Physics of Atomic Nuclei, Vol. 64, No. 9, 2001, pp. 1541–1548. Translated from Yadernaya Fizika, Vol. 64, No. 9, 2001, pp. 1619–1627.

NUCLEI
Experiment

Electrooptical Separation of Ca Isotopes for Nuclear-Physics Experiments

Sh. Sh. Nabiev*, L. P. Sukhanov, Yu. V. Gaponov, and L. V. Inzhechik**

Russian Research Centre Kurchatov Institute, pl. Kurchatova 1, Moscow, 123182 Russia

Received May 4, 2000

Abstract—The needs of experimental nuclear physics for the ^{48}Ca isotope for solving some fundamental problems are analyzed and justified. A new method is proposed for the separation of calcium isotopes. This method is based on the threshold dependence of the dipole moment of the CaF_2 molecule on the vibrational quantum number of large-amplitude motions. The conditions necessary for implementing the electrooptical method of isotope separation are formulated on the basis of examining a number of molecular systems. © *2001 MAIK "Nauka/Interperiodica".*

1. INTRODUCTION

At present, there is a constant need in experimental nuclear physics for the ^{48}Ca isotope. This nucleus, consisting of 20 protons and 28 neutrons, is likely to have the highest neutron excess among stable nuclei, which determines its features that are of importance for employing this nuclide in some fields of experimental nuclear physics.

Experimental investigation of the double-beta decay of nuclei is one of these fields. At present, these investigations pursue two basic objectives:

(i) measurement of the half-life for the standard two-neutrino ($2\beta2\nu$) mode of double-beta decay,

$$N(Z,A) \to N(Z+2,A) + 2e^- + 2\nu; \qquad (1)$$

(ii) searches for the exotic neutrinoless ($2\beta0\nu$) mode,

$$N(Z,A) \to N(Z+2,A) + 2e^-. \qquad (2)$$

The former process is observed and extensively studied in experiments. Measurement of the $2\beta2\nu$ half-life of nuclei is important for verifying the standard model of weak interaction. Moreover, relevant experimental data are necessary for improving methods for calculating nuclear matrix elements, since nuclear structure is substantial in theoretical calculations of the 2β decay. Because of the high neutron excess, the ^{48}Ca nucleus is characterized by a relatively high probability of $2\beta2\nu$ decay. However, theoretical estimates of the decay half-life $T_{1/2}(2\beta2\nu)$ yield very uncertain results from 10^{13} to 10^{18} yr [1]; therefore, new reliable experimental data would make it possible to obtain deeper insights into the phenomenon under investigation.

The second process, $2\beta0\nu$ decay, is forbidden in the standard theory of weak interaction and has not yet been observed. At the same time, current theoretical concepts of the nature of weak interaction go beyond the standard model. In particular, there is the popular hypothesis that the neutrino is a Majorana particle with a nonzero mass. The Majorana hypothesis implies that the neutrino and the antineutrino are identical and that the lepton number is not conserved. This hypothesis allows the neutrinoless mode of double-beta decay. Observation of the $2\beta0\nu$ decay mode would be of fundamental importance for weak-interaction physics because this would be direct experimental evidence for the failure of the standard theoretical model of weak interaction. Observation of this decay mode or even a determination of an upper limit on the decay probability would very important at present for a comparison with neutrino-oscillation data obtained by the Kamiokande collaboration (Japan) in 1998 [2]. If these extremely intriguing experimental results are not an artifact, they can be attributed only to the existence of a neutrino rest mass, which also contradicts the standard model.

The neutron-rich ^{48}Ca nucleus is very interesting for experimental investigation of double-beta decay. Studying this process with $CaCO_3$ samples that had a total mass of 42.2 g and which were enriched in ^{48}Ca to 73% by the electromagnetic method at the Kurchatov Institute, Balysh *et al.* [3] obtained the value $T_{1/2}^{2\nu2\beta}(^{48}\mathrm{Ca}) = (4.3^{+2.4}_{-1.1}[\mathrm{stat.}] \pm 1.4[\mathrm{syst.}]) \times 10^{19}$ yr for the two-neutrino process. For the ^{48}Ca nucleus, the ordinary beta-decay mode is also possible, but theoretical calculations predict that its probability

*e-mail: nabiev@imp.kiae.ru
**e-mail: inzhechik@imp.kiae.ru

is much lower than the double-decay probability. The current experimental constraint on $T_{1/2}^{0\nu 2\beta}$ for the neutrinoless process is $T_{1/2}^{0\nu 2\beta}(^{48}\mathrm{Ca} \to {}^{48}\mathrm{Ti}) > 9.5 \times 10^{21}$ yr [4].

To improve considerably experimental sensitivity and to obtain physically significant results on the neutrinoless mode of the 2β decay of the ^{48}Ca nucleus, it is necessary to have kilograms of this isotope with extremely low (10^{-12}–10^{-14} g/g) content of radioactive impurities. In addition, experimental investigation of the two-neutrino mode of the 2β decay in ^{48}Ca samples of a few kilograms would make it possible to reduce errors in measuring the probability of the process by one to two orders of magnitude and to refine the shape of the emitted-electron spectrum. This information would provide a quantitative test of the standard model of the 2β decay and would make it possible to estimate model parameters more accurately. More precise experimental data on 2β decay in ^{48}Ca would also be of use for developing methods for calculating its nuclear structure.

The accelerator physics of medium-mass and heavy nuclei is another experimental field where the use of the ^{48}Ca nucleus is of interest. In addition to ^{48}Ca beams, accelerated beams of ^{36}S, ^{58}Fe, ^{64}Ni, and other neutron-rich nuclei are used in accelerator experiments, but the ^{48}Ca nucleus is the most interesting and promising projectile at present. Having the highest neutron excess among stable nuclides, ^{48}Ca is used to bombard targets with the aim of synthesizing superheavy $Z > 110$ nuclei of the so-called stability island. Some nuclear-matter models predict that the decay period will increase at still greater values of Z, with the result that such superheavy nuclei become stable. For this reason, attempts at synthesizing superheavy nuclei are of substantial importance for verifying this prediction and for developing fundamental nuclear physics and its applications.

Such investigations are being extensively performed at JINR (Dubna) [5] and at GSI (Darmstadt) [6]. At the Laboratory of Nuclear Reactions, JINR, the team headed by Yu.Ts. Oganessian obtained $Z = 112$ nuclei with a half-life of about 100 s and $Z = 114$ nuclei through bombarding uranium and plutonium targets by accelerated ^{48}Ca nuclei [5, 7, 8],

$$^{48}\mathrm{Ca} + {}^{238}\mathrm{U} \to {}^{283}112 + 3n, \qquad (3)$$
$$^{48}\mathrm{Ca} + {}^{244}\mathrm{Pu} \to {}^{289}114 + 3n.$$

Active researches in this field are also performed at the Lawrence Berkeley National Laboratory by scientists from Berkeley and Oregon State University under the supervision of Ken Gregorich. They briefly reported that $Z = 118$ and 116 nuclei were synthesized through bombarding a ^{208}Pb target by ^{86}Kr ions accelerated to an energy of 449 MeV at an 88-inch cyclotron [9].

Thus, experimental data corroborate, at first glance, the existence of the stability island. These very interesting results will undoubtedly lead to the extension of studies devoted to synthesizing superheavy nuclei. Such experiments will obviously be developed at other research centers worldwide that employ beams of accelerated medium-mass ions.

Experimental data on unstable light and medium-mass nuclei with a high neutron excess are also of importance for developing nuclear physics. At present, such nuclei are obtained in the fragmentation of a stable neutron-rich projectile interacting with a target at rest. In these experiments, ^{48}Ca nuclei are also preferable for acceleration and further fragmentation. There is a program of systematic investigations along these lines that requires a regular use of ^{48}Ca nuclei.

Accelerated-beam substance is irreversibly consumed in experiments. Therefore, intensification of accelerator investigations with ^{48}Ca requires stable and even increasing amounts of this isotope. One might expect that the total need for ^{48}Ca at accelerator centers worldwide will attain 5–50 g/yr in the next 2–5 years. Note that the use of the ^{48}Ca isotope in experimental nuclear physics is restricted to a considerable extent by its high commercial cost. Therefore, development of cheaper and more efficient methods for separating Ca isotopes can contribute to considerable advances both in nuclear-physics techniques employing calcium and in fundamental physics.

At present, Ca isotopes are separated exclusively by the electromagnetic method, which is among the most power-consuming and low-output techniques used for the commercial production of isotopes. Searches for an alternative method of higher output therefore seem very promising. In this study, we examine the possibility of separating ^{48}Ca on the basis of the electrooptical method that was proposed previously for selecting nonrigid molecules [10–12].

2. BASIC PRINCIPLES OF THE ELECTROOPTICAL METHOD FOR SELECTING NONRIGID MOLECULES

Calcium ($Z = 20$, $A = 40$–48) is a typical element in the middle of the periodic system. Available methods for separating isotopes at the molecular level, including laser methods, are based on the selective multiphoton excitation and dissociation of molecules in infrared laser fields. Since calcium does not form volatile compounds, it is virtually impossible to apply

them to calcium. For this reason, calcium falls within the so-called dead zone of isotopes of some elements.

In [13, 14], a three-step selective photoionization of calcium atoms was implemented experimentally with aid of dye lasers. The first step in [13] was nonselective because the triplet metastable $4p$ state was excited by an electron impact and because the transition $4s4p\ ^3P_2 \to 4s5s\ ^3S_1$ was induced by 616.2-nm radiation. In contrast to [13], the intercombination $4s^2\ ^1S_0 \to 4s4p\ ^3P_1$ ($\lambda = 657.3$ nm) transition was selectively excited at the first stage in [14], and extra excitation occurred through the $4s4p\ ^3P_1 \to 4s5s\ ^3S_1$ ($\lambda = 612.2$ nm) transition. The full ionization of calcium atoms was achieved identically in [13, 14] by means of 488.0-nm argon-laser radiation. Although the authors of [13, 14] demonstrated that the separation of ^{48}Ca atoms is in principle possible, those studies were unfortunately not developed further.

In the past 10–15 years, a new class of nonrigid molecules whose individual atoms or fragments can move almost freely along some directions within distances commensurate with the dimensions of the molecular system, not causing its dissociation, has been revealed owing to application of precise experimental methods for studying molecular systems and to considerable advances in a computer simulation of such systems. These displacements, referred to as large-amplitude motions (LAMs), result in the anomalous behavior of the dipole moments of some nonrigid molecules. According to [15–17], the dipole moment μ of such molecules depends sharply on the vibrational quantum number n of LAMs, so that the difference of the dipole moments in the ground vibrational state [$\mu(n = 0)$] and in excited vibrational states [$\mu(n \neq 0)$] can be as large as about 10 D.

Electrooptical manifestations of large-amplitude motions can be used in the new molecule-selection method that was proposed in [10–12] and which makes it possible to obtain the isotopes of almost all elements of the periodic table, including those from the dead zone, through selecting nonrigid molecules in infrared-laser and nonuniform electric fields. This removes the existing limitation of molecular isotope-separation methods that is due to the incompatibility of the volatility of the objects to be separated with the productivity and the degree of enrichment.

The basic principles of the electrooptical selection method for nonrigid molecular systems become the clearest when they are considered for L[MX_{k+1}] molecules, where L is an alkali-metal atom; M is an element of the IIA, IIIA, or VA groups of the periodic system; X = H, F, O; and $k = 2, 3$. Figure 1 shows the layout of a setup for laser separation of isotopes entering into the composition of L[MX_{k+1}] molecules.

A crucible containing inorganic L[MX_{k+1}] salts that include ^{a}Z and ^{b}Z isotopes in natural amounts is heated to a temperature of $T \sim 1000$ K, at which the vapor over the molten salts is dominated by monomeric nonrigid molecules of the same composition. A nonrigid-molecule beam emitted from the crucible to a vacuum chamber is exposed to infrared laser radiation, which selectively excites molecules containing the ^{a}Z isotopes to the upper vibrational state with a small dipole moment $\mu(n \neq 0) \ll 10$ D. Molecules containing the ^{b}Z isotopes remain in the ground vibrational state with a large dipole moment $\mu(n = 0) \sim 10$ D. When occurring in the 20-cm-long region of a nonuniform electric field of gradient $\nabla E = 5$ CGS units, the nonrigid-molecule beam is separated in space, within the lifetime of the vibrational excitation, into two isotopic components, which are transversally spaced $\Delta S \sim 1$ cm apart at a molecule mass of $M \sim 10^{-22}$ g and a beam speed of $V \sim 10^4$ cm/s:

$$\Delta S = [\mu(n = 0) - \mu(n \neq 0)]\nabla E[l^2/(2MV^2)]. \quad (4)$$

As a result, an acceptable spatial separation of the ^{a}Z and ^{b}Z isotopes is achieved even at weak fields ($E \leqslant 10^3$ V/cm).

The electrooptical method [10–12] for selecting nonrigid molecules makes it possible to reduce the electric field by a factor of about 10^4 in relation to that in the previously available method [18, 19], where rigid symmetric AB_4 molecules of the spherical-rotor type that have T_d symmetry and which do not have a dipole moment in the ground vibrational state acquire it through the excitation of degenerate vibrations in a strong electrostatic field. A vibrationally excited spherical rotor develops a constant dipole moment of about 0.1 D owing to the presence of a mechanical and an electrooptical molecular anharmonicity. Since this method requires creating sufficiently strong (up to 10^7 V/cm) electric fields E, its applications are seriously restricted in practice [18, 19].

Although a nonrigid structure is known to be inherent in a fairly wide range of molecular systems, the electrooptical method [10–12] is applicable to only a relatively small number of compounds, because such compounds must simultaneously satisfy the following basic criteria [20]:

(i) They must be light, since the spatial separation of two isotopic components is inversely proportional to the molecular mass ($\Delta S \sim 1/M$).

(ii) Among similar melt–vapor systems, the partial pressure of the nonrigid-molecule vapor over molten salts of the same composition must be high at comparatively low vapor temperature.

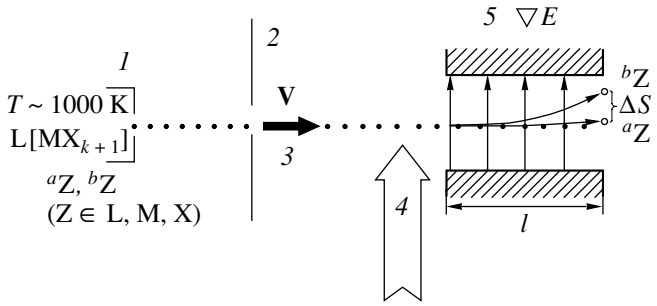

Fig. 1. Layout of a setup for laser separation of isotopes entering into the composition of nonrigid molecules: (*1*) crucible containing inorganic L[MX$_{k+1}$] salts that include ^{a}Z and ^{b}Z isotopes, (*2*) vacuum chamber, (*3*) nonrigid-molecule beam, (*4*) infrared laser, and (*5*) region of a nonuniform electric field whose gradient is ∇E.

(3) The dipole moment $\mu(n)$ of a specific nonrigid molecule must sharply depend on the vibrational quantum number n of the large-amplitude motions.

(4) A transition of a nonrigid molecule to an excited vibrational state characterized by a small dipole moment must be available.

(5) The time and isotope shift must be sufficient for selection of nonrigid molecules in a molecular beam.

The spectroscopic and electrooptical features of L[MX$_3$] molecules that were most comprehensively studied in [15–17] among nonrigid molecules are listed in Table 1. For these molecules, Fig. 2 shows the characteristic dependences of the dipole moment $\mu(n)$ on the vibrational quantum number n of large-amplitude motions that are actually the internal rotations of the cation L$^+$ about the anion [MX$_3$]$^-$.

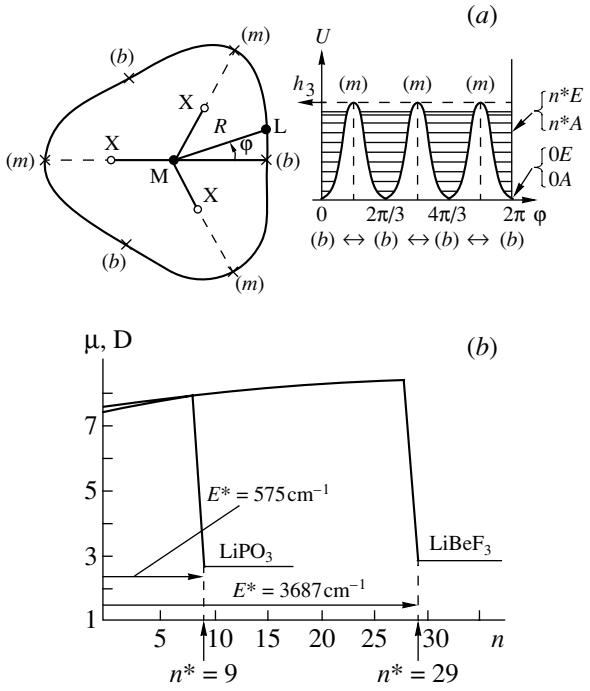

Fig. 2. (*a*) Internal rotations of the cation L$^+$ about the anion [MX$_3$]$^-$ in the plane of the complex L[MX$_3$] molecule and potential-energy curve along these rotations; (*b*) dipole moment $\mu(n)$ of the L[MX$_3$] molecule as a function of the vibrational quantum number n of internal rotations.

According to the data in Table 1 and in Fig. 2, the $LiPO_3$ molecule, which was studied in a number of experiments, is a nonrigid molecule optimally satisfying the basic criteria of applicability of the electrooptical isotope-separation method. Through one of the rigid modes, this molecule can undergo a transition to an excited vibrational state with a small dipole moment of $\mu(n^* = 9) = 2.7$ D (see, for example, [21]). The corresponding threshold energy $E^* = 575$ cm^{-1} is attainable for available laser sources, and the lifetime of the necessary vibrational excitation is about 3 s.

Because of extremely low volatility, L[MH$_3$] hydrides are unsuitable for the separation of the constituent isotopes. In all probability, this is one of the reasons why there are no experimental data on the gaseous phase of these compounds. Moreover, the data in Table 1 indicate that the threshold energies E^* for the L[MH$_3$] hydrides fall within the region that is virtually inaccessible to a vibrational excitation of a molecule with a small dipole moment. For the same reason, L[MF$_3$] fluorides show little promise for isotope separation by the electrooptical method. Substitution of heavier elements for L and M from the corresponding subgroups of the periodic system increases not only the molecular mass but also the threshold energy E^* (the case of L = K is no exception here).

It is obvious that optimal objects for isotope separation by the electrooptical method [10–12] can be sought not only among L[MX$_3$] molecules but also among other types of nonrigid molecules. The nonrigid CaF_2 molecule provides an illustrative example where the electrooptical method can be used to separate ^{48}Ca.

Table 1. Spectroscopic and electrooptical parameters of internal rotations in L[MX_3] molecules

Molecule	h_3, kcal/mole	B, cm^{-1}	τ	n^*	$\mu(n=0)$, D	$\mu(n^*)$, D	E^*, cm^{-1}	t, s
$LiBeF_3$	13.7	0.501	4774.9	29	7.7	2.8	3687	$7\times10^{-3} \ll t < 0.2$
$NaBeF_3$	14.3	0.229	10951.9	>29	>7.7		>3687	
$LiMgF_3$	22.7	0.364	10918.8	>29	7.3		>3687	
$LiPO_3$	3.2	0.485	1153.8	9	7.6	2.7	575	$0.1 \ll t < 2.7$
$LiBeH_3$	20.4	3.154	1131.1	10	7.1	2.5	4068	$5\times10^{-4} \ll t < 1\times10^{-2}$
$NaBeH_3$	15.1	2.868	920.7	8	9.4	3.2	2699	$1\times10^{-3} \ll t < 1\times10^{-2}$

Note: Here, h_3 is the height of the potential barrier separating the b and m molecular configurations (see Fig. 2a); B is the effective constant of intermolecular rotations; $\tau = h_3/2B$; n^* is that vibrational quantum number of internal rotations at which the dipole moment of the molecule sharply changes (see Fig. 2b); μ is the dipole moment of the molecule; E^* is the threshold energy corresponding to n^* (see Fig. 2b); and t is the time over which molecules in the molecular beam are separated by a nonuniform electric field (see Fig. 1).

Table 2. Basic physicochemical parameters of fluorite [22, 23]

Parameter	Value
Abundance [%]:	
$^{40}CaF_2$	96.94
$^{42}CaF_2$	0.65
$^{43}CaF_2$	0.13
$^{44}CaF_2$	2.09
$^{46}CaF_2$	3×10^{-3}
$^{48}CaF_2$	0.19
Density [g/cm^3]	3.181
Formation heat, ΔH_{298} [kJ/mole]	−1221
Melting point, T_{melt} [K]	1691
Melting heat, ΔH_{melt} [kJ/mole]	29.7
Boiling point, T_{boil} [K]	2803
Boiling heat, ΔH_{boil} [kJ/mole]	305
Energy of bond break $CaF_2 \rightarrow CaF + F$ [kJ/mole]	585
Angle between bonds F–Ca–F [deg]	142 ± 2
Spacing between nuclei Ca–F [nm]	0.210
Pressure of CaF_2 monomers over the melt at $T \cong 1700$ K [mm Hg]	$\cong 0.8$

3. SELECTION OF NONRIGID CaF_2 MOLECULES

For separating ^{48}Ca, we took fluorite (CaF_2), whose basic physicochemical parameters are presented in Table 2. This choice was motivated by the following reasons. Fluorite, which is sometimes referred to as fluorspar, is abundant in nature. In contrast to atomic calcium, which is characterized by a high chemical activity, CaF_2 is inert even in the presence of chemically aggressive compounds; in addition, a large formation heat (see Table 2) makes fluorite highly resistant to reducing agents (primarily, to molten metals) even at high temperatures [24]. In contrast to the majority of three-atom metal halides of the $XHal_2$ type, where X is an alkaline-earth metal and Hal = F, Cl, Br, I, which have a linear structure of $D_{\infty h}$ symmetry, CaF_2 molecules have a bent configuration whose point symmetry is $C_{2\nu}$

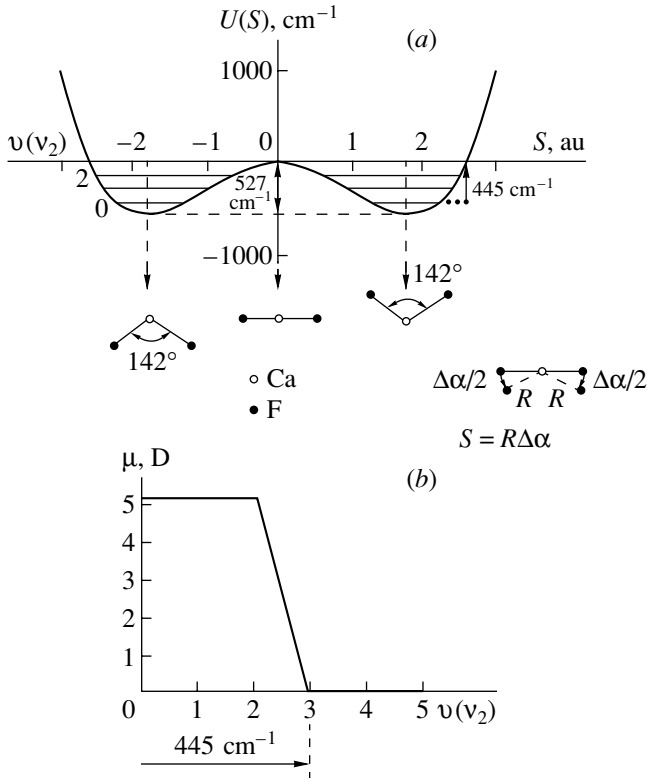

Fig. 3. (*a*) Potential-energy curve and energy levels of the large-amplitude motions in the CaF_2 molecule and (*b*) the dipole moment as a function of the vibrational quantum number $v(\nu_2)$ of large-amplitude motions.

[25]. The calcium fluoride molecule has three normal vibrations that are characterized by the symmetries

$$\Gamma_{\text{vib}} = 2A_1 + B_1 \qquad (5)$$

and which are manifested both in the infrared and in the Raman spectrum. Because of the physicochemical features of fluorite (see Table 2), the vibrational spectra of CaF_2 have been obtained to date only for molecules isolated in low-temperature noble-gas host surroundings [25–27]. The frequencies of all three vibrations of the $^{40}CaF_2$ and $^{44}CaF_2$ molecules are given in Table 3, along with the experimental values of the isotope shifts of these vibrations [25–27]. In addition, the lower part of Table 3 presents the frequencies ν_i and isotope shifts $\Delta\nu_i$ that we estimated for all three vibrational bands of the $^{48}CaF_2$ isotopic modification using data from [25–27].

In what is concerned with spectroscopic and electrooptical manifestations of nonrigid structure (the latter being, of course, of greatest importance for our purposes), the CaF_2 molecule is unique in some respect. The point is that, in contrast to some nonrigid molecules examined in [15–17], a vibrational excitation of the CaF_2 molecule is accompanied by a very sharp transition from the bent configuration of $C_{2\nu}$ symmetry to a linear structure of $D_{\infty h}$ symmetry and, hence, by a complete disappearance of the dipole moment. This process is characterized by a low energy barrier, which was estimated at 527 cm^{-1} in [28] between CaF_2 structures of $C_{2\nu}$ and $D_{\infty h}$ symmetries. Owing to this, there can occur a multiphoton transition of the CaF_2 molecule, through one of the vibrational modes, to an excited vibrational state with zero dipole moment (see Fig. 3).

Because all three vibrations of the CaF_2 molecule can be involved in dipole transitions, an implementation of the $CaF_2(C_{2\nu}) \rightarrow CaF_2(D_{\infty h})$ structural transition through a multiphoton excitation of molecules in an infrared laser field requires choosing the wavelength of laser radiation in such a way that this radiation is in resonance with the corresponding vibrational transition. It is obvious that the nonrigid deformation mode $\nu_2(A_1)$ is preferable for a multiphoton excitation, since it is the mode that is predominantly responsible for the disappearance of the dipole moment of the CaF_2 molecule. However, the absence of laser sources with generation frequencies in the range 150–200 cm^{-1} and a comparatively small isotope shift $\Delta\nu_1^{40-48}$ (see Table 3) dash the hopes that could be associated with this mode. For excitation through the symmetric mode ν_1, which has the same symmetry A_1 as the deformation vibration ν_2, the problem of a small isotope shift $\Delta\nu_1^{40-48}$ (see Table 3) remains, even though lasers whose frequencies can be varied within the range 450–500 cm^{-1} are available. We deem that excitation through the antisymmetric mode ν_3 of B_1 symmetry is preferable in view of the existence of laser sources in the relevant frequency range and of a fairly large isotope shift.

The layout of a setup for laser-radiation-induced calcium-isotope separation based on the use of the anomalous dependence of the dipole moment of the CaF_2 nonrigid molecule on the vibrational quantum number of large-amplitude motions can be similar to that in Fig. 1.

The crucible or Knudsen cell containing natural fluorite is heated to a temperature of about 1700 K, at which the vapor phase is dominated by monomeric CaF_2 molecules. The beam of CaF_2 molecules emitted from the cell to a vacuum chamber is exposed to selective infrared laser radiation whose frequency coincides with the frequency of the ν_3 mode of the $^{48}CaF_2$ isotope. Radiation of the required wavelength can be obtained from lasers that are excited via resonance optical pumping and which are characterized by an energy in a pulse of duration about 100 ns not less than 10 mJ (this can be, for example, C_2D_2 or NOCl lasers radiating in the frequency range 510–580 cm^{-1}). Under the effect of this radiation, the

Table 3. Vibrational frequencies and isotope shifts of bands in the infrared spectrum of the mixture $^{40}CaF_2$: $^{44}CaF_2 = 1:1$ in the argon host surrounding at a temperature of $T = 10$ K

Molecule and its isotope shift	$\nu_1(A_1)$, cm^{-1}	$\nu_2(A_1)$, cm^{-1}	$\nu_3(\beta_1)$, cm^{-1}
$^{40}CaF_2$	487.5	163.4	559.8
$^{44}CaF_2$	485.4	161.2	548.0
$\Delta\nu_i^{40-44}$	2.1	2.2	11.6
$^{48}CaF_2$	483.3	159.0	536.2
$\Delta\nu_i^{40-48}$	4.2	4.4	23.6

dipole moment of $^{48}CaF_2$ molecules vanishes completely. At the same time, molecules containing other calcium isotopes remain in the ground vibrational state and have a nonzero dipole moment. Unfortunately, the experimental value of the dipole moment of the CaF_2 molecule is not known. The quantum-chemical calculations performed in [28] revealed that the dipole moment of the CaF_2 molecule is quite large (about 5 D). In the 35-cm-long region of a nonuniform electric field of gradient about 50 CGS units, the molecular beam moving at a speed of $V \cong 345$ m s^{-1} is spatially separated predominantly into two components spaced $\Delta S \cong 1$ cm apart [28]. As a result, the spatial separation of the beam components that is necessary for collecting $^{48}CaF_2$ molecules is achieved at relatively weak fields ($E \approx 15 \times 10^3$ V/cm).

There are some open problems, including that of the relaxation deexcitation of thermally populated vibrational levels of the CaF_2 molecule and that of the contribution of "hot" bands to the excitation formation of the spectrum. However, estimations performed with allowance for the above electric fields, the pressure of CaF_2 vapor over molten fluorite at a temperature of 1700 K (see Table 2), and relatively weak laser fields demonstrate that the desired $^{48}CaF_2$ isotope, whose content in the natural mixture is 0.19%, can efficiently be separated and collected at a rate of about 5–10 mg/h, which is more than one order of magnitude higher than the rate achieved with a medium-power electromagnetic separator at the total ion current of up to 15 mA [29].

4. CONCLUSION

The method proposed here for separating Ca isotopes is based on the threshold dependence of the dipole moment of the CaF_2 molecule on the vibrational quantum number of large-amplitude motions. The structure of the energy levels of the CaF_2 molecule and a fairly large isotope shift (23.6 cm^{-1}) of the antisymmetric valence vibration make it possible to employ infrared laser radiation to excite selectively the CaF_2 molecule to a state where its dipole moment is zero (that is, to overcome the energy barrier separating the molecular structures of $C_{2\nu}$ and $D_{\infty h}$ point symmetries). Experience gained in studying the separation of molecular beams gives every reason to hope that the principle described above will be implemented as an efficient and relatively economical procedure for separating calcium isotopes.

Development of this proposal seems topical because, as was indicated above, many lines of current experimental investigations in nuclear physics require the ^{48}Ca isotope in amounts of a few kilograms (from time to time) and a few grams (regularly). Moreover, it can be assumed that the reduction of the cost of the isotope will give further impetus to relevant nuclear-physics investigations, with the result that more of it will be needed. Taking into account the uniquely high neutron excess in the ^{48}Ca nucleus, we can conclude that, for many nuclear experiments, there is no alternative to this nuclide.

REFERENCES

1. K. Grotz and H. V. Klapdor, *Die Schwache Wechselwirkung in Kern-, Teilchen- und Astrophysik* (Teubner, Stuttgart, 1989; Mir, Moscow, 1992).
2. Takaaki Kajita (for the SuperKamiokande and Kamiokande Collabs.), in *Proceedings of the 18th International Conference on Neutrino Physics and Astrophysics "NEUTRINO-98," Takayama, Japan, 1998*.
3. A. Balysh *et al.,* Phys. Rev. Lett. **77**, 5186 (1996).
4. Ke You *et al.,* Phys. Lett. B **265**, 53 (1991).
5. Yu. Ts. Oganessian *et al.,* Preprint No. E7-98-212, OIYaI (Joint Inst. for Nuclear Research, Dubna, 1998).
6. S. Hofmann, V. Ninov, F. P. Heβberger, *et al.,* Z. Phys. A **354**, 229 (1996).
7. Yu. Ts. Oganessian *et al.,* Preprint No. E7-99-53, OIYaI (Joint Inst. for Nuclear Research, Dubna, 1999); CERN Courier, Article No. 18 (1999).
8. Yu. Ts. Oganessian *et al.,* Yad. Fiz. **63**, 1979 (2000) [Phys. At. Nucl. **63**, 1315 (2000)].
9. http://user88.lbl.gov/element 118.html; submitted to Phys. Rev. Lett.
10. L. P. Sukhanov and A. I. Boldyrev, USSR Inventor's Certificate No. 1620120 (1990).
11. L. P. Sukhanov and Sh. Sh. Nabiev, *Proceedings of the 2nd All-Russia Scientific Conference "Physicochemical Processes Accompanying the Selection of Atoms and Molecules," Zvenigorod, 1997* (TsNIIAtominform, Moscow, 1998), p. 39.

12. L. P. Sukhanov and Sh. Sh. Nabiev, *Proceedings of the 3rd All-Russia Scientific Conference "Physicochemical Processes Accompanying the Selection of Atoms and Molecules," Zvenigorod, 1998* (TsNIIAtominform, Moscow, 1998), p. 154.
13. U. Brinkman, W. Hartig, H. Telle, *et al.,* Appl. Phys. **5**, 109 (1974).
14. A. P. Babichev, É. B. Gel'man, I. S. Grigor'ev, *et al.,* Kvantovaya Élektron. (Moscow) **15**, 860 (1988).
15. A. V. Romanets and L. P. Sukhanov, in *Proceedings of the 12th Symposium and School on High-Resolution Molecular Spectroscopy, St. Petersburg, 1996,* Proc. SPIE **3090**, 98 (1997).
16. A. V. Romanets and L. P. Sukhanov, Zh. Fiz. Khim. **71**, 839 (1997).
17. Sh. Sh. Nabiev and L. P. Sukhanov, Izv. Akad. Nauk, Ser. Khim., No. 8, 1415 (1999).
18. S. S. Alimpiev, N. V. Karlov, A. M. Prokhorov, *et al.,* Pis'ma Zh. Éksp. Teor. Fiz. **21**, 257 (1975) [JETP Lett. **21**, 117 (1975)].
19. N. V. Karlov and A. M. Prokhorov, Usp. Fiz. Nauk **118**, 583 (1976) [Sov. Phys. Usp. **19**, 285 (1976)].
20. Sh. Sh. Nabiev and L. P. Sukhanov, in *Collection of Presented at the MEPI Scientific Session* (Mosk. Inzh.-Fiz. Inst., Moscow, 1999), Vol. 5, p. 130.
21. F. Ramondo, L. Bencivenni, R. Caminiti, *et al.,* J. Chem. Phys. **145**, 27 (1990).
22. A. A. Radtsig and B. M. Smirnov, *Reference Data on Atoms, Molecules, and Ions* (Atomizdat, Moscow, 1980; Springer-Verlag, Berlin, 1985).
23. A. I. Efimov, L. P. Belorukova, L. V. Vasil'kova, *et al., Properties of Inorganic Compounds* (Khimiya, Leningrad, 1983).
24. F. A. Cotton, and G. Wilkinson, *Advanced Inorganic Chemistry* (Wiley, New York, 1980, 4th ed.).
25. Sh. Sh. Nabiev, Preprint No. 5310/12, IAÉ (Inst. of Atomic Energy, Moscow, 1991).
26. G. V. Calder, D. E. Mann, K. S. Seshardi, *et al.,* J. Chem. Phys. **51**, 2093 (1969).
27. F. Ramondo, V. Rossi, and L. Bencivenni, Mol. Phys. **64**, 514 (1988).
28. Sh. Sh. Nabiev, L. P. Sukhanov, Yu. V. Gaponov, *et al.,* in *Proceedings of 3rd All-Russia Scientific Conference "Physicochemical Processes Accompanying the Selection of Atoms and Molecules," Zvenigorod, 1998* (TsNIIatominform, Moscow, 1998), p. 159.
29. V. G. Bondarenko and R. N. Kuz'min, in *Isotopes: Properties, Production and Application,* Ed. by V. Yu. Baranov (IzdAT, Moscow, 2000), Part 6.1, p. 227.

Translated by R. Tyapaev

Physics of Atomic Nuclei, Vol. 64, No. 9, 2001, pp. 1549–1563. From Yadernaya Fizika, Vol. 64, No. 9, 2001, pp. 1628–1642.

NUCLEI
Experiment

Multifragmentation of Gold Nuclei by Light Relativistic Ions: Thermal Breakup versus Dynamical Disintegration*

S. P. Avdeyev, V. A. Karnaukhov, L. A. Petrov, V. K. Rodionov, V. D. Toneev, H. Oeschler[1)], O. V. Bochkarev[2)], L. V. Chulkov[2)], E. A. Kuzmin[2)], A. Budzanowski[3)], W. Karcz[3)], M. Janicki[3)], E. Norbeck[4)], A. S. Botvina[5)], W. A. Friedman[6)], K. K. Gudima[7)], and P. A. Rukoyatkin

Joint Institute for Nuclear Research, Dubna, Moscow oblast, 141980 Russia

Received July 17, 2000; in final form, October 11, 2000

Abstract—The multiple emission of intermediate-mass fragments (IMF) is studied for collisions of p, ^{4}He, and ^{12}C on Au with the 4π FASA setup. The mean multiplicities of IMF saturate at a value of around 2 for incident energies above 6 GeV. An attempt at describing the observed IMF multiplicities in the two-stage scenario, a fast cascade followed by a statistical multifragmentation, fails. Agreement with the measured IMF multiplicities is obtained by introducing an intermediate expansion phase and modifying empirically the excitation energies and masses of remnants. The angular distributions and energy spectra from p-induced collisions are in agreement with the scenario of "thermal" multifragmentation of a hot and expanded target spectator. In the case of ^{12}C + Au (22.4 GeV) and ^{4}He (14.6 GeV) + Au collisions, deviations from a pure thermal breakup are seen in the fragment energy spectra, which are harder than those both from model calculations and from the measured ones for p-induced collisions. This difference is attributed to a collective flow with the expansion velocity at the surface of about $0.1c$ (for ^{12}C + Au collisions). © *2001 MAIK "Nauka/Interperiodica"*.

1. INTRODUCTION

Nuclear fragmentation was discovered in cosmic rays 60 years ago [1, 2] as a puzzling phenomenon in which nuclear fragments are emitted from collisions of relativistic protons with various targets. The observed fragments were heavier than α particles but lighter than fission fragments. Now, they are commonly called intermediate-mass fragments (IMF), $3 \leq Z \leq 20$. Later on, in the 1950s, this phenomenon was first observed in accelerator experiments [3] and then studied leisurely for three decades. The situation changed dramatically after 1982, when the multiple emission of IMF was discovered in the ^{12}C (1030 MeV) irradiation of emulsion at the CERN synchrocyclotron [4]. These findings stimulated the development of many theoretical models to put forward an attractive idea that copious production of IMF may be related to a liquid–gas phase transition in nuclear matter [5–8]. A recent survey of multifragmentation can be found in [9].

About a dozen sophisticated experimental devices were created to investigate this process by using heavy ion beams, which are well suited for producing extremely hot systems. But in the case of heavy projectiles, nuclear heating is accompanied by compression, fast rotation, and shape distortion which may cause dynamical effects in the multifragment disintegration, and it is not easy to disentangle all these effects and extract information on the thermodynamic properties of hot nuclear systems. The situation becomes more transparent if light relativistic projectiles are used. In this case, dynamical effects are expected to be negligible. Another advantage is that all the fragments are emitted by a single source: a slowly moving target remainder. Its excitation energy might be almost entirely thermal. Light relativistic projectiles therefore provide a unique possibility of studying thermal multifragmentation.

*This article was submitted by the authors in English.

[1)]Institut für Kernphysik, Technische Universität Darmstadt, 64289 Darmstadt, Germany.

[2)]Russian Research Centre Kurchatov Institute, pl. Kurchatova 1, Moscow, 123182 Russia.

[3)]Niewodniczanski Institute of Nuclear Physics, PL-31-342 Cracow, Poland.

[4)]University of Iowa, Iowa City, IA 52242, USA.

[5)]Istituto Nazionale di Fisica Nucleare, Sezione di Bologna and Dipartimento di Fisica, Università di Bologna, Viale C. Berti Pichat, n. 6/2, I-40127 Bologna, Italy.

[6)]Physics Department, University of Wisconsin, Madison, WI 53706, USA.

[7)]Institute of Applied Physics, Chisinau, Moldova.

The time scale of IMF emission is a crucial question for understanding this decay mode: Is it a "slow" sequential process of independent emission of IMF, or is it a new (multibody) decay mode with "simultaneous" ejection of fragments governed by the total accessible phase space? Only the latter process is usually called multifragmentation. Simultaneous emission means that all fragments are liberated within a time smaller than the characteristic time of $\tau_c \approx 10^{-21}$ s [10], which is the mean time for the Coulomb acceleration of fragments. Within this time, IMF emission is not independent, but IMF interact via Coulomb forces and are accelerated after freeze-out in a common electric field. Measurement of the emission time $\tau_{\rm em}$ for IMF (i.e., the mean time between two successive events of fragment emission) is a direct way to answer the question about the nature of the multifragmentation phenomenon. An analysis of the IMF–IMF correlation function with respect to the relative velocity and also with respect to the relative angle involves two procedures for extracting information about the emission time.

By now, it has been shown that thermal multifragmentation does indeed occur in collisions of light relativistic projectiles (p, $\bar{p}$, ^{3}He, ^{4}He, π^-) with a heavy target and that fragments are emitted from an expanded, excited residue driven, after an expansion, by the thermal pressure [11–16]. Deduced from IMF–IMF correlation data, the fragment emission time is less than 100 fm/c. This value is considerably smaller than the characteristic Coulomb time. Thus, the trivial mechanism of multiple IMF emission (independent fragment evaporation) is excluded [17–19].

In this paper, we present results of the experimental study of the multifragment emission induced by relativistic helium and carbon ions and compare them with our data [13] obtained for p + Au collisions. The measured fragment multiplicities, energy, charge, and angular distributions are analyzed within the combined approach: cascade model followed by the statistical multifragmentation model (SMM). Emphasis is put on the question of thermalization and on a study of a transition from a pure statistical process to a behavior showing dynamical effects.

2. DESCRIPTION OF THE EXPERIMENT

2.1. Experimental Setup

The experiments were performed with the beams from the JINR synchrophasotron in Dubna by using the modified [20] 4π FASA setup [21]. The device consists of two main parts: (i) five ΔE (ionization chambers) $\times$ E (Si) telescopes (they are located at $\theta = 24°$, 68°, 87°, 112°, and 156° with respect to the beam direction and together cover a solid angle of 0.03 sr), which serve as a trigger for the readout of the system allowing measurement of the charge and energy distributions of IMF at different angles; (ii) a fragment multiplicity detector (FMD) consisting of 64 CsI(Tl) counters (with thicknesses around 35 mg/cm^2), which covers 89% of 4π. The FMD gives the number of IMF in an event and their spatial distribution. Thin polycrystalline CsI(Tl) films are prepared by thermal vacuum evaporation onto 2-mm Plexiglass backings, which are shaped as hexagons or pentagons. The light is transported onto photomultipliers of the FEU-110 type by hollow metal tubes using diffuse reflection. Using such lightguides instead of solid ones made from Plexiglass significantly reduces the background caused by beam halo (up to a level of a few percent). The background was continuously controlled by means of a double-gate mode in processing the photomultiplier pulses. The scintillator faces were covered with aluminized Mylar (0.2 mg/cm^2) to exclude light cross talk.

A self-supporting Au target 1.5 mg/cm^2 was located at the center of the FASA vacuum chamber (about 1 m in diameter). The following beams are used: protons at energies of 2.16, 3.6, and 8.1 GeV; ^{4}He at energies of 4 and 14.6 GeV; and ^{12}C at 22.4 GeV. The average beam intensity was 7×10^8 p/spill for protons and helium and 1×10^8 p/spill for carbon projectiles with a spill length of 300 ms and a spill period of 10 s.

2.2. Analysis of Fragment Multiplicities

By using the FMD array, the associated IMF multiplicity distribution $W_A(M_A)$ is measured in events triggered by a fragment in at least one of the telescopes. The triggering probability is proportional to the multiplicity M of an event (primary IMF multiplicity). Hence, the contribution of events with higher multiplicities in $W_A(M_A)$ is enhanced. This is a reason why $W_A(M_A)$ should differ from the primary multiplicity distribution $W(M)$. Another reason is that the FMD efficiency is less than 100% and depends on the detection threshold of scintillator counters being adjusted in such a way as to reduce the admixture of $Z \leq 2$ particles in the counting rate of IMF up to the level not exceeding 5%. These distributions are mutually related via the FASA response matrix $Q(M_A, M)$:

$$W_A(M_A) = \sum_{M=M_A+1} Q(M_A, M) W(M). \quad (1)$$

The response matrix includes the triggering probability, which is proportional to M, and the probability of detecting (in the FMD) M_A fragments among the

remaining $M-1$ fragments. The latter probability is described by the binomial distribution, and one gets

$$Q(M_A, M) = \frac{M!}{M_A!(M-1-M_A)!}\,\varepsilon^{M_A}\,(1-\varepsilon)^{M-1-M_A}, \quad (2)$$

where ε is the detection efficiency.

The FMD efficiency ε was calibrated as described in [20, 21]. We have the possibility of controlling its value experimentally using IMF coincidences in the trigger telescopes. From Eqs. (1) and (2), one finds that $\langle M_A\rangle$ and the moments of the primary multiplicity distribution are related by the equation

$$\frac{\langle M_A\rangle}{\varepsilon} = \frac{\langle M^2\rangle}{\langle M\rangle} - 1. \quad (3)$$

This expression gives the mean IMF multiplicity (without one) for events selected by the trigger.

The right-hand side of this equation can also be obtained from the coincidence rate n_{12} for IMF in the triggering telescopes:

$$\frac{n_{12}}{n_1 p_2} = \frac{\langle M^2\rangle}{\langle M\rangle} - 1. \quad (4)$$

Here, n_1 is the counting rate in telescope 1, and p_2 is the detection probability for a coincident fragment in telescope 2.

The value of p_2 is largely determined by the efficiency of the second telescope, ε_2, but it also depends on its position (θ_2) and the relative angle θ_{12}: $p_2 = \varepsilon_2\, f(\theta_1)\, g(\theta_{12})$. These last corrections are found from the measured angular distributions and relative angle correlations. Combining Eqs. (3) and (4), one gets the following relation for the FMD efficiency:

$$\varepsilon = \langle M_A\rangle / \frac{n_{12}}{n_1 p_2}. \quad (5)$$

There are two options for obtaining the primary multiplicity distribution $W(M)$ from the measured one $W_A(M_A)$. The first is to parametrize the distribution $W(M)$, to fold it with the experimental filter according to Eq. (1), and then to find the parameters of the parametrization by fitting the result to the experimental distribution. This was done under the assumption that $W(M)$ is shaped like the Fermi function, as motivated by calculations within the statistical multifragmentation model (see below).

The second option is the direct reconstruction of $W(M)$ by using the inverse matrix $Q^{-1}(M, M_A)$:

$$W(M) = \sum_{M_A=0}^{M-1} Q^{-1}(M, M_A)\, W_A(M_A). \quad (6)$$

Both procedures yield similar results. In Fig. 1, the multiplicity distributions obtained for the gold-target fragmentation by 14.6-GeV alphas and 22.4-GeV carbon ions are compared with those for p(8.1 GeV) + Au collisions. In these cases, the mean values $\langle M\rangle$ are always about 2.1–2.2 (see table), being close to that obtained by the ISIS group for ^{3}He + Au collisions at 4.8 GeV [22]. These values correspond to events with at least one IMF emitted. In this definition, M is never less than unity. The mean multiplicity for all inelastic events is smaller by the factor $[1-P(0)]$, where $P(0)$ is the probability of having no IMF in a collision event.

The mean values of the IMF multiplicity can also be obtained from the counting rates of coincidences for telescopes by using the relation between $(\langle M^2\rangle/\langle M\rangle - 1)$ and $\langle M\rangle$ [23]. It was calculated for systems at different excitation energies by the statistical multifragmentation model (SMM; see below), which faithfully reproduces the IMF-multiplicity distributions, as is seen in Fig. 1.

3. MODEL CALCULATIONS

The reaction mechanism for light relativistic projectiles is usually divided into two steps. The first one consists of a fast energy-deposition stage, within which very energetic light particles are emitted and a nuclear remnant (spectator) is excited. The second one is the decay of the target spectator. The fast stage is usually described in terms of a kinetic approach. We use a refined version of the intranuclear-cascade model [24] to get the distributions of nuclear remnants in charge, mass, and excitation energy. The second stage can be described by multifragmentation models. The SMM [25] and the expanding emitting source (EES) model [26] are employed here. It will be discussed below whether the assumption of thermoequilibrium behavior is justified.

3.1. Refined Cascade Model

The refined cascade (RC) model is a version of the quark–gluon string model developed in [27] and extended to intermediate energies in [28]. This is a microscopic model that is based on a relativistic Boltzmann-type transport equations and the string phenomenology of hadronic interactions. Baryons and mesons belonging to the lowest two $SU(3)$ multiplets, along with their antiparticles, are included. The interactions between the hadrons are described by a collision term, where the Pauli exclusion principle is applied to the final states. This includes elastic collisions, as well as hadron production and resonance decay processes. The formation time $\tau_f = 1$ fm/c for product particles is incorporated. At moderate energies in the limit $\tau_f \to 0$, this treatment reduces to the conventional cascade model [24].

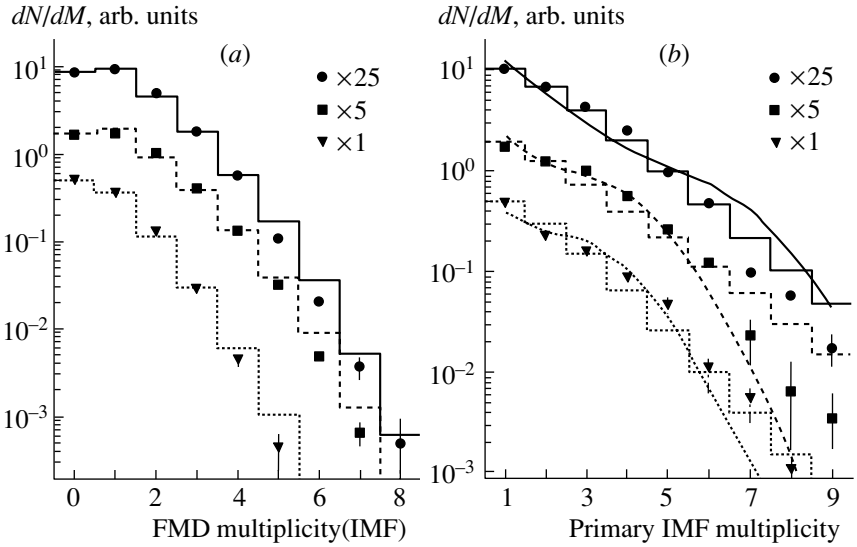

Fig. 1. (*a*) Measured IMF-multiplicity distributions (symbols) and fits with a Fermi function (folded with the experimental filter, histograms) associated with a trigger fragment for p + Au collisions at 8.1 GeV (circles, solid histogram), ^{4}He + Au at 14.6 GeV (squares, dashed histogram), and ^{12}C + Au at 22.4 GeV (triangles, dotted histogram). (*b*) Reconstructed primary IMF distributions (symbols; the notation is identical to that in Fig. 1*a*) and the Fermi distributions used to fit the data in Fig. 1*a* (histograms). The smooth curves were calculated within the RC + α + SMM model (see main body of the text).

Mean-field dynamics is neglected in our consideration. However, we keep the nuclear scalar potential to be defined for the initial state in the local Thomas–Fermi approximation, changing in time only the potential depth according to the number of knocked-out nucleons. This "frozen mean-field" approximation allows us to take into account nuclear binding energies and the Pauli exclusion principle, as well as to estimate the excitation energy of the residual nucleus by counting excited particle–hole states. This approximation is good for hadron–nucleus or peripheral nucleus–nucleus collisions, where there is no large disturbance of the mean field, but it is questionable for violent central collisions of heavy ions. However, in central collisions, the fraction of spectator matter is small and the available phase space for baryons is enlarged, so that the role of nuclear binding and the Pauli effect can be expected to decrease.

It is traditionally assumed that, after the completion of the cascade stage, the excited residual nucleus is in an equilibrium state. In general, this is not evident. The RC model includes the possibility of describing the attainment of thermodynamical equilibrium in terms of the preequilibrium exciton (PE) model [24, 29, 30]. During this equilibration process, some preequilibrium particles may be emitted, which will lead to a change in the characteristics of thermalized residual nuclei.

Typical results for the distributions of residual masses A_R versus their excitation energies E_R in this model are shown in Fig. 2.

3.2. Statistical Multifragmentation Model

Within the SMM [25], the probability of equilibrium decay through a given channel is proportional to its statistical weight. The breakup volume determining the Coulomb energy of the system is a key parameter. It is taken to be $V_b = (1 + k)A/\rho_0$, where A is the mass number of the fragmenting nucleus, ρ_0 is the normal nuclear density, and k is a free parameter. In [12, 13, 18], it was shown that breakup occurs at low densities. To reach these density values, it is assumed that the system expands before breakup. Primary fragments may be excited, and their deexcitation is taken into account to get final IMF distributions. Figure 3 shows the IMF multiplicity as a function of the excitation energy calculated for $k = 2$ and $k = 5$, which corresponds to the freeze-out densities of about $1/3\,\rho_0$ and $1/6\,\rho_0$, respectively. The calculations have been performed with the RC + SMM combined approach for ^{4}He + Au collisions at 14.6 GeV. The fragment multiplicity increases with excitation energy up to a maximum and then decreases because of vaporization of the overheated system. This so-called "rise and fall" of multifragmentation is well visible in Fig. 3 and was first demonstrated experimentally by the ALADIN group for collisions of ^{197}Au at 600 MeV/nucleon with Al and Cu targets [31].

The choice of the breakup density has only a slight effect on $\langle M \rangle$. The kinetic energies of fragments are more affected because they are determined mainly

Calculated properties of nuclear remnants from projectile + Au collisions

E_{proj}, GeV	Projectile	Experiment	Calculations							Model
		M_{IMF}	M_{IMF}	Z_R	A_R	Z_{MF}	A_{MF}	E_R	E_{MF}	
2.16	p	1.7±0.2	1.82	77	189	76	185	310	589	RC + SMM
			1.02	72	176	62	145	119	266	RC + PE + SMM
			1.69	77	188	75	183	288	564	RC + α + SMM
3.6	p	1.9±0.2	2.52	76	187	74	181	371	676	RC + SMM
			1.34	70	171	55	134	148	385	RC + PE + SMM
			1.89	75	184	73	175	282	568	RC + α + SMM
8.1	p	2.1±0.2	3.58	75	183	73	175	488	808	RC + SMM
			1.85	68	167	53	128	177	462	RC + PE + SMM
			2.0	72	176	67	158	259	529	RC + α + SMM
4.0	^{4}He	1.7±0.2	3.89	75	184	73	177	484	836	RC + SMM
			1.56	68	167	54	130	176	428	RC + PE + SMM
			1.77	73	177	69	161	238	502	RC + α + SMM
14.6	^{4}He	2.2±0.2	4.47	71	173	66	159	723	1132	RC + SMM
			3.06	63	153	48	116	377	824	RC + PE + SMM
			2.19	64	154	48	103	183	404	RC + α + SMM
22.4	^{12}C	2.2±0.3	4.04	67	163	64	153	924	1216	RC + SMM
			2.85	60	146	47	113	638	1026	RC + PE + SMM
			2.17	59	139	41	86	207	415	RC + α + SMM

Note: The quantity M_{IMF} is the mean number of IMF for events with at least one IMF, while Z_R, A_R, and E_R are the mean charge, the mass number, and the excitation energy (in MeV), respectively, averaged over inelastic collisions, the analogous quantities Z_{MF}, A_{MF}, and E_{MF} being averaged only over residues decaying through IMF emission.

by the Coulomb field in the system, which depends noticeably on its size. The use of a larger value of the parameter ($k = 5$) results in the underestimation of the fragment kinetic energies in relation to the data from [32]. In further calculations, we use $k = 2$, based on our analysis of the correlation data [18].

All calculations are performed in an event-by-event mode.

4. RESULTS AND DISCUSSION

4.1. Fragment Multiplicity and Excitation Energy of the System

The mean IMF multiplicities, measured and calculated, are shown in Fig. 4 versus the total beam energy for various projectiles. The data exhibit a saturation in $\langle M \rangle$ for energies above a value of about 6 GeV, in good agreement with findings of [13, 33, 34]. This so-called limiting fragmentation may be caused by a saturation of the residual excitation energy, while the fragment multiplicity is strongly energy-dependent. Other possible reasons for the saturation effect are discussed in [33].

The dashed line in Fig. 4 was obtained by means of the combined RC + SMM approach. The calculated mean multiplicities are significantly higher than the measured ones, with the exception of those from the measurement at the lowest beam energy. This fact indicates that the model overestimates the residue excitation energy. May the emission of preequilibrium light particles be responsible for this discrepancy? The inclusion of preequilibrium emission after the cascade stage (RC + PE + SMM) leads to a significant decrease in the excitation energy of the fragmenting target spectator and reduces the mean IMF multiplicity (dotted line in Fig. 4). However, the reduction of the multiplicity proves to be overly large for $E_{\mathrm{proj}} < 8$ GeV, predicting $\langle M \rangle$ to be smaller than the measured ones. Although the calculated value of $\langle M \rangle$ for the p(8.1 GeV) + Au collisions coincides

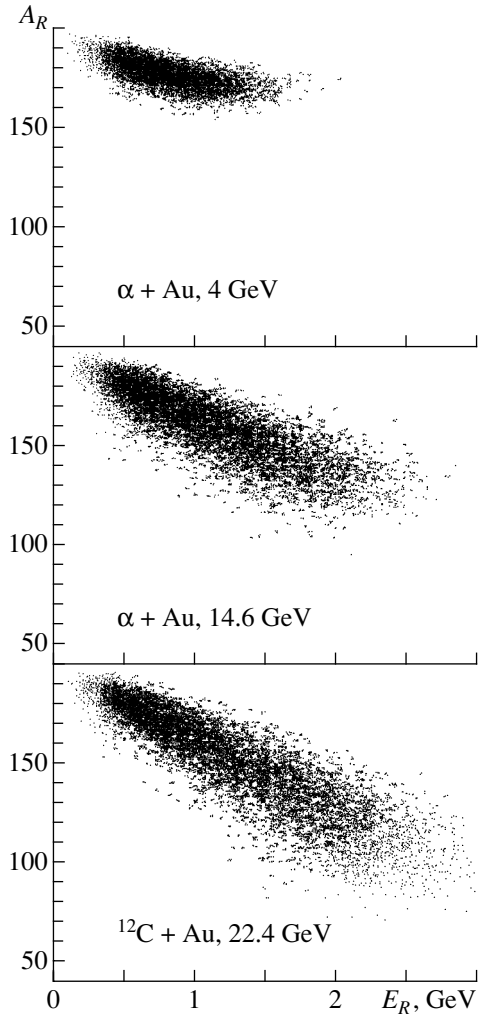

Fig. 2. Distribution of residual masses A_R versus excitation energies E_R after the cascade calculation for ^{4}He + Au at (top) 4 and (middle) 14.6 GeV and (bottom) ^{12}C + Au at 22.4 GeV.

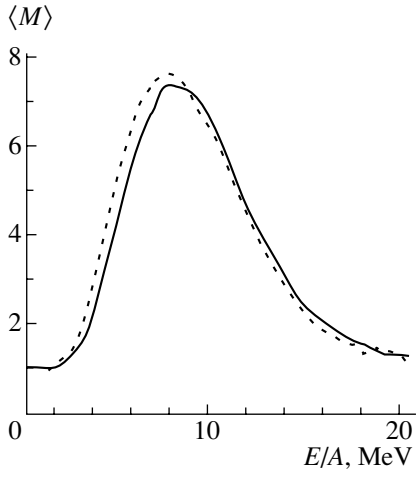

Fig. 3. Mean fragment multiplicities versus the thermal excitation energy according to SMM calculations for freeze-out densities of about (solid curve) $1/3\,\rho_0$ and (dashed curve) $1/6\,\rho_0$.

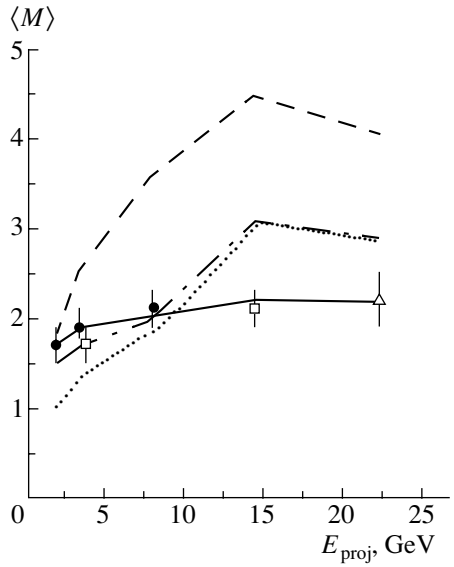

Fig. 4. Mean IMF multiplicities (for events with at least one IMF) versus the beam energy. The points represent experimental data. The dashed and dotted lines are drawn through the values calculated within the RC + SMM and within the RC + PE + SMM approach at the beam energies used. The solid and the dash-dotted lines were obtained by using the RC + α + SMM and the RC + EES approach, respectively. For the sake of simplicity, only one curve is drawn for a given model calculation neglecting the dependence on projectile mass.

with experimental data, the model predictions for the fragment kinetic energies within this approach are significantly lower than the experimental values, as was shown in [13]. Because the IMF energies are determined predominantly by the Coulomb field of the source, the RC + PE + SMM approach underestimates the charge Z of the target residue. In addition, at higher ^{4}He-beam energies, the decrease in the excitation energy after preequilibrium emission is not even sufficiently strong to get the observed fragment multiplicities. All these facts may suggest another possible mechanism for the energy loss before the IMF emission.

Calculations with the EES model [26] were performed by using the same characteristics of the RC remnants. As can be seen from Fig. 4, the values obtained for the mean fragment multiplicities are in accord with data for the beam energies below 10 GeV, but there is disagreement between the theory and experiment at higher energies.

We conclude that neither RC nor RC + PE is able to describe the properties of the target spectator over

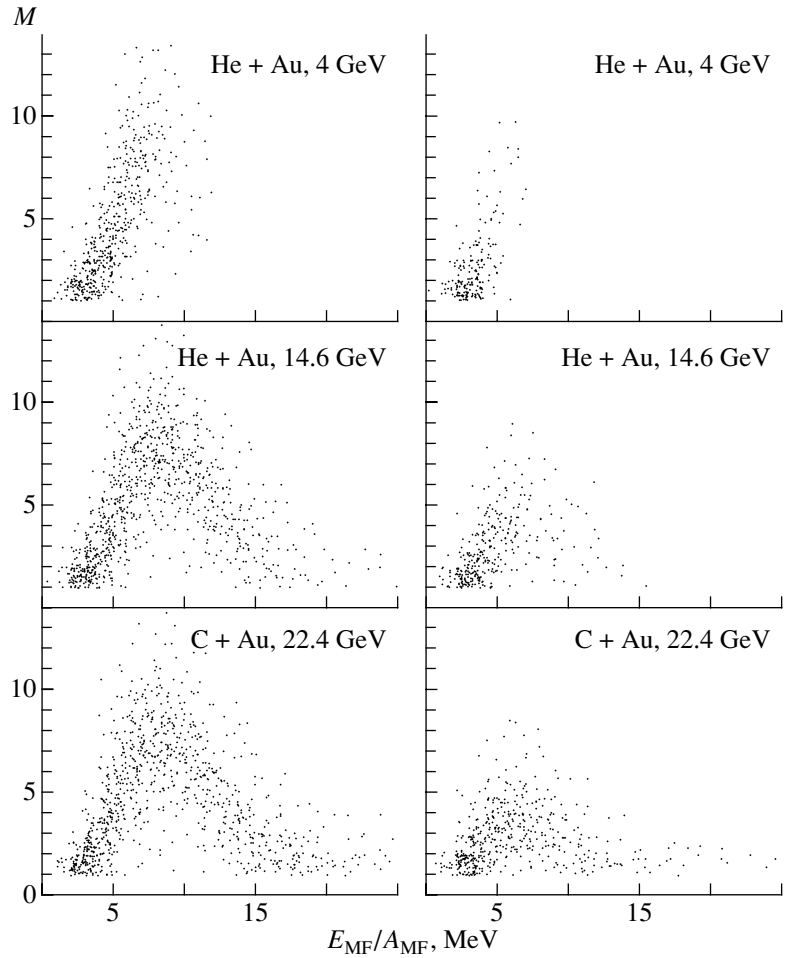

Fig. 5. Calculated event distribution in the $M-E_{MF}/A_{MF}$ plane: (left) RC + SMM approach and (right) RC + α + SMM approach for ^{4}He + Au (top) 4 GeV and (middle) 14.6 GeV and (bottom) ^{12}C + Au at 22.4 GeV.

a wide range of projectile energies. One should look for an alternative approach.

An example of an empirical approach to this problem was given by the authors of [35], who analyzed experimental data on multifragmentation in the reactions of ^{197}Au on C, Al, Cu, and Pb targets at $E/A = 600$ MeV. The parameterized relations (with seven parameters) were developed to get the mass and energy distributions of highly excited thermalized nuclear systems formed as the spectator parts of colliding nuclei. This distribution was used as an input for SMM calculations, and the parameters were adjusted to fit experimental results on the multiplicity distributions of IMF and their yield. It should be emphasized that the suggested parameterization is specific to the reaction under consideration.

In our approach, we start from the results of the cascade calculation and modify them empirically. In [36], the excitation energies of the cascade remnants were reduced by a factor α (see below) on an event-by-event basis, with the mass being unchanged. This was motivated by the guess that the frozen-mean-field approximation in the cascade calculation may result in an overestimation of the high-energy tail of the distribution. The mean IMF multiplicities obtained by this procedure are in accord with data for p + Au collisions in the projectile-energy range 2–8 GeV.

At the next step of our analysis of the same reactions [13], the drop in the excitation energy is accompanied by a mass loss. This combination holds both for preequilibrium emission in the spirit of the exciton model [30] and for particle evaporation during the expansion, as considered by the EES model [26].

In the present study, we follow the last approach. The excitation energies E_R^{RC} of the residual nuclei A_R given by the RC code are reduced by a fitting factor α to get the excitation energy of a multifragmenting state, E_{MF}; i.e., $E_{\mathrm{MF}} = \alpha E_R^{\mathrm{RC}}$. In other words, the drop in the excitation energy is equal to $\Delta E = (1-\alpha)E_R^{\mathrm{RC}}$. As is known from the cascade calculations, E_R^{RC} is proportional to the nucleon loss

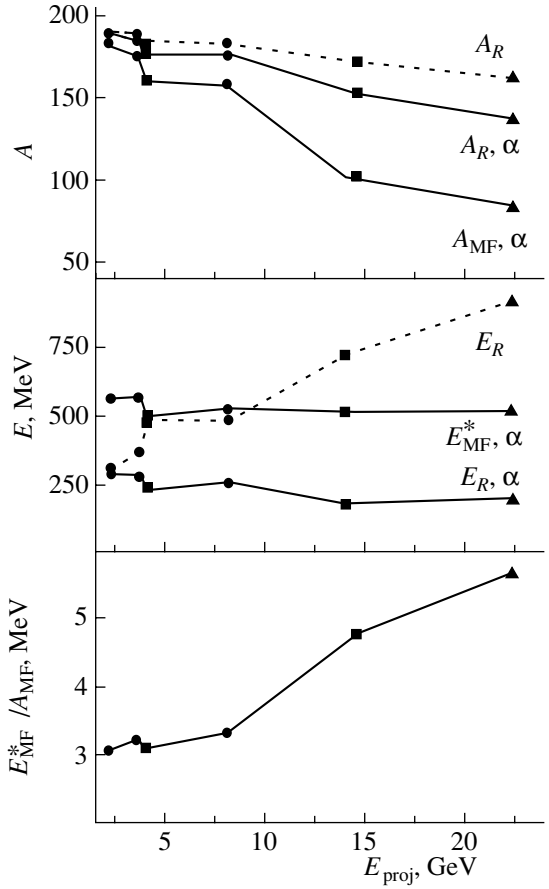

Fig. 6. Mean values of the remnant excitation energies and mass numbers according to the table: E_R and A_R are for averaging over all inelastic collisions, while $E_{\rm MF}$ and $A_{\rm MF}$ are for fragmenting residues. The calculations within the RC + α + SMM approach are labeled with "α." Points present data for (circles) proton, (squares) helium, and (triangles) carbon beams.

during the cascade, $\Delta A^{\rm RC}$; therefore, $\Delta E = (1-\alpha)\varepsilon_1 \Delta A^{\rm RC}$, where ε_1 is the mean excitation energy per ejected cascade nucleon. The loss of mass, ΔA, corresponding to this drop in the excitation energy is $\Delta A = \Delta E/\varepsilon_2$, where ε_2 is the mean energy removed by a nucleon. Assuming that $\varepsilon_2 \approx \varepsilon_1$, one gets $\Delta A = (1-\alpha)\Delta A^{\rm RC}$. We denote this empirical combined model as RC + α + SMM.

In [13], the simple relation

$$\alpha = \frac{\langle M_{\rm exp}\rangle}{\langle M_{\rm RC+SMM}\rangle}$$

could be applied for p + Au collisions because the excitation-energy range corresponded to the rising part of the energy dependence of $\langle M\rangle$ shown in Fig. 3. However, due to the rise-and-fall effect in $\langle M\rangle$, this relation fails for heavier projectiles. For these systems, the values of α are empirically adjusted to reproduce the measured mean IMF multiplicities. The charge, mass, and energy characteristics of fragmenting nuclei resulting from this fitting procedure are presented in the table for various colliding systems. The corresponding values for the p + Au case differ slightly from those given in [13] because a new cascade code is used here. The values of the parameter α can be found in the table by calculating the ratio E_R(RC + α + SMM)/E_R(RC + SMM), which gives 0.93, 0.76, and 0.53 (for p + Au); 0.49 and 0.25 (for He + Au); and 0.22 (for C + Au), respectively.

As follows from the above values of the parameter α, a rather large decrease in the residual excitation energy is required by this empirical procedure to reproduce the observed saturation effect in $\langle M\rangle$, which is caused mainly by a saturation in $E_{\rm MF}$. This is illustrated in Fig. 5, which shows the population of events in the M–$E_{\rm MF}/A_{\rm MF}$ plane calculated in both the RC + SMM (left panel) and the RC + α + SMM (right panel) scenario. According to the first approach, the excitation-energy distribution is rather wide and populates states along both the rising and the falling parts of the multiplicity curve. In the RC + α + SMM scenario, events are mainly situated in the rising part, hardly approaching the region of maximal values of the IMF multiplicity, which is in agreement with the measured data.

Note that the excitation energies of fragmenting nuclei given in the table are thermal by definition. As will be shown in Subsection 4.3 for both C(22.4 GeV) + Au and He(14.6 GeV) + Au collisions, the systems at breakup also have a collective expansion energy, which is estimated to be about 100–130 MeV for both cases. The total excitation energy $E^*_{\rm MF}$ for these cases is in fact larger by that value than the values shown in the table. This is taken into account in Fig. 6, which presents the calculated values of the mean residual excitation energies and mass numbers. The total excitation energy $E^*_{\rm MF}$ changes slightly with increasing incident energy. At the same time, the excitation energy per nucleon increases, while the residual mass decreases; the mean IMF multiplicity is almost constant.

It would be of interest to compare the extracted masses and excitation energies of fragmenting nuclei with those obtained by the EOS collaboration for Au(1 GeV/nucleon) + C collisions (in inverse kinematics) [37]. In that study, the mass- and energy-balance relations are applied with use of the measured kinetic energies of all outgoing charged particles after separation from the prompt stage of the reaction. The neutron contribution was taken into account on the basis of cascade and statistical model simulations. Our value of $E^*_{\rm MF}/A_{\rm MF}$ is close to that from [37] if the collective energy is added. As to the mean mass $A_{\rm MF}$, the value obtained in the present study (about 90) is

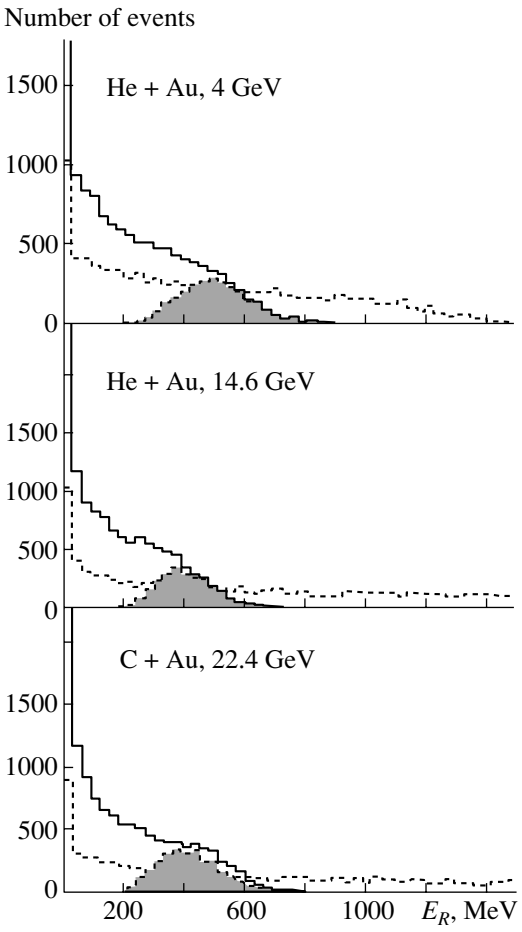

Fig. 7. Distribution of excitation energies obtained within (dashed histograms) the RC and (solid histograms) the RC + α approach and (hatched area) the fraction decaying by multifragmentation according to the RC + α + SMM calculation.

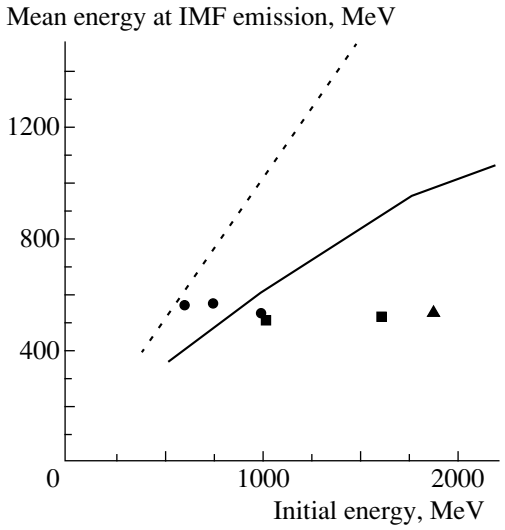

Fig. 8. The loss in the excitation energy during the expansion calculated by RC + EES model (solid line) is compared with the empirically deduced drop. The dashed line represents the initial energy (after RC stage). Points are data for proton (circles), helium (squares), and carbon (triangle) beams.

remarkably lower, being caused by the larger mass loss induced by the projectile with twice the energy.

Some examples of the excitation-energy distributions are displayed in Fig. 7. The IMF emission occurs on the tail of the distributions; therefore, the mean excitation of the fragmenting nuclei is much higher than that averaged over all target spectators.

In Fig. 8, the value obtained for the energy E^*_{MF} is confronted with the values predicted by the EES model [26]. The excitation energy after the cascade stage is taken as the initial one for the process of the energy (and mass) loss during the expansion of the system. Data for p + Au collisions are close to the predicted values if the excitation energy was corrected according to the above procedure, while, in all the cases of ^{4}He and ^{12}C beams, the EES model overestimates the excitation energy after expansion. This may be an indication of a possible contribution from an additional mechanism of the energy loss (e.g., preequilibrium emission).

4.2. Angular and Charge Distributions

Let us now consider the question of thermalization of the system at breakup. To check how close the emitting system is to thermal equilibrium, the plot of the fragment probability distribution in terms of the longitudinal–transverse velocity components is presented in Fig. 9 for ^{4}He + Au and C + Au collisions. The symbols correspond to constant invariant cross sections taken for emitted carbon fragments in the energy region above the spectral peak. The lines connecting experimental points form circles demonstrating an isotropic emission in the frame of a moving source, indicating that the fragment emission proceeds from a thermalized state. The center positions of the circles determine the source velocity, β_{source}. The mean values of β_{source} are in the range of (0.01–0.02)c, which is close to an estimate within the RC + α + SMM approach for all cases, with the exception of ^{4}He + Au at 4 GeV, where calculations underestimate the source velocity. The calculated mean β_{source} values are 0.76×10^{-2}, 1×10^{-2}, 1.36×10^{-2} and 1.7×10^{-2} for p(8.1 GeV) + Au, ^{4}He(4 GeV) + Au, ^{4}He(14.6 GeV) + Au, and C(22.4 GeV) + Au collisions, respectively. The accuracy of β_{source} determination is about 5%. The variation of β_{source} with the IMF velocity, β_{IMF}, is shown in Fig. 10.

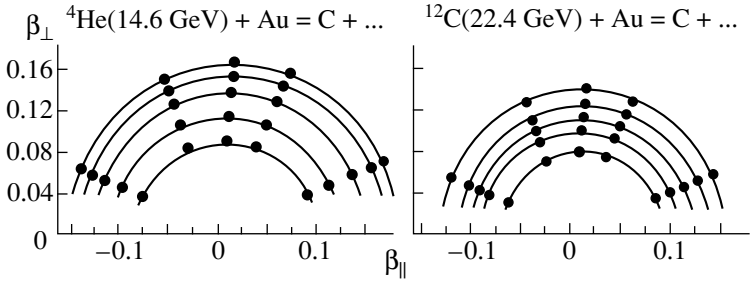

Fig. 9. Transverse versus longitudinal velocity plot for emitted carbon isotopes produced in ^{4}He (14.6 GeV) and ^{12}C (22.4 GeV) collisions with an Au target. Circles are drawn through points of equal invariant cross section corresponding to the isotropic emission of fragments in the moving-source frame.

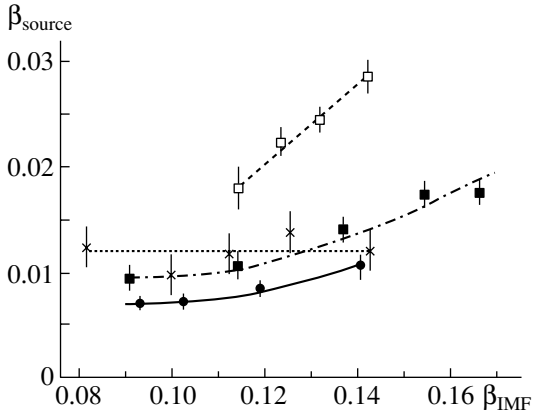

Fig. 10. Source velocities $\beta_{\rm source}$ versus the fragment velocity $\beta_{\rm IMF}$ for (closed circles) p(8.1 GeV) + Au, (closed squares) ^{4}He(14.6 GeV) + Au, (open squares) ^{4}He(4 GeV) + Au, and (crosses) ^{12}C(22.4 GeV) + Au collisions.

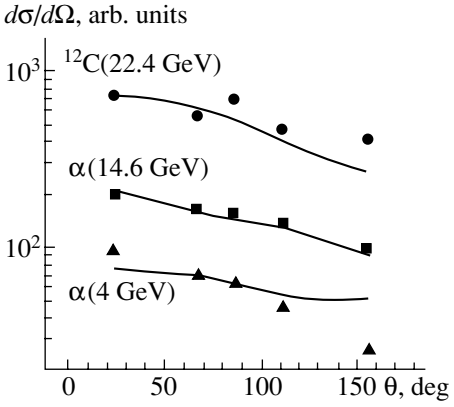

Fig. 11. Angular distributions of carbon (in laboratory frame) for ^{4}He + Au and ^{12}C + Au collisions. The curves were calculated by the RC + α + SMM approach.

The fragment angular distribution in the laboratory frame exhibits a forward peak caused by the source motion, as is shown in Fig. 11 for carbon fragments (points). The data are well reproduced by the model calculations for all cases, with the exception of the helium beam case at the lowest energy. The measured distribution here is more forward-peaked, which may be considered as an indication that the momentum transfer is larger than what is predicted.

The charge distributions of IMF are shown in Fig. 12. The results of the calculations for the RC + α + SMM scenario agree nicely with the data. The general trend of the IMF charge (or mass) distributions is well described by the power law $Y(Z) \sim Z^{-\tau}$. The values obtained for the exponent are $\tau = 1.9 \pm 0.1$, 2.0 ± 0.1 and 2.1 ± 0.1 for, respectively, a 4-GeV helium beam, a 14.6-GeV helium beam, and carbon projectiles (Fig. 12, right panel).

In earlier studies on multifragmentation [5, 38], the power-law behavior of the IMF yield was interpreted as an indication of the proximity of the decaying state to the critical point for a liquid–gas phase transition in nuclear matter. This was stimulated by the application of the classical Fisher's droplet model [39], which predicted a pure power-law droplet-size distribution with $\tau = 2$–3 at the critical point. According to [40], the fragmenting system is not very close to the critical point. Now, the power law is well explained at temperatures far below the critical point. As is seen from Fig. 12, the pure thermodynamical SMM predicts that the IMF charge distribution is very close to a power law at freeze-out temperatures of 5–6 MeV, while the critical temperature (i.e., where the surface tension vanishes) is $T_c = 18$ MeV. In [41], it was also shown that several results concerning the fragment size distribution can be rendered well by using the kinetic model of condensation beyond the vicinity of the liquid–gas critical point.

Thermal multifragmentation can be considered as a first-order phase transition of nuclear matter inside a spinodal region characterized by an instability of the liquid–gas phase. Indeed, it was proven experimentally that fragmentation occurs after expansion

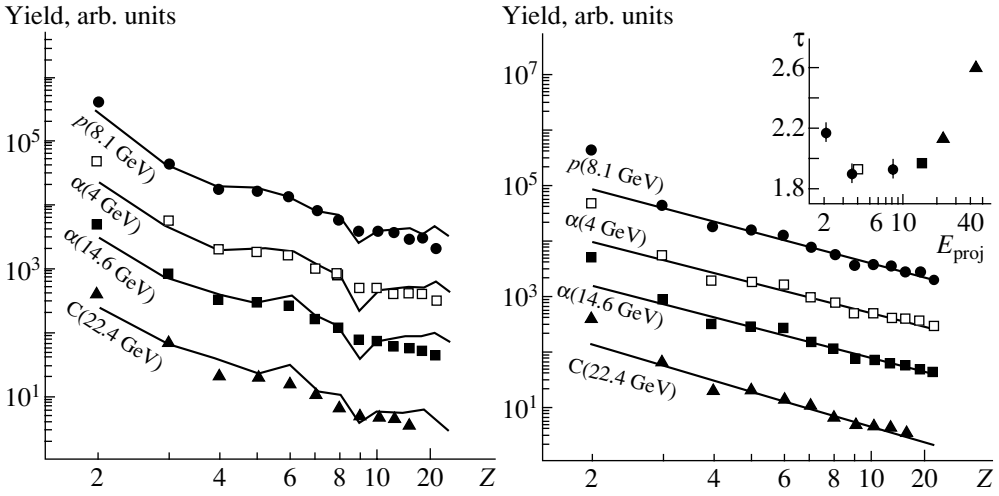

Fig. 12. Fragment charge distributions obtained at $\theta = 89^\circ$ for p + Au at 8.1 GeV, ^{4}He + Au at 4 GeV, ^{4}He + Au at 14.6 GeV, and ^{12}C + Au at 22.4 GeV. The curves (left side) were calculated within the RC + α + SMM approach (normalized at $Z = 3$). Power-law fits are shown in the right panel with τ parameters given in the inset as a function of the beam energy. The last point in the inset is for ^{12}C + Au collisions at 44 GeV (from a preliminary experiment).

driven by thermal pressure [12–14] and that the decomposition time is short (less than 100 fm/c) [17–19]. In fact, the final state of this transition looks like a nuclear fog [42]: liquid drops of IMF surrounded by a gas of nucleons and light clusters (d, t, and α particles). This interpretation is in line with the SMM [43]. Later, it was employed in other approaches (see, for example, [44]).

4.3. Energy Spectra of Fragments

In general, the kinetic energy of fragments is determined by four terms: thermal motion, Coulomb repulsion, rotation, and collective expansion energies of the system at freeze out: $E = E_{\rm th} + E_{\rm C} + E_{\rm rot} + E_{\rm flow}$. The additivity of the first three terms is quite obvious. For the last term, its independence from the others may be considered only approximately when the evolution of the system after freeze-out is driven only by the Coulomb force. The Coulomb term is significantly larger than the thermal one. It was shown in [18] that, for ^{4}He (14.6 GeV) + Au collisions, the Coulomb part of the mean energy of the carbon fragment is three times larger than the thermal energy. These calculations were performed within the RC + SMM scenario, where the volume emission of fragments from a dilute system was taken into consideration.

The contribution of a collective flow for p + Au collisions at an incident energy of 8.1 GeV was estimated in [13]. This was done by comparing the measured IMF spectra with those calculated within the SMM, which includes no flow. This analysis did not reveal any significant enhancement in the measured energy spectra, constraining the mean flow velocity as $v_{flow} < 0.02c$. For the case of heavy-ion collisions, a collective flow was observed, and it is the most pronounced in central Au + Au collisions [45]. In this respect, it would be quite interesting to analyze the fragment spectra from He + Au and C + Au collisions with reference to searches for a possible manifestation of collective flows. The carbon spectra for proton, helium, and carbon collisions with

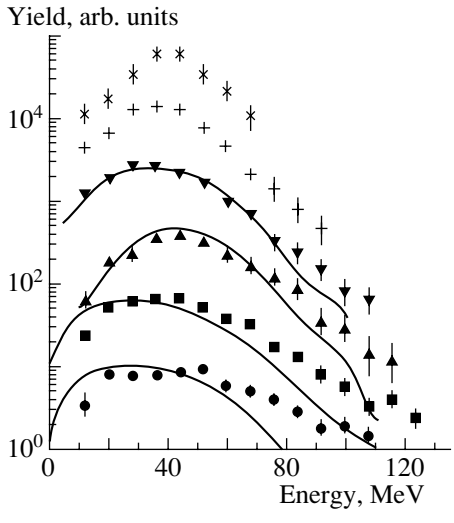

Fig. 13. Energy distribution of carbon isotopes obtained for various collision systems at $\theta = 89^\circ$. The curves were calculated within the RC + α + SMM scenario under the assumption of no flow. Stars, crosses, inverted triangles, triangles, squares, and circles correspond to p (2.1 GeV), p (3.6 GeV), p (8.1 GeV), ^{4}He (4 GeV), ^{4}He (14.6 GeV), and ^{12}C(22.4 GeV) projectiles, respectively.

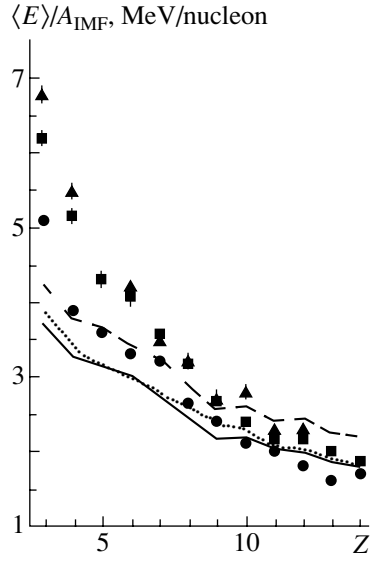

Fig. 14. Mean kinetic energies per nucleon of outgoing fragments measured at $\theta = 89°$ for (circles, dashed line) p (8.1 GeV), (squares, solid line) ^{4}He (14.6 GeV), and (triangles, dotted line) ^{12}C (22.4 GeV) collisions with Au. The lines were calculated by using the RC + α + SMM approach and assuming no flow.

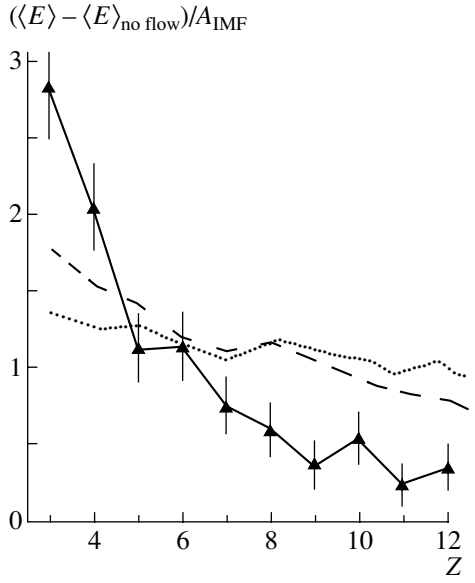

Fig. 15. Flow energy per nucleon (triangles) obtained as the difference of the measured fragment kinetic energies and the values calculated under assumption of no flow in the system for ^{12}C (22.4 GeV) + Au collisions. The curves represent calculations assuming a linear radial profile of the expansion velocity with $v^0_{\rm flow} = 0.1c$ (dotted line) and quadratic profile with $v^0_{\rm flow} = 0.2\,c$ (dashed line).

a Au target are presented in Fig. 13. The calculated carbon spectrum for p + Au collisions (at 8.1 GeV) is consistent with the measured one. A similar situation is observed for ^{4}He + Au collisions at 4 GeV, but not for ^{4}He(14.6 GeV) + Au and ^{12}C + Au interactions: the measured spectra are harder than the calculated ones.

The mean kinetic energies per fragment nucleon are displayed in Fig. 14, where only statistical errors are shown. There is a remarkable enhancement in the reduced kinetic energy for light fragments from He + Au and C + Au collisions in relation to the p(8.1 GeV) + Au case. The calculated values of the mean fragment energies (shown by lines) were obtained within the RC + α + SMM approach by many-body Coulomb trajectory calculations on an event-by-event basis. In the initial state, all charged particles are assumed to have only a thermal velocity. The measured energies are close to the calculated ones for p + Au collisions in the range of the fragment charges between 4 and 9. However, for ^{4}He + Au and ^{12}C + Au interactions, experimental data are definitely above the calculated values.

The observed deviation cannot be attributed to the effect of the angular momentum. To estimate the rotational part of energy, $E_{\rm rot}$, we consider the uniform classical rotation of the system with mass number A and total rotational energy E_L. The mean rotational energy of a fragment with mass $A_{\rm IMF}$ is

$$\langle E_{\rm rot}\rangle/A_{\rm IMF} = \frac{5}{3}\langle\frac{E_L}{A}\rangle\frac{\langle R_Z^2\rangle}{R_{\rm sys}^2}, \qquad (7)$$

where R_Z and $R_{\rm sys}$ are the radial coordinate of the fragment and the radius of the system, respectively. According to the RC calculations for C + Au collisions, the mean angular momentum of the target spectator is $L = 36\hbar$. It might be reduced by a factor of 1.5 due to the mass loss along the way to the freeze-out point. Finally, $\langle E_L\rangle$ is estimated to be only 5 MeV and $\langle E_{\rm rot}\rangle/A_{\rm IMF} \approx 0.04$ MeV/nucleon, which is an order of magnitude smaller than the energy enhancement for light fragments. We believe that this enhancement is caused by the expansion of the system, which is assumed to be radial, since the velocity plot (Fig. 9) does not show any significant deviation from circular symmetry.

An estimate of the fragment flow energy can be obtained as the difference of the measured IMF energies and those calculated without taking into account any flow in the system. This difference for C + Au collisions is shown in Fig. 15. The error bars include both statistical and systematic contributions. The latter one is associated with the calibration of the energy scale and is estimated at about 5%. In an attempt at describing the data, we replaced the SMM code by RC + α + SMM by including a radial velocity boost for each particle at freeze-out. In other words, a radial expansion velocity was superimposed

on thermal motion in the calculation of the many-body Coulomb trajectories. A self-similar radial expansion is assumed, where the local flow velocity is linearly dependent on the distance of the particle from the center of mass. The expansion velocity of particle Z located at radius R_Z is given by

$$\mathbf{v}_{\rm flow}(Z) = v^0_{\rm flow}\,\frac{\mathbf{R}_Z}{R_{\rm sys}}, \qquad (8)$$

where $v^0_{\rm flow}$ is the radial velocity at the surface of the system. In this case, the density distribution changes in the course of dynamical evolution in a self-similar way, being a function of the scaled radius $R_Z/R_{\rm sys}$. The use of a linear profile for the radial velocity is motivated by the hydrodynamic-model calculations for an expanding hot nuclear system (see, for example, [46]). The value of $v^0_{\rm flow}$ was adjusted to describe the mean kinetic energy measured for the carbon fragment. The results are also presented in Fig. 15 as the difference of the fragment energies calculated for $v^0_{\rm flow} = 0.1c$ and $v^0_{\rm flow} = 0$. The data deviate significantly from the calculated values for Li and Be. This may be caused in part by the contribution of particle emission, during the early stage of expansion, from a hotter and denser system. This is supported by the fact that the extra energy of Li fragments with respect to the calculated value is clearly seen in Fig. 14 even for proton-induced fragmentation, where no significant flow is expected. This feature of light fragments was noticed by the ISIS group for ^{3}He + Au collisions at 4.8 GeV [22].

As to fragments heavier than carbon, the calculated curve in Fig. 15 is above the data and only slightly decreases with increasing fragment charge. In general, such a behavior should be expected. The mean fragment flow energy is proportional to $\langle R_Z^2\rangle$. This quantity changes only slightly with fragment charge in the SMM code because of the assumed equal probability for fragments of a given charge to be formed at any point of the available breakup volume. This assumption is a consequence of the model simplification that considers the system to be uniform with $\rho(r) = \text{const}$ for $r \le R_{\rm sys}$. The discrepancy between the data and the calculations in Fig. 15 indicates that the density distribution is not uniform. The dense interior of the expanded nucleus favors the appearance of larger IMF if fragments are formed via density fluctuations. This observation is also in accord with the analysis of the mean IMF energies performed in [13, 38] for proton-induced fragmentation. It is also seen from Fig. 14 that, for p + Au collisions, the measured energies are below the theoretical line for fragments heavier than Ne. This may be explained by the preferential location of heavier fragments in the interior region of the freeze-out volume, where the Coulomb field is reduced. The deviation of data from the calculations becomes less, but it still remains if one assumes the quadratic radial profile of the expansion velocity. The result of such a calculation shown in Fig. 15 was obtained with $v^0_{\rm flow} = 0.2c$, which was chosen to be close to the data at $Z = 6$. An interesting feature of a reduced flow energy for heavier fragments is also observed for central heavy-ion collisions (see the review article [47]). This effect is increasingly important at energies $\le 100\,A$ MeV, and this is in accord with our suggestion on its relation to the density profile of the hot system at freeze-out.

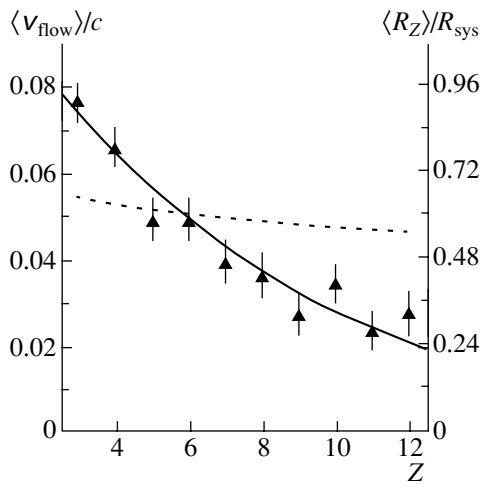

Fig. 16. Experimentally deduced mean flow velocities (triangles) for ^{12}C + Au collisions versus the fragment charge (left scale) and the mean relative radial coordinates of fragments (right scale) as obtained under the assumption of a linear radial profile for the expansion velocity. The dashed line shows the mean radial coordinates of fragments according to the SMM code.

The difference of the measured IMF energies and calculated ones (no flow) was used to estimate the mean flow velocities of fragments. The results are presented in Fig. 16. The values for Li and Be are considered as upper limits because of the possible contribution of preequilibrium emission. The corresponding values of $\langle R_Z\rangle/R_{\rm sys}$, obtained under the assumption of a linear radial profile for the expansion velocity, are plotted on the right-hand scale of the figure. Again, the reduced radius value for the carbon fragment is chosen to coincide with the calculated one. The dashed line shows the mean radial coordinates of fragments according to the SMM code. As was noted above, the calculated values of $\langle R_Z\rangle/R_{\rm sys}$ decrease only slightly with Z, in contrast to the data.

Effects of the radial collective energy for Au + C collisions at 1 GeV per nucleon (in inverse kinemat-

ics) were considered in [48] by analyzing the transverse kinetic energies K_t of fragments with $Z = 2$–7. This was done for two charged-particle-multiplicity bins corresponding to peripheral ($M1$) and central ($M3$) collisions. The Berlin statistical model code [49] was used with allowance for a radial velocity chosen properly to explain the experimental values of $\langle K_t \rangle$. In the case of peripheral collisions, the resulting expansion velocities are close to those given in Fig. 16, but the corresponding mean IMF multiplicities (in our definition) are less than 1.5. For central collisions ($\langle M_{\rm IMF} \rangle \simeq 4$), the expansion velocities are greater by a factor of about 1.5. It would be desirable to compare our data with those for the intermediate case (bin $M2$), which are unfortunately not available. Making an interpolation, one may see that our analysis gives slightly lower values of $v_{\rm flow}(Z)$ than those in [48]. This may be caused by the fact that the MMMC model [49] underestimates the Coulomb part of the fragment kinetic energy (see [32]), since the freeze-out density used is too small ($\rho_f = 1/6\rho_0$).

The total expansion energy can be estimated by integrating the nucleon flow energy [taken according to Eq. (8)] over the available volume at freeze-out. For a uniform system, one gets

$$E^{\rm tot}_{\rm flow} = \frac{3}{10} A\, m_N\, (v^0_{\rm flow})^2\, (1 - r_N/R_{\rm sys})^5, \qquad (9)$$

where m_N and r_N are the nucleon mass and radius. For ^{12}C + Au collisions, this yields $E^{\rm tot}_{\rm flow} \simeq 100$–$130$ MeV, which corresponds to a flow velocity at the surface of 0.1 c. Similar results are obtained for ^{4}He(14.6 GeV) + Au collisions.

5. CONCLUSION

The emission of intermediate mass fragments has been studied for p(2.1, 3.6, and 8.1 GeV) + Au, ^{4}He(4 and 14.6GeV) + Au, and ^{12}C(22.4 GeV) + Au interactions. The measured IMF multiplicities (for events involving at least one IMF) saturate at a value around 2 for incident energies above 6 GeV, irrespective of the projectile size. The angular distributions of IMF are slightly forward-peaked; the yield distributions of parallel versus perpendicular velocities exhibit circular symmetry. These results show that IMF are emitted from a source that moves with a rather low velocity (0.01–0.02) c. These findings support the interpretation of thermal multifragmentation, a breakup of an expanded system.

Model calculations for the IMF multiplicities using a two-stage concept with a cascade followed by the SMM fail to describe the measured values. This might originate partly from too high an excitation energy predicted by the cascade model used. Taking into account preequilibrium particle emission before attainment of thermal equilibrium in the system decreases the number of IMF but still cannot predict the observed multiplicity saturation. The employment of the EES model also fails to reproduce the measured multiplicities over the whole available energy range. Only if one applies an empirical modification of the calculated excitation energies E_R and residual masses A_R after the cascade used as input for the SMM calculations can the IMF multiplicity saturation effect be reproduced. This study shows that the widely used approach of dividing the nuclear multifragmentation process into two distinct stages is much oversimplified.

The energy spectra of IMF prove to be very sensitive observables. In p + Au collisions, the energy spectra are well described by the empirically modified cascade–SMM calculations. However, for ^{4}He- and ^{12}C-induced reactions, the number of higher energy IMF is larger than that which is given by the calculations. This effect is not caused by any variation of the residual masses. We attributed this observation to the occurrence of collective (expansion) flow in the system possibly caused by a higher thermal pressure. Under the assumption of a linear radial profile of flow velocity, its value at the surface is estimated at about 0.1c both for ^{4}He- and ^{12}C-induced reactions. However, a detailed inspection of the variation of the kinetic energies of fragments, together with their charges, reveals that the flow velocities are not constant. This is in contrast with expectations that assume equal probabilities for the formation of fragments of a given charge at any available point of the system with uniform density. The discrepancy between the extracted flow velocities and the simple assumption indicates that heavier fragments are formed predominantly in the interior of the system, possibly due to a density gradient.

This study of multifragmentation using a range of projectiles from protons to light nuclei seems to be quite attractive, furnishing new information on the various aspects of multifragmentation from a "thermal decay" to a disintegration governed by collision dynamics.

ACKNOWLEDGMENTS

We are grateful to Prof. A. Hrynkiewicz, Prof. A.M. Baldin, Prof. N.A. Russakovich, and Prof. S.T. Belyaev for support.

The work was supported in part by the Russian Foundation for Basic Research (project no. 00-02-16608), the Polish State Committee for Scientific Research (grant no. 2P0312615), the Collaborative Linkage (grant no. PST.CLG.976861), INTAS (grant no. 94-2249), Bundesministerium für Forschung und Technologie (contract no. 06DA453), and by the US National Science Foundation.

REFERENCES

1. E. Schopper, Naturwissenschaften **25**, 557 (1937).
2. I. I. Gurevich *et al.,* Dokl. Akad. Nauk SSSR **18**, 169 (1938).
3. O. V. Lozhkin and N. A. Perfilov, Zh. Éksp. Teor. Fiz. **31**, 913 (1956) [Sov. Phys. JETP **4**, 790 (1956)].
4. B. Jacobsson *et al.,* Z. Phys. A **307**, 293 (1982).
5. P. J. Siemens, Nature **305**, 410 (1983).
6. H. R. Jaqaman *et al.,* Phys. Rev. C **27**, 2782 (1983); **29**, 2067 (1984).
7. M. W. Curtin *et al.,* Phys. Lett. B **123B**, 289 (1983).
8. J. H. Rose *et al.,* Phys. Rev. Lett. **53**, 344 (1984).
9. "*Multifragmentation," Proceedings of International Workshop XXVII on Gross Properties of Nuclei and Nuclear Excitations, Hirschegg, Austria, 1999,* Ed. by H. Feldmeier, J. Knoll, W. Nörenberg, and J. Wambach (GSI, Darmstadt, 1999).
10. O. Shapiro and D. H. E. Gross, Nucl. Phys. A **573**, 143 (1994).
11. S. J. Yennello *et al.,* Phys. Rev. Lett. **67**, 671 (1991).
12. Bao-An Li, D. H. E. Gross, V. Lips, and H. Oeschler, Phys. Lett. B **335**, 1 (1994).
13. S. P. Avdeyev *et al.,* Eur. Phys. J. A **3**, 75 (1998).
14. K. Kwiatkowski *et al.,* Phys. Rev. Lett. **74**, 3756 (1995).
15. L. Beaulieu *et al.,* Phys. Lett. B **463**, 159 (1999).
16. T. Lefort *et al.,* nucl-ex/9910017.
17. V. Lips *et al.,* Phys. Lett. B **338**, 141 (1994).
18. S. Y. Shmakov *et al.,* Yad. Fiz. **58**, 1735 (1995) [Phys. At. Nucl. **58**, 1635 (1995)].
19. G. Wang *et al.,* Phys. Rev. C **53**, 1811 (1996); **57**, R2786 (1998).
20. S. P. Avdeyev *et al.,* Prib. Tekh. Éksp., No. 2, 7 (1996).
21. S. P. Avdeyev *et al.,* Nucl. Instrum. Methods Phys. Res. A **332**, 149 (1993).
22. E. R. Foxford *et al.,* Phys. Rev. C **54**, 749 (1996).
23. S. P. Avdeyev *et al.,* Preprint No. E1-2000-152, OIYaI (Joint Inst. for Nuclear Research, Dubna, 2000).
24. V. D. Toneev and K. K. Gudima, Nucl. Phys. A **400**, 173c (1983).
25. J. Bondorf *et al.,* Phys. Rep. **257**, 133 (1995); Nucl. Phys. A **444**, 476 (1985); A. S. Botvina, A. S. Iljinov, and I. N. Mishustin, Nucl. Phys. A **507**, 649 (1990); A. S. Botvina *et al.,* Yad. Fiz. **57**, 667 (1994) [Phys. At. Nucl. **57**, 628 (1994)].
26. W. A. Friedman, Phys. Rev. C **42**, 667 (1990).
27. V. D. Toneev *et al.,* Nucl. Phys. A **519**, 463c (1990).
28. N. S. Amelin *et al.,* Yad. Fiz. **52**, 272 (1990) [Sov. J. Nucl. Phys. **52**, 172 (1990)].
29. K. K. Gudima *et al.,* Yad. Fiz. **21**, 602 (1975) [Sov. J. Nucl. Phys. **21**, 138 (1975)].
30. M. Blann, Annu. Rev. Nucl. Sci. **25**, 123 (1975).
31. C. A. Ogilvie *et al.,* Phys. Rev. Lett. **67**, 1214 (1991).
32. H. Oeschler *et al.,* Part. Nucl. Lett., No. 2[99]-2000, 70 (2000).
33. K. B. Morlet *et al.,* Phys. Lett. B **355**, 52 (1995).
34. N. T. Porile *et al.,* Phys. Rev. C **39**, 1914 (1989).
35. A. S. Botvina *et al.,* Nucl. Phys. A **584**, 737 (1995).
36. S. P. Avdeyev *et al.,* JINR Rapid Commun., No. 2[82]-97, 71 (1997).
37. J. A. Hauger *et al.,* Phys. Rev. Lett. **77**, 235 (1996).
38. A. S. Hirsch *et al.,* Phys. Rev. C **29**, 508 (1984).
39. M. E. Fischer, Phys. (N.Y.) **3**, 255 (1967).
40. V. A. Karnaukhov, Yad. Fiz. **60**, 1780 (1997) [Phys. At. Nucl. **60**, 1625 (1997)].
41. J. Schmelzer, G. Ropke, and F.-P. Ludwig, Phys. Rev. C **55**, 1917 (1997).
42. P. J. Siemens, Nucl. Phys. A **428**, 189c (1984).
43. I. N. Mishustin, Nucl. Phys. A **447**, 67c (1985).
44. A. Guarnera *et al.,* Preprint GANIL, No. P-95-05 (1995).
45. W. Reisdorf *et al.,* Nucl. Phys. A **612**, 493 (1997); G. D. Kunde *et al.,* Phys. Rev. Lett. **74**, 38 (1995).
46. J. P. Bondorf *et al.,* Nucl. Phys. A **296**, 320 (1978).
47. W. Reisdorf and H. G. Ritter, Annu. Rev. Nucl. Part. Sci. **47**, 663 (1997).
48. J. Lauret *et al.,* Phys. Rev. C **57**, R1051 (1998).
49. D. H. E. Gross, Rep. Prog. Phys. **53**, 605 (1990).

Physics of Atomic Nuclei, Vol. 64, No. 9, 2001, pp. 1564–1580. Translated from Yadernaya Fizika, Vol. 64, No. 9, 2001, pp. 1643–1659.

NUCLEI
Theory

Emission Properties of Fission Fragments and Their Isomeric Ratios

O. T. Grudzevich

Institute of Atomic Power Engineering, Obninsk, Kaluga oblast, 249020 Russia

Received February 7, 2000; in final form, May 25, 2000

Abstract—The properties of neutron emission from fragments formed in the spontaneous fission of ^{252}Cf and in the thermal-neutron-induced fission of ^{235}U are analyzed on the basis of the statistical model of nuclear reactions. Upon extracting the mean excitation energies of fission fragments from experimental data on the mean multiplicities of neutrons, the observables of neutron emission can be described over wide ranges of total kinetic energies and masses. The observed values of mean fragment spins are also reproduced. A method for calculating the isomeric ratios of the independent yields of fission fragments that is based on the cascade–evaporation model of excited-nucleus decay is employed to describe experimental data on ^{235}U fission induced by thermal neutrons and on ^{238}U fission induced by alpha particles. The effect exerted on the isomeric ratios for fission fragments by two different assumptions on the spin distributions of primary-fragment populations—the assumption of the distribution associated with rotational degrees of freedom and the assumption of the distribution associated with the internal degrees of freedom of fully accelerated fragments—is investigated. © *2001 MAIK "Nauka/Interperiodica".*

INTRODUCTION

Since the fission of nuclei is accompanied by a radical redistribution of the nuclear charge and mass and by the formation of severely deformed and highly excited fragments, theoretical analysis of the process involves formidable difficulties. For this reason, a detailed description of its dynamics and mechanism has not yet been developed. As an advancement toward creating a unified theory of the fission process, it would therefore be reasonable, in describing specific features of fission, to invoke consistent theoretical models that were successfully employed to study the properties of different reactions.

In the present article, the formation of fission fragments prior to neutron emission and the deexcitation of these fragments via neutron and photon emission are chosen as the subject of investigation. It seems obvious that the deexcitation of fission fragments must be of a statistical character, because the fission process itself proceeds through the stage of a compound nucleus. Hence, the application of the statistical model of nuclear reactions [1–3] is quite a logical, albeit rather complicated (from the practical point of view), step.

The observables of the deexcitation of excited fragments are averaged over many variables, including charges, masses, excitations, kinetic energies, and total angular momenta. This is precisely the reason why it is difficult to describe theoretically these features—the calculations should involve a great number of parameters. That nuclei appearing as fission products are usually formed only in the fission process, with the result that their properties are poorly known, further aggravates the situation.

In order to successfully apply the statistical model of nuclear reactions to describing the properties of fission fragments, it is necessary to answer one question of fundamental importance—specifically, it is necessary to establish the character of the excitation-energy and the angular-momentum distribution of fission fragments. Knowing these distributions and sidestepping difficulties associated with uncertainties in the parameters of neutron-rich nuclei, one can compute almost any observable of fission-fragment deexcitation, including the neutron and photon multiplicities and spectra, isomeric ratios, and even the yields of nuclei.

Investigation of the process through which isomeric states of nuclear-fission fragments are produced may furnish information about the mechanism of formation and magnitudes of the total angular momenta of the fragments. The practical aspect of such investigations is that more detailed and accurate data on the activities and composition of spent nuclear fuels are required at the current stage of development of nuclear power engineering, when the efforts of researchers are concentrated on creating new-generation reactors of higher reliability and on studying the possibility of transmuting and destroying radioactive wastes of operating reactors.

In the present study, the theoretical approach that was successfully employed to compute isomers in

various reactions [4–6] and the spectra of photons from the spontaneous fission of ^{252}Cf [7] is applied to evaluating the yields of the isomers of fission fragments originating from the reactions $^{235}\mathrm{U}(n_{\mathrm{th}}, f)$ and $^{238}\mathrm{U}(\alpha, f)$. The applicability of the statistical model of nuclear reactions to calculating the emission properties of fission fragments is substantiated by analyzing experimental data on neutron emission from fission fragments over wide ranges of the total kinetic energies and masses, by extracting the mean excitation energies of fission fragments from experimental data, and by testing the balance of the resulting energies.

1. THEORETICAL MODEL

The statistical model of nuclear reactions within the Hauser–Feshbach–Moldauer formalism [1, 2] and its generalization to the case of gamma decay of excited nuclei in the form of the cascade–evaporation model [3] are successfully used in theoretical analyses of the emission of photons and particles of nonzero mass, as well as in analyses of the yield of isomeric levels from various nuclear reactions [4–6]. The application of the statistical model of nuclear reactions and of the cascade–evaporation model to describing processes that involve emission from fission fragments is hindered by a number of factors. Listed immediately below are the most important of these:

(i) Since the total kinetic energy of fission fragments lies between 140 and 220 MeV, the excitation energy of fragments can vary between 0 and 50 MeV. The distribution of the excitation energy among the complementary fragments is not known.

(ii) That the excitation energy can vary within a wide range must lead to significant changes in the total-angular-momentum distribution of populations, but the mechanism of formation of these distributions in fission fragments is poorly known.

(iii) In order that calculations be able to reproduce mean observables of the fission process, it is necessary to perform such calculations for a wide range of nuclei.

Basic relations of the statistical model of nuclear reactions are well known and were implemented as a standard procedure in many computer codes (GNASH [8], STAPRE [9]). It is therefore not necessary to quote these relations here. We only note that the results obtained by calculating the emission spectra according to the statistical theory of nuclear reactions are determined by two model-dependent functionals: the level density of excited nuclei in the input and the output reaction channel and the penetrabilities for particles of finite mass and for photons. The level density was calculated on the basis of the generalized superfluid-nucleus model in the version proposed in [10]. These calculations were performed with the parameter values quoted in the dedicated LDPL-98 library [7], which contains the asymptotic level-density parameters $\tilde{a}$, the shell corrections δW, the corrections δ for even–odd distinctions, the quadrupole-phonon energies ω_{2^+}, and the diagrams of discrete levels of the excitation spectrum for nearly 2000 nuclei. The penetrability factors for neutrons were computed on the basis of the optical model of the nucleus with the parameters of the global optical potential from [11].

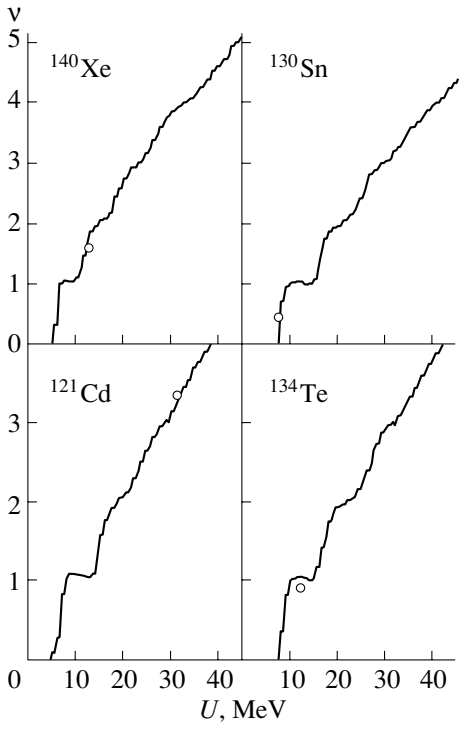

Fig. 1. Number of neutrons as a function of the excitation energy of the emitting nucleus for ^{121}Cd, ^{130}Sn, ^{134}Te, and ^{140}Xe. Closed circles represent the experimental values of $\langle\nu\rangle$ for the fragments of ^{252}Cf [13].

2. NEUTRON EMISSION

The spectra of neutrons are faithfully reproduced within the statistical model of nuclear reactions if the reaction being considered proceeds through a compound nucleus—that is, there is no coupling between the input and the output reaction channel, with the exception of those couplings that are associated with the laws of energy, total-angular-momentum, and parity conservation. From this point of view, it is reasonable to deem that the process leading to the formation of fragments and of their properties is fully consistent with the requirements ensuring the applicability of the statistical model of nuclear reactions.

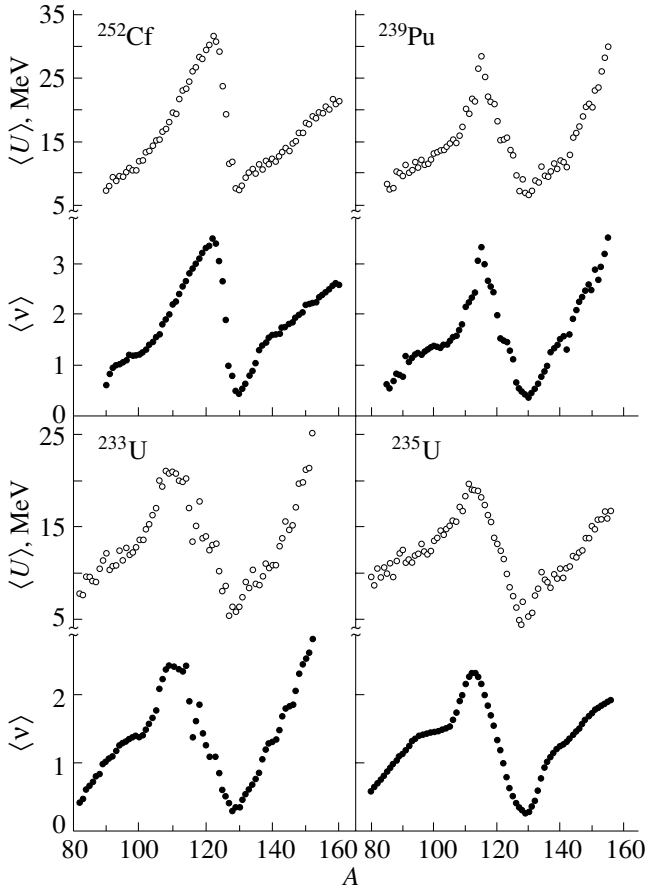

Fig. 2. Mean excitation energies of fission fragments and mean multiplicities of neutrons versus the mass of the fragments originating from the thermal-neutron-induced fission of ^{233}U, ^{235}U, and ^{239}Pu nuclei and from the spontaneous fission of a ^{252}Cf nucleus.

In conventional nuclear reactions, such as $(n \ldots \alpha, xn)$, the excitation energy of the nucleus emitting neutrons is known to a high precision. In nuclear fission, the excitation energies of fission fragments can vary within a broad range between 0 and 50 MeV. Therefore, the first step in applying the statistical model of nuclear reactions must be that of determining the mean excitation energy of fragments.

Excitation energy of fragments. Information about the excitation energies of fission fragments prior to neutron emission can be extracted from data on the mean number of neutrons under the assumption that neutrons are emitted from fully accelerated and fully formed products of nuclear fission [7]. The reliability of data obtained on the basis of this approach is ensured by the fact that the number of neutrons unambiguously depends on the excitation energy of a given nucleus. In order to demonstrate typical dependences of the number ν of emitted neutrons on the excitation energy of a uranium nucleus, we choose nuclei that appear as the fragments produced in ^{252}Cf fission and which have the highest (^{121}Cd) or the lowest (^{130}Sn) multiplicity of neutrons [12], as well as nuclei characterized by the maximum yield (^{140}Xe) or by the ν value corresponding to the plateau in the dependence $\nu(U)$ (^{134}Te) (Fig. 1). The greatest error in determining the excitation energy may be 2 to 3 MeV and is due to the fact that, in the dependence $\nu(U)$, there is a plateau around $\nu = 1$ (Fig. 1). This error becomes smaller if the procedure employs the dependence averaged over a few fragments rather than the dependence for one nucleus.

The probabilities of emission of various numbers of neutrons from fission fragments excited to energies not exceeding 80 MeV were calculated for four processes, the thermal-induced-fission of ^{233,235}U and ^{239}Pu nuclei and the spontaneous fission of ^{252}Cf. The calculations were performed for $A = 70$–160 fragments, whose yields do not fall below 0.1 of the maximum yield of a fragment with a specific mass. The input data were taken from the LDPL-98 library of level-density parameters [7]. The distributions of the yields of fragments with a specific charge and

mass, $Y(Z, A)$, were computed on the basis of the model developed in [12]. The dependences $\nu(Z, A, U)$ were averaged with the weights associated with the corresponding yields, whereupon the quantities $\langle U \rangle$ were determined from a comparison of the calculated values of $\nu(A, U)$ and the experimental values $\langle \nu(A) \rangle$ [12–14]. The resulting mean excitation energies of fission fragments and the mean neutron multiplicities used [12–14] are displayed in Fig. 2 versus fragment masses. Obviously, the sawtooth structure of $\langle \nu(A) \rangle$ must be reproduced and is indeed reproduced in the dependences $\langle U(A) \rangle$. It is important to emphasize that the experimental values of $\langle \nu(A) \rangle$ are often known to a poor precision. By way of example, we indicate that, for ^{252}Cf, the precision is 15% around $A = 120$ and that, for ^{235}U, the scatter of data presented by different authors is as large as 40% around $A = 115$–125 [12].

The extracted mean excitation energies of fragments of various masses are shown in Fig. 3 versus the mean number of neutrons. Use was additionally made there of data from [15] for various values of the total kinetic energy of fragments. It is noteworthy that, for seven cases, the dependences $\langle U(\nu) \rangle$ obtained here are similar to a considerable extent and can be described by the formula

$$\langle U \rangle = 5 + 4\nu + \nu^2. \quad (1)$$

That the function in (1) is nonlinear is indicative of an increase in the mean energy carried away by neutrons with increasing number of these neutrons as the residual nucleus approaches the stability band. In the ensuing calculations, use is made of the resulting mean energies for fragments of specific masses at mean total kinetic energies. Considering that the variance of the total kinetic energies is about 10–12 MeV and that the width of the distribution affects only slightly the extracted mean excitation energies, we adopt a value of 5 MeV for the root-mean-square deviation in the relevant Gaussian distribution.

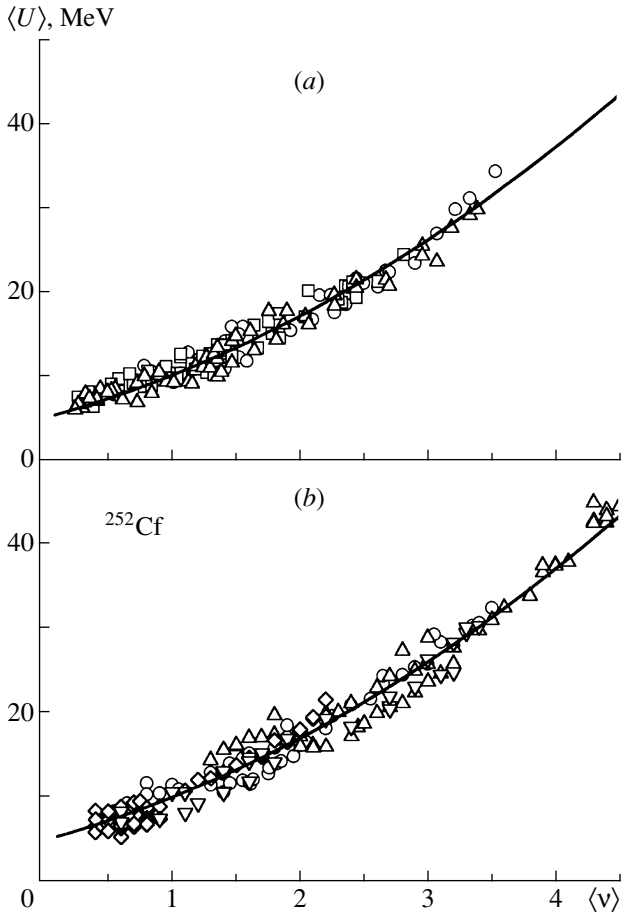

Fig. 3. Mean excitation energy of fragments as a function of the mean number of emitted neutrons for (*a*) the thermal-neutron-induced fission of (squares) ^{233}U, (triangles) ^{235}U, and (circles) ^{239}Pu nuclei and (*b*) the spontaneous fission of a ^{252}Cf nucleus for the fragment total kinetic energies of (circles) 187, (inverted triangles) 14, (triangles) 167, and (diamonds) 207 MeV. The curves represent the results of the calculations by formula (1).

Energy balance. The procedure used here to extract mean excitation energies of fission fragments takes no account of the energy balance in the fission process; therefore, its results can be verified by comparing the total mean energy of the complementary fragments, $\langle U(A_\mathrm{L}, A_\mathrm{H}) \rangle = \langle U(A_\mathrm{L}) \rangle + \langle U(A_\mathrm{H}) \rangle$, with the available energy $\mathrm{TXE}(A_\mathrm{L}, A_\mathrm{H})$ calculated by the formula

$$\mathrm{TXE}(A_\mathrm{L}, A_\mathrm{H}) = Q(A_\mathrm{L}, A_\mathrm{H}) - \mathrm{TKE}(A_\mathrm{L}, A_\mathrm{H}), \quad (2)$$

where Q is the reaction energy; TKE is the total kinetic energy; and A_L and A_H are the masses of, respectively, a light and the complementary heavy fragment. The present calculations were performed with the experimental $\mathrm{TKE}(A_\mathrm{L}, A_\mathrm{H})$ values from [13, 16] and with nuclear binding energies from [17]. A comparison of $\langle U(A_\mathrm{L}, A_\mathrm{H}) \rangle$ and $\mathrm{TXE}(A_\mathrm{L}, A_\mathrm{H})$ is illustrated in Fig. 4 for the fission of ^{252}Cf and ^{235}U nuclei. Satisfactory agreement between the values under comparison indicates that the procedure used to extract mean excitation energies of fragments leads to results compatible with the energy-conservation law and that the available energy of fission is converted almost completely into the excitation energy of fragments. That $\mathrm{TXE}(A_\mathrm{L}, A_\mathrm{H})$ exceeds $\langle U(A_\mathrm{L}, A_\mathrm{H}) \rangle$ by about 10 MeV for ^{235}U in the region of mass-symmetric fission can probably be explained by considerable uncertainties in $\langle \nu_\mathrm{expt} \rangle$.

The verification of the energy balance is incomplete if the energy transfer to fragments is not broken down into the components carried away by neutrons and photons. On one hand, this partition would make

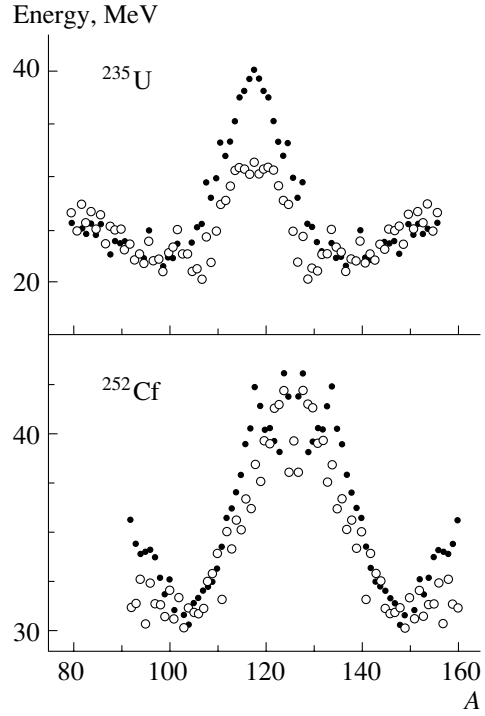

Fig. 4. Available energies TXE $= Q -$ TKE (closed circles) and sums of mean excitation energies of the complementary fragments, $\langle U(A_{\rm L}, A_{\rm H}\rangle = \langle U(A_{\rm L}\rangle + \langle U(A_{\rm H})\rangle$, (open circles) versus the fragment mass for the spontaneous fission of ^{252}Cf and for the thermal-neutron-induced fission of ^{235}U.

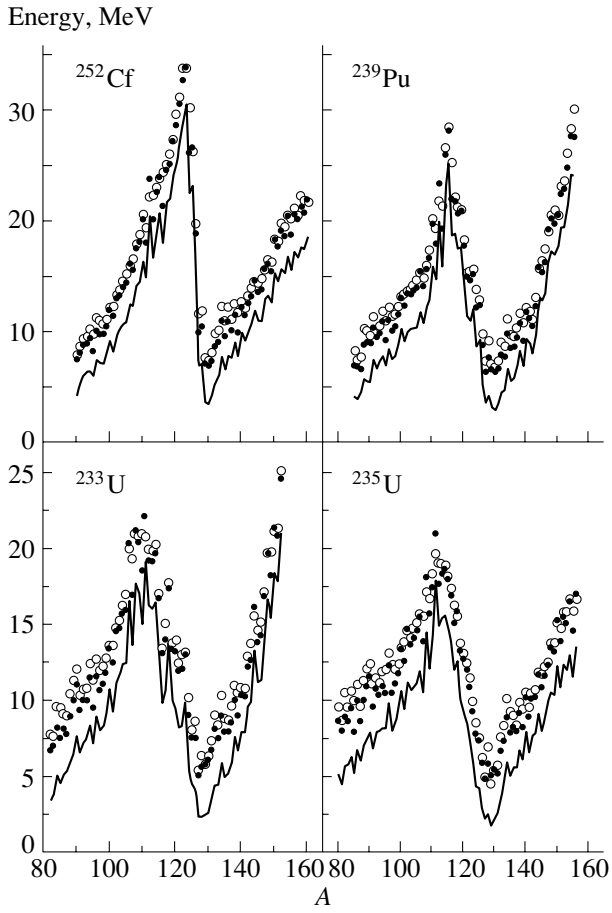

Fig. 5. Mean excitation energies of fission fragments (open circles), sum of the mean energies carried away by neutrons and photons (closed circles), and mean energies carried away by neutrons (curves).

it possible to test the widely used assumption that the photon energy E_γ is approximately half the neutron binding energy ($E_\gamma \approx B_n/2$); on the other hand, it provides yet another check upon the procedure for extracting mean excitation energies of fission fragments [7].

That the calculated multidimensional matrices of the neutron and photon spectra—$N_n(Z, A, U, \varepsilon_n)$ and $N_\gamma(Z, A, U, \varepsilon_\gamma)$, respectively—are available enables one to obtain theoretical values for any observables of fission fragments [7]. In particular, the energies carried away by neutrons and photons can be calculated as

$$E_n = \nu(\langle\varepsilon_n\rangle + \langle B_n\rangle), \quad E_\gamma = \mu\langle\varepsilon_\gamma\rangle, \qquad (3)$$

where the mean energies ($\langle\varepsilon_n\rangle$, $\langle\varepsilon_\gamma\rangle$) and multiplicities ($n$, μ) are obtained from the corresponding spectra.

Thus, a comparison of $\langle U(A)\rangle$ with $(E_n + E_\gamma)$ and of $E_{\gamma\,\rm calc}$ with $E_{\gamma\,\rm expt}$ would make it possible to demonstrate that the approach used does indeed take correctly into account all channels of the radiation of energy. For four fissile systems, the excitation energies of fragments are displayed in Fig. 5, along with the energies carried away by neutrons and photons. As might have been expected, the balance of the energies transferred to the fragments in the fission process and the energies carried away in the deexcitation of these fragments is obviously fulfilled. Some modest deviations are explained by the fact that the energy balance is verified for mean values.

Photons emitted by fission fragments carry away up to 50% of the excitation energy (Fig. 5); therefore, it is of paramount importance to verify whether the theoretical model used provides a correct description of the radiative deexcitation channel. For the fragments formed in thermal-neutron-induced fission of ^{235}U and ^{239}Pu, the experimental mean values of photon energies [18, 19] are contrasted in Fig. 6 against the calculated values. It is found that $E_{\gamma\,\rm calc}$ and $E_{\gamma\,\rm expt}$ are in satisfactory agreement. It is interesting that E_γ ranges between 20 and 90% of the neutron binding energy.

The experimental photon multiplicities $\mu_{\rm expt}$ [18, 19] as functions of the fragment mass have a sawtooth

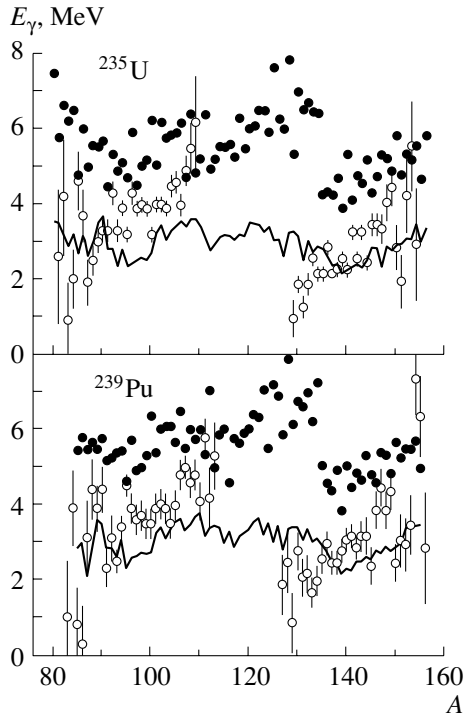

Fig. 6. Data on the mean energies carried away by photons from fragments originating from ^{235}U and ^{239}Pu fission induced by thermal neutrons: (open circles) experimental data from [18, 19] and (curves) results of the calculations. Closed circles represent the mean neutron binding energies in emitting nuclei.

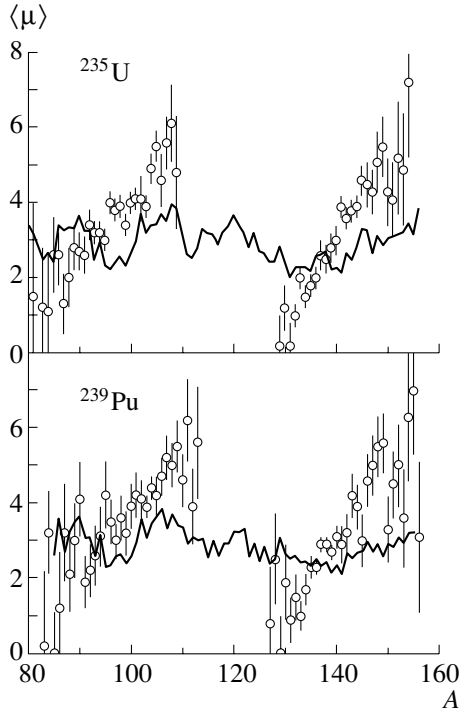

Fig. 7. Data on the multiplicities of photons from fragments formed in thermal-neutron-induced fission of ^{235}U and ^{239}Pu: (points) experimental data from [18, 19] and (curves) results of the calculations.

structure (see Fig. 7) similar to that of the dependence $\langle\nu(A)\rangle$. The calculations failed to reproduce this dependence. The reason may lie in the disregard of the radiation mechanism associated with transitions between the members of rotational bands of excited nuclei. Qualitatively, this conjecture is confirmed by a characteristic increase in the number of emitted photons as one recedes from the $A = 130$ spherical fragment toward deformed fission fragments with mass numbers in the range $A = 140$–150 (see Fig. 7).

Level density. The extracted quantities $\langle U(A)\rangle$ depend on the parameters of models used to calculate the neutron and photon spectra—above all, on the level-density parameters. In cases where the calculations poorly reproduce the spectra of neutrons, the values of mean excitation energies will be strongly distorted. It is therefore of great interest and importance to test the description of the spectra of neutrons originating from fission fragments. In Fig. 8, the spectra calculated on the basis of the statistical model of nuclear reactions with the parameter values from the LDPL-98 library [7] are contrasted against the experimental spectra of neutrons from [20]. Satisfactory agreement between these spectra indicates that the data in the LDPL-98 library are quite correct and that the statistical model of nuclear reactions can be successively applied to describing the emission properties of fission fragments. A comparison of the parameters from LDPL-98 with the corresponding empirical values obtained from the neutron spectra in [13, 20] (Fig. 9) would be an indirect check upon these parameters. A detailed accurate description of the shell structure that manifests itself in $A = 130$ fragments is the most compelling evidence of the predictive power of the level-density model [10] used in creating the LDPL-98 library. It should be borne in mind that the procedure employed in [13, 20] to extract level-density parameters is not free from drawbacks. First, the data were obtained for nuclei emitting neutrons, but it is well known that the spectra are determined by the parameters of residual nuclei; second, there exists a procedure for extracting the absolute value of the level density from the emission spectra [21], but it was not applied; and, third, the temperature t in the expression $U = at^2$, which was employed to obtain the parameter a, does not comply with that which is extracted from the spectra according to the Le Couteur–Lang relation [22].

Neutron multiplicities. The relations between the excitation energies were obtained for the mean values of the total kinetic energies of pairs of complementary fragments. The experimental values $\nu_{\text{expt}}(\text{TKE}, A)$ from [13, 23] make it possible to verify these relations over a wider range of excitation

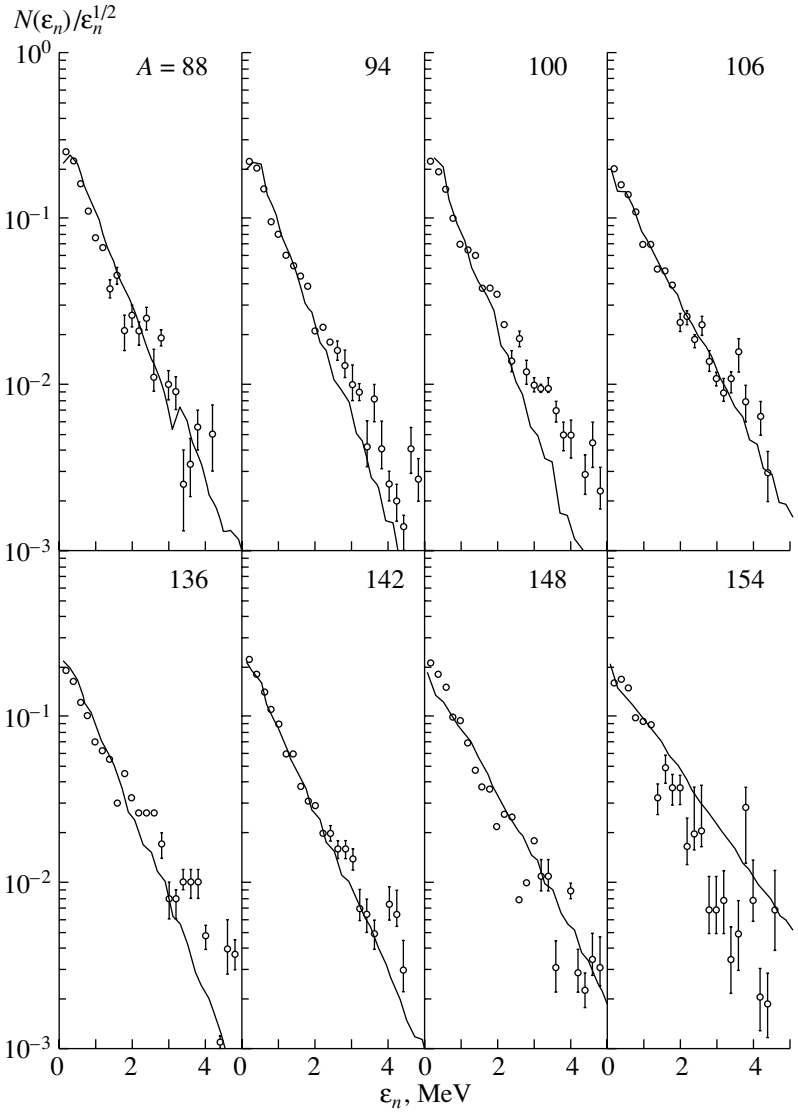

Fig. 8. Spectra of neutrons from fragments formed in thermal-neutron-induced fission of ^{235}U: (points) experimental data from [20] and (curves) results of the calculations.

energies. Since $\mathrm{TXE}(A_\mathrm{L}, A_\mathrm{H})$ is the sum of the excitation energies of two fission fragments, the distribution of this energy among the fragments will affect the calculated dependences $\nu_{\mathrm{calc}}(\mathrm{TKE}, A)$. In the calculations, the excitation energy of a given fragment was set to

$$U(A_{L,H}) = [Q - \mathrm{TKE}(A_L, A_H)]\frac{\langle U(A_{L,H})\rangle}{\langle U(A_L, A_H)\rangle}; \quad (4)$$

that is, it was assumed to be proportional to the ratio of the mean kinetic energies that was obtained above. In Fig. 10, the experimental values of $\nu(\mathrm{TKE}, A)$ from [13] are contrasted against their calculated counterparts for six pairs of complementary fragments (125, 127; 123, 129; 122, 130; 121, 131; 120, 132; 124, 128) originating from the spontaneous fission of ^{252}Cf, for four light fragments (115, 117, 118, 119), and for mass-symmetric fission. That the dependences $\nu_{\mathrm{expt}}(\mathrm{TKE}, A)$ and $\nu_{\mathrm{calc}}(\mathrm{TKE}, A)$ are in agreement over a wide range of total kinetic energies seems quite compelling, the excitation energies of individual fragments varying between 0 and 40 MeV. Some discrepancies between the absolute values are due to distinctions between TXE and $\langle U\rangle$ (see Fig. 4). A similar comparison of experimental data from [23] with the results of the calculations for ^{235}U is illustrated in Fig. 11. Since the data from [14] were used to extract mean energies and since the values $\nu_{\mathrm{expt}}(\mathrm{TKE}, A)$ were borrowed from [23], the calculated dependences had to be renormalized with allowance for the distinctions between the $\langle\nu\rangle$ values in [14] and [23]. For six pairs of complementary

fragments originating from ^{235}U fission induced by thermal neutrons, the calculated and the experimental values of ν(TKE, A) agree over wide ranges of total kinetic energies (150–190 MeV) and fragment masses (90–146) (Fig. 11). Thus, we can conclude that, in the majority of the cases, neutrons are emitted from fission fragments occurring at an equilibrium deformation. A sharp decrease in ν_{expt}(TKE, A) for TKE $\sim$ 150 MeV suggests that, for one reason or another, the fragments are excited to a lesser degree.

Thus, we have obtained a satisfactory description of the neutron spectra and multiplicities and have been able to reproduce faithfully the level-density parameters for $A \approx 130$ fragments. In view of this, a nearly twofold discrepancy between the calculated and experimental values of the mean neutron energies $\langle\varepsilon_n\rangle$ for the mass range 125–135 (Fig. 12) is quite surprising. In this connection, the experimental values of $\langle\varepsilon_n\rangle \approx 1.5$–$1.8$ MeV at emitting-nucleus excitation energies of 5–7 MeV seem unjustifiably large. For fragments of different masses, the agreement between $\langle\varepsilon_n\rangle_{\text{expt}}$ and $\langle\varepsilon_n\rangle_{\text{calc}}$ is quite acceptable.

Thermodynamic equilibrium. Knowledge of mean excitation energies of complementary fragments makes it possible to test the energy condition for the scission of a fissile nucleus—that is, to assess the available-fission-energy fraction that is transferred to a given fragment or the proportion in which the available fission energy is shared between complementary fragments. The thermodynamical-equilibrium condition—that is, the equality of the temperatures of the light and the heavy fragment (t_L and t_H, respectively) at the instant of scission—is often used for this purpose. From this condition, it follows that the excitation energy of a given fragment is given by

$$U_{L,H} = \frac{U}{1 + a_{H,L}/a_{L,H}}, \qquad (5)$$

where U is the total excitation energy of complementary fragments and a is the level-density parameter. Since the parameter a depends on the excitation energy within the level-density model proposed in [10], an iterative procedure was used to solve Eq. (5).

For four fissile systems, a comparison of "true" excitation energies of fission fragments (Fig. 2) and the values computed by formula (5) with $U = \langle U(A_L, A_H)\rangle$ is illustrated in Fig. 13. Since the level-density parameters depend on the excitation energy and on shell corrections, the distributions of $U_{L,H}$ are similar to the distributions of $\langle U(A)\rangle$. As might have been expected, it is inappropriate to apply expression (5) to the case of spontaneous fission, because a nucleus undergoes spontaneous fission from the ground state. In the case of induced fission, the results are much better, although the excitation energy of a compound nucleus per fission fragment (3–4 MeV) constitutes only a small fraction of its total excitation energy.

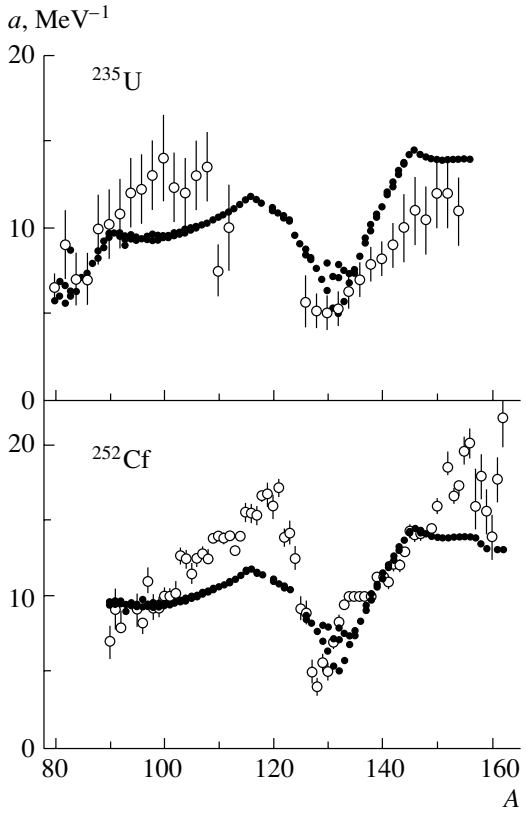

Fig. 9. Parameters of the level densities in primary fragments produced in the spontaneous fission of ^{252}Cf and in the thermal-neutron-induced fission of ^{235}U versus the fragment mass: (open circles) empirical values obtained in [13, 20] from neutron spectra and (closed circles) data from LDPL-98 library [7] that were rescaled to mean excitation energies.

In summary, it has been shown that, over wide ranges of the total kinetic energies and masses of fission fragments, the observed emission properties of such fragments can be reproduced on the basis of the statistical model of nuclear reactions. As a next step in studying the emission properties of fission fragments within the approach combining the statistical model of nuclear reactions with the cascade–evaporation model, we proceed to examine the population of the isomeric states of fragments.

3. ISOMERIC RATIOS

At present, the isomeric ratios of independent yields [24, 25] are usually calculated by the method that was proposed in [26] and which is based on the assumption that the total-angular-momentum (J)

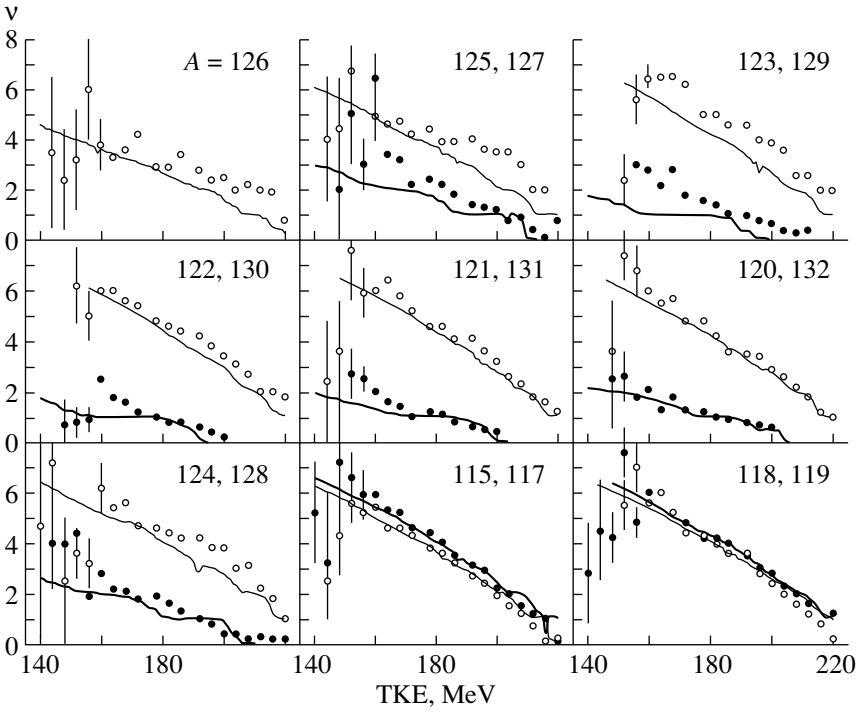

Fig. 10. Multiplicities of neutrons emitted by fragments originating from the spontaneous fission of ^{252}Cf versus the total kinetic energy. Points represent experimental data from [13] for (open circles) light and (closed circles) heavy fragments. The curves show the results of the calculations.

distribution of isomeric-nucleus populations is proportional to the spin distribution of the density of excited levels; that is,

$$W(J) \sim (2J+1)\exp\left(-\frac{(J+1/2)^2}{2\sigma^2}\right), \quad (6)$$

where σ^2 is the spin-cutoff parameter. According to [26], an isomeric state is populated via a few gamma transitions whose probability is determined by the density of final-state levels. It is assumed here that the spin-cutoff parameter σ is independent of excitation energy. The method proposed in [26] was tested by using it to analyze experimental isomeric ratios for the radiative capture of thermal and resonance neutrons and the isomeric ratios in (γ, n) reactions on some nuclei. By varying, within reasonable limits, the parameter σ and the number μ of photons emitted in the process leading to the population of the isomeric state, it was possible to obtain a reasonable description of currently available data for 28 nuclei in (n, γ) reactions. In photonuclear reactions, the situation is different. For example, experimental data on the reaction ^{115}In(γ, n) could be described only by making σ tend to infinity.

Physically, the method proposed in [26] is based on the assumption that the isomeric ratio is formed by a photon cascade that accompanies the decay of the isomeric nucleus being considered. This assumption is confirmed by an analysis of isomeric cross sections for many reactions [4–6]. By way of example, it can be recalled that, even for (n, γ) reactions induced by 14-MeV neutrons, a direct population of an isomer following neutron emission is insignificant; that is, the main contribution to the isomeric cross section comes from photon cascades removing the excitation that remained after neutron emission [6]. However, the shape of the distribution of populations prior to photon emission that leads to the formation of an isomer may differ significantly from that in (6) if the states of the isomeric nucleus are formed owing to neutron emission and if the relevant compound nucleus is excited to high energies. In this case, the extracted value of the parameter σ will be overestimated, which was demonstrated in [26]. Since the excitation energy of fission fragments prior to neutron emission can be quite sizable (up to 50 MeV), it would be incorrect to apply the method developed in [26] to an analysis of the isomeric ratios of independent yields.

As was demonstrated in a great number of studies, the most consistent way to compute the cross sections for isomer formation and isomeric ratios is to make use of the approach combining the statistical model of nuclear reactions with the cascade evaporation model [1–3]. It was found that a fairly good description of experimental data could be obtained for

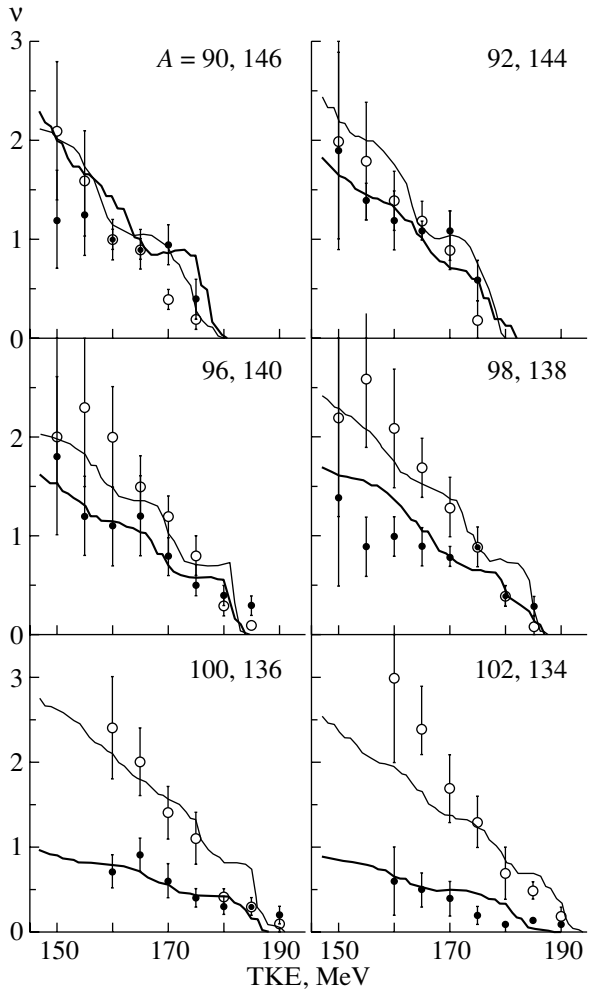

Fig. 11. As in Fig. 10, but for ^{235}U fission induced by thermal neutrons. Points represent experimental data from [23].

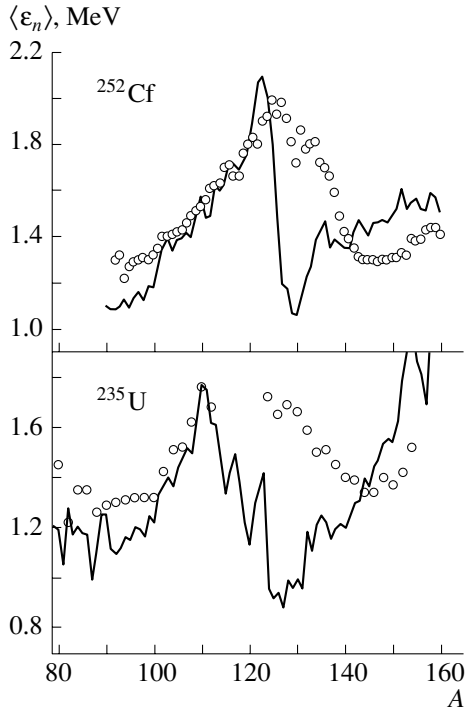

Fig. 12. Mean energies of neutrons emitted by fragments originating from the spontaneous fission of ^{252}Cf and from the thermal-neutron-induced fission of ^{235}U versus the primary-fragment mass: (points) experimental data from [13, 20] and (curves) results of the calculations.

a wide range of projectile species (from photons to alpha particles), a wide range of nuclear mass numbers (from 20 to 240), and a wide energy range (from thermal energies to 40 MeV). For isomers formed in the fission process, the above approach has not been used so far, however, because of additional complications and because of uncertainties in the input conditions. Since the mean excitation energies of fission fragments have already been established and since the library of the parameter values has been tested, there are no serious limitations that would restrict the application of the approach combining the statistical model of nuclear reactions and the cascade–evaporation model.

Mechanism of population of fission-fragment isomers. According to the cascade–evaporation model, a specific state of a nucleus that emerges as a product of the fission process can be populated in the following ways: (i) in the fission process (cold fission), (ii) upon neutron emission, or (iii) upon a photon cascade (the channel involving both neutron emission and a photon cascade is also possible). According to this mechanism of isomer population, the isomeric ratio of independent yields for a (Z, A) nucleus can be calculated by the formula

$$R = \frac{\sum\limits_{i=0}^{n} Y_i(Z, A+i)\langle P_i r_i\rangle}{\sum\limits_{i=0}^{n} Y_i(Z, A+i)\langle P_i\rangle}, \qquad (7)$$

where Y_i is the independent yield of a $(Z, A+i)$ fragment that emits i neutrons, P_i is the probability of emission of this number of neutrons, and r_i is the isomeric ratio for the case where i neutrons are emitted. Summation in (7) is performed from zero (the isomeric nucleus in question was directly formed in the fission process) to some number n of neutrons such that the isomeric nucleus is formed upon the emission of precisely this number of neutrons. Thus, $(n+1)$ nuclei appearing as products of the fission process participate in the formation of the isomeric state. Here, averaging is performed over the excitation energies of relevant primary fragments with allowance for the distribution function $f(U)$. In calculating P_i and r_i, it is necessary to specify, in

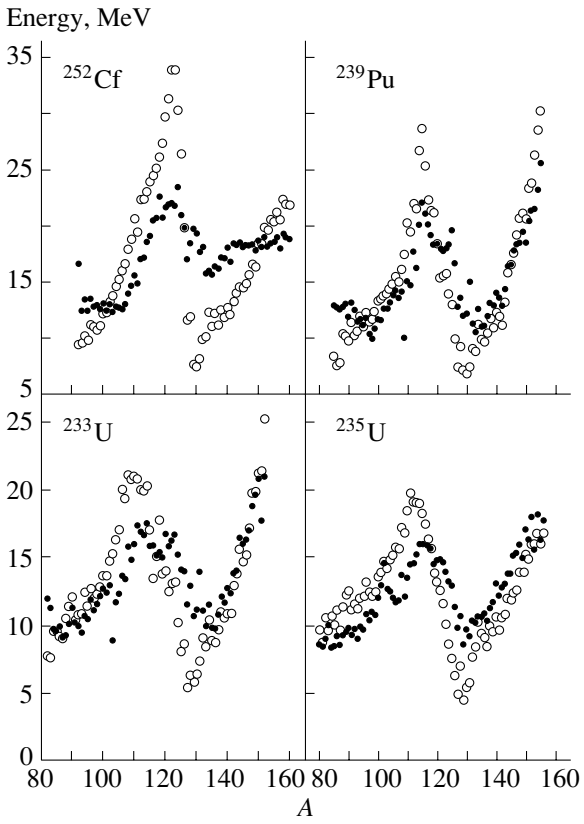

Fig. 13. Distribution of the excitation energy among the fragments originating from the thermal-neutron-induced fission of ^{233}U, ^{235}U, and ^{239}Pu and from the spontaneous fission of ^{252}Cf: (open circles) mean energies obtained from neutron multiplicities and (closed circles) values calculated by formula (5).

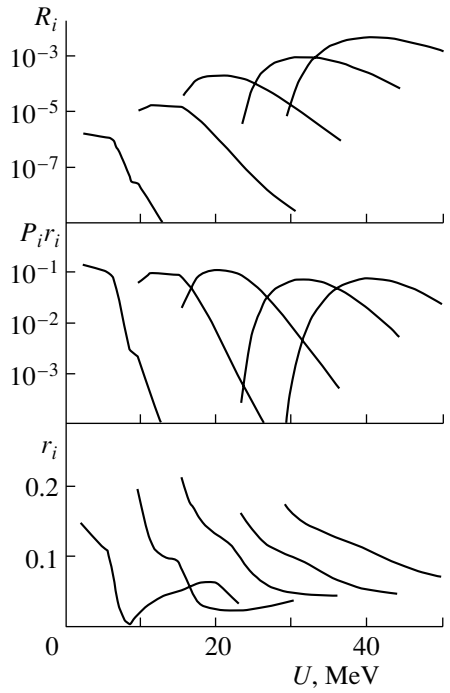

Fig. 14. Isomeric ratios $r_i(U)$, probabilities $P_i(U)r_i(U)$ of the population, and yields $R_i(U)$ of the isomer $^{123}\mathrm{Sn}(3/2^+)$ upon the emission of $\nu = 0, 1, 2, 3, 4$ neutrons (from left to right) as functions of energy.

addition to the distribution of excitation energies, the initial total-angular-momentum distribution of the populations of the levels involved.

In Fig. 14, the quantities appearing in expression (7) are displayed versus the excitation energy of the relevant nucleus after the emission of various numbers of prompt neutrons that results in the formation of an isomer in the ^{123}Sn nucleus. Since the metastable state of the ^{123}Sn nucleus is characterized by a low spin value ($J^\pi = 3/2^+$), an increase in the excitation energy leads to a decrease in the probability of population of this state in all channels of ^{123}Sn formation after the emission of neutrons ($\nu = 1$–4) and photons ($\nu = 0$). Multiplication of the function $r(U)$ by $P(U)$ leads to bell-shaped functions having nearly identical maxima. Finally, the terms in the numerator on the right-hand side of (7) that are obtained upon taking into account the dependence $Y(A+i)$ are such that, even at $\langle U\rangle = 10$–15 MeV, it is necessary to allow for the emission of four to five neutrons in the calculations. Thus, the isomer is populated through a few channels having commensurate probabilities. If we admit that isomers can also be formed upon the emission of delayed neutrons, the calculations become so involved that they require a dedicated investigation.

Radiative strength functions. The probabilities of isomer population upon neutron and photon emission depend on radiative strength functions. This issue was comprehensively studied in [27], where a method was proposed for parametrizing radiative strength functions f_{E1} for electric dipole transitions (modified Kadmensky–Markushin–Furman method) and where the effect of various procedures for calculating f_{E1} on the results of the calculation of isomeric cross sections and spectra in the deexcitation of uniformly excited nuclei was analyzed. For ^{235}U fission induced by thermal neutrons, the effect of f_{E1} on the calculated gamma spectra is illustrated in Fig. 15. The calculations took into account photons emitted by fission fragments with mass numbers $A = 80$–160. It can be seen that the description of experimental data compiled in [28] is considerably improved upon applying the modified Kadmensky–Markushin–Furman method, and that is why this was done in the present calculations. The reasons behind the discrepancies between the calculated and experimental spectra at energies in

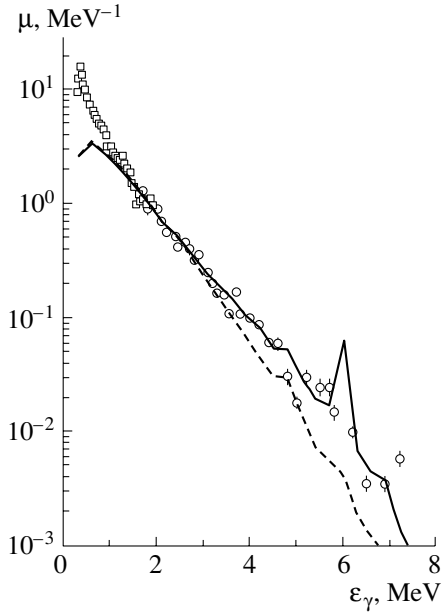

Fig. 15. Spectra of photons from fragments produced in ^{235}U fission induced by thermal neutrons: (points) experimental data from [28], (dashed curve) results of calculations employing a Lorentzian form of f_{E1}, and (solid curve) results of the calculation based on the modified Kadmensky–Markushin–Furman method [27].

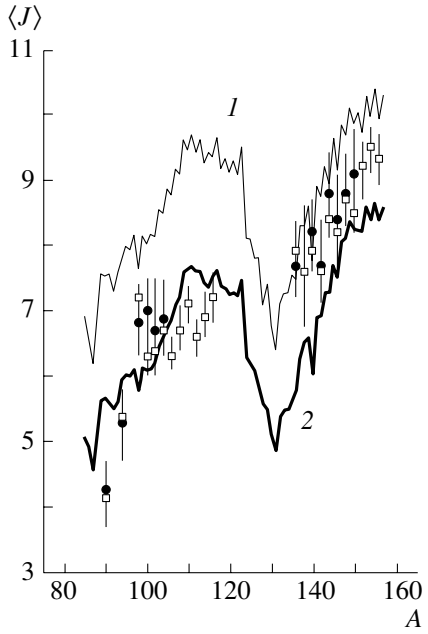

Fig. 16. Mean spins of fragments originating from (closed circles) the thermal-neutron-induced fission of ^{235}U and (open boxes) the spontaneous fission of ^{248}Cm: (points) data from [30] and (curves) results of the calculations with (*1*) $F = F_{\text{rig}}$ and (*2*) $F = F_{\text{rig}/2}$.

the region $E_\gamma \leqslant 1$ MeV and the possible means for removing these discrepancies are discussed in [7].

Mean fission-fragment spins. In order to apply the statistical model of nuclear reactions, which takes into account the laws of total-angular-momentum and parity conservation, to calculating the emission properties of fission fragments, it is necessary to know the spin distributions of their populations, $W_0(U, J)$, prior to neutron emission—specifically, mean spin values $\langle J \rangle$ and the form of the dependence $W_0(U, J)$. In other words, one should specify, in consistently applying the statistical model of nuclear reactions, the fission-barrier penetrability as a function of the orbital angular momentum of the relative motion of fission fragments at the instant of scission of the nucleus undergoing fission, $T_f(l)$. This issue, which is of only marginal importance in calculating the spectra of radiation from fragments [7], comes to the fore in calculating isomeric ratios. If, as follows from the analysis reported in [29], $T_f(l)$ is independent of the orbital angular momentum l, the total-angular-momentum dependence of the initial populations of the fragments has the form

$$W_0(U, J) \sim (2J + 1)\rho(U, J). \qquad (8)$$

The assumption in (8) can be verified by using data on the mean spins $\langle J \rangle$ of fission fragments [30] (see Fig. 16). Although the results presented in [30] are not purely experimental (in order to derive them, use was made of the results obtained by calculating the mean angular momenta carried away by neutrons and photons), they are sufficiently imformative for a comparison. By using the mean excitation energies of primary fragments (these energies were discussed above in connection with the data in Figs. 2–4) and two limiting values of the nuclear moment of inertia F—that for a rigid nucleus, F_{rig}, and that for a semirigid nucleus, $F_{\text{rig}/2}$—the mean spins $\langle J \rangle$ were calculated under the assumption specified by Eq. (8). It can be seen that, as a rule, the data from [30] lie within the corridor determined by the results of the calculations. Hence, the use of this assumption in the calculations leads to a satisfactory agreement with observed values of the mean spins of primary fragments.

Spin distribution of populations. On the basis of the mean spins of fission fragments, it is impossible to verify the assumption on the shape of the J dependence in (8), because different dependences can lead to identical values of $\langle J \rangle$. The broad distribution in (8) can be formed if single-particle levels are predominantly populated in the fission fragment being considered and if they are coupled to levels of rotational bands. Otherwise—that is, if nuclear fission populates collective states and if there is no coupling between levels of different origins—the distribution

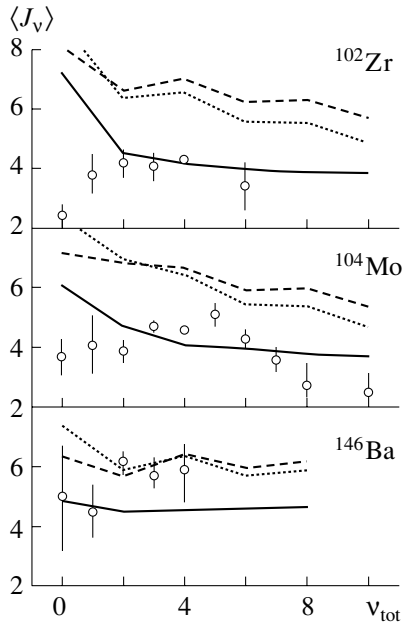

Fig. 17. Mean spins of ^{102}Zr, ^{104}Mo, and ^{146}Ba nuclei produced as fragments in the spontaneous fission of ^{252}Cf versus the number of neutrons emitted by a pair of complementary fragments: (points) experimental data from [31, 32]; (dashed and dotted curves) results of the calculations performed under the assumption in (8) with the parameters σ^2_{rig} and $\sigma^2_{\text{rig}/2}$, respectively; and (solid curves) results of the calculations performed under the assumption in (9) with the parameter $\sigma^2_{\text{rig}/2}$.

$W_0(U, J)$ must have the form

$$W_0(U, J) = \delta(J - \langle J\rangle), \qquad (9)$$

where $\langle J\rangle$ is determined according to (8) or from observable values and δ is a Dirac delta function. From Fig. 16, we can see that the mean spins of fission fragments are better reproduced by the calculation with $F = F_{\text{rig}/2}$; in the following, we therefore use this version in conjunction with the assumption in (9).

Data from [31, 32] on the mean angular momenta of the rotational bands in fragments produced in the spontaneous fission of ^{252}Cf nuclei (these data were obtained from an analysis of gamma transitions) may be of use for verifying the assumptions specified by Eqs. (8) and (9).

The mean spins of fission fragments of mass A upon the emission of ν neutrons can be determined from the dependence of J_ν on the excitation energy of a primary fragment. Specifically, we have

$$J_\nu(U) = \frac{\int\limits_0^{U-B_\nu} \sum\limits_J JW_\nu(x, J)dx}{\int\limits_0^{U-B_\nu} \sum\limits_J W_\nu(x, J)dx}, \qquad (10)$$

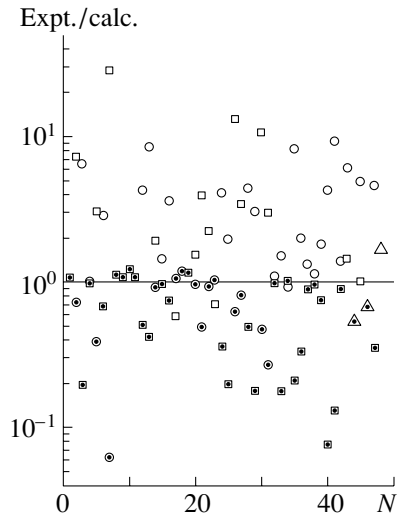

Fig. 18. Ratio of the experimental ([25]) and calculated [under the assumption specified by Eq. (8)] isomeric ratios of the independent yields of fragments produced in ^{235}U fission induced by thermal neutrons: (open circles) ground states, (open squares) first metastable levels, (open triangles) second metastable levels, and (closed circles) data for levels of higher spin values.

where W_ν is the population of the nuclear state under study after the emission of ν neutrons. Integration of the dependence $J_\nu(U)$ with respect to the excitation energy of a primary nucleus with the weight equal to the product of the distribution function $f(U)$ and the probability $P_\nu(U)$ of the emission of a given number of neutrons yields the mean fragment spin:

$$\langle J_\nu\rangle = \int\limits_0^{U_{\max}} J_\nu(U)P_\nu(U)f(U)dU. \qquad (11)$$

The mean spins of ^{102}Zr, ^{104}Mo, and ^{144}Ba nuclei produced as fragments in the spontaneous fission of ^{252}Cf upon neutron emission are displayed in Fig. 17. The mean spins as calculated under the assumption specified by Eq. (8) considerably exceed the experimental values even if we take into account experimental errors and uncertainties in the nuclear moment of inertia $\langle J\rangle$, a basic model parameter that has the strongest effect on the results of the calculations. It can be seen that, in this case, a fit to the experimental values of $\langle J\rangle$ requires anomalously low values of the nuclear moment of inertia. At the same time, satisfactory agreement with experimental data from [31, 32] was obtained under the assumption specified by Eq. (9). Thus, data on the mean angular momenta of fission fragments favor, in calculations for low-energy fission, the use of the spin distribution of primary-fragment populations in the form (9).

Isomeric ratios of independent yields. Experimental data on the isomeric ratios of independent

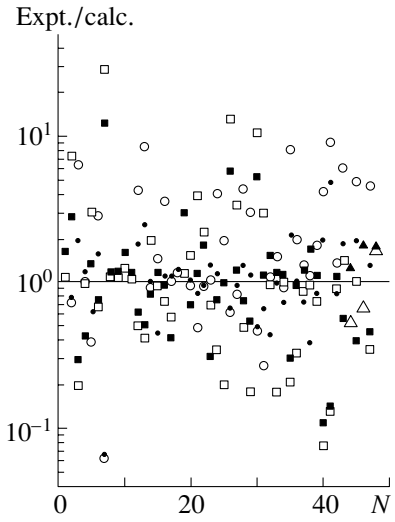

Fig. 19. Ratio of the experimental ([25]) and calculated isomeric ratios of the independent yields of fragments originating from ^{235}U fission induced by thermal neutrons: (open symbols) results obtained under the assumption specified by Eq. (8) and (closed symbols) results obtained under the assumption specified by Eq. (9).

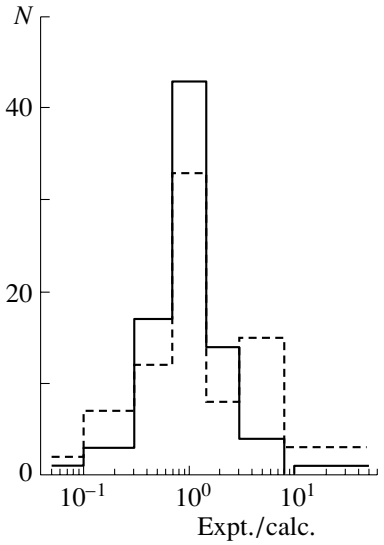

Fig. 20. Distribution of deviations of the ratios of the experimental and calculated isomeric ratios of independent yields of fragments originated from ^{235}U fission induced by thermal neutrons: (solid-line histogram) results obtained under the assumption specified by Eq. (9) and (dashed-line histogram) results obtained under the assumption specified by Eq. (8).

yields for ^{235}U fission induced by thermal neutrons [25] are available for 48 isomeric pairs of nuclear fragments with mass numbers in the range $A = 79$–148. The basic features of the isomeric levels of the nuclei under study are compiled in the table. It is important to note that the features of isomeric levels are not unique—as a rule, the difference of the spin values between the ground-state and a metastable level amounts to a few units of $\hbar$. At first glance, the description of the isomeric ratios of the independent yields of these levels should not therefore involve serious difficulties [4–6]. This is not so only for three high-spin isomeric levels of the ^{120,122,130}In nuclei.

The experimental isomeric ratios of independent yields from [25] are displayed in Fig. 18, along with their theoretical counterparts calculated under the assumption specified by Eq. (8). It is noteworthy that the calculated isomeric ratios are systematically in excess of the experimental values for high-spin levels and are systematically below them for low-spin levels, irrespective of whether the level being considered is ground-state or metastable. Variations in the parameters of nuclei—for example, a transition from the spin-cutoff parameter corresponding to the rigid-body moment of inertia to the value corresponding to the semirigid-body moment of inertia—or modifications to the method for calculating radiative strength functions lead only to slight changes in Fig. 18, but they do not distort the overall pattern.

A comparison of the experimental isomeric ratios of independent yields and the isomeric ratios calculated under the two limiting assumptions (8) and (9) on the total-angular-momentum distribution of primary-fragment populations is illustrated in Figs. 19 and 20. It can be seen that the use of the distribution in (9) leads to a radical improvement of the description of experimental data; no such improvement could be achieved by other methods for all nuclei simultaneously. Of course, there remain some discrepancies after the application of the distribution in (9), but they may probably be removed upon improving the description of soft-photon spectra (Fig. 15) or upon refining the diagrams of discrete levels in isomeric nuclei appearing as fission fragments.

The conditions under which the spins of fission fragments are formed and a further evolution of these spins during the Coulomb acceleration of the fragments can be different for different fissile systems—for example, in the fission processes induced by thermal neutrons, on one hand, and by alpha particles, on the other hand. The excitation energy of a compound nucleus is 5 to 6 MeV in the first case, but it may be as high as a few tens of MeV in the second case. It is obvious that, while, in (n_{th}, f) reactions, the distribution given by (9) is dominant, in (α, f) reactions, the contribution of (8) must be enhanced. This can be proven by analyzing the energy dependences of the isomeric ratios of independent yields for the latter reactions. Figure 21 shows experimental data on isomeric ratios for eight nuclei versus their mean excitation energies $\langle U \rangle$; these data were obtained with allowance for multichance fission and neutron emission [33]. The same figure displays the results of

Features of the isomeric levels of nuclei produced in ^{235}U fission induced by thermal neutrons (the relevant isomeric ratios were measured in [25]; presented in the table are the spin–parities J^π of the ground-state and metastable levels and the energies E_m of the metastable levels)

No.	Nucleus	J_g^π	J_m^π	E_m, MeV	No.	Nucleus	J_g^π	J_m^π	E_m, MeV
1	^{79}Ge	$1/2^-$	$7/2^+$	0.188	2	^{81}Ge	$9/2^+$	$1/2^+$	0.679
3	^{82}As	1^+	5^-	0.022	4	^{83}Se	$9/2^+$	$1/2^-$	0.231
5	^{84}Br	5^-	2^-	0.048	6	^{90}Rb	1^-	4^-	0.107
7	^{99}Nb	$9/2^+$	$1/2^-$	0.367	8	^{113}Ag	$1/2^-$	$7/2^+$	0.046
9	^{115}Ag	$1/2^-$	$7/2^+$	0.043	10	^{116}Ag	2^-	5^+	0.083
11	^{117}Ag	$1/2^-$	$7/2^+$	0.022	12	^{118}Ag	1^+	5^+	0.130
13	^{119}Cd	$1/2^+$	$11/2^-$	0.149	14	^{120}Ag	5^+	0^+	0.205
15	^{121}Cd	$1/2^+$	$11/2^+$	0.149	16	^{123}Cd	$3/2^+$	$11/2^+$	0.149
17	^{123}In	$9/2^+$	$1/2^-$	0.322	18	^{123}Sn	$11/2^-$	$3/2^+$	0.027
19	^{124}In	3^+	8^-	0.192	20	^{125}In	$9/2^+$	$1/2^-$	0.182
21	^{126}In	6^+	3^+	0.152	22	^{127}In	$9/2^+$	$1/2^-$	0.162
23	^{127}Sn	$11/2^-$	$3/2^+$	0.070	24	^{128}In	2^+	7^-	0.192
25	^{128}Sn	0^+	7^+	2.093	26	^{128}Sb	8^-	5^+	0.107
27	^{129}In	$9/2^+$	$1/2^-$	0.200	28	^{129}Sn	$3/2^+$	$11/2^-$	0.037
29	^{130}Sn	0^+	7^-	1.949	30	^{130}Sb	8^-	5^+	0.022
31	^{132}Sb	4^+	8^-	0.022	32	^{133}Te	$3/2^+$	$11/2^-$	0.336
33	^{133}I	$7/2^+$	$19/2^+$	1.636	34	^{133}Xe	$3/2^+$	$11/2^-$	0.235
35	^{134}Sb	0^-	7^-	0.020	36	^{134}I	4^+	8^-	0.318
37	^{135}Xe	$3/2^+$	$11/2^-$	0.529	38	^{136}I	2^-	6^-	0.642
39	^{138}Cs	3^-	6^-	0.082	40	^{146}La	2^-	6^-	0.022
41	^{148}Pr	1^-	6^-	0.092	42	^{148}Pm	1^-	6^-	0.140
43	^{120}In	1^+	3^+	0.200	44	^{120}In	1^+	8^-	0.302
45	^{122}In	1^+	4^+	0.102	46	^{122}In	1^+	8^-	0.222
47	^{130}In	1^-	10^-	0.052	48	^{130}In	1^-	5^+	0.402

the calculations performed under two assumptions on the form of the spin distribution of primary-fragment populations, that in (8) and that in (9). It can be seen that, as a rule, the observed isomeric ratios fall within the corridor determined by the calculated curves. As might have been expected, the rotation distribution in (9) prevails at low excitation energies, while the thermal distribution (8) is dominant at high excitation energies. This conclusion is also confirmed by data on the reaction ^{235}U(n_{th}, f) that are analyzed from the point of view of the fragment excitation energy (Fig. 22). Indeed, a transition from the distribution in (8) to the distribution in (9) improves the description of experimental data most radically for $\langle U\rangle = 6$–10 MeV; for $\langle U\rangle = 14$–20 MeV, a similar effect is much less pronounced.

Thus, the spins of fission fragment can be formed through two mechanisms: the rotational motion of a fragment upon the scission of a fissile nucleus and the internal motion of fragment nucleons. During the ac-

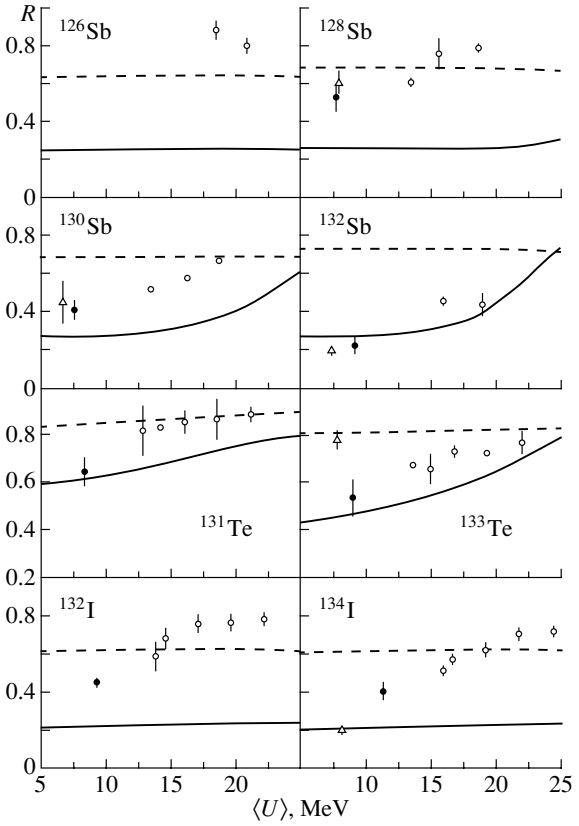

Fig. 21. Data on the isomeric ratios for nuclei produced in the reactions (open circles) ^{238}U(α, f), (closed circles) ^{241}Pu($n_{\rm th}$, f), and (open triangles) ^{235}U($n_{\rm th}$, f) [25]. The results of the calculations performed under the assumptions specified by Eqs. (9) and (8) are represented by the solid and dashed curves, respectively.

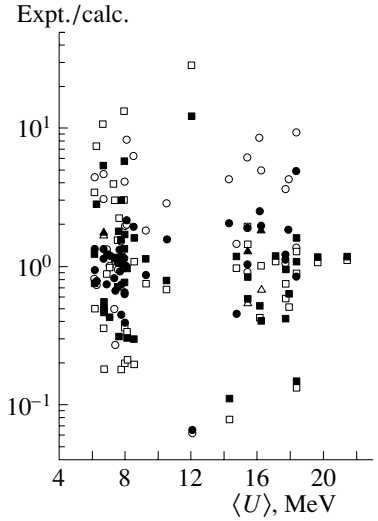

Fig. 22. As in Fig. 19, but versus the mean excitation energy of a fission fragment.

celeration of fission fragments, which is accompanied by the transformation of the potential energy of deformation into internal energy, the primary distribution of the form (9) is smeared in such a way that it takes the form (8), which is caused by the density of internal noncollective types of motion.

4. CONCLUSION

The statistical model of nuclear reactions and the cascade–evaporation model for the decay of excited nuclei have been used to analyze the emission properties of fragments formed in low-energy fission and their isomeric ratios. In order to justify the applicability of the approach combining these two models, the mean excitation energies of fission fragments as functions of their mass have been determined from experimental data on the mean multiplicities of neutrons and have been tested by using the condition of energy balance. The observed spectra of neutrons emitted by fission fragments of various masses have been reproduced by calculating the spectra of emitting nuclei at excitation energies equal to the mean excitation energies of fission fragments. The experimental dependences of the neutron multiplicities on the total kinetic energy of complementary fragments have been described in a model-dependent way under the basic assumption that the total available fission energy is distributed among fission fragments in proportion to the extracted mean excitation energies. The mean fission-fragment spins calculated at the mean excitation energies by using the assumption that the fission-barrier penetrability is independent of the orbital angular momentum agree with the analogous values extracted from experimental data. Two assumptions on the character of the distribution of the total angular momenta of fission fragments after their full acceleration—that using a distribution of a rotational origin and that using a distribution associated with single-particle motion—have been analyzed. It has been shown that the form of the spin distribution of primary-fragment populations is one of the key factors that affect the isomeric ratios of independent yields. It has turned out that, in order to describe the observed isomeric ratios, it is necessary to assume that this distribution may involve a component characterized by a fixed value of the total angular momentum.

ACKNOWLEDGMENTS

I am grateful to A.A. Goverdovski and W.I. Furman for stimulating discussions and advice.

This work was supported by INTAS (project no. 1929).

REFERENCES

1. W. Hauser and H. Feshbach, Phys. Rev. **87**, 366 (1952).
2. P. A. Moldauer, Phys. Rev. **135**, B642 (1964).
3. E. S. Troubetzkoy, Phys. Rev. **122**, 212 (1961).
4. S. M. Qaim, A. Mushtaq, and M. Uhl, Phys. Rev. C **38**, 645 (1988).
5. M. B. Chadwick and P. G. Young, Nucl. Sci. Eng. **108**, 117 (1991).
6. O. T. Grudzevich, Yad. Fiz. **61**, 29 (1998) [Phys. At. Nucl. **61**, 24 (1998)].
7. O. T. Grudzevich, Yad. Fiz. **64**, 11 (2001) [Phys. At. Nucl. **64**, 9 (2001)].
8. P. G. Young and E. D. Arthur, Los Alamos National Laboratory Report LA-6947 (1977).
9. M. Uhl and B. Strohmaier, Report IRK 76/01 (Vienna, 1976).
10. O. T. Grudzevich, A. V. Ignatyuk, and V. I. Plyaskin, in *Proceedings of International Conference on Nuclear Data for Science and Technology, Mito, Japan, 1988,* p. 1221.
11. D. Wilmore and P. E. Hodgson, Nucl. Phys. **55**, 673 (1964).
12. A. C. Wahl, At. Data Nucl. Data Tables **39**, 1 (1988).
13. C. Budtz-Jorgensen and H. H. Knitter, Nucl. Phys. A **490**, 307 (1988).
14. J. W. Boldeman, A. R. L. Musgrove, and R. L. Walsh, Aust. J. Phys. **164**, 1520 (1967).
15. I. During, V. Jahnke, and H. Marten, in *Proceedings of the Workshop on Nuclear Fission and Fission-Product Spectroscopy, Grenoble, France, 1994,* p. 202.
16. H. H. Knitter, F. J. Hamsch, and C. Budtz-Jorgensen, Z. Naturforsch. Teil A **42**, 786 (1987).
17. G. Audi and A. H. Wapstra, Nucl. Phys. A **595**, 409 (1995).
18. F. Pleasonton, R. Ferguson, and H. W. Schmitt, Phys. Rev. C **6**, 1023 (1972).
19. F. Pleasonton, Nucl. Phys. A **213**, 413 (1973).
20. K. Nishio, I. Kimura, and Y. Nakagome, *ISINN-7* (Dubna, 1997), p. 325.
21. H. Vonach, in *Proceedings of the IAEA Advisory Group Meeting, New York, 1983,* p. 247.
22. K. J. LeCouteur and D. W. Lang, Nucl. Phys. **13**, 32 (1959).
23. M. S. Samant, R. P. Anand, R. K. Choudhury, *et al.,* Phys. Rev. C **51**, 3127 (1995).
24. D. G. Madland and T. R. England, Nucl. Sci. Eng. **64**, 859 (1977).
25. G. Rudstam, in *Proceedings of a Specialists' Meeting on Fission Product Nuclear Data, Tokai, Japan, 1992,* p. 271.
26. J. P. Huizenga and R. Vandenbosch, Phys. Rev. **120**, 1305 (1960).
27. O. T. Grudzevich, Yad. Fiz. **62**, 227 (1999) [Phys. At. Nucl. **62**, 192 (1999)].
28. *Physics of Nuclear Fission,* Ed. by V. S. Stavinskiĭ (Gosatomizdat, Moscow, 1963).
29. A. L. Barabanov and V. I. Furman, in *Proceedings of XIII Meeting on Physics of Nuclear Fission, Obninsk, 1995,* p. 52.
30. J. L. Durell, in *Proceedings of 3rd International Conference "Dynamical Aspects of Nuclear Fission," Dubna, 1996,* Ed. by J. Kliman, p. 270.
31. G. A. Popeko *et al.,* in *Proceedings of International Conference on Fission and Properties of Neutron-Rich Nuclei, Florida, 1997,* p. 645.
32. G. M. Ter-Akopian *et al.,* Flerov Laboratory of Nuclear Reactions, Scientific Report 1995–1996, JINR (Dubna, 1997), p. 81.
33. H. Naik *et al.,* Nucl. Phys. A **648**, 45 (1999).

Translated by A. Isaakyan

Physics of Atomic Nuclei, Vol. 64, No. 9, 2001, pp. 1581–1593. Translated from Yadernaya Fizika, Vol. 64, No. 9, 2001, pp. 1660–1672.

NUCLEI
Theory

Statistical and Dynamical Aspects of the Description of the Cross Section for ^{238}U Fission Induced by 1- to 55-MeV Neutrons

M. I. Svirin

Institute of Physics and Power Engineering,
pl. Bondarenko 1, Obninsk, Kaluga oblast, 249020 Russia

Received April 20, 2000; in final form, July 13, 2000

Abstract—On the basis of statistical theory and on the basis of the Kramers and Grange–Weidenmüller diffusion model of fission, the cross section $\sigma_f(E_n)$ for ^{238}U fission induced by 1- to 55-MeV neutrons is calculated under the assumption that dynamical effects are damped at low excitation energies. It is shown that the structure of the fission cross section from a statistical calculation differs substantially from that in a dynamical description. The reduced coefficient of nuclear friction (viscosity) is found to be $\beta = 4.1 \times 10^{21}$ s^{-1}. This value and the estimate $\beta \geqslant 5 \times 10^{21}$ s^{-1}, which was obtained by analyzing the mean multiplicity of prefission neutrons in heavy-ion-induced fission reactions, suggest supercritical damping and the one-body mechanism of nuclear viscosity. © *2001 MAIK "Nauka/Interperiodica".*

1. INTRODUCTION

In [1], the effect of nuclear viscosity (friction) on fissility within the diffusion model was considered in analyzing the energy dependence of the fission probability, $P_f(E)$, for preactinide nuclei. For the fission reaction $^{238}\mathrm{U}(x, xn'f)$, the statistical and the dynamical approach are used in the present study to describe the cross section by decomposing it into terms corresponding to different numbers ($x = 0, 1, \ldots$) of prefission neutrons (so-called chance structure of the cross section). An analysis of data on the fission cross sections for actinide nuclei, $\sigma_f(E_n)$, revealed [2, 3] that the statistical model reproduces satisfactorily the absolute values and the energy dependence of $\sigma_f(E_n)$ in the traditional region of bombarding-neutron energies ($E_n < 20$ MeV). Within this framework, the parameters of the statistical description (neutron-absorption cross sections, fission barriers, level-density parameters, and so on) have physically reasonable values. Difficulties arise, for example, when attempts are made to reproduce the absolute values of experimental fission cross sections at higher energies of $E_i \geqslant 20$ MeV [4]. This disagreement between the theory and experimental data may partly be due to nuclear friction, which is disregarded within the statistical description. A fit to experimental data that is based on varying parameters—for example, the absorption cross section in [4]—can mask an actually existing physical phenomenon.

By studying the effect that dissipative processes caused by nuclear-matter viscosity can have on various features of the fission process, one can deduce information about the magnitude of the coefficient of nuclear viscosity and clarify the nontrivial physics behind dissipation and viscosity (or friction) in nuclei. So far, such data have been insufficiently accurate to pinpoint the theory (that of one-body or that of two-body dissipation) adequately describing dynamical effects. The type of viscosity operative in the processes has a profound effect on the dynamics of collective motion. The mechanism of one-body dissipation predicts a large viscosity of nuclear matter and supercritical damping of nuclear motion. At the same time, two-body dissipation within a nucleus may appear to be weak because of the Pauli exclusion principle suppressing two-body collisions, which has a less drastic effect only in the surface region. In relation to the case of zero friction, one-body (two-body) dissipation leads to less (more) prolate configurations at the scission point [5].

Analyses of the mass–energy distributions [6] and of the yields [5] of prefission neutrons seems to suggest collective motion undergoing supercritical damping, favoring the hypothesis of one-body (rather than two-body) dynamics. Unfortunately, independent information about the magnitude of the coefficient of the nuclear friction is not precise. In order to obtain deeper insights into dissipation in nuclei, it is advisable to extend the analysis of traditionally used data by including new experimental information about the features of the fission process.

By considering the reaction $^{238}\mathrm{U}(n, xn'f)$ by way of example, it will be shown in this study that, by analyzing the experimental cross sections for the fission

of actinide nuclei (these cross sections were measured over a sufficiently wide range of bombarding-neutron energy) within the statistical model at low energies ($E_n < 20$ MeV) and within the diffusion model proposed by Kramers [7] and by Grange and Weidenmüller [8] at high energies ($E_n > 20$ MeV), one can deduce information about the coefficient of nuclear-matter viscosity. It should be borne in mind that, in describing fissility, the application of the diffusion model is complicated by an almost complete absence of theoretical and experimental information about the temperature dependence of the coefficient of viscosity. In the low-temperature region corresponding to $E_n < 20$ MeV, we can assume that this coefficient is close to zero, because the statistical model provides here an acceptable description of experimental data. In the high-temperature region corresponding to $E_n > 20$ MeV, it is believed that the coefficient of viscosity is nonzero and is virtually independent of the excitation energy. In the intermediate region, between the two values (zero and constant) of the coefficient of viscosity, its energy dependence was simulated with the aid of a function that describes the damping of dynamical effects at low energies. This function had the form of a smoothed step and ensured continuity of the computed features over the entire neutron-energy range under investigation in going over from the statistical to the diffusion branch of the calculation.

2. STATISTICAL DESCRIPTION OF THE FISSION CROSS SECTION

An analysis of the fission cross section for actinide nuclei and its chance structure has been performed predominantly in the bombarding-neutron-energy region $E_n < 20$ MeV, which is traditionally studied and which contains the bulk of experimental data on cross sections for the fission of heavy nuclei. As a rule, relevant theoretical estimates were obtained within the statistical model. In deducing them, it was assumed that the nonequilibrium decay mechanism contributes only at the first stage of the emission cascade and that, at all the remaining stages, neutron emission is purely evaporative.

In previous studies, the statistical calculation included nearly the entire variety of concepts of the density $\rho_{\text{in}}\,(U, J)$ of excited states—that is, the constant-temperature model, the Fermi gas model, the superfluid model [9], combinatorial calculations [10], and hybrid approaches combining different models in a unified description [11, 12]. This is one of the main sources of discrepancies between the results of the calculations and analyses of $\sigma_f\,(E_n)$.

In the statistical description of the cross section for ^{238}U fission, use is made here of the basic results obtained in [3] from an analysis of $\sigma_f(E_n)$ and its chance structure up to $E_n < 20$ MeV for a chain of nuclei from ^{233}U to ^{238}U. The calculations of the single-particle spectrum in [3] were performed for a deformed Woods–Saxon potential, and this spectrum was then used as a basis for evaluating the density $\rho_{\text{in}}(U, J)$ of internal excitations within the superfluid model of the nucleus [9]. In contrast to the noninteracting-particle (Fermi gas) model, the superfluid model of the nucleus takes into account, at low energies, residual pair interaction of the correlation type. A consistent description of the level density with allowance for collective excitations of nuclei has yet to be obtained. Their contribution is estimated in the adiabatic approximation [13], where the excitations of various physical origins are taken into account in terms of factors [9] as

$$\rho(U, J) = \rho_{\text{in}}(U, J) \times K_{\text{rot}}(U) \times K_{\text{vib}}(U), \qquad (1)$$

where K_{rot} and K_{vib} are the coefficients of, respectively, rotational and vibrational enhancement of the level density. In the case of sufficiently hot nuclei, K_{vib} can easily be estimated by the formula obtained within the liquid-drop model [9]. As a rule, the possible distinction between K_{vib} values in the fission and in the neutronic channel was ignored in this study. This was motivated by the smallness of K_{vib} and its variations in relation to K_{rot}. The best that we can do is to set $K_{\text{vib},f} = K_{\text{vib},n}$. The coefficients of the rotational and the vibrational enhancement of the level density K_{rot} depend strongly on the symmetry of the nuclear shape (see below).

Let us briefly dwell on the basic elements of a statistical calculations of $\sigma_f\,(E_n)$. Reactions of a type $(n, xn'f)$ involving various numbers x of prefission neutrons are often referred to as fission chances. Specifically, the fission of the primary nucleus A—^{239}U in our case—is the first chance; accordingly, the fission of the $A - x$ nucleus is the $(x + 1)$th chance. After the emission of x neutrons, the $(x + 1)$th fission chance comes into play if the excitation energy of the primary nucleus A satisfies the condition

$$E \geqslant B_f^{A-x} + \sum_{i=1}^{x} B_n^{A+1-x} = E_x, \qquad (2)$$

where B_f and B_n are, respectively, the height of the fission barrier and the deuteron binding energy for nuclei whose mass numbers are indicated in the superscripts. At $x = 1$, the entire right-hand side of inequality (2)—that is $B_f^{A-1} + B_n^A = E_1$, reduces to the threshold for emission fission. The fission cross section $\sigma_f\,(E)$ is the sum of the partial cross sections $\sigma_{fx}\,(E)$ for individual chances:

$$\sigma_f(E) = \sum_{x=0}^{x_{\max}(E)} \sigma_{fx}(E). \qquad (3)$$

For $x = x_{\max}(E) + 1$, the fission of residual nuclei $A - x$ is not favored energetically. In calculating $\sigma_{fx}(E)$ and, accordingly, $\sigma_f(E)$, we can use the Hauser–Feshbach formalism (codes of the STAPRE type) or relationships of the statistical model in the semiclassical approximation [9, 14]. In the energy region under consideration, the two approaches lead to similar estimates of the cross sections. In [3], the calculation was based on the STAPRE code. In describing fissility on the basis of the diffusion model, use is made here of the semiclassical approach, which admits a convenient inclusion of nuclear-viscosity effects.

According to general concepts of the compound-nucleus model, the relations for fissility (fission probability) can be represented in the form

$$P_f(E) = \frac{\sigma_f(E)}{\sigma_c(E)} \tag{4}$$
$$= \sum_J \sigma_c^J(E) \frac{\Gamma_f J}{\Gamma_f^J + \sum_i \Gamma_i^J} \Big/ \sum_J \sigma_c^J(E),$$

where σ_c^J is the cross section for the formation of a compound nucleus having the excitation energy $E = E_n + B_n$ and a fixed value of the angular momentum J, $\sigma_c = \sum_J \sigma_c^J$ is the total cross section for the formation of a compound nucleus, Γ_f^J is the fission width, and Γ_i^J stands for the widths with respect to decays competing with fission ($i = n, \gamma$, and so on). By using the formula for the level density in the fissile nucleus for the transition state and a similar formula for the level density in the competing channel—the neutronic one in the present case—the ratio of the fission width and the neutronic width can be represented in the form [9, 15]

$$\Gamma_f^J / \Gamma_n^J = \gamma(J) \Gamma_n / \Gamma_n, \tag{5}$$

where all factors dependent on the angular momentum are included in the factor $\gamma(J)$ and where Γ_f and Γ_n are, respectively, the fission width and the neutron widths at zero angular momentum ($J = 0$).

Within the model of a two-humped barrier, the mean fission width is described by the relation [9, 16]

$$\overline{\Gamma f}(E) \tag{6}$$
$$= \Gamma_{fA}(E) \Gamma_{fB}(E) / (\Gamma_{fA}(E) + \Gamma_{fB}(E)),$$

where

$$\Gamma_{fi} = \frac{1}{2\pi \rho_c(E, 0)} \tag{7}$$
$$\times \int_0^{E - B_{fi}} \left[1 + \exp\left(\frac{2\pi k}{\hbar \omega_i}\right)\right]^{-1} \rho_{fi}(E - B_{fi} - k) dk$$

are the fission widths for the humps ($i = A, B$) and B_{fi} and $\hbar\omega_i$ are, respectively, the heights and the curvature parameters of the humps. At $J = 0$, the neutronic-channel width has the form

$$\Gamma_n(E) = \frac{1}{2\pi^2 \rho_c(E, 0)} \tag{8}$$
$$\times \int_0^{E - B_n} g_n k_n^2(\varepsilon_n) \sigma_{cn}(\varepsilon_n, U) \rho_n(U, 0) d\varepsilon_n.$$

Here, $g_n k_n^2 = (2s_n + 1) 2 m_n \varepsilon_n / \hbar^2$, where s_n, m_n, and ε_n are, respectively, the spin, mass, and energy of the emitted neutron; E, U, ε_n, and B_n are related by the balance equation $E = U + \varepsilon_n + B_n$; $\rho_j(U, 0)$ is the nuclear-level density for zero angular momentum; and the index $j = c, f, n$ labels quantities referring to the compound nucleus, fission channel, and the neutronic channels, respectively. In Eq. (8), the cross section $\sigma_{cn}(\varepsilon_n, U)$ for the inverse reaction is set to the cross section for compound-nucleus formation in bombarding the ground-state target nucleus ($U = 0$) by neutrons with an energy ε_n and is calculated on the basis of the optical model. Within the Brink–Axel model [17], we can estimate the radiative width Γ_γ, thereby taking into account the competition of the γ channel.

In relation (4), the cross section σ_c^J for compound-nucleus formation is determined by the expression

$$\sigma_c^J = \pi \lambda_n^2 g_J T_J(E_n), \tag{9}$$

where λ_n is the wavelength of the incident neutrons, $g_J = (2J + 1) / (2s_n + 1)(2I_0 + 1)$ is a statistical factor, and T_J stands for sticking coefficients. In order to simplify the description, we can use, in (4) and (9), the semiclassical estimate of the sticking coefficients,

$$T_J = \begin{cases} 1 & \text{for } J \leqslant J_{\max} \\ 0 & \text{for } J > J_{\max}. \end{cases} \tag{10}$$

It is reasonable to determine the maximal angular momentum $J_{\max}$ on the basis of the optical calculations:

$$J_{\max}^2 = \frac{2 \sum\limits_J (2J + 1) T_J J(J + 1)}{\sum\limits_J (2J + 1) T_J} = 2 \langle J^2 \rangle_{\text{opt}}. \tag{11}$$

In the semiclassical approximation, expression (4) for the fissility (without allowance for the competition of photons) can be represented in the form

$$P_f(E) = J_{\max}^{-2} \int_0^{J_{\max}} \frac{(2J + 1)\, dJ}{1 + \sum\limits_{i = A, B} \gamma_i^{-1} \Gamma_n / \Gamma_{fi}}. \tag{12}$$

Similar expressions can be obtained for the differential and for the integrated probabili-

ty $[dP_n(\varepsilon_n, E)/d\varepsilon_n$ and $P_n(E)]$ of neutron emission [14]. The fission cross section, the spectrum, and the total cross section for equilibrium neutron emission are given by

$$\sigma_f = \sigma_c P_f, \quad d\sigma_n/d\varepsilon_n = \sigma_c dP_n/d\varepsilon_n, \qquad (13)$$
$$\sigma_n = \sigma_c P_n.$$

The cross section σ_c for compound-nucleus formation is related to the neutron-absorption cross section $\sigma_{\rm abs}$ by the equation

$$\sigma_c = \sigma_{\rm abs} - \sigma_{\rm pr} = \sigma_{\rm abs}[1 - q_{\rm pr}(E)], \qquad (14)$$

where $\sigma_{\rm pr}$ and $q_{\rm pr}(E)$ are, respectively, the cross section for nonequilibrium (preequilibrium) neutron emission and its fraction in $\sigma_{\rm abs}$. These quantities can be estimated within the exciton model for preequilibrium decay [18]. The total spectrum of first-chance neutrons ($x = 1$) is the sum of the spectra of equilibrium and preequilibrium neutrons:

$$d\sigma_{n1}/d\varepsilon_n = \sigma_c dP_n(\varepsilon_n, E)/d\varepsilon_n \qquad (15)$$
$$+ \sigma_{\rm abs} dP_{\rm pr}(\varepsilon_n, E)/d\varepsilon_n.$$

It is assumed that the spectra of second-chance neutrons and of neutrons of further chances ($x \geqslant 2$) are formed by the purely evaporation mechanism of the reaction.

The above relations are valid for the calculation of the decay features of the primary nucleus A at a fixed value of the excitation energy E. The formulas for calculating analogous features of $A - x$ nuclei formed after the emission of x neutrons ($x \geqslant 1$) become somewhat more complicated [14] since these nuclei are distributed in excitation energy U between 0 and $U^{\max}_{A-x} = E - \sum_{i=1}^{x} B_{n\,A+1-i}$. The quantities σ_{fA-x} and $d\sigma_{nx+1}/d\varepsilon_n$ can be obtained by integrating $P_f(U_{A-x})$ and $dP_n(\varepsilon_n, U_{A-x})/d\varepsilon_n$ with respect to the excitation energy for the residual nuclei $A - x$ (for more details, see [14]).

3. EFFECT OF THE DAMPING OF THE ROTATIONAL-MODE CONTRIBUTION TO THE LEVEL DENSITY ON THE DESCRIPTION OF THE FISSION CROSS SECTION

The dependence of the coefficient of rotational enhancement of the level density, $K_{\rm rot}(U)$, in (1) on the symmetry of nuclear shapes was investigated in [13], where one can also find adiabatic estimates of $K_{\rm rot}(U)$, which are valid at sufficiently low excitation energies. That the mode of the single-particle motion in a nucleus and its rotation as a discrete unit are independent indicates that the problem of calculating $K_{\rm rot}(U)$ is adiabatic, the ratio of the temperature T to the quadrupole deformation ε being the measure of the deviation from adiabaticity. The temperature at which the assumption of adiabaticity becomes meaningless was estimated in [13] as

$$T_0 = \hbar\bar{\omega}_0\varepsilon \approx 41A^{-1/3}\varepsilon, \qquad (16)$$

where $\bar{\omega}_0$ is the mean frequency for an anisotropic oscillator potential. For $T \geqslant T_0$, there must occur a damping effect that is associated with the interaction of internal and collective (rotational) degrees of freedom of a deformed nucleus and which is manifested in reduction of $K_{\rm rot}(U)$ in relation to the adiabatic estimate, with $K_{\rm rot}(U)$ tending to unity in the limit of large U values.

In all probability, Ignatyuk *et al.* [19] were the first who made an attempt at taking into account the damping of rotational modes in describing the probability of deformed-nucleus fission. The damping function was determined empirically and was assumed to be the same in the fission channel and in the neutronic channel. This contradicts the theoretical estimates that were presented in [13] and which showed that this function depends greatly not only on the excitation energy but also on the nuclear deformation. The more recent numerical calculations of Hansen and Jensen [20], who used the $SU(3)$ single-particle shell model to investigate the energy dependence of the level density in nuclei characterized by various forms of ground-state symmetry, confirmed the estimates from [13]. These authors also established that the rotational-mode contribution can decrease with increasing temperature because of a gradual disappearance of the asymmetry of nuclear shapes. By way of example, we indicate that, at energies of $U \geqslant 20$ MeV, the level density in a nucleus having the shape of a three-axis ellipsoid in the ground state ($K^{\rm ad}_{\rm rot} = \sqrt{\frac{\pi}{2}}\sigma_x\sigma_y\sigma_z \approx \sqrt{\frac{\pi}{2}}\sigma_\parallel\sigma_\perp^2$) does not differ from those in axisymmetric and mirror-symmetric nuclei ($K^{\rm ad}_{\rm rot} = \sigma_\perp^2$); at still higher excitation energies, it does not differ from the level density in a spherical nucleus ($K^{\rm ad}_{\rm rot} = 1$).

In connection with practical applications, it is convenient to represent $K^{\rm ad}_{\rm rot}(U)$ for a deformed nucleus as the product of two factors,

$$K^{\rm ad}_{\rm rot}(U) = K^{\rm ad}_1(U) \times K^{\rm ad}_2(U). \qquad (17)$$

The factor $K^{\rm ad}_1(U)$, which characterizes an additional enhancement of the level density in axisymmetric and mirror-symmetric nuclei [$K^{\rm ad}_{\rm rot}(U) = \sigma_\perp^2 = K^{\rm ad}_2(U)$] owing to the disappearance of the nuclear-shape symmetry, is given by

$$K_1^{\rm ad}(U) = \begin{cases} 2 & \text{for axisymmetric nuclei that display mirror asymmetry} \\ \sqrt{\pi/2\sigma_\parallel} & \text{for nuclei that do not possess symmetries other than that} \\ & \text{with respect to a rotation through an angle of } 180^\circ \text{ about three axes} \\ \sqrt{2\pi}\sigma_\parallel & \text{for axially asymmetric nuclei that possess mirror symmetry} \\ \sqrt{8\pi}\sigma_\parallel & \text{for nuclei that do not possess rotational symmetry.} \end{cases} \quad (18)$$

The damping of each of the quantities $K_i^{\rm ad}(U)$ can be approximated by the expression [20]

$$K_i(U) = 1 - F_i(U) + F_i(U)K_i^{\rm ad}(U), \quad (19)$$

where the damping function has the form

$$F_i(U) = [1 + \exp(U - U_i)/d_i]^{-1.} \quad (20)$$

Here, the parameters U_i and d_i depend greatly on deformation values that characterize specific symmetry violations ($i = 1$ for axial symmetry and $i = 2$ for spherical symmetry).

The approximate relations for determining U_i and d_i can be found in [20]. The estimated values show a large scatter. On the basis of the numerical calculations for the nuclear-level density from [20], it can be stated with confidence that, for $U \geqslant 20$ MeV, there is no difference in this respect between axisymmetric and mirror-symmetric nuclei, on one hand, and nuclei displaying shape asymmetry in the ground state, on the other hand. This means that $K_1(U) = 1$ for $U \geqslant 20$ MeV. In describing nuclear fissilities, the fact that, for axisymmetric nuclei, the characteristic energies are proportional to the square of the deformation, $U_2 \approx 120A^{1/3}e^2$ [20], leads to important consequences. The damping of $K_2(U) = K_2^{\rm ad}(U)$ because of the transition from the axial shape at the saddle point ($\varepsilon_A \sim 0.6$, $\varepsilon_B \sim 0.8$) to the spherical shape can be disregarded in the region of intermediate energies, $U \leqslant 100$ MeV. In the neutronic channel ($\varepsilon \sim 0.24$), deviations of $F_2(U)$ from unity become noticeable at energies of $U \geqslant 50$ MeV.

In the present analysis of the cross section for ^{238}U fission induced by 1- to 55-MeV neutrons, estimates of the fission width and of the neutronic width were obtained at $K_2(U) = K_2^{\rm ad}(U)$. Because the inner hump A is mirror-symmetric and axially asymmetric ($N \geqslant 146$) and because the outer hump B is, on the contrary, axisymmetric and mirror-asymmetric [21], we have $K_1^{\rm ad} = \sqrt{2\pi}\sigma_\parallel$ and 2 for A and B, respectively. It can be seen from Fig. 1 that, without taking into account the damping of the asymmetric component, the calculated values of $\sigma_f(E_n)$ for ^{238}U can be matched with experimental data up to $E_n = 16$ MeV. For $E_n > 16$ MeV, the calculated curve lies much higher than the experimental points, which represent the standard values of the cross section for neutron-induced fission of ^{238}U from [22]. The cross section $\sigma_f(E_n)$ was calculated with model parameters (including fission barriers and level-density parameters) set to values that are rather close to those that were obtained by analyzing the experimental cross sections for $^{232-238}$U nuclei within the approach developed in [3]. The neutron-absorption cross section $\sigma_{\rm abs} = \sigma_r - \sigma_{\rm dir}$ for ^{238}U was determined on the basis of calculating the reaction cross section σ_r and the cross section $\sigma_{\rm dir}$ for the direct excitation of low-lying states in inelastic neutron scattering within the coupled-channel method as implemented in the ECIS code [23] with the optical-model parameters for the deformed Young potential [24].

The theoretical calculations of the cross section for the neutron-induced-fission of $^{233-283}$U that were performed in [4] up to the neutron energy of $E_n = 100$ MeV with the same Young optical potential and which were based on the assumption that the shape of the fissile nuclei in question at the saddle point has no rotational symmetry ($K_1^{\rm ad} = \sqrt{8\pi}\sigma_\parallel$) considerably overestimate $\sigma_f(E_n)$ at $E_n = 7$ MeV and higher energies. Those calculations employed the internal-excitation density according to the single-particle spectrum of the Nilsson model. The authors of [4] included, in their calculations, the damping of the asymmetric component of the rotational enhancement of the level density at the saddle point according to (19) and (20) with parameter values close to $U_1 = 7$ MeV and $d_1 = 0.8$ MeV. This enabled them to match the theoretical description with the experimental results up to an energy of 17 MeV. At higher energies E_n, the statistical calculation overestimates the fission cross section.

For two parameter sets—(i) $U_1 = 7$ MeV, $d_1 = 0.8$ MeV and (ii) $U_1 = 16$ MeV, $d_1 = 1.2$ MeV—Fig. 1 illustrates the effect that the damping of the coefficient $K_1(U)$ of rotational enhancement of the level density as given by Eqs. (19) and (20) exerts on the results of cross-section calculations. In relation to the results of the original calculation without damping, which agree with data in the range $E_n = 1-15$ MeV, the curve corresponding to the calculations with the first parameter set begins to deviate from experimental points at an energy value as low

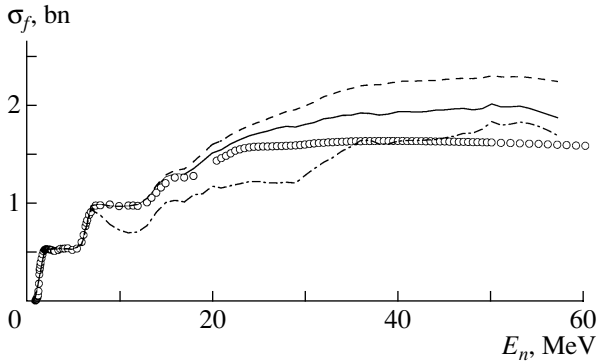

Fig. 1. (○) Standard values of the cross section for the neutron-induced fission of ^{238}U [22] along with a statistical description represented by the curves that correspond to (dashed curve) the calculations employing the adiabatic estimate of the coefficient of rotational enhancement of the level density and the calculations allowing for the damping of the asymmetric component $K_1(U)$ at the saddle point according to (19) with the damping function (20) at (dash-dotted curve) $U_1 = 7$ MeV and $d_1 = 0.8$ MeV and (solid curve) $U_1 = 16$ MeV and $d_1 = 1.2$ MeV.

as $E_n \geqslant 7$ MeV. The second parameter set provides the best description of $\sigma_f^{\exp}(E_n)$, but there is still no perfect agreement with experimental data. The corresponding curve lies closer to the experimental points than the curve computed without damping, but it nevertheless goes noticeably higher than the experimental fission cross section for $E_n \geqslant 18$ MeV.

Lestone and Gavron [4] were able to obtain a satisfactory description of the experimental data over the entire range of E_n under investigation using an adjustable factor by which they multiplied the absorption cross section $\sigma_{\rm abs}(E_n)$. The value of this factor changed from 1 at $E_n = 17$ MeV to 0.82 at 100 MeV. The required modification to $\sigma_{\rm abs}(E_n)$ can be obtained by the method proposed in [25]. Specifically, the Young potential proposed in [24] and taken as a basis was modified in [25]. At high energies, this potential leads to smaller values of the cross section $\sigma_{\rm abs}(E_n)$ than the original Young potential. Such ad hoc tricks are not quite correct. Their application is not motivated by any actual physical grounds. By considering the example of ^{238}U fission, it will be shown below that the discrepancy between the statistical estimates of the fission cross section and experimental results can be removed by taking into account, in theoretical calculations, effects associated with nuclear-matter viscosity.

4. FISSION CROSS SECTION IN DIFFUSION MODEL

The application of principles of Brownian motion in a force field to the problem of propagation of a nuclear system through a barrier proved to be very efficient, for example, in explaining the systematic excess of the experimental multiplicity of prefission neutrons in heavy-ion reactions [5, 26] over the results of the calculations within the statistical model. In the diffusion model, the fission variable x (deformation) and the conjugate momentum $p = \mu u$ are considered as classical variables. The time evolution of a nuclear system in two-dimensional phase space is described in terms of the distribution function (probability density) $W(x, u, t)$ satisfying the Fokker–Planck equation [8, 27]

$$\frac{\partial W(x,u,t)}{\partial t} = -u\frac{\partial W(x,u,t)}{\partial x} - k(x)\frac{\partial W(x,u,t)}{\partial u} + \beta\frac{\partial [uW(x,u,t)]}{\partial u} + \vartheta\frac{\partial^2 W(x,u,t)}{\partial u^2}, \quad (21)$$

where $k(x) = -\mu^{-1}\partial V(x)/\partial x$, $V(x)$ being the potential energy of deformation; $\beta = \eta/\mu$ is the reduced coefficient of nuclear friction (the ratio of the coefficient η of nuclear friction to the reduced mass μ of the nuclear system); and $\vartheta = \beta T/\mu$ is the diffusion coefficient, $T = (E/a)^{1/2}$ being the temperature of the nucleus (heat bath). The reduced mass $\mu = M_1M_2/(M_1 + M_2)$ (M_1 and M_2 are the masses of complementary fragments) is equal to $\mu = M/4$ at $M_1 = M_2 = M/2$.

On the basis of principles of Brownian motion, it is very difficult to obtain a general solution to the problem of overcoming a potential barrier by using the Fokker–Planck equation. Of special interest is the particular case where the initial quasistationary and the intermediate state are physically significant. This means that the potential-barrier height corresponding to the deformation $x = x_0$ is much greater than the energy of the thermal motion; that is, the condition $B_f \gg T$ is satisfied. This condition is necessary for the applicability of the transition-state method within a statistical analysis of the problem, where it is assumed that internal degrees of freedom are in equilibrium with collective degrees of freedom (which are associated with fission). In contrast to the statistical approach, the diffusion model takes into account the interaction between them, which was simulated in [7] by nuclear friction ($\beta \neq 0$). In this case, an equilibrium distribution cannot be established at all values of x. By virtue of the condition $B_f \gg T$, only in a close vicinity of the first minimum of the potential energy $V(x)$, $x = x_1$, can the actual distribution be

approximated, to a high precision, by the equilibrium Maxwell–Boltzmann distribution

$$W^{MB}(x,u) = C\exp[-(\mu u^2/2 + V(x))/T]. \quad (22)$$

It can easuly be verified that the function in (22) satisfies the Fokker–Planck Eq. (21). For $x > x_0$, it is assumed that the level density is much less than that which would follow from the equilibrium distribution (22). A slow diffusion occurring through the barrier tends to restore equilibrium conditions at all values of x.

Assuming that the quasistationarity conditions $\partial W(x,u,t)/\partial t = 0$ hold everywhere and approximating the deformation energy $V(x)$ in the vicinity of the saddle point $x = x_0$ and in the vicinity of the first minimum $x = x_1$ by the quadratic forms

$$V_i(x) = \begin{cases} B_f - \mu\omega_0^2(x-x_0)^2/2 & \text{around } x = x_0 \\ \mu\omega_1^2(x-x_1)^2/2 & \text{around } x = x_1, \end{cases} \quad (23)$$

where ω_0 and ω_1 are the oscillator frequencies associated with the curvature of $V(x)$ at the saddle point $x = x_0$ and in the first potential well $x = x_1$, respectively, one can obtain a solution to the Fokker–Planck equation in the form

$$W_i(x,u) = \begin{cases} W_0^{\mathrm{MB}}(x,u)[(a-\beta)/2\pi\vartheta]^{1/2}\displaystyle\int_{-\infty}^{\xi}\exp[-(a-\beta)z^2/2\vartheta]dz, \text{ in the vicinity of} x = x_0, \\ W_1^{\mathrm{MB}}(x,u), \text{ in the vicinity of}(x = x_1), \end{cases} \quad (24)$$

where $W_i^{\mathrm{MB}}(x,u) = C\exp[-(\mu u^2/2 + V_i(x))/T]$, $a = (\beta^2/4 + \omega_0^2)^{1/2} + \beta/2$, and $\xi = u - a(x - x_0)$. The fission width according to Kramers [7], which is associated with the time-independent solution to the Fokker–Planck equation is given by

$$\Gamma_f^{\mathrm{K}} = \hbar J_0/N_1 \quad (25)$$
$$= (\hbar\omega_1/2\pi)\exp(-B_f/T)$$
$$\times\left\{\left[(\beta/2\omega_0)^2 + 1\right]^{1/2} - (\beta/2\omega_0)\right\},$$

where

$$J_0 = \int_{-\infty}^{+\infty} W_0(x = x_0, u)u\,du = C(T/\mu)$$
$$\times[(a-\beta)/a]^{1/2}\exp(-B_f/T)$$

is the diffusion current through the saddle point $x = x_0$ and

$$N_1 = \int_{-\infty}^{+\infty}\int_{-\infty}^{+\infty} W_1(x,u)dx\,du = C(2\pi T/\mu\omega_1)$$

is the number of nuclei (states) in the first well of the potential energy of deformation. If there is no dynamical friction (that is, under the condition $\beta \to 0$), we have

$$\Gamma_f^{\mathrm{K}}(\beta \to 0) = (\hbar\omega_1/2\pi)\exp(-B_f/T). \quad (26)$$

Expression (26) is sometimes referred to as the approximation of the transition-state method.

For $E - B_f \geqslant 3$ MeV, the fission width determined by the popular Bohr–Wheeler formula

$$\Gamma_f^{\mathrm{BW}} = \hbar\frac{J_0(E - B_f)}{N_1(E)} \quad (27)$$
$$= \hbar\frac{(dE/2\pi\hbar)\int_0^{E-B_{\mathrm{f}}}\rho(E - B_{\mathrm{f}} - k)\,dk}{\rho(E)\,dE},$$

with the level density corresponding to the constant-temperature model, $\rho(U) = C\exp(U/T)$, can be approximated, to a high precision, by the expression

$$\Gamma_f^{BW} = (T/2\pi)\exp(-B_f/T). \quad (28)$$

As was shown by Strutinsky [28], the factors in front of the exponential $\exp(-B_f/T)$ in (28) and (26) are different ($T/2\pi$ and $\hbar\omega_1/2\pi$, respectively) because collective-motion states were disregarded in determining the number of the initial state, $N_1(E)$, in (27). But it is precisely the space of these states that should be considered in estimating the current $J_0(E - B_f)$ at the fission barrier. With allowance for collective motion, the number of the initial states of nuclei having excitation energies between E and $E + dE$ is given by

$$N_1(E) = (dE/2\pi\hbar) \quad (29)$$
$$\times\int dx\int dp\rho(E - E_{col}(x,p)).$$

If we assume, as is usually done, that $E \gg E_{col}$, the correct formula (29) yields

$$N_1(E) = (T/\hbar\omega_1)\rho(E)dE. \quad (30)$$

The corresponding fission width $\Gamma_f'^{BW}$, which differs by the factor $\hbar\omega_1/T$ from that which is traditionally used, coincides with (26):

$$\Gamma_f'^{BW} = (\hbar\omega_1/T)\Gamma_f^{BW} = \Gamma_f^{\mathrm{K}}(\beta \to 0). \quad (31)$$

The relationship between $\Gamma_f^{\mathrm{K}}(E,\beta)$ according to Kramers and $\Gamma_f'^{\mathrm{BW}}(E)$ according to Bohr and

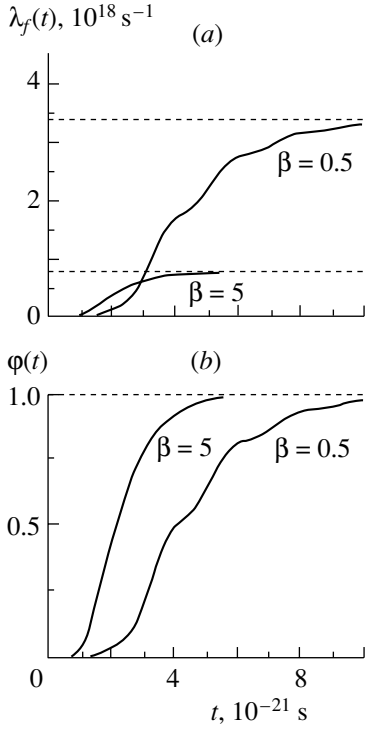

Fig. 2. Characteristics of the transient process in the fission of the excited nucleus ^{239}U at temperature $T =$ 1.5 MeV for two values of the coefficient of friction β (in units of 10^{21} s^{-1}): (a) time dependence of the fission rate $\lambda_f(t)$ calculated at the saddle point (the dashed curves represent the Kramers quasi-steady-state values λ_f^{K}) and (b) function $\varphi(t) = \lambda_f(t)/\lambda_f^{\mathrm{K}}$ demonstrating how the quasi-steady-state value Γ_f^{K} (dashed curve) is established.

Wheeler (with allowance for the factor $\hbar\omega_1/T$) has the form

$$\Gamma_f^{\mathrm{K}}(E,\beta) = \Gamma_f'^{\mathrm{BW}}(E) \times \left[\sqrt{(\beta/2\omega_0)^2+1} - (\beta/2\omega_0)\right] = \Gamma_f'^{\mathrm{BW}}(E)\tilde{\gamma}(\beta/2\omega_0). \quad (32)$$

In many studies, the factor $\hbar\omega_1/T$, by which Γ_f^{K} differs from Γ_f^{BW} in the case of low friction, was disregarded in the calculations. It follows from (32) that, for the steady-state case, the presence of nuclear-matter viscosity ($\beta > 0$) leads to a reduction of the fission width in relation to $\Gamma_f'^{BW}$, since $\tilde{\gamma}(\beta/2\omega_0) < 1$. This is due to a decrease in the probability of penetration of the fissile system through the barrier. The critical damping occurs at $\beta/2\omega_0 = 1$ ($\tilde{\gamma}(1) = \sqrt{2}-1$).

As a matter of fact, the quasi-steady-state flux through the fission barrier is established after a lapse of some characteristic time $\tau(\beta)$ (not instantaneously) that depends on the reduced coefficient β of nuclear friction. The time $\tau(\beta)$ characterizes the interaction of the fission degree of freedom with the rest of the system (heat bath). The problem of the time-evolution of a fissile system can be solved analytically with the aid of the time-dependent Fokker–Planck equation (21) [8] if $V(x)$ is approximated by the harmonic oscillator (23) in the vicinities of x_0 and x_1. In this case, the fission width is given by

$$\Gamma_f(t) = \hbar\lambda_f(t) = \frac{\hbar\sigma_u\sqrt{1-\phi^2}}{2\pi\sigma_x} \times \left[1 - \frac{\vartheta}{(\beta+A)\,\sigma_u^2(1-\phi^2)-\vartheta}\right]^{1/2} \times \exp\left[-\frac{B_{\mathrm{f}}}{(1-\phi^2)\,\sigma_x^2\mu\omega_1^2}\right]. \quad (33)$$

Here, $\phi = \exp(-\beta t)$,

$$\sigma_x^2 = \frac{T}{\mu\omega_1^2} \times \left\{1-\phi\left[2\frac{\beta^2}{\beta_1^2}\sinh^2\left(\frac{1}{2}\beta_1 t\right)+\frac{\beta}{\beta_1}\sinh(\beta_1 t)+1\right]\right\},$$

$$\sigma_u^2 = \frac{T}{\mu} \times \left\{1-\phi\left[2\frac{\beta^2}{\beta_1^2}\sinh^2\left(\frac{1}{2}\beta_1 t\right)-\frac{\beta}{\beta_1}\sinh(\beta_1 t)+1\right]\right\},$$

$$A(t) = -\alpha(t) - \Omega[C\exp(-2\Omega t)+1]\,/\,[C\exp(-2\Omega t)-1],$$

where $\beta_1 = \sqrt{\beta^2-4\omega_1^2}$, C is an arbitrary constant determined by the initial conditions of the problem,

$$\alpha(t) = \beta/2 - \vartheta/\left[\sigma_u^2\left(1-\phi^2\right)\right],$$

$$\Omega^2(t) = \alpha^2(t) + \omega_0^2 + 2\vartheta\phi\omega_0^2/\left[\sigma_u\sigma_x\omega_1^2\left(1-\phi^2\right)\right].$$

Expression (33) is bounded and real-valued even when β_1 is zero or imaginary. Imaginary values of β_1 ($\beta/2\omega_1 < 1$) correspond to low friction, while its real values ($\beta/2\omega_1 > 1$) are realized in the case of high friction. In the limit $t \to \infty$, expression (33) reduces to expression (32) for calculating the steady-state fission width according to Kramers.

For the fissile nucleus ^{239}U, Fig. 2 shows the function $\lambda_f(t,\beta)$ and the dimensionless quantity $\varphi(t) = \lambda_f(t,\beta)\Big/\lambda_f^{\mathrm{K}}(\beta)$, which demonstrate how the Kramers equilibrium value is established in the course of the time-evolution process at low and large values of the coefficient of friction β.

The duration τ of the transient process—it is defined as the time over which the width $\Gamma_f(t,\beta) = \varphi(t)\Gamma_f^{\mathrm{K}}(\beta)$ achieves the value of $0.9\Gamma_f^{\mathrm{K}}$—was obtained by numerically solving the equation $\varphi(\tau) - 0.9 = 0$. It can be seen from Fig. 3*a* that τ depends differently on β for low ($\beta/2\omega_1 < 1$) and high ($\beta/2\omega_1 > 1$) values of the coefficient of friction. In the calculations, we set $\hbar\omega_0 = 0.6$ MeV and $\hbar\omega_1 = 1$ MeV. In the first case, an increase in β leads to an increase in the strength of the interaction between the internal and collective degrees of freedom, with the result that the transient time τ decreases as

$$\tau \approx \beta^{-1} \ln(10B_f/T). \qquad (34)$$

In the second case, collective vibrations are damped aperiodically and the diffusion process is moderated, which leads to

$$\tau \approx \left(\beta/2\omega_1^2\right) \ln(10B_f/T). \qquad (35)$$

The probability of first-chance fission is given by [8]

$$P_f(E,\beta) = \int_0^\infty dt \frac{\Gamma_n}{\hbar} \exp\left(-\frac{\Gamma_n}{\hbar}t\right) \qquad (36)$$

$$\times \left[1 - \exp\left(-\frac{\Gamma_f^{\mathrm{K}}}{\hbar}\int_0^t \varphi(t')dt'\right)\right].$$

For the steady-state case, where $\varphi(t) = 1$, expression (36) yields

$$P_f = P_f^{\mathrm{K}} = \frac{\Gamma_f^{\mathrm{K}}}{\Gamma_n + \Gamma_f^{\mathrm{K}}}. \qquad (37)$$

Figure 3*a* also shows the mean time $\tau_n(E) = \hbar/\Gamma_n(E)$ required for the emission of the first-chance neutron versus the excitation energy of ^{239}U. The factor $f(E,\beta) = P_f(E,\beta)/P_f^{\mathrm{K}}$ obtained by numerically integrating Eq. (36) is presented in Fig. 3*b* as a function of the excitation energy E at various values of the parameter β. This dependence illustrates the effect of the transient process on the fission probability with respect to the Kramers fission probability. For all β values, we can see the trend toward a decrease in the fissility with increasing excitation energy, but the slope of this dependence, $|df(E,\beta)/dE|$, depends greatly on the coefficient of friction. In the case where it is possible to obtain an analytic representation of $f(E,\beta)$, the effect of the parameter β is manifested more clearly. For example, the approximation of the transient-process function by a step—$\varphi(t) = 0$ for $t < \tau$ and $\varphi(t) = 1$ for $t > \tau$—leads to the analytic result

$$f(E,\beta) = \exp\left[-\tau(\beta)/\tau_n(E)\right], \qquad (38)$$

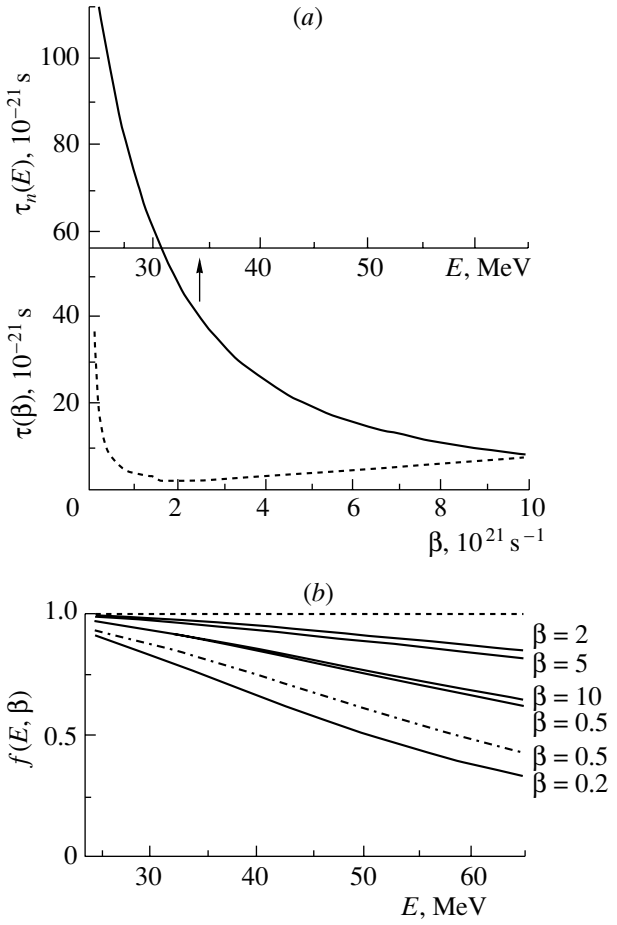

Fig. 3. (*a*) Duration of the transient process, $\tau(\beta)$ as a function of the reduced coefficient of friction β (dashed curve) and mean time $\tau_n(E)$ it takes for the emission of a first-chance neutron as a function of the excitation energy E (solid curve); (*b*) energy dependence of the function $fE,\beta)$ determining the effect of the transient process on the fission probability with respect to the Kramers fission probability for various values of β (in units of 10^{21} s^{-1}): (dashed curve) quasi-steady-state solution and (dash-dotted curve) approximation of the transient-process function $\varphi(t)$ by a step.

where $\tau_n(E)$ determines the energy dependence of $f(E,\beta)$, while $\tau(\beta)$ determines the slope of the curve with respect to the steady-state level $f(E,\beta) = 1$. As can be seen from Fig. 3*b*, the simulation of the transient process by a step function leads to a slope $|df(E,\beta)/dE|$ larger than that following from the actual dependence $\varphi(t)$ (see Fig. 2) at the same value of β. Deviations of $f(E,\beta)$ from unity for the actual transition process (solid curves in Fig. 3*b*) become sizable at $E \geqslant 40$ MeV for $\beta \leqslant 0.5 \times 10^{21}$ and $\beta \geqslant 10 \times 10^{21}$ s^{-1}.

Thus, the factors $\tilde{\gamma}(\beta/2\omega_0)$ and $f(E,\beta)$, which are dependent on β, have different effects on the fis-

sion probability:

$$P_f(E,\beta) = \frac{\Gamma_f'^{\rm BW}\tilde{\gamma}(\beta/2\omega_0)}{\Gamma_n(E)+\Gamma_f'^{\rm BW}\tilde{\gamma}(\beta/2\omega_0)} f(E,\beta). \quad (39)$$

The factor $f(E,\beta)$ affects the energy dependence of the fission probability, and its role becomes more important with increasing excitation energy. At low energies ($E \leqslant 20$ MeV, which corresponds to $T \leqslant 1$ MeV), we have $f(E,\beta) \approx 1$. The Kramers factor $\tilde{\gamma}(\beta/2\omega_0)$ is independent of E, and its effect on the fission probability decreases with decreasing β. Since there is virtually no information confirming the excitation-energy dependence of viscosity (temperature dependence of β), it is impossible at present to answer the question of how dynamical effects are damped with increasing energy, if at all. By damping, we mean here the vanishing of nuclear friction ($\beta/2\omega_0 \to 0$) at specific values of the excitation energy.

That the traditional statistical approach was successfully used in analyses of experimental data, including the fission cross section [2, 3] for $E_n < 20$ MeV, indirectly confirms that nuclear-friction effects are inoperative at low energies. The results of the statistical calculation and experimental data begin to deviate at higher energies (a few tens of MeV and higher). By way of example, we indicate that, within the standard statistical model, the experimental multiplicity of prefission neutrons, $\bar{\nu}_{\rm pre}(E)$, in heavy-ion reactions [5] cannot be reproduced without including, in the description of the fission probability $P_f(U)$, effects associated with the viscosity of nuclear matter. The results obtained from an analysis of the mass–energy distributions of fission fragments [6] and prefission neutrons [5] give sufficient grounds to conclude that $\beta > 1 \times 10^{21}$ s^{-1}. This corresponds to temperatures of $T \geqslant 2$ MeV. At low temperatures ($T \leqslant 1$ MeV), there is no need for invoking the diffusion model for estimating the fission probability because, in this region, the statistical concepts are consistent with experimental data. This gives every reason to assume that, at low energies, nuclear friction is extremely low: $\beta/2\omega_0 \approx 0$—that is, $\tilde{\gamma} \approx 1$. In going over from the statistical description at low energies (Bohr–Wheeler fission probabilities) to the description within the diffusion model at high energies (Kramers fission probability), the continuity of the calculated characteristics can be ensured by including, in the description of $P_f(U)$ (39), the energy dependence of the coefficient of viscosity in the form

$$\tilde{\beta}(U) = \beta Q(U), \quad (40)$$

$$Q(U) = \left[1+\exp\left(\frac{U_{\rm d}-U}{\delta U}\right)\right]^{-1}.$$

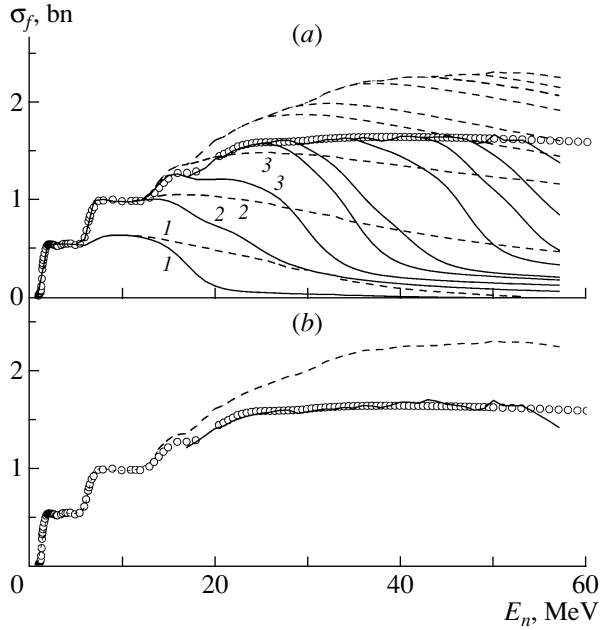

Fig. 4. Results of the theoretical calculation of the cross section for the neutron-induced-fission of ^{238}U: (a) cross section $\sigma_f(E_n)$ and its components (curves *1*) σ_{f0}, (curves *2*) $\sigma_{f0}+\sigma_{f1}$, (curves *3*) $\sigma_{f0}+\sigma_{f1}+\sigma_{f3}$, etc. The dashed curves represent a statistical description (these data are analogous to those shown by the dashed curve in Fig. 1, but the contributions of various chances are additionally shown here), and the solid curves were computed on the basis of the diffusion model ($\beta = 4.1 \times 10^{21}$ s^{-1}) with allowance for the damping of the asymmetric component $K_1(U)$ at the saddle point. (b) Data shown in Fig. 1 by the dashed curve and open circles (dashed curve and open circles, respectively) and results of the calculation of $\sigma_f(E_n)$ on the basis of the diffusion model with $\beta = 10 \times 10^{21}$ s^{-1} and with the adiabatic estimate for the coefficient of rotational enhancement of the level density (solid curve).

At low excitation energies, the function describing the damping of dynamical effects is chosen by analogy with the function describing the damping of the rotational effects at high energies [see Eq. (19)]. The function $Q(U)$ has the form of a smoothed step at $U = U_d$, its smearing being determined by the parameter δU. If the parametrization in (40) correctly reflects the dependence of nuclear friction on the excitation energy, it must be universal—that is, its extension to a wide range of nuclei must ensure the description of the fission cross section over the entire energy range. Relation (40) has no theoretical validation. The parameters U_d and δU are empirically adjusted.

Figure 4*a* presents the results obtained from an analysis of the cross section for ^{238}U fission and its chance structure for two versions of the calculation: (i) a statistical description (dashed curves) employing the adiabatic estimate for the coefficient of rotational enhancement of the level density (these data

are analogous to those represented by the dashed curve in Fig. 1, but they additionally display the chance structure of the fission cross section) and (ii) a calculation on the basis of the diffusion model with allowance for the damping of the asymmetric component $K_1\,(U)$ (19) at the saddle point with parameters $U_1 = 16$ MeV and $d_1 = 1.2$ MeV for (20). A satisfactory description of experimental data over the entire range of E_n is achieved at the coefficient of friction equal to $\beta = 4.1 \times 10^{21}$ s^{-1} and the parameter values of $U_d = 24$ MeV and $\delta U = 1.5$ MeV for the function in (40), which describes the damping of dynamical effects at low excitation energies. If we disregard the damping of the asymmetric component—that is, if we set $K_1(U) = K_1^{\rm ad}(U)$—the overestimation of the experimental data within the statistical description can also be compensated within the diffusion model, but the larger value of $\beta = 10 \times 10^{21}$ s^{-1} must then be taken for the coefficient of viscosity. The results of the calculations are shown in Fig. 4*b*. Thus, an analysis of the cross sections for neutron-induced fission can furnish additional and independent information about the magnitude of the reduced coefficient of friction β. This is especially important because information about this parameter of the diffusion model is not fully reliable. At present, there is no commonly accepted concept of the mechanism of nuclear viscosity. The assumptions of the two-body and one-body viscosity mechanisms lead to β values that differ by one order of magnitude. The estimates of β that are obtained in the present study and the results deduced from an analysis of the neutron yields in (HI, xnf) heavy-ion reactions ($\beta \geqslant 5 \times 10^{21}$ s^{-1} [29]) favor supercritical damping ($\beta/2\omega_0 > 1$).

It can be seen from Fig. 4*a* that the inclusion of nuclear friction in calculating $\sigma_f(E_n)$ leads to changes in the relative contributions of the different chances, $R_x = \sigma_{fx}(E_n)/\sigma_f(E_n)$, and in the energy dependence of the cross section for each individual chance, $\sigma_{fx}(E_n)$. The chances in the dynamical description are damped much faster with increasing energy than the corresponding chances in the statistical description.

An analysis of the chance structure in the energy dependence of the fission cross section shown in Fig. 4*a* makes it possible to calculate directly the mean multiplicity of prefission neutrons as a function of the excitation energy $E = E_n + B_n$. Specifically, we have

$$\bar{\nu}_{\rm pre}(E) = \sum_{x=0}^{x_{\max}(E)} xR_x(E), \qquad (41)$$

where $xR_x = \bar{\nu}_{{\rm pre}\,x}$ is the contribution of the fission chance upon the emission of x neutrons to the total multiplicity $\bar{\nu}_{\rm pre}$. Relation (41) determines the yield

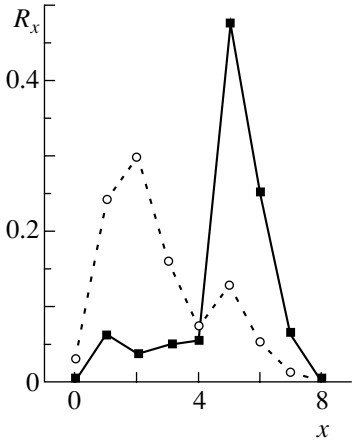

Fig. 5. Relative contributions of different chances, $R_x = \sigma_{fx}\,(E_n)\,/\sigma_f\,(E_n)$, at $E_n = 45$ MeV: (open circles) statistical description and (closed boxes) description within the diffusion model.

of prefission neutrons that have been emitted by the excited primary nucleus before it reaches the saddle point. It should be noted that the approach used here gives no way to estimate the mean multiplicity of prefission neutrons being emitted over the time over which the fissle nucleus evolves from the saddle to the scission point.

Figure 5 shows the relative yield of various chances, $R_x = \sigma_{fx}(E_n)/\sigma_f(E_n)$ ($\sum_x R_x = 1$), at $E_n = 45$ MeV for the same versions of theoretical description of the fission cross section as in Fig. 4*a*. If the dynamical delay of fission according to (39), as described by the diffusion model due to Kramers [7] and Grange–Weidenmüller [8], is taken into account, the maximum of the distribution of $R_x^{(d)}$ is shifted toward greater x values with respect to the maximum of the statistical distribution of $R_x^{(\rm s)}$. As a result, the prediction of the diffusion model for the prefission-neutron emission proves to be markedly different from that of the statistical model ($\overline{\nu}_{\rm pre}^{(d)} = \sum_x xR_x^{(d)} = 4.68$ versus $\overline{\nu}_{\rm pre}^{(\rm s)} = \sum_x xR_x^{(\rm s)} = 2.68$). It is obvious that a variation $k \times \sigma_{\rm abs}\,(E_n)$ of the cross section in the input reaction channel with the aid of the scale factor k, while changing the value of the calculated fission cross section [4], will introduce no changes in the relative contributions of different chances, $R_x = (k \times \sigma_{fx}(E_n))/(k \times \sigma_f(E_n))$, and, hence, in $\bar{\nu}_{\rm pre}$.

The mean number $\bar{\nu}_{pre}(E)$ of prefission neutrons that was estimated for the reaction ^{238}U$(n, xn'f)$ under the assumption that neutrons are emitted before the saddle point [see Eq. (41)] is presented in Fig. 6 versus the excitation energy, along with the experimental values $\bar{\nu}_{\rm pre}^{\rm expt}(E)$ for the U–Cm actinides with

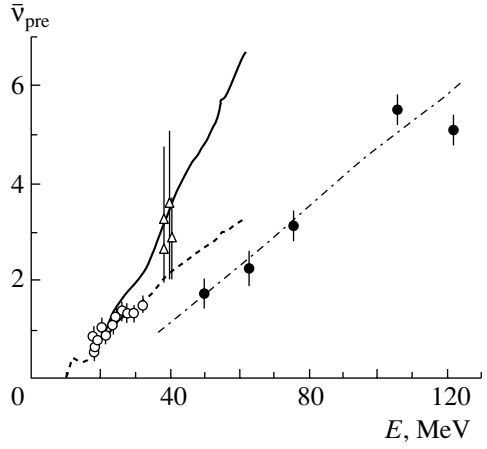

Fig. 6. Results of calculations of $\bar{\nu}_{\rm pre}$ and experimental values for the actinides in the U–Cm region ($Z = 91$–96) versus the excitation energy E: (open circles and triangles) reaction induced by light charged particles (protons and alpha particles, respectively), (closed circles) heavy-ion reactions, (dash-dotted curve) empirical systematics from [30], (dashed curve) statistical description, and (solid curve) results of the calculation within the diffusion model.

mass numbers in the range 239–243. A compilation of $\overline{\nu}_{\rm pre}^{\rm expt}(E)$ was given in [30]. Open symbols represent data for the reaction induced by light charged particles: (circles) $p + {}^{235,236,238}{\rm U} \to {}^{236,237,239}{\rm Np}$ [31] and (triangles) $\alpha + {}^{232}{\rm Th}$, ${}^{233,238}{\rm U}$, ${}^{239}{\rm Pu} \to {}^{236}{\rm U}$, ${}^{237,242}{\rm Pu}$, ${}^{243}{\rm Cm}$ [32]. The closed circles correspond to data obtained in the heavy-ion reactions [33] ${}^{20}{\rm N} + {}^{209}{\rm Bi} \to {}^{229}{\rm Np}$, ${}^{7}{\rm Li} + {}^{232}{\rm Th} \to {}^{239}{\rm Np}$, and ${}^{28}{\rm Si} + {}^{208}{\rm Pb} \to {}^{236}{\rm Cm}$. Experimental information about $\bar{\nu}_{\rm pre}^{\rm expt}(E)$ in reactions induced by light charged particles includes a data set in the narrow energy range $E = 20$–40 MeV. Here, the measurement errors for (α, xnf) reactions are large. Unfortunately, there are no data on $\overline{\nu}_{\rm pre}^{\rm expt}(E)$ for neutron-induced reactions. The experimental procedure that makes it possible to obtain such data was implemented only by authors of [34] about forty years ago. All this complicates a verification of the diffusion model on the basis of a simultaneous analysis of the fission cross sections and the multiplicity of prefission neutrons. Nevertheless, we can state for a first approximation that the solid curve representing $\bar{\nu}_{\rm pre}(E)$ in Fig. 6 and corresponding to the chance decomposition within the diffusion model lies closer to the experimental points for (α, xnf) reactions in the vicinity of $E =$ 40 MeV than the dashed curve corresponding to the traditional statistical description. By using the set of data on (p, xnf) reactions that does not include three boundary points lying on the dashed curve in the vicinity of $E = 30$ MeV, it is hardly possible to discriminate between the two descriptions of $\bar{\nu}_{\rm pre}(E)$.

Kozulin *et al.* [30] noticed a feature that manifests itself in matching the high-energy data ($\bar{\nu}_t, \bar{\nu}_{\rm post}, \bar{\nu}_{\rm pre}$) measured in $({\rm HI}, xnf)$ reactions with low-energy data measured in reactions induced by neutrons ($\bar{\nu}_t$) and light charged particles ($\bar{\nu}_t, \bar{\nu}_{\rm post}, \bar{\nu}_{\rm pre}$). For the example of $\bar{\nu}_{\rm pre}$ in Fig. 6, this feature consists in that the empirical systematics based on the analysis of data on heavy-ion reactions in the energy region $E \leqslant 40$ MeV yields values of the prefission-neutron multiplicity that are lower than the values $\bar{\nu}_{\rm pre}^{\rm expt}$ measured in (p, xnf) and (α, xnf) reactions and the values of $\bar{\nu}_{\rm pre}$ as obtained on the basis of a theoretical description of the fission cross section by decomposing it into individual chances for the reaction ${}^{238}{\rm U}(n, xn'f)$. The authors of [30] indicated that this cannot be explained by different contributions from nonequilibrium neutron emission in reactions of different types. Partly, the effect can be associated with the rotational energy $E_{\rm rot}$, by which we must reduce, according to [29], the excitation energy for the values $\bar{\nu}_{\rm pre}^{\rm expt}$ measured in $({\rm HI}, xnf)$ reactions. This energy, which can be disregarded for light particles, is converted in the fission process into gamma radiation. It is obvious that available experimental data in the region of heavy actinide nuclei are insufficient both for matching the results of measurements in heavy-ion reactions and reactions induced by light particles and for testing theoretical models.

5. CONCLUSIONS

An analysis of the cross section for ${}^{238}{\rm U}$ fission induced by 1- to 55-MeV neutrons has been performed with the parameters of the optical model for the deformed Young potential [24]. The basic conclusions drawn from this analysis are the following:

(i) Within the standard statistical model, it is possible to fit the results of the calculations to experimental data on $\sigma_f\,(E_n)$ for $E_n < 16$ MeV. At higher energies, the calculated curve lies considerably higher than experimental data.

(ii) Perfect agreement between the calculated and the experimental cross section cannot be achieved by including, in the statistical description, the damping of the asymmetric component of the coefficient of rotational enhancement of the level density at the saddle point.

(iii) Within the diffusion model, the inclusion of dynamics at high energies makes it possible to describe the fission cross section over the entire energy range under investigation and to obtain information about the magnitude of the reduced coefficient β of

the nuclear viscosity (friction). The values of β as estimated in the present study are in agreement with the results that are obtained from an analysis of the prefission-neutron yield in heavy-ion reactions and of the mass–energy distributions of fission fragments and which furnish evidence in favor of supercritical damping.

(iv) Simultaneous experimental investigations of the fission cross section and the mean multiplicity of prefission neutrons and their global analysis in reactions induced by neutrons and light charged particles may prove to be useful in testing the diffusion model and in matching it with the statistical description at low energies.

REFERENCES

1. E. M. Rastopchin, S. I. Mul'gin, Yu. B. Ostapenko, *et al.,* Yad. Fiz. **53**, 1200 (1991) [Sov. J. Nucl. Phys. **53**, 741 (1991)].
2. A. V. Ignatyuk, V. M. Maslov, and A. B. Pashchenko, Yad. Fiz. **47**, 355 (1988) [Sov. J. Nucl. Phys. **47**, 224 (1988)].
3. G. A. Kudyaev, Yu. B. Ostapenko, V. V. Pashkevich, *et al.,* Yad. Fiz. **56** (1), 51 (1993) [Phys. At. Nucl. **56**, 29 (1993)].
4. J. P. Lestone and A. Gavron, Yad. Fiz. **57**, 1268 (1994) [Phys. At. Nucl. **57**, 1200 (1994)].
5. J. O. Newton, Fiz. Élem. Chastits At. Yadra **21**, 821 (1990) [Sov. J. Part. Nucl. **21**, 349 (1990)].
6. G. D. Adeev, I. I. Gonchar, V. V. Pashkevch, *et al.,* Fiz. Élem. Chastits At. Yadra **19**, 1231 (1988) [Sov. J. Part. Nucl. **19**, 529 (1988)].
7. H. A. Kramers, Physica **7**, 284 (1940).
8. P. Grange and H. A. Weidenmüller, Phys. Lett. B **96B**, 26 (1980) P. Grange, Li Jun-Qing, and H. A. Weidenmüller, Phys. Rev. C **27**, 2063 (1983).
9. A. V. Ignatyuk, *Statistical Properties of Excited Nuclei* (Énergoatomizdat, Moscow, 1983).
10. A. I. Vdovin, V. V. Voronov, L. A. Malov, *et al.,* Fiz. Élem. Chastits At. Yadra **7**, 952 (1976) [Sov. J. Part. Nucl. **7**, 380 (1976)].
11. A. Gilbert and A. G. W. Cameron, Can. J. Phys. **43**, 1446 (1965).
12. G. V. Antsilov, V. A. Kon'shin, V. M. Maslov, *et al.,* Vopr. At. Nauki Tekh., Ser.: Yad. Konst. **3**, 25 (1985).
13. S. Bjornholm, A. Bohr, and B. R. Mottelson, in *Proceedings of Symposium "Physics and Chemistry of Fission," Rochester, 1973* (Vienna, 1974), Vol. 1, p. 367; A. Bohr and B. R. Mottelson, *Nuclear Structure* (New York, Amsterdam, 1974), Vol. 2.
14. M. I. Svirin, G. N. Lovchikova, and A. M. Trufanov, Yad. Fiz. **60**, 818 (1997) [Phys. At. Nucl. **60**, 727 (1997)].
15. A. V. Ignatyuk, G. N. Smirenkin, M. G. Itkis, *et al.,* Fiz. Élem. Chastits At. Yadra **16**, 709 (1985) [Sov. J. Part. Nucl. **16**, 307 (1985)].
16. E. V. Gaĭ, A. V. Ignatyuk, N. S. Rabotnov, and G. N. Smirenkin, Yad. Fiz. **10**, 542 (1969) [Sov. J. Nucl. Phys. **10**, 311 (1970)].
17. D. M. Brink, Doctoral Thesis (Oxford Univ., Oxford, 1955); P. Axel, Phys. Rev. **126**, 671 (1962).
18. R. Nowotny and M. Uhl, *Handbook on Nuclear Activation Data*, STI/DOC/10/273 (IAEA, Vienna, 1987).
19. A. V. Ignatyuk, K. K. Istekov, and G. N. Smirenkin, Yad. Fiz. **30**, 1205 (1979) [Sov. J. Nucl. Phys. **30**, 626 (1979)].
20. G. Hansen and A. Jensen, Nucl. Phys. A **406**, 236 (1983).
21. H. C. Britt, in *Proceedings of Symposium "Physics and Chemistry of Fission," Jülich, 1979* (IAEA, Vienna, 1980), Vol. 1, p. 3; S. Bjornholm and J. E. Lynn, Rev. Mod. Phys. **52**, 725 (1980).
22. 1982 INDC/NEANDC Nuclear Standards File, Technical Report No. 227 (IAEA, Vienna, 1983); *Update to Nuclear Data Standards for Nuclear Measurements,* Ed. by H. Wienke, INDC(NDS)-368 (IAEA, Vienna, 1997).
23. J. Raynal, *Optical Model and Coupled-Channel Calculations in Nuclear Physics,* IAEA Report SMR-9/8 (1970).
24. P. G. Young, INDC(NDS)-335 (IAEA, Vienna, 1994), p. 109.
25. V. M. Maslov , Yu. V. Porodzinskij, A. Hasegawa, and K. Shibata, JAERI-Reaseach 98-040 (1998).
26. D. J. Hinde, R. J. Charity, G. S. Foote, *et al.,* Nucl. Phys. A **452**, 550 (1986).
27. S. Chandrasekhar, Rev. Mod. Phys. **15**, 1 (1943).
28. V. M. Strutinsky, Yad. Fiz. **19**, 259 (1974) [Sov. J. Nucl. Phys. **19**, 127 (1974)].
29. A. Gavron, A. Gayer, J. Boissevain, *et al.,* Phys. Rev. C **35**, 579 (1987).
30. É. M. Kozulin, A. Ya. Rusanov, and G. N. Smirenkin, Yad. Fiz. **56** (2), 37 (1993) [Phys. At. Nucl. **56**, 166 (1993)].
31. M. Strecker, R. Wien, P. Plischke, and W. Scobel, Phys. Rev. C **41**, 2172 (1990).
32. Z . Fraenkel, I. Mayk, J. P. Unik, *et al.,* Phys. Rev. C **12**, 1809 (1975).
33. D. J. Hinde, H. Ogata, M. Tanaka, *et al.,* Phys. Rev. C **39**, 2268 (1989).
34. Yu. A. Vasil'ev, Yu. S. Zamyatnin, E. I. Sirotinin, and É. F. Fomushkin, At. Énerg. **9**, 499 (1960).

Translated by A. Isaakyan

Physics of Atomic Nuclei, Vol. 64, No. 9, 2001, pp. 1594–1599. Translated from Yadernaya Fizika, Vol. 64, No. 9, 2001, pp. 1673–1679.

NUCLEI
Theory

Ground State of the $^{17}_{\Lambda}$O Nucleus within the $4\alpha + \Lambda$ Cluster Model

I. N. Filikhin and S. L. Yakovlev

Institute of Physics (Petrodvorets Branch), St. Petersburg State University, Ul'yanovskaya ul. 1, Petrodvorets, 198904 Russia

Received September 16, 1999; in final form August 9, 2000

Abstract—The s-wave bound state of the $4\alpha + \Lambda$ system is investigated. The relevant solution to the Schrödinger equation is expanded in the basis formed by the eigenfunctions of Hamiltonian for the 4α subsystem. Differential equations for Yakubovsky components are employed to calculate basis functions. Phenomenological potentials for $\alpha\alpha$ and $\alpha\Lambda$ interactions are used. In the 4α system, additional three-particle potentials for the interaction between α clusters are introduced in such a way as to reproduce the experimental data on the binding energies, the root-mean-square radii, and the charge form factors for the ^{12}C and the ^{16}O nucleus. The binding energy, the root-mean-square radius, and the hyperon distribution in the ground state of the $^{17}_{\Lambda}$O nucleus are calculated. The results of the calculations are in good agreement with those obtained on the basis of the ^{16}O + Λ two-particle model with the phenomenological Woods–Saxon potential. © *2001 MAIK "Nauka/Interperiodica".*

1. INTRODUCTION

The *nucleus plus* Λ *hyperon* two-particle cluster model has long since been used to describe hypernuclei. A local s-wave potential for the (*nucleus plus* Λ) system makes it possible to reproduce the experimental values of the Λ-hyperon separation energy for medium-mass and heavy nuclei. In [1], it was proposed to take the potential in the Woods–Saxon form

$$V(r) = \frac{V_0}{1 + \exp(\frac{r-r_0}{a})}. \qquad (1)$$

Various sets of values for the parameters of this potential were presented in [1, 2], and the analytic dependence of the parameter r_0 on the hypernucleus atomic number was obtained there. An attempt was made in [3] to estimate the hyperon binding energy in the $^{17}_{\Lambda}$O hypernucleus, for which the experimental value of the binding energy is not known. The inputs used there included the potential (1) with the parameter values from [2]. The potential (1) was also employed in [4] to calculate the binding energy of hyperons in double hypernuclei.

The objective of the present study is to describe the hyperon state in the $^{17}_{\Lambda}$O nucleus within the α-particle cluster model, where this nucleus is treated as a system of five particles (four α clusters and a Λ hyperon). In view of what was said about the use of *nucleus plus* Λ *hyperon* two-particle model [1, 2], it is natural to assume that the s-wave approximation will be sufficient for this purpose. It is of course necessary to ensure, in this approximation, a satisfactory description of the ^{16}O core of this nucleus—in particular, the core binding energy, root-mean-square radius, and charge form factor must be reproduced. A correct description of the behavior of the charge form factor would suggest that the wave function of the 4α cluster subsystem closely approximates the wave function of the ^{16}O nucleus. In [5], we proposed the s-wave α cluster model for the nucleus ^{16}O and showed that this model makes it possible to reproduce satisfactorily experimental data on the aforementioned features for the ^{12}C and ^{16}O nuclei. In addition to the two-particle $\alpha\alpha$ potential, this model involves three-particle potentials [5, 6] acting in the 3α subsystem. In the present study, we use the results from [5]. In order to describe the $\alpha\alpha$ and $\Lambda\alpha$ interactions, we choose phenomenological potentials that faithfully reproduce two-particle data and the binding energy of the $^{13}_{\Lambda}$C hypernucleus ($\alpha\alpha\alpha\Lambda$ system) [7].

In order to solve the Schrödinger equation for the $^{17}_{\Lambda}$O nucleus, we use the simplest version of the coupled-channel method for the case of strong coupling [8]. Within this method, the required solution is expanded in a basis that is formed by the eigenfunctions of the Hamiltonians for the subsystem, which are treated as bound clusters. In the $4\alpha + \Lambda$ system, it is the eigenfunctions of the Hamiltonian for the 4α subsystem that appear to be the basis functions. Upon taking projections onto the basis elements, the

Schrödinger equation reduces to a set of two equations for the functions describing the relative motion of two clusters, 4α and Λ. It should be noted that, in the $4\alpha\Lambda$ system, the pronounced degree of $4\alpha + \Lambda$ clustering is expected to ensure a high rate of convergence of the basic expansion. In order to calculate the basis in the 4α subsystem, we apply the differential equations for Yakubovsky components. These equations, which were first obtained and analyzed in [9], are solved numerically on the basis of the cluster-reduction method that we proposed in [10].

The ensuing exposition is organized as follows. In Section 2, we give an account of our method for solving the Schrödinger equation for the $4\alpha + \Lambda$ cluster system. In Section 3, we describe the s-wave potential model based on the effective equations obtained in Section 2. In Section 4, we present the features of the $^{17}_{\Lambda}$O nucleus that were calculated in the s-wave approximation and compare these results with those produced by the *nucleus plus* Λ *hyperon* model employing the potential (1). In the conclusions, we formulate the basic results of our study.

2. DESCRIPTION OF THE FORMALISM

We consider the $4\alpha\Lambda$ system, which consists of four bosons (α particles) and one fermion (Λ hyperon). The Schrödinger equation for this system has the form

$$(H_0 + V_3 + V_{\rm C} + V_{\alpha\alpha} + V_{\Lambda\alpha} - E)\Psi = 0, \qquad (2)$$

where H_0 is the kinetic-energy operator, $V_{\alpha\alpha}$ ($V_{\Lambda\alpha}$) is the sum of the two-particle potentials for the $\alpha\alpha$ ($\Lambda\alpha$) interaction, $V_{\rm C}$ represents the Coulomb interaction between the α clusters, and V_3 is the sum of the three-particles potentials for the interaction of the α clusters. It is obvious that the total wave function Ψ for the system must be symmetric with respect to permutations of the α clusters.

In order to describe the system in configuration space, we use Jacobi coordinates $\mathbf{x}$, $\mathbf{y}$, $\mathbf{z}$, and $\mathbf{r}$, which can be explicitly expressed in terms of the radius vectors of the particles constituting the system [11]. Among the possible sets of Jacobi coordinates, we choose here those that correspond to the $4\alpha + \Lambda$ clustering of the system. The Jacobi coordinates associated with this clustering are displayed schematically in Figs. 1*a* and 1*b*. The coordinates in Fig. 1*a* (1*b*) correspond to the $3 + 1$ ($2 + 2$) Jacobi coordinates in the 4α subsystem.

The wave function for the $4\alpha\Lambda$ system can be expanded in the complete basis formed by the eigenfunctions of the Hamiltonians for the subsystems. Taking into account the $4\alpha + \Lambda$ clustering, we choose the eigenfunctions of the Hamiltonian for the 4α subsystem for this basis. The basis functions are

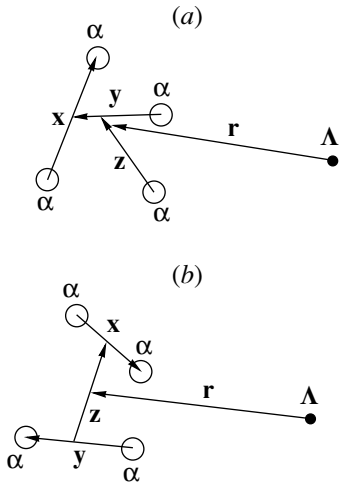

Fig. 1. Jacobi coordinates for the $4\alpha + \Lambda$ system that correspond to the (*a*) $3 + 1$ and (*b*) $2 + 2$ Jacobi coordinates in the 4α subsystem.

denoted by $\psi_i(\mathbf{X})$, $i = 1, 2, \ldots$, where $\mathbf{X} = \{\mathbf{x}, \mathbf{y}, \mathbf{z}\}$. The functions $\psi_i(\mathbf{X})$ are solutions to the Schrödinger equation

$$(H_{0X} + V_3 + V_{\rm C} + V_{\alpha\alpha} - E_i)\psi_i(\mathbf{X}) = 0, \qquad (3)$$

where E_i are the corresponding eigenvalues and H_{0X} is the kinetic-energy operator for the 4α subsystem. To construct the basis, we use here the differential formalism of Yakubovsky equations [11]. The wave function $\psi_i(\mathbf{X})$ can be broken down into a set of components that satisfy the relevant set of integro-differential equations. In the case of identical particles, this set is reduced to two equations for the components U_i^1 and U_i^2 [5],

$$\begin{aligned}(H_{0X} + \bar{V}_{\alpha\alpha} + V_{\rm c} + V_3 - E_i)U_i^1 \qquad (4)\\ +\bar{V}_{\alpha\alpha}(P_4^+ + P_4^-)U_i^1\\ = -\bar{V}_{\alpha\alpha}\left[(P_1^+ + P^+)U_i^1 + (P_1^+ + P_4^+)U_i^2\right],\\ (H_{0X} + \bar{V}_{\alpha\alpha} + V_{\rm c} + V_3 - E_i)U_i^2 + \bar{V}_{\alpha\alpha}(P^+P^+)U_i^2\\ = -\bar{V}_{\alpha\alpha}(P^+ + P_1^+)P^+U_i^1,\end{aligned}$$

where $\bar{V}_{\alpha\alpha}$ is the two-particle potential of the $\alpha\alpha$ interaction and $P^\pm$ and $P_i^\pm$ are the operators of cyclic permutations of, respectively, four and three particles (the subscript indicates the number of the particle not involved in a specific permutation). The component U_i^1 (U_i^2) corresponds to the $3 + 1$ ($2 + 2$) partition of the system. The wave function ψ_i can be obtained by applying the particle-permutation operators to U_i^1 and U_i^2:

$$\begin{aligned}\psi_i = (I + P^+ + P^+P^+ + P^-)(I + P_4^+ \qquad (5)\\ +P_4^-)U_i^1 + (I + P_1^+ + P_1^-)(I + P^+P^+)U_i^2.\end{aligned}$$

The functions $U_i^1(\mathbf{X})$ and $U_i^2(\mathbf{X})$ satisfy the conditions

$$U_i^k(\mathbf{X})|_{\Gamma(R)} = 0, \quad k = 1, 2,$$

at the boundary $\Gamma(R)$ of the region whose typical size is determined by the radius R. The basis functions $\psi_i(\mathbf{X})$ are numbered in the order of increase in the eigenvalues. At a sufficiently large value of the parameter R, the function $\psi_1(\mathbf{X})$ coincides with the total wave function of the 4α system (^{16}O nucleus) in the ground state.

Once the orthogonal basis $\psi_i(\mathbf{X})$, $i = 1, 2, \ldots$, has been constructed, we can write the expansion of the total wave function for the system in the form

$$\Psi(\mathbf{X}, \mathbf{r}) = \sum_{i=0}^{\infty} \psi_i(\mathbf{X}) f_i(\mathbf{r}). \tag{6}$$

It should be noted that, owing to the representation in (5), the function $\Psi(\mathbf{X}, \mathbf{r})$ in (6) is automatically symmetric under permutations of the α clusters [11]. Projecting Eq. (2) onto the basis elements, we find that the functions $f_i(\mathbf{r})$, which describe the relative motion of the 4α subsystem and the Λ particle, satisfy the equation

$$(H_{0r} - E + E_i) f_i(\mathbf{r}) \tag{7}$$
$$+ \sum_{j>0} \left[\langle \psi_i(\mathbf{X}) | \sum_{k=1}^{k=4} \bar{V}_{\Lambda\alpha}(|\mathbf{r} - \mathbf{r}_k|) | \psi_j(\mathbf{X}) \rangle \right] f_j(\mathbf{r}) = 0,$$

where H_{0r} is the kinetic-energy operator for the relative motion of the 4α subsystem and the Λ particle, $\bar{V}_{\Lambda\alpha}$ is the two-particle potential of $\Lambda\alpha$ interaction, and $\mathbf{r}_k$ are radius vectors of the α clusters. In taking into account the completeness of the basis $\psi_i(\mathbf{X})$, we perform summation in expansion (6) over a finite number of terms ($N_{\max}$) in order to obtain the numerical results [thereby, the set of Eqs. (7) is reduced to a finite set]. In view of this, it is of paramount importance to study the convergence of the results versus $N_{\max}$. The efficiency of the aforementioned cluster reduction of Eq. (2) is entirely determined by this parameter.

3. DESCRIPTION OF THE MODEL

We consider the bound state of the system formed by four α particles and a Λ hyperon. The total angular momentum of the system itself as a discrete unit and the angular momenta of its subsystems are taken to be zero (that is, we perform our analysis in the s-wave approximation). The interaction between the Λ hyperon and the α clusters is described by the potential [12]

$$\bar{V}_{\Lambda\alpha}(r) = V_0 \exp(-r^2/\beta_0^2), \tag{8}$$

where $V_0 = -43.97$ MeV and $\beta_0 = 1.566$ fm. This potential faithfully reproduces the binding energy of the Λ hyperon in the $^5_\Lambda$He hypernucleus ($E_\Lambda = -3.11$ MeV).

To describe the two-particle interaction of the α clusters, we use the s-wave component of the potential [13] (version "a"),

$$\bar{V}_{\alpha\alpha}(r) = V_1 \exp(-r^2/\beta_1^2) + V_2 \exp(-r^2/\beta_2^2), \tag{9}$$

where $V_1 = 120.0$ MeV, $\beta_1 = 1.53$ fm, $V_2 = -30.18$ MeV, and $\beta_2 = 2.85$ fm.

In the subsystem of α-particle clusters, we introduce an additional three-particle potential $\bar{V}_3$ that ensures the existence of a bound state in the subsystems. This potential is taken in the form

$$\bar{V}_3(\rho) = V \exp(-(\rho/\beta)^2), \tag{10}$$

where $\rho^2 = \sum_{i=1}^{i=3} \mathbf{r}_i^2$, $\mathbf{r}_i$ being the radius vector of the ith particle in the c.m. frame. For the four-particle system, we have introduced two three-particle potentials $V_3^{\mathrm{I}}(\rho)$ and $V_3^{\mathrm{II}}(\rho)$. Of these, the first ensures the existence of a bound state in the three-particle cluster, while the second specifies interaction between the fourth particle and each pair of particles in the three-particle cluster. These potentials are chosen in the form (10), with the parameters being denoted by V^{I}, β^{I} and V^{II}, β^{II}, respectively. In this way, we take explicitly into account the $3\alpha + \alpha$ cluster structure in the 4α four-particle system.

In [5], we showed that the parameters of these potentials can be chosen from a fit to experimental data on the binding energy, the root-mean-square radius, and the charge form factors for the ^{12}C and ^{16}O nuclei. In constructing this fit, we assumed that the α-particle clusters in the bound cluster system are deformed in relation to the free α particle. The deformation coefficient is defined as

$$A = (R_\alpha/R_c)^2,$$

where R_α and R_c are the root-mean-square radii of the α particle (R_α =1.47 fm) and the α cluster, respectively. The potential model constructed in [5] reproduces not only the ground state but also the 0_2^+ excited s-wave state of the ^{16}O nucleus, its binding energy being -8.8 MeV (to be compared with the experimental value of -8.34 MeV).

The parameters of the three-particle potential $V_3^{\mathrm{I}}(\rho)$ are $V^{\mathrm{I}} = -24.32$ MeV and $\beta^{\mathrm{I}} = 3.795$ fm. In the present article, the parameters V^{II} and β^{II} of the three-particle potential $V_3^{\mathrm{II}}(\rho)$ from [5] were changed. We choose the values of $V^{\mathrm{II}} = -5.59$ MeV and $\beta^{\mathrm{II}} = 5.71$ fm. In this case, the coefficient A of the α-cluster deformation takes the values of $A = 3$ both for the 3α and for the 4α system, while the

charge form factor calculated according to [5] for the 4α-cluster system reproduces qualitatively the experimental behavior of the ^{16}O form factor at high momentum transfers. Hence, the wave function for the cluster system being considered can be close to the ^{16}O wave function at sufficiently small distances. In Fig. 2, the solid curve represents the behavior of the form factor for the 4α-cluster system, while the closed squares correspond to experimental data from [14] on the ^{16}O form factor.

In [7], the potentials (8)–(10) were employed to study the $^{13}_{\Lambda}$C nucleus on the basis of the $\alpha\alpha\alpha\Lambda$ cluster model; there, the experimental value of the ground-state binding energy for the $^{13}_{\Lambda}$C nucleus ($E_B = -18.7$ MeV) was reproduced and the result of Hiyama *et al.* [15], who predicted an s-wave excited bound state in the $\alpha\alpha\alpha\Lambda$ system, was confirmed.

In the s-wave approximation, the set of Eqs. (7) takes the form

$$[-a_s\partial_r^2 - (\varepsilon - \varepsilon_i)]f_i(r) + \sum_{j=1}^{j=N_{\max}} \langle\psi_i| \sum_{k=1}^{k=4} \bar{v}_{\Lambda\alpha}(R_k)|\psi_j\rangle f_j(r) = 0, \quad (11)$$

where

$$a_s = \frac{4m_\alpha + m_\Lambda}{8m_\Lambda},$$

m_α and m_Λ being, respectively, the α-particle and the Λ-hyperon mass; $\bar{v}_{\Lambda\alpha}(x) = \bar{V}_{\Lambda\alpha}(x)m_\alpha/\hbar^2$; $\varepsilon = Em_\alpha/\hbar^2$; $\varepsilon_i = E_i m_\alpha/\hbar^2$; and $r = |\mathbf{r}|$. The matrix elements $\langle\psi_i|\bar{v}_{\Lambda\alpha}(R_k)|\psi_j\rangle$ are calculated by the formula

$$\langle\psi_i|\bar{v}_{\Lambda\alpha}(R_k)|\psi_j\rangle = \int_0^R\int_0^R\int_0^R\int_\Omega dxdydzd\omega \times \bar{v}_{\Lambda\alpha}(R_k)\psi_i(x,y,z,u,v,w)\psi_j(x,y,z,u,v,w),$$

where

$$d\omega = \sin\Theta_x d\Theta_x \sin\Theta_y d\Theta_y \sin\Theta_z d\Theta_z d\phi_y d\phi_z$$

(Θ_x, Θ_y, and Θ_z; ϕ_y; and ϕ_z are the spherical angles of the vectors $\mathbf{x}$, $\mathbf{y}$, and $\mathbf{z}$, respectively);

$$v = \sin\Theta_x \sin\Theta_y \cos\phi_y + \cos\Theta_x \cos\Theta_y;$$

$$u = \sin\Theta_x \sin\Theta_z \cos\phi_z + \cos\Theta_x \cos\Theta_z;$$

$$w = \sin\Theta_y \cos\phi_y \sin\Theta_z \cos\phi_z + \sin\Theta_y \sin\phi_y \sin\Theta_z \sin\phi_z + \cos\Theta_y \cos\Theta_z;$$

$x = |\mathbf{x}|$, $y = |\mathbf{y}|$, $z = |\mathbf{z}|$,

$$R_1^2 = (z/4)^2 + (y/3)^2 + (x/2)^2 + r^2 - xyv/3 + zyw/6 - zxu/4 - zr\cos(\Theta_z/2) - 2yr\cos(\Theta_y/3) + xr\cos\Theta_x;$$

$$R_2^2 = (z/4)^2 + (y/3)^2 + (x/2)^2 + r^2 + xyv/3 + zyw/6 + zxu/4 - zr\cos(\Theta_z/2) - 2yr\cos(\Theta_y/3) - xr\cos\Theta_x;$$

$$R_3^2 = (z/4)^2 + (2y/3)^2 + r^2 - zyw/3 - zr\cos(\Theta_z/2) + 4yr\cos(\Theta_y/3);$$

$$R_4^2 = (3z/4)^2 + r^2 - 3zr\cos(\Theta_z/2).$$

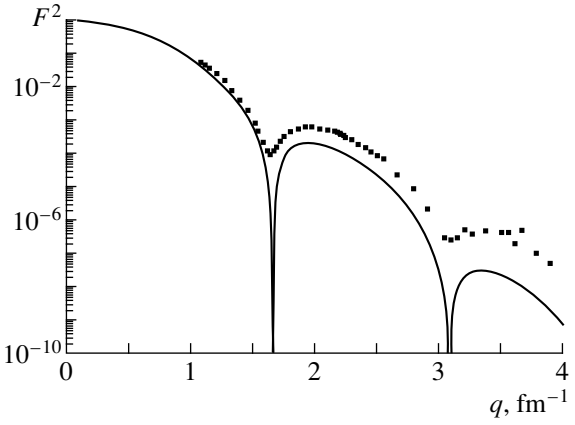

Fig. 2. Charge form factor for the nucleus ^{16}O. Solid curve represents the charge form factor of the 4α-cluster system at $A = 3$, dots correspond to the experimental data from [14].

The functions $\psi_i(x,y,z,u,v,w)$, $i = 1,2,\ldots,N_{\max}$, are normalized by the condition

$$\langle\psi_i|\psi_j\rangle = \int_0^R\int_0^R\int_0^R\int_\Omega dxdydzd\omega \times \psi_i(x,y,z,u,v,w)\psi_j(x,y,z,u,v,w) = \delta_{ij}. \quad (12)$$

In configuration space, the parameter R specifies the rectangular region (in the calculations, we took the value of 25 fm for this parameter) where the basis functions $\psi_i(x,y,z,u,v,w)$ were calculated according to expression (5).

4. RESULTS OF THE CALCULATIONS

The cluster reduction of Eq. (2) reduces the problem to solving the effective Eqs. (11) for the functions describing the relative motion of the constituent clusters. A numerical solution to the set of Eqs. (11) was constructed by using a finite-difference approximation on an equidistant mesh. The basis functions necessary for performing the reduction procedure were obtained by solving numerically [5] Eqs. (4) for the Yakubovsky components of the total wave function for the 4α subsystem; the basis functions $\psi_i(\mathbf{X})$, $i = 1,2,\ldots$, were calculated according to (5).

The results obtained by calculating the binding energy of the Λ hyperon in the $4\alpha + \Lambda$ system are

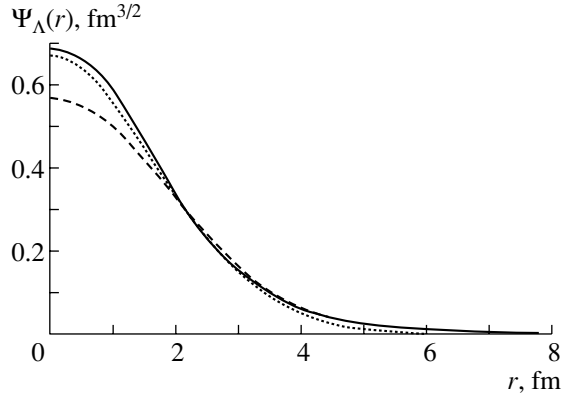

Fig. 3. Distribution of the Λ hyperon in the $^{17}_{\Lambda}$O nucleus: results of our calculations (solid curve) within the $4\alpha + \Lambda$ model and (dashed curve) within the ^{16}O+Λ two-particle model involving the Woods–Saxon potential with the parameter values from [2] and (dotted curve) results from [16], where the parameters of the Woods–Saxon potential were determined from a fit to the hyperon binding energy obtained within the microscopic approach in [16].

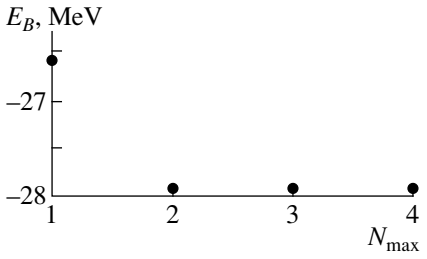

Fig. 4. Binding energy E_B in the ground state of the $4\alpha\Lambda$ system as a function of the number $N_{\max}$ of the basis functions involved.

presented in the table. Since there are no experimental data on the binding energy of the Λ hyperon in the $^{17}_{\Lambda}$O nucleus, our result is contrasted against the results of other calculations. By way of example, we indicate that, in [3], the binding energy was estimated on the basis of data deduced from an analysis of the experimental values of the binding energies of medium-mass and heavy hypernuclei. The value of -13.0 ± 0.4 MeV, which can be referred to as an experimental one in this sense, was thus obtained in [3]. From the table, we can see that the value calculated here for the ground-state energy of $^{17}_{\Lambda}$O agrees with this experimental result. The results of the calculations performed by other authors exhibit a rather broad scatter. The authors of [16] and [17] used the microscopic approach involving the reasonable Jülich potential (version B), but their results differ considerably from one another. Also presented in the table are the results of our calculations for the hyperon binding energy within the *nucleus plus* Λ *hyperon* two-cluster model for the $^{17}_{\Lambda}$O nucleus with the Woods–Saxon potential whose parameters were taken to be identical to those from [2].

For the Λ hyperon in the $^{17}_{\Lambda}$O nucleus, we have also calculated its distribution $\Psi_\Lambda(r)$ defined as

$$\Psi_\Lambda(r) = \sqrt{\sum_{i=1}^{i=N_{\max}} (f_i(r)/r)^2}$$

and normalized by the condition

$$\int_0^\infty \Psi_\Lambda^2(r) r^2 dr = 1.$$

In Fig. 3, the distribution function $\Psi_\Lambda(r)$ is shown by the solid curve. For the sake of comparison, the distribution of the Λ hyperon in the $^{17}_{\Lambda}$O nucleus according to the calculation within the *nucleus plus* Λ *hyperon* two-particle model involving the Woods–Saxon potential is shown in the same figure (dashed curve) for the case where the potential parameters were taken to be identical to those from [2] and (dotted curve, borrowed from [16]) for the case where these parameters were determined from a fit to the hyperon binding energy ($E_\Lambda = -11.83$ MeV) calculated within the microscopic approach in [16]. The root-mean-square radius of the Λ-hyperon distribution in the $^{17}_{\Lambda}$O nucleus was calculated by the formula

$$R_\Lambda = \frac{4m_\alpha}{4m_\alpha + m_\Lambda} \sqrt{\int_0^\infty \Psi_\Lambda^2(r) r^4 dr}.$$

The results of calculations are also quoted in the table.

Generally, we can conclude that the results that we obtained for the features of the $^{17}_{\Lambda}$O nucleus (binding energy, root-mean-square radius, and hyperon distribution) agree with the results of the calculations within the *nucleus plus* Λ *hyperon* model involving the local potential (1). In our opinion, this indicates that the ground state of the $^{17}_{\Lambda}$O nucleus can be treated as an s-wave state of the $4\alpha\Lambda$ system, which undergoes clustering predominantly in the $4\alpha + \Lambda$ form. In order to clarify this statement, we consider the rate of convergence of the results obtained within the cluster-reduction method because, from these results, it can be deduced whether there is (or there is no) clustering in the subsystems [10]. The binding energy calculated for the $4\alpha\Lambda$ system versus the number $N_{\max}$ of basis functions retained in expansion (6) is displayed in Fig. 4. It can be seen from the figure that, for the convergence of the calculation of the binding energy, it is sufficient to take into account the first two basis functions. These basis functions correspond to the ground state and to the first excited state of the ^{16}O nucleus, with their

Binding energy E_Λ and root-mean-square radius R_Λ for the distribution of the Λ hyperon in the $^{17}_{\Lambda}$O nucleus

References	E_Λ, MeV	R_Λ, fm
[16]	-11.83	2.47
[17]	-15.54	—
[3] ("Experiment")	-13.0 ± 0.4	—
Present study	-13.5	2.05
(^{16}O + Λ) model from [2]	-13.4	2.18

binding energy being equal to -14.4 and -8.8 MeV, respectively. Hence, the $4\alpha\Lambda$ system is well clustered in the form $4\alpha + \Lambda$. It should be noted that the s-wave $4\alpha + \Lambda$ cluster model [involving $\Lambda\alpha$ interaction described by the potential (8)] cannot be reduced to the ^{16}O + Λ *hyperon* model with a two-particle s-wave local potential. Indeed, only at $N_{\max} = 1$ can the set of Eqs. (11) be reduced to an equation similar to the two-particle Schrödinger equation. In this case, the calculated value of the Λ-hyperon binding energy is less (in absolute value) than the "experimental" one (see Fig. 4). The binding energy calculated with allowance for the excitation of the core (^{16}O nucleus) complies with the experimental value. The contribution of the core excited state to the wave function for the system does not exceed 5%. The numerical estimate was obtained in the following way. The probability P that the bound state of the $4\alpha\Lambda$ system is clustered in the form ^{16}O + Λ was calculated by the formula

$$P = \langle \psi_1 f_1 | \Psi \rangle,$$

where Ψ is the total wave function for the system, ψ_1 is the wave function for the ground state of the 4α system (^{16}O nucleus), and f_1 is the function that describes the relative motion of the nucleus and the Λ hyperon. Obviously, the probability of finding the $4\alpha\Lambda$ system in the $^{16}\mathrm{O}(0^+_2) + \Lambda$ form is $1 - P$. For P, the calculations yield the value of 0.95.

5. CONCLUSION

It has been shown that the ground state of the $^{17}_{\Lambda}$O hypernucleus can be described, to a high precision, within the s-wave $4\alpha + \Lambda$ cluster model where three-particle potentials representing the interactions between the α-particle clusters have been introduced in addition to the two-particle $\Lambda\alpha$ and $\alpha\alpha$ potentials. The idea that the ground state of the nucleus $^{17}_{\Lambda}$O is clustered predominantly in the $4\alpha + \Lambda$ form has been confirmed. The ^{16}O+Λ two-particle model [1, 2] involving a local potential provides a good approximation for describing the hyperon states in the $^{17}_{\Lambda}$O nucleus. In order to treat the $^{17}_{\Lambda}$O nucleus more accurately, it is necessary to take into account the excitation of the core (^{16}O nucleus).

ACKNOWLEDGMENTS

This work was supported by the Contest Center at the Ministry for Higher Education of the Russian Federation (grant no. 97-0-14.3-23) and by the Russian Foundation for Basic Research (project no. 98-02-18190).

REFERENCES

1. A. Bouyssy, Nucl. Phys. A **381**, 445 (1982).
2. D. J. Milliner, C. B. Dover, and A. Gal, Phys. Rev. C **38**, 2700 (1988).
3. A. A. Usmani, S. C. Pieper, and Q. N. Usmani, nucl-th/9502008.
4. J. Caro, C. García-Recia, and J. Nieves, nucl-th/9801065.
5. I. N. Filikhin and S. L. Yakovlev, Yad. Fiz. **63**, 409 (2000) [Phys. At. Nucl. **63**, 343 (2000)].
6. K. Fukatsu, K. Kato, and H. Tanaka, Prog. Theor. Phys. **81**, 736 (1989); O. Portilho and S. A. Coon, Z. Phys. A **290**, 93 (1979); H. Ogasawara and J. Hiura, Prog. Theor. Phys. **59**, 655 (1978); D. V. Fedorov and A. S. Jensen, Phys. Lett. B **389**, 631 (1996).
7. I. N. Filikhin, Yad. Fiz. **63**, 830 (2000) [Phys. At. Nucl. **63**, 760 (2000)].
8. V. P. Zhigunov and V. N. Zakhar'ev, *Methods of Strong Channel Coupling in Quantum Scattering Theory* (Atomizdat, Moscow, 1974).
9. S. P. Merkur'ev and S. L. Yakovlev, Dokl. Akad. Nauk SSSR **262**, 591 (1982) [Sov. Phys. Dokl. **27**, 39 (1982)]; Teor. Mat. Fiz. **56**, 60 (1983).
10. S. L. Yakovlev and I. N. Filikhin, Yad. Fiz. **56** (12), 98 (1993) [Phys. At. Nucl. **56**, 1676 (1993)]; **58**, 817 (1995) [**58**, 754 (1995)]; **60**, 1962 (1997) [**60**, 1794 (1997)]; nucl-th/9809041; I. N. Filikhin and S. L. Yakovlev, Yad. Fiz. **62**, 1585 (1999) [Phys. At. Nucl. **62**, 1490 (1999)]; **63**, 63 (2000) [**63**, 55 (2000)]; **63**, 79 (2000) [**63**, 69 (2000)]; **63**, 402 (2000) [**63**, 336 (2000)].
11. S. P. Merkur'ev and L. D. Faddeev, *Quantum Scattering Theory for Few-Body Systems* (Nauka, Moscow, 1985).
12. H. Bando, K. Ikeda, and T. Motoba, Prog. Theor. Phys. **66**, 344 (1981); **67**, 508 (1982).
13. S. Ali and A. R. Bodmer, Nucl. Phys. **88**, 99 (1966).
14. I. Sick and J. S. McCarthy, Nucl. Phys. A **150**, 631 (1970).
15. E. Hiyama, M. Kamimura, T. Motoba, *et al.,* Prog. Theor. Phys. **97**, 881 (1997).
16. I. Vidana, A. Polls, A. Ramos, and M. Hjorth-Jensen, Nucl. Phys. A **644**, 201 (1998); nucl-th/9805032.
17. S. Fujii, R. Okamoto, and K. Suzuki, nucl-th/9901055.

Translated by O. Chernavskaya

Physics of Atomic Nuclei, Vol. 64, No. 9, 2001, pp. 1600–1617. Translated from Yadernaya Fizika, Vol. 64, No. 9, 2001, pp. 1680–1697.

NUCLEI
Theory

Probing the Mesonic Structure of the Nucleon by Means of Exclusive Quasielastic Pion Knockout in $(e, e'\pi)$ Reactions at High Energies

V. G. Neudatchin, L. L. Sviridova, and N. P. Yudin

Institute of Nuclear Physics, Moscow State University, Vorob'evy gory, Moscow, 119899 Russia

Received February 29, 2000; in final form, November 10, 2000

Abstract—By including the Z diagram in an analysis performed in the laboratory frame (instantaneous form of dynamics), the notion of quasielastic pion knockout by protons and electrons [$(p, 2p)$ and $(e, e'p)$ reactions treated in terms of the relevant pole diagrams] is generalized to the relativistic case where a meson is quasielastically knocked out of a nucleon by an electron having an energy of a few GeV. The concept of the wave function is introduced for the pion (and for other mesons), and its relation to the vertex constant $G_{\pi NN}$ and the vertex function $g_{\pi NN}(k^2)$ is indicated. The spectroscopic factor S_N^{BM} is defined as the normalization of the wave function for the meson M. It is shown by two methods that, under the kinematical conditions of quasielastic knockout that include the condition $E_\pi \gg m_\pi$ (E_π is the energy of the knock-on pion) and the condition that the square Q^2 of the virtual pion mass is large, the competing tree diagram is suppressed in relation to the pole diagram (this is not so in the case of pion photoproduction). From data of a $p(e, e'\pi^+)n$ experiment involving longitudinal virtual photons γ_L^*, the momentum distribution $\left|\Psi_p^{n\pi}(k)\right|^2$ of pions in the nucleon is extracted for the first time over the entire range of significant momenta k, and this result is used to determine the cutoff constant $\Lambda_\pi = 0.7$ GeV/c and the value of $S_p^{n\pi} \approx 0.2$. The momentum distribution of positive rho mesons in the soft section of the spectrum is determined from experimental data on the process $p(e, e'\pi^+)n$ proceeding through the mechanism $\rho^+ + \gamma_T^* \to \pi^+$ involving transverse photons. A way to determine the momentum distribution of omega mesons through data on the process $p(e, e'\pi^0)p$ is indicated. Two forms of dynamics—instantaneous form and that of light-front dynamics (the latter does not involve the Z diagram)—are compared for the example where the calculations are performed for the spectroscopic factor S_N^{BM}. © *2001 MAIK "Nauka/Interperiodica".*

1. INTRODUCTION

At present, it is commonly recognized that QCD is the fundamental theory of strong interactions that has been sought by the scientific community over many decades. That the class of processes described by this theory can be effectively partitioned into perturbative and nonperturbative processes (the latter type includes strong QCD processes) is peculiar to QCD. In the perturbative region, one is dealing directly with fundamental degrees of freedom (quarks and gluons) and applies the formalism of perturbation theory in the coupling constant. In the nonperturbative region, perturbation theory is inapplicable, so that a considerable part of hadron structure and dynamics should be analyzed in terms of some effective degrees of freedom that are formed in this region. On the basis of first principles alone, it is, however, very difficult to pinpoint the effective degrees of freedom that must be taken into account; therefore, experimental data and physical intuition are of prime importance here.

For this reason, it comes as no surprise that very different hadron models—for example, models of quark interaction through gluon strings [1–3] or models of interaction via meson exchange [4–6]—are being discussed in the literature.

In connection with the construction of the Continuous Electron Beam Accelerator Facility (CEBAF) at Newport News (USA), interest in studying the structure of hadrons—in particular, nucleons—has quickened considerably. The problem of assessing the degree to which the properties of a hadron (nucleon) are determined by effective (mesonic) degrees of freedom (so-called question of the mesonic structure of the nucleon) [8, 9] is one of the important problems that have been widely discussed in these realms. Here, the debates that began as far back as the 1970s [10] are being continued at a new level.

In the present survey that summarizes our recent investigations, we consider the possibility of probing the mesonic structure of the nucleon by the simplest mechanism of pion knockout by high-energy electrons. This makes it possible to determine reliably, from exclusive coincidence experiments, the momentum distribution of mesons in the nucleon for various channels.

1063-7788/01/6409-1600$21.00

Investigation into the structure of a composite system by means of quasielastic knockout of its constituents has been playing an extremely important role in the physics of microcosm [11, 12].

In a broad sense, the term "quasielastic knockout" means the following: a high-energy projectile (electron, proton, etc.) instantanously knocks out a constituent—an electron from an atom, a nucleon or a cluster from a nucleus, or a meson or a quark from a nucleon or a nucleus—transferring a high momentum to it and leading to controllable changes in its internal state, whereof one can take advantage.

Use can be made of quasielastic effects both in inclusive and in exclusive experiments. Information about the structure of a composite system from inclusive experiments is much less definitive than information from exclusive experiments, but even the former can furnish valuable results [13–18].

Exclusive experiments resolve individual states of the final system (different channels of the virtual decay of the initial composite system into a constituent and the final system in a given excited state). As a result, the quasielastic mechanisms singled out in such cases provide more detailed information about the structure of the composite state being studied.

First of all, it should be noted that coincidence experiments of this type measure the missing momentum and energy (that is, the momentum of the constituent and its binding energy in the channel being considered). By varying kinematical conditions, one can directly measure the momentum distribution of constituents in various channels. By way of example, we indicate that, for nuclei, such experiments make it possible to determine the momentum distributions of nucleons in various shells. Second, it is possible to measure spectroscopic factors (probabilities) for constituent separation in various channels. For nuclei and atoms, spectroscopic factors determine the probabilities of excitation of the states of the $A-1$ nucleus upon nucleon knockout from the ground state of the A nucleus (structure of relevant fractional-parentage coefficients) [19]. The sum of the spectroscopic factors over all channels is equal to the total "effective" number of constituents in the system that belong to the type being studied.

In the present review article, we address the problem of how experience gained in studying the exclusive quasielastic knockout of nucleons and clusters from nuclei can be extended to the case of pion electroproduction on nucleons. In doing this, we rely both on previous investigations along these lines [20] and on our recent results [21–23]. We consider the exclusive knockout of pions and other mesons as a step that must follow inclusive experiments.

However, this step is nontrivial since, in the kinematical region being considered, quasielastic pion knockout from nucleons is essentially relativistic. In particular, pion knockout considered in the laboratory frame receives a significant contribution from the Z diagram, which represents the decay of a virtual photon into a meson–antimeson pair.

Quasielastic pion knockout is analyzed here in the initial-proton rest frame (laboratory frame). It is the frame where the momentum of the spectator-baryon (N') recoil is low in relation to the momentum of the knock-on meson (this is the most important signature of the quasielastic-knockout process).

2. DESCRIPTION OF THE FORMALISM

2.1. General Points

Pion electroproduction on nucleons in (e,e') processes belongs to the general class of reactions described by the Feynman diagram in Fig. 1. The element of the cross section for such processes is given by the well-known expression [24]

$$d\sigma = (2\pi)^4 \frac{\overline{|\mathcal{M}_{fi}|^2}}{4\mathcal{I}} \frac{d\mathbf{p}'_e}{(2\pi)^3 2p'_{e0}} \times \frac{d\mathbf{p}_x}{(2\pi)^3 2E_x} \frac{d\mathbf{p}_R}{(2\pi)^3 2E_R} \delta^4(q + p_T - p_x - p_R), \quad (1)$$

where $\mathcal{M}_{fi}$ is the relevant invariant amplitude (an overbar denotes averaging over spins); $\mathcal{I} = \left[(p_T p_e)^2 - m_e^2 M_T^2\right]^{1/2}$ is the Møller invariant flux; $(p_{e0}, \mathbf{p}_e)$ is the initial-lepton (electron) 4-momentum; $(p'_{e0}, \mathbf{p}'_e)$ is the final-lepton (electron) 4-momentum; $\mathbf{p}_x$ and E_x are, respectively, the momentum and the energy of the product particle (pion); $\mathbf{p}_R$ and E_R are, respectively, the momentum and the energy of the final particle (baryon); $q_\mu = (p_e - p'_e)$ is the virtual-photon 4-momentum; p_T is the 4-momentum of the target particle; and M_T is its mass.

Having expressed $\mathcal{M}_{fi}$ in terms of the relevant matrix elements of the hadron current J_μ,

$$\mathcal{M}_{fi} = \frac{-e\bar{u}\gamma^\mu u \langle p_x p_R | J_\mu | p_T \rangle}{Q^2}$$

(here, $\overline{u}$ and u are the Dirac spinors for the electrons, and $Q^2 = -q_0^2 = -q^2 + \mathbf{q}^2$ is the sign-reversed square of the virtual-photon 4-momentum), and performed summation and averaging over spins, we represent the fivefold-differential cross section as

$$\frac{d^5\sigma}{dE'_e d\Omega_e d\Omega^*_x} = \frac{\alpha}{(4\pi)^4} \frac{E'_e}{M_T} \frac{|p^*_x|}{W} \frac{4}{Q^4} \cos^2(\theta_e/2) \frac{Q^2}{\mathbf{q}^2} \frac{1}{\varepsilon} \times \left\{ \varepsilon |J_0|^2 + \frac{1}{2}\left(|J_{+1}|^2 + |J_{-1}|^2\right) + \sqrt{2\varepsilon(1+\varepsilon)} Re\left(J_0 (J_{+1} - J_{-1})^*\right) \cos\varphi_x \right. \quad (2)$$

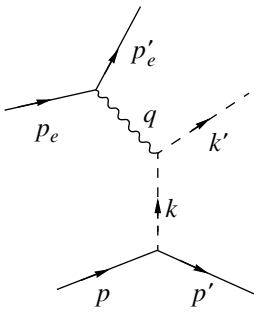

Fig. 1. Diagram for pion electroproduction on a nucleon: (p_e, p'_e) momenta of the incident and the scattered electron, respectively; (q) virtual-photon momentum; (k) virtual-meson momentum; (p) initial-nucleon momentum; (p') final-nucleon momentum; and (k') product-pion momentum.

$$- \varepsilon Re\left(J_{+1}J^*_{-1}\right)\cos 2\varphi_x\Big\},$$

where E'_e is the energy of the final electron; Ω_e is its scattering angle; $W^2 = (p_x + p_R)^2$ is the invariant mass of final hadrons; $J_\lambda = J_\mu e^\mu_\lambda$, e^μ_λ being photon-polarization unit vectors; $\mathbf{p}^*_x$ and $d\Omega^*_x$ are, respectively, the c.m. momentum of particle x and its c.m. scattering angle; φ_x is the angle between the plane spanned by the (e, e') momenta and the plane spanned by the final-hadron momenta; and the quantity

$$\varepsilon = \left[1 + \frac{2\mathbf{q}^2}{Q^2} tan^2 \frac{\theta_e}{2}\right]^{-1}$$

characterizes the degree of longitudinal polarization of the virtual photon.

Apart from a factor, the matrix elements $\langle p_x p_R | J_\mu | p_T\rangle$ coincide with the invariant amplitude for the transition

$$\gamma^* + p_T \to p_x + p_R,$$

where γ^* is a virtual photon. Therefore, the differential cross section $d^5\sigma/dE'_e d\Omega_e d\Omega^*_x$ is usually expressed in terms of the cross sections $d\sigma_L/dt, d\sigma_T/dt, d\sigma_{LT}/dt$, and $d\sigma_{TT}/dt$ for the production of particle x by a virtual photon, where $t = k^2 = (p_x - q)^2$. Here, $d\sigma_L/dt$ and $d\sigma_T/dt$ are the cross sections for the cases of, respectively, transverse and longitudinal polarization, while $d\sigma_{LT}/dt$ and $d\sigma_{TT}/dt$ are interference terms. Obviously, the cross sections $d\sigma_i/dt$, $i = L,\ T, LT, TT$, must be proportional to bilinear combinations of currents (amplitudes) that we denote, by convention, as $\langle J^2\rangle_i$,

$$d\sigma_L/dt \sim \langle J^2\rangle_L = |J_{\lambda=0}|^2,$$
$$d\sigma_T/dt \sim \langle J^2\rangle_T = 1/2\Big\{|J_{\lambda=1}|^2 + |J_{\lambda=-1}|^2\Big\}, \quad (3)$$
$$d\sigma_{LT}/dt \sim \langle J^2\rangle_{LT} = Re\{J_{\lambda=0}\,(J_{\lambda=-1} - J_{\lambda=1})^*\},$$
$$d\sigma_{TT}/dt \sim \langle J^2\rangle_{TT} = Re\{J_{\lambda=1}J_{\lambda=-1}\}.$$

The proportionality factors are introduced by analogy with the definition of the cross section for a real photon. For the real-photon-induced photoproduction of particle x by a real photon, the differential cross in the c.m. frame of the final hadrons Rx is given by

$$\frac{d\sigma_T}{d\Omega^*_x} = \frac{\langle J^2\rangle_T}{(8\pi W)^2}\frac{|\mathbf{p}^*_x|}{|\mathbf{q}^*_r|}, \quad (4)$$

where $\mathbf{q}^*_r$ is the real-photon momentum in this frame. As a rule, the cross sections $d\sigma_i/dt$ for electroproduction mediated by a virtual photon are defined by analogy with expression (4), but this is done in such a way that the momentum $\mathbf{q}^*_r$ and the invariant mass W of final hadrons are related by the equation

$$|\mathbf{q}^*_r| = \frac{W^2 - M_T^2}{2W},$$

which is valid for a real photon. For the electroproduction, we therefore have

$$\frac{d\sigma_i}{d\Omega^*_x} = \frac{\langle J^2\rangle_i}{(8\pi W)^2}\frac{|\mathbf{p}^*_x|}{|\mathbf{q}^*_r|}, \quad (5)$$

but, here, $\mathbf{q}^*_r$ is taken to be the photon momentum by convention.

With allowance for the aforesaid, we can represent the differential cross section (2) in the form

$$\frac{d^5\sigma}{dE'_e d\Omega_e d\Omega^*_x} = \Gamma_t\left\{\varepsilon\frac{d\sigma_L}{dt} + \frac{d\sigma_T}{dt}\right. \quad (6)$$
$$\left. + \sqrt{2\varepsilon(1+\varepsilon)}\frac{d\sigma_{LT}}{dt}\cos\varphi_x + \varepsilon\frac{d\sigma_{TT}}{dt}\cos 2\varphi_x\right\},$$

where

$$\Gamma_t = \frac{\alpha}{(2\pi)^2}\frac{E'_e}{E_e}\frac{W^2 - M_T^2}{Q^2 M_T^2}\frac{1}{1-\varepsilon} \quad (7)$$

plays the role of the virtual-photon flux and

$$\frac{d\sigma_i}{dt} = \frac{d\sigma_i}{d\Omega^*_x}\frac{\pi}{|\mathbf{q}^*||\mathbf{p}_x|}. \quad (8)$$

We note that, in (8), $\mathbf{q}^*$ is the virtual-photon momentum in the c.m. frame. Its square is given by

$$\mathbf{q}^{*2} = \frac{\left(W^2 - Q^2 - M_T^2\right)^2}{4W^2} + Q^2.$$

Instead of E'_e, Ω_e, and Ω_x, use is often made of the invariant variables $Q^2 = 4E_e E'_e sin^2(\theta_e/2)$, $W^2 = M_T^2 + 2M_T(E_e + E'_e) - 4E_e E'_e \sin^2(\theta_e/2)$, and $t = k^2$. In this case, we have

$$\frac{d^4\sigma}{dW^2 dQ^2 dt d\varphi_x} = 2\pi\Gamma\frac{d^2\sigma}{dt d\varphi_x} \quad (9)$$
$$= \Gamma\Big\{\varepsilon\frac{d\sigma_L}{dt} + \frac{d\sigma_T}{dt}$$

$$+\sqrt{2\varepsilon(\varepsilon+1)}\frac{d\sigma_{LT}}{dt}\cos\varphi_x+\varepsilon\frac{d\sigma_{TT}}{dt}\cos 2\varphi_x\Big\}.$$

Here, Γ is a different flux of virtual photons:

$$\Gamma=\frac{\alpha}{(4\pi)^2}\frac{W^2-M_T^2}{Q^2E_e^2M_T^2}\frac{1}{1-\varepsilon}. \qquad (10)$$

Experimental results are presented in terms of $d\sigma_i/dt$.

2.2. Quasielastic Meson Knockout from a Nucleon

The formulas presented in the preceding section are quite general: they are applicable to atoms, molecules, nuclei, and hadrons, and no specific reaction mechanism is implied in them. We will now specify these formulas for the process of quasielastic meson knockout from nucleons, in which case the virtual-photon momentum is entirely transferred to the product pion. We define the relevant kinematical variables as $p_T=p_N=p$, $p_R=p'$, and $p_x=k'$.

In quasielastic knockout, the energy transfer q_0 and the momentum transfer $|\mathbf{q}|$ must be such that $|\mathbf{q}|\gg|\mathbf{k}|$, where $\mathbf{k}$ is the virtual-meson momentum ($\mathbf{k}=\mathbf{k}'-\mathbf{q}$), and that $q_0\gg E_B-M_N$, where E_B stands for the final-baryon energies. That the diagram in Fig. 2 is dominant formally expresses the quasielasticity of the process. Postponing the discussion of the question concerning dominance of the pole diagram to the end of this section, we are now going to comment on the formal aspects of quasielasticity.

If antiparticle degrees of freedom can be disregarded, the differential cross section $d^5\sigma/dE'_ed\Omega_ed\Omega^*_\pi$ for the case of the quasielastic mechanism (Fig. 2) can be expressed in terms of the wave function for the meson $м$ in the nucleon and the cross section for the scattering process $e+м\to e'+\pi$.

In this case, the invariant amplitude $\mathcal{M}_{fi}$ can indeed be represented in the form

$$\mathcal{M}_{fi}=\frac{\mathcal{M}(p\to p'k)\mathcal{M}(p_ek\to p'_ek')}{2\varepsilon_{\mathbf{k}}(E_p-E'_p-\varepsilon_{\mathbf{k}})}, \qquad (11)$$

where $\mathcal{M}(p\to p'k)$ and $\mathcal{M}(p_ek\to p'_ek')$ are the invariant amplitudes for the processes indicated parenthetically; $\varepsilon_{\mathbf{k}}=\sqrt{m_м^2+\mathbf{k}^2}$, $m_м$ being the meson (pion) mass; and $E_{\mathbf{p}}$ and $E'_{\mathbf{p}}$ are the energies of, respectively, the initial and the final nucleon. It goes without saying that all the required kinematical variables must appear in these amplitudes. According to conventional rules of field theory [25], the quantity $\mathcal{M}(p\to p'k)/\left(E_{\mathbf{p}}-E'_{\mathbf{p}}-\varepsilon_{\mathbf{k}}\right)$ specifies the matrix element $\langle p'|a_{\mathbf{k}m}|p\rangle$, which will be referred to as the wave function for the meson $м$ in the target T:

$$\Psi_T^{Rx}(\mathbf{k},m)=\left\langle p'\right|a_{\mathbf{k}m}\left|p\right\rangle=\frac{e_m^{\mu*}\mathcal{M}_\mu(p\to p'k)}{E_{\mathbf{p}}-E'_{\mathbf{p}}-\varepsilon_{\mathbf{k}}}, \qquad (12)$$

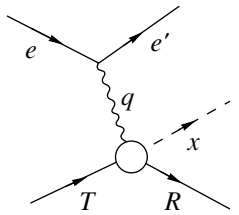

Fig. 2. Diagram for the electroproduction of particle x on a composite system T.

where $a_{\mathbf{k}m}$ is the annihilation operator for the meson $м$ of momentum $\mathbf{k}$, m being the projection of the meson spin.

For the amplitude in (11), the general formula (2) for the cross section $d^5\sigma/dE'_ed\Omega_ed\Omega^*_\pi$ takes the form

$$\frac{d^5\sigma}{dE'_ed\Omega_ed\Omega^*_\pi}=E'^2_e\frac{\overline{\left|\Psi_T^{Rм}(\mathbf{k},m)\right|^2}}{(4\pi)^3E_{\mathbf{p}}E'_{\mathbf{p}}\varepsilon_{\mathbf{k}}} \qquad (13)$$
$$\times\left(1-\frac{E'_{\mathbf{k}}}{|\mathbf{k}'|}\cos\theta_\pi\right)\frac{d\sigma^{\rm el}}{d\Omega_\pi},$$

where θ_π is the angle between the momenta of the emitted electron and pion, $d\sigma^{\rm el}/d\Omega_\pi$ is the cross section for elastic electron–meson scattering, and the overbar denotes averaging over spin projections.

The wave function is normalized by the condition

$$\int\overline{\left|\Psi_T^{Rм}(\mathbf{k},m)\right|^2}d\tau=S_T^{Rм}, \qquad (14)$$

where $S_T^{Rм}$ is the spectroscopic factor that was discussed in the Introduction, while the integration measure is given by

$$d\tau=d^3\mathbf{k}/\left[(4\pi)^3\,\varepsilon_kE_{\mathbf{p}}E'_{\mathbf{p}}\right].$$

The cross section for elastic electron–meson scattering—it appears in expression (13)—formally corresponds to the situation where the meson is bound in the nucleon in the initial state (the binding energy $E_{\rm b}$ of the meson being on the same order of magnitude as its mass), but is free in the final state, appearing to be high in a continuum. But in our case, where the energy of the knock-on meson is much greater than $E_{\rm b}$ and where, accordingly, its final momentum k' is much greater than its initial momentum k in the nucleon, the cross section for free $e\pi$ scattering under relevant kinematical conditions provides a highly accurate approximation to the cross section being discussed, and this fact is employed in expression (13). In other words, off-mass-shell effects in the amplitude can be disregarded in our case in dealing with the pole diagram. A similar problem is widely discussed in considering the quasielastic knockout of nucleons and nucleon clusters from nuclei [26]. But in the case of the tree diagram, such off-mass-shell effects for a virtual nucleon play an

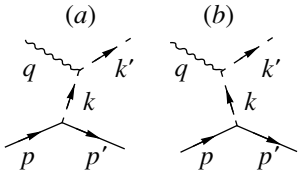

Fig. 3. Mechanisms of pion production on a proton under the effect of a virtual photon: (*a*) direct meson knockout by a virtual photon and (*b*) pion production through a meson-antimeson pair.

important role (see below). Further, the interaction of the knock-on pion and the spectator nucleon is disregarded in (13)—that is, use is made there of the plane-wave impulse approximation (PWIA) rather than distorted-wave impulse approximation (DWIA) (for a comparison of these two approximations in extracting the momentum distributions of the knock-on particle from experimental data, see [27]). In discussing specific results below, we will take qualitatively into account, however, the consequences of replacing plane waves by distorted ones.

The sum

$$\sum_R S_T^{R\mu} = N_\mu \qquad (15)$$

over final states determines the total number of μ-type mesons in the meson cloud of the nucleon.

The parametrization (13) of the cross section $d^5\sigma/dE'_e d\Omega_e d\Omega^*_\pi$ is very convenient in nonrelativistic physics. A vast body of valuable information about the structure of nuclei, atoms, and molecules was obtained on its basis [11, 12]. As a rule, this parametrization is not used in relativistic physics—experimentalists present their results in terms of the parametrization specified by Eqs. (6) and (9), because it is much more general than the parametrization in (13): the former includes, in a natural way, many mechanisms (in particular, resonance ones) and is valid not only in the quasielastic region. But it is because of this that it is much less efficient in the narrow quasielastic region than the quasielastic parametrization (13) proper.

Since the Feynman diagram in Fig. 2 involves not only meson knockout but also the production of meson pairs, it is necessary to generalize expression (13) in such a way as to incorporate the momentum distribution in it. This point will be discussed below.

2.3. Probing Meson Cloud

A. Pion cloud of the nucleon. Evaluation of the Feynman diagram in Fig. 2 is formally very simple, but it raises two questions of physical significance. First, these are the relationship between the contributions of the time-ordered diagrams in Figs. 3*a* (quasielastic knockout proper) and 3*b* (*Z* diagram describing meson-pair production) and the possibility of extracting the contribution corresponding to Fig. 3*a* from that associated with the sum of the diagrams. Second, mesons of the diagram in Fig. 2 are effective degrees of freedom. In this connection, there arises the problem of parametrizing the relevant vertices ($NN\mu$ and $\mu\pi\gamma$) and including form factors.

These questions are common to all mechanisms. We will consider them for the simplest example of the pion cloud. We emphasize once again that we perform our analysis in the laboratory frame, where the recoil momentum of the final baryon is low. It was indicated above that, for a first approximation, we can disregard off-mass-shell effects for the pion. Accordingly, the matrix element of the current J_λ (amplitude for the diagram in Fig. 2) is given by the obvious expression

$$J_\lambda = e\frac{\mathcal{M}(p\to n\pi)}{k^2-m_\pi^2}F_\pi(Q^2)(k+k')e_\lambda, \qquad (16)$$

where $F_\pi\left(Q^2\right)$ is the pion form factor, which was set to the free-pion form factor [28],

$$F_\pi\left(Q^2\right) = [1+Q^2/0.5\ (\mathrm{GeV}/c)^2]^{-1};$$

$\mathcal{M}(p\to n\pi)$ is the pion-absorption (pion-emission) amplitude; and $1/\left[k^2-m_\pi^2\right]$ is the conventional pion propagator. From Eq. (16), it can be seen that general principles of the diagram technique—the presence of only one amplitude for the two diagrams in Figs. 3*a* and 3*b*—make it possible to relate the contributions of these diagrams through the wave function as

$$\frac{\mathcal{M}(p\to n\pi)}{k^2-m_\pi^2} = \frac{\mathcal{M}(p\to n\pi)}{2\varepsilon_{\mathbf{k}}}\frac{1}{k_0-\varepsilon_{\mathbf{k}}}$$
$$\times\left[1-\frac{k_0-\varepsilon_{\mathbf{k}}}{k_0+\varepsilon_{\mathbf{k}}}\right] = \frac{\Psi_p^{n\pi}(\mathbf{k},m)}{2\varepsilon_{\mathbf{k}}}\left[1-\frac{k_0-\varepsilon_{\mathbf{k}}}{k_0+\varepsilon_{\mathbf{k}}}\right];$$

that is,

$$\frac{\mathcal{M}(p\to n\pi)}{k^2-m_\pi^2} = \frac{\Psi_p^{n\pi}(\mathbf{k},m)}{\varepsilon_{\mathbf{k}}}. \qquad (17)$$

In deriving Eq. (17), we considered that, for $\left|k^2\right| \leqslant 0.2\ (\mathrm{GeV}/c)^2$, the final neutron is nonrelativistic; therefore, $k_0 \ll \varepsilon_{\mathbf{k}}$.

It should also be emphasized that the total amplitude (that is, the sum of the amplitudes for the diagrams in Figs. 3*a* and 3*b*) is approximately twice as great as the amplitude for the diagram in Fig. 3*a*.

The wave function in turn can be related to the form factor $g_{\pi NN}(k^2)$ for the πNN vertex. For the πNN interaction in the pseudoscar version used most often [29] (in the situation considered here, the pseudoscalar and the pseudovector version are equivalent), we have

$$\Psi_p^{n\pi}(\mathbf{k},m) = \frac{\mathcal{M}(p\to n\pi)}{k_0-\varepsilon_{\mathbf{k}}} \qquad (18)$$

$$= \sqrt{2} G_{\pi NN}\, g_{\pi NN}(k^2) \frac{\bar{u}(p')\gamma^5 u(p)}{k_0 - \varepsilon_{\mathbf{k}}},$$

where $u(p')$ and $u(p)$ are the Dirac spinors for the initial and final nucleon, respectively; $G_{\pi NN}$ is the πNN-vertex constant; $g_{\pi NN}\left(k^2\right)$ is the corresponding form factor; and

$$\gamma^5 = \begin{pmatrix} 0 & -I \\ -I & 0 \end{pmatrix}$$

is the conventional Dirac matrix. The form factor $g_{\pi NN}\left(k^2\right)$ is usually taken in the form

$$g_{\pi NN}(k^2) = \frac{\Lambda_\pi^2 - m_\pi^2}{\Lambda_\pi^2 + k^2},$$

where Λ_π is the cutoff parameter.

Taking the modulus squared on both sides of Eq. (18) and performing summation and averaging over spins, we obtain

$$\overline{\left|\Psi_p^{n\pi}(\mathbf{k}, m)\right|^2} = 2 G_{\pi NN}^2\, g_{\pi NN}^2(k^2) \frac{\left|k^2\right|}{\left(k_0 - \varepsilon_{\mathbf{k}}\right)^2}. \quad (19)$$

It is convenient to define the radial part of the wave function in such a way that, in the laboratory frame, it is normalized to the spectroscopic factor as

$$\frac{\overline{\left|\Psi_p^{n\pi}(\mathbf{k}, m)\right|^2}}{(4\pi)^3 E_N(\mathbf{k}) M_N \varepsilon_{\mathbf{k}}} = \frac{\left|R_p^{n\pi}(k)\right|^2}{4\pi}, \quad (20)$$

where $E_N(\mathbf{k}) = \sqrt{M_N^2 + \mathbf{k}^2}$ and

$$\int \left|R_p^{n\pi}(k)\right|^2 k^2 dk = S_p^{n\pi}. \quad (21)$$

With the aid of (17), we represent the differential cross sections in the form

$$\frac{d\sigma_i}{dt} = \frac{1}{16} \frac{\alpha}{W^2 |\mathbf{q}|\, |\mathbf{q}_r|} \quad (22)$$
$$\times \frac{\overline{\left|\Psi_p^{n\pi}(\mathbf{k}, m)\right|^2}}{\varepsilon_{\mathbf{k}}^2} F_\pi^2(Q^2) \left|(k + k')_i\right|^2,$$

where $i = L, T$ and

$$\left|(k + k')_L\right|^2 = \frac{4}{Q^2}(q_z k_0' - q_0 k_z')^2,$$

$$\left|(k + k')_T\right|^2 = 2\left(k_x'^2 + k_y'^2\right)^2.$$

Expression (12) defines the wave function in the most direct way. It is of course interesting to compare this result with other ways of introducing the pion wave function in the nucleon. They are based on reconstructing the wave function on the basis of πN potentials that describe phase shifts for elastic πN scattering [30, 31].

The potential for πN scattering is defined in terms of a set of diagrams that cannot be broken down into parts by cutting only a nucleon or only a pion line. The sum of the pole and the contact diagram is taken here for the potential (Fig. 4). The first diagram has a pole at the bare-nucleon mass, while the second is approximated by the factorized potential

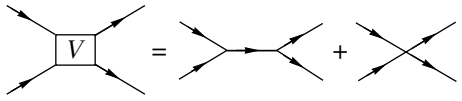

Fig. 4. Diagram representation of the πN-interaction potential (this potential was used in [30, 31]).

$$V(k, k', E) = \frac{f_0(k) f_0(k')}{E - M_{N_0} + i\delta} - h_0(k) h_0(k'), \quad (23)$$

where M_{N_0} is the bare-nucleon mass and M_N is the physical-nucleon mass. The functions $f_0(k)$ and $h_0(k)$ are chosen in such a way as to obtain a satisfactory description of the phase shifts for πN scattering.

The radial part of the pion wave function in the nucleon (this is the quantity of our prime interest) is determined from the residue of the exact πN propagator (a model one in the present formulation of the problem) $G(k, k', E)$:

$$G(k, k', E)\,|_{E \to M_N} = \frac{f(k, M_N) f(k', M_N)}{E - M_N}. \quad (24)$$

We then have

$$R_p^{n\pi}(k) = \frac{\sqrt{2} f(k, E = M_N)}{M_N - \varepsilon_{\mathbf{k}} - \varepsilon_{N_0}(\mathbf{k})}, \quad (25)$$

where

$$\varepsilon_{N_0}(\mathbf{k}) = \sqrt{\mathbf{k}^2 + M_{N_0}^2}.$$

The function $f(k, E)$ and the mass of the bare nucleon N_0 can easily be found from the equations presented in [31]:

$$f(k, E) = f_0(k, E) + h_0(k)\tau_0(E) \quad (26)$$
$$\times \int k'^2 dk' h_0(k') f_0(k') D_{\pi N}(k', E),$$

$$D_{\pi N}(k, E) = \left[E - \varepsilon_{\mathbf{k}} - \varepsilon_{N_0}(\mathbf{k}) + i\delta\right]^{-1},$$

$$\tau_0(E) = -\left[1 + \int k^2 dk \left|h_0(k)\right|^2 D_{\pi N}(k, E)\right]^{-1}.$$

Since there is a pole term in the potential, the wave function $R_p^{n\pi}(k)$ satisfies the nontrivial normalization condition [32]

$$\int \left|R_p^{n\pi}(k)\right|^2 k^2 dk \quad (27)$$
$$+ \frac{1}{(M_N - M_{N_0})^2} \left(\int R_p^{n\pi}(k) k^2 dk\right)^2 = 1,$$

which can be used, in particular, to test the results of a calculation.

Expression (22), which includes, in relation to the relativistic formalism, the new, essentially relativistic effect of the Z diagram, specifies the wave function in terms of the cross section without intermediate integrations, which would appear for diagrams that are more complicated than the pole one. But this is precisely our eventual objective. Following the same line of reasoning as above, we will generalize below expression (22) to the case where an electron impact converts various mesons into pions.

B. Rho-meson cloud of the nucleon. It will be seen below that, in the quasielastic region, the cross section $d\sigma_T/dt$ is determined by the diagram in Fig. 2, where a rho meson appears to be a virtual particle. Therefore, experimental data on the cross section $d\sigma_T/dt$ can be used to determine the structural features of the rho-meson cloud of the nucleon—specifically, its momentum distribution and spectroscopic factor.

However, formulas that relate the cross section $d\sigma_T/dt$ to the rho-meson wave function are more cumbersome than the analogous formulas that relate the cross section for longitudinal polarization to the pion wave function.

In order to find these relations, we will need effective Lagrangians for the ρNN and the $\rho\pi\gamma$ interaction. For these, we took the traditionally used expressions [33]

$$L_{\rho NN} = -G_{\rho NN} g_{\rho NN}(k^2) \times \bar{\Psi}\left(\gamma^\mu - \frac{\kappa}{2M_N}\sigma^{\mu\nu} i\partial_\mu\right)\tau\varphi_\nu\Psi, \quad (28)$$

$$L_{\rho\pi\gamma} = \frac{g_{\rho\pi\gamma}}{m_\pi}\varepsilon^{\alpha\beta\nu\mu}\partial_\alpha A_\beta \varphi \partial_\nu \varphi_\mu,$$

where φ and φ_μ are the isovector fields of pseudoscalar pions and vector rho mesons; Ψ is the nucleon field; A_β is the photon field; γ^μ are the Dirac matrices; $\sigma^{\mu\nu} = 1/2 \times [\gamma^\mu, \gamma^\nu]$; M_N and m_π are, respectively, the nucleon and the pion mass; $g_{\rho NN}\left(k^2\right)$ is the form factor for the ρNN vertex; $g_{\rho\pi\gamma}$ is the $\rho\pi\gamma$ vertex constant; κ is the vector magnetic moment of the nucleon; and $\tau = (\tau_1, \tau_2, \tau_3)$ are the isospin Pauli matrices. In accordance with [33], the constants were taken to be the following: $G_{\rho NN} = 2.9$, $g_{\rho\pi\gamma} = 0.0378/e$, and $\kappa = 6.1$; $e = 0.3027$ is the electron charge.

Further, the matrix element of the operator responsible for absorption of a rho meson carrying the vector index μ is related to the amplitude

$$\mathcal{M}^\mu\left(p \to n\rho^+\right) = \sqrt{2} G_{\rho NN} g_{\rho NN}\left(k^2\right)\bar{u}\left(p'\right)\Gamma^\mu u\left(p\right)$$

$$\left(\Gamma^\mu = \gamma^\mu + \frac{\kappa}{2M_N}\sigma^{\mu\nu}k_\mu\right)$$

for the virtual decay $p \to n\rho^+$ by the equation

$$\frac{\mathcal{M}^\mu(p \to n\rho)}{k_0 - \varepsilon_{\mathbf{k}}} = \left\langle p'\middle|a^\mu_\rho(\mathbf{k})\middle|p\right\rangle, \quad (29)$$

which is analogous to that for the case of pions [25]. Here,

$$a^\mu_\rho(\mathbf{k}) = a_{\mathbf{k}m} e^\mu_m, \quad (30)$$

where $a_{\mathbf{k}m}$ is the operator describing the absorption of a ρ^+ meson characterized by the spin projection m onto the quantization axis and

$$e^\mu_m = \left(\frac{(\mathbf{k}\cdot\mathbf{e}_m)}{m_\rho}, \mathbf{e}_m + \frac{\mathbf{k}(\mathbf{k}\cdot\mathbf{e}_m)}{m_\rho(\varepsilon_{\mathbf{k}} + m_\rho)}\right) \quad (31)$$

are the unit vectors of free-rho-meson polarization [$e_{m=0} = (0, 0, 1)$, $e_{m=\pm1} = \pm\frac{1}{\sqrt{2}}(-m, -i, 0)$].

Relation (29) is somewhat nontrivial. The point is that the quantity $\langle p'|a^\mu_\rho(\mathbf{k})|p\rangle$, which appears in the residues of the Fourier transform of the Green's function $\langle n|T\{\varphi^\mu(x)\varphi^{\nu+}(x')\}|n\rangle$ (n is a neutron), corresponds to the amplitude that is determined by the total set of diagrams converting a proton into a neutron and a rho meson and which is multiplied by the rho-meson (that is, particle) part of the propagator $D_{\mu\nu}(k)$ ρ for the rho-meson field. However, the vector-particle propagator

$$D_{\mu\nu}(k) = \frac{1}{k^2 - m^2_\rho}\left[-g_{\mu\nu} + \frac{k_\mu k_\nu}{m^2_\rho}\right]$$

can no longer be represented [34] as the sum of the particle and the antiparticle propagator—in addition, it involves a contact term,

$$D_{\mu\nu}(k) = \frac{1}{(k_0 - \varepsilon_{\mathbf{k}})2\varepsilon_{\mathbf{k}}}\left[-g_{\mu\nu} + \frac{k'_\mu k'_\nu}{m^2_\rho}\right] - \frac{1}{(k_0 + \varepsilon_{\mathbf{k}})2\varepsilon_{\mathbf{k}}}\left[-g_{\mu\nu} + \frac{k''_\mu k''_\nu}{m^2_\rho}\right] - \frac{1}{m^2_\rho}\delta_{\mu0}\delta_{\nu0},$$

where $k'^\mu = \left(\sqrt{m^2_\rho + \mathbf{k}^2}, \mathbf{k}\right)$ and $k''^\mu = \left(\sqrt{m^2_\rho + \mathbf{k}^2}, -\mathbf{k}\right)$.

The contact part $-\delta_{\mu0}\delta_{\nu0}/m^2_\rho$ of the propagator for the rho-meson field is disregarded in (29). In our case, this part corresponds to direct $\gamma\pi NN$ interaction not mediated by a meson and seems to have no bearing on the problems concerning the structure of the rho-meson cloud that are discussed here.

In just the same way as was done for pions, the quantity $\langle p'|a_{\mathbf{k}m}|p\rangle$ will be referred to as the rho-meson wave function in the nucleon.

Expressions (3) for the effective electroproduction cross section involve bilinear matrix elements of the

hadronic current J_λ that are related to the amplitude $\mathcal{M}^\mu(p \to n\rho)$ by the equation

$$J_\lambda = e\frac{\mathcal{M}_\mu(p\to n\rho)}{k^2-m_\rho^2}\left(-g^{\mu\nu}+\frac{k_\mu k_\nu}{m_\rho^2}\right) \times \varepsilon^{\mu\nu\alpha\beta}e_{\lambda\nu}q_\alpha k_\beta\frac{g_{\rho\pi\gamma}}{m_\pi}F_{\pi\rho}(Q^2) \quad (32)$$

or, since we have $\mathcal{M}^\mu k_\mu = 0$,

$$J_\lambda = e\frac{\mathcal{M}_\mu(p\to n\rho)}{k^2-m_\rho^2}\varepsilon^{\mu\nu\alpha\beta}e_{\lambda\nu}q_\alpha k_\beta\frac{g_{\rho\pi\gamma}}{m_\pi}F_{\rho\pi}(Q^2), \quad (33)$$

where $\varepsilon^{\mu\nu\alpha\beta}$ is an antisymmetric tensor, $e_{\lambda\nu}$ is the photon polarization vector, and $F_{\rho\pi}\left(Q^2\right)$ is the form factor for the $\rho\pi\gamma$ transition. Following [35], we set

$$F_{\rho\pi}\left(Q^2\right) = [1+q^2/(3m_\rho)^2]^{-2}.$$

Thus, the problem consists in expressing the bilinear combinations $J_\lambda J_\lambda^*$ of the current in terms of the radial part of the wave function $R_p^{n\rho}(\mathbf{k},m)$. This relation was established by invoking the $g_{\rho NN}\left(k^2\right)$ form factor.

Taking the square of the modulus of $\Psi_p^{n\rho}\left(\mathbf{k},m\right)$ and performing summation and averaging over the spins of the nucleons and the rho-meson involved, we can easily obtain

$$\overline{|\Psi_p^{n\rho}(\mathbf{k},m)|^2} = \frac{\overline{\left|e_m^{\mu*}\mathcal{M}_\mu(p\to n\rho)\right|^2}}{\left(k_0-\varepsilon_\mathbf{k}\right)^2}, \quad (34)$$

where the overbar denotes the aforementioned averaging.

By directly evaluating the quantity $\overline{\left|e_m^{\mu*}\mathcal{M}_\mu(p\to n\rho)\right|^2}$ in the target rest frame, we find that $\left|R_p^{n\rho}(k)\right|^2$ and $g_{\rho NN}\left(k^2\right)$ can be related as

$$\left|R_p^{n\rho}(k)\right|^2 = \frac{G_{\rho NN}^2 g_{\rho NN}^2(k^2)}{(k_0-\varepsilon_\mathbf{k})^2}\frac{2}{3}\frac{1}{(4\pi)^2E_N(\mathbf{k})M_N\varepsilon_\mathbf{k}} \times\left[2(1+\kappa)^2\left(2M_N(M_N-k_0+\varepsilon_\mathbf{k})\frac{\mathbf{k}^2}{m_\rho^2} - (E_N(\mathbf{k})M_N-M_N^2)\right)\right. + \left(\frac{\kappa^2}{2M_N}(E_N(\mathbf{k})+M_N)-2(1+\kappa)\right) \left.\times(2M_N-k_0+\varepsilon_\mathbf{k})^2\frac{\mathbf{k}^2}{m_\rho^2}\right], \quad (35)$$

where $\varepsilon_\mathbf{k}=\sqrt{m_\rho^2+\mathbf{k}^2}$, $E_N(\mathbf{k})=\sqrt{M^2+\mathbf{k}^2}$, and $\mathbf{k}$ is the rho-meson momentum in the laboratory frame.

Accordingly, the bilinear combinations $\left\langle J^2\right\rangle_{L,T}$ of the currents are given by

$$\overline{|J_L|^2} = B\cdot 2(1+\kappa)^2(E_N(\mathbf{k})M_N-M_N^2)Q^2(k_x^2+k_y^2), \quad (36)$$

$$\overline{|J_T|^2} = B\left[M_N^2\left\{4(1-\kappa^2)+\frac{2\kappa^2}{M_N}(E_N(\mathbf{k})+M_N)\right\}\frac{\mathbf{q}^2}{2}(k_x^2+k_y^2)\right. \quad (37)$$
$$\left.-2(1+\kappa)^2M_N(E_N(\mathbf{k})-M_N)\left\{\frac{Q^2}{2}(k_x^2+k_y^2)-(q_zk_0-q_0k_z)^2\right\}\right],$$

where

$$B = 2e^2G_{\rho NN}^2\frac{g_{\rho NN}^2(k)}{\left(k^2-m_\rho^2\right)^2}\frac{g_{\rho\pi\gamma}^2}{m_\pi^2}F_{\pi\rho}^2(Q^2)$$

and k_x, k_y, and k_z are the components of the virtual-rho-meson 3-momentum.

We note that, in the literature, $g_{\rho NN}\left(k^2\right)$ is usually parameterized as

$$g_{\rho NN}(k^2) = \frac{\Lambda_\rho^2-m_\rho^2}{\Lambda_\rho^2+k^2}, \quad (38)$$

where Λ_ρ is the cutoff parameter.

C. Omega-meson cloud of the nucleon. That vector mesons make a dominant contribution to the pion-electroduction cross section σ_T for the case of transverse polarization provides a unique possibility of probing the omega-meson cloud of the nucleon. This is achieved in experiments implementing the exclusive quasielastic knockout of neutral pions by electrons. In contrast to what occurs in the case of charged pions, there is no direct knockout of neutral pions here (the matrix element $\left\langle\pi^0|J^\mu|\pi^0\right\rangle$ of the electromagnetic current vanishes because of charge symmetry), so that all neutral pions arise via the deexcitation of ρ^0 and ω mesons by virtual photons.

That ρ^0 and ω mesons are simultaneously involved here makes it possible to determine not only the parameters of the omega-meson cloud—the momentum distribution and the spectroscopic factor—but also the relative sign of the constants $G_{\rho NN}$ and $G_{\omega NN}$.

A general formalism for analyzing quasielastic

neutral-pion knockout is identical to that outlined in the subsection devoted to the rho-meson cloud. In the case being considered, the matrix element J_λ of the hadronic current has the form

$$J_\lambda = J_\lambda^{(\rho)} + J_\lambda^{(\omega)}, \tag{39}$$

where

$$J_\lambda^{(\rho)} = -eG_{\rho NN} g_{\rho NN}(k) \frac{\bar{u}\Gamma^{(\rho)\mu} u}{k^2 - m_\rho^2} \frac{g_{\rho\pi\gamma}}{m_\pi} F_{\rho\pi}(Q^2) \varepsilon_{\lambda\mu}^{(\rho)}, \tag{40}$$

$$J_\lambda^{(\omega)} = -eG_{\omega NN} g_{\omega NN}(k^2) \times \frac{\bar{u}\Gamma^{(\omega)\mu} u}{k^2 - m_\omega^2} \frac{g_{\omega\pi\gamma}}{m_\pi} F_{\omega\pi}(Q^2) \varepsilon_{\lambda\mu}^{(\omega)}.$$

Here, $G_{\omega NN}$ is the constant of omega-meson coupling to nucleons; $g_{\omega NN}\left(k^2\right)$ is a form factor; m_ω is the ω-meson mass; $\Gamma^{(\rho,\omega)\mu}$ stands for the effective vertices for ρ^0- and ω-meson emission from nucleons,

$$\Gamma^{(\rho,\omega)\mu} = \gamma^\mu + \frac{\kappa_{\rho,\omega}}{2M_N} \sigma^{\mu\nu} k_\mu;$$

$F_{\rho\pi}\left(Q^2\right)$ and $F_{\omega\pi}\left(Q^2\right)$ are the form factors for the $\rho^0 \to \pi^0$ and $\omega \to \pi^0$ transitions induced by a virtual photon; and $\varepsilon_\lambda^\mu \equiv \varepsilon^{\mu\sigma\alpha\beta} e_{\lambda\sigma} q_\alpha k_\beta$, $\varepsilon^{\mu\sigma\alpha\beta}$ being a unit antisymmetric tensor in Minkowski space.

In order to determine $d\sigma_L/dt$ and $d\sigma_T/dt$, we need the quantities

$$\overline{|J_\lambda|^2} = \overline{\left|J_\lambda^{(\rho)} + J_\lambda^{(\omega)}\right|^2} = \overline{\left|J_\lambda^{(\rho)}\right|^2} + \overline{\left|J_\lambda^{(\omega)}\right|^2} + 2Re\left(\overline{J_\lambda^{(\rho)} J_\lambda^{(\omega)*}}\right), \tag{41}$$

where the overbar denotes averaging and summation over spins.

We denote by $\mathrm{B}_{\rho\omega}$ the following combination of factors:

$$B_{\omega\rho} = 2e^2 G_{\omega NN} G_{\rho NN} \times \frac{g_{\omega NN}(k) g_{\rho NN}(k)}{\left(k^2 - m_\omega^2\right)\left(k^2 - m_\rho^2\right)} \frac{g_{\omega\pi\gamma} g_{\rho\pi\gamma}}{m_\pi^2} F_{\pi\omega}(Q^2) F_{\pi\rho}(Q^2). \tag{42}$$

Similarly, we will denote by B_ρ or B_ω a product of the form (42) with the substitution $\omega \to \rho$ or $\rho \to \omega$, respectively. The quantity $|J_\lambda^{(\rho)}|^2$ was obtained above, while $|J_\lambda^{(\omega)}|^2$ can be derived from $|J_\lambda^{(\rho)}|^2$ by means of the substitution $\rho \to \omega$. For $\mathrm{Re}(J_\lambda^{(\rho)} J_\lambda^{(\omega)*})$ in the laboratory frame, we have

$$\overline{\left|Re\left(J_{\lambda=0}^{(\rho)} J_{\lambda=0}^{(\omega)*}\right)\right|} = B_{\omega\rho} 2(1+\kappa)^2 (E_N(\mathbf{k}) M_N - M_N^2) Q^2 (k_x^2 + k_y^2),$$

$$\overline{\left|Re\left(J_{\lambda=\pm1}^{(\rho)} J_{\lambda=\pm1}^{(\omega)*}\right)\right|} = B_{\sigma\rho}\left[M_N^2\left\{4(1-\kappa_\omega\kappa_\rho) + \frac{2\kappa_\omega\kappa_\rho}{M_N}(E_N(\mathbf{k}) + M_N)\right\}\frac{\mathbf{q}^2}{2}(k_x^2 + k_y^2)\right. \tag{43}$$

$$\left. -2(1+\kappa_\omega)(1+\kappa_\rho) M_N (E_N(\mathbf{k}) - M_N)\left\{\frac{Q^2}{2}(k_x^2 + k_y^2) - (q_z k_0 - q_0 k_z)^2\right\}\right],$$

where $g_{\rho NN}$ and $g_{\omega NN}$ are functions of k^2. Instead of them, we can introduce the ρ^0- and ω-meson wave functions

$$\left|R_p^{n\rho(\omega)}(k)\right|^2 = A_{\rho(\omega)}(k) g_{\rho(\omega)NN}^2(k^2), \tag{44}$$

where

$$A_{\rho(\omega)}(k) = \frac{1}{\left(k_0 - \varepsilon_{\mathbf{k}}^{\rho(\omega)}\right)^2} \frac{2}{3} \frac{1}{(4\pi)^3 \varepsilon_{\mathbf{k}}^{\rho(\omega)} E_N(\mathbf{k}) M_N} \tag{45}$$

$$\times\left[2(1+\kappa_{\rho(\omega)})^2\left(2M_N(M_N - k_0 + \in_{\mathbf{k}}^{\rho(\omega)})\frac{\mathbf{k}^2}{m_{\rho(\omega)}^2} - (pp' - M_N^2)\right)\right.$$

$$\left. + \left(\frac{1}{2}\frac{\kappa_{\rho(\omega)}}{M_N^2}(pp' + M_N^2) - 2(1+\kappa_{\rho(\omega)})\kappa_{\rho(\omega)}\right)(2M_N - k_0 + \in_{\mathbf{k}}^{\rho(\omega)})^2 \frac{\mathbf{k}^2}{m_{\rho(\omega)}^2}\right].$$

2.4. Problems Associated with Dominance of Diagrams Involving a Pole in the t Channel

We have already indicated that, in the relativistic energy region, where particles can transform into one another, the concept of quasielastic knockout can run into difficulties, which will be exemplified here by considering pion knockout. Needless to say, a pion cloud exists in the nucleon, and a virtual photon can

transfer its momentum and energy directly to a pion from the cloud. In addition to the pion-in-flight process (pole diagram in Fig. 2), there is, however, quite a peculiar shake-off mechanism (Fig. 5) consisting in that the proton that has first absorbed the virtual photon shakes off a pion (tree diagram). The amplitudes of these diagrams cannot be separated and must generally be taken into account simultaneously [36]. As a result, the total amplitude for pointlike particles must have the form

$$J_\lambda = ie\sqrt{2}G_{\pi NN}\bar{u}'\gamma^5\frac{(\hat{p}+\hat{q})+M}{(p+q)^2-M^2}\gamma^\mu e_{\lambda\mu}u$$
$$+ ie\sqrt{2}G_{\pi NN}\frac{\bar{u}'\gamma^5 u}{k^2-m_\pi^2}\left(k+k'\right)e_\lambda,$$

where $\hat{p} = p_\mu\gamma^\mu$.

We will demonstrate that, in the case of quasielastic-knockout kinematics, the tree diagram is strongly suppressed because of high photon virtuality, to a considerable extent. Since, in the dominant pole diagram, off-mass-effects for the meson can be disregarded in the region being considered, the case in question is governed by free $e\pi$ interaction, which can be straightforwardly chosen in a gauge-invariant form. Thus, we will discuss the contributions of the diagrams in Figs. 2 and 5 in various situations.

For the case of transverse polarization, the cross sections for the photo- and the electroproduction channel at $W = 2$ GeV and $Q^2 = 1$ $(\mathrm{GeV}/c)^2$ are displayed in Figs. 6*a* and 6*b*, respectively. Off-mass-shell effects are disregarded for the virtual nucleon and the pion. From these figures, it can be seen that, for the case of transverse polarization, either diagram makes a sizable contribution to the cross section. It should be emphasized, however, that the tree diagram in Fig. 5 reduces the cross section significantly. This highlights the importance of taking into account the rho meson.

For the case of longitudinal polarization, Figs. 7*a* and 7*b* display the pion-electroproduction cross sections. It can be seen that, without the form factors, the tree diagram makes but a marginal contribution to the cross section for longitudinal polarization. The inclusion of the form factors $F_\pi(Q^2) = (1+Q^2/0.5)^{-1}$ and $F_N(Q^2) = (1+Q^2/0.7)^{-2}$ leads to a further strong suppression of the tree diagram. As a result, there arises a situation where the cross section for a longitudinal polarization must actually be interpreted in terms of the quasielastic-knockout mechanism exclusively. For the sake of completeness, it is also necessary to take into account off-mass-shell effects. For pions, this is of secondary importance in the case of the pole diagram because of the smallness of k^2 in relation to k'^2 [27]. For a virtual proton (Fig. 5), off-mass-shell effects could be

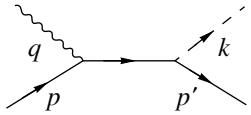

Fig. 5. Tree diagram for pion electro- and photoproduction.

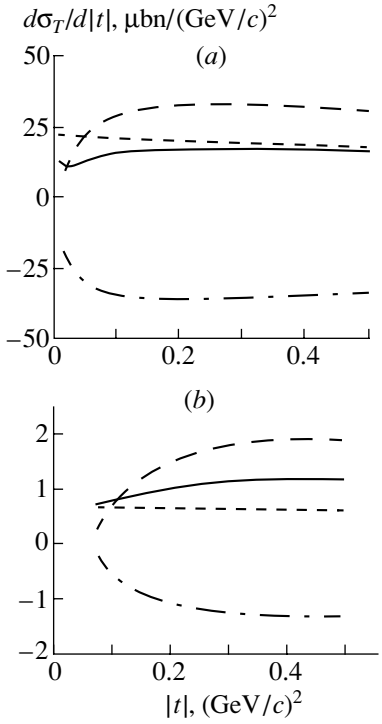

Fig. 6. Cross sections $d\sigma_T/dt$ for pion (a) photo- and (b) electroproduction on a proton for transverse polarization according to calculations that take into account only the diagrams in Figs. 2 and 5: (solid curve) total cross section, (long dashes) contribution of the pion-in-flight mechanism, (short dashes) contribution of the tree mechanism, and (dash-dotted curve) interference of the two mechanisms ($W = 2$ GeV, $Q = 1$ $(\mathrm{GeV}/c)^2$).

of importance for the tree diagram; for the right-hand vertex involving the pionic decay of a virtual nucleon, it may prove to be necessary to include, along with the form factor (38), the form factor

$$F(W^2) = \left(1+\frac{W^2-M^2}{\Lambda^2}\right)^{-2}, \qquad (46)$$

where W is the total energy of the virtual nucleon and where it is the quantity $W^2 - M^2$ that characterizes its virtuality.

This question is addressed in analyzing the contribution of pions to the deep-inelastic scattering of electrons [9], but, for the exclusive processes considered here, there are no visible grounds to assume that it is different from unity—that is, there are no grounds

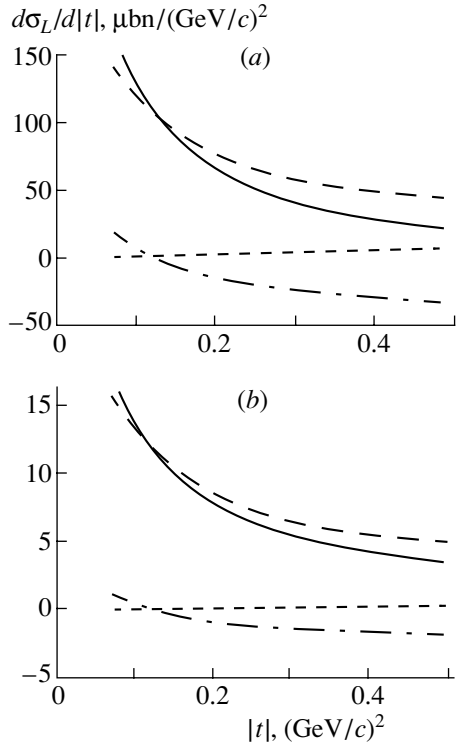

Fig. 7. Cross section $d\sigma_L/dt$ for pion electroproduction on a proton for longitudinal polarization: (*a*) result obtained in the approximation of pointlike pions and nucleons and (*b*) result obtained with allowance for their electromagnetic form factors. The notation for the curves is identical to that in Fig. 6.

to eliminate the tree diagram from the analysis of pion photoproduction.

By and large, the above analysis compellingly confirms, from the formal point of view, that, in [21–23], it was legitimate to use the pole approximation in the kinematics of quasielastic pion knockout by electrons. In those studies, we relied on the simplest criterion: for the pole diagram, the momentum distribution of knock-on pions in the nucleon as determined from experimental data according to relevant formulas is independent of the kinetic energy of the knock-on pion, provided that this energy is sufficiently high.

The studies reported in [20] and [35] are especially close to the range of problems that we address. Pion electroproduction on a nucleon for the case where the energy transfer from the electron and the virtual-photon mass satisfy the conditions $\nu > 2.2$ GeV and $Q^2 < 1$ (GeV/c)^2, respectively, was discussed by Guttner *et al.* [20], who employed the impulse approximation and factorized the cross section. In line with the general theory of inclusive experiments that makes use of light-front dynamics, they introduced, however, the Bjorken variable x and extracted, from experimental data, the distribution of pions,

$$G_{\pi/p}(x) = 1/(8\pi^2)$$
$$\times \int_{-\infty}^{t_{\min}} dt(-t)G_{\pi NN}F^2_{\pi NN}(t)/(t-m_\pi^2),$$

where $t_{\min} = -x^2M_N^2/(1-x)$ and where the momentum distribution of pions that is discussed in the present study appears as the integrand; here, $F_{\pi NN}(t)$ is the pion–nucleon form factor expressed in [20], in a model-dependent way, in terms of the quark-bag radius R as a parameter. In a similar formulation of the problem, Speth and Zoller [35] discussed the pion and the rho-meson wave function. These wave functions are also parametrized in terms of the bag radius R, which is estimated on the basis of the experimental cross sections $d\sigma_L/d\Omega_\pi$ and $d\sigma_T/d\Omega_\pi$. Thus, we develop the ideas presented in [20] and [35], going over, in the kinematical region where the pole diagram is dominant, to the instantaneous form of dynamics in the laboratory frame. That this results in the doubling of the number of pole diagrams does not present any serious problem since the underlying mechanism is quite simple. This made it possible to formulate, for the first time, the problem of directly extracting, from experimental data, the momentum distributions $\left|\Psi_N^{N'\pi}(k)\right|^2$, $\left|\Psi_N^{N'\rho}(k)\right|^2$, $\left|\Psi_N^{N'\omega}(k)\right|^2$, etc., at sufficiently low values of $\mathbf{k}$ (in the laboratory frame), which correspond to quasielastic kinematics, and at sufficiently high values of the virtual-photon mass squared Q^2, which are peculiar to the quasielastic mechanism, and to demonstrate that the more complicated mechanism associated with the tree diagram is inoperative here (that there is an asymptotic trend toward this with increasing Q^2 was indicated in [35]). A specific relationship between the aforementioned two forms of dynamics will be discussed by considering the example of spectroscopic factors.

2.5. Relationship between the Instantaneous Form of Dynamics and Light-Front Dynamics

The above formulas were obtained within the instantaneous form of dynamics [37]. Meanwhile, there recently appeared a great number of studies [9, 36–39] where phenomena allied to those that we consider were analyzed within light-front dynamics [37, 40].

Here, we will discuss only the relationship between the spectroscopic factors within these two forms of dynamics.

It is well known (see [41]) that the instantaneous form of dynamics and light-front dynamics are equivalent in the infinite-momentum frame of the initial

proton. By virtue of the geometric law of transformations under boosts, results found within light-front dynamics in the infinite-momentum frame must coincide with the corresponding results in any other reference frame related to it by Lorentz transformations.

As we have already seen, the spectroscopic factor in the proton rest frame is given by

$$S_p^{n\mu} = \int \frac{d^3\mathbf{k}}{(4\pi)^3 M_N E_N(\mathbf{p}')\varepsilon_{\mathbf{k}}} \times \frac{\overline{|\mathcal{M}|^2}}{(M_N - E_N(\mathbf{p}') - \varepsilon_{\mathbf{k}})^2}. \quad (47)$$

In an arbitrary rest frame, the spectroscopic factor can be written as

$$S_p^{n\mu} = \int \frac{d^3\tilde{\mathbf{k}}}{(4\pi)^3 E_N(\mathbf{p})E_N(\mathbf{p}')\varepsilon_{\tilde{\mathbf{k}}}} \times \frac{\overline{|\mathcal{M}|^2}}{(E_N(\mathbf{p}) - E_N(\mathbf{p}') - \varepsilon_{\tilde{\mathbf{k}}})^2}, \quad (48)$$

where $\tilde{\mathbf{k}}$ is the meson momentum and $\mathbf{p}$ and $\mathbf{p}'$ are the momenta of, respectively, the initial and the final nucleon. Going over to the limit $p_z \to \infty$, we can easily obtain

$$S_{p\infty}^{n\mu} = \int \frac{d\tilde{\mathbf{k}}_\perp}{(4\pi)^3}\frac{dx}{x(1-x)}\frac{4\overline{|\mathcal{M}|^2}}{(M_N^2 - W^2(\tilde{\mathbf{k}}_\perp, x))^2}, \quad (49)$$

where x is given by

$$x = \tilde{k}_z/p_z, \quad (50)$$

$$W^2(\tilde{\mathbf{k}}_\perp, x) = \frac{M_\perp^2}{1-x} + \frac{m_\perp^2}{x}. \quad (51)$$

Here, $\tilde{\mathbf{k}}_\perp$ is the transverse component of the momentum $\tilde{\mathbf{k}}$, $M_\perp^2 = M_N^2 + \tilde{\mathbf{k}}_\perp^2$, and $m_\perp^2 = m_\mu^2 + \tilde{\mathbf{k}}_\perp^2$. Instead of x and $\tilde{\mathbf{k}}_\perp$, it is more convenient to introduce the light-front momentum in the initial-proton rest frame. This momentum is given by the relations

$$\tilde{\mathbf{k}}_\perp = \mathbf{k}_\perp, \qquad x = \frac{\varepsilon_{\mathbf{k}} + k_z}{\varepsilon_{\mathbf{k}} + E_N(\mathbf{k})}. \quad (52)$$

In the new variables, expression (51) reduces to the form $W^2(\tilde{\mathbf{k}}_\perp, x) = W^2(\mathbf{k})$, where $W(\mathbf{k}) = \sqrt{M_N^2 + \mathbf{k}^2} + \sqrt{m_\mu^2 + \mathbf{k}^2}$. We then have

$$S_{p\infty}^{n\mu} = \int \frac{d\tilde{\mathbf{k}}_\perp}{(4\pi)^3}\frac{dx}{x(1-x)}\frac{4\overline{|\mathcal{M}|^2}}{(M_N^2 - W^2(\tilde{\mathbf{k}}_\perp, x))^2} \quad (53)$$

$$= \int \frac{d^3\mathbf{k}}{(4\pi)^3 M_N E_N(\mathbf{p}')\varepsilon\mathbf{k}}\frac{\overline{|\mathcal{M}|^2}}{(M_N - E_N(\mathbf{p}') - \varepsilon\mathbf{k})^2}C_k,$$

where

$$C_k = 4M_N W(\mathbf{k})\frac{(M_N - W(\mathbf{k}))^2}{\left(M_N^2 - W^2(\mathbf{k})\right)^2} = \frac{4M_N W(\mathbf{k})}{M_N^2 + W^2(\mathbf{k})} < 1. \quad (54)$$

Since $C_k < 1$ and since $|\mathcal{M}|^2$, which is an invariant, takes the same value in the two reference frames, then

$$S_{p\infty}^{n\mu} < S_p^{n\mu}. \quad (55)$$

Actually, the difference of these two quantities is quite small.

3. DISCUSSION OF PHYSICAL RESULTS

3.1. Pion Cloud

The underlying point of our analysis is that the contribution of the pole diagram is dominant in the kinematical region specified by the inequalities $Q^2 \geqslant 1\ (\mathrm{GeV}/c)^2$ and $|k^2| \leqslant 0.2\ (\mathrm{GeV}/c)^2$. This circumstance makes it possible

(i) to extract the momentum distribution $|R_p^{n\pi}(k)|^2$ of pions in the $n\pi^+$ channel from experimental data on electroproduction;

(ii) to refine the cutoff parameter Λ_π in a popular parametrization of this distribution;

(iii) to relate investigations of the phase shifts for πN scattering to pion-electroproduction data through the πN potential and the pion wave function in the nucleon;

(iv) to find the spectroscopic factor in the $n\pi^+$ channel, an extremely important feature of the pion cloud indeed.

The pion-electroproduction cross section $d\sigma_L/dt$ for the case of longitudinal polarization generally receives contributions both from the pion and from the rho-meson cloud. However, our calculations revealed that the rho-meson contribution to this cross section is very small (see Fig. 8). For a first approximation, we therefore disregard the rho-meson contribution to $d\sigma_L/dt$. From experimental data reported in [42, 43] for $d\sigma_L/dt$, we found the cutoff parameter Λ_π for the form factor $g_{\pi NN}(k^2)$. The result is 0.7 GeV/c, which is one-third as great as that for the Bonn potential [44].

Figure 9 shows the radial parts of the pion wave function in the nucleon. The thick solid curve represents the results of the calculation by formula (19) with the form factor $g_{\pi NN}(k^2)$ found previously, while the thin solid and the dashed curve were computed by formula (25) on the basis of the potentials from [30] and [31], respectively. Figure 10 displays the

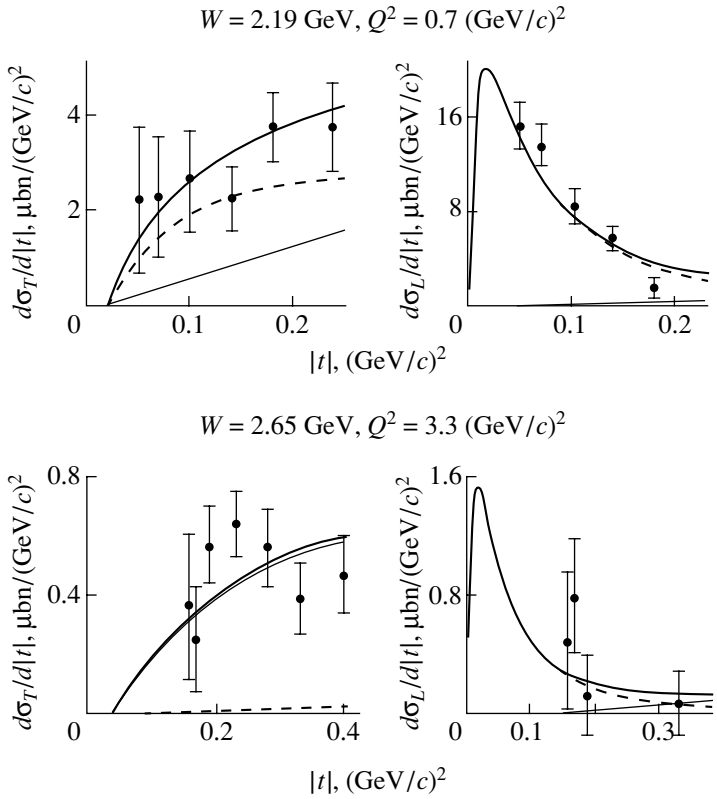

Fig. 8. Pion-electroproduction cross section for the cases of (left panel) transverse and (right panel) longitudinal polarization: (dashed curve) contribution of the diagram in Fig. 2 involving a virtual pion, (thin solid curve) contribution of the diagram in Fig. 2 involving a virtual rho meson, and (thick solid curve) total cross section. Experimental data were borrowed from [44, 45].

corresponding cross sections. It can be seen that the wave function from [31] is not compatible with experimental data on electroproduction in the quasielastic-knockout region. On the contrary, the results from [30] lead to satisfactory agreement with experimental data. It should be noted that either separable potential, that from [30] or that from [31], provides a good description of low-energy data on πN scattering. Thus, an experimental study of quasielastic knockout can be considered as an additional check on πN potentials.

The pion spectroscopic factor is given by the integral

$$\int \left|R_p^{n\pi}(k)\right|^2 k^2 dk = S_p^{n\pi} \qquad (56)$$

and, for the pion cloud, can be found directly from experimental data. It proves to be $S_p^{n\pi} = 0.13$; however, this value is underestimated, because we disregard final-state interaction—that is, the escape of pions from the πN channel. Relying on experience gained in intermediate-energy nuclear physics, where the corresponding result is underestimated by a factor of about 1.5, and bearing in mind that we have taken into account the important off-mass-shell effect (which is immaterial for loosely bound nucleons in outer nuclear shells), we adopt the value of $S_p^{n\pi} = 0.2$, which we believe to be quite reliable. Similar values were obtained in [9], where the pion content in the nucleon was calculated by perturbation theory within light-front dynamics.

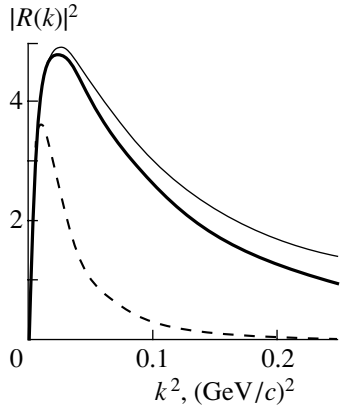

Fig. 9. Radial part of the pion wave function (momentum distribution) in the nucleon: (thick solid curve) result of the calculation by formula (19), (thin solid curve) result of the calculation by formula (25) on the basis of the potential from [30], and (dashed curve) result of the calculation by formula (25) on the basis of the potential from [31].

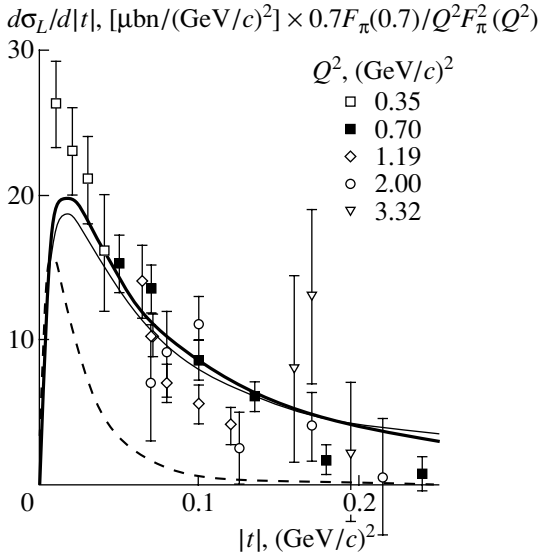

Fig. 10. Cross sections $d\sigma_L/dt$ for the case of longitudinal polarization that correspond to the following momentum distributions: (thick solid curve) wave function in the monopole parametrization, (thin solid curve) wave function from [30], and (dashed curve) wave function from [31]. Experimental data were borrowed from [44].

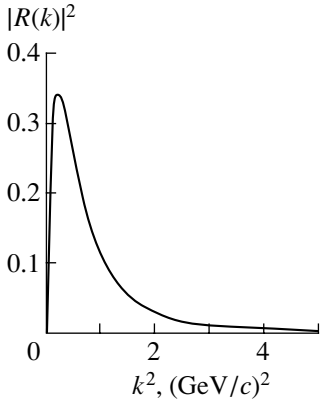

Fig. 11. Radial part of the rho-meson wave function in the proton.

It is interesting to note the Saito–Afnan wave function [30] normalized by the condition in (27) leads to the same value of the spectroscopic factor. If use is made of the parametrization $g_{\pi NN}(k^2) = \Lambda_\pi^2 - m_\pi^2/\Lambda_\pi^2 + k^2$, $S_p^{n\pi}$ depends greatly on Λ_π. At $\Lambda_\pi = 0.7$ GeV/c, we obtain $S_p^{n\pi} = 0.18$.

3.2. Rho-Meson Cloud

The contributions of the pion and of the rho-meson cloud to the cross sections $d\sigma_L/dt$ and $d\sigma_T/dt$ describing quasielastic pion knockout from a proton for the cases of, respectively, longitudinal and transverse polarization are displayed in Fig. 8. It can be seen that, at $Q^2 = 0.7$ (GeV/c)^2, the contribution of the rho-meson cloud to the cross section $d\sigma_L/dt$ for longitudinal polarization is small—this cross section is determined almost exclusively by the contribution of the pion cloud; as to the cross section $d\sigma_T/dt$, the contributions to it from pions and rho mesons are on the same order of magnitude. With increasing Q^2, the situation changes—at $Q^2 = 3.3$ (GeV/c)^2, the cross section $d\sigma_T/dt$ for transverse polarization is determined almost exclusively by the contribution of the rho-meson cloud; this is not so for the cross section $d\sigma_L/dt$, which, as before, receives the main contribution from pions.

It follows that analysis of the cross section $d\sigma_T/dt$ at $Q^2 = 3.3$ (GeV/c)^2 can in principle answer the same questions for the rho-meson cloud as those posed in discussing the pion cloud. However, available experimental and theoretical data on the rho-meson cloud are relatively scanty—for example, ρN phase shifts have not yet been analyzed, and experimental data have been obtained in the narrow region $|k^2| \leqslant 0.2$ (GeV/c)^2 (the wave function is entirely concentrated in this region in the case of pions, but it goes far beyond it in the case of rho mesons). Even on the basis of the available data, we can nevertheless draw some conclusions on the properties of the rho-meson cloud.

Figure 11 displays the momentum distribution of rho mesons in the proton according to the calculation by formula (35) with the cutoff constant Λ_ρ determined for the vertex function $g_{\rho NN}(k^2)$ by fitting the cross section $d\sigma_T/dt$ at $Q^2 = 3.3$ (GeV/c)^2 for transverse polarization to experimental data. Satisfactory agreement is achieved at $\Lambda_\rho = 1.4$ GeV/c.

However, only at relatively low values of $|k^2| \leqslant 0.2$ (GeV/c)^2 is it possible to extract the momentum distribution directly from experimental data. Therefore, a determination of the spectroscopic factor will be much less reliable here than in the case of the pion cloud. The spectroscopic factor depends greatly on Λ_ρ and, at $\Lambda_\rho = 1.4$ GeV/c, takes the value of 0.07.

3.3. Omega-Meson Cloud

Figure 12 shows the differential cross section $d\sigma_T/dt$ describing neutral-pion electroproduction for the case of transverse polarization. We consider these results as a guideline for performing future experiments—there are presently no data on the quasielastic knockout of neutral pions. Figure 12*a* corresponds to quite accessible values of $Q^2 = 3.3$ (GeV/c)^2 and $W = 2.65$ GeV, at which the

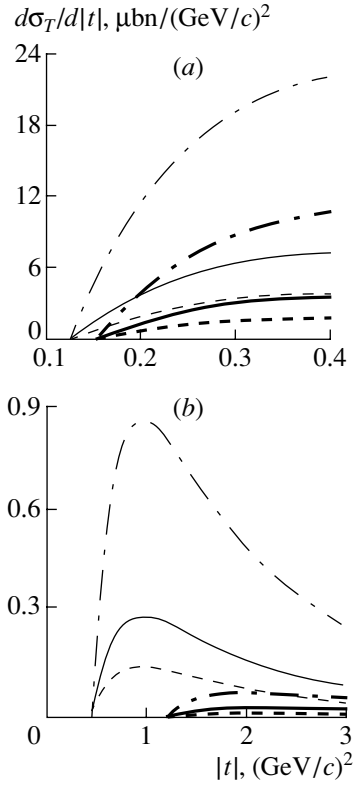

Fig. 12. Neutral-pion-production cross section for transverse polarization at $G^2_{\omega NN}/4\pi =$ (dashed curves) 5, (solid curves) 10, and (dash-dotted curves) 30 [thin (thick) curves correspond to identical (opposite) signs of the constants $G_{\omega NN}$ and $G_{\rho NN}$]: (*a*) $Q^2 = 3.3$ (GeV/c)^2, $W = 2.65$ GeV and (*b*) $Q^2 = 15$ (GeV/c)^2, $W = 2.65$ GeV.

reaction $p(e, e'\pi^+)n$ was investigated in experiments reported in [43, 44]. This is compatible with the k^2 range 0–0.4 (GeV/c)^2 considered here (in the quasielastic-knockout region, we have $k^2 \ll Q^2$, in which case off-mass-shell corrections are immaterial).

In the calculations, we used the values of $g^2_{\omega\pi\gamma}/g^2_{\rho\pi\gamma} = 10$ [45, 46] and $\kappa_\omega = 0.14 \pm 0.20$ [47]. The values chosen for the constants $g_{\rho\pi\gamma}$, $G_{\rho NN}$, and κ_ρ were quoted above. For the cutoff constant Λ_ω, to which the results presented in Fig. 12*a* are weakly sensitive, we adopted the value of $\Lambda_\omega = \Lambda_\rho = 1.4$ GeV/c.

Owing to the presence of the interference term in expression (41), the result depends on the relative sign of the constants $G_{\rho NN}$ and $G_{\omega NN}$; as can be seen from Fig. 12*a*, this sign can be established experimentally. Concurrently, the quantity $G^2_{\omega NN}/4\pi$, for which there is a scatter from 5 to 30 [48], will be refined.

In order to determine reliably the quantity Λ_ω (and to test Λ_ρ), it is obviously necessary to expand the k^2 range to 3 (GeV/c)^2; this in turn requires increasing Q^2 to about 15 (GeV/c)^2. Figure 12*b*, which displays the expected differential cross section for the aforementioned values of Λ_ω and Λ_ρ, corresponds to these kinematical conditions, which are more difficult for exclusive experiments.

4. SUMMARY AND OUTLOOK

The basic point of our analysis has been that, in the quasielastic-knockout region, where the recoil momentum k is much less than the momentum k' of the knock-on pion and, in addition, $k' \gg m_\pi$, the pole mechanism represented by the diagrams in Fig. 3 is dominant. In favor of this, we have adduced an analytic argument in Subsection 2.4 and an experimental one based on the observation that the momentum distribution of knock-on pions undergoes no changes in response to variations in the final energy of the knock-on pion.

The quasielastic-knockout concept adopted in nonrelativistic physics has been generalized by including the Z diagram in Fig. 3*b* in the analysis performed in the laboratory frame (it is in this frame that one can single out low values of k).

Further, we have introduced the notion of the wave function for the pion (and for vector mesons) in the nucleon and indicated how this function is expressed in terms of the vertex constant $G_{\pi NN}$ and the vertex function $g_{\pi NN}(k^2)$.

For a fixed $N \to B + м$ virtual decay channel, we have introduced the spectroscopic factor for the product meson in the nucleon.

From experimental data on pion electroproduction by longitudinal virtual photons [43], we have extracted the momentum distributions of pions in the channel $p \to n + \pi^+$ and, as a normalization of the momentum distribution, the pion spectroscopic factor ($S_p^{n\pi} \approx 0.2$). The shape of the momentum distribution has enabled us to determine reliably the cutoff parameter Λ_π for the vertex function $g_{\pi NN}(k^2)$, $\Lambda_\pi = 0.65 \pm 0.05$ GeV/c. This result is in good agreement with that presented by Loucks *et al.* [49], who analyzed data on pion electroproduction in the delta-isobar region, where the amplitudes of a few diagrams interfere, but it differs markedly from the value of $\Lambda_\pi = 2.1$ GeV/c, which is used in the Bonn potential [44]. A generalization of the approach discussed here to the case of quasielastic pion knockout from a nucleus is quite obvious. Although the relevant experiment will inevitably be inclusive ($\Delta E >$ 10 MeV), it will become possible, for the first time, to deduce information about the form of the pion

wave function in a nucleus (more specifically, to find out whether it reduces to a superposition of the pion wave functions in individual nucleons) and assess the number of pions in a nucleus [50].

The problem of the relationship between the pion spectroscopic factors within the instantaneous form of dynamics and light-front dynamics (the former being employed in our studies) has been considered.

By using preliminary, incomplete, experimental data on pion electroproduction by virtual transverse photons [42, 43] and taking into account the results from [35], which demonstrate that these processes are dominated by the contribution from the spin-flip nondiagonal $\rho^+ + \gamma_T \to \pi^+$ amplitude, we have been able to assess qualitatively, at low values of the rho-meson momentum [$|k^2| < 0.4$ (GeV/c)^2], the momentum distribution of the rho meson in the channel $p \to \rho^+ + n$ and to estimate the rho-meson spectroscopic factor roughly at $S_p^{n\rho} = 0.07$ and the cutoff parameter roughly at $\Lambda_\rho = 1.4$ GeV/c. In order to determine this momentum distribution over the entire region $|k^2| \geq 1.2$ (GeV/c)^2 [in this respect, the case being presently discussed differs from that of pions, for which the region $|k^2| \leqslant 0.5$ (GeV/c)^2, which was actually studied, is quite sufficient], electron beams of energy not lower than 10 GeV are required, and this is of paramount importance (here, it should be borne in mind that the eta and phi mesons and negative kaons, as well as tensor mesons, are of positive parity; see below). The reaction $p^+ + \gamma_T \to \pi^+$ and the possibility of extracting the momentum distribution of rho mesons are so important since, even in the case of quasielastic kinematics, the most natural process $p + e \to \rho^+ + n + e'$ proceeds according to a totally different scheme (through an intermediate Pomeron) because of vector dominance [50] and gives absolutely no way to explore the aforementioned momentum distribution of the rho meson in a nucleon.

The momentum distribution and the $S_p^{n\pi}$ value deduced for the channel $p \to \pi^+ + n$ have been compared (in terms of the wave function $\Psi_p^{n\pi}$) with what is obtained for the pion wave function in the nucleon with various πN potentials determined from a fit to the energy dependences of the phase shifts for πN scattering. Excellent agreement has been found for the case of the πN potential from [30] (it should be emphasized that the wave function for a pion bound in a nucleon was not considered there). This is yet another argument in favor of our approach.

The possibility of probing the omega-meson cloud of the nucleon in experiments exploring quasielastic neutral-pion knockout has been considered. Such experiments would enable an independent determination of the wave function $\Psi_p^{p\omega}(k)$—in particular, the magnitude of the constant $G_{\omega NN}$ and its sign. This is possible owing to the interference between the $\rho^0 + \gamma_T^* \to \pi^0$ amplitude (which is determined by the independent reaction $\rho^+ + \gamma_T^* \to \pi^+$) and the $\omega + \gamma_T^* \to \pi^0$ amplitude being discussed. The required electron beams of energy not less than 10 GeV would make it possible to obtain the entire set of wave functions $\Psi_p^{B\pi}(k)$ (where B can be, for example, the Roper resonance), $\Psi_p^{\Lambda K^+}(k)$, $\Psi_p^{\Sigma K}(k)$, and $\Psi_p^{p\eta}(k)$.

The question of whether it is possible to single out the quasielastic-knockout mechanism (e, e′φ) against the background of the diffractive production of a vector phi meson (which has the $\bar{s}s$ structure) [51] has been discussed. In addition, there exists yet another method that can be used to single out, in the nucleon, the cloud of positive-parity mesons, $м^+$. This possibility has been deduced from our experience gained in studying quasielastic alpha-particle knockout from light nuclei by protons [52] and electrons [53] of energy about 1 GeV. Namely, the probability of finding, in a nucleus, a virtual excited alpha particle with various values of the intrinsic orbital angular momentum $L_{\text{intr}} \neq 0$ is quite high [52]. A bombarding particle scattered on one or a few nucleons of this virtual cluster knocks it out of the nucleus; moreover, the amplitude for the transition of the knock-on cluster to the ground state, $\alpha^* \to \alpha^0$, proves to be sufficiently large in the process. Owing to a change in L_{intr}, different partial-wave amplitudes interfere, with the result that the momentum distributions of the recoil nucleus $(A-4)_f$ that are expressed in terms of the angles of orientation of the recoil momentum k with respect to the beam axis and to the plane of fast-particle scattering develop anisotropy. The predicted anisotropy is very strong in the reaction $A(p, p\alpha)A-4$ [52] and is quite sizable in the reaction $A(e, e\alpha)A-4$ [53], where scattering actually occurs on only one proton of the cluster. Here, we imply the physically observable momentum distribution of recoil nuclei $A-4$ in a specific excited state f; for this, it is not necessary, however, to record the recoil nucleus itself—measurement of p and α or of e and α pair correlations furnishes the entire body of needed information.

Thus, the process $e + м^{(+)} \to e'\pi$ can in principle be recognized by the above anisotropy of the momentum distributions of recoil nucleons, because the intrinsic orbital angular momenta of the mesons $м^{(+)}$ and of the pions are $L_{\text{intr}} = 1$ and $L_{\text{intr}} = 0$, respectively. Here, a key question is that of the magnitude of the off-diagonal amplitudes $\gamma_T^* + м^{(+)} \to \pi$ or $\gamma_L^* + м^{(+)} \to \pi$ in relation to those amplitudes that have been analyzed in the present review article. This is problem for the nearest future.

When the energy of knock-on mesons exceeds 1 GeV, the quasielastic-knockout reaction $(p, p\mathcal{M})$ can also be of use, in principle, since proton beams of energies in excess of 10 GeV are available in a few laboratories worldwide. But even in the simplest experiment of the $^1\mathrm{H}(p, p\pi^+)n$ type, the situation is partly complicated by strong diffractive pp interaction in the initial and in the final state. However, the off-diagonal amplitudes for meson knockout can independently be studied in pion scattering on protons that is inelastic in the meson state.

In addition, one can also discuss quasielastic-knockout reactions of the $(\pi, \pi\mathcal{M})$ type, which have been known for a long time in the $(\pi, 2\pi)$ version, but which have hitherto been used only to determine the phase shifts for $\pi\pi$ scattering [54]. The only question to be solved here is that of whether it is possible to obtain intense secondary pion beams of energy in excess of 10 GeV that are characterized by a comparatively small energy spread.

To conclude, we note that, although we have described here the meson cloud of the nucleon in purely phenomenological terms for the sake of simplicity, one has eventually to address the more fundamental problem of the hadronization of the quark–gluon vacuum polarized by the baryon charge of the nucleon. More specifically, the problem consists in projecting quark–gluon wave functions onto $B + \mathcal{M}$ cluster channels [55]; to some extent, this is similar to projecting the multinucleon wave functions for the A nucleus onto $(A-4)_f + \alpha^*$ channels. Various models have been proposed for this [56]. For example, the relations between the coupling constants $G_{\mathcal{M}BB}$ for various mesons $\mathcal{M}$ and baryons B were analyzed along these lines in [57]. The scopes of such an analysis can be substantially expanded by invoking the results obtained from an investigation of quasielastic meson knockout.

ACKNOWLEDGMENTS

This work was supported by the Russian Foundation for Basic Research (project no. 00-02-16117).

REFERENCES

1. P. Geiger and N. Isgur, Phys. Rev. D **41**, 1595 (1990); **47**, 5050 (1993).
2. S. Capstick and N. Isgur, Phys. Rev. D **34**, 2809 (1986); S. Godfray and N. Isgur, Phys. Rev. D **32**, 189 (1985).
3. T. Barnes, F. E. Close, and E. S. Swanson, Phys. Rev. D **52**, 5242 (1995).
4. L.-F. Li and T. P. Cheng, hep-ph/9709293.
5. K. F. Liu, D. D. Dong, *et al.,* hep-ph/9806491.
6. G. Ya. Glozman and D. O. Riska, Phys. Rep. **268**, 263 (1996).
7. C. E. Carlson, Nucl. Phys. A **622**, 66 (1997).
8. J. D. Sullivan, Phys. Rev. D **5**, 1732 (1972).
9. J. Speth and A. W. Thomas, Adv. Nucl. Phys. **268**, 263 (1997).
10. V. S. Murzin and L. I. Sarycheva, *Interaction of High-Energy Hadrons* (Nauka, Moscow, 1983); A. A. Bel'kov, S. A. Bunyatov, K. N. Mukhin, and O. O. Patarakin, *Pion–Nucleon Interaction* (Nauka, Moscow, 1983).
11. D. G. Ireland and G. van der Steenhoven, Phys. Rev. C **49**, 2182 (1994); M. Traini, Phys. Rev. C **55**, 160 (1997); Yahne Jin *et al.,* Phys. Rev. C **48**, R964 (1993).
12. V. G. Neudachin, Yu. V. Popov, and Yu. F. Smirnov, Usp. Fiz. Nauk **169**, 1111 (1999).
13. G. A. Leksin, Zh. Éksp. Teor. Fiz. **32**, 445 (1957) [Sov. Phys. JETP **5**, 378 (1957)].
14. L. S. Azhgireĭ, I. K. Vzorov, V. P. Zrelov, *et al.,* Zh. Éksp. Teor. Fiz. **33**, 1185 (1957) [Sov. Phys. JETP **6**, 911 (1958)].
15. D. I. Blokhintsev, Zh. Éksp. Teor. Fiz. **33**, 1295 (1957) [Sov. Phys. JETP **6**, 995 (1957)].
16. M. Breidenbach, J. I. Friedman, H. W. Kendall, *et al.,* Phys. Rev. Lett. **23**, 935 (1969).
17. D. J. Bjorken, Phys. Rev. **179**, 1547 (1969); R. P. Feynman, Phys. Rev. Lett. **23**, 1415 (1969).
18. R. K. Bhaduri, *Models of the Nucleon* (Addison-Wesley, New York, 1988).
19. V. G. Neudachin and Yu. F. Smirnov, *Nucleon Clusters in Light Nuclei* (Nauka, Moscow, 1969).
20. F. Guttner, G. Chanfray, H. J. Pirner, and B. Povh, Nucl. Phys. A **429**, 389 (1984).
21. V. G. Neudachin, N. P. Yudin, and L. L. Sviridova, Yad. Fiz. **60**, 2020 (1997) [Phys. At. Nucl. **60**, 1848 (1997)].
22. N. P. Yudin, L. L. Sviridova, and V. G. Neudachin, Yad. Fiz. **61**, 1689 (1998) [Phys. At. Nucl. **61**, 1577 (1998)].
23. N. P. Yudin, L. L. Sviridova, and V. G. Neudachin, Yad. Fiz. **62**, 694 (1999) [Phys. At. Nucl. **62**, 645 (1999)].
24. V. Dmitrasinovich and F. Gross, Phys. Rev. C **40**, 2479 (1989); P. J. Mulders, Phys. Rep. **185**, 83 (1990); S. Boffi, C. Giusi, and F. D. Pacati, Phys. Rep. **226**, 1 (1993).
25. L. D. Blokhintsev, I. Borbeĭ, and É. I. Dolinskiĭ, Fiz. Élem. Chastits At. Yadra **8**, 1189 (1977) [Sov. J. Part. Nucl. **8**, 485 (1977)]; R. N. Faustov, V. O. Galkin, and A. I. Mishurov, Phys. Lett. B **356**, 516 (1995).
26. J. Hiura and I. Shimodaia, Prog. Theor. Phys. **34**, 861 (1965); V .V. Balashov and J. V. Mebonia, Nucl. Phys. A **107**, 369 (1968); J. W. Watson, H. G. Pugh, P. G. Roos, *et al.,* Nucl. Phys. A **172**, 513 (1971); D. de Forest, Nucl. Phys. A **392**, 232 (1983).
27. D. S. J. Findley and R. O. Owens, Nucl. Phys. A **292**, 53 (1977); P. G. Roos, N. S. Chant, A. A. Cowley, *et al.,* Phys. Rev. C **15**, 69 (1976).
28. A. Braton, Nucl. Phys. A **623**, 357c (1997).
29. S. S. Schweber, *An Introduction to Relativistic Quantum Field Theory* (Row, Peterson and Co.,

Evanston, 1961; Inostrannaya Literatura, Moscow, 1963).
30. T.-Y. Saito and I. R. Afnan, Few-Body Syst. **18**, 101 (1995).
31. S. Nozawa, B. Blankleider, and T.-S. H. Lee, Nucl. Phys. A **513**, 459 (1990).
32. W. Hangeveld, W. H. Dickhoff, and K. Albert, Nucl. Phys. A **451**, 269 (1986).
33. M. Benmerrouch, N. C. Mukhopodhay, and J. F. Zhang, Phys. Rev. D **51**, 3237 (1995).
34. S. Weinberg, Phys. Rev. **133**, B1318 (1964).
35. J. Speth and V. R. Zoller, Phys. Lett. B **351**, 533 (1995).
36. N. N. Nikolaev, J. Speth, and G. T. Garvey, Z. Phys. A **349**, 59 (1994).
37. A. Szscurek and J. Speth, Nucl. Phys. A **570**, 765 (1994).
38. A. Szczurek and J. Speth, Nucl. Phys. A **555**, 249 (1993).
39. A. Szczurek, V. Ulechenko, H. Holtman, and J. Speth, Nucl. Phys. A **624**, 495 (1997).
40. G. P. Lepage and S. T. Brodsky, Phys. Rev. D **22**, 2157 (1980).
41. J. B. Kogut and D. E. Soper, Phys. Rev. D **1**, 2901 (1970).
42. P. Brauel, T. Canzler, D. Cords, *et al.,* Z. Phys. C **3**, 101 (1979).
43. C. J. Bebek, C. N. Brown, S. D. Holmes, *et al.,* Phys. Rev. D **17**, 1693 (1978).
44. K. Holinde, Phys. Rep. **68**, 121 (1981); J. Haidenbauer, K. Holinde, and A. W. Thomas, Phys. Rev. C **49**, 2331 (1994).
45. J. Hamilton and G. C. Oades, Nucl. Phys. A **424**, 447 (1984).
46. W. Grein and P. Kroll, Nucl. Phys. A **338**, 332 (1980).
47. W. Grein, Nucl. Phys. B **131**, 255 (1977).
48. G. Hohler, E. Pietarinen, I. Sabba-Stefanescu, *et al.,* Nucl. Phys. B **114**, 505 (1976).
49. S. Loucks, V. R. Phandaripande, and R. Shiavilla, Phys. Rev. C **49**, 342 (1994); Phys. Rep. **149**, 1 (1987).
50. A. Donnachie and P. V. Landshoff, Phys. Lett. B **185**, 403 (1987) T. Gousset, Nucl. Phys. A **622**, 130c (1997) M. G. Ryskin and Yu. M. Shabelski, Yad. Fiz. **62**, 1047 (1999) [Phys. At. Nucl. **62**, 980 (1999)].
51. E. M. Henley, G. Krein, and A. G. Williams, Phys. Lett. B **281**, 178 (1992); A. I. Titov, Y. Oh, S. N. Yang, and T. Morii, Phys. Rev. C **58**, 2429 (1998).
52. V. G. Neudachin, A. A. Sakharuk, V. V. Kurovskiĭ, and Yu. M. Chuvil'skiĭ, Yad. Fiz. **58**, 1234 (1995) [Phys. At. Nucl. **58**, 1155 (1995)].
53. A. A. Sakharuk, V. G. Zelevinsky, and V. G. Neudatchin, Phys. Rev. C **60**, 014605 (1999).
54. O. O. Patarakin, V. N. Tikhonov, and K. N. Mukhin, Nucl. Phys. A **598**, 335 (1996).
55. D. S. Isert, S. P. Klevansky, and P. Rehberg, Nucl. Phys. A **643**, 275 (1998).
56. L. Ya. Glozman, Z. Papp, W. Plessas, *et al.,* Phys. Rev. C **57**, 3406 (1998); L. Ya. Glozman, Nucl. Phys. A **629**, 121c (1998); I. T. Obukhovsky, A. Faessler, G. Wagner, and A. J. Buchmann, Phys. Rev. C **60**, 035207 (1999).
57. V. G. J. Stoks, Nucl. Phys. A **629**, 205c (1998).

Translated by A. Isaakyan

Physics of Atomic Nuclei, Vol. 64, No. 9, 2001, pp. 1618–1623. Translated from Yadernaya Fizika, Vol. 64, No. 9, 2001, pp. 1698–1704.

ELEMENTARY PARTICLES AND FIELDS
Experiment

A Dependence of the Cross Sections for the Cumulative Production of Pions and Protons in Proton–Nucleus and Nucleus–Nucleus Interactions

V. K. Bondarev, A. G. Litvinenko, A. I. Malakhov, and S. G. Reznikov

Joint Institute for Nuclear Research, Dubna, Moscow oblast, 141980 Russia

Received May 30, 2000

Abstract—The behavior of the inclusive cross sections for the cumulative production of $\pi^{\pm}$ mesons and protons in pA, DA, and ^{4}HeA interactions is studied versus the atomic mass number of fragmenting nuclei. The primary-beam momenta were 4.5 GeV/c per nucleon. Secondary pions and protons were recorded with a fixed momentum of 0.5 GeV/c at an angle of 120°. Specifically, the experiment explored the fragmentation of D, He, ^{6}Li, ^{7}Li, C, Si, ^{58}Ni, ^{64}Ni, ^{64}Zn, ^{114}Sn, ^{124}Sn, and Pb nuclei. The energy spectra of π^+ and π^- mesons and protons with momenta in the range 0.3–0.7 GeV/c (the emission angle being 120°) were measured in an 8.9-GeV/c proton beam for Ni, Zn, and Sn isotopes. The special features in the behavior of the cross sections are found and discussed, and a comparison is drawn with the results of other studies.

1. INTRODUCTION

The majority of the experiments that studied the cumulative production of particles ($\pi^{\pm}$, $K^{\pm}$, p, n, $\bar{p}$, and nuclear fragments) were performed in proton beams of incident energies in the range 1–400 GeV. The term "cumulative" implies that the production of particles with specific features (momenta, masses, emission angles) is forbidden by the kinematics of free-nucleon collisions. Cumulative particles can be observed both in the target- and in the projectile-fragmentation region. In the first case, the particles are recorded at emission angles in the range 90°–180° (backward hemisphere). In the present study, we are dealing with cumulative particle production in the target-fragmentation region.

At present, a vast body of experimental information about cumulative particle production has been collected in various scientific centers [1–6]. The original premises of the cumulative effect in relativistic nuclear interactions are presented in [1]; the pioneering results on cumulative production are summarized in [2]; and the theoretical models of cumulative processes are considered in [3–5]. Experimental data within various conceptual frameworks and the possible mechanisms of cumulative particle production are discussed in [6], which is the latest review on the subject. The quoted articles contain an exhaustive list of references to relevant experimental and theoretical studies.

Investigations into cumulative production revealed [1–6] that the spectra of cumulative particles are similar for various nuclei, irrespective of the energy and the type of the incident beam. The A dependence of the cross sections appeared to be an equally universal feature. The energy dependences of the cross sections for various particles are reproduced quite satisfactorily by many theoretical models [3–5]. The A dependence of the cross sections remains incomprehensible in many aspects. The frequently used approximation of the cross section in terms of a power-law form like A^n is quite satisfactory for a limited number of nuclei within the mass-number range $A \simeq 30$–240. In some cases, the exponent n depends on the mass numbers of nuclei in a rather specific manner. This concerns the behavior of the cross sections for isotopically enriched nuclei, which are usually used in relevant measurements [6]. Here, we mean the so-called isotopic effect [7], which consists in that the inclusive cross sections for the production of π^+ and K^+ mesons and of protons (that is, of positively charged particles) are independent of the excessive neutron content at a fixed charge of fragmenting nuclei (^{58}Ni, ^{64}Ni, ^{114}Sn, ^{124}Sn).

In this article, the results on the cumulative production of $\pi^{\pm}$ mesons and protons in beams of protons, deuterons, and He nuclei with momenta of 4.5 GeV/c per nucleon are presented for the case where secondaries are emitted at an angle of 120° with a fixed momentum of 0.5 GeV/c. The experiment was performed with D, He, ^{6}Li, ^{7}Li, C, Si, ^{58}Ni, ^{64}Ni, ^{64}Zn, ^{114}Sn, ^{124}Sn, and Pb as fragmenting

1063-7788/01/6409-1618$21.00

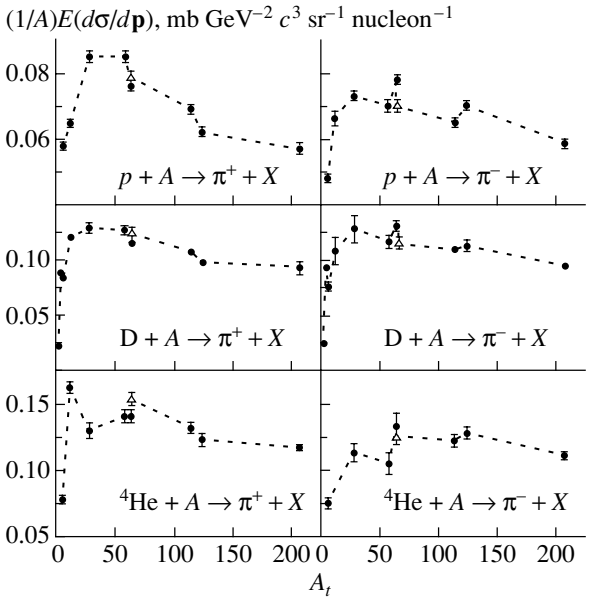

Fig. 1. *A* dependence of the inclusive cross sections for the production of 0.5 GeV/c π^+ and π^- mesons at an emission angle of 120° in beams of protons, deuterons, and ^{4}He nuclei with a momentum of 4.5 GeV/c per nucleon (A_t is the mass number of target nuclei; the open triangles correspond to the results for the ^{64}Zn nucleus).

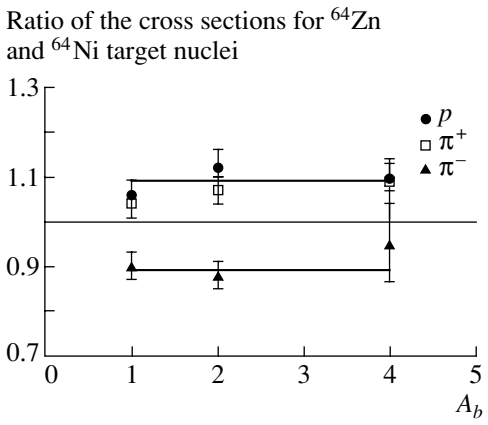

Fig. 2. Ratios of the cross sections for the production of protons and pions on ^{64}Zn and ^{64}Ni nuclei versus the beam type (A_b is the mass number of beam nuclei; all incident beams have the same momentum of 4.5 GeV/c per nucleon; the emission angle is 120°).

nuclei. For the same value of the emission angle, the spectra of protons and pions with momenta in the range 0.3–0.7 GeV/c were additionally measured in an 8.9-GeV/c proton beam. In that case, ^{58}Ni, ^{64}Ni, ^{64}Zn, ^{114}Sn, ^{124}Sn, and Pb were used as fragmenting nuclei. The above sets of fragmenting nuclei allowed us to obtain the overall pattern of the cross sections as functions of A and to trace finer details of this dependence under the same experimental conditions. The entire set of the aforementioned fragmenting nuclei was used in the deuteron beam.

Our experimental data were obtained with the DISK setup, which includes a time-of-flight spectrometer and which makes it possible to combine data from it with a magnetic analysis of the momenta of secondary particles and with measurements of ionization losses and of the intensity of Cherenkov light. The beam of secondary particles was focused onto scintillation counters by the doublet of quadrupole lenses. A detailed description of the experimental procedure can be found in [6, 8]. The tabulated data on the cross sections for the production of pions, kaons, protons, and deuterons were reported in [6, 9].

2. EXPERIMENTAL RESULTS

We would like to note those special features in the behavior of pion and proton cross sections that did not attract much attention in previous studies. For cross sections, we will henceforth use the representation [6, 9]

$$\frac{1}{A}E\frac{d\sigma}{d\mathbf{p}} = \frac{1}{A}\frac{E}{p^2}\frac{d^2\sigma}{dp\,d\Omega}$$
$$(\text{mb GeV}^{-2}\,c^3\,\text{sr}^{-1}\text{nucleon}^{-1}).$$

Figure 1 shows the A dependence of the cross sections for the production of $\pi^\pm$ mesons in proton, deuteron, and helium beams. Two features inherent in the behavior of the cross sections in all types of beams considered here are worthy of special note. First, the A dependences of the pion cross sections are similar for all beam types. Moreover, the similarity manifests itself in minute detail, since the isotopic effect is peculiar to all beams. It should be emphasized that, here, the isotopic effect becomes noticeable at an incident proton momentum one-half as great as that at which it was observed in the pioneering studies. Another fact is a noticeable growth of the cross sections in the mass-number range $A \simeq 50$–60 and their reduction on either side of this range. This type of behavior is peculiar to the specific binding energy of nuclei. Figure 1 also demonstrates that the isotopic effect for pions is the most spectacular in proton beams.

Let us consider a pair of ^{64}Zn and ^{64}Ni nuclear species. They are isobars (that is, they have equal mass numbers). We use the ratios of the cross sections for the production of π^+ and π^- mesons and of protons on these nuclei and compare the behavior of these ratios in the different beams. The results are illustrated in Fig. 2, which shows that there is virtually no dependence on the beam type in these ratios. A fit to a constant yields

$$0.89 \pm 0.02,\ \chi^2 = 0.3 \text{ for } \pi^-; 1.06 \pm 0.02,$$
$$\chi^2 = 0.5 \text{ for } \pi^+; 1.09 \pm 0.02,\ \chi^2 = 0.8 \text{ for } p.$$

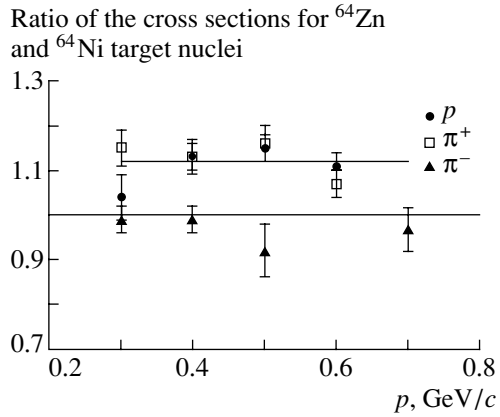

Fig. 3. Ratios of the cross sections for the production of protons and pions on ^{64}Zn and ^{64}Ni target nuclei versus the momenta of these particles (the momentum of the incident proton beam is 8.9 GeV/c; the emission angle is 120°).

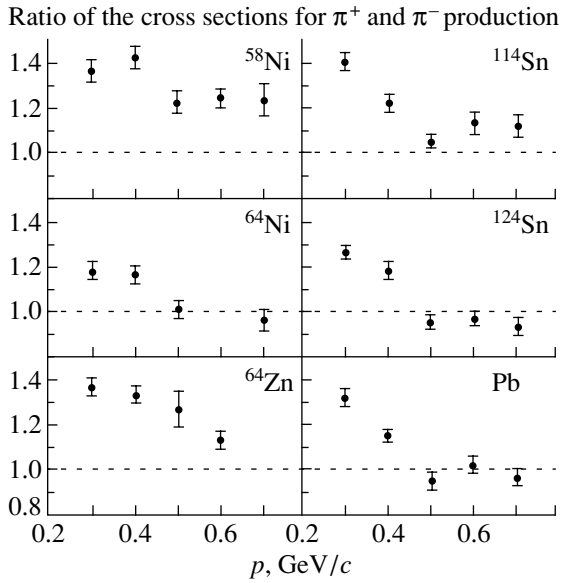

Fig. 4. Ratios of the cross sections for the production of π^+ and π^- mesons on different nuclei versus the pion momentum (the momentum of the incident proton beam is 8.9 GeV/c; the emission angle is 120°).

That the ratios of the cross sections for the production of protons and π^+ mesons on the nuclei of nickel and zinc isotopes are nearly equal (Fig. 2; the pion and proton momentum is 0.5 GeV/c) gives every reason to expect that this will be the case for other proton and pion momenta. Indeed, Fig. 3 (data obtained in an 8.9-GeV/c proton beam) confirms these expectations. In this case, however, the cross sections for π^- mesons are equal for the nickel and zinc isotopes within the experimental errors, in contrast to what was observed at 4.5 GeV/c. A fit to a constant yields

$$0.98 \pm 0.02,\ \chi^2 = 0.4 \text{ for } \pi^-; 1.12 \pm 0.02,$$

$$\chi^2 = 1.5 \text{ for } \pi^+; 1.12 \pm 0.02, \chi^2 = 1.3 \text{ for } p.$$

The kinetic-energy ranges 47–232 and 191–574 MeV for protons and pions, respectively, correspond to the proton- and pion-momentum range 0.3–0.7 GeV/c. The values of the scaling variable x in the range 0.6–1.4 for pions and in the range 1.2–1.7 for protons correspond to the same momentum range (for an 8.9-GeV/c proton beam at an emission angle of 120°). The definition of the scaling variable x can be found, for example, in [6] (it is traditionally used in studying cumulative particle production). We assume that experimentally measured values are more convenient for illustrating the results that we obtained. We can conclude that, for the momenta of secondaries in the range 0.3–0.7 GeV/c, the very specific behavior of the ratios of the pion and proton cross sections for nuclei with equal mass numbers is still observed at the incident-proton momentum nearly twice as great as that for which we discussed it first. The data in Figs. 2 and 3 suggest an isobaric effect in pion and proton production.

Nucleonic compositions of isotopic nuclei of targets

Target nucleus	Z	N	N/Z	Enrichment, %
^{58}Ni	28	30	1.07	99.7
^{64}Ni	28	36	1.29	93.1
^{64}Zn	30	34	1.13	98.7
^{114}Sn	50	64	1.28	92.0
^{124}Sn	50	74	1.48	97.2

The ratio of the cross sections for π^+ and π^- production on nuclei is one of the interesting features of cumulative production. As was established in various experiments (see [6] and the references therein), this ratio is close to unity not only for isoscalar nuclei but also for nuclei with a high relative content of neutrons. For a typical example of the latter, we can indicate the Pb nucleus, for which N/Z is 1.5. A feature peculiar to our study of this problem is a specific choice of fragmenting target nuclei. Their nucleonic compositions are given in the table.

The ratios of the cross sections for π^+ and π^- production that were obtained in our study are shown in Fig. 4 versus the pion momentum. The behavior of these ratios looks quite peculiar for various nuclei. First, there are some distinctions between the values of the ratio at low and high pion momenta (by convention, it is adopted here that these are momenta below and above 0.5 GeV/c, respectively; it should be noted

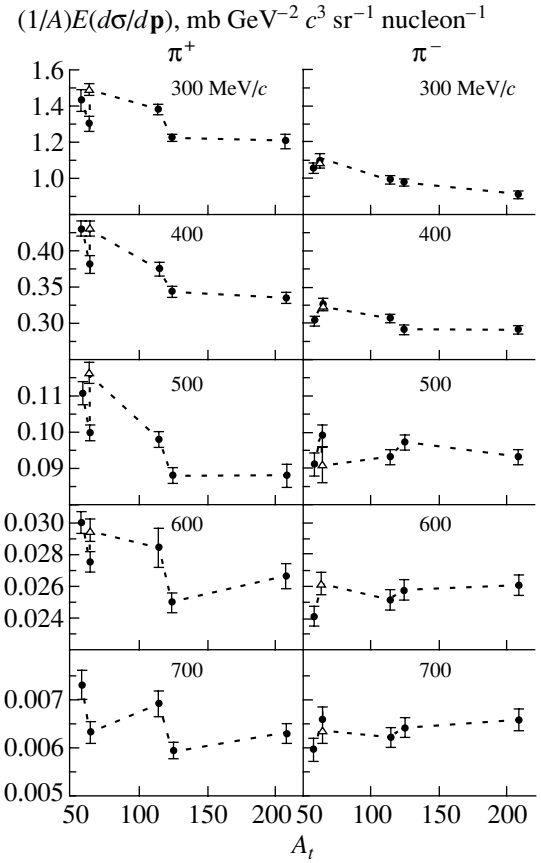

Fig. 5. Isotopic and isobaric effects in the pion-production cross sections versus the pion momentum (the momentum of the incident proton beam is 8.9 GeV/c; the emission angle is 120°). The open triangles correspond to the results for the ^{64}Zn nucleus.

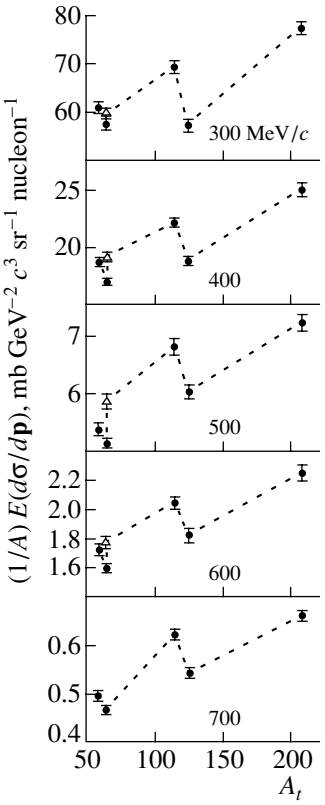

Fig. 6. As in Fig. 5, but for protons.

that the scaling variable x, which is traditionally used in cumulative production, takes a value close to unity for 0.5-GeV/c pions). Second, there is no correlation between the π^+/π^- ratios and the N/Z values. The ratios of the pion-production cross sections are equal or close to unity for the Pb, ^{124}Sn, ^{114}Sn, and ^{64}Ni nuclei in the momentum region around 0.5 GeV/c and above. The situation is absolutely different for the ^{58}Ni and ^{64}Zn nuclei. Thus, we see that, under the conditions of the present experiment, the ratio of the cross sections for π^+ and π^- production depends on the pion momenta and on the particular type of target nuclei.

The available data on cumulative pion and proton production in an 8.9-GeV/c incident proton beam make it possible to study the behavior of the relevant inclusive cross sections for nickel, zinc, and tin isotopes versus momentum. Figures 5 and 6 show the results for pions and protons, respectively. The isotopic effect in pion and proton production is observed there in the momentum range 0.3–0.7 GeV/c. For the presentation to be more emphatic, a special notation is used in the figures for the points corresponding to the ^{64}Zn nucleus.

3. DISCUSSION OF THE RESULTS

We have considered cumulative particle production in various types of incident beam and on various fragmenting nuclei. A rich variety of fragmenting target nuclei has enabled us to measure comprehensively the A dependence of the cross sections for pion and proton production. A comparison of data obtained in the beams of protons and helium nuclei has revealed that the A dependences of the pion cross sections are similar. The behavior of the cross sections for the separated isotopes of nuclei exhibits a detailed similarity. The shape of the A dependences of the pion cross sections resembles the behavior of the specific binding energy of nuclei (a maximum in the mass-number range $A \simeq 50$–60, a reduction on either side of the maximum, and irregularities for magic nuclei and those close to them).

This shape of the A dependence of the cross sections was obtained in other studies as well that were devoted to measurements for light nuclei. We would like mention the article of Gavrishcuk *et al.* [10], who presented experimental data on pion production at an angle of $\vartheta = 159°$ in incident proton beams of momenta in the range 15–65 GeV/c. In particular,

the cross sections for the production of 250- and 500-MeV/c pions on Be, C, Al, Ti, Mo, and W nuclei exhibit a similar shape of the A dependence. For higher pion momenta, statistics were insufficient there for studying the shape of the A dependence. Pion production at $\vartheta = 119°$ on Be, Al, Cu, and Ta nuclei exposed to a 10-GeV proton beam was investigated in [11]. According to data obtained in that study, there is an enhancement in the cross sections for $A \simeq 50$–60 at a pion momentum of 0.6 GeV/c, which was the initial pion momentum used there; no such enhancement was observed for the pion momentum of 1.077 GeV/c (the cross sections per nucleon for the production on Cu and Ta nuclei are identical within the experimental errors). There are some data on $K^{\pm}$-meson production in the same beams [12, 13]; however, large errors in the experimental data give no way to draw a definitive conclusion on the shape of the A dependence of the kaon cross sections, although the cross sections for K^+ and K^- mesons show markedly different types of behavior in those studies. In [14], the cross sections for antiproton production at an angle of 97° were measured in a 10-GeV proton beam. According to those data, the shape of the A dependence of the cross sections for antiproton momenta in the range 0.6–1.05 GeV/c is similar to that for pions. In addition, we would like to mention the data from [6, 9] on the production of 0.5-GeV/c π^+ mesons at 120° in a carbon-nucleus beam of momentum 4.5 GeV/c per nucleon. The shape of the A dependence of the pion cross section there is similar to that in the beams of protons, deuterons, and ^{4}He nuclei (Fig. 1).

According to the semiempirical formula for the binding energy of nuclei, the shape of the curve is determined by the total contribution of the volume, the surface, the symmetry, and the Coulomb energy. It is possible that the shape of the A dependence of the pion-production cross section obtained in this study is determined by the same factors. The A dependence of the proton cross section is different from that for pions—it is an increasing function of the nuclear mass number (Fig. 6).

Let us now address the results for the isotopically enriched nuclei. Their properties are listed in the table. We can see that there are two pairs of isotopes and a single pair of isobars. A change in the number of neutrons (the number of nn pairs) at an invariable nuclear charge leads to an isotopic effect in pion and proton production. In the case of the ^{64}Ni and ^{64}Zn nuclei, differing by the replacement of a pp pair by an nn pair, there is an isobaric effect for pions and protons. Additionally, we would like to note that, in [15], the neutron yield was found to be independent of the excess content of protons in the nucleus (isotonic effect). Thus, all available types of nuclei manifest themselves in the processes under study. The typical scale of these effects amounts to 10–20%. In particular, the distinction between the values of the cross sections for positively charged particles (protons and π^+ mesons; see Fig. 2) is close to 10% and is commensurate with the ratio of ^{64}Zn and ^{64}Ni charges, which is equal to 1.07. For π^- mesons, the ratio of the cross sections for the same nuclei is about 0.9, the ratio of the number of neutrons in them being 0.94. On the whole, the cross sections for the production of π^+ and π^- mesons on ^{64}Zn and ^{64}Ni nuclei differ by about 20%. Figure 3 shows that the isobaric effect is independent of the pion and proton momenta—it does not disappear at the nearly doubled momentum of incident protons, amounting to about 10%. The isobaric effect was also observed in the production of 0.5-GeV/c protons at an angle of 180° on ^{58}Ni and ^{58}Fe nuclei exposed to an 8.9-GeV/c proton beam [16]. Its magnitude was 1.14 ± 0.04, which is commensurate with the data of our study.

On a larger scale, these effects manifest themselves in the ratios of the cross sections for π^+- and π^--meson production on specially selected nuclei of ^{58}Ni, ^{64}Ni, ^{64}Zn, ^{114}Sn, ^{124}Sn, and Pb (Fig. 4). As was mentioned above, both effects appear in this case, and they depend on the pion momenta differently.

Since the effects being discussed are associated with charged particles, it is natural to assume that they are caused by electromagnetic interaction, which discerns particles by their electric charges. It is hardly probable that this is a purely Coulomb interaction, since, under the conditions of our study, there is no dependence on the type or energy of incident beams. Nor do secondaries show any dependence on their momenta in the measured region. The isotopic effect has the same scale on nickel and tin isotopes, whose nuclear charges are markedly different (see table). The variation in the charge of incident beams (those of protons and helium nuclei; Fig. 2) does not change the scale of the effect.

In [17], Coulomb effects were studied in the process Ne + NaF $\to \pi^{\pm}$ at energies of 380 and 164 MeV per nucleon and in some other processes for which protons and neutrons were detected. There, Coulomb corrections to the π^-/π^+ and n/p ratios were calculated on the basis of the fireball model. The kinematical conditions of our study differ substantially from those considered in [17], so that we need here calculations that are relevant to the particular experimental conditions and which are based on a specific model of cumulative production.

The results obtained in our study highlight an appreciable role of the nuclear structure, which, in

our opinion, must be taken into account in a theoretical description of cumulative particle production in hadron–nucleus and nucleus–nucleus interactions. As a matter of fact, a detailed study of the A dependence of the pion and proton cross sections reduced to exploring the properties of the nucleus as a bound system. The isotopic and isobaric effects, which reflect these properties, appeared to be independent of the properties or energies of the beams used or the pion and proton momenta. The ratio of the cross sections for π^+ and π^- production on the specially selected group of nuclei appeared to be the only property showing a specific momentum dependence. Further studies are required for assessing the degree to which the effects discovered here are universal. As obvious extensions of the experiment, we could propose recording a wider range of particles (for example, one could include $K^\pm$ mesons and antiprotons) and increasing the charge of incident nuclei or, in contrast to this, employing neutron beams to eliminate electromagnetic interaction at the initial stage. These problems are described in detail elsewhere [6].

Fragmentation and multifragmentation are other processes where nuclear effects on isotopically enriched target nuclei could manifest themselves to a greater degree. The first piece of evidence for the isotopic effects in these processes was obtained as far back as in [18] in studying ^{3}H, ^{3}He, ^{4}He, ^{6}Li, and ^{7}Li fragments produced on nickel and tin isotopes in a 660-MeV incident-proton beam.

4. CONCLUSIONS

The basic results of the present study can be summarized as follows:

(i) The inclusive cross sections for $\pi^\pm$ mesons produced on an extended set of fragmenting nuclei cannot be described by a simple power-law dependence of the A^n type; their behavior is similar to that of the specific binding energy of nuclei. This is confirmed by the data of the other studies.

(ii) The inclusive cross sections for $\pi^\pm$ mesons produced with a momentum of 0.5 GeV/c on ^{64}Zn and ^{64}Ni isobars vary within about 20%, irrespective of the beam type (protons, deuterons, and ^{4}He nuclei with a momentum of 4.5 GeV/c per nucleon).

(iii) For 8.9-GeV/c incident-proton beams, the inclusive cross sections for production processes occurring on ^{64}Zn and ^{64}Ni isobars are different for π^+ mesons and protons and show no variations within the experimental errors for π^- mesons. This is so for product-particle momenta in the range 0.3–0.7 GeV/c.

(iv) The ratios of the cross sections for π^+- and π^--meson production on ^{58}Ni, ^{64}Ni, ^{64}Zn, ^{114}Sn, ^{124}Sn, and Pb nuclei depend on the pion momenta and on the kind of nuclei.

(v) The isotopic and isobaric effects in pion and proton production induced by an incident beam of 8.9-GeV/c protons are observed in the momentum range 0.3–0.7 GeV/c.

ACKNOWLEDGMENTS

This work was supported by the Russian Foundation for Basic Research (project no. 96-02-17207).

REFERENCES

1. A. M. Baldin, Fiz. Élem. Chastits At. Yadra **8**, 429 (1977) [Sov. J. Part. Nucl. **8**, 175 (1977)].
2. V. S. Stavinskiĭ, Fiz. Élem. Chastits At. Yadra **10**, 949 (1979) [Sov. J. Part. Nucl. **10**, 373 (1979)].
3. V. K. Luk'yanov and A. I. Titov, Fiz. Élem. Chastits At. Yadra **10**, 815 (1979) [Sov. J. Part. Nucl. **10**, 321 (1979)].
4. M. I. Strikman and L. L. Frankfurt, Fiz. Élem. Chastits At. Yadra **11**, 571 (1980) [Sov. J. Part. Nucl. **11**, 248 (1980)].
5. A. V. Efremov, Fiz. Élem. Chastits At. Yadra **13**, 613 (1982) [Sov. J. Part. Nucl. **13**, 254 (1982)].
6. V. K. Bondarev, Fiz. Élem. Chastits At. Yadra **28**, 13 (1997) [Phys. Part. Nucl. **28**, 5 (1997)].
7. V. K. Bondarev *et al.,* in *Proceedings of the VIII International Workshop on Problems of High Energy Physics, Dubna, 1986,* D1, 2-86-668, p. 243.
8. T. V. Avericheva *et al.,* Soobshch. Ob'edin. Inst. Yad. Issled., Dubna, No. 1-11317 (1978).
9. V. K. Bondarev *et al.,* Preprint No. E1-93-84, OIYaI (Joint Inst. for Nuclear Research, Dubna, 1993).
10. O. P. Gavrishcuk *et al.,* JINR Rapid Commun., No. 4[55]-92, 4 (1992).
11. S. V. Boyarinov *et al.,* Yad. Fiz. **46**, 1472 (1987) [Sov. J. Nucl. Phys. **46**, 871 (1987)].
12. I. M. Belyaev *et al.,* Yad. Fiz. **56** (10), 135 (1993) [Phys. At. Nucl. **56**, 1378 (1993)].
13. S. V. Boyarinov *et al.,* Yad. Fiz. **50**, 1605 (1989) [Sov. J. Nucl. Phys. **50**, 996 (1989)].
14. S. V. Boyarinov *et al.,* Yad. Fiz. **54**, 119 (1991) [Sov. J. Nucl. Phys. **54**, 71 (1991)].
15. V. B. Gavrilov *et al.,* Preprint ITÉF-121 (Inst. of Theoretical and Experimental Physics, Moscow, 1985).
16. A. M. Baldin *et al.,* Soobshch. Ob'edin. Inst. Yad. Issled., Dubna, No. R1-83-432 (1983).
17. M. Gyulassy and S. K. Kauffmann, Nucl. Phys. A **362**, 503 (1981).
18. V. I. Bogatin *et al.,* Yad. Fiz. **19**, 32 (1974) [Sov. J. Nucl. Phys. **19**, 16 (1974)].

Translated by E. Kozlovskiĭ

Physics of Atomic Nuclei, Vol. 64, No. 9, 2001, pp. 1624–1627. Translated from Yadernaya Fizika, Vol. 64, No. 9, 2001, pp. 1705–1708.

ELEMENTARY PARTICLES AND FIELDS
Theory

Neutrino Oscillations in the Field of a Linearly Polarized Electromagnetic Wave

M. S. Dvornikov* **and A. I. Studenikin****

Department of Theoretical Physics, Faculty of Physics, Moscow State University, Vorob'evy gory, Moscow, 119899 Russia

Received May 5, 2000; in final form, February 19, 2001

Abstract—Neutrino oscillations $\nu_{iL} \leftrightarrows \nu_{jR}$ in the field of a linearly polarized electromagnetic wave are studied on the basis of a recently proposed effective Hamiltonian that describes the evolution of a spin in an arbitrary electromagnetic field. The condition of resonance amplification of the oscillations is analyzed in detail. A method is developed for qualitatively studying solutions to the equation of neutrino evolution in the resonance region. This method can be used to explore neutrino oscillations in fields of various configurations. © *2001 MAIK "Nauka/Interperiodica".*

The electromagnetic properties of the neutrino—in particular, the interaction of the neutrino with electromagnetic fields—present one of the basic problems in neutrino physics. The reason is that nonvanishing electromagnetic form factors for the neutrino, together with a nonvanishing neutrino mass, would indicate that it is necessary to go beyond the Glashow–Salam–Weinberg Standard Model (SM) of electroweak interactions.

In the majority of studies performed so far, the effect of electromagnetic fields on the neutrino and neutrino oscillations arising under such conditions (see, for example, [1–11]) was considered for the specific case of a magnetic field $\mathbf{B}_\perp$ that is constant in time and which is orthogonal to the neutrino velocity. Recently, an effective Hamiltonian for in the Schrödinger equation describing the evolution of neutrinos was derived in [12, 13] from the Bargmann–Michel–Telegdi equation generalized to the case of neutrino motion in a classical electromagnetic field. This Hamiltonian makes it possible to consider helicity-flip transitions $\nu_{iL} \leftrightarrows \nu_{jR}$ between neutrinos of both the same generation and the different generations.

The use of the new Hamiltonian allowed the first analyses of neutrino transitions $\nu_{iL} \leftrightarrows \nu_{jR}$. This resulted in the prediction of a resonance amplification of the corresponding neutrino oscillations in the field of a circularly polarized electromagnetic wave and in the electromagnetic-field configurations involving a nonzero magnetic field $\mathbf{B}_\parallel$ along the neutrino velocity.

*e-mail: maxim_dvornikov@aport.ru
**e-mail: studenik@srdlan.npi.msu.su

In the present study, we consider neutrino oscillations in the field of a linearly polarized electromagnetic wave. We propose a method for determining and qualitatively studying a solution in the resonance region. This method is particularly efficient in the cases where it is impossible to find an exact solution to the Schrödinger equation that describes transitions between two neutrino states. The proposed approach can be used to study neutrino oscillations in electromagnetic fields of various configurations.

Let us consider the system of two neutrinos $\nu = (\nu_R, \nu_L)$ of different helicity states. The evolution of ν in the field of an electromagnetic wave of frequency ω can be described by the equation

$$i\frac{\partial \nu}{\partial t} = H\nu, \tag{1}$$

where the Hamiltonian H can be represented in the form [12, 13]

$$H = (\mathbf{n}\cdot\sigma)\left(\frac{\Delta m^2 A}{4E} - \frac{V_{\text{eff}}}{2}\right) - \frac{\mu(\sigma\cdot\mathbf{B}^0)}{\gamma}, \tag{2}$$

where $\mathbf{n}$ is a unit vector directed along the neutrino velocity β, $\sigma = (\sigma_1, \sigma_2, \sigma_3)$ are the Pauli matrices, V_{eff} is the difference of the effective potentials representing the interaction of the neutrino with matter, A is a function of the vacuum mixing angle (the explicit form of A for various transitions of the $\nu_{iL} \leftrightarrows \nu_{jR}$ type can be found in [9–11]), $\mathbf{B}^0$ is the strength of the magnetic field in the frame where the neutrino is at rest, and $\gamma = (1-\beta)^{-1/2}$. We use here the system of units in which $c = \hbar = 1$.

We denote by $\mathbf{e}_3$ a unit vector parallel to $\mathbf{n}$ and by ϕ the angle between $\mathbf{e}_3$ and the direction of wave propagation. By using Lorentz transformations for

1063-7788/01/6409-1624$21.00

electromagnetic fields, we then find that, in the particle rest frame, there arises the magnetic field

$$\mathbf{B}^0 = \gamma\Big[(\cos\phi - \beta)B_1\mathbf{e}_1 + (1 - \beta\cos\phi)B_2\mathbf{e}_2 - \frac{\sin\phi}{\gamma}B_1\mathbf{e}_3\Big], \quad (3)$$

where the vectors $\mathbf{e}_{1,2,3}$ are unit vectors orthonormal to one another.

In the case of a linearly polarized electromagnetic wave, we have

$$B_1 = \cos\alpha\cos\psi, \quad B_2 = \sin\alpha\cos\psi, \quad (4)$$

where $\psi = \omega t(1 - \beta/\beta_0 \times \cos\phi)$ is the phase of the wave, β_0 is its velocity (which, in general, may be less than unity; $\beta_0 \leq 1$), and α is the angle specifying the orientation of the plane of wave polarization.

Substituting expressions (3) and (4) into the general formula (2) and expanding it in powers of the small parameter $1/\gamma \ll 1$, we reduce the Hamiltonian to the form

$$H = -\tilde{\rho}\sigma_3 - A_0\cos\psi(\sigma_1\cos\alpha - \sigma_2\sin\alpha), \quad (5)$$

where $A_0 = -\mu B(1 - \beta\cos\phi)$ and $\tilde{\rho} = V_{\text{eff}}/2 - \Delta m^2 A/4E$.

For the ensuing investigation, it is convenient to introduce the evolution operator $V(t)$ that relates the neutrino state $\nu(t)$ at the instant t to the initial state $\nu(0)$: $\nu(t) = V(t)\nu(0)$. From (1) and (5), we find that $V(t)$ satisfies the equation

$$\dot{V}(t) = i\,[\tilde{\rho}\sigma_3 + A_0\cos\psi \times (\sigma_1\cos\alpha - \sigma_2\sin\alpha)]V(t). \quad (6)$$

Note that the operator $U(t)$ defined as

$$U(t) = \exp\left(-i\sigma_3\frac{\alpha}{2}\right)V(t)\exp\left(i\sigma_3\frac{\alpha}{2}\right)$$

satisfies the equation

$$\dot{U}(t) = i\,[\tilde{\rho}\sigma_3 + A_0\sigma_1\cos\psi]\,U(t). \quad (7)$$

Thus the dynamics of $\nu_{iL} \leftrightarrows \nu_{jR}$ neutrino transitions is independent of the orientation of the polarization plane.

Seeking a resonance in neutrino oscillations, we substitute, in Eq. (7), the condition

$$\tilde{\rho} = 0. \quad (8)$$

A solution to Eq. (7) then has the form

$$U_1(t) = \exp(i\sigma_1 f(t)), \quad (9)$$

where $f(t) = A_0/\dot{\psi}\sin\dot{\psi}t$. For the probability of neutrino transitions, we obtain

$$P_{ij}(t) = |\langle\nu_R|V(t)|\nu_L\rangle|^2 = \sin^2 2f(t) = \sin^2\left(\frac{A_0}{\dot{\psi}}\sin\dot{\psi}t\right). \quad (10)$$

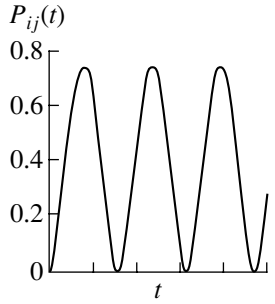

Fig. 1. Transition probability P_{ij} as a function of time t for the case of $|A_0/\dot{\psi}| = 1 < \pi/2$. The zeros of the function $P_{ij}(t)$ are determined from the equation $\sin\dot{\psi}t = 0$.

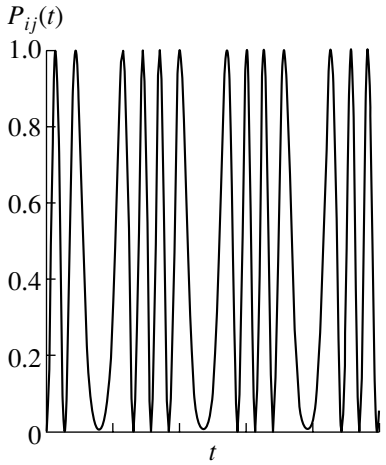

Fig. 2. Transition probability P_{ij} as a function of time t for the case of $|A_0/\dot{\psi}| = 6.2 > \pi/2$. The zeros of the function $P_{ij}(t)$ are determined from the equation $6.2\sin\dot{\psi}t = \pi n$, $n = 0, 1$.

From this formula, it follows that the transition probability can attain the value of unity, provided that

$$\left|\frac{A_0}{\dot{\psi}}\right| \geq \frac{\pi}{2}. \quad (11)$$

This condition can set limits on the quantities characterizing the neutrino (μ, β) and the electromagnetic wave $(\omega, B, \phi, \beta_0)$.

That condition (11) is necessary for the emergence of a resonance $[P_{ij}(t) = 1]$ can be illustrated by the graphs representing the dependence $P_{ij}(t)$ for various values of $\xi = |A_0/\dot{\psi}|$ (see Fig. 1 for $\xi < \pi/2$ and Fig. 2 for $\xi > \pi/2$). These graphs show that only if the subsidiary condition (11) is met can the probability take the value of unity. For $\xi \geq \pi/2$, the basic concept of an effective oscillation length becomes meaningless, because the maxima of the probability do not alternate with the minima at regular intervals.

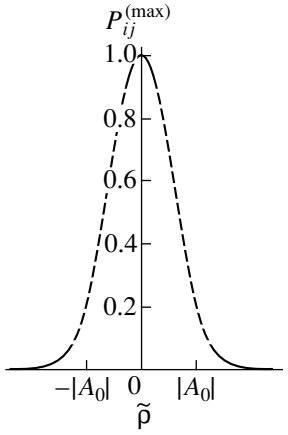

Fig. 3. Maximum value of the transition probability as a function of the parameter $\tilde{\rho}$ for $|\tilde{\rho}| \ll |A_0|$ and $|\tilde{\rho}| \gg |A_0|$.

Let us now investigate condition (8) in more detail. Suppose that $\tilde{\rho} \gg A_0$; from (7), we then obtain the equation

$$\dot{U} = i\tilde{\rho}\sigma_3 U. \tag{12}$$

A solution to this equation can be represented in the form

$$U = \exp(i\sigma_3\tilde{\rho}t).$$

The transition probability vanishes in this case:

$$P_{ij} = \left|\langle\nu_R|\exp(i\sigma_3\tilde{\rho}t)|\nu_L\rangle\right|^2 = 0.$$

We will now prove that the relation in (8) is actually the condition of resonance amplification of $\nu_{iL} \leftrightarrows \nu_{jR}$ oscillations. For this, we consider a small deviation from the condition in (8); that is, we set $\tilde{\rho} = \varepsilon$, where ε is a small parameter. Equation (7) then takes the form

$$\dot{U} = i(\varepsilon\sigma_3 + H_1)U, \quad H_1 = A_0\sigma_1\cos\psi. \tag{13}$$

We seek a solution to Eq. (13) in the form

$$U = U_1 F,$$

where U_1 [see Eq. (9)] satisfies the equation

$$\dot{U}_1 = iH_1U_1. \tag{14}$$

For the matrix F, we obtain the equation

$$\dot{F} = i\varepsilon H_\varepsilon F,\ H_\varepsilon = \sigma_3\cos 2f(t) + \sigma_2\sin 2f(t). \tag{15}$$

It is natural to represent a solution to Eq. (15) as the series

$$F = \sum_{k=0}^{\infty}\varepsilon^k F^{(k)},$$

where $F^0 = \hat{1}$ is an identity matrix. The quantities $F^{(k)}$ satisfy the recursion relation

$$F^{(k+1)}(t) = i\int_0^t H_\varepsilon(\tau)F^{(k)}(\tau)d\tau. \tag{16}$$

To terms of order ε^2 inclusive, this yields

$$F(t) = \hat{1} + i\varepsilon(\sigma_2\gamma(t) + \sigma_3\delta(t)) + \varepsilon^2(-\mathcal{A}(t) + i\sigma_1\mathcal{B}(t)) + O(\varepsilon^3),$$

where

$$\gamma(t) = -\int_0^t \sin 2f(\tau)d\tau,$$

$$\delta(t) = \int_0^t \cos 2f(\tau)d\tau,$$

$$\mathcal{A}(t) = \int_0^t [\delta(\tau)\cos 2f(\tau) - \gamma(\tau)\sin 2f(\tau)]d\tau,$$

$$\mathcal{B}(t) = \int_0^t [\gamma(\tau)\cos 2f(\tau) + \delta(\tau)\sin 2f(\tau)]d\tau.$$

The $\nu_{iL} \leftrightarrows \nu_{jR}$ transition probability is then given by

$$P_{ij} = \sin^2 f + \varepsilon^2[2\sin f(\mathcal{B}\cos f - \mathcal{A}\sin f) + (\gamma\cos f - \delta\sin f)^2] + O(\varepsilon^4). \tag{17}$$

Suppose that the condition in (11) is satisfied. We consider the values of the probability at the points $f(t) = \pi/2 + \pi k$, $k \in Z$, where it is at a maximum. Relation (17) then takes the form

$$P_{ij}^{(\max)} = 1 + \varepsilon^2(\delta^2 - 2\mathcal{A}).$$

It can be shown that, at the points $f(t) = \pi/2 + \pi k$, the following strict inequality holds:

$$\delta^2 - 2\mathcal{A} = \left(\int_0^t \sin 2f(\tau)d\tau\right)^2 < 0,$$

whence it follows that $P_{ij}^{(\max)}(\varepsilon \neq 0) < 1$. Thus, we have shown that, if there is a small deviation from the resonance condition (8), the probability cannot reach the value of unity. The dependence of $P_{ij}^{(\max)}$ on $\tilde{\rho}$ under the condition (11) is illustrated in Fig. 3.

In conclusion, we discuss the origin of the subsidiary condition (11) in more detail. In the case of oscillations in a constant transverse magnetic field, the resonance condition can be expressed in terms of only one relation [similar to Eq. (8)] [4, 5]. In the case considered here, the emergence of the subsidiary condition (11) is associated with the special configuration of the electromagnetic field.

Indeed the evolution of a spin was described here within the approach that was developed in [12, 13] and which is based on an analog of the Bargmann–Michel–Telegdi equation [14]. In this approach, the quantum evolution operator $V(t)$ has the meaning

of the evolution matrix for the spin-tensor $S = (\sigma \mathbf{S})$, where $\mathbf{S}$ is the particle spin vector. In the presence of an electromagnetic field, the particle spin precesses about a fixed vector $\mathbf{l}$ whose direction is determined by a particular configuration of the electromagnetic field. The resonance amplification of spin oscillations occurs in the case where the vector $\mathbf{l}$ forms a right angle with the neutrino velocity. For this reason, the condition $\tilde{\rho} = 0$ dictates the required direction of the vector $\mathbf{l}$.

In a linearly polarized electromagnetic wave, however, the magnetic-field-induction vector $\mathbf{B}$ oscillates in a plane. Under such conditions, the spin vector $\mathbf{S}$ rotates in opposite directions in the cases where the vector $\mathbf{B}$ is parallel and antiparallel to the $\mathbf{e}_1$ axis. As a consequence, the spin vector oscillates, in our problem, about the direction orthogonal to the neutrino velocity. For the emergence of effective neutrino oscillations it is necessary that their amplitude be greater than or equal to π. A detailed analysis reveals that, for this to occur, one must impose a constraint on the amplitude of the magnetic field and that this constraint coincides with the condition in (11).

REFERENCES

1. R. Cisneros, Astrophys. Space Sci. **10**, 87 (1971).
2. J. Schechter and J. Valle, Phys. Rev. D **24**, 1883 (1981).
3. M. B. Voloshin, M. I. Vysotskiĭ, and L. B. Okun', Yad. Fiz. **44**, 677 (1986) [Sov. J. Nucl. Phys. **44**, 440 (1986)].
4. C.-S. Lim and W. Marciano, Phys. Rev. D **37**, 1368 (1988).
5. E. Akhmedov, Phys. Lett. B **213**, 64 (1988).
6. J. Vidal and J. Wudka, Phys. Lett. B **249**, 473 (1990).
7. A. Yu. Smirnov, Phys. Lett. B **260**, 161 (1991).
8. E. Akhmedov, S. Petcov, and A. Smirnov, Phys. Rev. D **48**, 2167 (1993).
9. G. G. Likhachev and A. I. Studenikin, Zh. Éksp. Teor. Fiz. **108**, 769 (1995) [JETP **81**, 419 (1995)].
10. A. Egorov, G. Likhachev, and A. Studenikin, in *Proceedings of Recontres de la Valle d'Aoste,* Ed. by M. Greco, Frascati Phys. Ser. (1995).
11. G. Likhachev and A. Studenikin, Grav. Cosm. **1**, 22 (1995).
12. A. M. Egorov, A. E. Lobanov, and A. I. Studenikin, in *New Worlds in Astroparticle Physics,* Ed. by A. Mourao, M. Pimento, and P. Sa (World Sci., Singapore, 1999); hep-ph/9902447.
13. A. M. Egorov, A. E. Lobanov, and A. I. Studenikin, Phys. Lett. B **491**, 137 (2000); hep-ph/9910476.
14. V. B. Berestetskiĭ, E. M. Lifshitz, and L. P. Pitaevskiĭ, *Quantum Electrodynamics* (Nauka, Moscow, 1980; Pergamon, Oxford, 1982).

Translated by R. Rogalyov

Physics of Atomic Nuclei, Vol. 64, No. 9, 2001, pp. 1628–1636. Translated from Yadernaya Fizika, Vol. 64, No. 9, 2001, pp. 1709–1717.

ELEMENTARY PARTICLES AND FIELDS
Theory

"Recoil"-Effect-Induced Contribution of Order $m\alpha^6$ to the Hyperfine Splitting of the Positronium Ground State

A. P. Burichenko[1)]

Received June 13, 2000

Abstract—The recoil-effect-induced part of the $m\alpha^6$ contribution to the hyperfine splitting of the positronium ground state is calculated. The method employed is based on noncovariant perturbation theory within QED. The result is $0.381(6)m\alpha^6$, which agrees well with the results of previous studies. This means that it deviates sizably from experimental data. © *2001 MAIK "Nauka/Interperiodica".*

1. INTRODUCTION

At present, the hyperfine splitting of the positronium ground state—that is, the difference of the energies of the 1^3S_1 and the 1^1S_0 state, which is denoted by $\Delta\nu$ in the following—has been measured to the highest precision among all features of positronium. The best two experimental results for this quantity were obtained in [1, 2] and [3]; they are, respectively,

$$\Delta\nu = 203387.5(1.6)\ \text{MHz} \tag{1}$$

and

$$\Delta\nu = 203389.10(0.74)\ \text{MHz}. \tag{2}$$

The $m\alpha^4$, $m\alpha^5$, and $m\alpha^6\ln\alpha$ contributions to $\Delta\nu$ were calculated in [4–9]. Their sum is given by

$$m\alpha^4\left[\frac{7}{12}-\frac{\alpha}{\pi}\left(\frac{8}{9}+\frac{1}{2}\ln 2\right)-\frac{5}{24}\alpha^2\ln\alpha\right] = 203400.29\ \text{MHz}. \tag{3}$$

In order to compare the experimental results presented in (1) and (2) with theoretical predictions, it is necessary to calculate $m\alpha^6$ contributions not involving logarithms. One can break them down into a few terms and calculate each such term separately. The contributions associated with one-, two-, and three-photon annihilation were calculated in [10, 11], [12], and [13, 14], respectively. The contributions that are formally proportional to $(Z\alpha)^4\alpha^2 m$ and $(Z\alpha)^5\alpha m$ (here, Ze is the charge of one of the constituent particles; for positronium, $Z=1$) were determined in [15, 16] and [17–19], respectively. There is also a $(Z\alpha)^6 m$ contribution. It is induced by the "recoil" effect and is represented by diagrams where each photon line links two fermion lines. In what follows, the sum of the $m(Z\alpha)^6$ and $m(Z\alpha)^6\ln\alpha$ terms in $\Delta\nu$ is denoted by $\Delta\nu_{\text{rec}}$; it was calculated in [20–23]. Here, we also consider this very contribution.

The results presented in [20–22] were different. The value obtained in [23], $0.3763m\alpha^6$, complies with that from [21], $0.3767(17)m\alpha^6$. Our present result is $0.381(6)m\alpha^6$, which is also in agreement, within the errors, with the aforementioned results from [21, 23]. Recently, the calculations from [22] were revised by their authors; the new value of $0.3764(35)m\alpha^6$ [24] is now consistent with those quoted immediately above.

In [20], so-called nonrelativistic QED (NRQED) was formulated and used to calculate $\Delta\nu_{\text{rec}}$. The calculations in [22] were performed within the Bethe–Salpeter formalism. In [21] (and, as matter of fact, in [23]), $\Delta\nu_{\text{rec}}$ was computed within the approach employing an effective nonrelativistic Hamiltonian. This approach is a combination of NRQED and old-fashioned noncovariant perturbation theory within QED. The latter was employed for the first time in [25] to calculate the spectrum of positronium.

In the present article, we also employ a formalism based on noncovariant perturbation theory within QED. In calculating relevant integrals with respect to loop momenta, we break them down into soft and hard components—that is, those that are associated with low and high momenta, respectively. Soft contributions are calculated analytically. In dealing with hard contributions, we reduce the sum of a large number of noncovariant diagrams to the sum of a few covariant ones, the latter being calculated numerically.

2. DESCRIPTION OF THE FORMALISM

The Schrödinger equation for the total (many-body) wave function can easily be reduced to an equation involving only a two-body component of this

[1)]Novosibirsk State Technical University, pr. K. Marksa 20, Novosibirsk, 630092 Russia.

wave function, with an effective Hamiltonian being dependent on energy. This equation has the form

$$(PHP + V_a(E) - E)|\psi_2\rangle = 0, \tag{4}$$

where $|\psi_2\rangle$ is the two-body component of the wave function; P is the operator of projection onto two-particle space; H is total QED Hamiltonian; and

$$V_a(E) = PHP_a\frac{1}{(E - P_aHP_a)}P_aHP,$$
$$P_a = 1 - P.$$

In order to calculate the energy spectrum determined by Eq. (4), we represent the corresponding effective Hamiltonian $PHP + V_a(E)$ as the sum of the unperturbed part $H^{(0)} \equiv PH_0P + V_0$ and the perturbation $V(E) \equiv V_a(E) + PV_NP - V_0$, where H_0 is the free-motion Hamiltonian of QED and V_N and V_0 are, respectively, the electromagnetic and the nonrelativistic Coulomb interaction.

The expansion of $V(E) + V_0$ in powers of the electromagnetic interaction can be illustrated in terms of two-particle-irreducible diagrams of noncovariant perturbation theory. The rules of the diagram technique in the noncovariant formulation can be found, for example, in [25].

Below, all the operators and wave functions used refer to the two-particle subspace. It is convenient to perform calculations in the c.m. frame, where the momentum $\mathbf{p}$ of the first particle is the only variable (apart from spins). We denote by V_c (V_m) the operator corresponding to the tree diagram involving the exchange of a Coulomb (magnetic) photon. We then rewrite V in the form

$$V(E) = V_1 + V_2 + V_3 + \ldots, \quad V_1 = V_{1c} + V_m, \tag{5}$$
$$V_{1c} \equiv V_c - V_0,$$

where V_2, V_3, etc., include irreducible diagrams featuring two, three, etc., photon lines, respectively. The recoil contribution $\Delta\nu$ correct to terms of order $m\alpha^6$ inclusive is

$$\langle\psi|V_1G'V_1G'V_1 + V_2G'V_1 + V_1G'V_2 \tag{6}$$
$$+ V_3 + V_1G'V_1 + V_2 + V_1\ |\psi\rangle|_{\sigma=0}^{\sigma=1}.$$

Here, $|\psi\rangle$ stands for the zero-order approximation of $|\psi_2\rangle$, that is, a solution to the equation

$$H^{(0)}|\psi\rangle = E_2|\psi\rangle; \tag{7}$$

σ is the positronium spin; and $G' = G'(E_2)$ is the Green's function for Eq. (7), where the ground-state contribution is subtracted.

It can be shown that, to a sufficient precision for the case being considered, we can represent the zero-order wave function as

$$|\psi\rangle \approx (1 + (S - S_0)V_0 \tag{8}$$
$$+ SV_0(S - S_0)V_0 + L\Delta T)|\varphi_0\chi\rangle.$$

Here, $L \equiv G'_0 - S_0 - S_0V_0S_0$, S_0 (S) is the free nonrelativistic (relativistic) two-particle Green's function, G'_0 stands for the Coulomb nonrelativistic Green's function where the ground-state contribution is subtracted, ΔT is the operator of the relativistic correction to the kinetic energy, χ represents the spin part of the wave function, and φ_0 (E_0) stands for the ground-state wave function (energy) for the ordinary nonrelativistic Coulomb problem. It is well known that $E_0 = 2m - \gamma^2/m$ and $\varphi_0(\mathbf{p}) = 8\gamma^{5/2}\pi^{1/2}f_p^{-2}$ (hereafter, we use the notation $\gamma \equiv \alpha m/2$ and $f_k \equiv \mathbf{k}^2 + \gamma^2$ for an arbitrary momentum $\mathbf{k}$). In (8) and everywhere below, all Green's functions are taken at E_0.

We now rearrange the various contributions in (6). To a sufficient degree of precision, we can first set $G' \approx S + SV_0S + L$. For an arbitrary operator X, we denote $\langle X\rangle \equiv \langle\varphi_0\chi|X|\varphi_0\chi\rangle|_{\sigma=0}^{\sigma=1}$; further, we use the notation $\langle X\rangle_{(n)}$ for the sum of the α^n and $\alpha^n\ln\alpha$ contributions to $\langle X\rangle$. Retaining only the terms of the required orders, we arrive at

$$\Delta\nu_{\rm rec} = \langle V_3 + V_2 + U_{V2} + U_C + U_M \tag{9}$$
$$+ U_{MM} + U_{MCM} + U_{MMM} + U_L\rangle_{(6)},$$

where

$$U_{V2} = V_2SV_m + V_2(SV_c - S_0V_0) + \text{h.c.}, \tag{10}$$

$$U_C = V_{1c} + U_{C2} + U_{C3}, \tag{11}$$

$$U_M = V_m + U_{M2} + U_{M3}, \tag{12}$$

$$U_{MM} = U_{MM2} + U_{MM3}, \tag{13}$$

$$U_{MCM} = V_mSV_cSV_m, \tag{14}$$

$$U_{MMM} = V_mSV_mSV_m, \tag{15}$$

$$U_L = V_mLV_m + (V_mL(\Delta T\ + V_{1c})\ + \text{h.c.}). \tag{16}$$

Here, we have

$$U_{C2} = V_{1c}SV_{1c} + (V_{1c}(S - S_0)V_0 + \text{h.c.}), \tag{17}$$

$$U_{M2} = V_m(SV_c - S_0V_0) + \text{h.c.}, \tag{18}$$

$$U_{MM2} = V_mSV_m, \tag{19}$$

$$U_{C3} = V_0(S - S_0)V_{1c}(S - S_0)V_0 \tag{20}$$
$$+ (V_{1c}SV_c(S - S_0)V_0 + \text{h.c.})$$
$$+ (V_{1c}SV_{1c}(S - S_0)V_0 + \text{h.c.}),$$

$$U_{M3} = (V_cS - V_0S_0)V_m(SV_c - S_0V_0) \tag{21}$$
$$+(V_mSV_c(SV_c - S_0V_0) + \text{h.c.}),$$

$$U_{MM3} = V_mSV_m(SV_c - S_0V_0) + \text{h.c.} \tag{22}$$

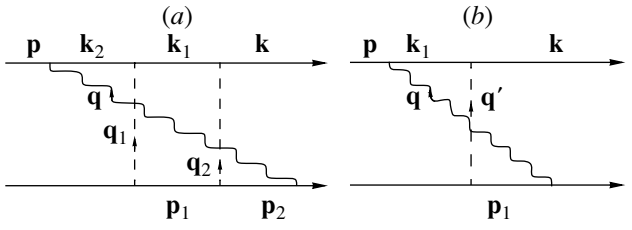

Fig. 1. Irreducible diagrams associated with the retardation effect (wavy and dashed lines denote, respectively, magnetic (transverse) and Coulomb photons).

3. COMPUTATIONAL METHOD

The various contributions to $\Delta\nu_{\rm rec}$ can be represented as integrals with respect to loop momenta. A contribution will be referred to as a hard one if it is controlled (to a sufficient degree of precision) by the region where all the loop momenta are of order m. Otherwise, a contribution is classed with soft ones. In order to separate soft and hard contributions, we expand relevant integrand in powers of momenta. In order to answer the question of whether one term of such an expansion or another involves a soft contribution, we assume that all the momenta are of order αm and, by counting the relevant powers, we then find out whether this region of momenta makes a contribution of order $m\alpha^6$ to $\Delta\nu_{\rm rec}$—if so, the expansion term being considered must obviously be associated with soft contributions. On the other hand, it appears that, in the problem addressed here, the absence of an $m\alpha^6$ contribution from the above region implies that there is no soft contribution in general (at least, within the computational algorithm presented below).

In breaking down an expression into a soft and a hard part, there is some degree of arbitrariness; hence, the soft part can always be chosen in such a way that its contribution to the integral is analytically calculable. In calculating the hard contribution, one can set $E_0 = 2m$ in the integrand, whereupon the resulting integral can easily be computed numerically.

The contributions to $\Delta\nu_{\rm rec}$ can be broken down into tree ($\langle V_{1c}, V_m\rangle_{(6)}$), one-loop ($\langle V_2, U_{C2}, U_{M2}, U_{MM2}\rangle_{(6)}$), and two-loop ($\langle V_3, U_{V2}, U_{C3}, U_{M3}, U_{MM3}, U_{MCM}, U_{MMM}\rangle_{(6)}$) ones (in the second and the third case, the expression in $\langle\ \rangle_{(6)}$ appears to be, respectively, a single and a double integral with respect to momenta). In addition, there is the contribution $\langle U_L\rangle_{(6)}$ corresponding to diagrams involving three or more loops. We consider the contributions of each type individually.

An arbitrary two-loop contribution has the form $\langle X_2\rangle_{(6)}$, where

$$X_2(\mathbf{p}, \mathbf{p}', \gamma) \tag{23}$$

$$= \alpha^3 \int \frac{d^3q_1}{(2\pi)^3}\frac{d^3q_2}{(2\pi)^3} Y_2(\mathbf{p}, \mathbf{p}', \mathbf{q}_1, \mathbf{q}_2, \gamma).$$

We define n as the degree of divergence of X_2; that is, $Y_2 \sim \delta^{n-6}$ for $p, p', q_1, \ldots, \gamma \sim \delta \ll m$. For all $n > 0$ terms, the main contribution to the integral comes from the region where $p \sim p' \sim \gamma$ and $q_1 \sim q_2 \sim |\mathbf{q}_1 - \mathbf{q}_2| \sim m$ and where the dependence of Y_2 on $\mathbf{p}$ and $\mathbf{p}'$ can be disregarded. As a result, we obtain

$$\langle X_2\rangle_{(6)} = \left|\varphi_0(\mathbf{r}=0)\right|^2 X_2\big|_{\sigma=0}^{\sigma=1}\big|_{\mathbf{p},\mathbf{p}',\gamma=0} \equiv \langle X_2\rangle_p. \tag{24}$$

For the sake of brevity, we still continue using the notation $\langle\ \rangle_p$ introduced in (24). The integral entering into the definition $\langle X_2\rangle_p$ is independent of the small parameter α and can easily be computed numerically.

In the case of $n \le 0$, we isolate a soft part Y_{21} from Y_2, so that Y_{21} and $(Y_2 - Y_{21})$ are characterized by $n \le 0$ and $n > 0$, respectively. It is convenient to do this in such a way that, for $p, p', q_1, \ldots \ll m$, Y_{21} is close to a homogeneous function (this is not done only for the contribution of the graph that is presented in Fig. 1*a* and which will be discussed in Section 4). It can be shown that, for all cases encountered in the ensuing calculations, this choice of Y_{21} makes it possible to calculate the hard part $\langle X_2\rangle_{(6)}$ according to (24). The result is

$$\langle X_2\rangle_{(6)} = \langle X_2 - X_{21}\rangle_p + \langle X_{21}\rangle_{(6)}, \tag{25}$$

where X_{21} is an integral of the form (23), where Y_{21} appears as the integrand. To ensure convergence of the integrals that determine the first and the second term in (25), the function Y_{21} must decrease at a sufficiently high rate for $q_1, q_2 \gg m$.

In calculating one-loop and tree contributions, we need to find first- and the second-order corrections in α to the leading contributions. The method for determining these corrections is obvious. To illustrate it, we will describe the calculation of $\langle X\rangle$, where $X = X(\mathbf{p}, \mathbf{p}')$ is a sufficiently smooth function independent of α and where the expansion of $X(\mathbf{p}, \mathbf{p}') - X(0,0)$ in $\mathbf{p}$ and $\mathbf{p}'$ begins from the third-order term. We represent $\langle X\rangle$ in the form

$$\langle X\rangle = A_0 + A_1 + A_2,$$

$$A_0 = |\varphi_0(\mathbf{r}=0)|^2 X(0,0)\big|_{\sigma=0}^{\sigma=1},$$

$$A_1 = \varphi_0(\mathbf{r}=0)\int \frac{d^3p}{(2\pi)^3}\varphi_0(\mathbf{p})(X(\mathbf{p},0) \tag{26}$$

$$+ X(0,\mathbf{p}) - 2X(0,0))\big|_{\sigma=0}^{\sigma=1},$$

$$A_2 = \int \frac{d^3p}{(2\pi)^3}\frac{d^3p'}{(2\pi)^3}\varphi_0^+(\mathbf{p}')\ (X(\mathbf{p},\mathbf{p}') \tag{27}$$

$$- X(\mathbf{p},0) - X(0,\mathbf{p}') + X(0,0))\big|_{\sigma=0}^{\sigma=1}\ \varphi_0(\mathbf{p}).$$

In order to calculate the first three terms of the expansion of $\langle X\rangle$ in α, we can replace $\varphi_0(\mathbf{p})$ in (26), (27) by $8\gamma^{5/2}\pi^{1/2}p^{-4}$, whereupon, A_0, A_1, and A_2 prove to be of order α^3, α^4, and α^5, respectively.

An arbitrary one-loop contribution has the form $\langle X_1\rangle_{(6)}$, where

$$X_1(\mathbf{p},\mathbf{p}',\gamma)=\int\frac{d^3q}{(2\pi)^3}\,\alpha^2\,Y_1(\mathbf{p},\mathbf{p}',\mathbf{q},\gamma). \quad (28)$$

Let n be such that $Y_1\sim\delta^{n-2}$ for $p,p',q,\ldots,\gamma\sim\delta\ll m$. In the case of $n\le 0$, we isolate a soft part Y_{11} from Y_1 in such a way that Y_{11} and (Y_1-Y_{11}) are characterized by $n\le 0$ and $n>0$, respectively. In choosing Y_{11}, it is convenient to require that, for $p,p',q,\gamma\ll m$, this soft part be close to a homogeneous function (this is not done only for the contribution of the graph that is presented in Fig. 1*b* and which will be discussed in Section 4). It can be shown that, for this choice of Y_{11}, the hard part $\langle X_1\rangle_{(6)}$ can be found according to a relation of the type in (26). The result is

$$\langle X_1\rangle_{(6)}=\langle((X_1-X_{11}) \quad (29)$$
$$-(X_1-X_{11})_0)S_0V_0+\text{h.c.}\rangle_p+\langle X_{11}\rangle_{(6)},$$

where we have used the notation $(\ )_0$ defined in such a way that $(X)_0(\mathbf{p},\mathbf{p}')\equiv X(\mathbf{p},\mathbf{p}')\big|_{\mathbf{p}=\mathbf{p}'=0}$ and where X_{11} is an integral of the form (28), where the integrand involves Y_{11}.

The tree contributions to $\Delta\nu_{\rm rec}$ ($\langle V_m\rangle_{(6)}$, $\langle V_{1c}\rangle_{(6)}$) are calculated in a similar way. Each of them is represented as the sum of the soft and the hard part, and the latter is calculated according to (27).

In Section 4, soft contributions are isolated in $\Delta\nu_{\rm rec}$ according to (25), (27), and (29), whereby it is found that

$$\langle V_3\rangle_{(6)}=\langle V_3-W_{V3}\rangle_p+E^S_{V3}, \quad (30)$$

$$\langle V_2+U_{V2}\rangle_{(6)}=\langle V_2SV_m+\text{h.c.}\rangle_p \quad (31)$$
$$+\langle(V_2SV_c-W_{V2})+\text{h.c.}\rangle_p+E^S_{V2},$$

$$\langle U_C\rangle_{(6)}=\langle V_cSV_cSV_c-W_C\rangle_p+E^S_C, \quad (32)$$

$$\langle U_M\rangle_{(6)}=\langle V_cSV_mSV_c-W_{M1}\rangle_p \quad (33)$$
$$+\langle(V_mSV_cSV_c-W_{M2})+\text{h.c.}\rangle_p+E^S_M,$$

$$\langle U_{MM}\rangle_{(6)} \quad (34)$$
$$=\langle(V_mSV_mSV_c-W_{MM})+\text{h.c.}\rangle_p+E^S_{MM},$$

$$\langle U_{MCM}\rangle_{(6)} \quad (35)$$
$$=\langle V_mSV_cSV_m-W_{MCM}\rangle_p+E^S_{MCM},$$

$$\langle U_{MMM}\rangle_{(6)}=\langle V_mSV_mSV_m\rangle_p, \quad (36)$$

where W_i ($i=V3$, $V2$, C, etc.) stand for the operators associated with the soft contributions and E^S_i are the analytically calculable soft contributions to $\Delta\nu_{\rm rec}$.

The first term of $\langle\ \rangle_p$ in each of expressions (30)–(36) is obtained by summing the contribution of a few noncovariant diagrams, their sum being equal to the sum of expressions for all two-loop noncovariant diagrams of the recoil type. It should be noted that, in applying the procedure $\langle\ \rangle_p$ to any diagram, its external legs occur on the mass shell. The sum of the corresponding integrands for all noncovariant diagrams having the same topological structure is equal to the integrand for an ordinary covariant Feynman diagram (after integration with respect to zero components of loop momenta). Owing to this fact, the sum of the contributions of many noncovariant diagrams can be reduced to the sum of the contributions of only a few covariant diagrams. Moreover, the sum of the integrands for all covariant diagrams is independent of gauge, so that the calculations can be performed in any gauge.

4. SOFT CONTRIBUTIONS

Here, we apply the general algorithm for extracting soft contributions to various terms in $\Delta\nu_{\rm rec}$. Beforehand, we note that any quantity averaged over the ground-state wave function can be replaced by its average over positronium polarizations (that is, over the directions of the total spin); as a result, the calculations are somewhat simplified.

Let us discuss the calculation of the retardation-induced contributions to $\langle V_m\rangle_{(6)}$, $\langle V_2\rangle_{(6)}$, and $\langle V_3\rangle_{(6)}$; in the last two cases, we imply the contributions of the diagrams in Figs. 1*b* and 1*a*. From the outset, it is convenient to consider, instead of the relevant operators, their spin–spin components averaged over the directions of the total spin. Each of these quantities can be represented as the sum of two terms,

$$\langle V_i\rangle_{(6)}=\langle V_i^{\rm ret}\rangle_{(6)}+\langle V_i'\rangle_{(6)},\quad i=m,2,3, \quad (37)$$

where

$$V_2^{\rm ret}(\mathbf{p},\mathbf{k})=\int\frac{d^3q}{(2\pi)^3}\alpha^2\frac{4}{3}\frac{\pi^2}{m^2}\boldsymbol{\sigma}_1\cdot\boldsymbol{\sigma}_2\frac{q}{q'^2} \quad (38)$$
$$\times\left(\frac{1}{(q+f_k)(q+f_{k_1})}+\frac{1}{(q+f_p)(q+f_{p_1})}\right),$$

$$V_3^{\rm ret}(\mathbf{p},\mathbf{k})=\int\frac{d^3q_1}{(2\pi)^3}\frac{d^3q_2}{(2\pi)^3}\alpha^3\frac{16}{3}\frac{\pi^3}{m^2}\boldsymbol{\sigma}_1\cdot\boldsymbol{\sigma}_2\frac{q}{q_1^2q_2^2}$$
$$\times\left(\frac{1}{(q+f_p)(q+f_{p_1})(q+f_{p_2})}\right. \quad (39)$$
$$\left.+\frac{1}{(q+f_k)(q+f_{k_1})(q+f_{k_2})}\right)$$

the notation for the momenta is indicated in Fig. 1,

$$V_m^{\rm ret}(\mathbf{p},\mathbf{k})=\frac{1}{2}V_{m0}\left[\frac{q}{q+f_p}+\frac{q}{q+f_k}\right]. \quad (40)$$

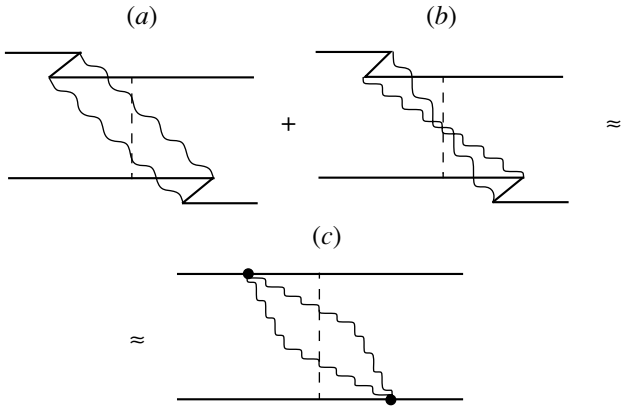

Fig. 2. Cancellation of soft contributions for irreducible diagrams involving two magnetic photons.

Here,

$$V_{m0} = V_s\big|_{\mathbf{p}\,=\,\mathbf{k}\,=\,\gamma\,=\,0} = \frac{2}{3}\frac{\alpha\pi}{m^2}\boldsymbol{\sigma}_1\cdot\boldsymbol{\sigma}_2, \quad \mathbf{q} = \mathbf{k} - \mathbf{p},$$

and V_s is the positronium-polarization-averaged spin–spin contribution to V_m. The softest contributions to $\langle V_i\rangle_{(6)}$ are entirely contained in the first terms on the right-hand side of (37). The second terms in (37) can be found by the method outlined in the preceding section.

It should be noted that the sum of the first terms in (37) is equal to zero. This can easily be demonstrated either by a straightforward evaluation or by means of the following argument. For a particle of mass $m/2$ moving in the field of a particle of large mass M, we consider, for this purpose, the calculation of the hyperfine splitting of the ground state taking into account terms of order $\alpha^6 m^2/M$. To a precision sufficient for the present case, we can disregard retardation effects from the outset, assuming the magnetic interaction to be instantaneous. But if we allow for retardation explicitly, the corresponding contributions must exactly cancel:

$$\langle V_m^{\mathrm{ret}} + V_2^{\mathrm{ret}} + V_3^{\mathrm{ret}}\rangle_{(6)} = \langle V_{m0}\rangle_{(6)} = 0. \qquad (41)$$

4.1. Contributions of Irreducible Diagrams

In order to calculate $\langle V_3\rangle_{(6)}$, we must find V_{30}—that is, that part of V_3 which is controlled by an integral featuring whose degree of divergence is $n = 0$—and then apply expression (25) with $X_{21} = V_{30}$. There are only three essentially different diagrams contributing to V_{30}. These are those in Figs. 2*a*, 2*b*, and 1*a*. However, the total contribution of the diagrams in Figs. 2*a* and 2*b* to V_{30} can be discarded, since, in the region of low loop momenta, their sum reduces to the diagram in Fig. 2*c*, where the effective two-photon vertex is independent of spins. Thus, V_{30} is determined by the diagram in Fig. 1*a* exclusively and can be set to V_3^{ret}. As a result, we arrive at expression (30) with

$$W_{V3} = V_3^{\mathrm{ret}}, \quad E_{V3}^S = \langle V_3^{\mathrm{ret}}\rangle_{(6)}.$$

In order to calculate $\langle V_2\rangle_{(6)}$, we follow a similar procedure. Specifically, we apply expression (29) with $X_{11} = V_{20}$, where V_{20} is the $n = 0$ component of V_2. Noticing that $\langle U_{V2}\rangle_{(6)} = \langle U_{V2}\rangle_p$, we arrive at (31) with

$$W_{V2} = (V_{20} + (V_2 - V_{20})_0)S_0V_0, \quad E_{V2}^S = \langle V_{20}\rangle_{(6)}.$$

The diagrams involving two Coulomb photons do not contribute to V_{20}. As to the contributions of the diagrams with two magnetic photons, they are cancelled, in just the same way as the analogous contributions to V_{30}.

Let us now consider the diagrams that involve one magnetic and one Coulomb photon and which contribute to V_2. The only diagram of this type not containing pairs is that in Fig. 1*b*. Its contribution to V_{20} can be set to V_2^{ret}. The set of diagrams featuring pairs can be broken down into two subsets associated with the covariant graphs A and B displayed in Fig. 3. The contribution of each subset to V_{20} can be chosen in the form

$$V_{20}^A(\mathbf{p},\mathbf{p}') = V_{20}^B = \int\frac{d^3q}{(2\pi)^3}\frac{4\alpha^2\pi^2}{3m^3} \qquad (42)$$
$$\times\,\boldsymbol{\sigma}_1\cdot\boldsymbol{\sigma}_2\frac{1}{q^2q'^2}((q^2+q'^2)R_q - k^2R_k)$$

(the notation for the momenta is indicated in Fig. 3, $\mathbf{k}\equiv\mathbf{p}'-\mathbf{p}$, and $R_l \equiv m^2/(m^2+l^2)$ for any $\mathbf{l}$). Their total contribution to E_{V2}^S is

$$E_P^S = (2/3)m\alpha^6\ln\alpha.$$

4.2. Contributions of Reducible Diagrams

We begin by evaluating $\langle U_L\rangle_{(6)}$. As a matter of fact, this is the contribution of the diagrams involving a Coulomb ladder that contain more than two loops. To the required accuracy, this contribution is controlled by the region where all loop momenta are of order $m\alpha$; hence, it can be calculated analytically. There are two types of such diagrams, those involving two or one magnetic photon and corresponding to the first or the second term in (16). The contribution of the diagrams involving two magnetic photons is independent, in the order being considered, on the details of the formalism employed; for the first time, it was calculated in [26]. The method that we use here to compute it is basically analogous to that from

[27] (calculations in the coordinate representation); the result is coincident with the previous one:

$$E^S_{LMM} = \left(\frac{791}{864} - \frac{\pi^2}{18}\right) m\alpha^6 \approx 0.3672 m\alpha^6. \quad (43)$$

The contribution of the diagrams involving one magnetic photon was calculated by two methods: in the coordinate representation (by a method similar to that from [27]) and by means of a straightforward integration in the momentum representation with the explicit expression for the function $L(\mathbf{p}, \mathbf{k})$, for example, from [26]. The results obtained by the two methods are identical:

$$E^S_{LM} = (1/64) m\alpha^6 \approx 0.01562 m\alpha^6. \quad (44)$$

Let us now calculate $\langle U_M \rangle_{(6)}$, the contribution of reducible graphs involving one magnetic photon (without the contribution of graphs that contain many loops and which were treated above). In doing this, we consider that $\langle V_m \rangle_{(6)} = \langle V_s \rangle_{(6)}$. We expand V_s in powers of momenta as

$$V_s = V^{\rm ret}_m + V_{m1} + V_{m2}, \quad (45)$$

where

$$V_{m1}(\mathbf{p}, \mathbf{k}) = \frac{1}{2m^2} V_{m0} \left[\frac{p^2 k^2}{q^2}(R_p + R_k) - \frac{1}{q^2}(p^4 R_p + k^4 R_k) - (p^2 R_p + k^2 R_k) \right], \quad (46)$$

where $\mathbf{q} = \mathbf{p} - \mathbf{k}$. It can be shown that $\langle V_{m2} \rangle_{(6)}$ is then determined by expression (27) with $X = V_{m2}$.

In order to calculate $\langle U_{M2} \rangle_{(6)}$ and $\langle U_{M3} \rangle_{(6)}$, we can use the expressions (29) and (25) with $X_{11} = V_{m0}(S_0 V_{11} + S_1 V_0) + \text{h.c.}$ and $X_{21} = V_{m0} S_0 V_0 (S_0 V_{11} + S_1 V_0) + \text{h.c.}$ Here, $S_1 \approx S - S_0$ in the region where the momenta are of order $m\alpha$; in this region, V_{11} is approximately equal to the difference $V_c - V_0$ averaged over the directions of the total spin.

After some simple algebra, we arrive at (33) with

$$W_{M1} = (V_c S V_m)_0 S_0 V_0 + \text{h.c.} + V_0 S_0 (V^{\rm ret}_m + V_{m1}) S_0 V_0 - ((V_0 S_0 (V^{\rm ret}_m + V_{m1}))_0 S_0 V_0 + \text{h.c.}),$$

$$W_{M2} = V_{m0} S_0 V_0 (S_0 V_{11} + S_1 V_0) + (V_m S_0 V_0 + V_{m0} S_1 V_0 + (V_m S V_c - V_m S_0 V_0 - V_{m0} S_1 V_0)_0) S_0 V_0,$$

$$E^S_M = \langle V^{\rm ret}_m + V_{m1} \rangle_{(6)} + 2\langle V_{m0}(S_1 V_0 + S_0 V_{11}) \rangle_{(6)} + 2\langle V_{m0} S_0 V_0 (S_0 V_{11} + S_1 V_0) \rangle_{(6)}.$$

We set $V_{11}(\mathbf{p}, \mathbf{k}) = \alpha\pi/m^2 R_p$ and $S_1(p) = -R_p/4 + \gamma^2/(2f_p) - \gamma^4/(4f_p^2)$;

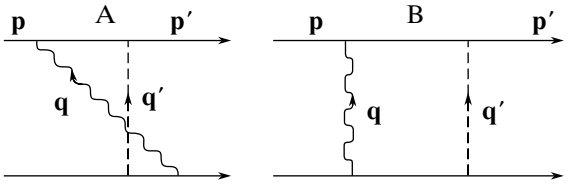

Fig. 3. One-loop covariant diagrams contributing to V_{20}.

we then have

$$E^S_M = m\alpha^6 \left(-\frac{1}{3}\ln\alpha + \frac{53}{192}\right) + \langle V^{\rm ret}_m \rangle_{(6)}.$$

The contribution of reducible diagrams involving only Coulomb photons—that is, $\langle U_C \rangle_{(6)}$—is calculated in a similar way. The result has the form (32), where one must set

$$W_C = V_0 S_0 V'_{1c} S_0 V_0, \quad E^S_C = \langle V'_{1c} \rangle_{(6)}. \quad (47)$$

Taking V'_{1c} in the form

$$V'_{1c}(\mathbf{p}, \mathbf{k}) = \frac{1}{24}\boldsymbol{\sigma}_1 \cdot \boldsymbol{\sigma}_2 \frac{\alpha\pi}{m^2} \left(-\frac{1}{2}\left(\frac{p^4}{q^2} - p^2 - \mathbf{p}\cdot\mathbf{k}\right) R_p + (\mathbf{p} \leftrightarrows \mathbf{k}) + \frac{p^2 k^2}{q^2} R_p \right),$$

we arrive at

$$E^S_C = -\frac{1}{48} m\alpha^6 \left(\ln\alpha + \frac{1}{4}\right).$$

We now calculate the contribution of reducible diagrams involving two magnetic photons (omitting the contribution of multiloop diagrams that was considered above). It is equal to $\langle U_{MM2} + U_{MM3} + U_{MCM} \rangle_{(6)}$. In order to calculate $\langle U_{MM2} \rangle_{(6)}$ and $\langle U_{MCM} \rangle_{(6)}$, we make use of expressions (29) and (25), where we set $X_{11} = V_{mb} S_0 R V_{mb}$ and $X_{21} = V_{mb} S_0 V_0 S_0 R V_{mb}$, with V_{mb} standing for that part of the Breit Hamiltonian which is induced by the exchange of a magnetic photon and R being the operator with kernel $R(\mathbf{pp'}) = (2\pi)^3 \delta^3(\mathbf{p} - \mathbf{p'}) R_p$. It can easily be seen that $\langle U_{MM3} \rangle_{(6)} = \langle U_{MM3} \rangle_p$. As a result, we obtain (34) and (35), where we must set

$$W_{MM} = V_{mb} S_0 R V_{mb} S_0 V_0 + (V_m S V_m - V_{mb} S_0 R V_{mb})_0 S_0 V_0,$$

$$W_{MCM} = V_{mb} S_0 V_0 S_0 R V_{mb},$$

$$E^S_{MM} = \langle V_{mb} S_0 R V_{mb} \rangle_{(6)} = \left(-\frac{3}{8}\ln\alpha - \frac{23}{96}\right) m\alpha^6,$$

$$E^S_{MCM} = \langle V_{mb} S_0 V_0 S_0 R V_{mb} \rangle_{(6)} = \left(-\frac{5}{48}\ln\alpha - \frac{5}{32} + \frac{\pi^2}{18}\right) m\alpha^6.$$

Table 1. Hard contributions to $\Delta\nu_{\rm rec}$ (in units of $m\alpha^6$) (also displayed are the results from [22])

Diagram	Contribution to $\Delta\nu_{\rm rec}$	Calculated value (in the notation of [22])	Contribution to $\Delta\nu_{\rm rec}$ (according to [22])
$4CCC$	-0.0039	$cccx$	-0.0039
$4CMC$	0.0042	$ctcx$	0.0043
$4MCC$	-0.0486	$cctx + tccx$	-0.0489
$4MCM$	-0.0230	$tctx$	-0.0230
$4MMC + 3MMC$	-0.0209	$(cttx + ttcx) + cttz$	-0.0209
$4MMM$	0.0042	$tttx$	0.0041
$3CCC$	0.0064	$cccz$	0.0063
$3MCC$	0.0268	$ctcz + cctz$	0.0283
$3CMM$	0.0530	$ttcz + tctz$	0.0534
$3MMM$	-0.0012	$tttz$	-0.0011
$2CCC$	-0.0184	$cccy + ccx$	-0.0186
$2MCC$	-0.0661	$tccy$	-0.0681
$2MCM$	0.0552	$tcty + ttcy$	0.0558
$2MMM$	-0.0011	$ttty$	-0.0011
$1MMM$	0.0694	$ttt0$	0.0694
$1CCC$	-0.0094	–	–
$1MCM$	-0.0745	–	–
$1CMM + 2CMM$	-0.5112	–	–
$3CCM$	-0.0104	–	–
$2CMC$	-0.0245	–	–
$1MCC$	0.1795	–	–
$1CMC$	-0.0092	–	–

This completes the evaluation of the soft contributions. Their sum is

$$\left(-\frac{1}{6}\ln\alpha + \frac{1393}{1728}\right) m\alpha^6 \approx \left(-\frac{1}{6}\ln\alpha + 0.8061\right) m\alpha^6.$$

In order to check the formalism employed and the procedure for calculating the soft contributions, we apply them to calculating the $(Z\alpha)^6 m^2/M$ contribution to the hyperfine splitting of the ground state of the hydrogen atom. In calculating this quantity (to the required order), we can actually reduce the two-particle problem to that of motion in an external field, so that the sought value can easily be calculated in the coordinate representation. The result, $4\alpha^6 m^2/M$, is identical to that obtained in the momentum representation by the method described in this article.

5. HARD CONTRIBUTIONS

There exist four two-loop covariant recoil-type diagrams that cannot be obtained from one another by particle permutations or time reversal (or by combining those two operations). They are displayed in Fig. 4. If magnetic and Coulomb photons are represented by different lines, we have 24 different diagrams. To indicate magnetic and Coulomb lines in referring to a specific diagram, we will henceforth use the indices "M" and "C," respectively, written in the order of the emergence of photons along the lower lines in diagrams 1–4 (Figs. 4) from left to right.

The hard contribution to $\Delta\nu_{\rm rec}$ was calculated by two methods. The first, based on the Coulomb gauge, consists in calculating the contribution of 24 diagrams separately. Within the second method, the total hard contribution was calculated as a whole by using Feynman gauge.

The result is $-0.424(6)m\alpha^6$ for the individual and $-0.426(6)m\alpha^6$ for the combined calculations. For the hard contribution, we take the average of these two values, $-0.425(6)m\alpha^6$. Adding this to the soft

Table 2. Contributions involving a soft part along with the results from [22, 24] (in units of $m\alpha^6$)

Calculated value	Calculated value (in the notation of [22])	Coefficient of $\ln\alpha$	Constant	Constant (according to [22, 24])
$E^H_{1CCC}+E^S_C$	$cc0+ccc0$	$-1/48$	-0.0146	-0.0148
$E^H_{1MCM}+E^S_{MCM}$	$tct0$	$-5/48$	0.3176	0.3138
$E^H_{1CMM+2CMM}+E^S_{MM}$	$ctt0+ttc0+ctty+$ $+tt0+ttx$	$-3/8$	-0.751	-0.749
E_M	E'_M	1/3	0.427	0.423

contribution, we obtain $0.381(6)m\alpha^6$ for the nonlogarithmic part of the recoil contribution, in perfect agreement with the results from [21, 23, 24].

Table 1 lists the results for the hard contributions of various diagrams. The errors of the calculations are not quoted there, since they never exceed 1% for an individual contribution.

The contribution of the 3-*MMC* and 4-*MMC* diagrams were calculated together, since these diagrams involve noncovariant diagrams in Figs. 2*a* and 2*b*, whose contributions to V_{30} cancel each other. For a similar reason, we combined the contributions of the 1-*CMM* and 2-*CMM* diagrams.

We can compare the results obtained by separately calculating the individual contributions with the results from [22], where $\Delta\nu_{\rm rec}$ was calculated within the Bethe–Salpeter formalism (in the Coulomb gauge). The point is that the correction to the energy can be represented as a power series in irreducible covariant diagrams (the tree diagram featuring the exchange of a Coulomb photon is not included here). It is clear that the numerical value of any term of this series is independent of the formalism employed. In addition, the contribution of the 1-*MCM* diagram in the order being considered must be exactly equal to the corresponding contribution from [22]. The majority of the terms of the expansion in irreducible diagrams involve only the hard part; their numerical values are presented in the first part of Table 1. The other terms of this expansion involve soft contributions as well; their values are given in Table 2. Tables 1 and 2 also quote the corresponding values from [22] (with allowance for further corrections reported by the authors). They agree well with our present results. For example, the value of E^H_{1CCC} in Table 2 means the hard part of the contribution of the 1-*CCC* diagram,

$$E_M \equiv E^H_{3CCM}+E^H_{2CMC}+E^H_{1MCC}+E^H_{1CMC}+E^S_{LM}+E^S_M+E^S_P,$$

$$E'_M \equiv (ct0+tc0)+ctc0+(ctx+tcx)+(cct0+tcc0)+(ctcy+ccty)+tccz+\Delta E^{\rm hfs}_{MP}(\Delta K_0 T+T\Delta K_0)+\Delta E^{\rm hfs}_d$$

(in the notation of [22]).

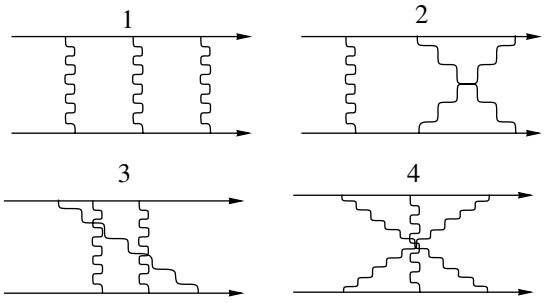

Fig. 4. Two-loop covariant diagrams of the recoil type (wavy lines photons in an arbitrary gauge).

6. CONCLUSION

We have calculated the recoil-effect-induced correction of order $m\alpha^6$ to the hyperfine structure of the positronium ground state [in general, its order is $(Z\alpha)^6 m$]. The calculation has been performed within the noncovariant formulation of perturbation theory in QED. The result,

$$\Delta\nu_{\rm rec} = m\alpha^6\left[-(1/6)\ln\alpha+0.381(6)\right],$$

is in accord with those obtained in [21, 23, 24]. Thus, we can state that $\Delta\nu_{\rm rec}$ has been reliably determined. However, this result is at odds with experimental data. Adding the recoil contribution to other contributions of the same order (which were also reliably determined), we find that the nonlogarithmic part of the total $m\alpha^6$ contribution to $\Delta\nu$ is

$$m\alpha^6(-0.3928) = -7.33\ \text{MHz} \qquad (48)$$

(in evaluating (48), we have taken, for $\Delta\nu_{\rm rec}$, the result from [23] as the most precise among three). Adding (48) to (3) (that is, to the $m\alpha^4, m\alpha^5$, and $m\alpha^6\ln\alpha$ contributions), we obtain the total theoretical result to order $m\alpha^6$ inclusive:

$$\Delta\nu_{th} = 203392.96\ \text{MHz}.$$

This value differs from the experimental result in (2) by five standard deviations.

The leading contribution of the next order in α (that is, the $m\alpha^7 \ln^2 \alpha$ contribution) was found in [28] to be

$$-(7/8\pi)m\alpha^7 \ln^2 \alpha \approx -0.92 \text{ MHz}.$$

With allowance for this correction, the difference between the theoretical and the experimental value of $\Delta\nu$ reduces to four standard deviations.

ACKNOWLEDGMENTS

I am grateful to I.B. Khriplovich, A.I. Milshtein, and A.S. Yelkhovsky for stimulating discussions and interest in this study. I am also indebted to G.S. Adkins for enlightening discussions.

Note added in proof. Presently, the $m\alpha^7 \ln \alpha$ contribution has been found [29–31]. Numerically, it is equal to 0.32 MHz.

REFERENCES

1. A. P. Mills, Jr., Phys. Rev. A **27**, 262 (1983).
2. A. P. Mills, Jr. and G. H. Bearman, Phys. Rev. Lett. **34**, 246 (1975)
3. M. W. Ritter, P. O. Egan, V. W. Hughes, and K. A. Woodle, Phys. Rev. A **30**, 1331 (1984).
4. J. Pirenne, Arch. Sci. Phys. Nat. **29**, 265 (1947).
5. V. B. Berestetskiĭ and L. D. Landau, Zh. Éksp. Teor. Fiz. **19**, 673 (1949).
6. R. Karplus and A. Klein, Phys. Rev. **87**, 848 (1952).
7. T. Fulton and P. Martin, Phys. Rev. **95**, 811 (1954)
8. G. P. Lepage, Phys. Rev. A **16**, 863 (1977).
9. G. T. Bodwin and D. R. Yennie, Phys. Rev. Lett. **41**, 1088 (1978).
10. G. S. Adkins, R. N. Fell, and M. Mitrikov, Phys. Rev. Lett. **79**, 3383 (1997).
11. A. H. Hoang, P. Labelle, and S. M. Zebarjad, Phys. Rev. Lett. **79**, 3387 (1997).
12. G. S. Adkins, Y. M. Aksu, and M. H. T. Bui, Phys. Rev. A **47**, 2640 (1993).
13. G. S. Adkins, M. H. T. Bui, and D. Zhu, Phys. Rev. A **37**, 4071 (1988).
14. A. Devoto and W. W. Repko, Phys. Rev. A **42**, 5730 (1990).
15. S. J. Brodsky and G. W. Ericson, Phys. Rev. **148**, 26 (1966).
16. R. Barbieri, J. A. Mignaco, and E. Remiddi, Nuovo Cimento A **11**, 824 (1972).
17. J. R. Sapirstein, E. A. Terray, and D. R. Yennie, Phys. Rev. D **29**, 2290 (1984).
18. K. Pachucki and S. G. Karshenboim, Phys. Rev. Lett. **80**, 2101 (1998).
19. A. Czarnecki, K. Melnikov, and A. Yelkhovsky, Phys. Rev. A **59**, 4316 (1999).
20. W. E. Caswell and G. P. Lepage, Phys. Lett. B **167B**, 437 (1986).
21. K. Pachucki, Phys. Rev. A **56**, 297 (1997).
22. G. S. Adkins and J. R. Sapirstein, Phys. Rev. A **58**, 3552 (1998).
23. A. Czarnecki, K. Melnikov, and A. Yelkhovsky, Phys. Rev. Lett. **82**, 311 (1999).
24. G. S. Adkins and J. R. Sapirstein, Phys. Rev. A **61**, 069902(E) (2000).
25. I. B. Khriplovich, A. I. Milstein, and A. S. Yelkhovsky, Phys. Lett. B **282**, 237 (1992); Phys. Scr. T **46**, 252 (1993).
26. W. E. Caswell and G. P. Lepage, Phys. Rev. A **18**, 810 (1978).
27. G. T. Bodwin, D. R. Yennie, and M. Gregorio, Rev. Mod. Phys. **57**, 723 (1985).
28. S. G. Karshenboĭm, Zh. Éksp. Teor. Fiz. **103**, 1105 (1993) [JETP **76**, 541 (1993)].
29. R. Hill, Phys. Rev. Lett. **86**, 3280 (2001).
30. K. Melnikov and A. Yelkhovsky, Phys. Rev. Lett. **86**, 1498 (2001).
31. B. A. Kniehl and A. A. Penin, Phys. Rev. Lett. **85**, 5094 (2000).

Translated by O. Chernavskaya

Physics of Atomic Nuclei, Vol. 64, No. 9, 2001, pp. 1637–1642. Translated from Yadernaya Fizika, Vol. 64, No. 9, 2001, pp. 1718–1723.

ELEMENTARY PARTICLES AND FIELDS
Theory

Constraint on Anomalous 4ν Interaction

K. M. Belotsky[1)], A. L. Sudarikov[2)], and M. Yu. Khlopov[1),2)]

Keldysh Institute of Applied Mathematics, Russian Academy of Sciences, Miusskaya pl. 4, Moscow, 125047 Russia

Received April 11, 2000; in final form, July 5, 2000

Abstract—The features of a hypothetical 4ν interaction considered as the possible reason for massive-neutrino instability required in the cosmological scenario that involve neutrino dark matter are discussed. New constraints on the 4ν-interaction constant G_χ are obtained: $G_\chi < (15–42)\,G_F$ for $m_\chi > m_Z$ (G_F is the Fermi constant of weak interaction; m_χ is the mass of the 4ν-interaction gauge boson, also known as χ boson; and m_Z is the Z-boson mass) and $G_\chi < (2.8–5.6)\,G_F$ for $m_\chi \ll m_Z$. These constraints virtually rule out the 4ν interaction as a possible version of solution to the cosmological neutrino-instability problem.

1. INTRODUCTION

The cosmology of unstable hidden mass is one of the possible solutions to the problem of dark matter in the Universe. As was shown in [1], a massive neutrino (of mass in the range 30–100 eV) can be a realistic candidate for a dark-matter particle if such a neutrino is unstable (the relevant lifetime must be in the range 10^8–10^9 yr) with respect to decays into other weakly interacting particles. In the case of stable neutrinos, the large-scale structure of the Universe would evolve overly fast, with the result that there would emerge a structure that is incompatible with observations. The decay of massive neutrinos leads to a reduction of the matter density in nonhomogeneities and, hence, to a moderation in the rate of structure evolution. In order to justify neutrino instability, it is necessary to extend the Standard Model (SM) of electroweak interaction. By way of example, we indicate that, in the horizontal-unification model, which supplements SM symmetry by the broken symmetry of fermion generations (for an overview, see [2]), there can occur the decay process $\nu_H \to \nu_L\alpha$, where ν_H and ν_L are, respectively, the heavy and the light neutrino, while α is the archion, a Goldstone boson in this theory. Other models with neutrino decay are also possible. In the present article, we consider the simplest version of realization of neutrino instability, that which does not require particles of a new type explicitly. Specifically, we discuss a hypothetical 4ν interaction, which leads to the decay $\nu_H \to 3\nu_L$.

As early as the 1960s and 1970s, such an interaction was considered in [3–5]. It was established that if a neutrino–neutrino exists, it can produce noticeable effects only if the dimensional coupling constant G_χ for the effective 4ν interaction is anomalously large. The most stringent constraint on G_χ ($G_\chi < 10^4 G_\mathrm{F}$, where G_F is the Fermi constant) was obtained in [5] from an analysis of the process $\nu_\mu + N \to \mu^+ + \nu_\mu + \nu_\mu +$ *hadrons* (see [6] for a more detailed analysis). In [6, 7], this 4ν interaction was considered as a version of solution to the cosmological problem of neutrino instability. Also, a wide variety of its possible manifestations—in particular, astrophysical manifestations—were discussed. It was concluded in [7] that this version of solution to the cosmological problem of neutrino instability (that is, for $G_\chi \geqslant 5 \times 10^3 G_\mathrm{F}$) can hardly be realized. It will be shown in the present study that this conjecture is confirmed and even strengthened by up-to-date experimental data, primarily on the Z-boson decay width.

2. PHENOMENOLOGY OF 4ν INTERACTION

We take the Lagrangian of 4ν interaction in the form [6]

$$L_{4\nu} = \frac{G_\chi}{\sqrt{2}} J^\mu J^+_\mu, \qquad (1)$$

where J^μ is the current-density operator (here, Greek indices are those of Minkowski space[3)]). In the most general case, this operator can be represented as

$$J^\mu = \sum_{a,b} \bar\nu_a \gamma^\mu (V_{ab} + A_{ab}\gamma^5)\nu_b,$$

[1)] Cosmion Scientific and Educational Center for Cosmoparticle Physics, Miusskaya pl. 4, Moscow, 125047 Russia.

[2)] Moscow State Engineering Physics Institute (Technical University), Kashirskoe sh. 31, Moscow, 115409 Russia.

[3)] In what follows, the indices of Minkowski space will appear only as subscripts.

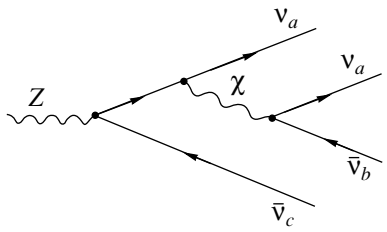

Fig. 1. One of the diagrams for the process of $Z \to \nu\bar{\nu}\nu\bar{\nu}$. The indices a, b, and c label different neutrino flavors.

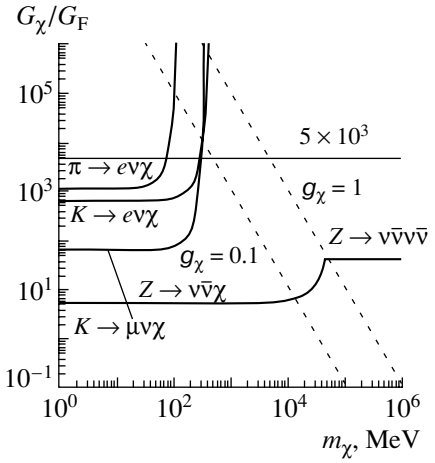

Fig. 2. Constraints on the 4ν-interaction coupling constant G_χ from an analysis of experimental data on various decays. The lower limit corresponding to cosmological models of unstable neutrinos ($G_\chi \geqslant 5 \times 10^3 G_F$) is indicated. The dashed lines are plotted for cases where the dimensionless coupling constant for 4ν interaction is $g_\chi = 1$ and 0.1.

where $\nu_{a,b}$ is the neutrino wave function; the overbar denotes Dirac conjugation; the indices a, b label neutrino flavors; and V_{ab} and A_{ab} are the parameters of, respectively, the vector and the axial-vector current.

By analogy with weak interaction, we assume that 4ν interaction has a mediator (χ boson) and that it can be characterized by a dimensionless coupling constant (g_χ). It is worth noting that the description of the interaction in terms of the Lagrangian in (1) is legitimate if, in the process being considered, the modulus of the χ-boson 4-momentum is much less than the χ-boson mass. Below, a constraint on G_χ is derived from experimental data on the Z-boson decay width that are analyzed on the basis of Lagrangian (1) for 4ν interaction (in the case at hand, the procedure used is valid for $m_\chi > m_Z$). We also obtain a constraint on G_χ for $m_\chi < m_Z$ using experimental data on the decays of the Z boson and of the π and K mesons. For the latter case, it is assumed that the dimensionless coupling constant g_χ, the χ-boson mass, and the dimensional constant G_χ are related by the equation

$$\frac{G_\chi}{\sqrt{2}} = \frac{g_\chi^2}{m_\chi^2}.$$

3. CONSTRAINT ON G_χ AT $m_\chi < m_Z$

If a 4ν interaction exists, it must contribute to all known neutrino processes. In the case of $m_\chi > m_Z$, which is considered in this section, the effective 4ν interaction is characterized by a dimensional constant G_χ; therefore, the contribution of this interaction to neutrino processes is proportional to $G_\chi^2\Delta^4$, where Δ is the energy release. For the case of Z-boson decay, the energy release is determined by a relatively large Z-boson mass, $\Delta \sim \dfrac{m_Z}{2}$. Therefore, the 4ν interaction would make a greater contribution to the neutrino decay of the Z boson than to other known processes. Moreover, the Z-boson decay width was measured to a high precision, so that these data can be highly sensitive to possible effects of 4ν interaction.

The decay $Z \to$ *invisible objects* receives contributions from diagrams of the type in Fig. 1. For the sake of definiteness, we assume that, in the final state, there are two neutrinos of the same flavor and two antineutrinos of two different flavors. The 4ν interaction is chosen in such a way that, in general, the lepton number is violated. For the purpose of illustration, the χ boson is shown in the figure; one can see there which transitions are possible between specific neutrino flavors. The total number of such diagrams is large (360; see below), because different types neutrino flavors can appear in the χ-boson vertices and because neutrinos and the χ boson can be permuted in various ways. Here, we present a calculation of only one diagram. The result is independent of its choice—the difference lies exclusively in the parameters V_{ab} and A_{ab}. The total contribution of all other diagrams will be roughly estimated according to their number.

For the sake of convenience, we introduce a notation for a set of diagrams involving fixed neutrino flavors in the final state. The matrix element for the set of such diagrams also contains crossed terms. Taking into account all possible permutations (for a permutation of identical neutrinos, special attention must be given to the sign of the contribution from the corresponding diagram to the total amplitude), one obtains eight diagrams with fixed final-neutrino flavors. For the set of the diagrams with neutrino

flavors identical to those in Fig. 1, we introduce the notation

$$\begin{pmatrix} a \\ a \\ \bar{b} \\ \bar{c} \end{pmatrix},$$

where the different indices a, b, and c correspond to different neutrino flavors. The square of the matrix element for this set of eight diagrams contains 64 terms. Among these, eight have the form $M_i M_i^+$, where M_i are matrix elements and where the "+" sign in the superscript denotes Hermitian conjugation. The remaining 56 terms are crossed terms that have the form $M_i M_j^+$, $i \neq j$. Using the above notation and taking into account all possible neutrino combinations in the final state, we can represent the total probability of the decay $Z \to 4\nu$ as

$$\Gamma(Z \to 4\nu) = \sum_{\substack{a,b,c \\ a \neq b \neq c}} \left\{ \begin{pmatrix} a \\ a \\ \bar{a} \\ \bar{a} \end{pmatrix} + \begin{pmatrix} a \\ b \\ \bar{a} \\ \bar{b} \end{pmatrix} + \begin{pmatrix} a \\ a \\ \bar{b} \\ \bar{b} \end{pmatrix} + \begin{pmatrix} a \\ a \\ \bar{a} \\ \bar{b} \end{pmatrix} + \begin{pmatrix} a \\ b \\ \bar{a} \\ \bar{a} \end{pmatrix} + \begin{pmatrix} a \\ b \\ \bar{a} \\ \bar{c} \end{pmatrix} + \begin{pmatrix} a \\ a \\ \bar{b} \\ \bar{c} \end{pmatrix} + \begin{pmatrix} b \\ c \\ \bar{a} \\ \bar{a} \end{pmatrix} \right\}. \quad (2)$$

The total number of terms is equal to the sum of the products of the number of terms associated with each column (this number is equal to 64) and the number of different neutrino flavors. For the first column, this number of types is 3, while, for the other seven columns, it is 6. Thus, the total number of terms is

$$N = 3 \times 64 + 7 \times 6 \times 64 = 2880. \quad (3)$$

The width with respect to decay process being considered can be represented as

$$\Gamma^{(4\nu)}_{Z\to 4\nu} = \Gamma_1 + \Gamma_2 + \cdots + \Gamma_{2880} = \Gamma_1(r_1 + r_2 + \cdots + r_{2880}),$$

where $r_i \equiv \Gamma_i/\Gamma_1$ (the numbering is arbitrary). The matrix element M_1 and the decay width Γ_1 for one diagram corresponding to the first column in (2) are given by

$$M_1 = \frac{\bar{g}}{4}\bar{\nu}_{a1}\hat{Z}(1+\gamma_5)\frac{1}{\hat{k}}\frac{G_\chi}{\sqrt{2}} \times \gamma_\mu(V_{aa} + A_{aa}\gamma_5)\nu_{\bar{a}2}\bar{\nu}_{a3}\gamma_\mu(V_{aa} + A_{aa}\gamma_5)\nu_{\bar{a}4},$$

$$\Gamma_1 = \frac{G_\mathrm{F} G_\chi^2 m_Z^7}{180(4\pi)^5\sqrt{2}}(V_{aa} + A_{aa})^2(V_{aa}^2 + A_{aa}^2) = \Gamma_{Z0}\left(\frac{G_\chi}{G_\mathrm{F}}\right)^2 \frac{(V_{aa} + A_{aa})^2}{4}\frac{V_{aa}^2 + A_{aa}^2}{2},$$

where $\bar{g}$ is the dimensionless coupling constant for weak interaction, Z is the Z-boson wave function, k is the 4-momentum of the propagator neutrino (a hat denotes contraction with the γ matrix; for example, $\hat{k} = k_\mu\gamma_\mu$), m_Z is the Z-boson mass, and $\Gamma_{Z0} \equiv \dfrac{G_\mathrm{F}^3 m_Z^7\sqrt{2}}{45(4\pi)^5} = 0.8345 \times 10^{-5}$ MeV. Introducing the additional notation

$$Z_Z \equiv \frac{(V_{aa} + A_{aa})^2}{4}\frac{V_{aa}^2 + A_{aa}^2}{2} \times (r_1 + r_2 + \cdots + r_{2880}),$$

we eventually obtain $\Gamma^{(4\nu)}_{Z\to 4\nu}$ in the form

$$\Gamma^{(4\nu)}_{Z\to 4\nu} = \Gamma_{Z0}\left(\frac{G_\chi}{G_\mathrm{F}}\right)^2 Z_Z.$$

The experimental value for the Z-boson decay width into invisible decay products is [8]

$$\Gamma^{(\mathrm{expt})}_{Z\to\mathrm{invisible}} = 499.9 \pm 2.5\,\mathrm{MeV}.$$

According to the SM, the $Z \to 2\nu$ decay width in the lowest order of perturbation theory is

$$\Gamma^{(\mathrm{SM})}_{Z\to 2\nu} = 3\frac{G_\mathrm{F} m_Z^3}{12\sqrt{2}\pi} = 497.7\,\mathrm{MeV}.$$

The decay width $\Gamma^{(4\nu)}_{Z\to 4\nu}$ should not exceed the value

$$\Delta\Gamma_{Z\to\mathrm{invisible}} = \Gamma^{(\mathrm{expt})}_{Z\to\mathrm{invisible}} - \Gamma^{(\mathrm{SM})}_{Z\to 2\nu} = 2.2 \pm 2.5\,\mathrm{MeV} \quad (4a)$$

or

$$\Delta\Gamma_{Z\to\mathrm{invisible}} < 5.4\,\mathrm{MeV} \quad (4b)$$

(at a 90% C.L.).

It follows that G_χ can be constrained as

$$G_\chi < \frac{0.80 \times 10^3}{\sqrt{Z_Z}} G_\mathrm{F}.$$

We set all the parameters V_{ab} and A_{ab} (a and b are arbitrary) to unity. We define the factor Z_Z under two assumptions: (i) $r_i = +1$ for all i, or (ii) all crossed terms in $\Gamma^{(4\nu)}_{Z\to 4\nu}$ are canceled. In the first case, the factor Z_Z is equal to the total number of terms (2880). In the second case, it is equal to the number of the diagrams [see Eq. (3)]; that is,

$$Z_Z = 3 \times 8 + 7 \times 6 \times 8 = 360.$$

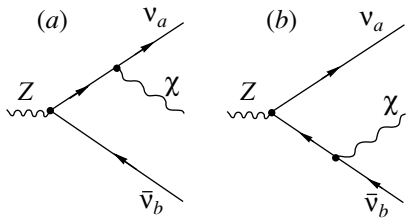

Fig. 3. Diagrams for the process $Z \to \nu\bar{\nu}\chi$ for the case of fixed neutrino flavors, a and b, in the final state.

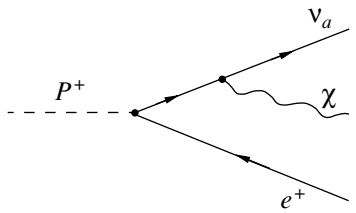

Fig. 4. Diagram for the process $P \to e\nu\chi$, where P stands for a π or a K meson, the index a corresponding to e, μ, and τ.

Using the above two values for Z_Z, we then obtain the following constraint on G_χ:

$$G_\chi < (15\text{–}42)G_\mathrm{F}.$$

These values provide rather rough upper limits. They are not rigorous for deriving a stringent upper limit on G_χ. At the same time, it is unlikely that a precise upper limit on G_χ would differ markedly from the values in the last inequality, because the dependence on the factor Z_Z is weak (it is of the square-root type). For the maximum possible values of G_χ, the region allowed by this inequality is shown in Fig. 2.

4. CONSTRAINT ON G_χ FOR $m_\chi < m_Z$

In the case of $m_\chi < m_Z$, there can occur the decay process $Z \to \nu\bar{\nu}\chi$, which also contributes to the width with respect to the decay $Z \to$ *invisible objects*. In addition, the π- and K-meson decays $\pi \to l\nu\chi$ and $K \to l\nu\chi$ become possible for $m_\chi < m_\pi$ and $m_\chi < m_K$, respectively.

In the lowest order of perturbation theory, the decay $Z \to \nu\bar{\nu}\chi$ resulting in the formation of fixed-flavor neutrinos in the final state is described by two diagrams in Figs. 3*a* and 3*b*. The neutrino-flavor type indices a and b are arbitrary in these figures. In just the same way as for $\Gamma^{(4\nu)}_{Z\to 4\nu}$, we take only one diagram to estimate the width $\Gamma_{Z\to\nu\bar{\nu}\chi}$. The matrix element and decay width corresponding to the diagram in Fig. 3*a* are given by

$$M_1 = g_\chi \bar{\nu}_a \hat{\chi}(V_{ab} + A_{ab}\gamma_5)\frac{1}{\hat{k}}\frac{\bar{g}}{4}\hat{Z}(1+\gamma_5)\nu_b,$$

$$\Gamma_1 = \Gamma_{Z\chi 0}\frac{G_\chi}{G_\mathrm{F}}F_Z\,(m_\chi/m_Z)\,\frac{(V_{ab}+A_{ab})^2}{4},$$

where χ is the χ-boson wave function,

$$F_Z(x) = 1 - 8x^2(1-x^4) - x^8 + 24x^4\ln(1/x),$$

and

$$\Gamma_{Z\chi 0} = \frac{G_\mathrm{F}^2 m_Z^5}{8(4\pi)^3} = 0.05404\ \mathrm{MeV}.$$

For a finite coupling constant g_χ, the above formulas are not valid in the limit $m_\chi \to 0$ (this is so for decays considered below as well). The point is that, in this case, we would have $G_\chi \to \infty$, which is incompatible with the constraints obtained below. For $m_\chi \to 0$ at a finite value of g_χ, there is an infrared divergence: $\Gamma \to \infty$. At very large Γ, it is necessary to consider next orders of perturbation theory, but, in the limit of its indefinite growth, perturbation theory becomes inapplicable. Moreover, the limit $m_\chi \to 0$ corresponds to a non-Abelian rigorous gauge group, since the 4ν interaction considered here violates lepton charge. However, this situation requires a dedicated analysis for matching the theory with current experimental data.

The total probability of the process $Z \to \nu\bar{\nu}\chi$ can be represented as

$$\Gamma_{Z\to\nu\bar{\nu}\chi} = \Gamma_{Z\chi 0}\frac{G_\chi}{G_\mathrm{F}}F_Z\,(m_\chi/m_Z)\,Z_{Z\chi}.$$

In the case of fixed final-neutrino flavors, there are two diagrams. In this case, the total number of terms is therefore equal to 4; among these, there are two terms of the form $M_i M_i^+$. The inclusion of all neutrino flavors (a and b) yields the factor of $3\times 3 = 9$. Setting all the parameters V_{ab} and A_{ab} (for arbitrary a and b) to unity, we obtain $Z_{Z\chi} = 9\times 2 = 18$ in the approximation $\sum_{i\neq j} M_i M_j^+ = 0$ and $Z_{Z\chi} = 9\times 4 = 36$ under the assumption that all terms are equal to each other ($M_i M_i^+ = M_i M_j^+$). From the condition $\Gamma_{Z\to\nu\bar{\nu}\chi} < \Delta\Gamma_{Z\to\mathrm{invisible}}$, where $\Delta\Gamma_{Z\to\mathrm{invisible}}$ is defined in (4a) and (4b), we obtain

$$G_\chi F_Z\,(m_\chi/m_Z) < \frac{100}{Z_{Z\chi}}G_\mathrm{F} = (2.8\text{–}5.6)G_\mathrm{F}.$$

In the G_χ–m_χ plane, the area allowed by this inequality is shown in Fig. 2 (here, we have taken the value of $5.6G_\mathrm{F}$); $F_Z(m_\chi/m_Z) \approx 1$ for $m_\chi \ll m_Z$.

Let us now consider π- and K-meson decays into e, ν, and χ. The diagrams for these decays are presented in Fig. 4. The symbol P stands for a π or a K meson. A constraint on G_χ can be obtained from the condition

$$\frac{\Gamma_{P\to e\nu\chi}}{\Gamma^{(\mathrm{theor})}_{P\to e\nu}} < \frac{\Gamma^{(\mathrm{expt})}_{P\to e\nu(\nu\bar{\nu})}}{\Gamma^{(\mathrm{expt})}_{P\to e\nu}}. \qquad (5)$$

The matrix element for the process has the form

$$M = \frac{G_\mathrm{F}\cos\theta_\mathrm{C}}{\sqrt{2}} f_P p_\mu \varphi_P$$
$$\times g_\chi \bar{\nu}\hat{\chi}(V_{ea} + A_{ea}\gamma_5)\frac{1}{\hat{k}}\gamma_\mu(1+\gamma_5)e,$$

where θ_C is the Cabibbo angle; f_P is the decay constant; p_μ is the P-meson 4-momentum; and φ_P and e are, respectively, the P-meson and the electron wave function. Neglecting the electron mass, we find for the width with respect to the decay $P \to e\nu\chi$ that

$$\Gamma_{P\to e\nu\chi} = \frac{G_\mathrm{F}^3\cos^2\theta_C f_P^2 m_P^5}{12(4\pi)^3\sqrt{2}}$$
$$\times \frac{G_\chi}{G_\mathrm{F}} F_P\,(m_\chi/m_P)\,Z_P,$$

where m_P is the π- or the K-meson mass, and the function $F_P(x)$ is given by

$$F_P(x) = 1 + 72x^4 - 64x^6$$
$$- 9x^8 - 24x^4(3+4x^2)\ln(1/x)\,.$$

In the case where the parameters V_{ea} and A_{ea} are independent of the index a labeling the neutrino flavor, the factor Z_P takes the form

$$Z_P = 3\frac{(V_{ea}+A_{ea})^2}{4}, \qquad (6)$$

where the factor of 3 stems from summation over the neutrino flavors. The width $\Gamma^{(\mathrm{theor})}_{P\to e\nu}$ is given by

$$\Gamma^{(\mathrm{theor})}_{P\to e\nu} = \frac{G_\mathrm{F}^2\cos^2\theta_\mathrm{C} f_P^2 m_P^3}{8\pi}\Delta(1-\Delta)^2, \qquad (7)$$

where $\Delta = (m_e/m_P)^2$, m_e being the electron mass. Setting V_{ea} and A_{ea} to unity, we arrive at

$$G_\chi F_P\,(m_\chi/m_\pi)$$
$$< 2.635\times 10^4 \frac{\Gamma^{(\mathrm{expt})}_{\pi\to e\nu(\nu\bar{\nu})}}{\Gamma^{(\mathrm{expt})}_{\pi\to e\nu}} G_\mathrm{F} \quad \text{for the } \pi \text{ meson},$$

$$G_\chi F_P\,(m_\chi/m_K)$$
$$< 168.3 \frac{\Gamma^{(\mathrm{expt})}_{K\to e\nu(\nu\bar{\nu})}}{\Gamma^{(\mathrm{expt})}_{K\to e\nu}} G_\mathrm{F} \quad \text{for the } K \text{ meson}.$$

The experimental values of the branching fractions for the relevant [see (5)] decays [8] are quoted in the table. By using these experimental data, we obtain

$$G_\chi F_P\,(m_\chi/m_\pi) < 1.1\times 10^3 G_\mathrm{F} \quad \text{for the } \pi \text{ meson},$$

$$G_\chi F_P\,(m_\chi/m_K)$$
$$< 0.65\times 10^3 G_\mathrm{F} \quad \text{for the } K \text{ meson}.$$

The areas of G_χ and m_χ values allowed by these inequalities are shown in Fig. 2. For $m_\chi \ll m_\pi$ or $m_\chi \ll m_K$, the function $F_P(m_\chi/m_K)$ can be set to unity.

For the decay process $K \to \mu\nu\chi$, all the above arguments remain in force (there are no experimental data for the analogous pion decay). The relevant decay width can be represented in the form

$$\Gamma_{K\to\mu\nu\chi} = \frac{G_\mathrm{F}^3\cos^2\theta_\mathrm{C} f_K^2 m_K^5}{12(4\pi)^3\sqrt{2}}$$
$$\times C\frac{G_\chi}{G_\mathrm{F}} F_K\,(m_\chi/m_K)\,Z_P,$$

where the function $F_K\,(m_\chi/m_K)$ is given by the integral expression

$$F_K(x) = \frac{12}{C}\int_{x^2}^{(1-\mu)^2} \frac{(s-x^2)^2(s+2x^2)((1+2\mu^2)s - s^2 + \mu^2(1-\mu^2))}{s^3}\sqrt{((1-\mu)^2-s)((1+\mu)^2-s)}\,ds,$$

$$C = 1 + 12\mu^4 - 16\mu^6 + 3\mu^8$$
$$- 24\mu^4\ln(1/\mu) = 0.946,$$

where $\mu = m_\mu/m_K$, m_μ being the muon mass; the factor Z_P is evaluated by formula (6); and the coefficient $12/C$ is determined by the requirement that the function $F_K\,(m_\chi/m_K)$ be equal to unity at zero χ-boson mass (that is, to the inverse value of the integral at $x = 0$). The quantity $\Gamma^{(theor)}_{K\to\mu\nu}$ is determined by Eq. (7) (with the substitution of m_μ for m_e). In this case, the constraint is

$$G_\chi F_K\,(m_\chi/m_K)$$
$$< 0.6927\times 10^7 \frac{\Gamma^{(\mathrm{expt})}_{K\to\mu\nu(\nu\bar{\nu})}}{\Gamma^{(\mathrm{expt})}_{K\to\mu\nu}} G_\mathrm{F}.$$

Substituting the corresponding experimental data from the table, we obtain

$$G_\chi F_K\,(m_\chi/m_K) < 65\,G_\mathrm{F}.$$

The area determined by this inequality is presented in Fig. 2. For $m_\chi \ll m_K - m_\mu = 388$ MeV, we have $F_K(m_\chi/m_K) \approx 1$.

Experimental values of the relevant branching fractions

Decay channel	π	K
$P \to e\nu(\nu\nu)$	$< 5 \times 10^{-6}$	$< 6 \times 10^{-5}$
$P \to e\nu$	$1.230(4) \times 10^{-4}$	$1.55(7) \times 10^{-5}$
$P \to \mu\nu(\nu\nu)$	–	$< 6.0 \times 10^{-6}$
$P \to \mu\nu$	0.9998770(4)	0.6351(18)

From Fig. 2, it can be seen that the most stringent constraint is obtained from data on Z-boson decay. The dashed curves in Fig. 2 correspond to the dimensionless-coupling-constant values of $g_\chi = 1$ and 0.1. For $g_\chi > 1$, perturbation theory is inapplicable; therefore, the constraints obtained in this region—in particular, from Z-boson decay for $m_\chi > m_Z$—should be considered only as estimates. Also displayed in Fig. 2 is the lower limit on G_χ corresponding to relevant cosmological models of unstable neutrinos. We emphasize once again that, in contrast to constraints from π and K decays, the constraint from Z-boson decay is very rough. Nevertheless, we can state with confidence that the present results rule out the 4ν interaction as a version of solution to the cosmological problem of neutrino instability.

REFERENCES

1. A. G. Doroshkevich, A. A. Klypin, and M. Yu. Khlopov, Pis'ma Astron. Zh. **11**, 483 (1985) [Sov. Astron. Lett. **11**, 201 (1985)]; M.Yu. Khlopov, *Cosmoparticle Physics* (World Sci., Singapore, 1999).
2. A. S. Sakharov and M. Yu. Khlopov, Yad. Fiz. **57**, 690 (1994) [Phys. At. Nucl. **57**, 651 (1994)].
3. Z. Bialynicka-Birula, Nuovo Cimento **33**, 1484 (1964).
4. D. Yu. Bardin, S. M. Bilenky, and B. Pontecorvo, Phys. Lett. B **32B**, 121 (1970).
5. S. M. Bilen'kiĭ, N. A. Dadayan, and E. Kh. Khristova, Yad. Fiz. **28**, 518 (1978) [Sov. J. Nucl. Phys. **28**, 264 (1978)].
6. A. V. Berkov, Yu. P. Nikitin, A. L. Sudarikov, and M. Yu. Khlopov, Yad. Fiz. **46**, 1729 (1987) [Sov. J. Nucl. Phys. **46**, 1034 (1987)].
7. A. V. Berkov, Yu. P. Nikitin, A. L. Sudarikov, and M. Yu. Khlopov, Yad. Fiz. **48**, 779 (1988) [Sov. J. Nucl. Phys. **48**, 497 (1988)].
8. Particle Data Group (R. M. Barnett *et al.*), Phys. Rev. D **54**, 1 (1996).

Physics of Atomic Nuclei, Vol. 64, No. 9, 2001, pp. 1643–1656. Translated from Yadernaya Fizika, Vol. 64, No. 9, 2001, pp. 1724–1737.

ELEMENTARY PARTICLES AND FIELDS
Theory

Anomalous Three-Boson Coupling Constants in the Single Production of W Bosons at a Future e^+e^- Linear Collider

V. V. Braguta[1)], A. A. Likhoded[2)], and A. E. Chalov[1)]

Received May 30, 2000

Abstract—The question of whether constraints on the anomalous parameters of $WW\gamma$ and WWZ three-boson interactions can be deduced from an analysis of data on the reaction $e^+e^- \to W^-e^+\nu$ that are expected to come from a future $\sqrt{s} = 500$-GeV e^+e^- linear collider of integrated luminosity of $L = 50$, 100, or 500 fb^{-1} is discussed. An analysis of relevant differential distributions reveals that, in contrast to pair W-boson production, the reaction mentioned immediately above is highly sensitive to the parameter λ_Z and that the resulting constraints can be viewed as those that supplement the constraints that follow from data on $e^+e^- \to W^+W^-$. For the experiment being discussed, two possible implementations of a detector are considered that correspond to the kinematical regions $|\cos\theta_{e^+}| \le \cos 7^\circ$ and $|\cos\theta_{e^+}| \le \cos 1.5^\circ$. It is indicated that the region of small positron-scattering angles is of importance for improving the sensitivity of the process. In setting constraints on the anomalous parameters, the SEWS scenario for anomalous boson coupling constants, where interactions responsible for electroweak-symmetry breaking are strongly coupled, is examined along with the case of the most general parametrization of the $WW\gamma(Z)$ three-boson vertices. © *2001 MAIK "Nauka/Interperiodica".*

INTRODUCTION

Measurement of the coupling constants for $WW\gamma$ and WWZ interactions is one of the most important problems for experiments at e^+e^- colliders. Within the Standard Model (SM), the $WW\gamma$ and WWZ vertices are strictly defined by the $SU(2)_L \times U(1)$ gauge invariance; therefore, precision measurements of the processes being discussed provide a unique test of the gauge structure of electroweak theory. In contrast to low-energy, high-precision experiments at the pole of the Z^0 resonance, collider experiments make it possible to measure directly—and, what is of importance, in a model-independent way—three-boson vertices. Presently, experiments at the LEP II collider, which are aimed at analyzing data on the pair production of W bosons, play a key role in such investigations (see, for example, [1]). For a number of reasons, however, which include a modest collider luminosity and a low sensitivity of the processes being analyzed to anomalous contributions at relevant energies, experiments at LEP would permit setting constraints on anomalous three-boson coupling constants at a level of 10%, which is by far insufficient for pinpointing the mechanism of anomalous boson interactions and for specifying the class of models that give rise to them. Searches for and investigations into anomalous boson interactions are among the main problems for next-generation linear colliders, like TESLA, where a high luminosity and a high energy guarantee the possibility of achieving a percent level of accuracy in determining anomalous boson parameters. Moreover, the properties of future colliders will make it possible to extend fully the analysis for $e^+e^- \to W^+W^-$ to reactions other than that, which include $e^+e^- \to We\nu$ and $e^+e^- \to e^+e^-W^+W^-$ and which are difficult for investigation at LEP either because of their small cross sections or because of their low sensitivity at LEP energies. Investigation of a few independent processes would permit separating contributions from different anomalous parameters that appear in the WWV vertices.

In the present study, we consider the constraints that an analysis of data on the process $e^+e^- \to e^+W^-\nu(e^-W^+\nu)$ from experiments at a 500-GeV e^+e^- collider of integrated luminosity $L = 50$, 100, or 500 fb^{-1} could yield for anomalous three-boson parameters.

1. WWV-INTERACTION VERTEX

For the three-boson interaction of two charged vector bosons with a neutral vector boson, the general

[1)]Moscow Institute for Physics and Technology, Institutskiĭ proezd 9, Dolgoprudnyĭ, Moscow oblast, 141700 Russia.

[2)]Institute for High Energy Physics, Protvino, Moscow oblast, 142284 Russia.

form of the vertex was extensively discussed in the literature [2]. The C-, P-, and Lorentz-invariant part of the Lagrangian for WWV interaction (where $V=\gamma, Z$) can be represented as

$$\mathcal{L}_{\text{eff}}/g_{WWV} = ig_1^V\left(W^\dagger_{\mu\nu}W^\mu V^\nu - W^\dagger_\mu V_\nu W^{\mu\nu}\right) + ik_V W^+_\mu W_\nu V^{\mu\nu} + \frac{i\lambda_V}{M_W^2}W^\dagger_{\lambda\mu}W^\mu_\nu V^{\nu\lambda}, \quad (1)$$

where $V=\gamma$, Z^0; W^μ is the W-boson field; $W_{\mu\nu}=\partial_\mu W_\nu - \partial_\nu W_\mu$; and $V_{\lambda\nu}=\partial_\lambda V_\nu - \partial_\nu V_\lambda$. The gauge coupling constants g_{WWV} for the photon and the Z^0 boson are given by

$$g_{WW\gamma}=e, \quad g_{WWZ}=e\cot\theta_{\text{W}}, \quad (2)$$

where e is the positron charge and θ_{W} is the Weinberg angle. For charged-vector-boson coupling to the photon, there exists, in the static limit, a simple interpretation of the parameters appearing in (1): g_1^γ determines the charge of the W boson, whereas the coefficients k_γ and λ_γ are related to the W-boson magnetic dipole (μ_W) and electric quadrupole (Q_W) moments as

$$\mu_W = \frac{e}{2M_W}(1+k_\gamma+\lambda_\gamma), \quad (3)$$

$$Q_W = -\frac{e}{M_W^2}(k_\gamma-\lambda_\gamma).$$

A similar interpretation is valid for the parameters k_Z and λ_Z of the WWZ^0 vertex. Within the SM, we have

$$g_1^V = k_V = 1, \quad \lambda_V = 0.$$

The requirement of gauge invariance leads to the equality $g_1^\gamma = 1$. Beyond the SM, the scenario being considered involves five independent parameters. These are g_1^Z, $k_{\gamma(Z)}$, and $\lambda_{\gamma(Z)}$ ($g_1^\gamma \equiv 1$).

The above parametrization corresponds to a model-independent approach to anomalous three boson interactions and includes all possible Lorentz structures that can contribute to the WWV vertices. In specific scenarios of going beyond the SM, the requirements of invariance under symmetry-group transformations may lead to relations between anomalous parameters and, hence, to a reduction of the total number of those that are independent. There exist various versions of extension of the SM that include various mechanisms of symmetry breaking. Within a wide class of models, it is assumed that interactions responsible for symmetry breaking are characterized by strong coupling, so that their effects must be experimentally manifested as deviations of observed coupling constants from the form dictated by the minimal SM—in particular, in the sector of vector-boson self-interaction.

Along with the case of the most general parametrization of anomalous three-boson vertices, we investigate here the class of effective models either not involving a Higgs boson or assigning it a very large mass (at least such that it is inaccessible to a direct observation at future colliders) and leading to the emergence of nonstandard coupling constants for multiboson interactions (so-called SEWS scenario).

Let us consider the minimal effective Lagrangian describing the interaction of gauge bosons in a theory where the original $SU(2)_L \times U(1)_Y$ gauge symmetry is spontaneously broken to $U(1)_Q$. In this case, that part of the Lagrangian which involves the mass and kinetic terms for gauge bosons has the form [3]

$$\mathcal{L}^{(2)} = \frac{v^2}{4}\text{tr}\left(D^\mu\Sigma^\dagger D_\mu\Sigma\right) - \frac{1}{2}\text{tr}\left(W^{\mu\nu}W_{\mu\nu}\right) - \frac{1}{2}\text{tr}\left(B^{\mu\nu}B_{\mu\nu}\right), \quad (4)$$

where $W_{\mu\nu}$ and $B_{\mu\nu}$ are the field-strength tensors corresponding to the $SU(2)$ and the $U(1)$ group; that is,

$$W_{\mu\nu} = \frac{1}{2}\left(\partial_\mu W_\nu - \partial_\nu W_\mu + \frac{i}{2}g[W_\mu, W_\nu]\right), \quad (5)$$

$$B_{\mu\nu} = \frac{1}{2}\left(\partial_\mu B_\nu - \partial_\nu B_\mu\right)\tau_3.$$

Here, $W_\mu \equiv W^i_\mu \tau_i$, and the Pauli matrices τ_i are normalized in such a way that $\text{tr}(\tau_i\tau_j)=2\delta_{ij}$.

The matrix $\Sigma \equiv \exp(i\boldsymbol{\omega}\cdot\boldsymbol{\tau}/v)$ involves a Goldstone boson ω_i that ensures the generation of the W- and Z-boson masses through the Higgs mechanism, and the $SU(2)_L \times U(1)_Y$-covariant derivative has the form

$$D_\mu\Sigma = \partial_\mu\Sigma + \frac{i}{2}gW^i_\mu\tau^i\Sigma - \frac{i}{2}g'B_\mu\Sigma\tau_3. \quad (6)$$

The first term in (4) is the $SU(2)_L \times U(1)_Y$-gauge-invariant mass term for W and Z. The physical masses are calculated at $v \approx 246$ GeV. This nonlinear realization of a spontaneous breakdown of symmetry leads to a low-energy phenomenology that coincides with the minimal SM where the Higgs boson is assigned a very large mass [3]. This theory is nonrenormalizable; it must be interpreted as an effective field theory below some scale of $\Lambda \leq 3$ TeV. In the lowest order, the interactions between the gauge bosons and fermions have the same form as in the minimal SM.

The "anomalous" couplings of gauge bosons correspond to other $SU(2)_L \times U(1)_Y$-gauge-invariant operators that can be written in addition to those in (4). For "low-energy" processes occurring at energies below the energy-breaking scale Λ, it is possible to represent the effective Lagrangian in a form that corresponds to an expansion of scattering amplitudes in powers of E^2/Λ^2. The next-to-leading-order (NLO) Lagrangian arising in this context was widely discussed in the literature [3–7].

Let us consider an effective Lagrangian involving NLO terms that preserve the original $SU(2)_C$ symmetry (apart from hypercharge coupling). The NLO effective Lagrangian conserving C and P invariance then has the form

$$\begin{aligned}\mathcal{L}^{(4)} = \frac{v^2}{\Lambda^2}\Bigg\{ & L_1\left[\mathrm{tr}\left(D^\mu\Sigma^\dagger D_\mu\Sigma\right)\right]^2 \\ & + L_2\mathrm{tr}\left(D_\mu\Sigma^\dagger D_\nu\Sigma\right)\mathrm{tr}\left(D^\mu\Sigma^\dagger D^\nu\Sigma\right) \\ & - igL_{9L}\mathrm{tr}\left(W^{\mu\nu}D_\mu\Sigma D_\nu\Sigma^\dagger\right) \\ & - ig'L_{9R}\,\mathrm{tr}\left(B^{\mu\nu}D_\mu\Sigma^\dagger D_\nu\Sigma\right) \\ & + gg'L_{10}\,\mathrm{tr}\left(\Sigma B^{\mu\nu}\Sigma^\dagger W_{\mu\nu}\right)\Bigg\}.\end{aligned} \tag{7}$$

The terms that involve L_i preserve the original $SU(2)_C$ symmetry; for all terms L_i to be $\mathcal{O}(1)$ quantities, the factor v^2/Λ^2 was introduced in the definition of $\mathcal{L}^{(4)}$. In the unitary gauge, where $\Sigma = 1$, Feynman rules can be obtained by expanding the Lagrangians in (4) and (7) [8]. Within the model considered here, it is possible to recover the correspondence between the parameters of the Lagrangians in (1) and (7). The results are given by

$$\begin{aligned} g_1^Z &= 1+\frac{e^2}{c_\mathrm{W}^2}\left(\frac{1}{2s_\mathrm{W}^2}L_{9L}+\frac{1}{(c_\mathrm{W}^2-s_\mathrm{W}^2)}L_{10}\right)\frac{v^2}{\Lambda^2}, \\ g_1^\gamma &= 1, \\ k_Z &= 1+e^2\left(\frac{1}{2s_\mathrm{W}^2c_\mathrm{W}^2}\left(L_{9L}c_\mathrm{W}^2-L_{9R}s_\mathrm{W}^2\right)\right. \\ &\quad \left.+\frac{2}{(c_\mathrm{W}^2-s_\mathrm{W}^2)}L_{10}\right)\frac{v^2}{\Lambda^2}, \\ k_\gamma &= 1+\frac{e^2}{s_\mathrm{W}^2}\left(\frac{L_{9L}+L_{9R}}{2}-L_{10}\right)\frac{v^2}{\Lambda^2}, \end{aligned} \tag{8}$$

where c_W and s_W are, respectively, the cosine and the sine of the Weinberg angle. It is worth noting that, in the scenario being considered, the terms that involve λ_V correspond to operators of higher dimensions and appear in higher orders of the expansion of the effective Lagrangian. Thus, the anomalous boson coupling constants are expressed in terms of three independent parameters (L_{9L}, L_{9R}, and L_{10}). It should be recalled that L_{10} is proportional to the parameter ϵ_3, which was measured at LEP I, so that there is a stringent constraint on it [9]. In view of this, there is no need for varying L_{10}. Hence, there only remains the set of two independent parameters.[3)]

[3)]For the ensuing numerical estimates, we fix the scale of new physics at $\Lambda = 2$ TeV.

In analyzing data on the process $e^+e^- \to eW\nu$, we will present below the results both for the case of a model-independent parametrization and for the SEWS scenario.

2. PROCESS $e^+e^- \to eW\nu$

In order to set constraints on the anomalous boson coupling constants, we analyze here the differential distributions of $e^+e^- \to e^+\mathrm{W}^-\nu$ events with respect to the scattering angle, transverse momentum, and energy of final-state particles (positron and reconstructed W boson). In the ensuing calculations, the values of $M_Z = 91.178$ GeV, $\sin\theta_W = 0.47688$, and $\alpha = 1/128$ are chosen for the input SM parameters. In calculating the differential distributions for the process being considered, use is made here of the helicity-amplitude method supplemented with a Monte Carlo integration over phase space (the accumulated statistics are sufficient for ensuring, in each bin of the distribution, a precision higher than 0.1% in calculating the relevant differential cross sections). The calculations were performed for a $\sqrt{s} =$ 500-GeV future linear collider of integrated luminosity $L\,dt = 50$, 100, or 500 fb^{-1}, which corresponds to the first stage of TESLA operation.

In our data analysis, we consider two cases of a cut on the positron scattering angle with respect to the incident-electron momentum:

$$\begin{aligned} &\text{(I)}\,|\cos\theta_e| \le \cos 7^\circ, \\ &\text{(II)}\,|\cos\theta_e| \le \cos 1.5^\circ. \end{aligned}$$

This choice of kinematical regions is dictated by a number of factors. In order to reconstruct the differential distributions of the cross section—in particular, with respect to the positron scattering angle, transverse momentum p_T, and energy—it is necessary that the facility used in the experiment being discussed involve a tracking system that would make it possible to record reliably final-state positrons. However, the existing designs of the detector for TESLA would provide the possibility of reconstructing the final-electron (final-positron) momentum and the quark-jet momenta only for scattering angles in excess of 7° (at the same time, the tracking system for muons would make it possible to cover the angular region down to 1.5°) [10]. If the importance of reconstructing the final-particle momenta in the region of small angles were nevertheless substantiated by sufficiently strong arguments, the design of the detector could be modified in such a way that it would become possible to reconstruct the q and e momenta down to angles of about 1.5°. In view of this, we will consider both these versions and assess the degree to which the sensitivity of data to anomalous contributions changes in

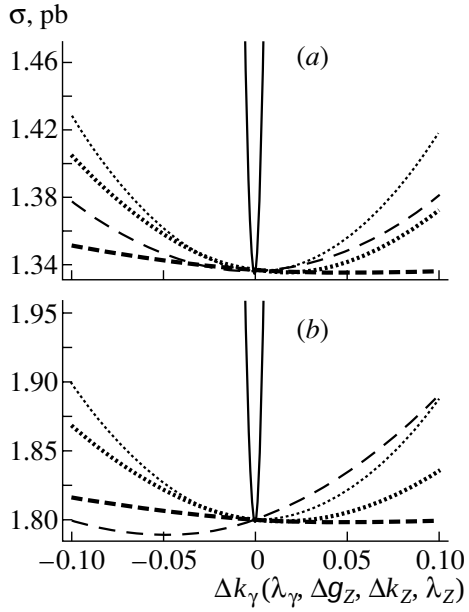

Fig. 1. Total cross section for the process $e^+e^- \to e^+W^-\nu$ versus variable anomalous parameters for cuts (*a*) I and (*b*) II . The solid, thin dashed, thick dashed, thin dotted, and thick dotted curves correspond to specific deviations of the parameters k_γ ($\Delta k_\gamma = 0.1$), λ_γ ($\lambda_\gamma = 0.1$), k_Z ($\Delta k_Z = 0.1$), λ_Z ($\Delta g_Z = 0.1$), and g_Z ($\lambda_Z = 0.03$), respectively, from the SM values.

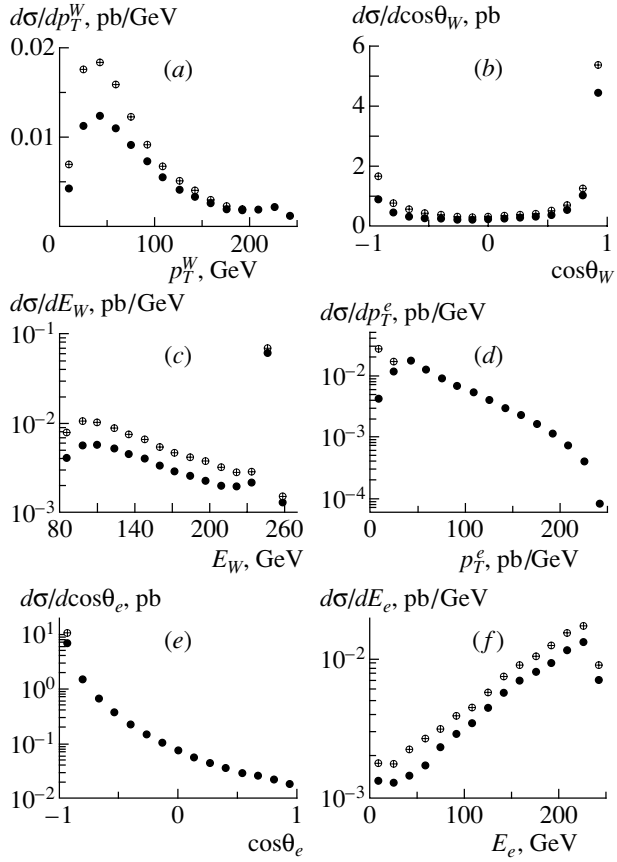

Fig. 2. Differential distributions of the cross section for the process $e^+e^- \to e^+W^-\nu$ with respect to (*a, d*) the W, e^+ transverse momenta; (*b, e*) the W, e^+ scattering angle; and (*c, f*) the W, e^+ energies. Closed circles (encircled crosses) correspond to cut I (II).

response to the inclusion of the positron-scattering-angle region from 1.5° to 7° in our analysis.

The calculation of the total cross section for the process $e^+e^- \to e^+W^-\nu$ within the SM at 500 GeV yields $\sigma_{\text{tot}} \simeq 1.34$ pb for cut I and $\sigma_{\text{tot}} \simeq 1.8$ pb for cut II. At the integrated luminosity of $L = 50$ fb^{-1}, this corresponds to statistics of 10^4–10^5 events. It should be noted that the reaction cross section is highly sensitive to deviations of the parameters g_1^Z, k_V, and λ_V from the values dictated by the SM. Figures 1*a* and 1*b* show the relevant cross sections versus variable anomalous parameters. From these figures, it can be seen that the process in question shows the highest sensitivity to the parameter λ_Z. Therefore, this process is especially interesting from the point of view of setting constraints on the anomalous parameters, since the competing process of pair W-boson production is weakly sensitive to deviations of this parameter from the SM value [1].

Figure 2 displays the differential distributions of the reaction cross section with respect to W-boson and positron transverse momentum, scattering angle, and energy. In Figs. 2*a*–2*f*, curves formed by closed circles (encircled crosses) correspond to cut I (II). From the transverse-momentum distribution of W bosons (Fig. 2*a*), it can be seen that the main contribution to the cross section comes from the region of small p_T and that the more lenient cut leads to a greater relative contribution of the low-p_T region to the cross section. The angular distribution of W bosons (Fig. 2*b*) shows a fast growth of the cross section in the region of small W-boson scattering angles. In the case being considered, a transition from cut I to cut II does not lead to a sizable change in the shape of the distribution; it is the common normalization of the differential cross section that changes predominantly here. A similar effect is observed in the distribution of the cross section with respect to the W-boson energy: when the more lenient cut is used, the region of low and intermediate values of E_W is saturated, but the main contribution to the cross section comes from the region of maximum energies (Fig. 2*c*). The differential distribution of the cross section with respect to positron transverse momentum exhibits regularities differing from those in the above cases (Fig. 2*d*). A transition to the more lenient cut deforms strongly the distribution at low values of the positron transverse momentum; at the same time,

the region of intermediate and high p_T^e values remains virtually intact. In the region of small scattering angles, the distribution with respect to the positron scattering angle has a pronounced peak (Fig. 2*e*), which is due to a dominant contribution of diagrams involving the exchange of a t-channel photon and the production of a W boson in the central region. A transition from cut I to cut II naturally enhances the contribution of the small-angle region. For the distribution with respect to the positron energy (Fig. 2*f*), the change in the cut leads to a change in the common normalization of the cross section, whose maximum receives the main contribution from the region of high positron energies.

In analyzing the dependence of the process on anomalous boson parameters, it is of interest to find out which of the distributions considered above possesses the highest sensitivity to the anomalous contributions and to pinpoint the kinematical region where the sensitivity is the highest. First, this will enable us to choose the optimum binning of the distributions for the subsequent χ^2 analysis of data; second, this will provide the possibility of preliminarily assessing the degree to which relaxing the kinematical cut on the positron scattering angle can improve the sensitivity of data to the anomalous parameters. For this purpose, we consider the relative deviations that the differential distributions being studied develop in response to variations in the anomalous parameters,

$$\left(\frac{d\sigma^{\mathrm{NEW}}}{dx} - \frac{d\sigma^{\mathrm{SM}}}{dx}\right) \Big/ \frac{d\sigma^{\mathrm{SM}}}{dx},$$

where $d\sigma^{\mathrm{SM}}/dx$ is the differential cross section for the reaction in question at the SM values of the parameters g_1^Z, k_V, and λ_V and $d\sigma^{\mathrm{NEW}}/dx$ is the differential cross section for this reaction in the case where one of the parameters $x = p_T$, $\cos\theta$, or E for the positron (W boson) deviates from the SM values. For the deviations of the parameters g_1^Z, k_V, and λ_V, we choose, by way of illustration, the values

$$\Delta g_1^Z = \Delta k_Z = \Delta k_\gamma = \lambda_\gamma = 0.1, \quad \lambda_Z = 0.03.$$

The choice of different values for the deviations of the parameters from the SM values would lead to a change in the common normalization of the resulting dependences, but this would not have a sizable effect on their shapes.[4)]

For W bosons and positrons, Fig. 3 displays the relative deviations of the differential cross sections for the process $e^+e^- \to e^+W^-\nu$ versus the variable anomalous parameters k_γ, λ_γ, g_Z, k_Z, and λ_Z (curves *1, 2, 3, 4*, and *5*, respectively). From Fig. 3*a*, it can be seen that the differential distribution with respect to the W-boson transverse momentum possesses the highest sensitivity to the anomalous parameters in the region of the highest values of p_T. Comparing Figs. 2*a* and 3*a*, we can conclude that a transition from the kinematical region I to the kinematical region II does not toughen substantially the constraints on the anomalous coupling constants from this distribution; the reason behind this is the following: when the kinematical cut is relaxed, it is the low-p_T region that is saturated, but the sensitivity to the anomalous contributions is low there. In the case of the distribution with respect to the W-boson scattering angle, one can expect that the resulting constraints will become more stringent upon relaxing the cut, since a transition from cut I to cut II changes the common normalization of the differential cross section (Fig. 2*b*)—in particular, at intermediate values of the angle, where the sensitivity to the anomalous contribution is maximal (Fig. 3*b*). Moreover, this distribution is especially sensitive to deviations of the parameter k_γ in the region of W-scattering into the backward hemisphere, where the differential cross section is nearly doubled upon relaxing the cut. Therefore, it is precisely for this parameter that one would expect the most pronounced toughening of the constraints in an expanded kinematical region. For the differential distribution with respect to the W-boson energy, the behavior of the relative deviations is more complicated (Fig. 3*c*); nonetheless, it can be shown that the highest sensitivity to the anomalous contributions is observed in the region of intermediate values of E_W for the parameter k_γ (curve *1*) and in the region of its maximum values for the other anomalous parameters. From an analysis of the behavior of the differential cross section (Fig. 2*c*), we can deduce that, in these regions, the differential cross section becomes noticeably larger upon relaxing the cut. This gives every reason to hope for the toughening of the resulting constraints for cut II in relation to those for cut I.

A somewhat different situation is observed for the distributions with respect to the positron transverse momentum, scattering angle, and energy. A transition to the more lenient kinematical cut modifies substantially the differential distributions with respect to p_T^e and $\cos\theta_e$ in the region of low p_T and small positron scattering angles (see Figs. 2*d* and 2*e*, respectively). However, these distributions show the highest sensitivity to the anomalous contributions at

[4)] For the parameter λ_Z, we chose a value different from other parameter values only because we wanted to obtain approximately identical scales of relative deviations of the differential cross sections—the point is that the sensitivity of the process to λ_Z is much higher than to other anomalous parameters.

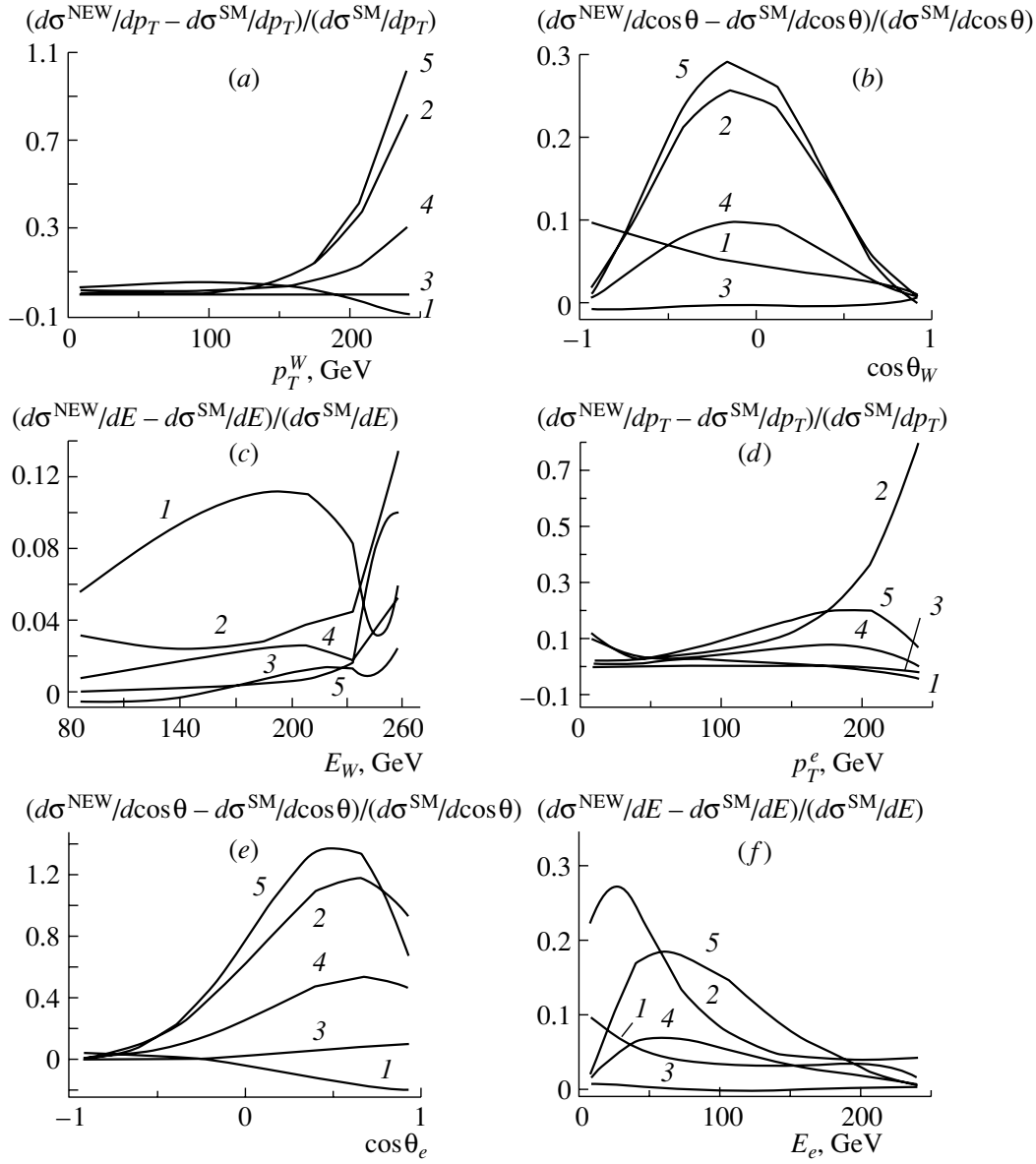

Fig. 3. Relative deviations of the differential distributions for the process $e^+e^- \to e^+W^-\nu$ with respect to (*a, d*) the W, e^+ transverse momenta; (*b, e*) the W, e^+ scattering angles; and (*c, f*) the W, e^+ energies. Curves *1*, *2*, *3*, *4*, and *5* correspond to specific deviations of the parameters k_γ ($\Delta k_\gamma = 0.1$), λ_γ ($\lambda_\gamma = 0.1$), k_Z ($\Delta k_Z = 0.1$), λ_Z ($\Delta g_Z = 0.1$), and g_Z ($\lambda_Z = 0.03$), respectively, from the SM values.

high p_T values (Fig. 3*d*) and at large positron scattering angles, which correspond to the scattering of the positron into the backward hemisphere (Fig. 3*e*). For the distribution with respect to the positron scattering angle, this effect is straightforwardly explained by the fact that the region of angles corresponding to positron scattering into the forward hemisphere is dominated by the diagram involving the t-channel exchange of a photon; this diagram does not contain anomalous vertices, representing, in this sense, a pure "background." Therefore, relaxing the kinematical cut can hardly have a pronounced effect on the resulting constraints, but an insignificant toughening may occur owing to a general increase in the cross section and, hence, in total statistics. On the other hand, the constraints on the anomalous parameters from the energy distribution of positrons are expected to become more stringent upon relaxing the kinematical cut, since this leads to a change in the general scale of the differential cross section over the entire region of electron energies (Fig. 2*f*), including the region of low and intermediate E_e values, where this distribution is especially sensitive to the anomalous parameters (Fig. 3*f*).

Thus, we have seen that, for the parameters k_γ, λ_γ, g_Z, k_Z, and λ_Z, the constraints that result from an analysis of some distributions can be toughened upon going over from the more stringent cut $|\cos\theta_e| \leq \cos 7^\circ$ on the positron scattering angle to the more lenient cut $|\cos\theta_e| \leq \cos 1.5^\circ$, but there are no grounds to expect drastic changes.

3. CONSTRAINTS ON ANOMALOUS PARAMETERS

3.1. Method for Setting Constraints

Prior to proceeding to consider the potential of a 500-GeV collider for setting constraints on the anomalous three-boson parameters, we are going to discuss the expected experimental situation. Detailed investigations for a future linear collider reveal [11] that the systematic error may amount to about 2%. This value receives contributions from the uncertainties in measurement of the luminosity ($\delta_L \simeq 1\%$), the error in the acceptance ($\delta_{\text{accep}} \simeq 1\%$), the uncertainties in the subtraction of background ($\delta_{\text{backgr}} \simeq 0.5\%$), and the systematic error in determining the relevant branching ratio ($\delta_{\text{Br}} \simeq 0.5\%$). Estimations assuming the efficiency ϵ_W of W-boson reconstruction to be in the range 0.5–1 and the integrated luminosity of the collider to be about 50 fb^{-1} show that the relative statistical error in the total cross section is about 0.5% and that it can be as large as a few percent in individual bins of the distribution. Thus, we can see that, for the process being discussed, the systematic error can be commensurate with the statistical errors; for this reason, we will take into account both kinds of error in our analysis.

For the ensuing estimates, we set the collider parameters to the values of $\sqrt{s} = 500$ GeV and $\int L\,dt =$ 50, 100, or 500 fb^{-1}; this corresponds to the first stage of TESLA operation.

3.2. Procedure for Data Analysis

Investigations similar to that reported here traditionally use SM predictions as experimental data and treat the possible effects of new physics as small deviations from these experimental values. Requiring that the predictions of a new model be in agreement with the experimental values within errors, one can then set constraints on the parameters of this model.

In setting constraints on the anomalous three-boson parameters, we will analyze the distributions presented above and use the simplest χ^2 functional defined as

$$\chi^2 = \sum_i \left(\frac{X_i - Y_i}{\Delta^i_{\text{exp}}}\right)^2,$$

where

$$X_i = \int_{z_i}^{z_{i+1}} \frac{d\sigma^{\text{SM}}}{dz}dz, \quad Y_i = \int_{z_i}^{z_{i+1}} \frac{d\sigma^{\text{NEW}}}{dz}dz$$

are the cross-section values in the ith bin of the z distribution (specifically, we will consider the distributions with respect to the W-boson and positron transverse momentum, energy, and scattering angle), respectively, within the SM and for the k_γ, λ_γ, g_Z, k_Z, and λ_Z values deviating from the SM values and Δ^i_{exp} are experimental errors in the bins. These errors, defined as

$$\Delta^i_{\text{exp}} = X_i\sqrt{\delta^2_{\text{stat}} + \delta^2_{\text{syst}}},$$

$$\delta_{\text{stat}} = \frac{1}{\sqrt{N_i}} = \frac{1}{\sqrt{\epsilon_W L X_i}},$$

$$\delta_{\text{syst}} = \sqrt{\delta L^2 + \delta^2_{\text{accep}} + \delta^2_{\text{backgr}} + \delta^2_{\text{Br}}},$$

include both systematic and statistical errors.[5)] Here, N_i is the number of events in a given bin of the distribution predicted by the SM, and L is the integrated luminosity of the collider.

3.3. Case of a Model-Independent Parametrization

In this subsection, the constraints on the anomalous parameters from an analysis of data on the differential cross sections for the process $e^+e^- \to e^+W^-\nu$ are considered for the case of a model-independent parametrization of three-boson vertices (the set of parameters includes k_γ, λ_γ, g_Z, k_Z, and λ_Z). Any differential cross section is a quadratic form in any anomalous parameter, whereas the functional χ^2 used in our data analysis is a power-law function of fourth degree. In the space spanned by five parameters k_γ, λ_γ, g_Z, k_Z, and λ_Z, a solution to the equation

$$\chi^2(k_\gamma, \lambda_\gamma, g_Z, k_Z, \lambda_Z) = \chi^2_{\min} + \Delta\chi^2 \qquad (9)$$

(where $\Delta\chi^2$ depends on the chosen confidence level) generally appears to be a complex surface; for this reason, we represent the resulting constraints in the form of the central cross sections of surface (9) by planes for each pair of the parameters (in doing this, we admit variations of a given pair of the parameters and fix the remaining parameters at the SM values).

Distributions for W. For the anomalous three-boson parameters, Fig. 4 shows constraints (at a 95% C.L.) that follow from an analysis of data on the differential distributions for the W boson with respect to its (solid curve) transverse momentum, (dotted curve) scattering angle, and (dashed curve) energy

[5)] In calculating the total error, we disregard the correlation between the statistical and the systematic error.

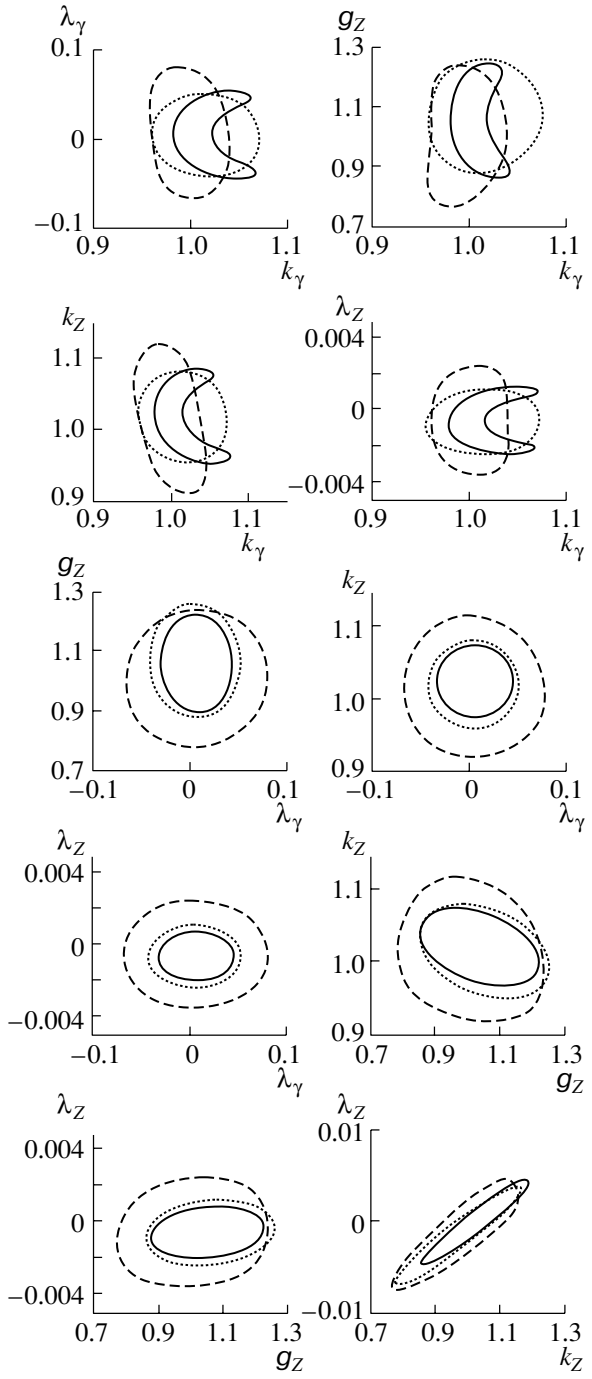

Fig. 4. Constraints on the anomalous three-boson parameters (at a 95% C.L.) from an analysis of data on the differential distributions for the W-boson (cut I) with respect to its (solid curve) transverse momentum, (dotted curve) scattering angle, and (dashed curves) energy. The regions of allowed parameter values are enclosed by the relavant contours.

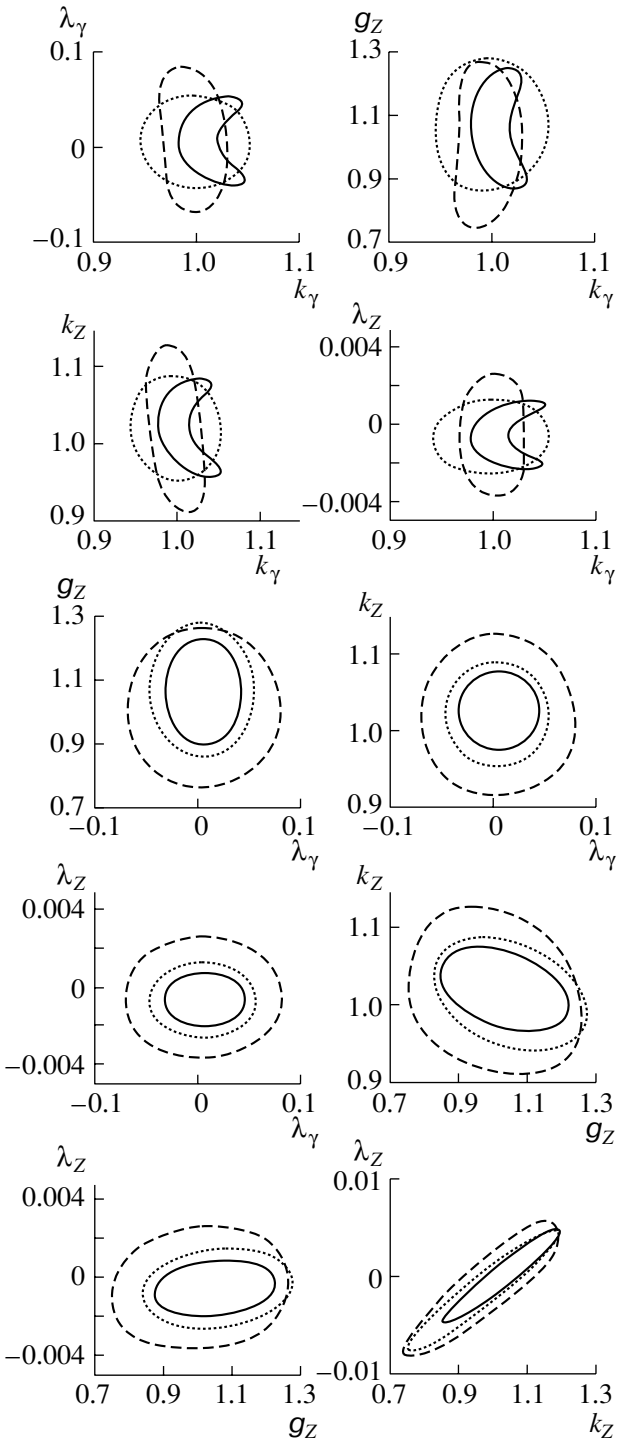

Fig. 5. As in Fig. 4, but for cut II.

for cut I. The regions of allowed parameter values are enclosed by the relevant contours. From Fig. 4, we can see that, for the planes of the g_Z–λ_γ, k_Z–λ_γ, λ_Z–λ_γ, k_Z–g_Z, and λ_Z–g_Z parameter pairs, the most stringent constraints are obtained from an analysis of data on transverse-momentum (p_T) distributions. For the remaining pairs of the parameters, more stringent constraints are achieved by combining data on p_T, $\cos\theta$, and E distributions. In the case where only one parameter is varied, with the remaining four being

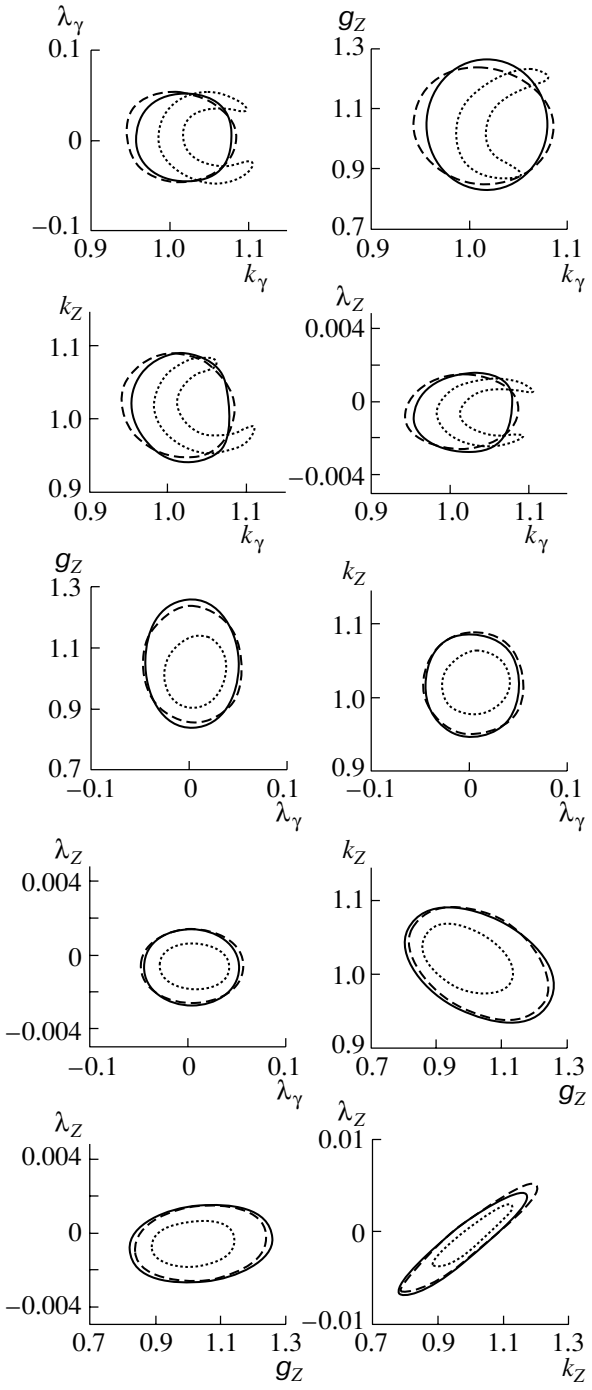

Fig. 6. Constraints on the anomalous three-boson parameters (at a 95% C.L.) from an analysis of data on the differential distributions for the positron (cut I) with respect to its (solid curve) transverse momentum, (dotted curve) scattering angle, and (dashed curve) energy. The region of allowed parameter values is enclosed by the relevant contours.

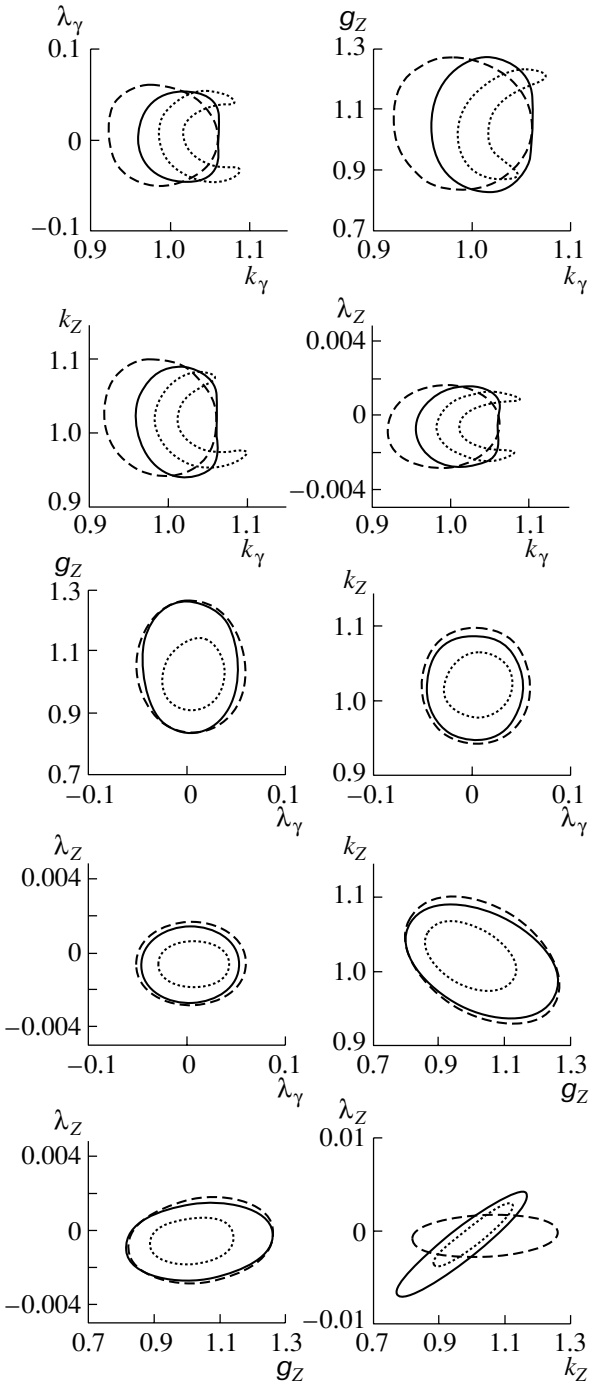

Fig. 7. As in Fig. 6, but for cut II.

fixed at the SM values, the individual constraints are the following:

$$0.98 \le k_\gamma \le 1.02,$$

$$\begin{gathered} -2.74 \times 10^{-2} \le \lambda_\gamma \le 4.1 \times 10^{-2}, \\ 0.9 \le g_Z \le 1.22, \\ 0.976 \le k_Z \le 1.074, \\ -2.0 \times 10^{-3} \le \lambda_Z \le 6.95 \times 10^{-4}. \end{gathered} \tag{10}$$

As might have been expected, the process being considered possesses an extremely high sensitivity to the parameter λ_Z—the constraints on λ_Z are an order of

magnitude more stringent than the constraints on the remaining parameters.

Figure 5 shows similar constraints on the anomalous parameters for cut II. In just the same way as in the case represented in Fig. 4, the distribution with respect to the W transverse momentum is that which possesses the highest sensitivity, although all the distributions used must be combined for obtaining some pair constraints. Here, the individual constraints are

$$\begin{gathered} 0.985 \le k_\gamma \le 1.02, \\ -2.75 \times 10^{-2} \le \lambda_\gamma \le 4.07 \times 10^{-2}, \\ 0.91 \le g_Z \le 1.22, \\ 0.976 \le k_Z \le 1.074, \\ -2.1 \times 10^{-3} \le \lambda_Z \le 7.0 \times 10^{-4}. \end{gathered} \tag{11}$$

We note that, although relaxing the cut did not render the individual constraints much more stringent, a comparison of Figs. 4 and 5 reveals that the areas of allowed regions in the planes of the parameter pairs decrease considerably. The reason behind this is that the expansion of the kinematical region (a transition from cut I to cut II) leads to the growth of the relative contribution to the cross section from terms associated with the crossed products of the anomalous parameters.

Distributions for e^+. For the anomalous parameters, Figs. 6 and 7 display pair constraints that follow from an analysis of the differential distributions with respect to the positron (solid curve) transverse momentum, (dotted curve) scattering angle, and (dashed curve) energy for cuts I and II, respectively. In contrast to the case of the distributions for the W boson, the most stringent constraints on the anomalous parameters here come from data on the angular distribution of positrons. For cut I, the individual constraints for each parameter are the following here:

$$\begin{gathered} 0.986 \le k_\gamma \le 1.018, \\ -2.5 \times 10^{-2} \le \lambda_\gamma \le 3.65 \times 10^{-2}, \\ 0.905 \le g_Z \le 1.13, \\ 0.978 \le k_Z \le 1.063, \\ -1.835 \times 10^{-3} \le \lambda_Z \le 6.055 \times 10^{-4}. \end{gathered} \tag{12}$$

In the present case, the individual constraints are determined, to a considerable extent, by the data on the angular distribution. For cut II, we have

$$\begin{gathered} 0.986 \le k_\gamma \le 1.017, \\ -2.51 \times 10^{-2} \le \lambda_\gamma \le 3.65 \times 10^{-2}, \\ 0.904 \le g_Z \le 1.13, \\ 0.978 \le k_Z \le 1.063, \\ -1.83 \times 10^{-3} \le \lambda_Z \le 6.05 \times 10^{-4}. \end{gathered} \tag{13}$$

In just the same way as in the case of data on the distributions for W bosons, relaxing the cut did not render the individual constraints more stringent, but the areas of the allowed parameter values in the planes of parameter pairs decrease as before. That this effect is due to the enhancement of the relative contribution to the cross section from terms associated with the crossed products of the anomalous parameters can be demonstrated by considering the example of changes undergone by the allowed region in the λ_Z–k_Z plane (compare Figs. 6 and 7): upon going over from the kinematical region I to the kinematical region II, the relative orientation of the allowed regions obtained from data on the angular and energy distributions of product positrons (regions enclosed by the dotted and the dashed curve) changes—in the case of cut I, the allowed regions appear to be coaxial ellipses, while, in the case of cut II, the ellipse of the allowed region from data on the positron energy rotates, which is obviously due to a change in the relative contribution to the cross section from the term associated with $\lambda_Z \times k_Z$. The resulting constraint is then represented by the intersection of the two ellipses.

By combining data on the distributions for W and e^+, one can obtain eventual constraints on the deviations of the parameters from the SM values (since the individual constraints for the two cuts differ insignificantly, in contrast to the allowed regions for the parameter pairs, we present these constraints for cut II):

$$\begin{gathered} -0.014 \le \Delta k_\gamma \le 0.017, \\ -2.5 \times 10^{-2} \le \lambda_\gamma \le 3.65 \times 10^{-2}, \\ -0.09 \le \Delta g_Z \le 0.13, \\ -0.022 \le \Delta k_Z \le 0.063, \\ -1.83 \times 10^{-3} \le \lambda_Z \le 6.05 \times 10^{-4}. \end{gathered} \tag{14}$$

We can compare these results with the constraints following from an analysis of data obtained at the Tevatron and LEP II.

For the anomalous three-boson parameters, the constraints (at a 95% C.L.) obtained from an analysis of Tevatron data under the assumption that the boson coupling constants are identical for $WW\gamma$ and WWZ vertices are as follows [12]:

$$\begin{gathered} -0.43 \le \Delta k_{\gamma,Z} \le 0.59, \\ -0.34 \le \lambda_{\gamma,Z} \le 0.36, \\ -0.60 \le \Delta g_Z \le 0.81. \end{gathered}$$

For the anomalous coupling constants, a fit to LEP II data that is aimed at searches for anomalous boson interactions (under the assumption that $\Delta k_Z = \Delta g_Z - \Delta k_\gamma \tan^2\theta_{\mathrm{W}}$ and $\lambda_Z = \lambda_\gamma$) yielded the values [1]

$$\begin{gathered} k_\gamma = 1.11^{+0.25}_{-0.25} \pm 0.17, \\ \lambda_\gamma = 0.10^{+0.22}_{-0.20} \pm 0.10, \end{gathered}$$

$$g_Z = 1.11^{+0.19}_{-0.18} \pm 0.10,$$

where the first and the second error are, respectively, statistical and systematic.

Comparing these constraints with the results that are presented in (14) and which are expected from experiments at a future linear collider, we can see that the existing constraints can be toughened by at least one order of magnitude.[6)] It should be emphasized that the constraints from data on the process $e^+e^- \to eW\nu$ studied at a future linear collider can compete with the constraints from data on the pair production of W bosons as well, since, in relation to $e^+e^- \to W^+W^-$, the process $e^+e^- \to eW\nu$, for example, possesses an anomalously high sensitivity to the parameter λ_Z.

The constraints in (14) on the anomalous parameters correspond to a future linear collider of integrated luminosity $L = 50$ fb^{-1}; however, versions of collider operation with an integrated luminosity of $L = 100$ or 500 fb^{-1} are considered to be quite realistic for the TESLA project. It would be of interest to trace the changes that the resulting constraints would undergo in response to the corresponding increase in the number of events of the reaction being considered. Since the most stringent constraints on the anomalous parameters come from an analysis of data on the distribution of the positron scattering angle, we will consider the constraints following from precisely this distribution at the above three values of the integrated luminosity. For the kinematical cut II, the allowed regions in the planes of parameter pairs are presented in Fig. 8 for $L =$ (dashed curve) 50 fb^{-1}, (dotted curve) 100 fb^{-1}, and (solid curve) 500 fb^{-1}. It can be seen that the increase in the luminosity leads to much more stringent (by about 50%) constraints both for individual anomalous parameters and for their pairs. This suggests that, for the process being considered, the statistical error is dominant in the bins of the distributions.

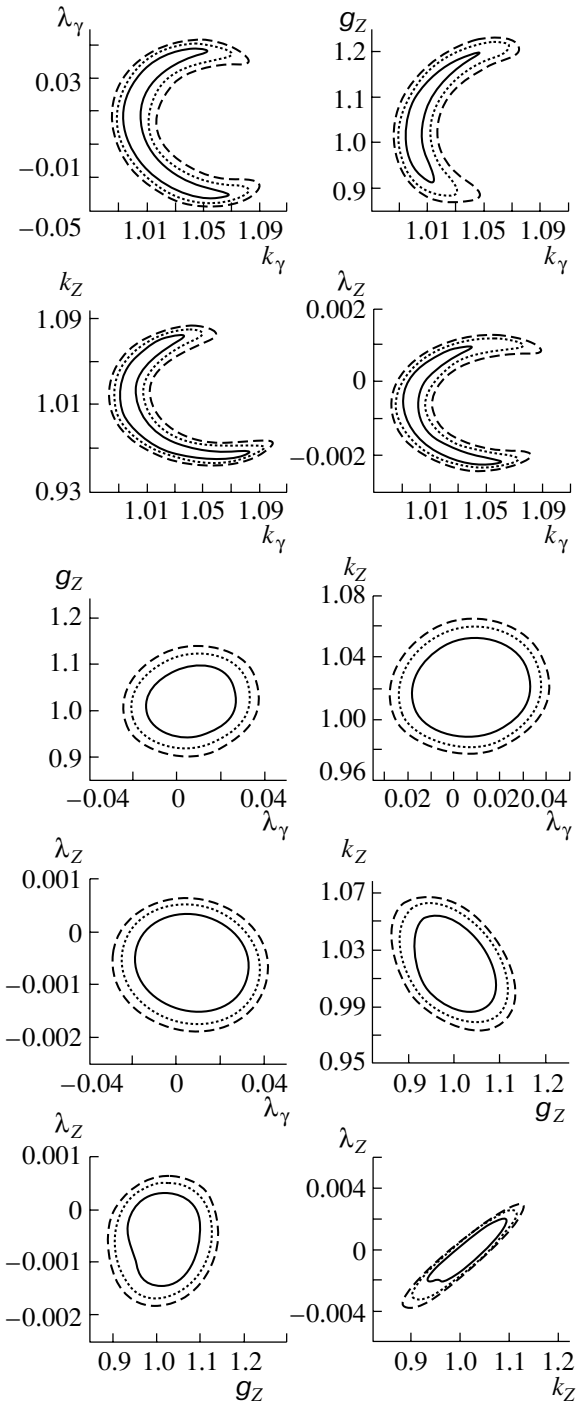

Fig. 8. Allowed regions in the planes of the parameter pairs at $L =$ (dashed curve) 50, (dotted curve) 100, and (solid curve) 500 fb^{-1} from an analysis of data on the positron angular distribution for the kinematical cut II.

3.4. SEWS Scenario

Within the SEWS scenario, the model-independent parametrization (1) and the parameters describing anomalous boson interactions in this scenario are related by Eqs. (8); owing to this, the number of independent parameters reduces to two (for the chosen new-physics scale of $\Lambda = 2$ TeV), L_{9L} and L_{9R}. The constraints on the parameters L_{9L} and L_{9R} (at a 95% C.L.) from an analysis of data on the transverse-momentum, angular, and energy distributions of W bosons are presented in Figs. 9*a* and 9*b* for cuts I and II, respectively. Analogous constraints from data on the positron distributions are displayed in Figs. 9*c* and 9*d*. It can be seen that

[6)] In Figs. 4–7, we do not present constraints from Tevatron and LEP II data, since these constraints considerably exceed the scale chosen for these figures.

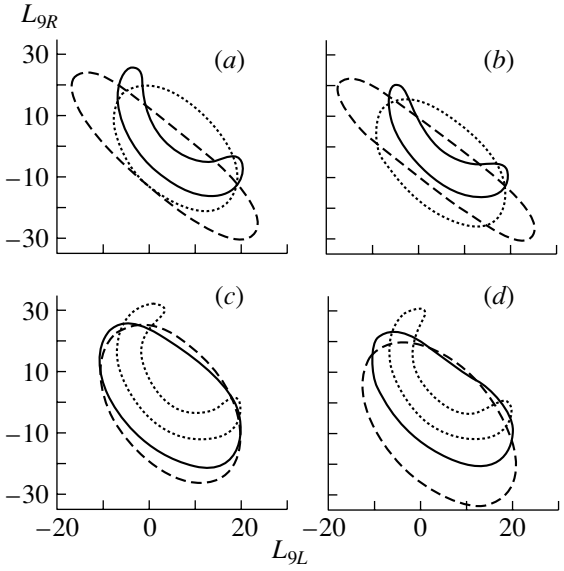

Fig. 9. Regions of allowed values of the SEWS parameters L_{9L} and L_{9R} (at a 95% C.L.) according to an analysis of data on (solid curve) the transverse-momentum, (dotted curve) the angular, and (dashed curve) the energy distributions of the (a, b) W boson and (c, d) positron in the case of cuts (a, c) I and (b, d) II. The allowed regions are enclosed by the relevant contours.

the most stringent constraints follow from data on the transverse-momentum distribution of the W boson and the angular distribution of the positron. These data determine individual constraints on the parameters L_{9L} and L_{9R}; at the same time, it is necessary to combine data on all distributions in order to constrain a region in the plane of the two parameters, since the resulting allowed region of their values appears to be the intersection of the allowed regions obtained from each of the distributions. From Fig. 9, it can be seen that a transition from cut I to cut II leads to a noticeable contraction of the allowed regions in the L_{9L}–L_{9R} plane.

An increase in the collider luminosity also toughens considerably the constraints on the parameters L_{9L} and L_{9R}. In Fig. 10, this effect is illustrated by the example of the evolution of the L_{9L}–L_{9R} allowed region obtained from data on the transverse-momentum distribution of the W boson for cut II.

By combining data on the distributions of the W boson and the positron, we can obtain individual constraints on the parameters L_{9L} and L_{9R}. For cut II, the table lists the resulting constraints (at a 95% C.L.) for the aforementioned three values of the collider luminosity. These results can be compared with the constraints from data obtained at other colliders. Precision measurements of the partial widths of the Z boson at LEP I [13] suggest that

$$-28 \le L_{9L} \le 27, \qquad (15)$$
$$-100 \le L_{9R} \le 190.$$

The constraints that are expected on the basis of the LEP II data are [14]

$$-41 \le L_{9L} \le 26, \qquad (16)$$
$$-100 \le L_{9R} \le 330.$$

Investigations for LHC (for $\sqrt{s} = 14$ TeV and an integrated luminosity of 100 fb^{-1}) reveal [15] that the LHC data would make it possible to constrain the parameter L_9 at a level of 10. It can be seen that the constraints on the parameters L_{9L} and L_{9R} from data on the process $e^+e^- \to eW\nu$ studied at a new linear

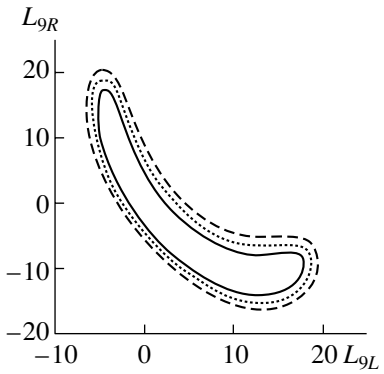

Fig. 10. Regions of allowed values of the SEWS parameters L_{9L} and L_{9R} (at a 95% C.L.) according to an analysis of data on the transverse-momentum distribution of the W boson for cut II at the collider integrated luminosity of $L =$ (solid contour) 500, (dotted contour) 100, and (dashed contour) 50 fb^{-1}.

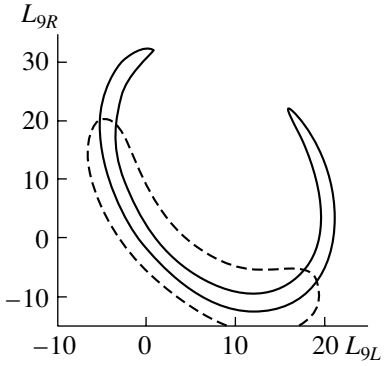

Fig. 11. Regions of allowed values of the parameters L_{9L} and L_{9R} for an electron–positron collider ($\sqrt{s} =$ 500 GeV, $L = 50$ fb^{-1}) from (region encircled by the solid contour) an analysis of data on the process $e^+e^- \to W^+W^-$ and (region encircled by the dashed contour) an analysis of data on the transverse-momentum distribution of the W boson originating from the reaction $e^+e^- \to eW\nu$ for cut II.

Table

L, fb^{-1}	L_{9L}	L_{9R}
50	−2.27–3.93	−4.60–6.95
100	−2.08–2.67	−3.48–4.63
500	−1.18–1.34	−1.97–2.28

collider will be much more stringent than constraints attainable at LEP and LHC.

The above constraints on the parameters L_{9L} and L_{9R} from data on the process $e^+e^- \to eW\nu$ supplement those that follow from data on pair W-boson production at a future linear collider. Figure 11 shows the regions of allowed values of the parameters L_{9L} and L_{9R} for an electron–positron collider ($\sqrt{s} = 500$ GeV, $L = 50$ fb^{-1}) (region encircled by the solid contour) according to an analysis of data on the process $e^+e^- \to W^+W^-$ [16] and (region encircled by the dashed contour) according to an analysis of data on the transverse-momentum distribution of the W boson in the process $e^+e^- \to eW\nu$ for cut II. As can be seen from the figure, the contours in question encircle different regions of L_{9L} and L_{9R} values, so that a global analysis of data on the two processes will make it possible to reduce considerably the resulting region of allowed parameter values.

4. CONCLUSION

We have analyzed the possibility of setting constraints on anomalous three-boson coupling constants on the basis of data on single W-boson production in the process $e^+e^- \to e^+W^-\nu$ that are expected to come from a future 500-GeV linear electron–positron collider. For the detector to be used in the relevant experiments, we have considered two possible implementations corresponding to the kinematical cuts $|\cos\theta_{e^+}| \le \cos 7^\circ$ and $|\cos\theta_{e^+}| \le \cos 1.5^\circ$ on the product-positron scattering angle. We have studied the case of a model-independent parametrization of anomalous boson interactions and the so-called SEWS scenario, which also leads to the emergence of anomalous $WWZ(\gamma)$ vertices and which is characterized by a strong coupling of interactions responsible for electroweak-symmetry breaking.

For the case of a model-independent parametrization, it has been shown that, in contrast to the process of pair W-boson production, the process $e^+e^- \to e^+W^-\nu$ is highly sensitive to the parameter λ_Z. By combining data on the distributions of the cross section for W and e^+ from the process $e^+e^- \to e^+W^-\nu$ as implemented at a future 500-GeV linear electron–positron collider of integrated luminosity 50 fb^{-1}, it will be possible to set the following constraints on the anomalous parameters (at a 95% C.L.):

$$-0.014 \le \Delta k_\gamma \le 0.017,$$
$$-2.5 \times 10^{-2} \le \lambda_\gamma \le 3.65 \times 10^{-2},$$
$$-0.09 \le \Delta g_Z \le 0.13,$$
$$-0.022 \le \Delta k_Z \le 0.063,$$
$$-1.83 \times 10^{-3} \le \lambda_Z \le 6.05 \times 10^{-4}.$$

These constraints are much more stringent than those that have already been obtained from LEP II and Tevatron data.

The corresponding constraints in the case of the SEWS scenario are

$$-2.27(\Lambda/2\ \text{TeV})^2 \le L_{9L} \le 3.93(\Lambda/2\ \text{TeV})^2,$$
$$-4.60(\Lambda/2\ \text{TeV})^2 \le L_{9R} \le 6.95(\Lambda/2\ \text{TeV})^2.$$

It has been shown that, both in the case of a model-independent parametrization and in the case of the SEWS scenario, relaxing the cut on the scattering angle leads to a sizable contraction of allowed regions in the planes of parameter pairs. The constraints that can be attained have also been analyzed for the collider-operation modes characterized by integrated luminosities of 100 and 500 fb^{-1}. It has been indicated that the constraints that follow from data on the process $e^+e^- \to eW\nu$ supplement those that were previously obtained on the basis of data on pair W-boson production.

ACKNOWLEDGMENTS

We are grateful to T. Ohl and A.K. Likhoded for stimulating discussions and enlightening comments.

This work was supported by the Russian Foundation for Basic Research (project nos. 00-15-96645 and 99-02-16558).

REFERENCES

1. L3 Collab. (M. Acciarri *et al.*), hep-ex/9910008.
2. K. Hagiwara *et al.,* Nucl. Phys. B **282**, 253 (1987).
3. T. Appelquist and C. Bernard, Phys. Rev. D **22**, 200 (1980); A. Longhitano, Nucl. Phys. B **188**, 118 (1981).
4. B. Holdom, Phys. Lett. B **258**, 156 (1991).
5. J. Bagger, S. Dawson, and G. Valencia, Nucl. Phys. B **399**, 364 (1993).
6. A. Falk, M. Luke, and E. Simmons, Nucl. Phys. B **365**, 523 (1991).
7. T. Appelquist and G. H. Wu, Phys. Rev. D **48**, 3235 (1993).
8. K. Cheung *et al.,* Phys. Rev. D **51**, 5 (1995).
9. G. Altarelli, Preprint CERN-TH-7045/93 (1993).
10. *Proceedings of the TESLA Meeting, DESY, Hamburg, 2000.*

11. M. Frank *et al.,* in *Proceedings of Workshop "e^+e^- Collisions at 500 GeV: the Physics Potential,"* Ed. by P. M. Zerwas (DESY, Hamburg, 1991), p. 223; G. Gounaris *et al.,* in *Proceedings of Workshop "e^+e^- Collisions at 500 GeV: the Physics Potential,"* Ed. by P. M. Zerwas (DESY, Hamburg, 1991), p. 735.
12. B. Abbott *et al.,* hep-ex/9912033.
13. D. Dawson and G. Valencia, Nucl. Phys. B **439**, 3 (1995); Phys. Lett. B **333**, 207 (1994).
14. F. Boudjema, in *Proceedings of Workshop "Physics and Experiments with Linear e^+e^- Colliders," 1993,* Ed. by F. A. Harris *et al.,* p. 713, and references therein.
15. H. Aihara *et al.,* hep-ph/9503425.
16. A. A. Likhoded and O. P. Yushchenko, Yad. Fiz. **60**, 72 (1997) [Phys. At. Nucl. **60**, 64 (1997)].

Translated by A. Isaakyan

Physics of Atomic Nuclei, Vol. 64, No. 9, 2001, pp. 1657–1666. Translated from Yadernaya Fizika, Vol. 64, No. 9, 2001, pp. 1738–1747.

ELEMENTARY PARTICLES AND FIELDS
Theory

Masses of the t and the b Quark and Their Mass Ratio m_b/m_t as a Consequence of a Dynamical Breakdown of $SU_L(2)$ Symmetry

I. T. Dyatlov

Petersburg Nuclear Physics Institute, Russian Academy of Sciences, Gatchina, 188350 Russia
Received July 24, 2000

Abstract—A model (of the type of the Nambu–Jona-Lasinio model) where the t and the b quark simultaneously acquire dynamical masses m_t and m_b is constructed to describe a dynamical breakdown of chiral and weak $SU_L(2)$ symmetry. That the ratio $x = m_b/m_t$ is small may imply that, at high energies, the energy scales of isoscalar vector exchange and isoscalar scalar exchange between the quarks are markedly different ($M_V \sim \sqrt{x}M_S$). The spectrum of composite scalar states of the model and the mechanism that causes the transformation of Goldstone bosons of the system under consideration into components of vector bosons of local $SU_L(2)$ symmetry are investigated. © *2001 MAIK "Nauka/Interperiodica".*

1. INTRODUCTION

Two unexpected features of third-generation quarks attract particular attention. These are a very large value of the t-quark mass, $m_t \simeq 170$–180 GeV, and a very large difference between the b- and the t-quark mass, $m_t/m_b \approx 40$.

In the Standard Model (SM), both factors are fixed by a direct choice of the corresponding Yukawa coupling constants that determine the interaction of t and b with the scalar field ϕ that is common to all quarks; that is,

$$\Delta L = -f_t[(\bar{t}_{Ri}\phi_C^{+a}q_{Li}^a) + \text{h.c.}] - f_b[(\bar{b}_{Ri}\phi^{+a}q_{Li}^a) + \text{h.c.}], \quad (1)$$

$$\phi = \begin{pmatrix}\phi_+\\ \phi_0\end{pmatrix}, \quad \phi_C = i\sigma_y\phi^*, \quad q_L = \begin{pmatrix}t\\ b\end{pmatrix}_L,$$
$$a = t, b, \quad i = 1, 2, \ldots, N_c,$$

where N_c is the number of colors and L and R are the quark helicities. The difference of m_t and m_b is directly represented in (1) with the aid of the phenomenological relation

$$f_t \simeq 40 f_b. \quad (2)$$

So large a difference does not seem appropriate for the interaction with the same fundamental field. Along with other numerical regularities found in the SM (for example, the hierarchies of the mass generations and of the elements of quark-mixing matrices), relation (2) furnishes yet another reason to conjecture that the SM and the numerical constants in it have profound dynamical foundations and that they are pieces of evidence in favor of the existence of a consistent high-energy scheme for which the Lagrangian in (1) is as an effective low-energy limit. In this case, f_t and f_b would be functions of high-energy properties. They could arise as different dynamical structures originating from markedly different sources. A considerable distinction between f_t and f_b (m_t and m_b) would then be quite natural. Searches for physical explanations of these puzzles began long ago.

The large value of the t-quark mass m_t led to the hypothesis that the Higgs field ϕ and particle emerging as the result of a spontaneous breakdown of chiral symmetry in the system of strongly interacting, originally massless t quarks have a composite character (t color [1]). The Nambu–Jona-Lasinio model [2] was proposed as appropriate example to analyze the possible occurrence of such a situation.

This model is based on four-fermion interaction. In order to choose its form that would be adequate to our further objectives, we use the method that, at low energies and for the simplest case of $f_b = 0$, leads to a system that reproduces the basic properties of the SM [3]. For this purpose, we integrate the system specified by Lagrangian (1) with respect to the "auxiliary" field ϕ at a large fixed mass scale M. At $f_b = 0$, we have

$$-f_t(\bar{t}_R\phi^+q_L) + \text{h.c.} - M^2\phi^+\phi \quad (3)$$
$$= -M^2\left|\phi + \frac{f_t}{M^2}(\bar{t}_Rq_L)\right|^2 + \frac{f_t^2}{M^2}(\bar{q}_Lt_R)(\bar{t}_Rq_L)$$
$$\to \frac{f_t^2}{M^2}(\bar{q}_Lt_R)(\bar{t}_Rq_L) \to G_t(\bar{q}_Lt_R)(\bar{t}_Rq_L).$$

The high-energy constant G_t is taken to be an arbitrary quantity that is different from f_t^2/M^2 (f_t is the low-energy Yukawa coupling constant).

At $N_c \gg 1$, the coupling G_t ensures chiral-symmetry breaking and the emergence of the mass $m_t \neq 0$ as a solution to the gap equation in the Nambu–Jona-Lasinio model [2]:

$$1 - \beta_t J(m_t) = 0, \quad (4)$$

$$J(m) = \frac{1}{M^2}\int \frac{d^4p}{\pi^2 i}\frac{1}{m^2 - p^2} f_M(p),$$

$$\beta_t = \frac{G_t N_c M^2}{8\pi^2}. \quad (5)$$

Here, M is the cutoff scale in the Nambu–Jona-Lasinio model. At energies $E \ll M$, there arises, in our model, a scalar state that is similar to the Higgs particle in the SM. An appealing feature of the critical problem in the Nambu–Jona-Lasinio is that almost all qualitative properties are independent of the choice of a cutoff function $f_M(p)$—that is, of the way in which the quadratically divergent integral in (4) is treated.

The nonrenormalized four-fermion coupling (3) can be considered as an effective low-energy ($E \sim m_t$) interaction for some consistent theory existing at energies $E \gg M$. On the other hand, this coupling (3) could arise as the high-energy limit ($E \gg m_t$) for such an SM where there is no fundamental Higgs boson, where the field ϕ is composite, and where the boundary conditions for the renormalization-group equations within the SM are dictated by the conditions of the composite nature of the field ϕ (the corresponding renormalization constants are $Z = 0$ for $p^2 > M^2$). The qualitative properties of such an SM and of the Nambu–Jona-Lasinio model are similar, and this similarity was comprehensively studied in [3].

As to the inclusion of the mass m_b and of the small ratio $x = m_b/m_t$ in the analysis, there are two approaches to explaining the the enormous distinction between m_b and m_t.

(i) The first employs independent spontaneous symmetry breaking associated with the f_b term [as in (3)]. Two massive scalars are present here at low energies [4]. Hence, the low-energy limit of the corresponding Nambu–Jona-Lasinio model appears to be a nonminimal SM involving two Higgs scalars ϕ_t and ϕ_b. The condition $x \ll 1$ is introduced phenomenologically by assuming that the relevant dynamical vacuum expectation values satisfy the strong inequality $\langle\phi_t\rangle \gg \langle\phi_b\rangle$.

(ii) In the second approach, radiative corrections in some new perturbative interaction generate a mass m_b that is expressed in terms of the dynamically arising mass m_t. A perturbative character of the new interaction explains the smallness of the ratio x. However, this approach obviously requires inventing new interactions and fields adequate to the pursued goal [5].

Apart from this, a small mass m_b is included in the scheme of the spontaneous generation of m_t in an ad hoc manner, in which case one neglects $SU_L(2)$ symmetry and resulting inconsistencies (see [3]).

The objective of this study is to construct and investigate a model where the dynamical generation of m_t and m_b occurs simultaneously. In this model, there arises, in the low-energy region ($E \sim m_t$), only one composite scalar state, as in the minimal SM. At SM energies, we want to have an effective Lagrangian of the type in (1) and to develop, for such systems, a physical interpretation of the resulting large distinction between the masses m_t and m_b .

The model in question partly reproduces mechanisms of the types in (1) and (2). Specific points of the model-parameter space correspond to these mechanisms. But apart from these points, a large distinction between m_t and m_b in the most natural and significant part of the parameter space can be interpreted as existence of two different energy scales, at high energies (much higher than the SM energies), for two different physical phenomena, scalar and vector exchanges between the quarks.

It is also shown how the vector W bosons develop a longitudinal component under the conditions of the complex phase transition being considered (see Appendix).

2. CHOICE OF MODEL

We reproduce the transformation in (3) with Lagrangian (1); that is, we integrate the system specified by Eq. (1) with respect to the imaginary and the real part of the auxiliary field ϕ. At the mass scale M, we obtain

$$-f_t[(\bar{t}_R\phi_C^{+a}q_L^a) + \text{h.c.}] - f_b[(\bar{b}_R\phi^{+a}q_L^a) + \text{h.c.}] \quad (6)$$
$$-M^2\phi^+\phi \to 2\{G_t(\bar{t}_Rq_L^a)(\bar{q}_L^at_R)$$
$$+G_b(\bar{b}_Rq_L^a)(\bar{q}_L^ab_R) + \frac{1}{2}\sqrt{G_tG_b}[(\bar{q}_R^aq_L^a)(\bar{q}_R^{a'}q_L^{a'})$$
$$-(\bar{q}_R^aq_L^{a'})(\bar{q}_R^{a'}q_L^a) + \text{h.c.}]\Big\},$$

where $G_a = f_a^2/M^2$ and $a, a' = t, b$. The last bracketed term on the right-hand side of Eq. (6) can be recast into the form

$$\sqrt{G_tG_b}[(\bar{t}_Rt_L)(\bar{b}_Rb_L) - (\bar{t}_Rb_L)(\bar{b}_Rt_L) + \text{h.c.}].$$

It should be borne in mind that, if we consider (6) as an effective interaction arising from a high-energy consideration, this formula does not involve all possible four-fermion terms—only those of them appear that affect the equations for masses and the spectra of scalar (pseudoscalar) particles.

Obviously, three terms in the braces on the right-hand side of (6) possess substantially different properties. The first two of these are invariant under

$SU_L(2)$ transformations. The symmetry of the third term is $SU_L(2) \times SU_R(2)$. If expression (6) is an effective low-energy interaction calculated within some theory that is consistent at high energies ($E > M$), the distinctions between these three terms in (6) must be due to dynamical reasons.

One possibility is obvious here. After the Fierz transformation, the first two terms on the right-hand side of (6) become vector–vector products of isosinglets and describe the coupled transitions $\bar{t}_R t_R \rightleftarrows \bar{q}_L q_L \rightleftarrows \bar{b}_R b_R$. These contributions appear to be a "result" of vector exchanges between the quarks, the helicity being conserved in their vertices ($L \rightleftarrows L, R \rightleftarrows R$). Exchanges generating the third term can have vector vertices in none of the channels. There, $R \rightleftarrows L$ transitions occur, which are characteristic of scalar (or tensor) exchanges. Therefore, we can deal with high-energy exchanges that are indeed dissimilar and which are characterized by physically different structures (see Section 1 above).

From the viewpoint of any physical hypothesis, however, it is difficult to explain, within this conceptual framework, the relation $G = \sqrt{G_t G_b}$ between three coupling constants of the Nambu–Jona-Lasinio model because of the independence of the contributions in Lagrangian (6). The only reasonable way out is to consider the model specified by Eq. (6) with fully independent constants G_t, G_b, and G. Again, these constants are not directly related ($\sim f_a^2/M^2$) to the low-energy constants f_t and f_b. But of course, G_t, G_b, and G are inversely proportional to the squares of their mass scales. Since the constants G_t and G_b describe the dynamically coupled channels, their scale factors must be identical. Therefore, it is natural for G_t and G_b to be close quantities, parameters on the same order of magnitude. At the same time, both the scalar scale and the constant G can have sharply different values.

In this study, we will therefore consider the model characterized by the interaction

$$L_{\text{int}} = G_t(\bar{t}_R q_L^a)(\bar{q}_L^a t_R) + G_b(\bar{b}_R q_L^a)(\bar{q}_L^a b_R) \quad (7)$$
$$+ \frac{1}{2}G[(\bar{q}_R^a q_L^a)(\bar{q}_R^{a'} q_L^{a'}) - (\bar{q}_R^a q_L^{a'})(\bar{q}_R^{a'} q_L^a) + \text{h.c.}].$$

Here, the parentheses imply summation over both the spinorial and N_c color indices. It should be recalled that, in the Nambu–Jona-Lasinio models, the number N_c of colors is large: $N_c \gg 1$.

To conclude this section, we note that the Lagrangian in (7) represents the most general form of an $SU_L(2)$-invariant four-fermion interaction that belongs to the type of a scalar–scalar product. Formula (7) is a direct generalization of the well-known $SU_L(2) \times SU_R(2)$-symmetric Lagrangian [6]

$$\delta L = G[(\bar{\psi}\psi)(\bar{\psi}\psi) + (\bar{\psi} i\gamma_5 \tau\psi)(\bar{\psi} i\gamma_5 \tau\psi)], \quad (8)$$

which is often used to simulate a spontaneous breakdown of chiral invariance and the generation of pseudoscalar states in QCD [7].

3. SET OF GAP EQUATIONS

If chiral symmetry is broken in quark interaction, the equations for the quark self-energy have nonvanishing solutions at a nonzero momentum ($p \neq 0$). Within Nambu–Jona-Lasinio models involving a large number of colors, these are precisely masses generated by symmetry breaking. They are order parameters in the problem, and it is customary to refer to these equations for masses as gap equations [2].

For Nambu–Jona-Lasinio models, a conventional procedure consists in taking into account, in the lowest order in N_c, the one-loop contributions to the equations for the self-energies [1–3]. For the interaction in (7), we therefore have

$$\beta_t J_t + \beta x J_b = 1, \qquad \beta_b J_b + \beta \frac{1}{x} J_t = 1, \quad (9)$$

where $J_t \equiv J(m_t)$ and $J_b \equiv J(m_b)$ [$J(m)$ is defined by the integral in (4)]. The parameters β_t, β_b, and β are expressed in terms of G_t, G_b, and G in just the same way as in (5), and $x = m_b/m_t$.

The quadratically divergent integrals $J(m)$, which depend on the type of cutoff, can be calculated by using the simplest cutoff form $f_M(p) = \vartheta(M^2 - |p|^2)$. The result is

$$J(m) = 1 - \frac{m^2}{M^2} \ln \frac{M^2}{m^2}. \quad (10)$$

If we are interested only in a qualitative pattern of the model, the representation in (10) is of no fundamental importance. But it can be used to get a clear idea of the specific form and properties of $J(m)$. The choice of cutoff function becomes of importance only when the Nambu–Jona-Lasinio model is used to obtain numerical estimates—for example, to calculate the masses of pseudoscalar bosons in QCD [7].

It can be seen from (10) that $J(m) \leq 1$ ($m > 0$), and this property remains unchanged for all reasonable forms of cutoff.

A spontaneous breakdown occurs if the set of Eqs. (9) has the solution $m_t > 0$ and $m_b > 0$. In the simplest model where $\beta_b = \beta = 0$, the equation

$$\beta_t J_t = 1 \quad (11)$$

has a nontrivial solution at $\beta_t \geq 1$ (owing to the property $J_t < 1$). The point $\beta_t = 1$ is the critical temperature of a phase transition; here, the masses (order parameters) vanish.

For the set of Eqs. (9), the domain of existence (or absence) of solutions depends on three parameters. This comes as no surprise—a similar situation arises

in phase transitions, when, in addition to temperature, other parameters of the system (external fields, pressure, and so on) are taken into account. The region where there is no chiral-symmetry breaking can easily be traced in Eqs. (9). It is the region where the parameters are relatively small. Upon leaving this region in various directions, we arrive at parameter values yielding $m_{t,b} > 0$; that is, a phase transition has already occurred.

By eliminating the explicit dependence on x from (9), we obtain

$$x = \frac{1-\beta_t J_t}{\beta J_b} = \frac{\beta J_t}{1-\beta_b J_b}. \qquad (12)$$

With the aid of (12), one can easily express J_b in terms of J_t, and vice versa,

$$J_b = \frac{1-\beta_t J_t}{(1-\beta_t J_t)\beta_b + \beta^2 J_t}, \qquad (13)$$
$$J_t = \frac{1-\beta_b J_b}{(1-\beta_b J_b)\beta_t + \beta^2 J_b},$$

and m_b in terms of m_t (or m_t in terms of m_b),

$$x = \frac{(1-\beta_t J_t)\beta_b + \beta^2 J_t}{\beta}, \qquad (14)$$
$$x = \frac{\beta}{(1-\beta_b J_b)\beta_t + \beta^2 J_b}.$$

Formulas (12)–(14) and the formula

$$(1-\beta_t J_t)(1-\beta_b J_b) - \beta^2 J_t J_b = 0, \qquad (15)$$

which is symmetric with respect to the interchange of b and t, are of use in the calculations performed in the sections that follow. From Eqs. (9), it can be seen that the substitutions $t \rightleftarrows b$, $x \rightleftarrows 1/x$ do not obviously change the above formulas. This symmetry is extensively used in Sections 4 and 5, and it is also helpful in checking the calculations. If the quark masses satisfy the condition $m_{t,b} \ll M$, relation (15) implies the need for the fine tuning of the parameters. Indeed, it follows from (10) and (15) that a nontrivial solution to the set of Eqs. (9) exists in the region

$$(1-\beta_t)(1-\beta_b) - \beta^2 \simeq O\left(\frac{m^2}{M^2}\right) \qquad (16)$$

[here, we have disregarded the term $\ln(M^2/m^2)$]. Such fine tuning is necessary for $m \ll M$ in any Nambu–Jona-Lasinio model [by way of example, we indicate that, for (11), $\beta_t \simeq 1 + O(m^2/M^2)$] and is one of the manifestations of the hierarchy problem [3].

Despite the approximate relation (16), we actually have three parameters for two equations in (9). Therefore, the existence of solutions with necessary properties is beyond any doubt. To demonstrate this, we invert the problem and, at given m_t and m_b (that is, at given x, J_t, and J_b), express β_t and β_b in terms of β:

$$\beta_t = \frac{1-\beta x J_b}{J_t}, \qquad \beta_b = \frac{1-\beta(1/x)J_t}{J_b}. \qquad (17)$$

The model being considered includes both approaches (i) and (ii) mentioned in the Introduction. Two low-energy scalars emerge in the region of very small values of β (at $\beta \lesssim m_{t,b}^2/M^2$, as will be seen in the next section) and when the critical parameters β_t and β_b are both greater than unity. The radiative version of the origin of m_b would correspond to $\beta_b = 0$—that is, $x = \beta J_t$—when the mass m_b is expressed in terms of m_t and the small constant $\beta \sim x$, as it must be in cases where the mass is calculated in terms of radiative corrections. On the other hand, $\beta > 0$ and β_t remains less than unity—that is, it does not reach the critical value: $m_t = 0$ if we set $\beta = 0$. If, at the same time, β emerged owing to perturbative scalar exchanges, we could neglect it without introducing substantial changes in the spectrum of the system. Therefore, there is actually no perturbative version of m_b generation in the model being considered (at least for $1 \gg x \gg m^2/M^2$).

Another possible version of a $x \ll 1$ solution could be realized is the case of three large parameters, $\beta \gg x$ and $\beta_t \sim x\beta_b$, $|\beta_b| \gtrsim 1$. Here, there of course arises some version of a nonperturbative mechanism . However, a large distinction ($\beta_t \sim x\beta_b$) between the uniform vector constants β_t and β_b seems a mere statement of the fact (as in Yukawa coupling constants within the SM) rather than a physical explanation of the phenomenon. The point is that the quantities $G_{t,b} \sim g_{t,b}/M_V^2$ ($\beta_{t,b} \sim G_{t,b}M^2$) cannot have different scale masses M_V, as was indicated above, since they describe the coupled transitions $\bar{t}_R t_R \rightleftarrows \bar{q}_L q_L \rightleftarrows \bar{b}_R b_R$. Therefore, the distinction between $G_{t,b}$ and $G_(b)$ is the distinction between the dimensionless numerical quantities g_t and g_b.

The region $|\beta| \sim x$, where β_t and β_b both appear to be close to the critical point—that is, $\beta_t \simeq 1 + O(x^2)$ and $\beta_b \simeq 1$ (β_t is greater or less than β_b, depending on the the sign of β)—is the most natural region for the emergence of a $x \ll 1$ solution. Here, the condition $x \ll 1$ must be interpreted as the distinction between the mass scales of vector and scalar exchanges:

$$M_V \sim \sqrt{x} M_S. \qquad (18)$$

In this region and for $x \gg m_{t,b}^2/M^2$, the disregard of small β (as has already been mentioned, this is possible if β emerges owing to switching on some perturbative coupling at high energies) does indeed strongly change the spectrum of the system: at $\beta > 0$, β_t and β_b are less than unity and we have a subcritical case; hence, $m_t = m_b = 0$. For $\beta < 0$, the inequality

$m_b > m_t$ would hold. Therefore, β is not a perturbative quantity. The version in (18) seems the simplest and most natural explanation of the large distinction between the masses of the t and the b quark in the case where both of them arise as the result of a spontaneous breakdown of chiral $SU_L(2)$ symmetry.

4. SCALAR AND PSEUDOSCALAR STATES

Composite bosons of the scalar and the pseudoscalar channel are also the standard subjects of investigation in Nambu–Jona-Lasinio model. We now recall how this is done for the simplest case of $\beta_b = \beta = 0$.

In the lowest approximation in N_c, the amplitude for $\bar{q}q$ scattering is represented as the sum of chain diagrams. Within each one-loop link, the helicity of the quark pair can either be conserved or change. Because of this, the link (one-loop contribution) A is a matrix in the helicity indices $\alpha = L, R$; $O_\alpha = 1/2(1 \pm \gamma_5)$. The amplitude B—that is, the sum of the chain contributions—is then expressed in terms of the matrix reciprocal to $1 - \beta A$:

$$B = \frac{8\pi^2\beta}{N_c M^2}\frac{1}{1-\beta A}. \tag{19}$$

Here, β is the four-fermion coupling constant (5), and the matrix $A_{\alpha\beta}$ can easily be written in an explicit form (for $q_\alpha\bar{q}_\beta$ with masses m_1 and m_2). In a form symmetric with respect to the interchange of m_1 and m_2, the one-loop contribution with incoming 4-momentum q has the form (see, for example, [8])

$$A_{\alpha\beta}(q) = -\frac{1}{M^2}\int\frac{d^4p}{\pi^2 i} \tag{20}$$
$$\times\frac{1}{2}\mathrm{tr}\left\{\frac{m_1 - (\hat{p}+\hat{q}/2)}{m_1^2-(p+q/2)^2}O_\alpha\frac{m_2-(\hat{p}-\hat{q}/2)}{m_2^2-(p-q/2)^2}O_\beta\right\}$$
$$A_{\alpha\beta}(q) = A_1^{(1,2)}\delta_{\alpha\beta} + A_2^{(1,2)}\delta_{\alpha-\beta}$$
$$A_1^{(1,2)} = -\frac{1}{M^2}\int\frac{d^4p}{\pi^2 i} \tag{21}$$
$$\times\frac{(p+q/2)(p-q/2)}{[m_1^2-(p+q/2)^2][m_2^2-(p-q/2)^2]},$$
$$A_2^{(1,2)} = -\frac{m_1 m_2}{M^2}I_{12}(q) \tag{22}$$
$$I_{12}(q) = \int\frac{d^4p}{\pi^2 i}\frac{1}{[m_1^2-(p+q/2)^2][m_2^2-(p-q/2)^2]}$$

(the cutoff function f_M is not presented explicitly). By using the relation

$$\left(p+\frac{q}{2}\right)\left(p-\frac{q}{2}\right) = -\frac{1}{2}\left[m_1^2-\left(p-\frac{q}{2}\right)^2\right] \tag{23}$$
$$-\frac{1}{2}\left[m_2^2-\left(p-\frac{q}{2}\right)^2\right]+\frac{1}{2}(m_1^2+m_2^2-q^2),$$

A_1 can be reduced to the form

$$A_1(q) = -\frac{1}{2}J_1 - \frac{1}{2}J_2 - \frac{q^2}{8M^2}c \tag{24}$$
$$+\frac{1}{2}\frac{m_1^2+m_2^2-q^2}{M^2}I_{12}(q),$$

where J_1 and J_2 are quadratically divergent integrals of the form (4) and c is a constant that depends on the choice of cutoff [$c = 1$ at $f_M = \vartheta(M^2 - p^2)$].

By setting $m_1 = m_2$ and taking into account (11), we obtain the ordinary statement [2] that there exists a scalar pole at $q^2 = 4m^2$ ($c = 0$) and a pseudoscalar Goldstone particle ($q^2 = 0$):

$$B_S(q) = \frac{(4\pi)^2}{N_c(I(q)+c/4)}$$
$$\times\frac{1}{4m^2/(1+c/(4I(q))-q^2} \tag{25}$$
$$B_{PS} = \frac{(4\pi)^2}{N_c[I(q)+c/4]}\frac{1}{-q^2}.$$

It should be noted that the residues at the poles do not depend explicitly on β (they depend on it only through the mass m).

For the model considered in this study, the coupling constant β and the quantities A and B are the matrix both in the helicity (α, β) and in the isotopic $(\bar{a}, \bar{b})$ indices. For the process $q_{\alpha\bar{a}} + \bar{q}_{\beta\bar{b}} \to q_{\alpha'\bar{a}'} + \bar{q}_{\beta'\bar{b}'}$, we write these matrices presenting all indices explicitly, although their number can be reduced because, in the leading approximation in N_c, the relations $\alpha = -\beta$ and $\alpha' = -\beta'$ hold in the vertices given by (7). Specifically, we have

$$\beta_{\alpha\bar{a},\beta\bar{b}}^{\alpha'\bar{a}',\beta'\bar{b}'} = [\beta_{\alpha\bar{a},\beta\bar{b}}\delta_{\alpha\alpha'}\delta_{\beta\beta'}\delta_{\bar{a}\bar{a}'}\delta_{\bar{b}\bar{b}'} \tag{26}$$
$$+\beta\delta_{\alpha\beta'}\delta_{\beta\alpha'}(\delta_{\bar{a}'\bar{b}'}\delta_{\bar{a}\bar{b}} - \delta_{\bar{a}'\bar{a}}\delta_{\bar{b}'\bar{b}})]\delta_{\alpha-\beta},$$

where $\beta_{Rt,L\bar{b}} = \beta_{L\bar{a}Rt} = \beta_t$ and $\beta_{Rb,L\bar{b}} = \beta_{L\bar{a}Rb} = \beta_b$.

In the expression for the one-loop contribution (all indices refer to the internal lines), the matrix is diagonal in the isotopic indices:

$$A_{\alpha\bar{a},\beta\bar{b}}^{\alpha'\bar{a}',\beta'\bar{b}'} \tag{27}$$
$$= \left(A_1^{\bar{a}\bar{b}}\delta_{\alpha'\alpha}\delta_{\beta'\beta} + A_2^{\bar{a}\bar{b}}\delta_{\alpha'-\alpha}\delta_{\beta'-\beta}\right)\delta_{\alpha-\beta}\delta_{\bar{a}\bar{a}'}\delta_{\bar{b}\bar{b}'}.$$

According to (26), we seek the reciprocal matrix $(1-\beta A)^{-1} = \bar{B}$ in the form

$$\delta_{\alpha\alpha'}\delta_{\beta\beta'}\left[\bar{B}_1\delta_{\bar{a}\bar{a}'}\delta_{\bar{b}\bar{b}'} + \bar{B}_2\left(\delta_{\bar{a}'\bar{b}'}\delta_{\bar{a}\bar{b}}\right.\right. \tag{28}$$
$$\left.\left.-\delta_{\bar{a}'\bar{a}}\delta_{\bar{b}'\bar{b}}\right)\right] + \delta_{\alpha-\alpha'}\delta_{\beta-\beta'}\left[\bar{B}_3\delta_{\bar{a}\bar{a}'}\delta_{\bar{b}\bar{b}'}\right.$$
$$\left.+\bar{B}_4\left(\delta_{\bar{a}'\bar{b}'}\delta_{\bar{a}\bar{b}} - \delta_{\bar{a}'\bar{a}}\delta_{\bar{b}'\bar{b}}\right)\right].$$

The quantities $\bar{B}_i$ depend on the isotopic indices of the scattering channel being considered. Written immediately below are the equations for $\bar{B}_i$ in various

channels (four equations for possible changes in the isotopic content and helicity).

(i) For $\bar{t}t \to \bar{t}t$ and $\bar{t}t \to \bar{b}b$ ($(1-\beta A)\bar{B}=1$), we have

$$\begin{gathered}(1-\beta_t A_1^{tt})\bar{B}_1^{tt} - \beta_t A_2^{tt}\bar{B}_3^{tt} \\ -A_2^{tt}\beta\bar{B}_2^{tb} - A_1^{tt}\beta\bar{B}_4^{tb} = 1, \\ -A_2^{tt}\beta_t\bar{B}_1^{tt} + (1-\beta_t A_1^{tt})\bar{B}_3^{tt} \\ -A_1^{tt}\beta\bar{B}_2^{tb} - A_2^{tt}\beta B_4^{tb} = 0, \\ -A_2^{bb}\beta\bar{B}_1^{tt} - A_1^{bb}\beta\bar{B}_3^{tt} \\ +(1-\beta_b A_1^{bb})B_2^{tb} - \beta_b A_2^{bb}B_4^{tb} = 0, \\ -A_1^{bb}\beta\bar{B}_1^{t}t - A_2^{bb}\beta\bar{B}_3^{tt} - \beta_b A_2^{bb}\bar{B}_3^{tb} \\ +(1-\beta_b A_1^{bb})\bar{B}_4^{tb} = 0.\end{gathered} \tag{29}$$

(ii) For $\bar{b}b \to \bar{b}b$ and $\bar{b}b \to \bar{t}t$, the set of equations is analogous to that in (29) with the substitution $t \Leftrightarrow b$, their determinants being coincident.

(iii) For the charged channels $\bar{t}b \to \bar{t}b$, we have

$$\begin{gathered}[(1-\beta_b A_1^{tb}) - \beta A_2^{tb}](\bar{B}_1 - \bar{B}_2)^{tb} \\ +(\beta A_1^{tb} - \beta_t A_2^{tb})(\bar{B}_3 - \bar{B}_4)^{tb} = 1, \\ (\beta A_1^{tb} - \beta_b A_2^{tb})(\bar{B}_1 - \bar{B}_2)^{tb} \\ +[(1-\beta_t A_1^{tb}) - \beta A_2^{tb}](\bar{B}_3 - \bar{B}_4)^{tb} = 0\end{gathered} \tag{30}$$

for t_R scattering and the analogous set of equations with the substitution $t \leftrightarrows b$ for t_R scattering, the determinant taking the same value in the two cases.

By substituting (22) and (24) into (29) and (30), we can calculate the determinants of these sets of equations, which characterize the possible scalar states. It should be emphasized that $|A_2| \ll |A_1|$ at $m_{t,b}^2, |q^2| \ll M^2$ and that there are small terms $\sim m^2/M^2$ in A_1, which seem negligible. However, the limiting transition $\beta \to 0$, in which there must arise independent low-energy states ϕ_t and ϕ_b and charged Higgs particles characteristic of a nonminimal SM, can be traced only if we retain all orders of smallness. In addition, this makes it possible to follow the fate of all four scalar states of each channel with increasing β and to prove that Goldstone states are present in the system under conditions (9), irrespective of relations between $m_{t,b}^2, q^2$, and M^2. In view of all this, the determinants of the sets of Eqs. (29) and (30) were calculated here without recourse to any approximation. The single simplification is that we set the constant c to zero in (24). This, however, does not change any of the significant features.

For the determinant of the set of Eqs. (29) (neutral channel), we thus have

$$\begin{aligned}\mathrm{Det}^{(0)} = \frac{-q^2}{M^2}\,\frac{m_t m_b}{M^2}\beta\left(I_t\frac{1}{x} + I_b x\right) \\ \times\left[\beta\left(I_t\frac{1}{x^2} + I_b x^2\right) + \frac{2m_t m_b}{M^2}\eta I_t I_b\right] \\ +\frac{1}{2}\left(\frac{-q^2}{M^2}\right)^2 I_t I_b\left[\beta^2 + 2\beta\left(I_t\frac{1}{x^2} + I_b x^2\right)\right. \\ \left.\times\frac{m_t m_b}{M^2}\eta + 2I_t I_b\left(\frac{m_t m_b}{M^2}\right)^2\eta^2\right] \\ +\frac{1}{4}\left(\frac{-q^2}{M^2}\right)^2\beta\left[I_t^2\left(\frac{\beta}{x^2} + \frac{2m_t m_b}{M^2}I_b\eta\right)\right. \\ \left.+ I_b^2\left(\beta x^2 + \frac{2m_t m_b}{M^2}I_t\eta\right)\right] \\ +\frac{1}{4}\left(\frac{-q^2}{M^2}\right)^3\eta I_t I_b\left[I_t\left(\frac{\beta}{x} + \frac{m_b^2}{M^2}I_b\eta\right)\right. \\ \left.+ I_b\left(\beta x + \frac{m_t^2}{M^2}I_t\eta\right)\right] + \frac{1}{16}\left(\frac{-q^2}{M^2}\right)^4\eta^2 I_t^2 I_b^2,\end{aligned} \tag{31}$$

where $I_t = I(q, m_t)$ and $I_b = I(q, m_b)$ are determined by (22) and $\eta = \beta_t\beta_b - \beta^2$ characterizes the deviation from the case where there is one Higgs boson and where we have $G^2 \equiv G_t G_b$ [see (6)].

In calculating Det^0 and in reducing the result to the form (31), use has extensively been made of (9) and (12)–(15). It is for this reason that formula (31) does not involve the quadratically divergent integrals J_t and J_b. The masses m_t and m_b appear as solutions to the set of Eqs. (9); therefore, we must take into account Eqs. (9) in going over to the limit associated with masses (for example, $m_b \to 0$) in (31). Solutions to Eq. (31) are composite scalars or pseudoscalars of the system under investigation. For the neutral channel, these are the poles of the amplitude for the three reactions

$$\bar{t}t \to \bar{t}t, \quad \bar{b}b \to \bar{b}b, \quad \bar{t}t \leftrightarrows \bar{b}b,$$

which conserve and change the helicity of particles and antiparticles.

As might have been expected on the basis of transformation (6), Eq. (31) at $\eta = 0$ has only two roots, that for $q^2 = 0$ and that for

$$\begin{aligned}q^2 = m_\phi^2 \approx 4m_t m_b\frac{I_t(1/x^2) + I_b x^2}{I_t(1/x) + I_b x} \\ = 4\frac{I_t m_t^4 + I_b m_b^4}{I_t m_t^4 + I_b m_b^4},\end{aligned} \tag{32}$$

which correspond to the Goldstone state and to a composite analog of the Higgs boson ϕ. At $m_t = m_b$—that is, at $x = 1$—we obtain the well-known Nambu–Jona-Lasinio formula $m_\phi^2 = 4m^2$ [2]. The functions $I_t(q)$ and $I_b(q)$ are given by (22) at $m_1 = m_2$. They depend logarithmically on q^2. We disregard this dependence.

Another limiting case, that of $\beta \to 0$, was mentioned in Section 3. For this case, we have

$$\mathrm{Det}^{(0)} = \frac{1}{4}\frac{4m_t^2 - q^2}{M^2}\,\frac{-q^2}{M^2}(\beta_t I_t)^2 \times \frac{1}{4}\frac{4m_b - q^2}{M^2}\,\frac{-q^2}{M^2}(\beta_b I_b)^2. \quad (33)$$

Here, the denominator in expression (19) for the scattering amplitude splits into two independent parts, the poles corresponding to the neutral components of two scalar isodoublets (composite Higgs fields ϕ_t and ϕ_b) that suffered a spontaneous breakdown of $SU_L(2)$ symmetry. There are four neutral states and, as will be seen below, four charged states. Three massless state form a Goldstone isovector. Four massive (two neutral and two charged) states and one massless state would be the candidates for observed bosons. The calculation of the amplitudes in (19) at $\beta = 0$ proves a nonminimal character of the system. By way of example, we indicate that, for the channel $\bar{b}b \to \bar{b}b$, which conserves the particle helicity, the denominator of the amplitude [it corresponds to the minor of Eqs. (29)] can be represented as

$$\beta_b \frac{2m_b^2 - q^2}{2M^2} I_b \frac{-q^2}{2M^2} I_t \cdot \frac{(4m_t^2 - q^2)}{2M^2}\beta_t^2. \quad (34)$$

Substituting this expression into (19) and taking into account (33), we then arrive at expression (25) with the pole at $4m_b^2$. A similar result is valid for other channels ($b \leftrightarrows t, m_b \leftrightarrows m_t$). The situation with two scalar fields is conserved up to $\beta \lesssim m_t m_b/M^2$.

Let us proceed to analyze the region $\beta \sim x \gg m_t m_b/M^2$. For $q^2 \ll M^2$, we obtain the approximate expression

$$\mathrm{Det}^{(0)} = \frac{-q^2}{M^2}\,\frac{m_t m_b}{M^2}\left\{\beta^2\left(I_t\frac{1}{x} + I_b x\right)^2 \times [m_\phi^2(q) - q^2] + O\left(\frac{m_t m_b}{M^2}, \frac{-q^2}{M^2}\right)\right\}, \quad (35)$$

where m_ϕ^2 is given by (32). Thus, we see that, at energies much lower than the cutoff value M, there are two scalar states corresponding to the minimally broken SM.

Knowing two roots of Eq. (31)—$q^2 = 0$ and $q^2 \approx m_\phi^2$—we can easily determine the positions of the two other roots. In the region being considered, $\beta \sim x$ and the approximate solution (correct to one power of $m_{t,b}^2/M^2$) makes it possible to find two more roots:

$$\left(\frac{-q^2}{M^2}\right)_1 \simeq -2\beta\frac{I_t(1/x) + I_b x}{\eta I_t I_b} + O\left(\frac{m_t^2, m_b^2, m_t m_b}{M^2}\right), \quad (36)$$

$$\left(\frac{-q^2}{M^2}\right)_2 \simeq -2\beta\frac{I_t(1/x) + I_b x}{\eta I_t I_b}.$$

The second root does not involve $\sim m_{t,b}^2/M^2$ contributions. It can be proven that $\sim m_{t,b}^2/M^2$ contributions do not vanish for $\beta \to 0$. It follows that, in this limit, one of the roots can be equal to zero, while the other provides a finite mass, this being consistent with our calculations for $\beta = 0$. In the region $m_{t,b}^2/M^2 \ll \beta \sim x \ll 1$, the roots occur near the cutoff boundary in the model. If we again disregard the weak dependence of $I_{t,b}$ on q^2, then

$$(q^2)_{1,2} \sim M^2\frac{\beta}{x}\frac{1}{\eta} \sim M^2. \quad (37)$$

Actually, there are therefore no roots (36) in the model (for $\beta > 0$, they can be tachyons); that is, their inclusion is meaningless within our consideration. It follows that, with the exception of the point $\beta \simeq 0$, the model specified by Eq. (7) corresponds to the minimal SM at energies $E \ll M$.

It only remains to perform a similar analysis for the charged channel. By substituting formulas (24) and (22) into the determinant of the set of Eqs. (30), we obtain ($c = 0$)

$$\mathrm{Det}^{(\pm)} = \frac{m_t^2 - m_b^2}{2M^2}[I_{tb}(q) - I_{tb}(0)] \times \left\{\beta_t - \beta_b + \eta\frac{m_t^2 - m_b^2}{2M^2}[I_{tb}(q) - I_{tb}(0)]\right\} + \frac{-q^2}{2M^2}I_{tb}(q)\left[\beta\left(x + \frac{1}{x}\right) + \eta\frac{m_t^2 + m_b^2}{M^2}I_{tb}(q)\right] + \left(\frac{-q^2}{2M^2}\right)^2\eta I_{tb}^2(q), \quad (38)$$

where the function $I_{tb}(q)$ is determined by the integral in (22) at $m_1 = m_t$ and $m_2 = m_b$. The dependence on the cutoff mass M is canceled in the difference $I_{tb}(q) - I_{tb}(0)$. At small q^2, we have

$$[I_{tb}(q) - I_{tb}(0)]\frac{1}{q^2} = \frac{1}{2}\frac{m_t^2 + m_b^2}{(m_t^2 - m_b^2)^2} + \frac{m_t^2 m_b^2}{(m_t^2 - m_b^2)^3}\ln\frac{m_t^2}{m_b^2}. \quad (39)$$

Formulas (12)–(15) have been again used widely to reduce $\mathrm{Det}^{(\pm)}$ to the form (38).

In $\mathrm{Det}^{(\pm)}$, the Goldstone root $q^2 = 0$ is also present, as it must. At $\eta = 0$, the other roots are absent and we are dealing directly with the minimally broken SM according to (6). At $\beta = 0$, the massive charged-scalar state

$$q^2 \simeq 2(m_t^2 + m_b^2) + O\left(\frac{m^2}{\ln(M^2/m^2)}\right) \quad (40)$$

manifests itself in addition to the Goldstone root.

In deriving (40), it should be borne in mind that, at $\beta = 0$, $\beta_t - \beta_b \sim (m_t^2/M^2)\ln(M^2/m_t^2)$ [this follows from the gap Eqs. (9)]. It was mentioned above that, at $\beta = 0$, there are in total four charged states of finite mass. Thus, the spectrum of the charged channels complements the picture up to a nonminimal SM that involves two Higgs scalars.

At $|\beta| \gg m_{t,b}^2/M^2$, a charged massive particle has a mass of about M—that is, on the order of cutoff boundary. There only remain the states that correspond to the minimal SM with a single composite Higgs particle.

Thus, we have constructed a model that describes a spontaneous breakdown of chiral $SU_L(2)$ symmetry and which is characterized by a simultaneous dynamical generation of the masses of both components of the weak doublet of quarks, t and b. At SM energies, there appears only one composite scalar boson. Hence, the low-energy situation in this model is fully analogous to the minimal SM.

The large difference of the t- and the b-quark mass, $x = m_b/m_t \ll 1$, can suggest that, at high energies, there exist phenomena whose energy scales differ considerably from one another.

ACKNOWLEDGMENTS

I am grateful to G.S. Danilov and L.N. Lipatov for stimulating discussions.

This work was supported by the Russian Foundation for Basic Research (project no. 98-02-17214).

APPENDIX

Here, we demonstrate how the well-known Higgs phenomenon (even the theorem) of the transformation of a Goldstone state into the longitudinal component of a weak massive vector meson W acts in the intricate situation being considered.

First, it is useful to recall how this occurs in the SM with the fundamental Higgs field ϕ, which is a doublet of weak $SU_L(2)$ symmetry. Breaking the symmetry, the field ϕ forms the condensate

$$\phi(x) = \frac{1}{\sqrt{2}}(\eta + \chi)\exp\left[i\varphi^a(x)\frac{\tau^a}{2}\right]\begin{pmatrix}0\\1\end{pmatrix}, \quad \text{(A.1)}$$

where η is a vacuum expectation value, $\chi(x)$ is the field of the massive Higgs boson, and $\varphi^a(x)$ is the isovector Goldstone field. The interaction between ϕ and W leads to the emergence of the longitudinal self-energy W not vanishing at $q = 0$, that is, to the mass M_W,

$$\Pi_{\mu\nu}(q) = \left(g_{\mu\nu} - \frac{q_\mu q_\nu}{q^2}\right)\frac{g_2^2\eta^2}{4},$$

$$M_W = \frac{g_2\eta}{2}, \quad \text{(A.2)}$$

where g_2 is the semiweak coupling constant. The point is that, owing to the interaction with the massless field $\varphi^a(x)$, W may transform into a Goldstone state. This leads to the existence of the pole in the self-energy W. Therefore, the propagator W (in an arbitrary gauge) has the form

$$D_{\mu\nu}(q) = \frac{g_{\mu\nu} - (q_\mu q_\nu/q^2)}{q^2 - M_W^2} + \frac{\alpha(q^2)}{q^2}\frac{q_\mu q_\nu}{q^2}$$
$$= \frac{g_{\mu\nu} - (q_\mu q_\nu/M_W^2)}{q^2 - M_W^2} + \frac{q_\mu q_\nu}{q^2}\left(\frac{1}{M_W^2} + \frac{\alpha}{q^2}\right). \quad \text{(A.3)}$$

For the sake of simplicity, we set $\alpha = 0$—otherwise, we would have to consider the Goldstone boson with mass $m_g^2 = -(1/2)M_W^2$ (it would be generated by the transition $\varphi \to W \to W \to \varphi$).

In quark–quark scattering processes, it is necessary to take into account both the exchange of a W boson and the exchange of a Goldstone boson φ. At $q^2 \approx 0$, the W-boson contribution is given by

$$\frac{q_\mu q_\nu}{q^2}\frac{1}{M_W^2}, \quad \text{(A.4)}$$

and the interaction of the W boson and the quark is

$$\bar{Q}g_2\hat{W}^a\frac{1}{2}(1+\gamma_5)\frac{\tau^a}{2}Q, \quad \hat{W}^a = W_\mu^a\gamma^\mu. \quad \text{(A.5)}$$

While the singular contribution of the Goldstone boson is $-q^{-2}$, the contribution of its interaction with quarks can be represented as

$$\bar{Q}m_Q i\gamma_5\frac{\tau^a\varphi^a}{2}Q. \quad \text{(A.6)}$$

Formulas (A.5) and (A.6) make it possible to calculate the residues of both poles at $q^2 = 0$.

The calculation of two singular contributions demonstrates that they are canceled. After that, there only remains the contribution of the massive part of the propagator in (A.3).

A similar cancellation of the singular parts must occur in the present model of a composite Higgs boson.

The self-energy W is the sum of the contributions of two diagrams in Fig. 1. But only the diagram in Fig. 1*b* involves the contribution of the Goldstone pole of the quark–quark scattering amplitude. This diagram determines exclusively M_W^2 and, hence, the singular parts of the self-energy (A.2) and of the W-exchange term in (A.4). The contribution of the diagram in Fig. 1*a* does not involve singularities and can determine only the renormalization of the charge g_2 (see [3]). This contribution involves a quadratically

divergent part, and the presence of this indeterminate form can be used to recast the total self-energy $\Pi_{\mu\nu}(q)$ into a gauge-invariant transverse form, including the singular contribution of the diagram in Fig. 1*b*. Let us fix the indeterminate form by setting $\Pi_{\mu\nu}q_\mu = \Pi_{\mu\nu}q_\nu = 0$. There is then no need for taking care that the singular contribution is transverse, and the mass W can be determined, as in (A.2), directly from the diagram in Fig. 1*b*. For the charged boson $W^\pm$, we have

$$\left(-\frac{g_2N_c}{\sqrt{2}}\right)\int\frac{d^4p}{(2\pi)^4i}\mathrm{tr}\left\{\gamma_\mu\frac{1}{2}(1+\gamma_5)\right.$$
$$\times\frac{m_b+(\hat{p}-\hat{q}/2)}{m_b^2-(p-q/2)^2}$$
$$\times\left[\frac{1}{2}(1+\gamma_5)\langle t_L\bar{b}_R|+\frac{1}{2}(1-\gamma_5)\langle t_R\bar{b}_L|\right]$$
$$\left.\times\frac{m_t+(\hat{p}+\hat{q}/2)}{m_t^2-(p+q/2)^2}\right\}|g\rangle\frac{1}{-q^2}\langle g|$$
$$\times\left(-\frac{g_2N_c}{\sqrt{2}}\right)\int\frac{d^4\ell}{(2\pi)^4i}\mathrm{tr}\left\{\gamma_\nu\frac{1}{2}(1+\gamma_5)\right.$$
$$\times\frac{m_t+(\hat{\ell}+\hat{q}/2)}{m_t^2-(\ell+q/2)^2}\left[\frac{1}{2}(1+\gamma_5)|t_R\bar{b}_L\rangle\right.$$
$$\left.\left.+\frac{1}{2}(1-\gamma_5)|t_L\bar{b}_R\rangle\right]\frac{m_b+(\hat{\ell}-\hat{q}/2)}{m_b^2-(\ell-q/2)^2}\right\}.$$

We have represented the amplitudes in the symbolic form $\langle t\bar{b}|g\rangle\langle g|t\bar{b}\rangle/(-q^2)$, since they are different for different processes. Upon evaluating the traces, we obtain

$$\Pi_{\mu\nu}^{\mathrm{sing}}(q)=\frac{1}{-q^2}2g_2^2\left[\frac{N_c}{(4\pi)^2}\right]^2\int\frac{d^4p}{\pi^2i}\frac{d^4\ell}{\pi^2i}$$
$$\times\left[m_t^2\left(p-\frac{q}{2}\right)_\mu\left(\ell-\frac{q}{2}\right)_\nu\langle t_R\bar{b}_L|t_R\bar{b}_L\rangle\right.$$
$$+m_b^2\left(p+\frac{q}{2}\right)_\mu\left(\ell+\frac{q}{2}\right)_\nu\langle t_L\bar{b}_R|t_L\bar{b}_R\rangle \qquad \text{(A.7)}$$
$$\left.+2m_tm_b\left(p_\mu\ell_\nu-\frac{1}{4}q_\mu q_\nu\right)\langle t_L\bar{b}_R|t_Rb_L\rangle\right]$$
$$\times\frac{1}{\left[m]t^2-(p+q/2)^2\right]\left[m_b^2-(p-q/2)^2\right]}$$
$$\times\frac{1}{\left[m_t^2-(\ell+q/2)^2\right]\left[m_b^2-(\ell-q/2)^2\right]}.$$

The brackets denote the residues of the amplitudes (coefficients of $-q^{-2}$). Apart from a constant under the logarithm sign in $\ln(M^2/(m_tm_b))$, the integrals in (A.7) can be expressed in terms of $I_{tb}(q)$ given by (22); that is,

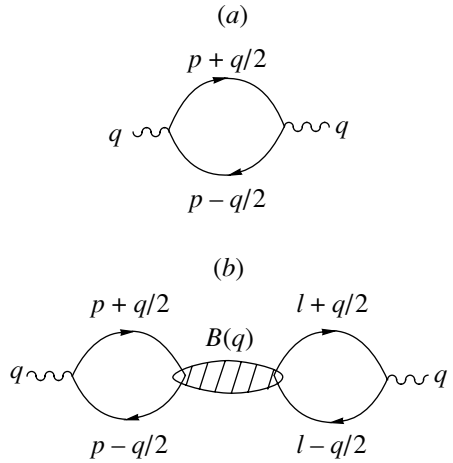

Fig. 1. Self-energy diagrams for the weak gauge boson W.

$$\int\frac{d^4p}{\pi^2i}\frac{(p\mp q/2)_\lambda}{[m_t^2-(p+q/2)^2][m_b^2-(p-q/2)^2]} \qquad \text{(A.8)}$$
$$=\mp\frac{1}{2}q_\lambda I_{tb}(q).$$

The charged-channel amplitudes are calculated according to (19) with the matrices β and $\bar{B}$ from formulas (26) and (30) in the approximation $x\sim|\beta|\gg m_tm_b/M^2$. For three residues written in (A.7), we obtain (recall that $x=m_b/m_t$)

$$B^{(\pm)}(q)=\frac{1}{-q^2}\frac{(4\pi)^2}{N_cI_{tb}(q)} \qquad \text{(A.9)}$$
$$\times\left(\frac{1}{1+x^2},\frac{x^2}{1+x^2},\frac{-x}{1+x^2}\right).$$

The substitution of (A.8) and (A.9) into (A.7) yields

$$M_W^2=\frac{1}{2}\frac{g_2^2N_c}{(4\pi)^2}(m_t^2+m_b^2)I_{tb}. \qquad \text{(A.10)}$$

In order to complete the calculation of the singular contribution (A.4), it is necessary to apply the product $q_\mu q_\nu$ to the quark vertices for the interaction in (A.5). For expression (A.7) or (A.9), we obtain

$$\frac{g_2^2}{2}(m_t^2,m_b^2,-m_tm_b). \qquad \text{(A.11)}$$

For the singular part of the contribution of W, we then have expression (A.9), but with the inverse sign.

To conclude, we present formulas resulting from analogous calculations for the neutral channels (W_3; the weak interactions of t and b have opposite signs). The hypercharge interaction (as in the SM) is not considered for the sake of simplicity.

The singular part $\Pi^{(0)}_{\mu\nu}(q)$ arises in the form (as before, brackets denote the corresponding residues at $q^2 = 0$)

$$\Pi^{(0)}_{\mu\nu}(q) = \frac{q_\mu q_\nu}{-q^2}\frac{g_2^2}{2}\left[\frac{N_c}{(4\pi)^2}\right]^2 \times \{m_t^2[\langle t_L\bar{t}_R|t_L\bar{t}_R\rangle - \langle t_L\bar{t}_R|t_R\bar{t}_L\rangle]I_t^2(q) + m_b^2[\langle b_L\bar{b}_R|b_L\bar{b}_R\rangle - \langle b_L\bar{b}_R|b_R\bar{b}_L\rangle]I_b^2(q) - 2m_t m_b[\langle t_L\bar{t}_R|b_L\bar{b}_R\rangle - \langle t_L\bar{t}_R|b_R\bar{b}_L\rangle]I_t(q)I_b(q)\}. \quad \text{(A.12)}$$

The residues can be calculated from the amplitudes of the corresponding processes [formulas (19), (26), and (29)] in the same approximation $x \sim \beta \gg m^2_{t,b}/M^2$. We present the results according to the order in which these processes appear in formula (A.12):

$$B^{(0)}(q) = \frac{8\pi^2}{N_c\,(I_t(1/x) + I_b x)} \times \frac{m_\phi^2(q)}{(-q^2)(m_\phi^2(q) - q^2)}\lambda, \quad \text{(A.13)}$$

$$\lambda = \left\{\frac{1}{x}\left(1 + 2\frac{-q^2}{m_\phi^2}\right), -\frac{1}{x}; \quad x\left(1 + 2\frac{-q^2}{m_\phi^2}\right), -x; -1, 1 + 2\frac{-q^2}{m_\phi^2}\right\}. \quad \text{(A.14)}$$

For the W_3 mass, we have

$$M^{(0)^2} = \frac{1}{2}\frac{g_2^2 N_c}{(4\pi)^2}(I_t m_t^2 + I_b m_b^2). \quad \text{(A.15)}$$

A comparison of the singular contributions from W and from the Goldstone particle shows that they of course cancel each other.

REFERENCES

1. Y. Nambu, in *Proceedings of XI International Symposium on Elementary Particle Physics, Kazimirz, Poland, 1988,* Ed. by Z. Ajduk *et al.* (World Sci., Singapore, 1989).
2. Y. Nambu and G. Jona-Lasinio, Phys. Rev. **122**, 345 (1961).
3. W. A. Bardeen, C. T. Hill, and M. Lindner, Phys. Rev. D **41**, 1647 (1990).
4. M. Suzuki, Phys. Rev. D **41**, 3457 (1990); M. A. Luty, Phys. Rev. D **48**, 1295 (1993).
5. R. N. Mohapatra and K. S. Babu, Phys. Rev. Lett. **66**, 556 (1991).
6. S. P. Klevansky, Rev. Mod. Phys. **64**, 649 (1992).
7. T. Hatsuda and T. Kunihiro, Phys. Rep. **297**, 221 (1994); V. Dmitrašinovič, H. J. Schulze, and R. Tegen, Ann. Phys. (N.Y.) **238**, 332 (1995).
8. I. T. Dyatlov, Yad. Fiz. **60**, 1650 (1997) [Phys. At. Nucl. **60**, 1504 (1997)].

Translated by A. Isaakyan

Physics of Atomic Nuclei, Vol. 64, No. 9, 2001, pp. 1667–1688. From Yadernaya Fizika, Vol. 64, No. 9, 2001, pp. 1748–1768.

ELEMENTARY PARTICLES AND FIELDS
Theory

Arguments against One-Boson-Exchange Models of Nuclear Forces and New Mechanism for Intermediate- and Short-Range Nucleon–Nucleon Interaction*

V. I. Kukulin, I. T. Obukhovsky, V. N. Pomerantsev, and A. Faessler[1)]

Institute of Nuclear Physics, Moscow State University, Vorob'evy gory, Moscow, 119899 Russia
Received August 2, 2000; in final form, November 24, 2000

Abstract—Arguments against the traditional Yukawa-type approach to NN intermediate- and short-range interaction due to scalar–isoscalar and heavy-meson exchanges are presented. Instead of the Yukawa mechanism for intermediate-range attraction, some new approach based on the formation of a symmetric six-quark bag in the state $|(0s)^6[6]_X, L=0\rangle$ dressed owing to strong coupling to π, σ, and ρ fields is suggested. This new mechanism offers a strong intermediate-range attraction, which replaces effective σ exchange (or excitation of two isobars in the intermediate state) in traditional force models. A similar mechanism with the production of a vector ρ meson in the intermediate six-quark state is expected to lead to a strong short-range spin–orbit nonlocal interaction in the NN system, which may resolve the long-standing puzzle of the spin–orbit force in baryons and in two-baryon systems. The effective interaction in the NN channel provided by the new mechanism will be enhanced significantly if the partial restoration of chiral symmetry is assumed to occur inside the six-quark symmetric bag. A simple illustrative model is developed that demonstrates clearly how well the suggested new mechanism can reproduce NN data. Strong interrelations have been shown to exist between the proposed microscopic model and one-component Moscow NN potential developed by the authors previously and also with some hybrid models and the one-term separable Tabakin potential. The new implications of the proposed model for nuclear physics are discussed.

1. INTRODUCTION

Since the mid-1930s, when Yukawa proposed [1] his classical theory of the nuclear force based on meson exchange between nucleons, this concept, although improved and also partially modified over the last half century (see, e.g., [2, 7] and some reviews of studies done until 1978 in the book of Brown and Jackson [8]), has basically remained the same: the nuclear force is assumed to originate from the exchange of one or a few mesons between isolated nucleons. Though other channels with one or two Δ isobars in the intermediate state have also been added to the nucleon one in the last two decades [5, 6], isobars interact via meson exchange.

A large variety of potential models based on this concept have been suggested in recent years to describe the NN interaction, which fit very accurately experimental data on NN scattering up to the energy of 300 MeV in the laboratory frame.

However, with the accumulation of many new data in the field of hadron physics, it has become more and more evident that traditional NN interaction models (i.e., those that are based on the meson-exchange concept) suffer from numerous inner inconsistencies and discrepancies—for example, the same meson–nucleon form factors must have different types of short-range behavior in describing very similar processes. In particular, the same functional form of the πNN form factor $F_{\pi NN}(q^2)$ must have very different cutoff parameters $\Lambda_{\pi NN}$ in describing elastic and inelastic NN scattering or in describing two-body $2N$ and three-body $3N$ forces [9], etc. (Some other examples of such inconsistencies are discussed in Section 2.)

At the same time, due to radical improvements in the accuracy and the reliability of dynamical few-nucleon calculations, one also begins to find some numerous disagreements between new experimental data and the results of the most accurate Faddeev calculations (for a list, although far from complete, of such disagreements in few-nucleon calculations see, e.g., [9]). It is very instructive that many of such disagreements cannot be removed by introducing phenomenological $3N$ forces in the calculations [9–12].

*This article was submitted by the authors in English.

[1)]Institut für Theoretische Physik, Universität Tübingen, Auf der Morgenstelle 14, D-72076 Tübingen, Germany.

Some recent studies in the field that are based on chiral perturbation theory (χPT) may serve as a very clear indicator of the degree of our understanding (or misunderstanding) of the fundamental NN interaction. This is especially true for the studies reported in [13, 14]. There, the authors showed that, within chiral perturbation theory, it is impossible to describe, without introducing any cutoffs, all the lowest partial waves even if one incorporates the excitation into intermediate Δ isobars and the exchanges of vector (ρ and ω) mesons. Thus, a quantitative description of the lowest partial waves with $L = 0$–2 up to $E_{\rm lab} = 300$ MeV requires going beyond the framework of χPT. This problem becomes more urgent in passing to the intermediate-energy region around $E_{\rm c.m.} \simeq 1$ GeV, where a strong coupling to meson-production channels will render the application of χPT even more complicated.

On the other hand, we consider critically here the problem of the existence and the role, in the fundamental NN force, of a scalar–isoscalar light meson, usually referred to as the σ meson. The exchange of a σ meson is considered in traditional one-boson-exchange (OBE) models as a main contribution responsible for the strong intermediate-range attraction between nucleons and eventually as the main component of nuclear binding (e.g., in the Walecka model). Very numerous attempts at finding a well-developed resonance in the S-wave $\pi\pi$ system have been undertaken in recent years (see, e.g., the recent review [15]). According to the latest data [16], there is only a smooth $\pi\pi$ resonance with a large width.

Moreover, very recent studies of different groups have demonstrated [13, 14, 17] that the exchange of a correlated $\pi\pi$ pair in an S state between nucleons leads to a repulsive rather than an attractive contribution to the NN interaction. Thus, we should attribute the NN intermediate-range attraction to the generation of two intermediate Δ isobars (or at least to an $N\Delta$ intermediate state) [13, 14]. But, as will be argued in Section 3, this intermediate $\Delta\Delta$ state strongly overlaps the symmetric six-quark state $|(0s)^6[6]_X,\ L = 0, 2\rangle$; thus, the above $\Delta\Delta$ state can be replaced by an intermediate symmetric six-quark state strongly coupled to the 2π channel. Thus, we have tried to circumvent the problem in the treatment of lower partial waves by refraining from the basic Yukawa idea of meson exchange between (isolated) nucleons and to develop some new interaction mechanism on the basis of a quark model where quarks are strongly coupled to chiral fields.

Our treatment is essentially based on group-theoretical considerations of symmetries, on algebraic recouplings in the six-quark system, and on the specific role played by the fully symmetric six-quark state $|(0s)^6[6]_X[f_{CS}]\rangle$ in the NN interaction in lower partial waves. In particular, one could even expect that such a fully symmetric $6q$ state, due to the maximal overlap of all six quarks (which implies some enhancement of $q\bar{q}$ fluctuations inside such a state), may lead in the direction of a phase transition of the chiral symmetry restoration. This Goldstone limit, or even just an approach to this limit, means, in accordance with the variational principle, the appearance of a strong additional attraction between quarks and, hence, also between two nucleons at an intermediate range (i.e., at distances of $r_{NN} \sim 0.7$–1.2 fm, where such a dressed six-quark bag is localized).

The proposed mechanism is illustrated by a simple model in Section 4. In particular, that simple model can describe perfectly all lower NN phase shifts in the rather wide energy range 0–600 MeV.

The organization of this paper is as follows. In Section 2, we offer a critical look on OBE models and discuss the difficulties of traditional meson-exchange models with anomalously high cutoff parameters Λ and also with respect to their application to few-nucleon problems. Section 2 also includes a critical discussion of the scalar-meson puzzle in the light of some new results. In Section 3, we describe in detail the new model for intermediate- and short-range interaction and compare it with the traditional Yukawa mechanism of σ and ρ exchange. A simple illustrative model that describes all lower NN phase shifts in the energy range 0–600 MeV is described in Section 4. Section 5 is devoted to interrelations between the NN-interaction model suggested in this study and other models proposed previously. In the Conclusion, we summarize the main results of our study. Some algebraic details required for deriving the basic formulas and some tables of the group-theoretical algebraic coefficients are presented in the Appendix.

2. CRITIQUE OF THE BASIC ASSUMPTIONS OF OBE MODELS AND THEIR PREDICTIONS

Despite the relative success in the description of low-energy NN scattering data up to $E_{\rm lab} = 350$ MeV, traditional OBE models based on the initial Yukawa meson-exchange mechanism for the nucleon–nucleon force suffer from some inner contradictions and inconsistencies. These contradictions concern not only with the description of NN data themselves but also with the description of few-body data. All these contradictions and inner inconsistencies seem to be hardly removable today, because they concern, as a rule, many independent experiments or various basic theories.

2.1. Range of the NN Force due to Heavy-Meson Exchange and Quark Radius of the Nucleon

While the range of the π-exchange force $\lambda_\pi \simeq 1.45$ fm is much larger than the quark radius of the nucleon, $\langle r_N \rangle \simeq 0.6$ fm, so that Yukawa π exchange may be considered to occur mainly between two separated nucleons, the exchange of heavy mesons (with masses $m \geq 600$ MeV) occurs mainly at distances of $r_m \simeq 0.2$–0.8 fm, where two nucleons strongly overlap. Thus, this heavy-meson exchange happens mainly in the field of all six quarks of the participating nucleons. Hence, in OBE models using such a heavy-meson mechanism, it is necessary, first of all, to justify the employment of "free-space" meson–nucleon coupling constants and cutoff form factors. As a result of this, all existing OBE models have severe problems with short-range cutoff parameters Λ [6, 7, 9, 18, 19] (see especially the severe critique in [18]). Thus, all short-range parts of OBE potentials are treated in a purely phenomenological way [5–8], but by using, at the same time, the Yukawa framework, which looks rather inadequate for such short ranges. Very recently, an attempt [13, 14] undertaken to refrain from this short-range phenomenology, but still staying within the framework of a meson-exchange model (with a perturbative chiral-field treatment of two-pion exchange), demonstrated very clearly that models that incorporate one- and two-boson exchange are able to describe only higher NN partial waves. Hence, the description of lower partial waves requires a nonperturbative dynamical treatment.

This difficulty with cutoff parameters is especially evident in the values of $\Lambda_{\pi NN}$, which can be derived from the theory of πNN form factors [18, 20–22] and even from direct $N(e, e'\pi)N'$ experiments in which a pion is knocked out from the pion cloud of the nucleon by fast electrons [23]. In any case, the values of $\Lambda_{\pi NN}$ taken in all OBE models to fit NN data lie in the interval $\Lambda_{\pi NN}^{\rm OBE} \simeq 1.3$–$2.0$ GeV [6, 18], while all the above-mentioned direct estimates and experiments result in the values of $\Lambda_{\pi NN}^{\pi N+\rm theor} \simeq 0.4$–$0.8$ GeV; i.e., the discrepancy is within a factor of 1/3 to 1/4 or even less. Moreover, the choice of the strongly increased values of $\Lambda_{\pi NN} \simeq 1.3$–$2.0$ GeV in microscopic nuclear models results in a strong enhancement of the pion field inside nuclei [24], which is in drastic disagreement with many observations (see numerous examples in the review article [24]).[2)] Also, high Λ values were found to be incompatible with recent experiments on the Drell–Yan process [27].

The large value of $\Lambda_{\pi NN} \simeq 1.3$–$2.0$ GeV also seems incompatible with the description of pion production in the process $pp \to pn\pi^+$ [28] and also with elastic backward $p + d$ scattering [19]. There are also many other pieces of evidence that point very unambiguously to the need for soft cutoff parameters $\Lambda_{\pi NN}$ and $\Lambda_{\rho NN}$ for both the πNN and ρNN form factors (see, e.g., [29]). Last but not least, the $3N$-force models (via pion exchanges), which describe accurately the $3N$ and $4N$ systems [30–32], still require a soft cutoff parameter $\Lambda_{\pi NN}$.

Quite a similar situation is observed for other mesons, like σ, ρ, and ω, as well. For these, one also needs large cutoff parameters Λ in OBE models in contradiction to values given, e.g., by the vector-dominance model (in the case of ρ mesons). In total, the problem with artificially enhanced values of the cutoff parameters seems almost unavoidable in OBE models. For example, in attempts at solving this problem, Ueda [33] proposed adding three-pion-exchange contributions in the form of $\pi\rho$ and $\pi\sigma$ terms and also some "heavy"-pion (Π) exchange. He found again that the cutoff parameter $\Lambda_{\Pi NN}$ for the Π meson should be about 3 GeV (!) to fit NN scattering data. A similar critique of the short-range part of the NN interaction in the current OBE models (but much less detailed than in the present paper) was presented by the Bochum group [18].

2.2. Few-Body Puzzles Originating from the Application of Conventional NN-Interaction Models to Precise Few-Nucleon Calculations

In recent years, serious disagreements with accurate modern experimental data were found in high-precision few-nucleon calculations that use the most realistic conventional NN potentials for low (<200 MeV) and intermediate energies (200–300 MeV) [12, 31, 34, 37].[3)]

(i) Long-standing disagreements have been found since the mid-1970s in $3N$- and $4N$-binding energies. A strong underbinding found in the $3N$ and $4N$ ground-state energies was explained long ago with a significant contribution from a meson-exchange $3N$ force [30, 31]. However, this $3N$ force did not help to understand quantitatively some other $3N$ puzzles. For example, it was demonstrated very recently [38, 39] that the conventional $3N$ forces used, while still

[2)] For example, the high sensitivity of the pion-cloud terms to the value of the cutoff $\Lambda_{\pi NN}$ in the πNN vertex and the enhancement of the pion light-cone momentum distribution in the nuclear medium were especially emphasized by Thomas [25] (see also [26]).

[3)] The present authors are deeply grateful to Prof. W. Gloeckle and his coworkers in Bochum for detailed discussions on their recent few-body calculations and our critique presented here.

helping to explain new $p\vec{d}$ data, fail in the treatment of new high-precision experiments that studied $\vec{p}d$ elastic scattering at energies $E_N \simeq 150$–300 MeV into the backward hemisphere.

(ii) There is the well-known puzzle of the analyzing power A_y for low-energy $\vec{n}d$ and $\vec{p}d$ scattering [40]. The contribution of the traditional three-nucleon force does not help to remove the A_y discrepancy.

(iii) Recently, it was found [38, 39, 41] that the so-called Sagara puzzle (disagreement for the backward Nd elastic scattering near the minimum of the cross section) increases with growing energy. At $E_N^{\rm lab} = 200$ MeV, the disagreement is as large as 30%.[4)]

(iv) Quite remarkable disagreements for electromagnetic processes, like the reactions $pp \to pp\gamma$ [42], $^3\mathrm{He}(e,e'p)$, and $^3\mathrm{He}(e,e'pp')$ at moderate to high momentum transfers and energies, were observed [43, 44].

(v) Some evident discrepancies with data were also found in recent four-nucleon calculations of the Lisbon [36] and Grenoble groups [12] even at very low energies in the range 1–6 MeV. However the theoretical results of both groups are in very good agreement with each other.

This list may be continued still further (see, e.g., the recent reviews [9]). It should also be noted here that the current conventional NN models are able to explain fully quantitatively many various data for few-nucleon systems, first of all, due to a precise fit of the on-shell NN amplitudes up to 400 MeV. However, the above few-body puzzles and disagreements found very recently, together with long-standing puzzles, clearly signal that the existing NN-force models (based on the meson-exchange mechanism) do not include some important nontrivial contribution at intermediate and short ranges.

2.3. Scalar-Meson Puzzle and Problem of the Intermediate-Range NN Force

The problem with scalar mesons and their role in the hadron–hadron interaction attracts much attention today (see, e.g., [15, 16, 45]). This interest focuses on the experimental identification of scalar mesons and on their contribution to the description of hadron collisions—in particular, to the NN interaction.

According to the traditional point of view advocated for a long time by many "constructors" of NN potentials (see, e.g., [5, 6]), the exchange of the $\pi\pi$ correlated pair in a relative S wave between two pions in conjunction with the excitation of intermediate Δ isobars is responsible for a strong intermediate-range attraction between nucleons [5, 6, 46]. Further, in the conventional picture, this strong attraction at short distances is fully compensated by a strong repulsion due to ω exchange [8, 47].

Very recently, however, it was found by two groups independently [14, 17] that the $\pi\pi$ S-wave correlation is unable to provide any intermediate-range attraction, but that it even results in a rather strong short- and intermediate-range repulsion between nucleons within the two-pion-exchange mechanism. Thus, in the conventional meson-exchange mechanism, the main intermediate-range attraction should be associated only with the excitation of intermediate-state Δ isobars. Some independent arguments in favor of this conclusion follow from the obvious failure to get this strong attraction from various microscopic models like the model of Skyrme soliton interaction and the resonating-group-model (RGM) treatment with qq interaction based on the Goldstone boson exchange [48] in which the $\Delta\Delta$-state (or ΔN-state) excitation was neglected.

A second important argument comes from the experimental search for the low-mass scalar–isoscalar meson [15, 45]. While the highly excited scalars $f_0(1370)$ and $f_0(1500)$ were identified more or less reliably in experiments, the identification of low-mass scalar meson resonances (which one often refers to as a σ meson and which one relates to the $\pi\pi$ S-wave resonance) is not well accepted. The scatter of the mass and width estimates for these states is extremely large [15]. The estimates accepted today are as follows [15]: $m_\sigma = 400$–1200 MeV and $\Gamma_\sigma = 300$–500 MeV; i.e., they are rather uncertain, although the latest data corroborating a wide scalar–isoscalar resonance in $\pi\pi$ scattering appeared quite recently [16]. However, as was noted above, the large contribution of the continuum part of $\pi\pi$ spectrum results in a repulsive rather than in an attractive contribution to the NN sector. Therefore, numerous attempts at interpreting the basic internucleon attraction as that which originates from a Yukawa-type exchange of a heavy scalar meson do not seem very conclusive.

Nevertheless, there is no doubt that some scalar-meson contribution (of the σ-exchange type) is necessary for understanding numerous processes in hadron physics, e.g., for πN and NN interactions. Hence, the above deep contradiction should be somehow resolved.

We propose here a new approach to solving this puzzle. This approach is in part based on the assumption that the particle-like scalar–isoscalar excitation of the QCD vacuum, which is conventionally referred

[4)] If, however, the conventional $3N$ force is taken into account, the disagreement is considerably reduced, but there instead appears some larger disagreement for the vector (A_y) and the tensor (A_{xx}) analyzing power at the same backward angles [38].

to as the σ meson, should not be associated with this wide resonance in the $\pi\pi$ system with a mass of $m_\sigma \sim 600$ MeV. Instead of this, the scalar excitation (with a much lower mass of $m_\sigma \sim 2m_\pi$) must be considered as some sort of a quasiparticle excitation inside hadrons—in particular, inside a multiquark bag [49]. On the basis of this assumption, it can be understood very naturally why it was impossible to date to observe this "light" scalar particle in the $\pi\pi$ final-state interaction. In [50], it was suggested that a similar light scalar meson with a mass of about $2m_\pi$ can be considered as a precursor of the chiral-symmetry-restoration effect. Therefore, one can conclude that such an exchange of a "light" scalar–isoscalar quasiparticle may occur very naturally in the field of a dense six-quark bag, but that such a "light" quasiparticle cannot couple to isolated nucleons in free space.

These ideas lead very naturally to a new basic mechanism of the intermediate-range NN interaction presented in the following section.

3. DRESSED-BAG MECHANISM FOR THE INTERMEDIATE- AND SHORT-RANGE NN FORCE

From previous studies (see, e.g., [49–51]) devoted to chiral-restoration effects in multiquark systems or in high-density nuclear matter, it follows that some phase transition may occur when the quark density or the temperature of the system is increased. This phase transition leads to a restoration of broken chiral symmetry. Whatever the particular mechanism of restoration of the chiral symmetry is, the most probable consequence of the (partial) restoration should be the strengthening of the σ-meson field in the NN overlap region. This could be simulated by the "dressing" of the most compact six-quark configurations $|s^6[6]_X L=0\rangle$ and $|s^5p[51]_X L=1\rangle$ inside the NN overlap region with an effective σ-meson field.

In order to give to the reader some clue to the proposed mechanism, we display the respective graphs in Fig. 1. The Yukawa one-meson-exchange mechanism displayed in Fig. 1*a* is confronted with the new s-channel mechanism of the dressed-bag intermediate state in Fig. 1*b*. The two-pion state produced in the lower vertex in Fig. 1*b* is modified in the high-density six-quark bag in which chiral symmetry may be at least partially restored [49]. The "σ" or a similar light scalar–isoscalar meson is assumed to exist only in a high-density environment and not in a vacuum, in contrast to the π and ρ mesons. It will be demonstrated here that this mechanism, being combined with an additional orthogonality requirement, can describe both the short-range repulsion and the intermediate-range attraction and can replace the t-channel exchange of σ and ω mesons in the conventional Yukawa-type picture of the NN force.

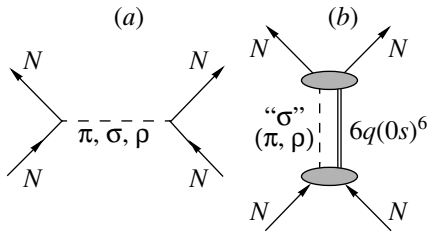

Fig. 1. (*a*) Traditional t-channel meson-exchange mechanism, along with the new s-channel "dressed"-bag mechanism (*b*) for NN interaction.

Instead of the light "σ" meson in Fig. 1*b*, other mesons like π and ρ can also be considered within this mechanism. The contributions of π, σ, and ρ mesons will depend on the total angular momentum and on the spin–isospin and permutation symmetry of the corresponding six-quark state. Thus, we adopt the s-channel quark–meson intermediate states, the transition amplitude being determined by s-channel singularities in sharp contrast to the Yukawa mechanism driven by t-channel meson exchange (see Fig. 1*a*). Surely, together with this specific six-quark mechanism, we should also take into consideration the traditional Yukawa mechanism for π, 2π, and ρ (but not σ) exchanges between isolated nucleons. However, these meson-exchange contributions are significant only at separations beyond the intermediate six-quark bag or in high partial waves ($L > 3$). In the lowest partial waves, the intermediate dressed six-quark bag makes a dominant contribution to the total NN interaction. It is appropriate to refer henceforth to the present microscopic force model as a Moscow–Tübingen dressed-bag model.

It is worth noting that the above-mentioned "compact" s^6 and s^5p $6q$ configurations are usually included in RGM calculations for the NN system, but they play quite a passive role in the standard RGM approach, providing only the "dying-out" of the NN wave function at a short range as the result of the destructive interference between the nonexcited s^6 and s^5p and the nearest excited $s^4p^2(L=0)$ and $s^3p^3(L=1)$ configurations in even- and odd-parity states. In our model, we use the "dressed bags" (DB) $\Psi^L_{\rm DB} = |s^6+\sigma\rangle$ or $|s^5p+\sigma\rangle$ instead of the "bare" quark configurations s^6 and s^5p in the RGM approach.

In this analysis, we employ the results of previous studies in this field [52–58]. The six-quark wave function in the NN-overlap region in low partial waves ($L=0$–3) can be represented as a restricted sum of the shell-model configurations satisfying the Pauli exclusion principle (with the restriction to configurations with only minimal numbers of harmonic-

oscillator quanta) [52–54, 57]:

$$\Psi_{6q} \to |(0s)^6[6]_X, [f_{CS}], L=0; ST\rangle \quad (1)$$
$$+\sum_{f'} C_{f'}|(0s)^4(1p)^2[42]_X, [f'_{CS}], L=0(2); ST\rangle$$

for even waves ($[f_{CS}] = [2^3]$ for $ST = 10$ and $[2^21^2]$ for $ST = 01$) and

$$\Psi_{6q} \to |(0s)^5(1p)[51]_X, [f_{CS}], L=1; ST\rangle \quad (2)$$
$$+\sum_{f'} C_{f'}|(0s)^3(1p)^3[3^2]_X, [f'_{CS}], L=1(3); ST\rangle$$

for odd waves ($[f_{CS}] = [2^21^2]$ for $ST = 00$ and [321] for $ST = 11$), where $[f'_{CS}] = [42]$, $[321]$, $[2^3]$, $[31^3]$, $[21^4]$ are all possible color–spin (CS) Young diagrams for the inner product $[2^3]_C \circ [42]_S$ for $S = 1$ and $[f'_{CS}] = [2^3]_C \circ [3^2]_S = [3^2]$, $[41^2]$, $[2^21^2]$, $[1^6]$ for $S = 0$.

For example, in the triplet S- and D-wave NN scattering (in the deuteron channel, $L = 0, 2$, $ST = 10$, $J^P = 1^+$), the allowed six-quark configurations

$$d_0 = |(0s)^6[6]_X, [2^3]_{CS}, L=0; ST=10\rangle, \quad (3)$$
$$d_{f'}^{L=0,2} = |(0s)^4(1p)^2[42]_X, [f'_{CS}],$$
$$L=0,\ 2; ST=10\rangle$$

correspond to state vectors of very different nature: while the unexcited six-quark state d_0 corresponds to the maximal overlap of all six quarks, the states with mixed symmetry $d^L_{f'}$, $L = 0, 2$ lead to cluster-like nodal NN relative-motion wave functions $|2s(r)\rangle$ and $|2d(\mathbf{r})\rangle$ (see, e.g., [56]):

$$\langle N(123)N(456)|d_0\rangle = \Gamma_{d_0} U^{NN}_{f_0} |0s(r)\rangle, \quad (4)$$
$$\langle NN|d^{L=0}_{f'}\rangle = \Gamma_{d_{f'}} U^{NN}_{f'} |2s(r)\rangle,$$
$$\langle NN|d^{L=2}_{f'}\rangle = \Gamma_{d_{f'}} U^{NN}_{f'} |2d(\mathbf{r})\rangle,$$

where $\mathbf{r} = \frac{1}{3}(\mathbf{r}_1 + \mathbf{r}_2 + \mathbf{r}_3 - \mathbf{r}_4 - \mathbf{r}_5 - \mathbf{r}_6)$, $|N(123)\rangle = |s^3[3]_X[21]_{CS}\rangle \sim \exp[-\frac{1}{2b}(\frac{1}{2}\rho_1^2 + \frac{2}{3}\rho_2^2)]$, b is the "quark radius" of the nucleon (about 0.6 fm), $\boldsymbol{\rho}_1 = \mathbf{r}_1 - \mathbf{r}_2$, $\boldsymbol{\rho}_2 = \frac{1}{2}(\mathbf{r}_1 + \mathbf{r}_2) - \mathbf{r}_3$, and f_0 and f' are the Young diagrams $f_0 = \{[1^6]_{CST}, [2^3]_{CS}\}$ and $f' = \{[f'_{CST}], [f'_{CS}]\}$. The quantities $\Gamma_{d_0} = 1$ and $\Gamma_{d^L_{f'}} = -\sqrt{\frac{4}{45}}$ ($L = 0, 2$) are the coordinate parts of the fractional-parentage coefficients (f.p.c.) of the translationally invariant shell model (TISM), while the $U^{NN}_{f_0}$ and $U^{NN}_{f'}$ are the respective CST parts of them.

Therefore, we propose that, at short NN distances, the total (antisymmetrized) six-quark wave function of the system $\Psi^L_{\rm tot}(6q)$ consists of two mutually orthogonal parts: the "proper NN component" $\Psi^L_{NN}(6q)$, which is dominated by the excited six-quark configurations s^4p^2 at $L = 0$ (or the s^3p^3 at $L = 1$), and the "proper $6q$ component" $\Psi^L_0(6q)$, which is dominated by the compact configuration s^6 (or the s^5p at $L = 1$). Thus, when projecting the component $\Psi^L_{NN}(6q)$ onto the $N(3q)N(3q)$ cluster channel, we obtain the NN wave function $\psi^L_{NN}(\mathbf{r}) = \langle N(123)N(456)|\Psi^L_{NN}(6q)\rangle$, which should be similar to the nodal NN wave function of the Moscow potential model [54, 58, 59].

In contrast to this clusterlike state $\Psi^L_{NN}(6q)$, the s^6 and s^5p configurations are dressed by an enhanced σ field (i.e., the DB components, e.g., $\Psi^L_{\rm DB} = |d_0 + \sigma(\pi\pi)\rangle$) and play the same role in the hadronic sector as the $\Delta\Delta + \pi\pi$ intermediate state in the standard (hadron) models of the NN interaction (see, e.g., [5, 6] and references therein). However, the dressed bag $|6q + \sigma(\pi\pi)\rangle$ has a much more extended physical content than the $\Delta\Delta + \pi\pi$ intermediate state in the traditional NN models: (i) The six-quark part of the DB implies a coherent sum over all possible baryon–baryon pairs in the cluster decomposition $3q + 3q$, e.g., $d_0 = a_{NN}NN + a_{\Delta\Delta}\Delta\Delta + \sum_{ij} a_{ij}C_iC_j$, where the factors $a_{B_1B_2}$ are the (total) f.p.c. (ii) The σ-meson (or $\pi + \pi$) part of the DB is probably enhanced owing to a (partial) chiral-symmetry restoration, which implies the reduction of the σ-meson and constituent quark masses [49, 51].

Thus, we can treat the DB states as a new component in Fock space or a new (closed) channel in the coupled-channel approach to the NN scattering and write the total NN six-quark wave function $\Psi^{LJ}_{\rm tot}$ in the form

$$\Psi^{LJ}_{\rm tot} = \begin{pmatrix} \Psi^{LJ}_{NN}(6q) \\ \Psi^{LJ}_{\rm DB}(6q+\sigma) \end{pmatrix}, \quad (5)$$
$$\Psi^{LJ}_{\rm DB}(6q+\sigma) = \Psi^{LJ}_0(6q) \times \sigma(\pi\pi),$$

where the "proper" NN wave function $\Psi^{LJ}_{NN}(6q)$ is orthogonal to the six-quark part of the DB component $\Psi^{LJ}_0(6q)$ [54, 58, 59]:

$$\langle \Psi^{LJ}_{NN}(6q)|\Psi^{LJ}_0(6q)\rangle = 0, \quad L = 0,\ 1. \quad (6)$$

Our first task here is to evaluate the amplitude of the transition from the proper NN state $\Psi^{L'J}_{NN}(6q)$ [satisfying the orthogonality condition (6)] to the DB state $\Psi^{LJ}_{\rm DB}(6q + \sigma)$. It implies the emission of a σ meson (or the S-wave correlated $\pi + \pi$ state) in a transition from the initial $s^4p^2(L' = 0,\ 2)$ (or s^3p^3 at

$L' = 1, 3$) six-quark configurations to the intermediate one $s^6(L=0) + (\pi\pi)$ [or $s^5p + (\pi\pi)$ at $L=1$] (see Fig. 2).

In the graph in Fig. 2, the pions are created in S waves owing to the conservation of parity and angular momentum. The intermediate six-quark configuration $s^5p[51]_X$ (denoted by a vertical dashed line in the graph) for $L = 0, 2$ even partial waves in the NN channel has fixed quantum numbers that are determined by the initial (NN) and intermediate ("dressed"-bag $6q + \sigma$) states. The second (after the first pion emission) state in the $ST = 01,\ J^P = 0^+$ channel has quantum numbers of the so-called d' dibaryon (see, e.g., [60, 61]):

$$|d'\rangle = |(0s)^5(1p)[51]_X[321]_{CS}, \quad LST = 110,\ J^P = 0^-\rangle. \tag{7}$$

The transition into the $ST = 10,\ J^P = 1^+$ channel proceeds via an intermediate state d'', which is a partner of d' with S and T interchanged:

$$|d''\rangle = |(0s)^5(1p)[51]_X[2^21^2]_{CS}, \quad LST = 101,\ J^P = 1^-\rangle. \tag{8}$$

It should be noted that both configurations d' and d'' cannot decay into two-nucleon states since the quantum numbers do not satisfy the Pauli exclusion principle for two nucleons. Due to this feature, they were considered previously as candidates for narrow dibaryon resonances that were suggested to be responsible for a resonance-like structure observed in (π^+, π^-) double-charge-exchange processes [60, 61].

The transition amplitude is calculated here within the well-known quark-pair-creation model (QPCM) [62] (see also [60, 61] for details). In the QPCM, the transition operator for the emission of the pion π^λ ($\lambda = 0, \pm$) by a single (e.g., the sixth) quark in a six-quark system can be written in the form [60]

$$H^{(6)}_\lambda(\mathbf{k}_6) = v\,\tau^{(6)}_{-\lambda} e^{i\frac{5}{6}\mathbf{k}_6\cdot\boldsymbol{\rho}'_5}\hat{O}^{(6)}(\boldsymbol{\rho}_5, \boldsymbol{\rho}'_5) \times \boldsymbol{\sigma}^{(6)}\left[\frac{\omega_\pi}{2m_q}\left(\frac{2}{i}\boldsymbol{\nabla}_{\rho_5} + \frac{5}{6}\mathbf{k}_6\right) + \left(1 + \frac{\omega_\pi}{12m_q}\right)\mathbf{k}_6\right], \tag{9}$$

where the nonlocal factor

$$\hat{O}^{(6)}(\boldsymbol{\rho}_5, \boldsymbol{\rho}'_5) = \exp[-i\frac{1}{2}\mathbf{k}_6(\boldsymbol{\rho}_5 - \boldsymbol{\rho}'_5)]\Psi_\pi(\boldsymbol{\rho}_5 - \boldsymbol{\rho}'_5),$$

$\boldsymbol{\rho}_5 = \frac{1}{5}(\mathbf{r}_1 + \mathbf{r}_2 + \ \ldots + \mathbf{r}_5) - \mathbf{r}_6$ is proportional to the pion wave function Ψ_π. For the calculation, we employ here shell-model quark configurations for the pion and the σ meson [63],

$$\pi^\lambda = |s\bar{s}[2]_X LST = 001\, T_z = \lambda\ J^P = 0^-\rangle, \tag{10}$$
$$\sigma = |s^2\bar{s}^2[4]_X, LST = 000, J^P = 0^+\rangle,$$

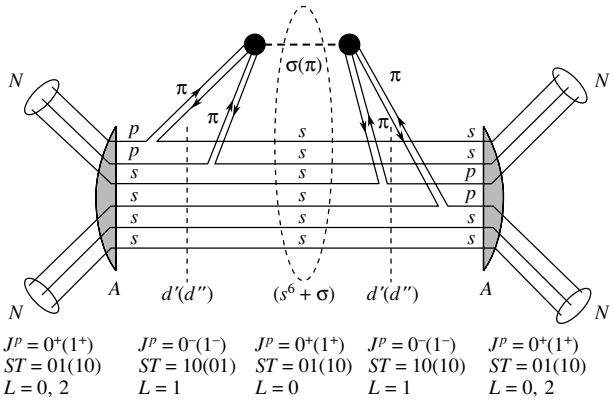

Fig. 2. Graph illustrating two sequential π-meson emissions and absorptions via an intermediate σ (or ρ) meson and the generation of a six-quark bag.

with Gaussian wave functions, e.g., $\Psi_\pi(\boldsymbol{\rho}_\pi) \sim \exp(-\rho^2_\pi/4b^2_\pi)$, $\boldsymbol{\rho}_\pi(ij) = \mathbf{r}_i - \mathbf{r}_j$, where b_π is the "quark radius" of the pion (about $0.5b \approx 0.3$ fm). In the limit of a pointlike pion [$b_\pi \to 0$; i.e., $\Psi_\pi(\boldsymbol{\rho}_\pi) \to \delta(\boldsymbol{\rho}_\pi)$], the operator $H^{(6)}_\lambda$ in (9) tends to the standard pseudovector (PV) quark–pion coupling and the phenomenological constant v in (9) becomes the PV coupling constant:

$$v = -i\,\frac{f_{\pi qq}}{m_\pi}\frac{1}{(2\pi)^{9/2}(2\omega_\pi)^{1/2}}; \tag{11}$$

here, $f_{\pi qq}$ should be normalized to the well-known pion–nucleon PV coupling constant: $f_{\pi qq} = \frac{3}{5}f_{\pi NN}$.

The $\pi + \pi \to \sigma$ transition amplitude was found [63] to be proportional to the overlap of the two pion and the σ-meson wave functions:

$$\langle\pi(\mathbf{k})\pi(\mathbf{k}')|H_{\pi\pi\sigma}|\,\sigma\rangle = f_{\pi\pi\sigma}F_{\pi\pi\sigma}((\mathbf{k} - \mathbf{k}')^2), \tag{12}$$
$$F(\mathbf{k}^2) = \exp\left(-\frac{1}{2}k^2b^2_\sigma\right).$$

Here, b_σ is a characteristic scale of the σ meson in the $\pi\pi$ channel. When this expression is compared with (9) and (11), it becomes obvious that

$$f_{\pi\pi\sigma} = \frac{g_{\pi\pi\sigma}}{(2\pi)^{3/2}(2\omega_\pi(k_6))^{1/2}(2\omega_\pi(k_5))^{1/2}(2\omega_\sigma(k))^{1/2}},$$

where $g_{\pi\pi\sigma}$ is the standard $\pi\pi\sigma$ coupling constant.

The $NN^{L=0,2}(s^4p^2) \to d'(d'') + \pi \to 6q(s^6) + \sigma$ transition amplitude can be written as a matrix element of the transition operator $\Omega_{NN\to d_0+\sigma}$ (the nondiagonal coupling potential for the nucleon–nucleon and bressed-bag states):

$$A^{L=0(2)}_{NN\to d_0+\sigma}(E;\mathbf{k}) = \int d^3r\,\Psi^{L=0(2)}_{NN}(E;\mathbf{r})\,\Omega_{NN\to d_0+\sigma}(E;\mathbf{r},\mathbf{k}). \tag{13}$$

Here, $\Psi_{NN}^{L=0(2)}(E;\mathbf{r})$ is the proper NN wave function in the sense of Eqs. (5) and (6), $E = 2m_N + p_N^2/m_N$, and the plane-wave approximation is used for the intermediate DB state [this plane-wave state is just included in the expression for $\Omega_{NN\to d_0+\sigma}$ in (13) through the elementary vertices $\langle\pi\pi|H_{\pi\pi\sigma}|\sigma\rangle$ and $\langle d'(d'')|H_{-\lambda}^{(5)}|d_0\rangle$; see below].

The operator (nondiagonal potential) $\Omega_{NN\to d_0+\sigma}$ corresponds to the left half of the graph in Fig. 2, the six-quark state being projected onto the two-nucleon clusters of the initial state. For the operator $\Omega_{NN\to d_0+\sigma}$, the total expression can be written as an integral of the elementary six-quark transition amplitude with respect to both inner coordinates of quark clusters [$N(123)$, $N(456)$, π, and σ] and the pion momenta $\mathbf{k}_5$ and $\mathbf{k}_6$ (see the triangle diagram in Fig. 3):

$$\Omega_{NN\to d_0+\sigma}(E;\mathbf{r},\mathbf{k}) = 15(2\pi)^3\int d^3k_5\int d^3k_6\,\delta(\mathbf{k}_5+\mathbf{k}_6-\mathbf{k})\sum_\lambda(-1)^\lambda \tag{14}$$
$$\times\frac{\sqrt{10}\,\langle NN|H_\lambda^{(6)}(\mathbf{k}_6)|\,d'(d'')\rangle\,\langle d'(d'')|H_{-\lambda}^{(5)}(\mathbf{k}_5)|\,d_0\rangle\,f_{\pi\pi\sigma}F_{\pi\pi\sigma}((\mathbf{k}_5-\mathbf{k}_6)^2)}{\left[m_{d'}+k_6^2/(2m_{d'})+\omega_\pi(k_6)-E\right]\left[m_{d_0}+k^2/(2m_{d_0})+\omega_\pi(k_5)+\omega_\pi(k_6)-E\right]}.$$

The numerical factor of 15 in front of the integral takes into account the number of qq pairs in the six-quark system. In calculating the amplitude in (13), it is reasonable first to project the initial NN state onto the basis of six-quark configurations $|n,f\rangle = |s^{n_s}p^{n_p}[f_X]\,[f_{CS}]LST,\ J^P\rangle$ by inserting the identity operator

$$I = \sum_{n,f}|n,f\rangle\langle n,f| \tag{15}$$

into the matrix element $\langle NN|H_\lambda^{(6)}(\mathbf{k}_6)|d'(d'')\rangle$ corresponding to the left vertex of the triangular graph in Fig. 3 (the symbols n and f are defined here as $n=\{n_s,n_p\}$, $f=\{[f_X],\,[f_{CS}]\}$).

In the case of the emission of S-wave pions, only the excited six-quark configurations $d_{f'}^{L=0(2)}$ in the sum (15) are important [while the baglike configuration d_0 does not contribute to the amplitude (13) because of the orthogonality condition (6) for the wave function $\Psi_{NN}^L(E)$]. Thus, one can decompose the vertex matrix element $N+N\to d'(d'')$ in the integrand of (14) as

$$\langle NN|H_\lambda^{(6)}(\mathbf{k}_6)|d'(d'')\rangle \tag{16}$$
$$=\sum_f\langle NN|d_f^{L=0(2)}\rangle\,\langle d_f^{L=0(2)}|H_\lambda^{(6)}(\mathbf{k}_6)|d'(d'')\rangle$$

and use the overlap factors from (4).

All matrix elements of interest are calculated by using the f.p.c. technique [53] (see also [60, 61] for details) and are reduced to a standard form of the vertex matrix element as the product of the vertex constant $vf_{\pi AB}$, the form factor $F_{\pi AB}(k_i^2)$, and the kinematical factor $\omega_\pi(k_i)/m_qb$ (as was determined earlier in [60]):

$$\langle d_f^{L=0(2)}|H_\lambda^{(6)}(\mathbf{k}_6)|d'\rangle \tag{17}$$
$$= v\frac{\omega_\pi(k_6)}{m_qb}f_{\pi d_fd'}^L F_{\pi d_fd'}^L(k_6^2)\,\Sigma^{d_fd'}\,T_{-\lambda}^{d_fd'},$$
$$\langle d'|H_\lambda^{(5)}(\mathbf{k}_5)|d_0\rangle$$
$$= v\frac{\omega_\pi(k_5)}{m_qb}f_{\pi d'd_0}F_{\pi d'd_0}(k_5^2)\,\Sigma^{d'd_0}\,T_{-\lambda}^{d'd_0}.$$

In (17), $\Sigma^{d_fd'}$ and $T_{-\lambda}^{d_fd'}$ are transition operators in the space of the total spin and isospin, respectively, of the six-quark states d_f and d'; the transition form factors F^L depend on the angular momentum $L=0(2)$ of the initial state: $F_{\pi d_fd'}^L(k_6^2) = (1+a_L5k_6^2b^2/24)\times\exp(-5k_6^2b^2/24)$ and $F_{\pi d_0d'}(k_5^2)=\exp(-5k_5^2b^2/24)$, where $a_{L=0}=4/19$ and $a_{L=2}=-13/43$.

Substituting the vertex amplitudes (12), (16), and (17) into (14), we find that, in the case of S and D partial waves in the initial NN channel, the transition operator (14) is given by the simple expression

$$\Omega_{NN\to d_0+\sigma}^L(E;\mathbf{r},\mathbf{k}) \tag{18}$$
$$= g_Le^{-5k^2b^2/48}D^L(E,k)\times\begin{cases}|2s(r)\rangle, L=0\\ |2d(\mathbf{r})\rangle, L=2,\end{cases}$$

where g_L stands for the effective strength constants for the transitions $N+N\to d_0+\sigma$ from the initial (clusterlike) NN states to the intermediate dressed-bag configuration. Specifically, they are given by

$$g_L = \frac{f_{\pi qq}^2}{m_\pi^2}\,\frac{g_{\pi\pi\sigma}}{m_q^2b^2}\,C_L, \tag{19}$$

$$C_L = 15\sqrt{10}\, f_{\pi d_0 d'} \sum_f f^L_{\pi d_f d'} \Gamma_{d_f} U^{NN}_f$$

$$= \frac{1}{81\sqrt{3}} \left\{ \begin{array}{c} -\dfrac{19\sqrt{5}}{6}, L=0 \\ \dfrac{43}{3}, L=2 \end{array} \right\} \approx \mp 10^{-1},$$

where the coefficients Γ_{d_f} and U^{NN}_f are defined according to (4) and the vertex constants $f_{\pi d_0 d'}$ and $g_{\pi\pi\sigma}$ are taken from (12) and (17).

The function $D^L(E,k)$ corresponds to the loop-integration in Fig. 3. By denoting the variable of integration as $\mathbf{q} = \mathbf{k}_5 - \mathbf{k}_6$, one can recast the integral in (14) into the form

$$D^L(E,k) = \frac{1}{128(2\pi)^3} \qquad (20)$$

$$\times \int d^3q \left[1 + \frac{5}{24} a_L \left(\frac{\mathbf{k}-\mathbf{q}}{2}\right)^2 b^2\right] e^{-q^2B^2}$$

$$\times \left[\left(m_{d_0} + \frac{k^2}{2m_{d_0}} + \omega_\pi(\frac{\mathbf{k}-\mathbf{q}}{2}) + \omega_\pi(\frac{\mathbf{k}+\mathbf{q}}{2}) - E\right)\right.$$

$$\left. \times \left(m_{d'} + \frac{1}{2m_{d'}}(\frac{\mathbf{k}-\mathbf{q}}{2})^2 + \omega_\pi(\frac{\mathbf{k}-\mathbf{q}}{2}) - E\right)\right]^{-1}$$

with $B^2 = 5b^2/48 + b^2_\sigma/8$ and $\omega_\pi(\frac{\mathbf{k}\pm q}{2}) = \sqrt{m^2_\pi + (\frac{\mathbf{p}\pm\mathbf{q}}{2})^2}$.

Thus, the calculation of the multiloop diagram in Fig. 2 results in a separable amplitude of the NN interaction, with left- and right-hand vertices being represented in the form (18) [with $D^L(E,k)$ being taken from (20)]; the loop integral over the intermediate $|0s^6 + \sigma\rangle$ state is expressed in terms of the function (a generalized propagator of the dressed bag)

$$G_{LL'}(E) = \frac{4\pi}{(2\pi)^3} \int_0^\infty k^2\, dk \qquad (21)$$

$$\times \frac{\exp\left(-\frac{5}{24}k^2b^2\right) D^L(E,k) D^{L'}(E,k)}{2\omega_\sigma(k)(E - \mathcal{E}(k))},$$

$$\omega_\sigma(k) = \sqrt{m^2_\sigma + k^2},\ \ \mathcal{E}(k) = m_{d_0} + \frac{k^2}{2m_{d_0}} + \omega_\sigma(k).$$

In accordance with this, the contribution of the mechanism displayed in the diagram in Fig. 2 to the NN interaction in the S and D partial waves can be expressed in terms of the matrix element

$$A^{L'L}_{NN\to d_0+\sigma\to NN} \qquad (22)$$

$$= \int d^3r' d^3r \Psi^{L'*}_{NN}(E;\mathbf{r}') V^{L'L}_E(\mathbf{r}',\mathbf{r}) \Psi^L_{NN}(E;\mathbf{r}),$$

where $V^{L'L}_E(\mathbf{r}',\mathbf{r})$ is a separable potential of the form

$$V^{L'L}_E(\mathbf{r}',\mathbf{r}) = \left(\begin{array}{cc} g_0^2 G_{00}(E) |2s(r')\rangle\langle 2s(r)| & g_0 g_2 G_{02}(E) |2s(r')\rangle\langle 2d(\mathbf{r})| \\ g_2 g_0 G_{20}(E) |2d(\mathbf{r}')\rangle\langle 2s(r)| & g_2^2 G_{22}(E) |2d(\mathbf{r}')\rangle\langle 2d(\mathbf{r})| \end{array} \right). \qquad (23)$$

This interaction operator mixes S and D partial waves in the triplet NN channel; thus, it leads to a specific tensor mixing with a range of about 1 fm (approximately equal to that of the intermediate DB state).

Thus, the proposed new mechanism of NN interaction at intermediate and short ranges that is induced by the intermediate dressed six-quark bag $|s^6 + 2\pi\rangle$ results in a specific matrix separable form of interaction with nodal (in S and P partial waves) form factors and a specific tensor mixing of new type (see also [64]). This nodal behavior of form factors makes it possible to explain, within this mechanism, the origin of the NN repulsive core by the nodes in transition form factors and by the conditions additionally requiring that NN and intermediate $6q$-bag components be orthogonal. We can then treat the expression derived for the NN-scattering amplitude as an energy-dependent potential and solve the Schrödinger equation with this potential. This means some way of summation of an infinite series of such loop diagrams.

In the case of (partial) restoration of chiral symmetry within the (compact) symmetric six-quark bag, the effective σ-meson mass and width should be lower than their vacuum values (m_σ tends to the two-pion mass [50, 51]). It is possible that the d_0 mass also becomes lower because of the respective reduction of the constituent quark mass. The position of the branch point $E_0 = m_{d_0} + m_\sigma$ of the function $G_{LL'}(E)$ in (21)–(23) must then be shifted lower on the energy scale, and the contribution of this (attractive) mechanism to the low-energy NN interaction must become more important. We suggest that just this shift of the branch point (and of the respective cut on the energy sheet) to lower energies because of a partial restoration of chiral symmetry may be responsible for the strong attraction at intermediate distances, which is usually attributed in conventional OBE models to

Table 1. Model parameters for various partial waves

$^{2s+1}L_J$	Λ, GeV	$r_0^{\rm orth}$, fm	λ_{11}	λ_{22}	λ_{12}	r_{01}, fm	r_{02}, fm	E_0, MeV	χ^{2*}
$^1S_0(< 600$ MeV)	0.65	0.3943	2.055			0.59686		356	1.09
$^1S_0(< 1.2$ GeV)	0.65	0.3943	4.565			0.5106		550	3.9
$^1D_2$	0.65		0.02463			0.79403		330	0.028
$^3S_1$–^3D	0.5936	0.3737	7.201	0.007928	0.2294	0.45469	0.65652	681	1.7
$^3D_2$	0.5527		0.01038			0.86037		800	0.062
$^3D_3$–$^3G_3$	0.5936		0.002927	0.1753	0.02624	0.89971	0.42893	800	0.11
$^1P_1$	0.7324	0.46572	28.74			0.44311		600	0.167
$^3P_0$	0.65	0.3445	0.02841			0.455		400	0.14
$^3P_1$	0.65	0.4491	3.195			0.51749		600	0.13
$^3P_2$–$^3F_2$	0.65		0.03124	−0.006486	0.000765	0.70995	0.75653	360	0.71

* The χ^2 value is defined here as usual: $\chi^2 = \frac{1}{N}\sum_{i=1}^{N}(\delta^{\rm PSA}(E_i) - \delta^{\rm theor}(E_i))^2$.

σ-meson exchange (in t channel) between two nucleons. In other words, instead of the (artificial) increase in the cutoff parameters in the πNN (σNN, ρNN, etc.) form factors, as in conventional OBE models, we adopt a (natural) decrease in the denominator in (21) due to (partial) restoration of chiral symmetry.

Thus, the proposed new mechanism can resolve a deep contradiction of the current NN force models based on the OBE mechanism with new results for the exchange of a 2π correlated pair [17]. In fact, it was found in [17] that the exchange of an S-wave correlated $\pi\pi$ pair between two unexcited nucleons cannot generate any strong attraction of nucleons but, instead of this, results in a strong repulsion at short and intermediate ranges. On the other hand, the excitation of two intermediate deltas with artificially enhanced $\pi N\Delta$ form factors may formally explain the intermediate-range attraction [5–7].

The complicated energy dependence dictated by (21) may be well approximated by a pole term proportional to $(E - \bar{E}_0)^{-1}$ with the effective pole position $\bar{E}_0$ either calculated from our formulas or simply fitted to NN phase shifts. In the next section, we develop a simple illustrative model to test the proposed new mechanism.

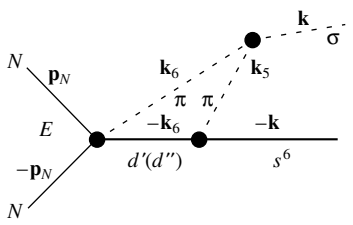

Fig. 3. Kinematical variables in the triangle diagram corresponding to the σ-meson (or ρ-meson) generation from two π mesons emerging in the transition of two p-shell quarks into the s orbit (see also Fig. 2).

4. SIMPLE MODEL

In this section we study the NN-interaction mechanism developed in preceding section by considering the example of a simple illustrative model. For this purpose, we parametrize the basic potential components involved in this model via a simple analytic form that includes the main features of the above mechanism. We want to emphasize that the simple model presented here serves only as an illustration rather than as a demonstration of the quality of the new formulation of the NN force. The new model includes only a few basic parameters (e.g., $q\pi\pi$, σNN, etc., coupling constants) for the NN force. But the full formulation of the model includes a rather tedious calculation for all intermediate loop integrals; for this reason, we postpone this calculation to future studies.

Thus, the model interaction consists of three terms: the orthogonalizing potential $V_{\rm orth}$ providing the condition of orthogonality between the proper NN channel and the six-quark intermediate bag in S and P waves; the one-pion-exchange (OPE) potential $V_{\rm OPE}$ with a soft dipole truncation; and the separable term V_{NqN} with an energy dependence described by a pole [which is the simplest approximation to a quark-induced interaction corresponding to the separable potential $V_E^{L'L}$ (23) of the virtual transition $NN \to (6q + 2\pi) \to NN$] as illustrated by the graph in Fig. 2: $V_{NN} = V_{\rm orth} + V_{NqN} + V_{\rm OPE}$, where

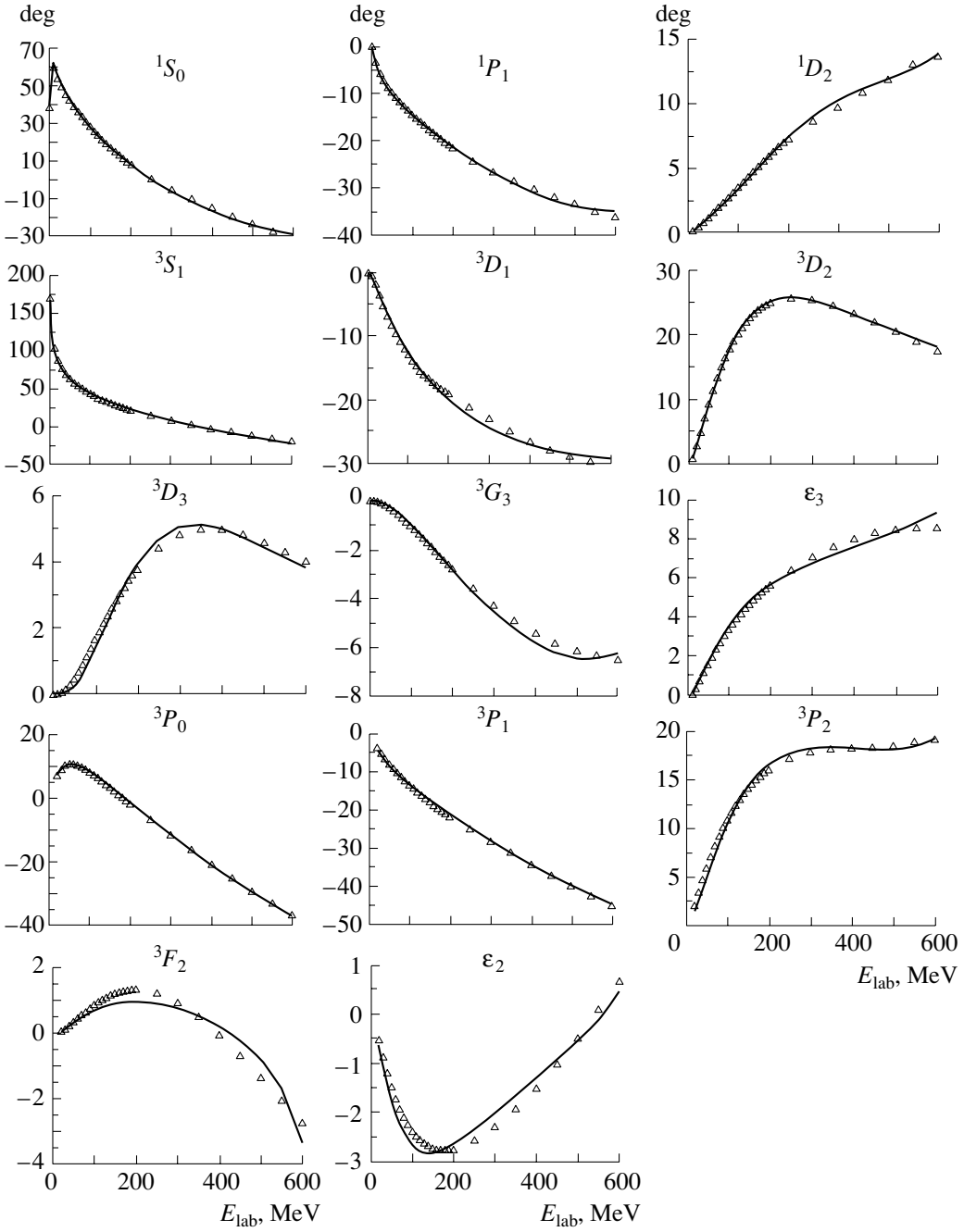

Fig. 4. *NN* phase shifts and mixing parameters in our simple model, along with data from a phase-shift analysis (SAID, solution SP99 [65]).

$V_{\text{orth}} = \lambda_0|\varphi_0\rangle\langle\varphi_0|$ and $\lambda_0 \to \infty$. In the momentum representation, the OPE term takes the form

$$V_{\text{OPE}}(\mathbf{k}) = \frac{f_\pi^2}{m^2}\frac{1}{\mathbf{k}^2+m^2}\left(\frac{\Lambda^2-m^2}{\Lambda^2+\mathbf{k}^2}\right)^2 \times (\boldsymbol{\sigma}_1\cdot\mathbf{k})(\boldsymbol{\sigma}_2\cdot\mathbf{k})\frac{(\boldsymbol{\tau}_1\cdot\boldsymbol{\tau}_2)}{3}.$$

For the single-channel case, the bag-induced term V_{NqN} is given by

$$V_{NqN} = \frac{E_0^2}{E-E_0}\lambda|\varphi\rangle\langle\varphi|,$$

while, for coupled channels, it is the 2×2 matrix [compare with (23)]

$$V_{NqN} = \frac{E_0^2}{E-E_0}\begin{pmatrix}\lambda_{11}|\varphi_1\rangle\langle\varphi_1| & \lambda_{12}|\varphi_1\rangle\langle\varphi_2| \\ \lambda_{21}|\varphi_2\rangle\langle\varphi_1| & \lambda_{22}|\varphi_2\rangle\langle\varphi_2|\end{pmatrix}, \quad (24)$$

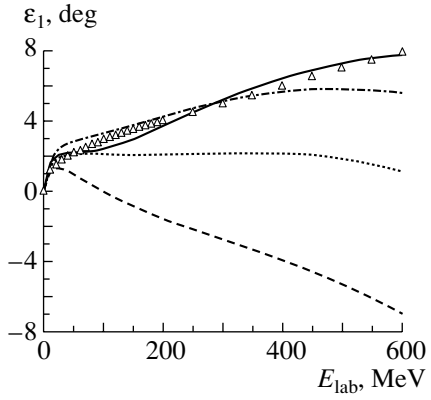

Fig. 5. Mixing parameter ε_1 for various values of the cutoff parameter $\Lambda_{\pi NN}$ (see main body of the text).

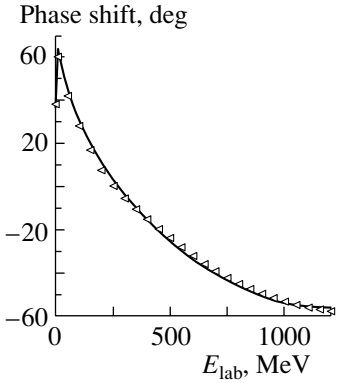

Fig. 6. $^1S_0$ phase shifts fitted by means of our simple model for $E_{\rm lab}$ up to 1200 MeV.

where it is assumed $\lambda_{12} = \lambda_{21}$. For all form factors $\varphi_i(r)$ in the above equations, we use the simple Gaussian form with one scale parameter r_0,[5)]

$$\varphi_i(r) = Nr^{L_i+1} \exp\left(-\frac{1}{2}\left(\frac{r}{r_0}\right)^2\right). \qquad (25)$$

In the calculations, we have used the averaged pion mass $m = (m_{\pi^0} + 2m_{\pi^\pm})/3$, the averaged pion–nucleon coupling constant $f_\pi^2/(4\pi) = 0.075$, and a soft cutoff parameter taking values in the range $\Lambda = \Lambda_{\rm dipole} = 0.50$–$0.75$ GeV.

The results of the fits of the model parameters λ_k (or λ_{jk}), r_0, and E_0 to the NN phase-shift analysis data are displayed in Figs. 4–6. It is quite evident that this simple model describes low NN partial waves up to $E_{\rm lab} = 600$ MeV very well. The model phase shifts and the mixing parameter ε_1 are compared in Figs. 4–6 with data of a recent phase-shift analysis (SAID, solution SP99 [65]). There are three adjustable parameters for each partial wave: λ (λ_k or λ_{jk} for coupled channels), r_0, and E_0. The parameters of the projection operators (r_0 for $V_{\rm orth}$) are taken from [54], where a deep local attractive potential (Moscow potential) was constructed as an effective NN one-component potential. The parameter E_0 corresponds to the sum of the six-quark-bag excitation energy and the effective σ-meson mass inside the six-quark bag (minus the mass of two nucleons, $2m_N$). Its value is taken here in the range 600–1000 MeV. In accordance with our suggestions, it should be the same for all partial waves of definite parity. We have found that the results depend on E_0 only weakly. All parameters found for S, P, and D waves are given in Table 1.

It is highly instructive to compare the present simple model based on the suggested new mechanism for NN interaction with the well-known phenomenological separable potential [66] (so-called Graz potential), which fits the same phase shifts up to $E_{\rm lab} = 500$ MeV. From a comparison, the reader can find that the number of free parameters in the Graz potential is much larger than that in our simple model, whereas the energy range is smaller and the quality of the fit is poorer for the Graz model. Thus, our simple model describes NN data more adequately than the Yamaguchi-type phenomenological model.

Moreover, it was very surprising to find that this simple model provides a very good description of the $^1S_0$ phase shifts even up to $E_{\rm lab} = 1200$ MeV (see Fig. 6) (there is presently no np phase-shift analysis at higher energies).

We want to discuss here especially the description of phase shifts in the $^3S_1$–$^3D_1$ triplet coupled channels. The crucial point is the behavior of the mixing parameter ε_1 with increasing energy. Without a separable (quark-bag-induced) mixing potential (i.e., at $\lambda_{12} = 0$), the behavior of ε_1 is correct only at very low energies, but it is in strong disagreement with the phase-shift analysis at energies higher than 50 MeV (see the dashed curve in Fig. 5). The increase in the cutoff parameter Λ up to values of 0.8 GeV does not help to obtain better agreement with the data; on the contrary, this destroys a good description at low energies (the dotted curve in Fig. 5). Introducing the quark-bag-induced mixing [$\lambda_{12} \neq 0$ in (24)] allows us to reproduce the behavior of ε_1 (and of the $^3S_1$–$^3D_1$ phase shifts as well) with a reasonable accuracy up to an energy as high as $E_{\rm lab} \sim 600$ MeV, but only for sufficiently small values of $\Lambda_{\pi NN}$. The best fit for the mixing parameter ε_1 is shown on Fig. 5 (solid curve), with the potential parameter values being given in Table 1, where $\Lambda_{\pi NN} = 0.5936$ GeV.

[5)] It is still in accordance with our general algebraic multiquark formalism due to the appearance of the additional orthogonality condition (see the respective orthogonalizing potential $V_{\rm orth}$ above).

In this case, the condition

$$\lambda_{12}^2 = \lambda_{11}\lambda_{22} \tag{26}$$

is satisfied. It is just this condition that follows approximately from our preliminary calculations of the loop integrals incorporated in the potential matrix (23). The increase in the value of $\Lambda_{\pi NN}$ up to 0.8 GeV results in the violation of condition (26) and in a significant deterioration of the description of ε_1 (see the curve in Fig. 5). Other phase shifts ($^3S_1$ and $^3D_1$) are reproduced for all four versions to the same good accuracy, so that we present, in Fig. 4, the results for only one version.

Thus, we can deduce, from the results of our simple model presented in this section, that the model is able to describe all phase shifts in low partial waves ($L = 0$–2) in a rather broad energy interval (0–600 MeV). This good description and the above comparison with the phenomenological Graz model seems to support the new dressed-bag mechanism proposed here for the intermediate-range interaction.

5. RELATIONSHIPS WITH OTHER INTERACTION MODELS

In this section, we will briefly discuss the interrelations of the new NN mechanism suggested here with other models proposed in previous years and clarify the microscopic grounds for some of them.

While the symmetry background of the Moscow potential models [54–59, 67, 68] is rather similar to that of the present model, the underlying mechanisms and the particular realizations are very different. In the above potential models, one starts with a subdivision of the possible spatial (permutational) six-quark symmetries of the total wave function into two types of different physical origins, $\Psi_{\rm bag}\left((0s)^6[6]\right) + \Psi_{NN}\left((0s)^4(1p)^2[42]\right)$, which are orthogonal to each other. By excluding the baglike components from the proper NN channel, one then arrives at an effective interaction Hamiltonian in the NN channel [58, 69] with an additional orthogonality-condition constraint:

$$\left(T_R + V_{\rm ME} + 10\frac{|f\rangle\langle f|}{E - E_0}\right)\tilde{\chi} = E\tilde{\chi}, \tag{27a}$$

$$\langle g|\tilde{\chi}\rangle = 0. \tag{27b}$$

In these equations, $\tilde{\chi}(R)$ is the wave function that describes NN relative motion and which is renormalized through the overlap kernel $\mathcal{N}(\mathbf{R}, \mathbf{R}')$ to have a probabilistic meaning [69]. Here, $V_{\rm ME}$ is the sum of conventional meson-exchange potentials cut off at the proper (i.e., soft) values of Λ_{mNN}; the form factor $f(\mathbf{R})$ in the separable term of (27a), $\langle \mathbf{R}|f\rangle \equiv f(\mathbf{R}) = \langle \psi_{6q}|H|\psi_N\psi_N\rangle$, is the matrix element that couples the six-quark and NN channels; and the function $g(\mathbf{R})$ in the orthogonality condition (27b) is taken to be $\langle \mathbf{R}|g\rangle \equiv g(\mathbf{R}) = \langle \psi_{6q}|\psi_N\psi_N\rangle$.

In the initial version of the one-channel Moscow NN potential [55, 58, 68], one then replaces both the separable term in (27a) and the orthogonality condition (27b) by one deep local potential, where deeply lying bound states (which are considered as "forbidden" states in the model) ensure fulfillment of the orthogonality condition (27b) due to the Hermicity of the underlying potential.

Thus, the previous Moscow NN potential model is essentially a local effective potential phase-shift-equivalent to a highly nonlocal and energy-dependent model (27). Our next step was the generalized orthogonality-condition model [54], where we still retained the deep local potential, but where we did not use the bound-state wave function in the orthogonality condition. Thus, from this point of view, the above-mentioned NN model can be considered as a generalized orthogonality-condition model initially proposed by Saito in nuclear cluster physics [70] as early as 1969. Very similar to the cluster model, the deep attractive well of the one-channel Moscow NN potential represents a local phase-shift-equivalent potential for a nonlocal and energy-dependent interaction term in (27a), together with the orthogonality-condition constraint (27b). As a result of the constraint, the NN phase shifts in low partial waves (S and P) display a behavior similar to that of phase shifts for local repulsive-core potentials [71]. The orthogonality condition results in a stationary (with respect to the energy variation) short-range node in the NN wave function of relative motion rather than in a strong damping of the latter near the origin. Moreover, the node position ($r_n \simeq 0.6$ fm) agrees very nearly with the radius of the repulsive core in the traditional force models like the Reid soft-core (RSC) model [71].

In this way, the short-range stationary node in the wave function for relative motion replaces a large portion of the repulsive core; thus, the coupling constant for ω-meson exchange can be reduced safely to moderate values of $g^2_{\omega NN}/4\pi \simeq 5$ dictated by $SU(3)$ symmetry. Thus, the new dressed-bag model presented in this study provides a microscopic quark–meson realization of previous Moscow-type NN models (e.g., it explains the strong intermediate-range attraction in the Moscow model).

There are also rather tight relationships between the current mechanism and hybrid models like QCB [72] suggested previously for NN interaction. The total wave function for the NN system in the hybrid models [72, 73] is composed, similarly to our basic assumption, from two components of different origins:

the quark compound-bag part at small distances $r \leq R_0$ and the proper clusterlike NN component in the peripheral region $r > R_0$, with R_0 being the matching radius between the two components. Analogously to our formal derivation [69], the baglike component is then eliminated in the QCB approach [72], and one arrives at an effective one-channel Schrödinger equation for the NN component analogous to (27a). However, in the hybrid models, in contrast to our model, two basic components—i.e., Ψ_{6q} and Ψ_{NN}—are taken to be nonorthogonal to each other.[6)] However, when the two channels are orthogonalized in the QCB approach, the scattering wave functions in the NN channel develop a short-range node rather similar to that in our case but with a violation of the continuity at the matching radius R_0.

But the main difference between the hybrid-model approach and the current model lies in the fact that a typical hybrid model essentially represents a phenomenological approach that does not consider any microscopic or field-theoretical aspects. However, the fact that, starting from absolutely independent arguments (in fact, we started, more than two decades ago, from the old phenomenological Moscow-type NN potential [74]), we arrive at a model that, in its formal aspects, has many similarities with hybrid models, shows that both models reflect the true underlying physical picture rather adequately.

There are also very interesting connections between our approach and the Tabakin potential. More than 30 years ago, Tabakin, to facilitate drastically Faddeev few-nucleon calculations, proposed [75] a phenomenological one-term separable potential "with repulsion and attraction." The characteristic feature of the Tabakin potential is an oscillating behavior of the potential form factor $g(p)$ in S waves: $V_{\rm T}(p,p') = \lambda g_{\rm T}(p) g_{\rm T}(p')$ with $g_{\rm T}(p) = (p^2 - p_0^2) f(p^2)$, where f is a smooth nodeless function.

At that time, the success of the Tabakin potential was considered to be somewhat "accidental" and puzzling.[7)] However, about a decade ago, Nakaishi-Maeda demonstrated [77] that the Tabakin potential can be considered, to a very good approximation, as the first term in the unitary-pole expansion of the t matrix for the deep local Moscow NN potential, while the scattering wave functions for both models display short-distance stationary nodes (at $r_n \simeq 0.6$ fm) in very similar ways. Moreover, it was shown [77] that the continuum bound state in the Tabakin potential has an energy of $E_{\rm lab} \simeq 300$ MeV and is very similar in structure to the "forbidden" bound state in the initial version of the Moscow potential.

However, the analogy between the new quark–meson mechanism suggested in the present study and the old Tabakin potential goes much further. In fact, the overlap factors (4) between three-quark nucleon clusters and six-quark configurations $|s^4p^2[42], L=0, ST\rangle$ and $|s^6[6], L=0, ST\rangle$ inevitably lead to nodal $2s$-type relative-motion form factors in our separable potential term V_{NqN}. In the momentum representation, this form factor has the form

$$g_{2s}(p) = N_{2s}(p^2 - p_0^2)\exp(-\frac{3p^2}{4p_0^2}), \qquad (28)$$

which exhibits the same nodal character with the same node position at p_0^2 as the Tabakin form factor. The use of the $2s$-type form factor (28) will project out all the admixtures of nodeless $0s$ components in NN scattering wave functions, giving, in this way, a stable short-range node in the S wave at $r_0 \simeq 0.6$ fm. Thus, the use of oscillating $2s$-type form factors replaces, to a good approximation, our orthogonality-condition constraints, resulting, as a matter of fact, in virtually the same scattering wave functions. This gives a quark microscopic interpretation for the success of the old phenomenological Tabakin potential. From here, one can conclude that there are many completely independent arguments in favor of our new interaction mechanism suggested here.

5. CONCLUSION

We have presented a critique of the conventional meson-exchange models of nuclear forces at intermediate and short ranges. We have provided many arguments clearly demonstrating inner inconsistencies and contradictions in modern OBE models for the short-range part of the interaction. There are also several observations in few-nucleon systems showing clearly that one cannot explain quantitatively and consistently many $3N$ and $4N$ experimental data with the existing NN models.

To find an alternative picture of the NN interaction, we have exploited the successful quark-motivated semiphenomenological models, viz., the Moscow model [54, 68, 69], the extensive microscopic studies of six-quark system in the shell-model approach [52, 56, 57, 60, 61], and Tübingen microscopic quark approaches [78–80], to develop them further. In this way, we have suggested, in the present study, some new mechanism for

[6)] This nonorthogonality of two basic components in QCB leads to an appearance of some ghost state at infinity, which can be considered as an analog of deeply bound "forbidden" states in our approach.

[7)] Almost simultaneously with the Tabakin study, we suggested [76] very similar separable potentials to describe cluster–cluster interaction for systems like ^{4}He^{4}He and ^{4}Hed, where all lowest partial phase shifts also change sign (from positive to negative) at rather low energies.

the intermediate- and short-range NN interaction. This mechanism differs from the traditional Yukawa concept of meson exchange in the t channel. We have introduced a concept of the dressed symmetric six-quark bag in the intermediate state with s-channel propagation. In a tight connection to this mechanism, we have also proposed a new interpretation of the "light" scalar–isoscalar σ meson as a quasiparticle. The new interaction mechanism proposed here has been shown to lead to separable energy-dependent s-channel resonance-like interaction terms with nodal form factors (in lowest partial waves) that result from the orthogonality-condition constraint.

In its final form, the proposed interaction depends only on a few fundamental constants (quark–meson or diquark–meson coupling constants and the intermediate-meson masses), so that, eventually, the total NN force can be parametrized in terms of only a few free parameters. However, at the present stage, we prefer to employ the derived form of the interaction to build a simple model whose main goal is to illustrate how well the suggested mechanism can work. We have found that, by adjusting only three parameters of the model in each partial wave, it is possible to describe excellently all lowest NN phase shifts in the broad energy interval 0–600 MeV and the S waves even up to 1200 MeV in the laboratory frame. This gives some strong evidence that the suggested new microscopic mechanism of the s-channel dressed symmetric bag should work adequately.

The proposed interaction model has been demonstrated to give a natural microscopic background for previous phenomenological interaction models like the Moscow NN potential and the Tabakin separable potential "with attraction and repulsion" and also for the various hybrid models. Thus, it also gives important bridges between absolutely disconnected (at first glance) models developed previously.

Another important result of the present model could be a possible solution to the long-standing puzzle of the weak vector-meson contribution to the baryon spectra and a strong spin–orbit splitting (due to the vector-meson contribution) in the NN interaction. If one assumes a significant quark–quark force due to vector-meson (or one-gluon) exchange, vector coupling will also immediately result in strong spin–orbit splitting in the baryon spectra. Recently, Glozman and Riska [81] suggested a new model for the qq interaction mediated essentially by Goldstone boson exchange to describe baryon spectroscopy. The model can naturally describe the absence of spin–orbit splitting in negative-parity excited baryon states. However, the model fails to explain strong spin–orbit splitting in the NN sector. Our explanation of the puzzle is based on the fact that there is no significant vector-meson contribution to qq forces (in the t channel) [81], but there is an important contribution of vector mesons to the dressing of the symmetric six-quark bag, thereby leading to strong spin–orbit effects in the NN interaction mediated by the dressed bag.

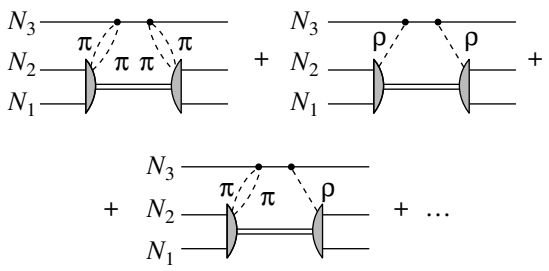

Fig. 7. Some graphs illustrating the new type of $3N$ forces.

Moreover, the proposed model will lead to the appearance of strong $3N$ and $4N$ forces mediated by 2π and ρ exchanges (see, e.g., $3N$-force graphs in Fig. 7). It is easy to see that the new $3N$ forces include both central and spin–orbit components. Such a spin–orbit $3N$ force is extremely desirable for explaining the low-energy puzzle of the analyzing power A_y in Nd scattering [12, 31] and also the behavior of A_y in the $3N$ system at higher energies of $E_N \simeq 250$–350 MeV at backward angles [38, 39]. The central components of the $3N$ and $4N$ forces are expected to be strongly attractive; thus, they must contribute to $3N$- and $4N$-binding energies, possibly resolving thereby the very old puzzle of the binding energies of the extremely light nuclei. Moreover, these strong contributions (as one can expect) of the above $3N$ and $4N$ forces mediated by the "σ-type" 2π exchange to nuclear binding, in combination with strong relativistic effects predicted by our model [9, 55, 59], can lead very naturally to relativistic hadrodynamics (i.e., the Walecka model), where the σ field constitutes the main agent for nuclear binding. The suggested new mechanism leads to a large number of new contributions for many nuclear-physics observables, like enhanced Coulomb displacement energies for isobar analog states [67, 69], more significant relativistic effects, and a new interpretation of meson-exchange-current contributions. Further studies must show the degree to which such expectations can be justified.

ACKNOWLEDGMENTS

We express our deep gratitude to many colleagues for continuous encouragement. We appreciate very much stimulating discussions with Prof. W. Gloeckle and his group on the nature of discrepancies found

Table 2. Scalar factors $\Gamma^{S=1}_{CS}([f_{CS}]([f'_{CS}]\times[f''_{CS}]), s_{56})$ of the Clebsch–Gordan coefficients for the group $SU(6)_{CS} \subset SU(3)_C \times SU(2)_S$ [see Eq. (A.9)]

	$[2^2]_{CS}\times[2]_{CS}$		$[21^2]_{CS}\times[1^2]_{CS}$	
	$[2^2]_C\times[2]_C$ $[2^2]_S\times[2]_S$	$[21^2]_C\times[1^2]_C$ $[31]_S\times[1^2]_S$	$[2^2]_C\times[2]_C$ $[31]_S\times[1^2]_S$	$[21^2]_C\times[1^2]_C$ $[2^2]_S\times[2]_S$
$[42]_{CS}$	$\sqrt{\frac{1}{20}}$	$-\sqrt{\frac{9}{20}}$	0	0
$[321]_{CS}$	$\sqrt{\frac{8}{15}}$	$-\sqrt{\frac{2}{15}}$	$\sqrt{\frac{2}{9}}$	$\sqrt{\frac{8}{27}}$
$[2^3]_{CS}$	$\sqrt{\frac{5}{12}}$	$\sqrt{\frac{5}{12}}$	$\sqrt{\frac{5}{18}}$	$-\sqrt{\frac{5}{54}}$
$[31^3]_{CS}$	0	0	$-\sqrt{\frac{1}{18}}$	$-\sqrt{\frac{25}{54}}$
$[21^4]_{CS}$	0	0	$\sqrt{\frac{4}{9}}$	$-\sqrt{\frac{4}{27}}$

in few-nucleon systems. Special thanks are due to Prof. S. Moszkowski for his permanent support of our studies. We also thank Prof. M. Rosina.

The work of the Russian authors was supported in part by the Russian Foundation for Basic Research (grant RFBR–DFG no. 92-02-04020) and by the Deutsche Forschungsgemeinschaft (grant no. Fa-67/20-1).

APPENDIX A

Details of Quark-Model Calculations

Here, we consider some details of the quark-model calculations of the two-pion-emission amplitude for the transition from the $^3S_1(^3D_1)$ NN state to the dressed six-quark bag $d_0+\pi+\pi$. We will demonstrate here how to use the known f.p.c. technique [52, 53, 56, 57, 60] in the calculations of the two-step process $d_f \to d'' + \pi \to d_0 + \pi + \pi$ in the $ST = 10$ $J^P = 1^+$ channel. First, we consider two-pion emission in the two-quark subsystem "56" (where "5" and "6" are the quark numbers in the six-quark system "123456"). We start from the $2s(2d)$ harmonic-oscillator state of the sixth quark in the d_f state [see Eqs. (3), (7), and (8) in Section 3], which, after S-wave pion emission, goes over to the $1p$ harmonic-oscillator state in the 56 subsystem of the intermediate d'' configuration. At the next step, the fifth quark of the 56 subsystem emits another S-wave pion and the intermediate d'' configuration goes over to the final d_0 configuration in which the 56 subsystem is in the $0s$ harmonic-oscillator state. Therefore, we must take into consideration the following five nonvanishing elementary $q \to q + \pi$ transition amplitudes in the harmonic-oscillator quark basis:

(i) the two amplitudes

$$T^{(6)}_{2s\to 1p}(j_{56}=0) \equiv \langle 1p, s_{56}=1(j_{56}=0), \quad t_{56}=0|H^{(6)}_{\pi qq}|2s, s_{56}=0, t_{56}=1\rangle = i\,v\sqrt{\frac{2}{3}}\frac{\omega_\pi(k_6)}{2m_q\alpha}(1/2||\sigma||1/2) \times\sqrt{\frac{1}{6}}(1/2||\tau||1/2)F_2^{L=0}(k_6^2), \tag{A.1}$$

$$T^{(5)}_{1p\to 0s}(j_{56}=0) \equiv \langle 0s, s_{56}=0, t_{56}=1|H^{(5)}_{\pi qq}|1p, s_{56}=1(j_{56}=0), t_{56}=0\rangle = i\,v\,\frac{\omega_\pi(k_5)}{2m_q\alpha'}(1/2||\sigma||1/2)\sqrt{\frac{1}{6}}(1/2||\tau||1/2)F_0(k_5^2)$$

should be taken if the total angular momentum of the 56 subsystem is $j_{56} = 0$, and

(ii) the three amplitudes

$$T^{(6)}_{2s\to 1p}(j_{56}=1) \equiv \langle 1p, s_{56}=0(j_{56}=1), \quad t_{56}=1|H^{(6)}_{\pi qq}|2s, s_{56}=1, t_{56}=0\rangle = -i\,v\,\frac{\sqrt{2}}{3}\frac{\omega_\pi(k_6)}{2m_q\alpha}(1/2||\sigma||1/2) \times\sqrt{\frac{1}{6}}(1/2||\tau||1/2)F_2^{L=0}(k_6^2), \tag{A.2}$$

$$T^{(6)}_{2d\to 1p}(j_{56}=1) \equiv \langle 1p, s_{56}=0(j_{56}=1), \quad t_{56}=1|H^{(6)}_{\pi qq}|2d, s_{56}=1, t_{56}=0\rangle = -i\,v\,\frac{\sqrt{2}}{3}\frac{\omega_\pi(k_6)}{2m_q\alpha}(1/2||\sigma||1/2) \times\sqrt{\frac{1}{6}}(1/2||\tau||1/2)F_2^{L=2}(k_6^2),$$

$$T^{(5)}_{1p\to 0s}(j_{56}=1) \equiv \langle 0s, s_{56}=1(j_{56}=0), t_{56}=0|H^{(5)}_{\pi qq}|1p, s_{56}=0, t_{56}=1\rangle = -i\,v\sqrt{\frac{1}{3}}\frac{\omega_\pi(k_6)}{2m_q\alpha'}(1/2||\sigma||1/2) \times \sqrt{\frac{1}{6}}(1/2||\tau||1/2)F_0(k_5^2)$$

should be taken in the case of $j_{56}=1$.

To simplify matters, we use the shorthand notation $T^{(6)}_{2s\to 1p}(j_{56}=1)$, $T^{(5)}_{1p\to 0s}(j_{56}=0)$, etc., for the elementary amplitudes and omit spin, isospin, and angular momentum projections (omitting summation over these quantum numbers in the ensuing expressions). A further shorthand notation is $\alpha=\sqrt{6/5}\,b$ and $\alpha'=-\sqrt{5/2}\alpha$, where b is the scale parameter (rms radius) of the harmonic-oscillator basis functions, and

$$F_0(k_5^2)=\exp\left(-\frac{5}{24}k_5^2b^2\right), \qquad (A.3)$$

$$F_2^L(k_6^2)=\left(1+\frac{5}{24}a_Lk_6^2b^2\right)\exp\left(-\frac{5}{24}k_6^2b^2\right),$$

where $a_L=4/19$ if $L=0$ and $a_L=-13/43$ if $L=2$. The functions in (A.3) provide the k^2 dependence of the form factors in the $\pi d''d_f$ and $\pi d_0d''$ vertices [see Eq. (17) in Section 3],

$$F_{\pi d_0d''}(k_5^2)=F_0(k_5^2),\ F^L_{\pi d''d_f}(k_6^2)=F_2^L(k_6^2). \qquad (A.4)$$

The reduced matrix elements $(1/2||\sigma||1/2)$ and $(1/2||\tau||1/2)$ of the spin(isospin)-flip operators (i.e., σ and τ matrices in the vertex operators $H^{(6)}_{\pi qq}$ and $H^{(5)}_{\pi qq}$) are defined here in accordance with the Wigner–Ekkart theorem. Standard calculations yield

$$(1/2||\sigma||1/2)=(1/2||\tau||1/2)=-\sqrt{6}. \qquad (A.5)$$

Recall that, for the desired amplitude, we use the parametrization

$$15\,\langle d_0|H^{(5)}_{\pi qq}(k_5)|d''\rangle\,\langle d''|H^{(6)}_{\pi qq}(k_6)|d_f\rangle = v^2\,\frac{\omega_\pi(k_5)\omega_\pi(k_6)}{m_q^2b^2}\,f_{\pi d_0d''}f^L_{\pi d''d_f} \times F_{\pi d_0d''}(k_5^2)\,F^L_{\pi d''d_f}(k_6^2) \qquad (A.6)$$

[see Eq. (17) in Section 3]. Now, one can calculate "the coupling constants" $f_{\pi d''d_f}$ and $f_{\pi d_0d''}$ in this parametrization, starting from the elementary amplitudes (A.1) and (A.2). For this purpose, one can apply f.p.c. to separate the two-quark subsystem "56" from the six-quark configurations d_f, d'', and d_0 for all possible color, spin, isospin, and coordinate states of the quark pair ($[f_{56}]_C=[2],[1^2]$; $s_{56}=0,1$; $t_{56}=0,1$; $j_{56}=0,1$ for the $2s$, $2d$, $1p$, and $0s$ radial and orbital states). Recall that the f.p.c. technique implies summation over all possible states of the separated two-quark subsystem instead of summation over all numbers of quarks in the interaction operator. This scheme is particularly handy for application of the group-theoretical algebraic methods.

We use the invariants (i.e., the Young diagrams $[f_C]$, $[f_S]$, $[f_{CS}]$, $[f_T]$, $[f_{CST}]$, and $[f_X]$) of the chain of symmetry groups (see, e.g., [57, 60])

$$SU(12)_{CST}\supset SU(6)_{CS}\times SU(2)_T\supset SU(3)_C \times SU(2)_S\times SU(2)_T, \qquad (A.7)$$
$$SU(24)_{XCST}\supset SU(12)_{CST}\times SU(2)_X$$

to classify six-quark, four-quark, and two-quark states in the systems "123456," "1234," and "56," respectively. The f.p.c. for separation of the pair "56" in the total $XCST$ space $\Gamma_{XCST}(q^6\to q^4\times q^2)$ is the product of the "scalar factors" of the Clebsch–Gordan coefficients of groups

$$SU(6)_{CS}\supset SU(3)_C\times SU(2)_S,$$
$$SU(12)_{CST}\supset SU(6)_{CS}\times SU(2)_T,$$
$$SU(24)_{XCST}\supset SU(2)_X\times SU(12)_{CST}$$

taken from the reduction chain (A.7) (Γ_{CS}, Γ_{CST}, and Γ_{XCST}) and "orbital" f.p.c. Γ_X of the TISM:

$$\Gamma_{XCST}(q^6\to q^4\times q^2) = \Gamma_{CS}\Gamma_{CST}\Gamma_{XCST}\Gamma_X. \qquad (A.8)$$

The following extended notation for the nontrivial scalar factors Γ_{CS} is used here (see, e.g., [57]):

$$\Gamma^{S=1}_{CS}([f_{CS}]([2^2]_{CS}\times[2]_{CS}),s_{56}=1) \equiv \left(\begin{array}{c|c|c} [2^3]_C[42]_S & \| & [f_{CS}] \\ ([2^2]_C\times[2]_C)([2^2]_S\times[2]_S) & \| & ([2^2]_{CS}\times[2]_{CS})\end{array}\right), \Gamma^{S=1}_{CS}([f_{CS}]([2^2]_{CS}\times[2]_{CS}),s_{56}=0)$$

$$\equiv \left(\begin{array}{c|c|c} [2^3]_C[42]_S & \| & [f_{CS}] \\ ([21^2]_C\times[1^2]_C)([31]_S\times[1^2]_S) & \| & ([2^2]_{CS}\times[2]_{CS})\end{array}\right), \Gamma^{S=1}_{CS}([f_{CS}]([21^2]_{CS}\times[1^2]_{CS}),s_{56}=1)$$

$$\equiv \left(\begin{array}{c|c} [2^3]_C[42]_S & [f_{CS}] \\ ([21^2]_C\times[1^2]_C)([2^2]_S\times[2]_S) & ([21^2]_{CS}\times[1^2]_{CS}) \end{array} \right),$$
$$\Gamma^{S=1}_{C\cdot S}([f_{CS}]([21^2]_{CS}\times[1^2]_{CS}), s_{56}=0) \qquad (A.9)$$
$$\equiv \left(\begin{array}{c|c} [2^3]_C[42]_S & [f_{CS}] \\ ([21^2]_C\times[1^2]_C)([31]_S\times[2]_S) & ([21^2]_{CS}\times[1^2]_{CS}) \end{array} \right).$$

Here, $[f_{CS}]$ are all the CS Young diagrams from the inner product

$$[f_{CS}] = [2^3]_C \circ [42]_S = [42],\ [321],\ [2^3],\ [31^3],\ [21^4]. \qquad (A.10)$$

The values of all necessary scalar factors (A.9) are given in Tables 2 and 3.

Only the Young diagrams $[f_{CST}] = [2^21^2]$, $[21^4]$, and $[1^6]$ are important for the configurations d_f, d'', and d_0 ($[f_{CST}] = [\tilde{f}_X]$, where $[\tilde{f}_X]$ is the Young diagram conjugate to $[f_X]$). All the necessary scalar factors

$$\Gamma^{T=0}_{CST}([f_{CST}] : [f_{CS}]([2^2]_{CS}\times[2]_{CS}), t_{56}=0)$$
$$\equiv \left(\begin{array}{c|c} [f_{CS}][3^2]_T & [f_{CST}] \\ ([2^2]_{CS}\times[2]_{CS})([2^2]_T\times[1^2]_T) & ([1^4]_{CST}\times[1^2]_{CST}) \end{array} \right), \qquad (A.11)$$
$$\Gamma^{T=0}_{CST}([f_{CST}] : [f_{CS}]([21^2]_{CS}\times[1^2]_{CS}), t_{56}=1)$$
$$\equiv \left(\begin{array}{c|c} [f_{CS}][3^2]_T & [f_{CST}] \\ ([21^2]_{CS}\times[2]_{CS})([31]_T\times[2]_T) & ([1^4]_{CST}\times[1^2]_{CST}) \end{array} \right)$$

are given in Table 4. The coefficients Γ_{XCST} are trivial weight factors $\Gamma_{XCST}([6]_X([4]\times[2])) = 1$, $\Gamma_{XCST}([51]_X([4]\times[2])) = \sqrt{1/5}$, and $\Gamma_{XCST}([42]_X([4]\times[2])) = \sqrt{1/9}$ dependent only on the dimensions of the irreducible representations of the symmetric group for given Young diagrams: $n_{[6]} = 1$, $n_{[51]} = 5$, and $n_{[42]} = 9$. The last factor on the right-hand side of (A.8), the orbital f.p.c. Γ_X of the TISM, depends on the configuration; i.e., only five different values of Γ_X are necessary:

$$\Gamma_X(s^6[6](s^4[4]\times s^2[2])) = 1, \qquad (A.12)$$
$$\Gamma_X(s^4p^2 - s^52s[6](s^4[4]\times s2s[2])) = \sqrt{1/5},$$
$$\Gamma_X(s^4p^2 - s^52d[6](s^4[4]\times s2d[2])) = \sqrt{1/5},$$
$$\Gamma_X(s^5p[51](s^4[4]\times sp[2])) = -\sqrt{3/5},$$
$$\Gamma_X(s^4p^2[42](s^4[4]\times p^2[2])L = 0, 2) = -\sqrt{3/10}.$$

Thus, the total transition amplitude (A.6) is expressed in terms of the product of factors (A.1), (A.2), (A.9), (A.11), and (A.12) summed over the states of the pair "56" (summation should be extended over all possible two-quark states, but fixed quantum numbers of the initial, intermediate, and final states impose the restriction that only summation over $j_{56} = 0,\ 1$ and $[f_{56}]_{CS} = [2],\ [1^2]$ is allowed):

$$15\,\langle d_0|H^{(5)}_{\pi qq}(k_5)|d''\rangle\,\langle d''|H^{(6)}_{\pi qq}(k_6)|d_f\rangle \qquad (A.13)$$
$$= 15\sum_{j_{56}=0,\,1}\ \sum_{[f_{56}]_{CS}=[2],[1^2]} \Gamma_{X\cdot CST}([6]_X([4]\times[2]))$$
$$\times [\Gamma_{XCST}([51]_X([4]\times[2]))]^2$$
$$\times \Gamma_{XCST}([42]_X([4]\times[2]))\Gamma_X(s^6[6](s^4[4]\times s^2[2]))$$
$$\times \left[\Gamma_X(s^5p[51](s^4[4]\times sp[2]))\right]^2$$
$$\times\Gamma_X(s^4p^2[42](s^4[4]\times p^2[2])L = 0, 2)$$
$$\times \Gamma^{S=1}_{CS}([2^3]_{CS}([f_{1234}]_{CS}\times[f_{56}]_{CS}), s_{56})$$
$$\times \left[\Gamma^{S=0}_{CS}([2^21^2]_{CS}([f_{1234}]_{CS}\times[f'_{56}]_{CS}), s'_{56})\right]^2$$
$$\times \Gamma^{S=1}_{CS}([f_{CS}]([f_{1234}]_{CS}\times[f_{56}]_{CS}), s_{56})$$
$$\times\Gamma^{T=0}_{CST}([1^6]_{CST}\colon [2^3]_{CS}$$
$$\times ([f_{1234}]_{CS}\times[f_{56}]_{CS}), t_{56})$$
$$\times \left[\Gamma^{T=1}_{CST}([21^4]_{CST}\colon [2^21^2]_{CS}\right.$$

Table 3. Scalar factors $\Gamma^{S=0}_{CS}([f_{CS}]([f'_{CS}]\times[f''_{CS}]), s_{56})$ of the Clebsch–Gordan coefficients for the group $SU(6)_{CS} \subset SU(3)_C \times SU(2)_S$ [see Eq. (A.9)]

	$[2^2]_{CS}\times[1^2]_{CS}$		$[21^2]_{CS}\times[2]_{CS}$	
	$[2^2]_C\times[2]_C$	$[21^2]_C\times[1^2]_C$	$[2^2]_C\times[2]_C$	$[21^2]_C\times[1^2]_C$
	$[2^2]_S\times[1^2]_S$	$[31]_S\times[2]_S$	$[31]_S\times[2]_S$	$[2^2]_S\times[1^2]_S$
$[2^21^2]_{CS}$	$-\sqrt{\frac{3}{4}}$	$\sqrt{\frac{1}{4}}$	$-\sqrt{\frac{1}{2}}$	$\sqrt{\frac{1}{2}}$

Table 4. Scalar factors $\Gamma^{T=0(1)}_{CST}([f_{CST}]([f_{CS}]([f'_{CS}]\times[f''_{CS}])), t_{56})$ of the Clebsch–Gordan coefficients for the group $SU(12)_{CST} \subset SU(6)_{CS}\times SU(2)_T$ [see Eq. (A.11)]

	$T=0$					$T=1$
	$[42]_{CS}$	$[321]_{CS}$	$[2^3]_{CS}$	$[31^3]_{CS}$	$[21^4]_{CS}$	$[2^21^2]_{CS}$
$[2^21^2]_{CST}$:						
$([2^2]_{CS}\times[2]_{CS})\circ([2^2]_T\times[1^2]_T)$	1	$-\sqrt{\frac{3}{8}}$	$-\sqrt{\frac{3}{5}}$	0	0	
$([21^2]_{CS}\times[1^2]_{CS})\circ([31]_T\times[2]_T)$	0	$\sqrt{\frac{5}{8}}$	$-\sqrt{\frac{2}{5}}$	1	1	
$[1^6]_{CST}$:						
$([2^2]_{CS}\times[2]_{CS})\circ([2^2]_T\times[1^2]_T)$	0	0	$-\sqrt{\frac{2}{5}}$	0	0	
$([21^2]_{CS}\times[1^2]_{CS})\circ([31]_T\times[2]_T)$	0	0	$\sqrt{\frac{3}{5}}$	0	0	
$[2^21^2]_{CST}$:						
$([2^2]_{CS}\times[2]_{CS})\circ([2^2]_T\times[1^2]_T)$						$-\sqrt{\frac{4}{9}}$
$([21^2]_{CS}\times[1^2]_{CS})\circ([31]_T\times[2]_T)$						$\sqrt{\frac{1}{6}}$

$$\times\left([f_{1234}]_{CS}\times[f'_{56}]_{CS}), t'_{56}\right)\Big]^2$$
$$\times\Gamma^{T=0}_{CST}([2^21^2]_{CST}\colon [f_{CS}]([f_{1234}]_{CS}$$
$$\times[f_{56}]_{CS}), t_{56})T^{(5)}_{1p\to 0s}(j_{56})T^{(6)}_{2s(2d)\to 1p}(j_{56}).$$

The spin and isospin of the quark pair, $s_{56}(s'_{56})$ and $t_{56}(t'_{56})$, in (A.13) depend on the color quantum numbers of the pair. For example, $t_{56}=1$ ($t'_{56}=0$) for $[f_{56}]_{CS}=[1^2]$ and $t_{56}=0$ ($t'_{56}=1$) for $[f_{56}]_{CS}=[2]$. A general rule for $s_{56}(s'_{56})$ is easy to understand from the right-hand side of Eqs. (A.9). One can indicate that, in the case of $L=2$ (the ${}^3D_1$ initial state), the value of $j_{56}=0$ does not contribute to the ${}^3D_1 \to {}^3S_1$ transition, so that only the $j_{56}=1$ term should be taken on the right-hand side of (A.13). As a result, the coupling constant $f_{\pi d'' d_f}$ takes different values for $L=0$ and 2, and this is indicated by the additional superscript L: $f^L_{\pi d'' d_f}$.

The calculated values of the product $f^L_{\pi d'' d_f} f_{\pi d_0 d''}$ are given in Table 5. Substituting these values into (19), one obtains the following expression for factors

Table 5. Products of the coupling constants, $f_{\pi d_0 d''}\, f^{L=0(2)}_{\pi d'' d_f}$, for the two-step transition $d_f \to d'' + \pi \to d_0 + \pi + \pi$ with the creation of a scalar–isoscalar $\pi + \pi$ pair ("σ meson") and overlap factor U_f^{NN} between the NN and d_f states

	Quantum numbers of d_f					
	$(s^4p^2 - s^5 2s(2d))[6]_X$	$s^4p^2[42]_X$				
	$[2^3]_{CS}$	$[42]_{CS}$	$[321]_{CS}$	$[2^3]_{CS}$	$[31^3]_{CS}$	$[21^4]_{CS}$
$81\times f_{\pi d_0 d''}\, f^{L}_{\pi d'' d_f}$: $L = 0$	$\sqrt{\frac{2}{15}}$	0	$-\frac{13}{12}\sqrt{\frac{3}{2}}$	$-\sqrt{\frac{1}{30}}$	$-\frac{1}{20}\sqrt{\frac{1}{15}}$	$-\frac{1}{5}\sqrt{\frac{2}{15}}$
$L = 2$	$\frac{13}{10}\sqrt{\frac{1}{6}}$	$\frac{9}{10}\sqrt{\frac{1}{30}}$	$-\frac{31}{20}\sqrt{\frac{1}{30}}$	$-\frac{17}{20}\sqrt{\frac{1}{6}}$	$-\frac{1}{8}\sqrt{\frac{1}{3}}$	$-\frac{1}{10}\sqrt{\frac{1}{6}}$
[4pt] U_f^{NN}	$\sqrt{\frac{1}{9}}$	$-\sqrt{\frac{9}{20}}$	$\sqrt{\frac{16}{45}}$	$\sqrt{\frac{1}{36}}$	$-\sqrt{\frac{1}{18}}$	0

g_L in the transition operator (18):

$$g_L = g_{\pi\pi\sigma}\frac{f^2_{\pi qq}}{m^2_\pi}\,\frac{1}{m_q^2 b^2}\,\frac{1}{81\sqrt{3}}\times\begin{cases} -\dfrac{19\sqrt{5}}{6} & \text{for } L=0 \\ \dfrac{43}{3} & \text{for } L=2. \end{cases} \quad \text{(A.14)}$$

REFERENCES

1. H. Yukawa, Proc. Phys. Math. Soc. Jpn. **17**, 48 (1935); H. Yukawa and S. Sakata, Proc. Phys. Math. Soc. Jpn. **17**, 397 (1935); **19**, 1084 (1937).
2. G. Breit, Phys. Rev. **120**, 287 (1960).
3. G. Breit, M. H. Hull, K. E. Lassila, and K. D. Pyatt, Phys. Rev. **120**, 2227 (1960).
4. V. G. J. Stoks and J. J. de Swart, Phys. Rev. C **47**, 512 (1993); **49**, 2950 (1994); S. Nagels, T. A. Rijken, and J J. de Swart, Phys. Rev. D **17**, 768 (1978).
5. R. Machleidt, K. Holinde, and Ch. Elster, Phys. Rep. **149**, 1 (1987).
6. R. Machleidt, Adv. Nucl. Phys. **19**, 189 (1989).
7. M. Lacombe, B. Loiseau, J. M. Richard, *et al.*, Phys. Rev. C **21**, 861 (1980); Phys. Lett. B **101B**, 139 (1981).
8. G. E. Brown and A. D. Jackson, *The Nucleon–Nucleon Interaction* (North-Holland, Amsterdam, 1976).
9. V. I. Kukulin, in *Proceedings of the V PNPI Winter School in Theoretical Physics, Gatchina, 1999,* p. 142; *Symposium on Current Topics in the Field of Light Nuclei, Cracow, Poland, 1999,* p. 1339.
10. A. Picklesimer, R. A. Rice, and R. Brandenburg, Phys. Rev. Lett. **68**, 1484 (1992); Phys. Rev. C **45**, 2045 (1992); **45**, 2624 (1992).
11. W. Tornow, H. Witala, and A. Kievsky, Phys. Rev. C **57**, 555 (1998); L. D. Knutson, Nucl. Phys. A **631**, 9c (1998).
12. *Proceedings of 16th European Conference on Few-Body Problems in Physics, Autrans, France, 1998,* Few-Body Syst. Suppl. 10 (1999).
13. M. Kaiser, R. Brockman, and W. Weise, nucl-th/9706045.
14. M. Kaiser, S. Gerstendörfer, and W. Weise, nucl-th/9802071.
15. S. Spanier and N. Törnqvist, Eur. Phys. J. C **3**, 390 (1998); http://pdg.lbl.gov.
16. *Proceedings of the International Conference on High-Energy Physics (Rochester Series), Kyoto, 2000* (in press).
17. E. Oset, H. Toki, M. Mizobe, and T. Takahashi, Prog. Theor. Phys. **103**, 351 (2000).
18. D. Plaemper, J. Flender, and M. F. Gari, Phys. Rev. C **49**, 2370 (1994).
19. O. Imambekov, Yu. N. Uzikov, and L. V. Shevchenko, Z. Phys. A **332**, 349 (1989); Yu. N. Uzikov, Yad. Fiz. **60**, 1603 (1997) [Phys. At. Nucl. **60**, 1458 (1997)].
20. D. Lu, S. C. Phatak, and R. Landau, Phys. Rev. C **51**, 2207 (1995).
21. R. Bökmann, C. Hanhart, O. Krehl, *et al.,* Phys. Rev. C **60**, 055212 (1999).
22. T. E. O. Ericsson and W. Weise, *Pions and Nuclei* (Clarendon Press, Oxford, 1988).
23. V. G. Neudatchin, N. P. Yudin, and L. L. Sviridova, Yad. Fiz. **60**, 2020 (1997) [Phys. At. Nucl. **60**, 1848 (1997)].
24. L. A. Sliv, M. I. Strikman, and L. L. Frankfurt, Usp. Fiz. Nauk **145**, 553 (1985) [Sov. Phys. Usp. **28**, 281 (1985)].
25. A. W. Thomas, Phys. Lett. B **216**, 97 (1989).
26. A. Szhzurek, M. Ericson, H. Holtmann, and J. Speth, Nucl. Phys. A **596**, 397 (1996); H. Holtmann, A. Szhzurek, and J. Speth, Nucl. Phys. A **596**, 631 (1996).
27. D. M. Alde *et al.,* Phys. Rev. Lett. **64**, 2479 (1990).

28. T.-S. H. Lee, Phys. Rev. C **29**, 195 (1984); T.-S. H. Lee and A. Matsuyama, Phys. Rev. C **32**, 516 (1985); A. Matsuyama and T.-S. H. Lee, Phys. Rev. C **34**, 1900 (1986); L. A. Kondratyuk, F. M. Lev, and L. V. Shevchenko, Yad. Fiz. **33**, 1208 (1981) [Sov. J. Nucl. Phys. **33**, 642 (1981)]; O. Imambekov and Yu. N. Uzikov, Yad. Fiz. **47**, 1089 (1988) [Sov. J. Nucl. Phys. **47**, 695 (1988)].
29. V. Dmitriev, O. Sushkov, and C. Gaarde, Nucl. Phys. A **459**, 503 (1986).
30. B. F. Gibson, Lecture Notes in Physics **260**, 511 (1986); B. F. Gibson *et al.,* Few-Body Syst. **3**, 143 (1988).
31. W. Gloeckle, H. Witala, D. Hueber, *et al.,* Phys. Rep. **274**, 107 (1996).
32. R. B. Wiringa, Nucl. Phys. A **631**, 70c (1998).
33. T. Ueda, Preprint OUAM 91-1-1 (1991).
34. D. Hueber, H. Witala, H. Kamada, *et al.,* Nucl. Phys. A **631**, 663 (1998).
35. Y. Koike and S. Ishikawa, Nucl. Phys. A **631**, 683c (1998).
36. A. C. Fonseca, in: *Book of Contributions, Proceedings of 16th European Conference on Few-Body Problems in Physics, Autrans, France, 1998,* p. 59; a talk at *Symposium on Current Topics in the Field of Light Nuclei, Cracow, Poland, 1999,* p. 1070.
37. H. Witala and W. Gloeckle, Nucl. Phys. A **528**, 48 (1991); H. Witala, D. Hueber, and W. Gloeckle, Phys. Rev. C **49**, R14 (1994); L. D. Knutson, Nucl. Phys. A **631**, 9c (1998).
38. H. O. Meyer, a talk at *Symposium on Current Topics in the Field of Light Nuclei, Cracow, Poland, 1999,* p. 858.
39. H. Sakae, a talk at *Symposium on Current Topics in the Field of Light Nuclei, Cracow, Poland, 1999,* p. 890.
40. D. Hueber, H. Witala, and W. Gloeckle, Few-Body Syst. **14**, 171 (1993).
41. K. Bodek, a talk at *Symposium on Current Topics in the Field of Light Nuclei, Cracow, Poland, 1999,* p. 306.
42. O. Scholten, a talk at *Symposium on Current Topics in the Field of Light Nuclei, Cracow, Poland, 1999,* p. 259.
43. J. Golak, a talk at *Symposium on Current Topics in the Field of Light Nuclei, Cracow, Poland, 1999,* p. 278.
44. H. Block, a talk at *Symposium on Current Topics in the Field of Light Nuclei, Cracow, Poland, 1999,* p. 423.
45. F. Bonutti, P. Camerini, *et al.,* Phys. Rev. C **60**, 018201 (1999).
46. J. W. Durso, A. D. Jackson, and B. J. VerWest, Nucl. Phys. A **345**, 471 (1980).
47. V. G. J. Stoks, R. A. M. Klomp, M. C. M. Rentmeester, and J. J. de Swart, Phys. Rev. C **48**, 792 (1993).
48. Fl. Stancu, S. Pepin, and L. Ya. Glozman, nucl-th/9705030.
49. T. Hatsuda and T. Kunihiro, Phys. Rep. **247**, 221 (1994).
50. T. Hatsuda, T. Kunihiro, and H. Shimizu, Phys. Rev. Lett. **82**, 2840 (1999).
51. P. Rehberg, L. Bot, and J. Aichelin, Nucl. Phys. A **653**, 415 (1999).
52. I. T. Obukhovsky, V. G. Neudatchin, Yu. F. Smirnov, and Yu. M. Tchuvil'sky, Phys. Lett. B **88B**, 231 (1979).
53. M. Harvey, Nucl. Phys. A **352**, 301 (1981); **352**, 326 (1981).
54. V. I. Kukulin, V. N. Pomerantsev, and A. Faessler, Phys. Rev. C **59**, 3021 (1999).
55. V. I. Kukulin and V. N. Pomerantsev, Prog. Theor. Phys. **88**, 159 (1992).
56. A. M. Kusainov, V. G. Neudatchin, and I. T. Obukhovsky, Phys. Rev. C **44**, 2343 (1991).
57. I. T. Obukhovsky, Prog. Part. Nucl. Phys. **36**, 359 (1996).
58. V. I. Kukulin and V. N. Pomerantsev, in *Proceedings of the XII European Few-Body Conference, Uzhgorod, 1990,* p. 80.
59. V. I. Kukulin, in *Proceedings of the Annual Meeting of Japanese Physical Society, 1990,* p. 59.
60. I. T. Obukhovsky, A. Faessler, G. Wagner, and A. J. Buchmann, Phys. Rev. C **60**, 035207 (1999).
61. G. Wagner, L. Ya. Glozman, A. J. Buchmann, and A. Faessler, Nucl. Phys. A **594**, 263 (1995); L. Ya. Glozman, A. J. Buchmann, and A. Faessler, J. Phys. G **20**, 149 (1994).
62. L. Micu, Nucl. Phys. B **10**, 521 (1969); A. Le Yaouanc, L. Oliver, O. Pene, and J. C. Raynal, Phys. Rev. D **8**, 2223 (1973); **9**, 1415 (1974).
63. T. Gutsche, R. D. Viollier, and A. Faessler, Phys. Lett. B **331**, 8 (1994).
64. V. I. Kukulin, V. N. Pomerantsev, R. Mackintosh, and S. Cooper, Few-Body Syst., Suppl. **10**, 439 (1999); Yad. Fiz. **62**, 1187 (1999) [Phys. At. Nucl. **62**, 1114 (1999)].
65. R. A. Arndt, Chang Heon Oh, I. I. Strakovsky, and R. L. Workman, Phys. Rev. C **56**, 3005 (1997), and SAID solution SP99.
66. W. Schweiger, W. Plessas, L. P. Kok, and H. van Haeringen, Preprint UNIGRAZ-UTP 02/82 (University of Groningen, 1982).
67. V. I. Kukulin and V. N. Pomerantsev, Nucl. Phys. A **631**, 456c (1998).
68. V. I. Kukulin, V. M. Krasnopolsky, V. N. Pomerantsev, and P. B. Sazonov, Phys. Lett. B **135B**, 20 (1984); **165B**, 7 (1985).
69. V. I. Kukulin, V. N. Pomerantsev, A. Faessler, *et al.,* Phys. Rev. C **57**, 535 (1998).
70. S. Saito, Prog. Theor. Phys. **41**, 705 (1969).
71. R. V. Reid, Ann. Phys. (N.Y.) **50**, 411 (1968).
72. Yu. A. Simonov, Nucl. Phys. A **416**, 109c (1984); Yu. S. Kalashnikova, I. M. Narodetsky, Yu. A. Simonov, and A. I. Veselov, Phys. Lett. B **155B**, 217 (1985).
73. L. S. Kisslinger, Phys. Lett. B **112B**, 1307 (1982); T. S. Cheng and L. S. Kisslinger, Nucl. Phys. A **457**, 602 (1986); Phys. Rev. C **35**, 1432 (1987).
74. V. G. Neudatchin, I. T. Obukhovsky, V. I. Kukulin, and N. F. Golovanova, Phys. Rev. C **11**, 128 (1975).

75. F. Tabakin, Phys. Rev. **174**, 1208 (1968).
76. V. I. Kukulin and V. G. Neudatchin, Nucl. Phys. A **157**, 609 (1970).
77. S. Nakaishi-Maeda, Phys. Rev. C **34**, 303 (1986); **51**, 1633 (1995).
78. A. Buchmann, Y. Yamauchi, I. Ito, and A. Faessler, J. Phys. G **14**, 1037 (1988).
79. A. Faessler, F. Fernández, G. Lübeck, and K. Shimizu, Phys. Lett. B **124B**, 145 (1983); Nucl. Phys. A **402**, 555 (1983).
80. A. Buchmann, Y. Yamauchi, and A. Faessler, Nucl. Phys. A **496**, 621 (1989); Phys. Lett. B **225**, 301 (1989); Prog. Part. Nucl. Phys. **24**, 333 (1990); Y. Yamauchi, A. Buchmann, and A. Faessler, Nucl. Phys. A **494**, 401 (1989).
81. L. Ya. Glozman and D. O. Riska, Phys. Rep. **268**, 263 (1996); L. Ya. Glozman, Z. Papp, and W. Plessas, Phys. Lett. B **381**, 311 (1996).

Physics of Atomic Nuclei, Vol. 64, No. 9, 2001, pp. 1689–1703. Translated from Yadernaya Fizika, Vol. 64, No. 9, 2001, pp. 1769–1783.

ELEMENTARY PARTICLES AND FIELDS
Theory

New Approach to Solving the Problem of Composite-Particle Scattering on Nuclei

O. A. Rubtsova* **and V. I. Kukulin**

Institute of Nuclear Physics, Moscow State University, Vorob'evy gory, Moscow, 119899 Russia

Received June 30, 2000; in final form, January 12, 2001

Abstract—An essentially new approach to solving the problem of elastic and inelastic scattering of a composite particle on stable nuclei is described. Within this approach, all channels of virtual breakup and stripping in the intermediate states are included in a nonlocal complex-valued interaction operator with the aid of the projection-operator technique. The three-particle continuum spectrum of the Hamiltonian for intermediate states in Q space is calculated within the orthogonalizing-pseudopotential method by introducing a pseudo-Hamiltonian, which is diagonalized in a full space in terms of a relevant oscillator basis. As was shown by a number of authors, the use of special quadratures makes it possible to reduce integration over the continuous spectrum of intermediate states to summation over a discretized continuum. On the basis of the formalism developed in this study, a closed Schrödinger equation with a nonlocal complex potential for partial waves is derived for describing elastic scattering of a composite particle by a target, and an explicit approximate formula for the amplitude of three-particle breakup is obtained on the same basis. This method has a number of obvious advantages over currently well-known approaches of the type of the discretized-continuum coupled-channel method, where solving the problem in question reduces to solving a cumbersome set of coupled equations. © *2001 MAIK "Nauka/Interperiodica"*.

1. INTRODUCTION

The present study is devoted to constructing a new method for solving the quantum problem of elastic and inelastic scattering of a composite particle on a nucleus with allowance for inelastic channels within the three-particle problem. Processes of this type are exemplified by the scattering or breakup of a deuteron or a ^{7}Li nucleus by a heavy nucleus. An exact solution to this problem is described either by the set of Faddeev equations (which is very difficult to solve in the realistic case of complex-valued potentials featuring Coulomb interaction) or within the Schrödinger formalism by an infinite (continual) set of integro-differential equations that relate the elastic-scattering channel to an infinite number of breakup and stripping channels. Since it is hardly possible to solve this set of equations exactly, a method is required for discretizing the three-particle continuum of the $A + 2N$ system in order to reduce the infinite continual set of coupled equations to a finite set of equations. Much effort has been devoted to developing such methods over the past 25 years [1–10]. They were dubbed discretized-continuum coupled-channel (DCCC) methods.

Originally, the DCCC method was developed to solve the problem of the elastic and the inelastic scattering (breakup) of a deuteron on a nucleus [1, 2]; later on, it was extended by Sakuragi *et al.* (see, for example, [3]) to the cases of the elastic scattering and the breakup of, say, ^{6,7}Li and ^{12}C nuclei only for the two-fragment channel of projectile breakup. This seems justified for ^{7}Li and hardly justified for ^{6}Li, ^{12}C, etc., nuclei.

Presently, two approaches of this type [9, 10] have been developed to the greatest extent. Either is based (for example, in the case of deuteron–nucleus scattering) on discretizing the continuum of excited states in the coordinate of the relative motion of the np pair. Within the first of these [1–5], the discretization is performed by partitioning the continuous spectrum of the sub-Hamiltonian h_{np} describing the relative motion of the np pair into bands, localized wave packets being constructed within each of these. Within the second approach [6–10], the discretization is performed by expanding the wave functions for the continuous spectrum of the np subsystem in terms of square-integrable functions. Upon discretization by one of the above methods, the number of breakup channels becomes finite. Further, the full three-particle wave function for the $A + d$ system is expanded in a series in a discrete set of functions that describe the relative motion of the np pair. Finally, one obtains a set of great, but finite, number of coupled

*e-mail: rubtsova@nucl-th.npi.msu.su

second-order differential equations, which is solved by numerical methods.

Within these approaches, a vast body of experimental data on the elastic and inelastic scattering, as well as breakup, of ^{2}H, ^{6,7}Li, ^{9}Be, ^{12}C, etc., nuclei on medium-mass and heavy nuclei was analyzed in the 1980s and 1990s, predominantly by Japanese scientists. It was shown that, in many cases, good agreement with experimental could be obtained at projectile energies of 10–50 MeV per nucleon [3, 6, 8, 10]. However, the DCCC method has some series drawbacks hindering the application of this method, for example, in the case of nonlocal interactions of fragments with a target nucleus or in currently very popular cases of the elastic scattering of unstable ^{6}He, ^{8,9,11}Li, ^{12}Be, etc., nuclei on a stable target, because these cases cannot be reduced to the two-particle (virtual or real) fragmentation of a projectile in the interactions with a target. In addition, attempts at including, in the calculations, virtual excitations of not only the projectile but also of the target run into formidable technical difficulties.

Apart from these drawbacks of a fundamental character, the DCCC approach involves many methodological difficulties, such as a rather slow (and, in all probability, nonuniform) convergence in the number of channels being included and also the unwieldiness of the calculations. This slow convergence, which is observed primarily at large scattering angles is probably due to the fact that, in the DCCC approach, the interaction between projectile constituents—for example, the np interaction in the case of deuteron scattering on a stable nucleus—is considered to be dominant. Therefore, the three-particle scattering wave functions $\Psi(\mathbf{k};\mathbf{r},\mathbf{R})$ are expanded in series in the eigenfunctions of the sub-Hamiltonian h_{np} for the np interaction. All intermediate states in the three-particle continuum are then considered as a deuteron occurring in an excited state and moving as a discrete unit in the field of the target nucleus, but this is correct only at large distances from the force center. At the same time, large-angle deuteron scattering is governed primarily by the pair interactions of the particles n and p with the target nucleus, the np interaction playing the role of a correction. This means that, in the vicinity of the target nucleus, intermediate states must have a structure where each projectile constituent moves in the nuclear field along its orbit, which is weakly perturbed by the other projectile constituents. In the scattering of loose nuclei, such as ^{2}H, ^{6,7}Li, and ^{9}Be, the main contribution is expected to come from those single-particle orbits whose energies and angular momenta correspond to the kinetic-energy and total-angular-momentum distributions of the projectile in accordance with the fragment masses.

The physical idea of the method formulated in the present study is based on the observation that, in the elastic scattering of a composite particle by a nucleus at medium and large angles, the scattering amplitude receives contributions only from the regions of the multiparticle configuration space that correspond to rather small distances between all projectile constituents and the target nucleus. In other words, only the intrinsic parts of multiparticle-continuum wave functions must be taken into account. Therefore, a discretization of the L_2 type on the basis of square-integrable functions similar to those that are used in the shell model [11] must be sufficient. In mathematical terms, this approach amounts to including, with the aid of the Feshbach projection-operator formalism, all three-particle breakup and stripping channels that appear as intermediate states for elastic scattering in the nonlocal operator of interaction between the composite particle and the target nucleus. Further, the exact wave functions appearing in this nonlocal interaction operator and corresponding to inelastic channels are expanded in a three-particle discrete oscillator basis. This is the way in which the total intermediate three-particle continuum is discretized. In this (projection-operator) formulation of the scattering problem, a full summation over the set of states of the discretized three-particle continuum occurs; therefore, we can hope that local errors of discretization in the intermediate states will not affect the final results.

The ensuing exposition is organized as follows.

The second section of our study is devoted to deriving an equation for the elastic-scattering wave function on the basis of the Feshbach projection-operator formalism by introducing the operators that project the full space of functions for the original Hamiltonian onto the subspace corresponding to the elastic-scattering channel and the subspace that is orthogonal to it and which is associated with breakup channels. We obtain two equations relating the elastic-scattering channel to inelastic-scattering channels. By formally eliminating the component $Q\Psi$ that corresponds to the sum of all inelastic channels from the above set of equations, we arrive at a single equation for the elastic-scattering component $P\Psi$. In this equation, the (virtual) contribution of all breakup and stripping channels is represented by a nonlocal energy-dependent operator including integration over the continuous spectrum of intermediate states. For the wave function describing the elastic scattering of a composite particle in a given partial wave, we eventually obtain a single wave equation with a nonlocal energy-dependent potential.

A method for constructing the spectrum of the three-particle Hamiltonian for intermediate states in the subspace Q, which is orthogonal to the intrinsic

wave function for the incident composite particle, and its implementation in practice are discussed in Section 3. In Section 4, we briefly describe the scheme of the discretization of the continuum for the case of the two-fragment projectile breakup on the target nucleus. In Section 5, we discuss all basic results of our study. In Section 6, we present a brief summary.

We have also included two appendices in this article. In Appendix A, we present explicit formulas for the matrix elements corresponding to transitions from the elastic channel to inelastic channels. In Appendix B, we describe a method for calculating the intermediate resolvent for the case of a loose composite particle like the deuteron or the ^{7}Li nucleus.

2. FORMALISM FOR SOLVING THE PROBLEM

2.1. Hamiltonian and Projection-Operator Formalism

Let us describe the proposed approach by considering the problem of the scattering of a composite particle $\{1, 2\}$ by a force center. The total Hamiltonian of the problem has the form

$$H = H_1(\mathbf{r}_1) + H_2(\mathbf{r}_2) + V_{12}(|\mathbf{r}_1 - \mathbf{r}_2|), \quad (1)$$

where $H_1 = T(\mathbf{r}_1) + V_1(r_1)$ and $H_2 = T(\mathbf{r}_2) + V_2(r_2)$ are the single-particle Hamiltonians for the motion of each of particles 1 and 2 in the force field. Here, $\mathbf{r}_1$ and $\mathbf{r}_2$ are the coordinates of particles 1 and 2 with respect to the force center, T stands for the kinetic energy operators, and V_1 and V_2 are the potentials describing the interaction of the particles with the center, and V_{12} is the potential representing the interaction between particles 1 and 2. For the sake of simplicity, we will assume that $m_1 = m_2 = m$ and $V_1 = V_2$ (that is, the particles are identical) and that the target-nucleus mass M is indefinitely large. These conditions simplify only algebraic transformations with the three-particle oscillator basis and can easily be removed, if required. In the case of deuteron scattering, V_1 and V_2 are the complex-valued optical potentials for the scattering of, respectively, the neutron and the proton on the nucleus. We further introduce the Jacobi coordinates for the relative motion of the constituents 1 and 2 of the composite particle with respect to its center of mass as

$$\mathbf{r} = \frac{1}{\sqrt{2}}(\mathbf{r}_1 - \mathbf{r}_2), \quad \mathbf{R} = \frac{1}{\sqrt{2}}(\mathbf{r}_1 + \mathbf{r}_2). \quad (2)$$

The corresponding momenta are

$$\mathbf{p} = \frac{1}{\sqrt{2}}(\mathbf{p}_1 - \mathbf{p}_2), \quad \mathbf{P} = \frac{1}{\sqrt{2}}(\mathbf{p}_1 + \mathbf{p}_2).$$

Under this change of coordinates, the total orbital angular momentum does not change:

$$\mathbf{\Lambda} = \mathbf{l}_1 + \mathbf{l}_2 = \mathbf{L} + \mathbf{l}. \quad (3)$$

In terms of the new coordinates, the Hamiltonian takes the form

$$H = T(\mathbf{R}) + V_1\left(\frac{|\mathbf{r} + \mathbf{R}|}{\sqrt{2}}\right) + V_2\left(\frac{|\mathbf{r} - \mathbf{R}|}{\sqrt{2}}\right) + h_{12}(\mathbf{r}), \quad (4)$$

where $h_{12} = T(\mathbf{r}) + V_{12}(\sqrt{2}r)$ is the sub-Hamiltonian for the $\{1, 2\}$ subsystem. We assume that h_{12} has only one bound s-wave state $\phi_0(\mathbf{r})$:

$$h_{12}\phi_0(\mathbf{r}) = \varepsilon_0\phi_0(\mathbf{r}), \quad \phi_0(\mathbf{r}) \equiv \phi_0(r)Y_0^0(\hat{\mathbf{r}}). \quad (5)$$

Now, we make use of the well-known Feshbach method. For this, we introduce the projection operators satisfying the conditions

$$P^2 = P,\ Q^2 = Q,\ P + Q = 1,\ QP = PQ = 0,$$

where P is the operator of projection onto the elastic channel and Q is the orthogonal operator of projection onto all inelastic channels.

The Schrödinger equation for the total Hamiltonian,

$$H\Psi = E\Psi,$$

then splits into two coupled equations for the components $P\Psi$ and $Q\Psi$; that is,

$$(PHP - E)P\Psi = -PHQ\Psi, \quad (QHQ - E)Q\Psi = -QHP\Psi. \quad (6)$$

We further introduce the operator Green's function $G_Q^{(+)}(E)$ for the operator QHQ:

$$G_Q^{(+)}(E) = [QHQ - (E + i\gamma)]^{-1}. \quad (7)$$

Proceeding in a conventional way, we now substitute the second equation from (6) into the first equation. For the function $P\Psi$, we then derive the equation

$$(PHP - E)P\Psi = PHQG_Q^{(+)}(E)QHP\Psi. \quad (8)$$

On the right-hand side of this equation, there appears the nonlocal operator representing the interaction of the $\{1, 2\}$ particle with the force center and taking into account all inelastic channels.

In our problem, the kernel of the operator P can be represented in the form

$$P(\mathbf{r}, \mathbf{R}; \mathbf{r}', \mathbf{R}') = \phi_0(\mathbf{r})\delta(\mathbf{R} - \mathbf{R}')\phi_0^*(\mathbf{r}'). \quad (9)$$

If $\Psi(\mathbf{r}, \mathbf{R})$ is an eigenfunction of the total Hamiltonian H, its P projection has the form

$$P\Psi = \phi_0(\mathbf{r})\Psi_0(\mathbf{R}),$$

where $\Psi_0(\mathbf{R}) \equiv \int \phi_0^*(\mathbf{r}')\Psi(\mathbf{r}', R)d\mathbf{r}'$ is the "external" part of the wave function corresponding to elastic scattering.

Let $\{\tilde{\Psi}_n\}$ be the set of bound eigenstates of the operator QHQ, and let $\{\tilde{\Psi}(E, \alpha)\}$ be the set of states

belonging to the continuous spectrum of this operator, the index α numbering the quantum numbers in which there is degeneracy in energy. In our case, the index α depends on the total orbital angular momentum Λ of the system as a discrete unit and on its projection M onto the z axis, $\alpha = (\Lambda, M)$. Suppose that the two sets form a complete system of functions (in the space of the Hamiltonian H):

$$1 = \sum_n |\tilde{\Psi}_n\rangle\langle\tilde{\Psi}_n| + \sum_\alpha \int dE |\tilde{\Psi}(E,\alpha)\rangle\langle\tilde{\Psi}(E,\alpha)|.$$

For the operator Green's function $G_Q^{(+)}(E)$ associated with the operator QHQ, we use the spectral expansion [12]

$$G_Q^{(+)}(E) = \sum_n \frac{|\tilde{\Psi}_n\rangle\langle\tilde{\Psi}_n|}{E_n - E} + \sum_\alpha \int dE' \frac{|\tilde{\Psi}(E',\alpha)\rangle\langle\tilde{\Psi}(E',\alpha)|}{E' - (E + i\gamma)}. \quad (10)$$

We also have

$$G_Q^{(+)}(E) = QG_Q^{(+)}(E)Q - \frac{P}{E + i\gamma}.$$

The operator $QG_Q^{(+)}(E)Q$ then takes the form

$$QG_Q^{(+)}(E)Q = \sum_{n'} \frac{|\tilde{\Psi}_{n'}\rangle\langle\tilde{\Psi}_{n'}|}{E_{n'} - E} + \sum_\alpha \int dE' \frac{|\tilde{\Psi}(E',\alpha)\rangle\langle\tilde{\Psi}(E',\alpha)|}{E' - E} + i\pi \sum_\alpha |\tilde{\Psi}(E,\alpha)\rangle\langle\tilde{\Psi}(E,\alpha)|. \quad (11)$$

In the last formula, the functions $|\tilde{\Psi}\rangle$ are subjected to the additional condition

$$P|\tilde{\Psi}\rangle = 0, \quad (12)$$

which leads to a distinction between the eigenfunctions of the operators $G_Q^{(+)}(E)$ and $QG_Q^{(+)}(E)Q$.

We now proceed to formulate the basic idea of our approach in these terms. The operator PHQ describing the transition from the initial elastic channel into the intermediate states of the three-particle continuum is localized both in the relative coordinate $\mathbf{r}$ and in the center-of-mass coordinate $\mathbf{R}$. We will show this by using the Hamiltonian in (4). Since the commutator $[P, T(\mathbf{R}) + h_{12}(\mathbf{r})]$ vanishes and since the orthogonality condition $PQ = 0$ is satisfied, we have $PHQ = P\{V_1 + V_2\}Q$; that is,

$$PHQ \to \langle\phi_0(\mathbf{r})|V_1 + V_2|\tilde{\Psi}(\mathbf{r},\mathbf{R})\rangle.$$

In the last expression, the three-particle intermediate-state wave functions $\tilde{\Psi}(\mathbf{r},\mathbf{R})$ are effectively cut off in the coordinates $\mathbf{r}$ and $\mathbf{R}$ owing to the short-range potentials V_1 and V_2 and the function ϕ_0. In the spectral expansion of the intermediate resolvent $QG_Q^{(+)}(E)Q$ (11), only the continuum three-particle wave functions for $|\mathbf{r}| < r_0$, $|\mathbf{R}| < R_0$, which are orthogonal to ϕ_0), are of importance, and this makes it possible to use efficiently the very convenient L_2 discretization for describing intermediate states.

This conclusion is confirmed by the results of the recent analysis from [5], where the authors showed explicitly that the use of well-localized (in the r space of the relative motion of particles 1 and 2) wave packets leads to a faster convergence to exact results than the direct use of nondecaying exact scattering wave functions for the relative motion of particles 1 and 2.

There is no such cutoff in the problem of the breakup of an incident composite particle. Therefore, we somewhat modify our approach in this case (see Section 4).

We now proceed to derive explicitly an equation for the elastic-scattering wave function. The right-hand side of Eq. (8) includes the nonlocal operator $PHQG_Q^{(+)}QHP$. As was explained above, the following relation holds:

$$PHQG_Q^{(+)}QHP = P\{V_1+V_2\}QG_Q^{(+)}Q\{V_1+V_2\}P.$$

It is important to emphasize now that, in order to calculate the intermediate Green's function $G_Q^{(+)}(E)$, we employ, in the ensuing derivation (see Section 3), its spectral expansion expressed in terms of the single-particle coordinates $\mathbf{r}_1$ and $\mathbf{r}_2$. Here, the expansion includes the entire spectrum (involving bound states and single-particle resonances) of the operators H_1 and H_2. This means that, if use is made of a sufficiently large expansion basis, the virtual and real (if the total initial energy is higher than the corresponding thresholds) stripping channels are naturally included in this spectral expansion along with a great number of breakup channels, where both constituents (1 and 2) occur in states belonging to the three-particle continuum. This treatment of the intermediate spectrum of the operator QHQ radically differs from that in DCCC approaches, where only breakup channels—but not stripping ones—are taken into account in intermediate states. That the spectrum of the operator QHQ (and, accordingly, the expansion of the resolvent $QG_Q^{(+)}Q$) contains no asymptotic states involving the bound state ϕ_0 of particles 1 and 2 as an internal function of the composite particle (according to the meaning of the projection operator Q) is an important circumstance here. Therefore, relative motion in the (1, 2) pair always occurs in the continuous spectrum.

We now make use of the spectral expansion of the operator $QG_Q^{(+)}(E)Q$ (11) and, after well-known simplifications, derive the required equation for the function $\psi_0(\mathbf{K},\mathbf{R})$ describing the elastic scattering of the center of mass of the {1, 2} particle by the force center. The result is

$$\left(T(\mathbf{R})+V(R)-\frac{1}{2}\mathbf{K}^2\right)\psi_0(\mathbf{K},\mathbf{R}) \qquad (13)$$
$$=\int d\mathbf{R}'F(E;\mathbf{R},\mathbf{R}')\psi_0(\mathbf{K},\mathbf{R}'),$$
$$K=\sqrt{2(E-\varepsilon_0)},$$

where ε_0 is the energy of bound state of the sub-Hamiltonian h_{12} [it is defined in Eq. (5)];

$$V(R)=\int d\mathbf{r}\phi_0^*(\mathbf{r})\left\{V_1\left(\frac{|\mathbf{r}+\mathbf{R}|}{\sqrt{2}}\right)\right. \qquad (14)$$
$$\left.+V_2\left(\frac{|\mathbf{r}-\mathbf{R}|}{\sqrt{2}}\right)\right\}\phi_0(\mathbf{r})$$

is the so-called folded potential (introduced by Vanatabe long ago); and the kernel of the nonlocal operator on the right-hand side of (13),

$$F(E;\mathbf{R},\mathbf{R}')=\sum_n\frac{U_n(\mathbf{R})U_n^*(\mathbf{R}')}{E_n-E} \qquad (15)$$
$$+\sum_{\Lambda M}\int dE'\frac{U_{\Lambda M}(E',\mathbf{R})U_{\Lambda M}(E',\mathbf{R}')}{E'-(E+i\gamma)},$$

is a nonlocal complex-valued potential involving the inelastic channels of virtual breakup and stripping. Here, we have introduced the notation

$$U_{\Lambda M}(E,\mathbf{R})=\int d\mathbf{r}\phi_0^*(\mathbf{r})\left\{V_1\left(\frac{|\mathbf{r}+\mathbf{R}|}{\sqrt{2}}\right)\right. \qquad (16)$$
$$\left.+V_2\left(\frac{|\mathbf{r}-\mathbf{R}|}{\sqrt{2}}\right)\right\}\tilde{\Psi}(E,\Lambda M;\mathbf{r},\mathbf{R})$$

and

$$U_n(\mathbf{R})=\langle\phi_0(\mathbf{r})|V_1+V_2|\tilde{\Psi}_n(\mathbf{r},\mathbf{R})\rangle. \qquad (17)$$

Let us expand the angular parts of the required solution $\psi_0(\mathbf{K},\mathbf{R})$ and of the nonlocal interaction operator $F(E;\mathbf{R},\mathbf{R}')$ in terms of spherical harmonics. We have

$$\psi_0(\mathbf{K},\mathbf{R})=\sum_{LM}Y_L^{*M}(\hat{\mathbf{K}})\frac{\chi_L(K,R)}{R}Y_L^M(\hat{\mathbf{R}}),$$

where χ_L are the scattering partial-wave functions, and

$$F(E;\mathbf{R},\mathbf{R}')=\sum_{LM}Y_L^M(\hat{\mathbf{R}})\frac{F_L(E;R,R')}{RR'}Y_L^{*M}(\hat{\mathbf{R}}'),$$

where

$$F_L(E;R,R')=\sum_n\frac{U_n^L(R)U_n^{*L}(R')}{E_n-E} \qquad (18)$$
$$+\int dE'\frac{U^L(E',R)U^{*L}(E',R')}{E'-E},$$

with

$$U^L(E,R)=R\int d\Omega_{\mathbf{R}}Y_L^{*M}(\hat{\mathbf{R}})U_{LM}(E;\mathbf{R}).$$

A similar expression is obtained for $U_n^L(R)$. We note that, in the last equality, the subscripts LM on the function U appearing on the right-hand side represent the total orbital angular momentum of the system and its projection in the intermediate state, respectively, while the superscript L on the left-hand side corresponds to the orbital angular momentum of the center of mass of the $\{1,2\}$ particle. This form of expansion is associated with the conservation of the total orbital angular momentum of the system.

We substitute these expansions into (15) and (13), multiplying them, as usual, by $Y_{l'}^{m'}$ and integrating the results with respect to the angles. In this way, we arrive at an equation for the partial-wave functions describing the scattering of the center of mass of the composite particle by a nucleus with allowance for the channels of three-particle breakup and stripping. Specifically, we have

$$\left[-\frac{d^2}{dR^2}+\frac{L(L+1)}{R^2}+2V(R)-K^2\right]\chi_L(K,R)$$
$$=2\int_0^\infty dR'F_L(E;R,R')\chi_L(K,R'). \qquad (19)$$

Although the right-hand side of this equation involves a nonlocal interaction potential, it can be shown that, in the limit $KR\to\infty$, the required solution takes the form

$$\chi_L(K,R)=B_L(K)\{\chi_L^{(-)}(KR) \qquad (20)$$
$$-\chi_L^{(+)}(KR)S_L\},$$

where $\chi^{(\pm)}$ are spherical Hankel functions (see [13]) and S_L are the S-matrix elements corresponding to the scattering of the center of mass of a composite particle by the total potential from Eq. (19).

Equation (19), together with the definition in (18), is the basic equation of our approach. It demonstrates that, in the scattering of a composite particle, all virtual processes of breakup and stripping can be included in the energy-dependent nonlocal operator of finite range. However, the exact form of the kernel of the operator $F_L(E;R,R')$ is still overly complicated for numerically solving, by direct methods, the equation that we obtained. In the next subsection, we therefore present a convenient scheme for its finite-dimensional approximation using a three-particle harmonic-oscillator basis, which is the extension of the shell-model basis for particles 1 and 2 over the target-nucleus core.

In the particular case where the incident particle consists of two loosely bound fragments, a still simpler approximation described in Appendix B can be used in analyzing large-angle scattering.

2.2. Discretization of the Continuum of Intermediate States

We will seek the eigenfunctions of the three-particle intermediate state Hamiltonian QHQ in the form of the oscillator expansions

$$\Psi(E,\Lambda M)=\sum_{\mathcal{N}}\sum_{u}C_u^{\mathcal{N}}(E)|n_1l_1,n_2l_2,\Lambda M\rangle \quad (21)$$
$$\equiv\sum_{\mathcal{N}}\sum_{t}A_t^{\mathcal{N}}(E)|nl,NL,\Lambda M\rangle,$$

where $|n_1l_1,n_2l_2,\Lambda M\rangle$ and $|nl,NL,\Lambda M\rangle$ are two-particle oscillator functions in terms of the coordinates $(\mathbf{r}_1,r_2)$ and $(\mathbf{r},\mathbf{R})$, respectively [14]. This form of expansion is associated with (3). The oscillator-basis functions in terms of the single-particle coordinates $(\mathbf{r}_1,\mathbf{r}_2)$ have the form

$$\langle\mathbf{r}_1,\mathbf{r}_2|n_1l_1,n_2l_2,\Lambda M\rangle \quad (22)$$
$$=\sum_{m_1m_2}C^{\Lambda M}_{l_1m_1,l_2m_2}\Psi_{n_1l_1m_1}(\mathbf{r}_1)\Psi_{n_2l_2m_2}(\mathbf{r}_2),$$

where C are Clebsch–Gordan coefficients and the single-particle oscillator functions are given by

$$\Psi_{nlm}(\mathbf{r})=R_{nl}(r)\cdot Y_l^m(\theta,\phi)\equiv|nlm\rangle,$$
$$R_{nl}(r)=\left[\frac{2\cdot n!}{\Gamma(n+l+\frac{3}{2})}\right]^{\frac{1}{2}} \quad (23)$$
$$\times r^l\exp\left(-\frac{1}{2}r^2\right)L_n^{l+\frac{1}{2}}(r^2).$$

Here, $L_n^\alpha(x)$ are the generalized Laguerre polynomials. In expression (21), $\mathcal{N}$ denotes the total number of oscillator quanta ($\mathcal{N}=2n_1+l_1+2n_2+l_2=2n+l+2N+L$), u numbers various (n_1,l_1,n_2,l_2) sets, and t numbers various (n,l,N,L) sets at fixed $\mathcal{N}$. It is remarkable that the coefficients A and C are related by the purely algebraic Talmi–Moshinsky transformation [14, 15]

$$A_t^{\mathcal{N}}(E)=\sum_u\langle nl,NL,\Lambda|n_1l_1,n_2l_2,\Lambda\rangle C_u^{\mathcal{N}}(E),$$

which, in the case of arbitrary masses m_1 and m_2 of the projectile constituents, is generalized to become the Talmi–Moshinsky–Smirnov transformation [16]. For the transformation brackets $\langle nl,NL,\Lambda|n_1l_1,n_2l_2,\Lambda\rangle$, there exist analytic formulas [14–16] and detailed tables [17]. These transformation brackets are nonzero only under the condition $2n+l+2N+L=2n_1+l_1+2n_2+l_2$, which corresponds to the conservation of the total number of oscillator quanta (that is, energy).

The basic approximation of the method consists in bounding the number of oscillator quanta from above by the maximum number $\mathcal{N}_{\max}$. Instead of an infinite number of eigenfunctions of the operator QHQ, we then obtain a finite basis for each set (Λ,M). Instead of the continuous energy spectrum, we obtain, in this case, the discrete set $\{E_p\}$. As the number $\mathcal{N}_{\max}$ or the oscillator radius is increased, the density of states in the discretized continuum also increases, which makes it possible to control quite straightforwardly the spectral density of continuum states. In this way, the spectrum of the operator QHQ is discretized with a controllable spectral density.

For the operator $QG_Q^{(+)}Q$, we obtain, instead of integration over the entire continuum of intermediate states, summation over a finite set of states of the discretized spectrum; as a result, we can easily find the nonlocal operator $F(E;\mathbf{R},\mathbf{R}')$.

We emphasize once again that, in the limit $\mathcal{N}_{\max}\to\infty$, this L_2 discretization of the intermediate continuum must lead to a uniform convergence to the exact solution to the full problem owing to the short-range character of the transition form factors $U_{\Lambda M}(E,\mathbf{R})$ and $U_n(\mathbf{R})$.

Two problems arise within the proposed approach. The first is associated with actually constructing the spectrum of the operator QHQ, while the second consists in developing an effective algorithm that would replace integration over the continuum spectrum in $F(E;\mathbf{R},\mathbf{R}')$ by summation over a finite set of the constructed states of the discretized continuum. The first problem is investigated in detail in the next part of this study. The second problem can be treated on the basis of the well-known Stieltjes–Chebyshev technique of moments or quadratures [18, 19]. A similar approach as applied to our problem will be developed elsewhere. Upon successfully solving both problems, we can construct a good approximation for the kernel of the operator $F_L(E;R,R')$ (18) and then solve the basic Eq. (19) by means of iterations. Finding further complex partial-wave phase shifts with the aid of (20), we can calculate the partial-wave amplitudes for the scattering of a composite particle. In this way, a full solution to our problem is obtained.

3. CONSTRUCTING EIGENFUNCTIONS OF THE OPERATOR QHQ: METHOD OF ORTHOGONALIZING PSEUDOPOTENTIALS

The problem of constructing the total spectrum of the operator QHQ is nontrivial even in a finite L_2 basis, because all basis functions must be orthogonalized with respect to the internal wave function of the

projectile nucleus. As a matter of fact, we have to deal with continuum functions, and methods that are similar to that due to Gram and Schmidt and which are well known in applied mathematics are inappropriate here, since orthogonalization (according to Schmidt) of all continuum functions to one function $\phi_0(\mathbf{r})$ yields functions that are nonorthogonal to one another and violates the completeness property of the initial basis.

In order to determine the eigenstates of the operator QHQ that satisfy the condition in (12), it is convenient to use the orthogonalizing-pseudopotential method proposed in [20, 21]. The idea of this method is as follows. Instead of the Hamiltonian QHQ, one introduces the pseudo-Hamiltonian $\tilde{H}$:

$$\tilde{H} = H + \lambda P. \tag{24}$$

Here, H is given by (4); P is the projection operator (9), which complements the projection operator Q to unity; and λ is a positive parameter. As was shown in [20, 21], the use of the pseudo-Hamiltonian $\tilde{H}$ makes it possible to work in the complete (not in the truncated) space; this simplifies all calculations significantly. The additional term λP plays the role of the penalty function. This operator is positive definite; therefore, that component of the eigenfunction of the operator $\tilde{H}$ which is not orthogonal to P will increase the energy eigenvalue. As λ is increased, the basis of the eigenfunctions of the operator H rotates in such a way as to shift the functions involving the P components upward on the energy scale. In accordance with the variational principle, the admixture of the P components in the eigenfunctions of the lower part of the spectrum of $\tilde{H}$ will approach zero for $\lambda \to \infty$. The problem of replacing the operator QHQ by the operator $\tilde{H}$ was comprehensively analyzed in [22], where the exact eigenfunctions of the operator QHQ and the eigenfunctions of the operator $\tilde{H}$ from (24) were compared for a two-level system. In that article, it was explicitly shown that the admixture of the forbidden P component ξ in the allowed Q eigenfunctions behaves as $\xi \sim O(1/\lambda^2)$ (see below).

In the present study, the eigenstates of the discretized continuum of the pseudo-Hamiltonian

$$\tilde{H} = T(\mathbf{r}_1) + T(\mathbf{r}_2) + V_1(r_1) + V_2(r_2) + \lambda P \tag{25}$$

are constructed for the potentials

$$V_1(r_1) = U_0 e^{-\beta r_1^2}(1 + \delta r_1^2), \tag{26}$$
$$V_2(r_2) = U_0 e^{-\beta r_2^2}(1 + \delta r_2^2),$$

which, for an appropriate choice of the parameters β and δ, faithfully reproduce single-particle potentials with a sharp edge like the Woods–Saxon potential. In formula (25), we disregarded the interaction V_{12} for the sake of simplicity. For the function $\phi_0(\mathbf{r})$ appearing in the projection operator P, we take the deuteron wave function expanded in Gaussian functions (see [23]).

Let us reduce the Hamiltonian to a dimensionless form with the aid of characteristic parameters of an oscillator having a frequency ω:

$$r_\omega = \sqrt{\frac{\hbar}{m\omega}}, \quad p_\omega = \sqrt{\hbar m\omega}, \tag{27}$$
$$H \to \frac{H}{\hbar\omega}, \quad V \to \frac{V}{\hbar\omega}.$$

It is convenient to expand the eigenfunctions of $\tilde{H}$ in terms of the functions of the symmetric two-particle oscillator basis corresponding to the same frequency [14]:

$$|n_1 l_1, n_2 l_2, \Lambda M\rangle_S = \frac{1}{\sqrt{2}}(|n_1 l_1, n_2 l_2, \Lambda M\rangle \tag{28}$$
$$+ (-1)^{l_1+l_2-\Lambda}|n_2 l_2, n_1 l_1, \Lambda M\rangle).$$

This basis is symmetric with respect to the interchange of particles 1 and 2. This choice is made because the spin and the isospin part of the wave function are taken to be symmetric and antisymmetric, respectively. Positive-parity (negative-parity) states are expanded only in those states in (28) for which $l_1 + l_2$ and, consequently, the total number of quanta $N = 2n_1 + l_1 + 2n_2 + l_2$ are even (odd). If $(n_1, l_1) = (n_2, l_2)$, the factor $1/\sqrt{2}$ must be replaced by $1/2$. In this case, the state in (28) exists only at even Λ.

Thus, we write the eigenfunction of $\tilde{H}$ in the form

$$\hat{\Psi}(E_p, \Lambda M; \mathbf{r}_1, \mathbf{r}_2) \equiv \hat{\Psi}_{p,\Lambda M}(\mathbf{r}_1, \mathbf{r}_2) \tag{29}$$
$$= \sum_{\mathcal{N}}^{\mathcal{N}_{\max}} \sum_u C_{pu}^{\mathcal{N}} \langle \mathbf{r}_1, \mathbf{r}_2 | n_1 l_1, n_2 l_2, \Lambda M\rangle_S.$$

The hat sign is placed over the function Ψ in order to distinguish it from the exact function (21). Eventually, the problem of determining the spectrum of $\tilde{H}$ reduces to diagonalizing the matrix

$$\|{}_S\langle n_1' l_1', n_2' l_2', \Lambda | H + \lambda P | n_1 l_1, n_2 l_2, \Lambda\rangle_S\| \tag{30}$$

in the basis in (28). Owing to the choice of basis, all matrix elements (30) admit a complete analytic calculation (see, for example, [14] and Appendix A).

For the total orbital angular momentum of $\Lambda = 0$ and the maximum number of oscillator quanta that is equal to $\mathcal{N}_{\max} = 14$, the spectrum of eigenvalues of the matrix corresponding to the Hamiltonian (30) was investigated as a function of the parameter λ. With increasing λ, the eigenvalues of some forbidden states are shifted upward on the energy scale (these are the states for which the expectation value of the operator P is close to unity); for the others, the eigenvalues are saturated—these are lower states, for which the expectation value of the operator P sharply decreases

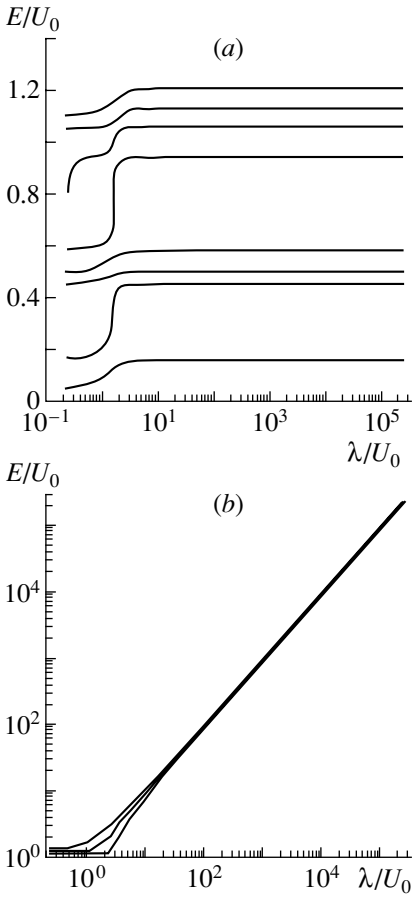

Fig. 1. Eigenvalues of the matrix of the Hamiltonian $\tilde{H}$ as functions of the parameter λ at $\mathcal{N}_{\max} = 14$ for some (a) lower and (b) upper states. The energies of the states and the parameter λ are presented in units of the dimensionless quantities E/U_0 and λ/U_0, respectively, where U_0 is the depth of the single-particle shell potential (26).

with increasing λ. It is noteworthy that the number of upper (forbidden) states at given $\mathcal{N}_{\max}$ and given total orbital angular momentum Λ is given by

$$K = \frac{1}{2}(\mathcal{N}_{\max} - \Lambda) + 1. \tag{31}$$

This can easily be explained by recasting the kernel of the projection operator into the equivalent form

$$P(\mathbf{r}, \mathbf{R}; \mathbf{r}', \mathbf{R}') \tag{32}$$
$$= \sum_{\Lambda M} \sum_{N} \langle \mathbf{r}, \mathbf{R} | \phi_0, N\Lambda M \rangle \langle \phi_0, N\Lambda M | \mathbf{r}', \mathbf{R}' \rangle.$$

In the last equality, we have used, instead of the delta function, the full sum over the single-particle oscillator basis $|N\Lambda M\rangle$ and taken into account the s-wave form of the function $\phi_0(\mathbf{r})$. That the total number of quanta of the two-particle basis is bounded from above ($2n + l + 2N + L \leq \mathcal{N}_{\max}$) and that the total orbital angular momentum of the system is fixed

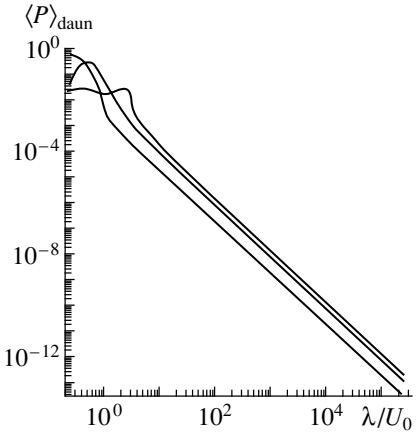

Fig. 2. Expectation values of the projection operator P for some lower states of the spectrum of $\tilde{H}$ as functions of the projection constant λ measured in units of U_0.

($\mathbf{\Lambda} = \mathbf{l} + \mathbf{L}$) mean that, instead the full sum in (32), one takes the sum involving K terms; that is,

$$P(\mathbf{r}, \mathbf{R}; \mathbf{r}', \mathbf{R}') \tag{33}$$
$$\approx \sum_{\Lambda M} \sum_{N=0}^{\frac{1}{2}(\mathcal{N}_{\max} - \Lambda)} \langle \mathbf{r}, \mathbf{R} | \phi_0, N\Lambda M \rangle \langle \phi_0, N\Lambda M | \mathbf{r}', \mathbf{R}' \rangle.$$

Figures 1a and 1b show some lower and upper energy eigenvalues of the pseudo-Hamiltonian $\tilde{H}$ as functions of λ. It can clearly be seen that, for lower eigenvalues, the saturation in λ occurs at values larger than some critical value (see Fig. 1a) and that the energy eigenvalues for upper levels grow in proportion to λ (Fig. 1b). These results are in perfect agreement with those from [22].

The expectation values of the projection operator P over some lower states are displayed in Fig. 2 versus λ. The sum of $\langle P \rangle$ averaged over all upper states is shown in Fig. 3 as a function of λ. In [22], the orthogonalizing-pseudopotential method was tested analytically for a simple two-level system, where one upper and one lower level are formed with increasing λ. According to [22], analytic dependences of the P values averaged over these states are given by

$$\langle P \rangle_{\text{lower}} = O\left(\frac{1}{\lambda^2}\right), \quad \langle P \rangle_{\text{upper}} = 1 - O\left(\frac{1}{\lambda^2}\right). \tag{34}$$

The results of our numerical calculations in the two-particle oscillator basis agree with (34) for lower states. For the sum averaged over all K upper states, we obtain the estimate

$$\frac{1}{K} \sum_{p=1}^{K} \langle P \rangle_{p,\text{upper}} = B - O\left(\frac{1}{\lambda^2}\right), \quad B < 1.$$

The distinction between this result and that in (34) is due to the fact that the truncated basis ceases to be complete. It should be noted that, in constructing the intermediate-state spectrum of the original problem, we need the wave functions of the lower states, which, within the method of orthogonalizing pseudopotentials, are therefore obtained to be orthogonal to the total projection operator (32).

As a result, we have shown that the orthogonalizing-pseudopotential method is well suited to determining the spectrum of the three-particle Hamiltonian QHQ for intermediate states.

4. SCHEME FOR INELASTIC SCATTERING: BREAKUP, STRIPPING, AND EXCITATION OF THE TARGET

In this section, we want to demonstrate that the representation of the three-particle resolvent in the oscillator basis can be effectively used to determine the cross sections for the stripping or breakup of a composite particle on a target at rest. However, we will use here a different approach that is based on the Faddeev formalism, since, in the last case (that is, for the breakup reaction), there are no explicit cutoff factors in the integrals for the relevant matrix elements—there are only the slowly decreasing factors of the $1/r$ type.

Let us define the following sub-Hamiltonians of the total Hamiltonian (1) of our system: $H_0 = T_1 + T_2$, which is associated with the free motion of particles 1 and 2; $H_3 \equiv H_1 + H_2 = H_0 + V_1 + V_2$, which is associated with the scattering of particles 1 and 2 in the field of a nucleus without allowance for the interaction between them; and $H_{12} = H_0 + V_{12}$, which takes into account the interaction only between particles 1 and 2. (We recall that T stands for the operators of the kinetic energies of the particles, H_1 and H_2 are the single-particle Hamiltonians for the interaction of the particles with the center, and V_{12} is the potential of the interaction between the particles.)

Let us introduce the Green's operators corresponding to the above sub-Hamiltonians:

$$G_{12}(E) = [H_{12} - (E + i0)]^{-1}, \qquad (35)$$
$$G_3(E) = [H_3 - (E + i0)]^{-1}.$$

According to [13], we further write the Faddeev equations for the exact wave function $\Psi_{\varepsilon_0,\mathbf{P}}$ describing the collision of the $\{1,2\}$ particle with the external potential field that correspond to the above partition of the total Hamiltonian:

$$\Psi_{\varepsilon_0,\mathbf{P}} = \Phi_{\varepsilon_0,\mathbf{P}} - G_{12}(V_1 + V_2)\Psi_{\varepsilon_0,\mathbf{P}}, \qquad (36)$$
$$\Psi_{\varepsilon_0,\mathbf{P}} = -G_3 V_{12}\Psi_{\varepsilon_0,\mathbf{P}}. \qquad (37)$$

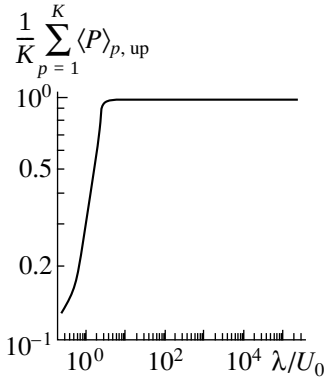

Fig. 3. Quantity obtained by averaging the sum of the matrix elements of the operator P over all up states, $\frac{1}{K}\sum_{p=1}^{K}\langle P\rangle_{p,\mathrm{up}}$, as a function of the projection constant λ measured in units of U_0.

Here, $\Phi_{\varepsilon_0,\mathbf{P}}$ is a function that specifies the state of the incident particle $\{1, 2\}$ before the collision event,

$$\Phi_{\varepsilon_0,\mathbf{P}} = \frac{e^{i\mathbf{P}\cdot\mathbf{R}}\phi_0(\mathbf{r})}{(2\pi\hbar)^{3/2}},$$

$\phi_0(\mathbf{r})$ describing the bound state of the $\{1,\ 2\}$ particle. Equations (36) and (37) must be solved simultaneously in order to ensure correct boundary conditions in all independent coordinates [13]. For this, a solution to the first equation can be substituted into the second equation, or vice versa.

By substituting (36) into (37), we obtain

$$\Psi_{\varepsilon_0,\mathbf{P}} = -G_3 V_{12}\Phi_{\varepsilon_0,\mathbf{P}} \qquad (38)$$
$$+ G_3 V_{12} G_{12}(V_1 + V_2)\Phi_{\varepsilon_0,\mathbf{P}} + \ldots.$$

In order to determine the breakup amplitude, we can use the conventional formula for the post-amplitude [13]:

$$T_{\mathrm{breakup}} = -\langle\phi^{(-)}_{\mathbf{K}_1}\phi^{(-)}_{\mathbf{K}_2}|V_{12}|\Psi_{\varepsilon_0,\mathbf{P}}\rangle. \qquad (39)$$

Here, $\phi^{(-)}_{\mathbf{K}_1}$ and $\phi^{(-)}_{\mathbf{K}_2}$ are the single-particle wave functions describing the scattering of particles 1 and 2 on the potentials V_1 and V_2, respectively, and corresponding to the continuous spectrum and the boundary conditions in the form of converging waves. Substituting (38) into (39) and retaining only the first term, we find that the breakup amplitude can be represented as

$$T_{\mathrm{breakup}} = -\langle\phi^{(-)}_{\mathbf{K}_1}\phi^{(-)}_{\mathbf{K}_2}|V_{12}G_3V_{12}|\Phi_{\varepsilon_0,\mathbf{P}}\rangle. \qquad (40)$$

As was defined above, the resolvent G_3 corresponds to the motion of two noninteracting particles 1 and 2 in a force field; therefore, it can be represented in the

form of the convolution of the single-particle Green's operators relevant to the Hamiltonians H_1 and H_2:

$$G_3(E) = \frac{1}{2\pi i}\int\limits_{-\infty}^{+\infty} d\epsilon g_1^{(+)}(\epsilon) g_2^{(+)}(E-\epsilon).$$

In calculating the breakup amplitude $\mathcal{T}_{\rm breakup}$, the functions appearing in the spectral expansion of this resolvent are strongly cut off only in the coordinate of the relative motion of particles 1 and 2 (in contrast to what occurs in the case of elastic scattering), the convergence of the relevant integrals in the single-particle coordinates $\mathbf{r}_1$ and $\mathbf{r}_2$ being ensured only by oscillations of wave functions in the continuum. Despite this, we deem it possible to use an oscillator basis in this very problem as well. This is due to the fact that, if we use wave packets instead exact continuum wave functions (it is precisely the underlying principle of the DCCC approach), these packets are well localized in space, admitting a convergent oscillator approximation. The representation of G_3 in the two-particle oscillator basis is considered in detail in Appendix B [see the final formula (A.18)].

If we now also represent the functions $\phi^{(-)}_{\mathbf{K}_1}$ and $\phi^{(-)}_{\mathbf{K}_2}$ in the form of the oscillator expansions, all integrals entering into (39) can be calculated analytically (by using the relation between the two-particle oscillator functions determined in the laboratory frame and in the c.m. frame of particles 1 and 2). The last circumstance is an important advantage of the proposed method.

The next term in the iteration series for multiple scattering has the form

$$\Delta T_{\rm breakup} \qquad (41)$$
$$= \langle \phi^{(-)}_{\mathbf{K}_1}\phi^{(-)}_{\mathbf{K}_2}|V_{12}G_3V_{12}G_{12}\{V_1+V_2\}|\Phi_{\varepsilon_0,\mathbf{P}}\rangle.$$

Such terms correspond to the rescattering of particles 1 and 2 in the final (or initial) state and are of importance for a low relative energy (that is, they take into account final-state-interaction effects of the Migdal–Watson type [13]), in which case the pole of the Green's function G_{12} is close to the physical region. In the remaining cases, these corrections for rescattering in higher orders must be small (an additional smallness in these corrections is due to the presence of the absorbing single-particle potential in the region of a nucleus: this leads to the suppression of any multiple-rescattering process in the internal region).

In a similar way, we can find the amplitude for stripping of, say, particle 1. For this, we use the formula from [13] for the stripping amplitude and the first term of the series in (38). As a result, we obtain

$$\mathrm{T}_{\rm stripping} = -\langle \phi_{\varepsilon_1}\phi^{(-)}_{\mathbf{K}_2}|V_{12}G_3V_{12}|\Phi_{\varepsilon_0,\mathbf{P}}\rangle, \qquad (42)$$

where ϕ_{ε_1} is the eigenstate of the Hamiltonian H_1 for the eigenvalues ε_1 of the discrete spectrum.

We now briefly discuss the generalization of the scheme presented in Section 2 to the case where target excitations are taken into account. Instead of the potential Hamiltonian H_1, there then appears its matrix analog $\hat{H}_1$. By way of example, we indicate that, for one rotational excitation of the target nucleus, we have

$$\hat{H}_1 = \begin{pmatrix} T_1 + V^{(11)} - \varepsilon_1 & V^{(12)} \\ V^{(21)} & T_1 + V^{(22)} - \varepsilon_2 \end{pmatrix}.$$

A similar matrix can be written for the sub-Hamiltonian $\hat{H}_2$. Here, ε_1 and ε_2 are the energies of, respectively, the ground and the first excited state of a target, while $V^{(12)}$ and $V^{(21)}$ are the potentials coupling the channels (for rotational excitations, these are ordinary the adiabatic folded potentials).

By way of example, we consider the problem of nucleon scattering by a deformed ^{12}C nucleus, taking into account coupling to the first 2^+ level in ^{12}C. When use is made of the matrix sub-Hamiltonians $\hat{H}_1$ and $\hat{H}_2$, the Green's function $\hat{G}_3$ also becomes the appropriate matrix (in the space of channels coupled to target-nucleus levels). The remaining part of the scheme (see Section 2) for solving the problem also assumes the matrix form without undergoing conceptual changing. Eventually, all intermediate summations (over the spectra of the operators $\hat{H}_1$ and $\hat{H}_2$) acquire an additional index that numbers the excited target states. In contrast to this, the inclusion of target excitations in the DCCC approach leads to a considerable increase in the number of channels, which was very large even in its original form. As a result, this approach becomes very cumbersome.

5. DISCUSSION OF THE RESULTS

Let us formulate basic results of this study. We have demonstrated that the problem of the elastic scattering of a composite particle on a nucleus with allowance for virtual breakup and stripping channels reduces to solving uncoupled Schrödinger equations for individual partial waves, the potentials in these equations being complex, nonlocal, and energy-dependent. Further, we have shown that the transition form factors PHQ are effectively cut off at small projectile-to-target distances. This makes it possible to use the L_2 discretization of the intermediate multiparticle continuum. For this discretization, we have used the two-particle oscillator basis, which made it possible to express all radial integrals entering into the nonlocal kernel in a simple analytic form.

The intermediate three-particle resolvent $QG_Q^{(+)}Q$ appearing in the kernel of the nonlocal operator is expressed in terms of the spectrum of the corresponding Hamiltonian QHQ; its spectrum in turn is obtained by diagonalizing the pseudo-Hamiltonian $\tilde{H} = H + \lambda P$ as the orthogonalizing constant λ increases.

We have also shown that the proposed method, which is based on discretizing the continuum of intermediate states and on subsequently approximating the three-particle resolvents, can be extended to the problem of the inelastic scattering of composite particles and also to the problem of taking into account target-nucleus excitations. A transition from integration over the full continuous spectrum of intermediate states to summation over the discretized continuum in the spectral expansion of the resolvent can be performed with the aid of quadrature methods (for example, the Stieltjes–Chebyshev methods [18, 19]). This problem will be considered in detail in our forthcoming publication.

As the result of the above complete reduction of the multiparticle-scattering problem, only one equation (with a complex-valued nonlocal potential expressed in analytic form) for the scattering wave function in each partial wave is obtained instead of the extremely cumbersome set of coupled equations within the method of the strongly coupled channels (in the DCCC approach) for calculating elastic scattering. This provides serious advantages in the practical implementation of this approach, which are briefly listed below:

(i) The entire scheme for numerically solving the problem is simpler and faster.

(ii) The number of intermediate channels that are taken into account and the spectral density of states of the discretized continuum can easily be controlled by increasing the dimension of the oscillator basis—that is, the total number of quanta $\mathcal{N}_{\max}$. As a matter of fact, the problem of discretizing the intermediate continuum can be reduced to diagonalizing the matrix of the effective Hamiltonian for the shell model, where considerable advances have recently been made in the realms of numerical implementation (for example, the Monte Carlo method for the shell model [24]); this makes it possible to take into account a great number of such intermediate states. It is important that codes for such calculations and the formalism for evaluating nuclear matrix elements are available.

(iii) It can easily be seen that the solution that we have obtained for the problem in question admits a direct generalization to the three- and four-particle fragmentation of the projectile nucleus and to the virtual excitation of the target nucleus (this is hardly possible within the DCCC method).

(iv) That all effects associated with the virtual and the real breakup of the projectile and with the stripping of its fragments are included in the nonlocal complex-valued operator that appears on the right-hand side of the basic equation and which can be treated as a correction to the main folding potential is an important advantage of the proposed scheme. Within such a consideration, the nonlocal operator of the dynamical polarization of a composite particle can easily be replaced (by using the inverse-problem method [25]) by an effective complex-valued local polarization potential, which illustrates the effects of the dynamical polarization of the incident composite particle.

6. CONCLUSION

We have proposed a new formalism for solving the problem of the elastic and inelastic scattering of a composite particle by a force center at rest. The method is based on the L_2 discretization of the continuous spectrum of intermediate states of the system in the two-particle oscillator basis. Inelastic channels have been included in the nonlocal operator describing the interaction of the incident particle as a discrete unit and the target nucleus. This operator involves summation over a great number of states of the discretized three-particle continuum; owing to this, it is very probable that random errors of discretization in the intermediate states do not affect the final result.

The simplicity of the method owing to the use of the oscillator basis, the possibility of including virtual stripping channels, convenience in using it in conjunction with inverse-problem methods, and the possibility of generalizing it to the case of scattering of particles consisting of three or four constituents are the most important advantages of our approach. The last circumstance is the most attractive, since the approaches developed so far (DCCC and so on) do not admit a viable generalization to four-body problems or problems involving a greater number of particles.

ACKNOWLEDGMENTS

We are grateful to Yu.F. Smirnov for a thorough verification of some formulas and valuable comments and to V.N. Pomerantsev for stimulating discussions and for placing at our disposal the code for calculating scattering wave functions.

APPENDIX A

In the Appendices, we everywhere assume that the potentials specifying the interaction of particles 1 and 2 with the target nucleus have the form (26).

We approximate the internal s-wave function of a composite particle by the sum of Gaussian functions:

$$\phi_0(\mathbf{r}) = \sum_{i=1}^{k} C_i e^{-\alpha_i r^2} Y_0^0(\hat{\mathbf{r}}). \tag{A.1}$$

For the folded potential $V(R) = \langle \phi_0(\mathbf{r}) | V_1 + V_2 | \phi_0(\mathbf{r}) \rangle$, which corresponds to the local part of the interaction between the composite particle and the target nucleus, we then have the analytic expression

$$V(R) = \sum_{i,j=1}^{k} (V_{10} + V_{20}) C_i C_j \frac{\sqrt{\pi}}{4} \frac{e^{-\gamma_{ij} R^2}}{(\alpha_i + \alpha_j + \beta)^{3/2}} \tag{A.2}$$

$$\times \left\{ 1 + \frac{3}{4} \frac{\delta}{\alpha_i + \alpha_j + \beta/2} + 2 \frac{\gamma_{ij}^2}{\beta^2} \delta R^2 \right\},$$

where

$$\gamma_{ij} = \beta \frac{\alpha_i + \alpha_j}{2\alpha_i + 2\alpha_j + \beta}. \tag{A.3}$$

The use of the oscillator basis makes it possible to derive analytic formulas for the transition form factors $U_{\Lambda M}(E; \mathbf{R})$, which appear in the nonlocal part of the interaction operator (15). We redefine

$$U_{\Lambda M}(E_p; \mathbf{R}) \to \hat{U}_{p,\Lambda M}(\mathbf{R})$$
$$= \langle \phi_0(\mathbf{r}) | V_1 + V_2 | \hat{\Psi}_{p,\Lambda M}(\mathbf{r}, \mathbf{R}) \rangle.$$

We now calculate this transition matrix element by using the oscillator expansion (29) of $|\hat{\Psi}_{p,\Lambda M}\rangle$ and formulas from [26]. We rewrite this form factor in the expanded form

$$\hat{U}_{p,\Lambda M}(\mathbf{R}) = \int d\mathbf{r} \phi_0^*(\mathbf{r}) \left(V_1 \left(\frac{|\mathbf{r} + \mathbf{R}|}{\sqrt{2}} \right) \right.$$
$$\left. + V_2 \left(\frac{|\mathbf{r} - \mathbf{R}|}{\sqrt{2}} \right) \right) \hat{\Psi}_{p,\Lambda M}(\mathbf{r}, \mathbf{R}),$$

where $\hat{\Psi}_{p,\Lambda M}$ is the wave function (29) represented in terms of the coordinates $(\mathbf{r}, \mathbf{R})$,

$$\hat{\Psi}_{p,\Lambda M}(\mathbf{r}, \mathbf{R}) = \sum_{\mathcal{N}}^{\mathcal{N}_{\max}} \sum_{t} A_{pt}^{\mathcal{N}} \langle \mathbf{r}, \mathbf{R} | nl, NL, \Lambda M \rangle,$$

with the coefficients A being related to the coefficients C by the Talmi–Moshinsky transformation brackets for symmetric functions (see Sections 2 and 3):

$$A_{pt}^{\mathcal{N}} = \sum_{u} \langle nl, NL, \Lambda | n_1 l_1, n_2 l_2, \Lambda \rangle_S C_{pu}^{\mathcal{N}}.$$

According to (28), the symmetric transformation brackets are expressed in terms of ordinary transformation brackets as

$$\langle nl, NL, \lambda | n_1 l_1, n_2 l_2, \lambda \rangle_S$$
$$= \frac{1}{\sqrt{2}} \left(\langle nl, NL, \lambda | n_1 l_1, n_2 l_2, \lambda \rangle \right.$$
$$\left. + (-1)^{l_1 + l_2 - \lambda} \langle nl, NL, \lambda | n_2 l_2, n_1 l_1, \lambda \rangle \right).$$

By taking into account relations associated with symmetries with respect to the permutation of indices on the transformation brackets [15], we obtain

$$\langle nl, NL, \lambda | n_1 l_1, n_2 l_2, \lambda \rangle_S \tag{A.4}$$
$$= \sqrt{2} \langle nl, NL, \lambda | n_1 l_1, n_2 l_2, \lambda \rangle,$$

the symmetric transformation brackets being nonzero only at even l. In the case of $(n_1, l_1) = (n_2, l_2)$, the factor $\sqrt{2}$ is omitted in the last formula.

Let us first calculate the integral for the Gaussian part of the potentials (26) (that is, at $\delta = 0$):

$$\tilde{U}_{p,\Lambda M}(\mathbf{R}) = \int d\mathbf{r} \phi_0^*(\mathbf{r}) (U_0 e^{-\beta r_1^2}$$
$$+ U_0 e^{-\beta r_2^2}) \hat{\Psi}_{p,\Lambda M}(\mathbf{r}, \mathbf{R}).$$

Owing to the conservation of the total orbital angular momentum of the system, the angular part is isolated in the form

$$\tilde{U}_{p,\Lambda M}(\mathbf{R}) = \frac{\tilde{U}_p^{\Lambda}(R)}{R} Y_{\Lambda}^{M}(\hat{\mathbf{R}}).$$

For the radial integral, the calculation yields

$$\tilde{U}_p^{\Lambda}(R) = U_0 \sum_{\eta,t} A_{pt}^{\eta} C_{l0,L0}^{\Lambda 0} \sqrt{\frac{(2l+1)(2L+1)}{2\Lambda + 1}} \tag{A.5}$$

$$\times \frac{\sqrt{\pi}}{2} A_{nl} A_{NL} \left(\frac{1}{2} \beta \right)^l \sum_{i=1}^{k} C_i \frac{(w_i - 1)^n}{w_i^{n+l+3/2}}$$
$$\times e^{-\gamma_i R^2} R^{l+L+1} L_N^{L+1/2}(R^2) L_n^{l+1/2}(\rho_i R^2),$$

where $L_m^{\alpha}(x)$ are generalized Laguerre polynomials (see [26]). Here, we have used the notation

$$w_i = \alpha_i + \frac{1}{2}\beta + \frac{1}{2},$$
$$\rho_i = \frac{\beta^2}{4 w_i (w_i - 1)}, \tag{A.6}$$
$$\gamma_i = \frac{1}{2} \left(1 + \frac{\beta(2\alpha_i + 1)}{2\alpha_i + \beta + 1} \right),$$
$$A_{nl} = \sqrt{\frac{2n!}{\Gamma(n + l + 3/2)}}.$$

It should be recalled that, in the calculations, we employ dimensionless quantities expressed in the oscillator units (27).

In order to determine the transition form factors relevant to the potentials (26) at $\delta \neq 0$, we can invoke the relation

$$\hat{U}_{p,\Lambda M}(\mathbf{R}) = \tilde{U}_{p,\Lambda M}(\mathbf{R}) - \delta \frac{\partial}{\partial \beta} \tilde{U}_{p,\Lambda M}(\mathbf{R}).$$

Thus, we can see that closed analytic formulas are obtained for the nonlocal operator representing the interaction between a composite particle and a nucleus.

Here, we present the results of the calculations for some matrix elements that appear if we use the oscillator basis.

(a) Let us consider the matrix element

$$ {}_S\langle n_1'l_1', n_2'l_2', \Lambda|\frac{1}{2}(\mathbf{p}_1)^2 + V_1(r_1) + \frac{1}{2}(\mathbf{p}_2)^2 + V_2(r_2)|n_1l_1, n_2l_2, \Lambda\rangle_S. \quad (A.7)$$

Considering that the wave function is symmetric with respect to the interchange of particles 1 and 2 and that the parameters β and δ in (26) for $V_1(r_1)$ and $V_2(r_2)$ are identical, we have

$$ {}_S\langle n_1'l_1', n_2'l_2', \Lambda|H_1 + H_2|n_1l_1, n_2l_2, \Lambda\rangle_S = 2\,{}_S\langle n_1'l_1', n_2'l_2', \Lambda|H_1|n_1l_1, n_2l_2, \Lambda\rangle_S.$$

The matrix element (A.7) is calculated in terms of the matrix elements

$$\langle n_1'l_1', n_2'l_2', \Lambda|\frac{1}{2}(\mathbf{p}_1)^2 + U_0e^{-\beta r_1^2}(1+\delta r_1^2)|n_1l_1, n_2l_2, \Lambda\rangle = \sum_{m_1', m_2'}\sum_{m_1, m_2} C^{\Lambda M}_{l_1'm_1', l_2'm_2'} C^{\Lambda M}_{l_1m_1, l_2m_2}$$

$$\times\langle n_1'l_1'm_1'|\frac{1}{2}(\mathbf{p}_1)^2 + U_0e^{-\beta r_1^2}(1+\delta r_1^2)|n_1l_1m_1\rangle \times \delta_{n_2'n_2}\delta_{l_2'l_2}\delta_{m_2'm_2}.$$

Let us consider the single-particle matrix element

$$\langle n_1'l_1'm_1'|\frac{1}{2}(\mathbf{p}_1)^2 + U_0e^{-\beta r_1^2}(1+\delta r_1^2)|n_1l_1m_1\rangle.$$

According to [14], we have

$$\langle n'l'm'|\frac{1}{2}(\mathbf{p})^2|nlm\rangle = \frac{1}{2}\left[\left(2n+l+\frac{3}{2}\right)\delta_{nn'} + \left[n\left(n+l+\frac{1}{2}\right)\right]^{1/2}\delta_{n'n-1} + \left[(n+1)\left(n+l+\frac{3}{2}\right)\right]^{1/2}\delta_{n'n+1}\right]\delta_{ll'}\delta_{mm'}. \quad (A.8)$$

Further, we calculate the matrix element $\langle n'l'm'|e^{-\beta r^2}|nlm\rangle \equiv \langle n'l|e^{-\beta r^2}|nl\rangle\delta_{l,l'}\delta_{m,m'}$. By using the formulas from [26], we obtain

$$\langle n'l|e^{-\beta r^2}|nl\rangle = \left[\frac{(l+\frac{3}{2})_n(l+\frac{3}{2})_{n'}}{n'!n!}\right]^{1/2} \times \frac{\beta^{n'+n}}{(\beta+1)^{n'+n+l+3/2}}\,{}_2F_1(-n', -n, l+3/2; 1/\beta^2), \quad (A.9)$$

where ${}_2F_1$ is a hypergeometric function, which, in our case, reduces to a polynomial, and

$$(l+3/2)_n = \mathbf{\Gamma}(l+3/2+n)/\mathbf{\Gamma}(l+3/2).$$

The matrix element $\langle n'l|e^{-\beta r^2}(1+\delta r^2)|nl\rangle$ is calculated by differentiating formula (A.9):

$$\langle n'l|e^{-\beta r^2}(1+\delta r^2)|nl\rangle = \langle n'l|e^{-\beta r^2}|nl\rangle - \delta\frac{d}{d\beta}\langle n'l|e^{-\beta r^2}|nl\rangle.$$

(b) Further, we consider the matrix elements of the projection operator P.

In order to calculate them, we need symmetric transition brackets:

$$ {}_S\langle n_1'l_1', n_2'l_2', \Lambda|P|n_1l_1, n_2l_2, \Lambda\rangle_S = \sum_{n', l', N', L'} {}_S\langle n_1'l_1', n_2'l_2', \Lambda|n'l', N'L', \Lambda\rangle \times \sum_{n, l, N, L} {}_S\langle n_1l_1, n_2l_2, \Lambda|nl, NL, \Lambda\rangle \times \langle n'l', N'L', \Lambda|\phi_0\rangle\langle\phi_0|nl, NL, \Lambda\rangle.$$

In the last formula, use has been made of the following condensed notation for the projection operator P:

$$P = |\phi_0\rangle\langle\phi_0|.$$

Let us consider the factor

$$\langle n'l', N'L', \Lambda|\phi_0\rangle\langle\phi_0|nl, NL, \Lambda\rangle = \langle n'l'|\phi_0\rangle\langle\phi_0|nl\rangle\delta_{NN'}\delta_{LL'},$$

where

$$\langle n'l'|\phi_0\rangle = \delta_{l'0}\int_0^\infty drr^2\phi_0(r)R_{n'0}(r). \quad (A.10)$$

Here, $\phi_0(r)$ is the radial part of the bound-state wave function $\phi_0(\mathbf{r})$. If we represent it in the form (A.1), the integral in (A.10) can easily be calculated by using, for example, (A.9).

APPENDIX B

The main objective of Appendix B is to demonstrate that, in some cases, the functions appearing in the spectral expansion (11) can be found by using a method simpler than that described in Section 3.

Let us consider the intermediate-state Hamiltonian QHQ. We now write the total Hamiltonian of the system in the form (1):

$$H = H_1(\mathbf{r}_1) + H_2(\mathbf{r}_2) + V_{12}(r).$$

We recall that the projection operator Q is orthogonal to the projection operator P (9). We conjecture the following:

(i) $QH_1Q \approx H_1$, since the P projection acts in the variables $(\mathbf{r}, \mathbf{R})$ which are "alien" for the variable $\mathbf{r}_1$. We can expect that the admixture of the P components in the eigenfunctions of the single-particle operator H_1 is small. A similar assumption is made for QH_2Q.

(ii) $\|QV_{12}Q\| \ll \|Q(H_1+H_2)Q\|$. This approximation is associated with the fact that the operator Q is orthogonal to the eigenfunction of the bound state in the potential V_{12}.

Thus, we want to make the substitution

$$QHQ \to H_1 + H_2 \tag{A.11}$$

and, in addition, the substitution

$$QG_Q^{(+)}(E)Q \to G_3^{(+)}(E) = [H_1+H_2-(E+i0)]^{-1}, \tag{A.12}$$

where $G_3^{(+)}(E)$ is the Green's function for two noninteracting particles in the field of the core.

The physical meaning of the above substitution is that, in the intermediate states, it is the interaction of particles 1 and 2 with the target nucleus (rather than the interaction between projectile constituents) that predominantly affects the composite particle at moderate projectile-to-target distances. These means that, conjecturing (i) and (ii), we assume, as a matter of fact, that, in the intermediate state, particles 1 and 2 diverge and move independently of each other in the field of the target nucleus. It should be emphasized, however, that this approximation is valid only in the Q subspace (from which the bound states of particles 1 and 2 are eliminated), but that it is not accurate in all probability in the full space.

Mathematically, the substitution in (A.12) means that, for the three-particle intermediate-state resolvent, we can use the convolution of the single-particle resolvents; that is,

$$QG_Q^{(+)}(E)Q \to \frac{1}{2\pi i}\int_{-\infty}^{+\infty} d\epsilon\, g_1^{(+)}(\epsilon)g_2^{(+)}(E-\epsilon), \tag{A.13}$$

where $g_1^{(+)}(\epsilon) = [H_1-(\epsilon+i0)]^{-1}$ and g_2 has the analogous form with the substitution $H_1 \to H_2$. We further consider the spectral expansion of the Green's function g_1 in the complete system of eigenfunctions $\{\psi_n, \psi(E, l_1m_1)\}$ of the Hamiltonian H_1:

$$g_1^{(+)}(\epsilon) = \sum_n \frac{|\psi_n\rangle\langle\psi_n|}{E_n-\epsilon} + \sum_{l_1m_1}\int_0^\infty \delta E' \frac{|\psi(E', l_1m_1)\rangle\langle\psi(E', l_1m_1)|}{E'-(\epsilon+i\gamma)}. \tag{A.14}$$

We can now use the discretization of the single-particle spectrum of the Hamiltonian H_1 in the finite-dimensional single-particle oscillator basis $\{|nlm\rangle\}$. For each $\{lm\}$, we obtain finite sets of eigenfunctions of the operator H_1 in the form

$$\psi_{p_1,l_1m_1}(\mathbf{r}_1) = \sum_{n_1=0}^{N_{\max}} A_{p_1n_1}^{l_1} R_{n_1l_1}(r_1)Y_{l_1}^{m_1}(\hat{\mathbf{r}}_1),$$

where R_{nl} is given by (23). For the resolvent g_1, we then obtain

$$g_1(\epsilon; \mathbf{r}_1, \mathbf{r}_1') = \sum_{p_1l_1m_1} \frac{\psi_{p_1,l_1m_1}(\mathbf{r}_1)\psi^*_{p_1,l_1m_1}(\mathbf{r}_1')}{E_{p_1l_1}-(\epsilon+i\gamma)}. \tag{A.15}$$

Here, the integral over the continuous spectrum of g_1 has been replaced by the sum over the states of the discretized continuum. The approximation in (A.15) is made for the case of $\gamma \neq 0$; in the limit $\gamma \to 0$, it is necessary to use special quadrature approximations [18, 19]. In order to evaluate the convolution in (A.13), it is sufficient to use the form (A.15) for g_1 and g_2 ($H_1 = H_2$). Calculating the integral in (A.13), we obtain

$$G_3^{(+)}(E; \mathbf{r}_1, \mathbf{r}_2; \mathbf{r}_1', \mathbf{r}_2') \approx \sum_{p_1l_1m_1}\sum_{p_2l_2m_2} \frac{|\psi_{p_1,l_1m_1}(\mathbf{r}_1)\psi_{p_2,l_2m_2}(\mathbf{r}_2)\rangle\langle\psi^*_{p_1,l_1m_1}(\mathbf{r}_1')\psi^*_{p_2,l_2m_2}(\mathbf{r}_2')|}{E_{p_1l_1}+E_{p_2l_2}-(E+i\gamma)}. \tag{A.16}$$

Let us perform rearrangement of the angular momenta, $(l_1m_1, l_2m_2) \to (l_1l_2, \Lambda M)$. As a result, we arrive at a convenient finite-dimensional representation for the convolution of two single-particle Green's functions. Specifically, we have

$$G_3^{(+)}(E) = \sum_{p_1l_1}\sum_{p_2l_2}\sum_{\Lambda=|l_1-l_2|,M}^{\Lambda=l_1+l_2} \frac{[\psi_{p_1l_1}\psi_{p_2l_2}]^{\Lambda M}[\psi^*_{p_1l_1}\psi^*_{p_2l_2}]^{\Lambda M}}{E_{p_1l_1}+E_{p_2l_2}-(E+i\gamma)}, \tag{A.17}$$

where

$$[\psi_{p_1l_1}\psi_{p_2l_2}]^{\Lambda M} = \sum_{m_1+m_2=M} C^{\Lambda M}_{l_1m_1,l_2m_2}\psi_{p_1,l_1m_1}\psi_{p_2,l_2m_2}.$$

Taking into account expression (22) for two-particle oscillator functions, we can eventually recast expression (A.17) into the form

$$G_3^{(+)}(E) = \sum_{p_1 n_1 l_1} \sum_{p_2 n_2 l_2} \sum_{\Lambda M} \frac{|A^{l_1}_{p_1 n_1}|^2 |A^{l_2}_{p_2 n_2}|^2 |n_1 l_1, n_2 l_2, \Lambda M\rangle\langle n_1 l_1, n_2 l_2, \Lambda M|}{E_{p_1 l_1} + E_{p_2 l_2} - (E + i\gamma)}. \quad \text{(A.18)}$$

This representation is convenient in that fully analytic expressions presented in Appendix A can used in calculating transition matrix elements and other similar quantities. In order to employ formula (A.18) in the limit $\gamma \to 0$, one can invoke the quadrature approximations from [18, 19]. This problem will be the subject of our forthcoming publication.

Thus we conclude that, if our conjectures (i) and (ii) and the substitution in (A.12) are correct, the problem of determining the spectrum of the intermediate-state resolvent $QG_Q^{(+)}Q$ is considerably simplified. Instead of diagonalizing the three-particle Hamiltonian according to the procedure described in Section 3, it is sufficient to find the spectrum of the single-particle Hamiltonian H_1 (and of H_2 if particles 1 and 2 are not identical). This makes it possible to enlarge considerably the number of basis functions used in the calculations and to simplify all formulas.

REFERENCES

1. J. P. Farrell, C. M. Vincent, and N. Austern, Ann. Phys. (N.Y.) **96**, 333 (1976).
2. M. Kawai and M. Kamimura, Prog. Theor. Phys. **59**, 674 (1978).
3. M. Kamimura, M. Yahiro, Y. Iseri, *et al.,* Prog. Theor. Phys. Suppl. **89**, 136 (1986).
4. N. Austern and M. Kawai, Prog. Theor. Phys. **80**, 694 (1988).
5. R. A. D. Piyadasa, M. Kawai, M. Kamimura, and M. Yahiro, Phys. Rev. C **60**, 044611 (1999).
6. B. Anders and A. Lindner, Nucl. Phys. A **296**, 770 (1978).
7. J. C. Johnson and P. C. Tandy, Phys. Rev. C **11**, 1152 (1975).
8. Z. C. Kuruoglu and F. S. Levin, Ann. Phys. (N.Y.) **163**, 120 (1985).
9. R. Y. Rasoanaivo and G. H. Rawitscher, Phys. Rev. C **39**, 1709 (1989).
10. V. I. Kukulin and V. N. Pomerantsev, Yad. Fiz. **50**, 27 (1989) [Sov. J. Nucl. Phys. **50**, 17 (1989)].
11. C. Manaux and H. A. Weidenmuller, *Shell-Model Approach to Nuclear Reactions* (North-Holland, Amsterdam, 1969).
12. R. G. Newton, *Scattering Theory of Waves and Particles* (McGraw-Hill, New York, 1966; Mir, Moscow, 1969).
13. A. I. Baz', Ya. B. Zel'dovich, and A. M. Perelomov, *Scattering, Reactions and Decays in Nonrelativistic Quantum Mechanics* (Nauka, Moscow, 1971, 2nd ed.; Israel Program for Scientific Translations, Jerusalem, 1966).
14. M. Moshinsky, *The Harmonic Oscillator in Modern Physics: From Atoms to Quarks* (Gordon and Breach, New York, 1969; Mir, Moscow, 1972).
15. M. Moshinsky, Nucl. Phys. **13**, 104 (1959).
16. Yu. F. Smirnov, Nucl. Phys. **27**, 117 (1961); M. A. Rashid, J. Phys. A **13**, 1977 (1980).
17. T. A. Brody and M. Moshinsky, *Tables of Transformation Brackets* (Wiley, New York, 1967).
18. J. R. Winick and W. P. Reinhardt, Phys. Rev. A **18**, 910 (1978).
19. I. Cacelli, V. Carravetta, A. Rizzo, and A. Moccia, Phys. Rep. **205**, 283 (1991).
20. V. M. Krasnopol'skiĭ and V. I. Kukulin, Yad. Fiz. **20**, 883 (1974) [Sov. J. Nucl. Phys. **20**, 470 (1975)].
21. V. I. Kukulin and V. N. Pomerantsev, Ann. Phys. (N.Y.) **111**, 330 (1978).
22. J. Mitroy and G. G. Ryzhikh, Comput. Phys. Commun. **123**, 103 (1999).
23. R. Beck, F. Dickmann, and R. J. Lovash, Ann. Phys. (N.Y.) **173**, 1 (1987).
24. Y. Alhassid, *Quantum Monte Carlo Methods for the Shell Model and Their Applications at Finite Temperature, Book of Contributions "Structure of the Nucleus at the Dawn of the Century, Bologna, 2000,"* p. 242.
25. V. I. Kukulin, V. N. Pomerantsev, and S.V. Zuev, Yad. Fiz. **59**, 428 (1996) [Phys. At. Nucl. **59**, 403 (1996)]; V. I. Kukulin, V. N. Pomerantsev, and J. Horacek, Phys. Rev. A **42**, 2719 (1990); S. G. Cooper and R. S. Mackintosh, Phys. Rev. C **43**, 1001 (1991); Nucl. Phys. A **517**, 285 (1990).
26. A. P. Prudnikov, Yu. A. Brychkov, and O. I. Marichev, *Integrals and Series* (Nauka, Moscow, 1983; Gordon and Breach, New York, 1986), Vols. 1-3.

Translated by A. Isaakyan

Physics of Atomic Nuclei, Vol. 64, No. 9, 2001, pp. 1704–1715. Translated from Yadernaya Fizika, Vol. 64, No. 9, 2001, pp. 1784–1795.

ELEMENTARY PARTICLES AND FIELDS
Theory

Model of a Hybrid Chiral Bag Involving Constituent Quarks

K. A. Sveshnikov[1),2)], S. M. Fedorov[2)], M. F. Khalili[2)], and I. O. Cherednikov[1),3),*]

Received January 13, 2000; in final form, August 18, 2000

Abstract—A three-phase modification of the hybrid quark-bag model is considered. In addition to the asymptotic-freedom and the hadronization phase, it includes the intermediate phase of constituent quarks. In the $(1+1)$-dimensional version of this model, a self-consistent solution is found with allowance for fermion-vacuum-polarization effects. Within this solution, the total bag energy, including the one-loop contribution from the Dirac sea, is investigated as a function of parameters that characterize bag geometry, the condition of a nonvanishing boson-condensate density in the internal region being imposed. It is shown that the ground-state bag configuration that is constructed on the basis of the solution found here, which minimizes the total energy, and which includes all three phases exists and is unique.

1. INTRODUCTION

Presently, the idea of describing a hadron as a bounded spatial region (bag) filled with quark and gluon fields seems the most natural way to construct an effective quantum field theory that provides the absolute confinement of color objects [1–12]. For such regions, boundary conditions are chosen so as to ensure, in a relativistically covariant way, color-particle confinement within a bag [1–3]. The possibility that such an object exists is associated with a change in the vacuum structure within a hadron. It is assumed that a nonperturbative vacuum within a strongly interacting particle is destroyed almost completely, with the result that there arises an excess of energy proportional to the bag volume [1–5]. The stability of the configuration is guaranteed by the valence-quark contribution to the total energy, this contribution being in inverse proportion to the bag radius. Even the first MIT bag model yielded fairly good results for the mass spectrum and the other static properties of hadrons at a relatively small number of parameters [6–8]. A further development of the model led to taking into account some effects associated with a spontaneous breakdown of chiral symmetry (one of the most important features of strong interactions at low energies) and to including meson fields in the theory that play the role of Goldstone bosons [9–11]. (These are the triplet of pions for the $SU(2)$ group or the octet of pions and kaons for the $SU(3)$ group.) Presently, the most consistent approach to describing the structure of hadrons on the basis of bag models has been developed within so-called hybrid chiral models [10–12]. In hybrid chiral models, the nucleon is considered as a small bag that confines quarks and gluons and which is surrounded by a large cloud of virtual mesons. This cloud can be described either by the hedgehog pion configuration of the Skyrme model or by more complicated models including vector mesons [13–15].

By and large, models of this type provide a correct scale for various static features of nonstrange baryons. At the same time, serious discrepancies in numerical values and even incorrect signs may occur for some individual quantities [12, 16]. Furthermore, the best results within hybrid chiral models are obtained at such values of relevant parameters (like the vacuum pressure B, the coupling constant α_s, the current quark masses, and the constant Z taking into account the Casimir energy) that differ from those derived by other methods [4, 5]. All this demonstrates that the conventional formulation of hybrid chiral models is not free from drawbacks.

The most subtle point in the hybrid chiral model is the Cheshire cat principle as a basis for breaking down the total configuration space into regions within which various phases are realized [17]. This principle essentially relies on the hypothesis [18] that fermionic theory within the bag and bosonic theory outside it are in fact equivalent and can be exactly transformed into each other by means of the bosonization procedure. As a result, no physical properties of such a bag depend on the choice of boundary surface,

[1)]Institute for Theoretical Problems of Microphysics, Moscow State University, Vorob'evy gory, Moscow, 119899 Russia
[2)]Faculty of Physics, Moscow State University, Vorob'evy gory, Moscow, 119899 Russia.
[3)]Joint Institute for Nuclear Research, Dubna, Moscow oblast, 141980 Russia.
[*]e-mail: igorch@goa.bog.msu.ru;igorch@thsun1.jinr.ru

and the boundary conditions are determined from the bosonization equations [19]. However, the bosonization procedure and, hence, the Cheshire cat hypothesis can be rigorously justified only in (1 + 1) dimensions. At the same time, a solution to the bosonization problem for the actual (3 + 1)-dimensioinal world has yet to be obtained. As a consequence, there exist, in (3 + 1)-dimensional hybrid chiral models based on the Cheshire cat hypothesis, only a small set of features (for example, the topological charge) that are actually independent of the bag radius [20]. At the same time, the phenomenology of strong interactions unambigously indicates that a characteristic scale confinement on the order of 0.5 fm does in fact exist—that is, irrespective of the degree to which the bosonization is justified in the (3 + 1)-dimensional case, the Cheshire cat principle must be strongly violated in realistic models.

Therefore, it seems quite natural to modify hybrid chiral models in such a way as to get rid of the Cheshire cat hypothesis and all constructions that it entails in the form of an infinitely thin boundary surface between the phases and the relevant surface action functional. Such a modification appears to be possible if the correlation between different bag phases, which are not assumed now to be equivalent in the sense of exact bosonization, is ensured by the actual interaction occurring in a finite-dimension region, which admits a natural interpretation as a third intermediate phase of a bag [21]. The emergence of this additional phase is quite appropriate, since it enables one to implement the chirally invariant mechanism of the dynamical generation of quark masses; owing to this, it is in part the phase of constituent quarks (it should recalled that the possibility of their existence is not considered in the original two-phase model). At the same time, constituent-quark models were successfully used in hadron spectroscopy. From this point of view, the physically most attractive situation would be that where free, virtually massless current quarks (this corresponds to high squares of momentum transfers, Q^2) are first converted, as the result of interactions, into dressed massive constituent quarks carrying the same color, flavor, and spin quantum numbers and only after that does there arise purely mesonic color-singlet phase.

The three-phase hybrid model involving an intermediate constituent-quark phase instead the boundary characterized by zero radial extension [21] is a first approximation to such a bag version. This model permits taking self-consistently into account three phases: the asymptotic-freedom phase featuring massless free quarks; the phase of constituent quarks acquiring effective masses owing to chirally invariant interaction with a boson field in the intermediate region of finite dimension; and the hadronization phase, where free-quark production is suppressed by an infinitely large mass and where the nonlinear dynamics of the boson field leads to the emergence of a boson condensate in the form of a soliton solution, which is eventually responsible for the quantum numbers of the entire bag.

In this study, we consider one version of such a model in (1 + 1) dimensions where, in an intermediate region, a one-flavor fermion field interacts in a chirally invariant way with a real scalar field possessing a nonlinear soliton solution in the external region. A self-consistent solution to the equations of the model is found with allowance for fermion-vacuum-polarization effects. Within this solution, the renormalized total bag energy is investigated as a function of parameters that characterize bag geometry, the condition of a nonvanishing boson-condensate density in the internal region being imposed. It is shown that, under specific conditions on the model parameters, the configuration that minimizes the total bag energy and which involves all three phases exists and is unique.

2. LAGRANGIAN AND EQUATIONS OF MOTION

The partition of the bag space into separate phases is implemented by the method described in [3, 22] by using the system of auxiliary fields $\theta(x)$. The fundamentals of the method are as follows. We consider the Lagrangian

$$\mathcal{L}_0 = \frac{1}{2}(\partial_\mu\phi)^2 - \theta V(\phi) + \frac{1}{2}(\partial_\mu\theta)^2 - g_0^2 W(\theta), \quad (1)$$

where the coupling constant g_0 for the self-interaction of the field θ is so large that, in the first approximation, we can neglect the effect of the matter fields ϕ on the dynamics of the field θ. The solutions to be obtained can then be used to control their dynamics [21, 22]. It is obvious that one can construct a Lagrangian involving the required number of fields $\theta(x)$ with a specific self-interaction that define a nearly rectangular partition of space into regions corresponding to different phases. Lorenz covariance will then be broken only spontaneously, at the level of solutions to the equations of motion; owing to this, the formalism of covariant group variables [23] can be used to restore covariance.

In the following, we assume that the auxiliary fields $\theta(x)$ have already formed the necessary bag configuration and proceed from the Lagrangian

$$\mathcal{L} = \bar\psi i\hat\partial\psi + \frac{1}{2}(\partial_\mu\varphi)^2 - \theta(x_1 < |x| < x_2) \quad (2)$$
$$\times \left(\frac{M}{2}\left[\bar\psi, e^{ig\gamma_5\varphi}\psi\right]_-\right) - \theta(|x| > x_2)$$

$$\times \left(\frac{M_0}{2} \left[\bar{\psi}, e^{ig\gamma_5\varphi}\psi \right]_- + V(\varphi) \right).$$

The commutator of fermion fields in the expressions specifying the chiral coupling between fermions and bosons ensures the charge symmetry of the model.

Thus, we originally have the theory of two fields, the spinor field ψ and the boson field φ. In region I ($|x| < x_1$), both fields are free and massless; in region II ($x_1 \le |x| \le x_2$), the field φ interacts with fermions in a chirally invariant way, whereby fermions acquire an effective mass M; and, in region III ($|x| > x_2$), the fermion effective mass becomes equal to M_0 and the self-interaction of the field φ comes into play, leading to a soliton solution for the boson field. It should be noted that, in the model being considered, the vacuum-pressure term appears to be redundant, since, as will be seen below, the polarization of the Dirac sea behaves in a very specific way owing to the presence of the intermediate region in this model, ensuring alone the required inward pressure. In addition, there is no need for valence fermions in our model, since all quantum numbers of the bag as a discrete unit—in the simplest case being considered, this is its baryon number—ensure a boson condensate in the form of a topological soliton. Thus, it would be difficult to validate the emergence of vacuum pressure from this standpoint as well.

In order to ensure the confinement of fermions, we further assume that the mass M_0 is very large, which leads to the dynamical vanishing of the fermion field in the external region III. In the internal region I, we have a free (decoupled from fermions) massless scalar field; this leads to a nonzero boson-condensate density in the asymptotic-freedom region. This possibility is compatible with the general concept of bag models and can be considered as one of the versions of the formulation of our three-phase model. Another version—the vanishing of the scalar field in the internal region—was investigated in detail elsewhere [21]. We also assume that an odd topological soliton-like configuration is a solution to the equation of motion for the boson field. The even case, where the scalar field can be nonzero in the internal region, is of no interest, because a trivial solution, with the scalar field being everywhere equal to a constant [one of the minima of the self-interaction potential $V(\varphi)$], is energetically favorable.

Let us consider the behavior of the fields in more detail. As is customary in hybrid models of the type in question, the boson field is considered in the mean-field approximation—that is, it is a c-number quantity. Ignoring, for the time being, a Lorentz-covariant description, we will consider the c.m. of the bag; the field $\varphi(x)$ will then be a time-independent classical field, against whose backgroundand the fermions evolve. The equations of motion for fields can be written as

$$i\hat{\partial}\psi = 0, \tag{3a}$$

$$\varphi'' = 0 \tag{3b}$$

in region I; as

$$\left(i\hat{\partial} - Me^{ig\gamma_5\varphi} \right)\psi = 0, \tag{4a}$$

$$\varphi'' = ig\frac{M}{2}\langle \left[\bar{\psi}, \gamma_5 e^{ig\gamma_5\varphi}\psi \right]_- \rangle \tag{4b}$$

in region II; and as

$$(i\hat{\partial} - M_0 e^{ig\gamma_5\varphi})\psi = 0, \tag{5a}$$

$$-\varphi'' + V'(\varphi) = 0 \tag{5b}$$

in region III. The angular brackets in Eq. (4b) denote averaging over a given bag state. In order to simplify the calculations, we further set $g = 1$, since the g dependence can easily be recovered by means of the substitution $\varphi \to \varphi/g$. The spectral problem for the wave functions ψ_ω describing fermions of given energy ω will then have the form

$$\omega\psi_\omega = -i\alpha\psi'_\omega + \beta e^{i\gamma_5\varphi}\left[M\theta(x_1 < |x| < x_2) + M_0\theta(|x| > x_2) \right]\psi_\omega. \tag{6}$$

In order to formulate the spectral problem correctly, it is necessary to specify the boundary conditions. They can be represented in the form

$$\pm i\gamma^1\psi_\omega(\pm x_2) + e^{i\gamma_5\varphi(\pm x_2)}\psi_\omega(\pm x_2) = 0 \tag{7}$$

and must be supplemented with the continuity condition for the function $\psi(x)$ at the boundaries between regions I and II. We note that the boundary conditions (7) are nothing but the standard chiral boundary conditions for hybrid models [9–12]. Here, however, they emerge as a natural consequence of an infinite fermion mass in region III [21, 24] and not arise from a local surface action functional (as a matter of fact, the latter is not quite correct). In region I, Eq. (6) is the equation for free massless fermions,

$$\omega\psi_{\rm I} = -i\alpha\psi'_{\rm I}, \tag{8}$$

while, in the intermediate-phase region (II), we have

$$\omega\psi_{\rm II} = -i\alpha\psi'_{\rm II} + \beta M e^{i\gamma_5\varphi}\psi_{\rm II}. \tag{9}$$

At the boundary between regions I and II, the wave functions $\psi_{\rm I}$ and $\psi_{\rm II}$ are matched on the basis of the continuity condition

$$\psi_{\rm I}(\pm x_1) = \psi_{\rm II}(\pm x_1); \tag{10}$$

at $|x| = x_2$, they satisfy the boundary conditions (7). In Eq. (9), the field φ is not arbitrary, but it is self-consistently determined from Eq. (4b) with the corresponding boundary conditions requiring that the field and its derivative be continuous at the points $|x| = x_{1,2}$.

3. SELF-CONSISTENT SOLUTION TO THE BAG EQUATIONS

That, in the closed intermediate region II of finite dimension $d = x_2 - x_1$, the self-consistent Eqs. (4) have a simple and physically meaningful solution, which would be inappropriate in an unbounded space, is an important feature of the present bag construction. In order to obtain this solution in the most consistent way, we first make, in region II, the chiral Skyrme rotation

$$\psi = \exp(-i\gamma_5\varphi/2)\chi, \tag{11}$$

whereupon Eq. (9) and the boundary condition (7) go over to

$$\left(\omega - \frac{1}{2}\varphi'\right)\chi_\omega = -i\alpha\chi'_\omega + \beta M\chi_\omega \tag{12}$$

and

$$\pm i\gamma^1\chi_\omega(\pm x_2) + \chi_\omega(\pm x_2) = 0, \tag{13}$$

respectively.

It is obvious from (12) and (13) that, if we postulate a linear behavior of the scalar field in region II,

$$\varphi' = \text{const} = 2\lambda, \tag{14}$$

then Eq. (12) is converted into the equation for massive free fermions,

$$\nu\chi = -i\alpha\chi' + \beta M\chi, \tag{15}$$

with eigenvalues $\nu = \omega - \lambda$. Thus, we can see that, as was conjectured from the outset, fermions that are massless in region I acquire, owing to the interaction with the field φ, a mass M in region II, whereby there arises the intermediate phase describing massive quasifree constituent quarks. From the condition requiring that the scalar field be odd and be continuous together with its derivative on the unification I + II, we obtain

$$\varphi(x) = 2\lambda x. \tag{16}$$

Equation (15) possesses the obvious sign symmetry, $\nu \to -\nu$. The unitary transformation of the fermion wave function corresponding to this symmetry has the form

$$\chi \to \tilde{\chi} = i\gamma_1\chi. \tag{17}$$

The axial-current density

$$j_5 = i\bar{\psi}\gamma_5 e^{i\gamma_5\varphi}\psi = i\chi^+\gamma_1\chi \tag{18}$$

does not change for the sign-symmetric states; that is,

$$j_5 = i\chi^+\gamma_1\chi = i\tilde{\chi}^+\gamma_1\tilde{\chi} = \tilde{j}_5. \tag{19}$$

However, the corresponding property for the fermion spectrum in the problem being considered does not generally follow from the sign symmetry $\nu \to -\nu$ in Eq. (15), because this equation is valid only in region II and because the spectrum is determined from the solution to the Dirac equation on the unification I + II. By directly solving Eqs. (8) and (9) with allowance for the boundary conditions (7) and relation (10), we find that, in general, the spectrum satisfies the equation

$$\exp(4i\omega x_1 - 2i\varphi_1) = \frac{1 - e^{-2ikd\frac{M-i(\nu+k)}{M-i(\nu-k)}}}{1 - e^{-2ikd\frac{M+i(\nu-k)}{M+i(\nu+k)}}}\frac{1 - e^{2ikd\frac{M-i(\nu-k)}{M-i(\nu+k)}}}{1 - e^{2ikd\frac{M+i(\nu+k)}{M+i(\nu-k)}}}, \tag{20}$$

where $\nu^2 = k^2 + M^2$ and $\varphi_1 = \varphi(x_1)$. By analyzing Eq. (20), it is straightforwad to show that the fermion spectrum has the sign symmetry $\nu \to -\nu$ if

$$4\lambda x_1 - 2\varphi_1 = \pi s, \tag{21}$$

where s is an integer, because, at such values of the derivative of the field $\varphi(x)$ in region II, the left-hand side of Eq. (20) reduces to $(-1)^s \exp(4i\nu x_1)$. In our case, however, $\varphi_1 = 2\lambda x_1$; therefore, Eq. (21) leads to a unique possibility, $s = 0$, but the parameter λ remains arbitrary. This is the point where our version of the three-phase model differs fundamentally from the case considered in [21], where $\varphi_1 = 0$ by virtue of the condition that the boson condensate vanishes in region I and where there arises a set of solutions with different $s \neq 0$, but Eq. (21) then leads to a nontrivial relation between λ and x_1.

We now note that, in region II, we have, on the right-hand side of Eq. (4b), which determines $\varphi''(x)$, the expectation value of the C-odd axial current

$$J_5 = \frac{1}{2}\left[\bar{\psi}, i\gamma_5 e^{i\gamma_5\varphi}\psi\right]_- = \frac{1}{2}\left[\chi^+, i\gamma_1\chi\right]_-. \tag{22}$$

By χ, we mean here the second-quantized Dirac field in the chiral representation (11),

$$\chi(x,t) = \sum_n b_n\chi_n(x)e^{-i\omega_n t}, \tag{23}$$

where $\chi_n(x)$ stands for the normalized solutions to the corresponding Dirac equation and b_n and b_n^+ are the fermion creation and annihilation operators obeying the canonical anticommutation relations

$$\left\{b_n, b_{n'}^+\right\}_+ = \delta_{nn'}, \quad \{b_n, b_{n'}\}_+ = 0. \tag{24}$$

By definition, averaging over a given bag state involves averaging over the filled sea of negative-energy states ($\omega_n < 0$ +) and the possible filled valence-fermion states with $\omega_n > 0$, which are omitted for the time being, since special attention will be given below to their status. As a result, we arrive at

$$\langle J_5\rangle = \langle J_5\rangle_{\text{sea}} = \left(\frac{1}{2}\sum_{\omega_n<0} - \frac{1}{2}\sum_{n>0}\right)\chi_n^+ i\gamma_1\chi_n. \tag{25}$$

It should be emphasized that, in formula (25), the partition into sea and valence fermions occurs in accordance with the sign of their eigenfrequencies ω_n,

which differ from the sign-symmetric frequencies ν_n by a shift of λ:

$$\omega_n = \nu_n + \lambda; \tag{26}$$

therefore, they do not possess $\omega \to -\omega$ symmetry. If, however, we additionally assume that ν_n and λ are such that, for all n, the signs of ν_n and ω_n coincide—that is, none of ν_n changes sign upon a shift of λ—the condition $\omega_n \gtrless 0$ in (25) is equivalent to the condition $\nu_n \gtrless 0$. By virtue of relation (19), we then have

$$\langle J_5 \rangle_{\text{sea}} = \left(\frac{1}{2} \sum_{\nu_n<0} - \frac{1}{2} \sum_{\nu_n>0} \right) \chi_n^+ i\gamma_1 \chi_n = 0. \tag{27}$$

But this in turn means that Eq. (4b) in region II reduces to $\varphi'' = 0$; this is in perfect agreement with our original assumption that $\varphi'(x) = \text{const}$ in region II. In other words, we obtain a solution to the coupled Eqs. (4) in region II in the form of the linear function (16) for the scalar field and expression (26) for the fermion energy spectrum, where ν_n is in turn determined from Eq. (20) with substitution of $\exp(4i\nu x_1)$ for the left-hand side.

The conceptual content behind the above solution involves the following key points. The first of these is the finiteness of the dimension d of the intermediate region since, for an unbounded region II, the solution in (16) is physically unacceptable for obvious reasons. In our case, however, the dimension of the intermediate region is always finite by construction and the boson field $\varphi(x)$ acquires a soliton character in region III owing to the self-interaction $V(\varphi)$. Here, the following circumstance manifests itself once again: in (1 + 1)-dimensional space, the chiral interaction $\bar{\psi} e^{i\gamma_5 \varphi} \psi$ alone cannot impart a soliton character to the dynamics of the scalar field only through fermion-vacuum-polarization effects—an additional boson self-interaction is necessary [25].

The second factor has a more profound reason and is associated with the use of the $\nu \to -\nu$ symmetry in calculating the expectation value of the axial current J_5 over the Dirac sea. The point is that, for expectation values of this type, another physically meaningful definition in terms of the η invariant is possible. This definition, which is often used in studying fermion-vacuum-polarization effects [26], has the form

$$\langle J_5 \rangle_{\text{sea}} = \lim_{\eta \to 0} \left[\frac{1}{2} \sum_{\omega_n<0} e^{-|\omega_n|\eta} \chi_n^+ i\gamma_1 \chi_n - \frac{1}{2} \sum_{\omega_n>0} e^{-\omega_n \eta} \chi_n^+ i\gamma_1 \chi_n \right]. \tag{28}$$

Since the spectrum ω_n is not symmetric, expression (28) already is no longer zero, in contrast to the expectation value in (27). By taking into account the relation between ω_n and ν_n, we can recast expression (28) into the form

$$\lim_{\eta \to 0} \left[\sinh \lambda\eta \left(\sum_{\nu_n>0} e^{-\nu_n \eta} \chi_n^+ i\gamma_1 \chi_n \right) \right]. \tag{29}$$

In the limit $\eta \to 0$, the sum over ν_n in (29) diverges in proportion to $1/\eta$; therefore, the quantity $\langle J_5 \rangle$ appears to be proportional to λ and does not vanish as long as $\lambda \neq 0$. The right-hand side of Eq. (4b) will then no longer be zero, and linear functions will not be a solution to this equation in region II.

Moreover, this is so for other fermion expectation values—in particular, for the vacuum expectation value of the fermion charge. Owing to the fact that the fermion spectrum is discrete, the result that our computational procedure yields for the vacuum expectation value of the charge vanishes for the same reason as the axial current does. Namely, if use is made of the C-odd expression for the charge,

$$Q = \frac{1}{2} \int dx \, [\psi^+, \psi]_-, \tag{30}$$

if the same conditions of correspondence of the signs of ω_n and ν_n are assumed for all n, we obtain

$$\langle Q \rangle = \langle Q \rangle_{\text{sea}} = \frac{1}{2} \sum_{\omega_n<0} - \frac{1}{2} \sum_{\omega_n>0} = \frac{1}{2} \sum_{\nu_n<0} - \frac{1}{2} \sum_{\nu_n>0} = 0. \tag{31}$$

But if $\langle Q \rangle_{\text{sea}}$ is determined in terms of the η invariant, we have

$$\langle Q \rangle_{\text{sea}} = \lim_{\eta \to 0} \left[\frac{1}{2} \sum_{\omega_n<0} e^{-|\omega_n|\eta} - \frac{1}{2} \sum_{\omega_n>0} e^{-\omega_n \eta} \right] \neq 0 \tag{32}$$

for $\lambda \neq 0$, because there is no $\omega \to -\omega$ symmetry. However, there are serious arguments in favor of relations (27) and (31) as those that form the most adequate basis for calculating expectation values over the sea in our problem. First, the η invariant is in fact the measure of the asymmetry of the Hamiltonian rather than the fermion charge in the ground state. Second, other ways of regularization of divergent sums of the type in $\langle J_5 \rangle$ and $\langle Q \rangle$, apart from the temperature regularization, are possible, and—this is the most important point—there are no grounds to state that the regularized expressions (28) and (32) will lead to the required quantities for $\eta \to 0$. It is easy to exemplify the situation where the parameter dependence in a sum or in an integral is not continuous—in particular, $F(k) = \int_0^\infty dx \ \sin kx/x = \pi/2$ for any $k > 0$, but $F(0) = 0$—that is, the limit of the integral

for $k \to 0$ and its exact value at $k = 0$ are different in this case.

Let us further consider an adiabatic change in the gradient λ of the boson field in region II from $\lambda = 0$. At the initial instant, we have $\omega_n = \nu_n$; therefore, all C-odd expectation values over the fermion sea obviously vanish: $\langle\ \rangle_{\text{sea}} \equiv 0$ for any reasonable way of regularization. Further, we consider that, in our case, the fermion spectrum is purely discrete and that the λ dependence of the spectrum is continuous; therefore, all ω_n will retain sign for sufficiently small values of λ. On the basis of general considerations, it can then be conjectured that, as previously, we have $\langle\ \rangle_{\text{sea}} = 0$, although the spectrum ω_n is no longer symmetric, with the result that the η invariant does not vanish. Therefore, we have every ground to believe that, for C-odd quantities (such as the axial current and the vacuum fermion charge), the temperature regularization can give, in this case, values not corresponding to the physics of the problem. It should be emphasized here that this situation is markedly different from that in the case of an unbounded space, where the spectrum is continuous—this is the reason why, in the latter case, any arbitrarily small variation in λ leads to changes in the density of states and, hence, in all expectation values, whereby there arises the phenomenon of induced fermion numbers [26].

Finally, we can try to check numerically whether the solution in (16) is self-consistent. The problem is then solved on a lattice; therefore, the number of all degrees of freedom and, as a consequence, the number of fermion levels are inevitably finite in this case, so that no regularization is required. The results of the calculations demonstrate that the linear dependence (16) and vanishing expectation values represent a unique self-consistent solution to this problem.

This result can be interpreted as follows. In our case, the boson field is continuous everywhere (it is nonzero in all regions, including region I) and is topologically equivalent to that odd soliton which would occur in the absence of fermions only owing to the self-interaction $V(\varphi)$. For this reason, the presence of spatial regions that contain fermions (regions I and II) and their dimensions has no effect on the topological charge of the boson field. On the other hand, the baryon charge of a hybrid bag is by definition the sum of the topological charge of the boson soliton and the fermion charge of the internal bag regions. The latter is zero in our case; therefore, the baryon charge of the bag is determined exclusively by the topological charge of the boson field and, as is required by the ideology of hybrid models, is independent of the dimensions of regions I and II, which contain fermions. Thus, we can see that, in our approach, a hadron essentially represents a particle formed by a boson soliton to which a fermion bag is pasted by means of interaction in the intermediate region II. We also note that, although the quantum numbers of this composite particle are determined by the soliton, this does not mean that the filled positive-energy fermion levels must be necessarily absent. This will be so only at sufficiently small values of the parameter λ. With increasing λ, the negative levels $\omega_n = -|\nu_n| + \lambda$ will inevitably begin to go over to the positive section of the spectrum. The change in sign of each such level will lead to the decrease in $\langle Q\rangle_{\text{sea}}$ by one unit of charge. But if we fill the arising positive vacant levels with a valence fermion, the sum $Q_{\text{val}} + Q_{\text{sea}}$ will be zero, as previously. Analogously, the total axial current will be equal to $J_{\text{val}} + J_{\text{sea}}$ and will not change either, which in turn ensures zero right-hand part of Eq. (4b) and preserves the status of the linear function (16) as a self-consistent solution to the equations of the model. In other words, the ground state of the bag is by definition the state in which all $\nu_n < 0$ levels are filled (the inequality is strict, since $\nu = 0$ levels can never exist in the case being considered). Therefore, the presence or the absence of valence fermions in our construction of the bag ground state depends on the relationship between λ and $|\nu_n|_{\min}$ and appears to be a dynamical characteristic like other bag parameters (dimensions and mass), which are determined by minimizing the total bag energy.

4. TOTAL BAG ENERGY

Thus, the boson soliton has, in our case, the form of the linear function (16) on the unification I + II. Upon changing the scale of the field according to the rule $\varphi \to \varphi/g$, this function is matched with the soliton solution (5b) in the external region by imposing the continuity condition on the function and its derivative. In order to avoid going into details of the structure of the field self-interaction $V(\varphi)$, we assume that, in region III, we can use the asymptotic expansion of solutions to Eq. (5b) at large $|x|$; that is,

$$\varphi_{\text{sol}}(x) = \frac{\pi}{g}\left(1 - Ae^{-mx}\right), \quad x > x_2, \qquad (33)$$

where m is the meson mass in the external bag region and, for $x < -x_2$, the field $\varphi_{\text{sol}}(x)$ is determined by considering that it is odd. The coefficient π/g indicates that we are dealing with a phase soliton; its topological charge must be an integral multiple of $2\pi/g$, since this is the period of the bare chiral interaction $\bar{\psi}\exp(i\gamma_5 g\varphi)\psi$. The constant A is determined by requiring that the boson field be continuous at the points $x = \pm x_2$. It should be noted that, in the external region, there can never be chiral symmetry for the following two reasons: the phenomenology of strong interactions, on one hand, and the special features of (1 + 1)-dimensional scalar models, where

the presence of a mass is a necessary condition for the formation of the required soliton profile, on the other hand.

The matching conditions at $x = \pm x_2$ yield

$$2\lambda x_2 = \pi\left(1 - Ae^{-mx_2}\right), \tag{34a}$$

$$2\lambda = \pi m A e^{-mx_2}. \tag{34b}$$

From here, we find that the parameter λ and the dimension of the bag are related by the equation

$$2\lambda = \pi\frac{m}{mx_2 + 1}. \tag{35}$$

The total energy of the boson soliton can now be represented in the form

$$E_\varphi = \frac{\pi^2}{g^2}\frac{m}{mx_2 + 1}. \tag{36}$$

The total bag energy is the sum of the total energy of the boson soliton, E_φ, and the fermion contribution E_ψ,

$$E_{\text{bag}} = E_\varphi + E_\psi. \tag{37}$$

As can easily be seen from (36), the energy of the boson field changes quite smoothly and decreases in the limit $x_2 \to \infty$; it does not therefore generate a vacuum pressure, although, in the region I + II, the gradient φ gives rise to the constant positive contribution $\varphi'^2/2 = 2\lambda^2$ to the energy density. This contribution could be identified with the vacuum pressure B in the standard hybrid chiral model. Actually, this is an artifact of the one-dimensional character of our problem. With increasing bag dimension, the gradient φ in the region I + II will always decrease according to (35) at the same rate for any number of space dimensions; at the same time, the volume of the region I + II in the one-dimensional case increases only as a linear function, not compensating for the decrease in λ, as would occur in two and three dimensions. Thus, we can state that, in the (1 + 1)-dimensional case, a nontrivial dependence of the total bag energy E_{bag} on the parameters of the problem can stem only from the fermion contribution to the energy E_ψ. In general, the fermion contribution is the sum of the term associated with the Dirac sea of filled negative-energy states and the the term associated with positive-energy valence fermions,

$$E_\psi = E_{\text{val}} + E_{\text{sea}}. \tag{38}$$

For the bag ground state that has the structure described in the preceding section, the sum in (38) can be reduced to a single universal expression by considering that, in the charge-symmetric case, the energy of the Dirac sea must be determined as [25, 27]

$$E_{\text{sea}} = \frac{1}{2}\sum_{\omega_n<0}\omega_n - \frac{1}{2}\sum_{\omega_n>0}\omega_n. \tag{39}$$

If, in going over from ω_n to ν_n, the sign is conserved for all n, there are no valence fermions in the bag ground state (otherwise, it is impossible to ensure the vanishing of the expectation values of the charge and of the axial current). From Eq. (39), we then obtain

$$E_\psi = E_{\text{sea}} = \frac{1}{2}\sum_{\nu_n>0}(-\nu_n + \lambda) \tag{40}$$

$$-\frac{1}{2}\sum_{\nu_n>0}(\nu_n + \lambda) = -\sum_{\nu_n>0}\nu_n.$$

But if the parameter λ is such that the initially negative-energy level $\omega_n = -|\nu_n| + \lambda$ changes sign and becomes a filled valence state, it is convenient to calculate E_ψ in two steps. First, we take into account the contribution to E_{sea} from all $|\nu_n| > \lambda$ states. By analogy with (40), this contribution is given by

$$E'_{\text{sea}} = -\sum_{\nu_m>\lambda}\nu_m. \tag{41}$$

To this expression, we must add the energy of the arising valence fermion, $E_{\text{val}} = -|\nu_n| + \lambda\text{K}$, and the contribution of the positive levels $\omega_n = \pm|\nu_n| + \lambda$ to the energy of the Dirac sea; for their sum, we have

$$E_\psi = -|\nu_n| + \lambda - \frac{1}{2}[(-|\nu_n| + \lambda) \tag{42}$$

$$+ (|\nu_n| + \lambda)] + E'_{\text{sea}} = -\sum_{\nu_n>0}\nu_n.$$

This expression is identical to that in (40), which which was obtained for the energy of fermions in the absence of filled valence states.

For a further analysis, we introduce a set of new parameters in terms of which the total bag energy is expressed in the most convenient form. First, we introduce the dimensionless quantities

$$\alpha = 2Mx_1, \quad \beta = 2Md, \quad \rho = 2Mx_2 \tag{43}$$

and analyze in detail Eq. (20), which determines the levels ν_n. It has two branches of roots; of these, the first corresponds to real values of k and, as expressed in terms of the parameters α and β, has the form

$$\tan\left(\alpha\sqrt{1+x^2}\right) = \frac{x}{\sqrt{x^2+1}} \tag{44}$$

$$\times\frac{x\cos\beta x + \sin\beta x}{-\cos\beta x + x\sin\beta x},$$

where the dimensionless quantity x, which is related to k by the equation $k = Mx$, so that we have $\nu = M\sqrt{1+x^2}$, appears to be an unknown. The domain of real-valued roots x_n is the semiaxis $0 \le x_n < \infty$, since, by virtue of the finite dimensions of the region where the fermions reside and by virtue of the boundary conditions at the ends, the fermion wave functions are in fact standing waves degenerate in the sign of k,

the corresponding frequencies ν_n lying in the range $M \le \nu_n < \infty$.

The second branch corresponds to purely imaginary $k = iMx$, so that $\nu = M\sqrt{1-x^2}$ $(0 \le x \le 1)$, and can be obtained from (44) by means of an analytic continuation:

$$\tan\left(\alpha\sqrt{1-x^2}\right) = \frac{x}{\sqrt{1-x^2}}\frac{x\cosh\beta x + \sinh\beta x}{\cosh\beta x + x\sinh\beta x - 1}. \quad (45)$$

For the second branch, ν_n changes within the range $0 < \nu_n \le M$.

Thus, ν_n and E_ψ appear to be functions of two independent dimensionless parameters α and β, whose sum determines the dimension ρ of the confinement region in dimensionless units,

$$\alpha + \beta = \rho. \quad (46)$$

Further, it is convenient to factor the constituent quark mass M out of the sea energy and the fermion frequencies in the form of a dimensional factor by setting

$$\varepsilon_n = \nu_n/M = \sqrt{1+x_n^2}, \quad (47)$$

so that $E_\psi = -M\sum_n \varepsilon_n$, and to introduce the dimensionless ratio of two mass parameters of the theory,

$$\mu = m/2M, \quad (48)$$

and the dimensionless total energy $\mathcal{E}_{\rm bag} = E_{\rm bag}/M$. For the last quantity, we eventually have the expression

$$\mathcal{E}_{\rm bag} = \mathcal{E}_\psi(\alpha,\beta) + \frac{\pi^2}{g^2}\frac{2\mu}{\mu\rho+1}. \quad (49)$$

Here, α and β are independent dimensionless parameters specifying the dimensions of the internal bag regions, while ρ is determined from (46). But these are the points where the present version of the three-phase model differs substantially from the version considered in [21], where α and β were unambiguously determined by μ and ρ. Thus, the total bag energy nontrivially depends on three dimensionless parameters μ, α, and β. The parameter μ is fixed by specifying the masses m and M, while the optimum values of α and β for the bag ground state at given μ are determined by minimizing the total energy, which we now proceed to study. For this, we must first regularize the dimensionless energy of the fermion sea in $\mathcal{E}_\psi$. This quantity obviously diverges at the upper limit; therefore, it must be renormalized with the aid of an appropriate subtraction procedure.

We begin by analyzing the asymptotic behavior of the roots of Eq. (44) in the ultraviolet region, where $x_n \gg 1$. For this, it is convenient to recast this equation into the form

$$\sin\left(\alpha\sqrt{1+x^2}\right) = \frac{1}{2}\left(\sqrt{1+x^2}+x\right) \quad (50)$$
$$\times \sin\left(\alpha\sqrt{1+x^2}+\beta x+\gamma\right) + \frac{1}{2}(\sqrt{1+x^2}-x)$$
$$\times \sin\left(\alpha\sqrt{1+x^2}-\beta x-\gamma\right),$$

where $\gamma = \arctan x$. From (50), we obtain

$$x_n(\alpha,\beta) = \frac{\pi/2+\pi n}{\rho} \quad (51)$$
$$+ \frac{(-1)^{n+1}\sin\left[(\pi/2+\pi n)\alpha/\rho\right]+1-\alpha/2}{\pi/2+\pi n} + O(1/n^2).$$

In expression (51), the first term leads to a quadratic and a linear divergence in $\sum_n \varepsilon_n$, while the second term involves a logarithmic divergence; that part of the second term which contains the sine does not lead to a divergence because of its oscillatory character. Thus, the renormalization problem reduces to compensating, in the asymptotic expression (51), the first term and the divergent contributions in the second term. As in any procedure of this type, the first step consists in using the obvious fact that it is not energy proper but the difference of two energy values that has a physical meaning. For our bag, it seems the most natural to choose, as the reference point for $\mathcal{E}_\psi$, the energy of the sea of free fermions contained in the same volume ρ. However, this subtraction method is inappropriate in our case, since, upon adding all meaningful counterterms, this energy appears to be larger than the energy of all configurations with $\beta \ne 0$ by an infinite value (see [21]). The presence of an infinite energy barrier between regularized $\mathcal{E}_\psi(\alpha,\beta)$ and the sea of free fermions is in line with the intuitive idea that free fermions can hardly be a good first approximation in the confinement problem.

As a result, we have a situation where there is no unambiguous prescription for choosing the subtraction point in renormalizing $\mathcal{E}_\psi(\alpha,\beta)$, this actually being a feature common to the majority of bag models [10, 12, 28]. In the classical renormalization procedure, arbitrariness associated with the ambiguity in choosing the subtraction point is removed by fixing the physical values of the relevant number of parameters. For obvious reasons, we will not address this problem in our toy (1 + 1)-dimensional model; instead, we consider the most direct method that makes it possible to compensate for the divergences in the original sum (42) and which preserves the continuous dependence of the result of subtraction on the parameters. The method essentially consists in that we subtract, from $\sum_n \varepsilon_n$, another divergent sum where the general term is identical to the divergent part of the asymptotic expression (51) and where summation is performed over the same index n. As a result, we obtain the finite quantity

$$\tilde{\mathcal{E}}_\psi = -\sum_n\left[\varepsilon_n - \left(\frac{\pi/2+\pi n}{\rho} + \frac{1+\beta/2}{\pi/2+\pi n}\right)\right]. \quad (52)$$

In this case, no counterterms must be added, because all divergences have already been compensated by the subtracted sum. It is natural that the physical meaning of this procedure is lost to some degree. It should be noted, however, that only in the $(1+1)$-dimensional case is the theory with the interaction $\mathcal{L}_{\rm I} = G\bar{\psi}(\sigma + i\gamma_5\pi)\psi$ (super)renormalized and do all counterterms have a clear physical meaning. As one goes over to a larger number of spatial dimensions, this is no longer so. Therefore, the procedure for compensating the energy divergences that is based on formula (52) should not be considered as a procedure motivated by no reasons. For the hybrid chiral model, the problem of extracting a finite part from the divergent energy of the Dirac sea was investigated in greater detail elsewhere [28–31].

We now proceed to analyze the regularized total bag energy

$$\mathcal{E}_{\rm bag} = \tilde{\mathcal{E}}_\psi(\alpha,\beta) + \frac{\pi^2}{g^2}\frac{2\mu}{\mu\rho+1} \qquad (53)$$

as a function of the parameters α and β. The first property of $\mathcal{E}_{\rm bag}$ follows from the analysis of the contribution to $\tilde{\mathcal{E}}_\psi$ from the convergent sum of a logarithmic order arising from the sine term in the asymptotic expansion (51). We recast it into the form

$$\left(\tilde{\mathcal{E}}_\psi\right)_{\log}(\alpha,\beta) \qquad (54)$$
$$= \frac{1}{\pi}\sum_{n\gg 1}(-1)^n\frac{\sin\left[(\pi\alpha/\rho)(n+1/2)\right]}{n+1/2}$$

and then use the well-known relation

$$\sum_{n=0}^{\infty}(-1)^n\frac{\sin\left[z(n+1/2)\right]}{n+1/2} = \ln\tan(\pi/4+z/4). \quad (55)$$

It can easily be seen that the sums in (54) and (55) involve the general term of the same form. For $z\to\pi$, the sum in (55) diverges in proportion to $-\ln(\pi-z)$, whence it follows that, for $\pi\alpha/\rho\to\pi$—that is, for $\beta\to 0$ or for $\alpha\to\infty$ and finite β—the sum in (54) behaves similarly:

$$\left(\tilde{\mathcal{E}}_\psi\right)_{\log}(\alpha,\beta) \to -\frac{1}{\pi}\ln(\beta/\alpha), \quad \beta/\alpha\to 0. \quad (56)$$

Thus, the regularized fermion energy (52), together with total bag energy, shows a logarithmic singularity for $\beta\to 0$ and, at the same time, a logarithmic growth for $\alpha\to\infty$ and finite β. From the occurrence of a singularity for $\beta\to 0$, it follows that, in fact, the three-phase bag model being considered does not feature a smooth transition into the two-phase configuration for $d\to 0$, although there was formally such a possibility at the level of the original Lagrangian (2). In other words, the radial extension of the boundary in such a three-phase model can be arbitrarily small but not equal identically to zero—to some extent, this corresponds to general physical ideas of the structure of multiphase systems.

The quantity $\mathcal{E}_{\rm bag}$ grows for $\beta\to\infty$ and finite α as well. In this case, $\pi\alpha/\rho\to 0$, since ρ inevitably grows together with β; therefore, the logarithmic term in (54) becomes negligibly small, so that the next terms of the expansion in $1/n$ become dominant. Technically, it is more convenient, however, to make use of the fact that, for $\rho\to\infty$, the fermion spectrum becomes quasicontinuous everywhere, with the exception of a narrow vicinity of the Fermi surface (zero of energy). This makes it possible to go over from sums over x_n to an integral with respect to x. In particular, an analysis of the distribution of roots of Eq. (44) reveals that, in this limit, $\sum_n \varepsilon_n$ is approximated by the (divergent) integral

$$\sum_n \varepsilon_n \to \frac{1}{\pi}\int dx\,\sqrt{1+x^2}\left(\beta + \frac{1}{1+x^2} \right. \qquad (57)$$
$$+ \alpha\frac{x^2}{x^2+\sin^2\left(\alpha\sqrt{1+x^2}\right)}$$
$$\left. - \frac{\sin\left(\alpha\sqrt{1+x^2}\right)\cos\left(\alpha\sqrt{1+x^2}\right)}{\sqrt{1+x^2}\left(x^2+\sin^2\left(\alpha\sqrt{1+x^2}\right)\right)}\right).$$

For the sum subtracted in (52), we obviously have

$$\sum_n\left(\frac{\pi/2+\pi n}{\rho} + \frac{1+\beta/2}{\pi/2+\pi n}\right) \qquad (58)$$
$$\to \frac{\rho}{\pi}\int dx\,\left(x + \frac{1+\beta/2}{\rho x}\right).$$

It can easily be seen that the integrals in (57) and (58) involve the common divergent part

$$\frac{1}{\pi}\int dx\,(\rho x + 1/x + \beta/2x),$$

so that their difference appears to be a convergent integral, as it must in accordance with the subtraction procedure. In this difference, taken with the (correct) inverse sign, $\beta/8\pi x^3$ is the leading term in the integrand. It is owing to this circumstance that, in $\tilde{\mathcal{E}}_\psi$ and, accordingly, in $\mathcal{E}_{\rm bag}$, there arises a positive contribution proportional to β. Finally, it immediately follows from the analysis reported in [21] that, for $\alpha\to 0$ and finite β, there are no singularities in $\tilde{\mathcal{E}}_\psi$ and $\mathcal{E}_{\rm bag}$. It was shown in [21] that renormalized $\tilde{\mathcal{E}}_\psi$ at $\alpha = 0$ and at finite $\beta\neq 0$ always differ solely by a finite value. In this region, the soliton energy $\mathcal{E}_\varphi$—in particular, the values of the parameters μ and g—therefore begins to play an important role. To be more specific, we note that, if μ is not overly small, the g dependence of $\mathcal{E}_\varphi$ is such that, at sufficiently small g,

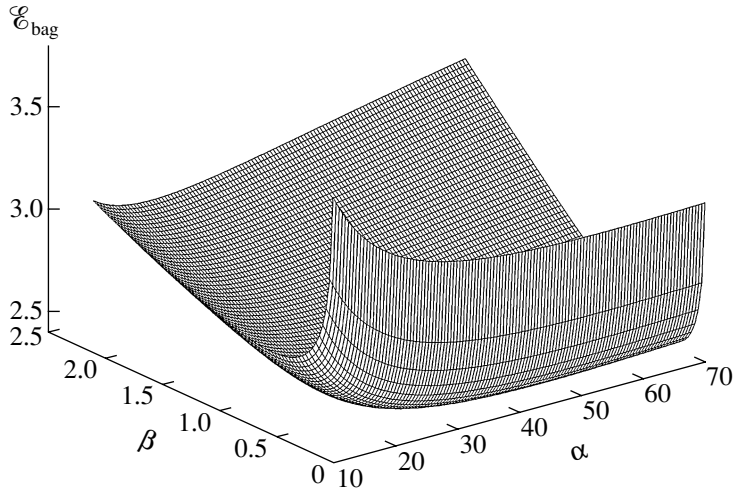

Fig. 1. Total dimensionless energy $\mathcal{E}_{\text{bag}}(\alpha, \beta)$ of a bag for $\mu = 0.25$.

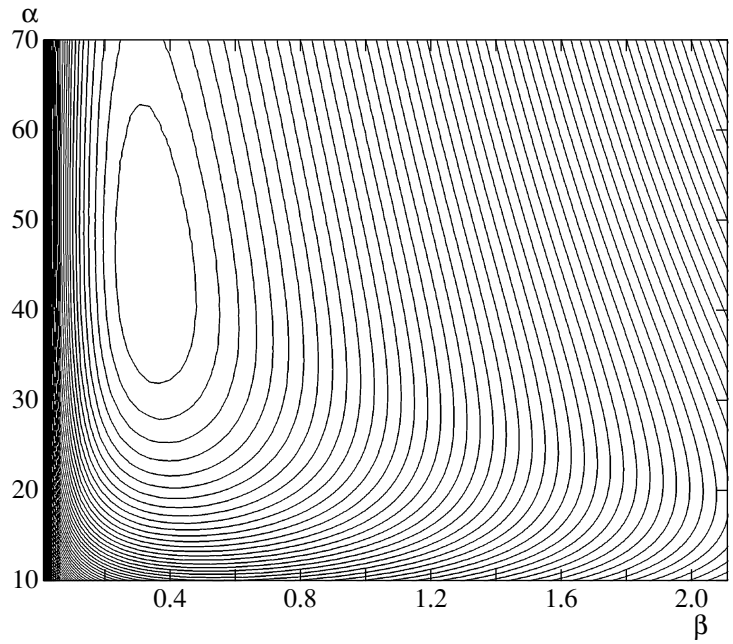

Fig. 2. Isolines for $\mathcal{E}_{\text{bag}}(\alpha, \beta)$ at $\mu = 0.25$. The minimum at $\alpha \simeq 40$–50 and $\beta \simeq 0.4$ is clearly seen.

$\mathcal{E}_{\text{bag}}$ grows sharply for $\alpha \to 0$ and finite β, whereby the presence of a pronounced minimum is ensured. On the contrary, a considerable increase in g or the vanishing of μ ($\mu \to 0$) can render the soliton energy $\mathcal{E}_\varphi$ negligibly small (nearly constant) over the entire region of variations in the bag dimensions. In this case, there can be no minimum in the total energy at all.

A numerical calculation fully confirms the above qualitative behavior of $\tilde{\mathcal{E}}_\psi$ and $\mathcal{E}_{\text{bag}}$. However, the presence of a minimum in the total bag energy as a function of α and β and, hence, the existence of a stable ground state of the bag at given values of μ and g can be proven or disproved only via a numerical calculation because there is no singularity in $\mathcal{E}_{\text{bag}}$ at $\alpha = 0$. In the present study, such a calculation was performed at $\mu = 0.25$, which approximately corresponds to the ratio $m_\pi/2m_Q$ if the constituent quark mass is taken to be 300 MeV and if $g = 1$. Qualitatively, the behavior of $\mathcal{E}_{\text{bag}}$ as a function of α and β is illustrated in Fig. 1, whence we can see that there is only one minimum in the total energy at nonzero values of α and β. Figure 2 shows relevant isolines, which make it possible to observe this minimum more

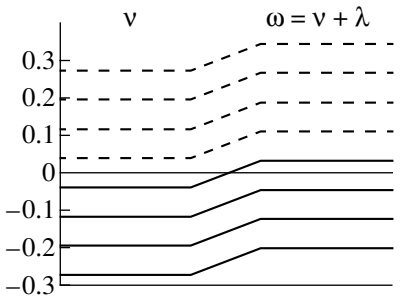

Fig. 3. Diagram of fermion levels for the bag ground state.

clearly. The values of α and β at the minimum differ approximately by two orders of magnitude; that is, the dimension of the intermediate region proves to be much less than the dimension of the internal region—to some extent, this transition region can be treated as a smeared boundary between the asymptotic-freedom region and the purely color-singlet phase. For this configuration, Fig. 3 displays the diagram of fermion levels in the vicinity of zero. It can be seen that, in this case, the ground state has one filled positive-energy valence level.

5. CONCLUSION

The objective of the present study has been to construct a consistent meaningful hybrid chiral model in which it is not assumed, from the outset, that the fermion and the boson (meson) phase are exactly equivalent. Our results have revealed that such a model can indeed be formulated in quite a consistent way and, in some points, can prove to be a means that describes low-energy hadron physics more efficiently than traditional hybrid chiral models.

First of all, we note that the original formulation of the model is a strictly local field theory and that, despite the abundance of classical solutions, which must be taken into account, covariance is broken here only spontaneously. This breakdown can be removed by means of the method developed in [23]—that is, by using covariant group variables of the center of inertia of the localized quantum-field system. Among the main advantages of our approach, we would like to mention the following: (i) The chiral boundary conditions are specified in a more correct form such that all components in the Lagrangian have a clear physical meaning. (ii) It leads to the existence of an intermediate phase that describes quasifree massive constituent quarks. (iii) Physically, the resulting behavior of the total energy of the bag as function of its dimensions is quite acceptable.

In addition, the fermion-confinement condition embedded in the model from the outset is manifested more clearly therein. This is reflected, in particular, in the fact that there is no need here for introducing a vacuum-pressure term (which, in the standard approach, is incorporated in the model on the basis of ad hoc considerations) since, in the case being considered, the polarization of the Dirac sea alone ensures an indefinite growth of energy at large distances.

A feature that distinguishes the problem considered here from that which was addressed in [21] is the following. Here, the condition of a nonzero boson-condensate density in the internal bag region radically affects the number of possible bag configurations realizing a local minimum of energy. In [21], the vanishing of the boson field in the internal region led to the emergence of an infinite series of such configurations that had indefinitely growing dimensions and energy and which differed from one another by the value of the gradient λ of the boson field in the intermediate region. In the present case, there is not more than one such configuration, if any, whereas high-energy bag states can be obtained only with the aid of extra valence fermions. Thus, we can see that the three-phase modification of the hybrid bag model admits a wide variety of types of description of composite particles such as hadrons and of their excited states.

It is necessary to emphasize once again that the problem of choosing a method for calculating expectation values over the Dirac sea for fermion bags is of fundamental importance. The method used here is based on the discrete character of the fermion energy spectrum and is capable of producing, via some obvious arguments, quite a simple solution to the self-consistent bag equations in the intermediate region. It should be recalled, however, that, despite the above argument in favor of precisely this method for computing expectation values over the Fermi sea, there are no grounds to reject, out of hand, alternative approaches like those that are based on temperature regularization. The problem of pinpointing a method that is the most adequate to the physics behind the problem can be resolved only by means of detailed investigations into realistic models.

ACKNOWLEDGMENTS

This work was supported by the Russian Foundation for Basic Research (project nos. 96-02-18097, 96-15-96674, and 00-15-96577) and by the St. Petersburg Contest Center for Fundamental Natural Sciences (grant no. 97-0-6.2-28). The work of I.O. Cherednikov was supported by a scholarship from the Council of Young Scientists at the Institute of Nuclear Physics, Moscow State University.

REFERENCES

1. A. Chodos, R. L. Jaffe, K. Johnson, *et al.,* Phys. Rev. D **9**, 3471 (1974).
2. W. A. Bardeen, M. S. Chanowitz, S. D. Drell, *et al.,* Phys. Rev. D **11**, 1094 (1975).
3. P. N. Bogolyubov and A. E. Dorokhov, Fiz. Élem. Chastits At. Yadra **18**, 917 (1987) [Sov. J. Part. Nucl. **18**, 391 (1987)].
4. E. W. Shuryak, Phys. Rep. **115**, 151 (1984).
5. A. E. Dorokhov, Yu. E. Zubov, and N. I. Kochelev, Fiz. Élem. Chastits At. Yadra **23**, 1192 (1992) [Sov. J. Part. Nucl. **23**, 522 (1992)].
6. A. Chodos, R. L. Jaffe, K. Johnson, and C. B. Thorn, Phys. Rev. D **10**, 2559 (1974).
7. T. DeGrand, R. L. Jaffe, K. Johnson, and J. Kiskis, Phys. Rev. D **12**, 2060 (1975).
8. K. Johnson, Acta Phys. Pol. B **6**, 865 (1975).
9. A. Chodos and C. B. Thorn, Phys. Rev. D **12**, 2733 (1975).
10. M. Rho, Phys. Rep. **240**, 1 (1994).
11. M. Rho, nucl-th/9812012.
12. H. Hosaka and O. Toki, Phys. Rep. **277**, 65 (1996).
13. I. Zahed and G. E. Brown, Phys. Rep. **142**, 1 (1986).
14. G. Holzwarth and B. Schwesinger, Rep. Prog. Phys. **49**, 825 (1986).
15. J. Schechter and H. Weigel, hep-ph/9907554.
16. M. Wakamatsu, Phys. Lett. B **349**, 204 (1995).
17. K. A. Sveshnikov and I. O. Cherednikov, Yad. Fiz. **62**, 1511 (1999) [Phys. At. Nucl. **62**, 1426 (1999)].
18. S. Nadkarni, H. B. Nielsen, and I. Zahed, Nucl. Phys. B **253**, 308 (1985); S. Nadkarni and H. B. Nielsen, Nucl. Phys. B **263**, 1 (1986); **263**, 23 (1986).
19. S. Coleman, Phys. Rev. D **11**, 2088 (1975); S. Mandelstam, Phys. Rev. D **11**, 3026 (1975).
20. M. Rho, A. S. Goldhaber, and G. E. Brown, Phys. Rev. Lett. **51**, 747 (1983); J. Goldstone and R. L. Jaffe, Phys. Rev. Lett. **51**, 1518 (1983).
21. K. A. Sveshnikov and P. K. Silaev, Theor. Math. Phys. **117**, 1319 (1998).
22. M. Creutz, Phys. Rev. D **10**, 1749 (1974); M. Creutz and K. Soh, Phys. Rev. D **12**, 443 (1975).
23. K. A. Sveshnikov, Phys. Lett. A **136**, 1 (1989); Teor. Mat. Fiz. **82**, 55 (1990).
24. R. Perry and M. Rho, Phys. Rev. D **34**, 1169 (1986).
25. D. K. Campbell and Y.-T. Liao, Phys. Rev. D **14**, 2093 (1976).
26. A. J. Niemi and G. W. Semenoff, Phys. Rep. **135**, 99 (1986).
27. R. Daschen, B. Hasslacher, and A. Neveu, Phys. Rev. D **12**, 2443 (1975).
28. G. Plumien, B. M. Muller, and W. Greiner, Phys. Rep. **134**, 87 (1986).
29. E. Elizalde, M. Bordag, and K. Kirsten, hep-th/9707083; E. Elizalde, M. Bordag, K. Kirsten, and S. Leseduarte, J. Phys. A **31**, 1743 (1998).
30. K. Milton, hep-th/9901011.
31. R. D. M. De Paola, R. B. Rodríguez, and N. F. Svaiter, hep-th/9905039.

Translated by A. Isaakyan

Physics of Atomic Nuclei, Vol. 64, No. 9, 2001, pp. 1716–1721. From Yadernaya Fizika, Vol. 64, No. 9, 2001, pp. 1796–1801.

ELEMENTARY PARTICLES AND FIELDS
Theory

Vibration of the QCD String*

Yu. S. Kalashnikova** **and D. S. Kuzmenko*****

Institute of Theoretical and Experimental Physics, Bol'shaya Cheremushkinskaya ul. 25, Moscow, 117259 Russia

Received August 30, 2000; in final form, December 6, 2000

Abstract—The large-distance behavior of adiabatic hybrid potentials is studied on the basis of the QCD string model. The calculated spectra are shown to result from the interplay of potential-type longitudinal and string-type transverse vibrations. © *2001 MAIK "Nauka/Interperiodica".*

General arguments from QCD and lattice data tell that the theory, even quenched in quarks, possesses a nontrivial spectrum, so that effective degrees of freedom for a constituent glue should be introduced to describe QCD in the nonperturbative region. As far as we know, the possibility for mesons with a gluonic lump to exist was first considered in [1] in 1976. Modern wisdom tells that the area-law asymptotic behavior of the Wilson loop implies a kind of string to be developed between a quark and an antiquark at large distances, and it is natural to identify the $q\bar{q}$ system connected by the string in its ground state with a conventional $q\bar{q}$ meson, while string vibrations are responsible for gluonic (hybrid) excitations. This picture, though physically appealing, does not follow directly from QCD, and one relies on models to describe these excitations. There are two main ideas on how to construct such models. One is to consider pointlike gluons confined by some potential-type force [2, 3], and the other is to introduce string phonons [4].

In principle, the best way to discriminate between these two possibilities is to compare predictions with experimental data on hybrid mesons. Indeed, there are many indications that hybrid mesons have already been found, but conclusive evidence has never been presented, nor have alternative explanations been completely excluded [5].

On the other hand, lattice calculations are now sufficiently accurate to provide reliable data on the properties of soft glue and to check model predictions. In this respect, recent measurements [6] of adiabatic hybrid potentials are of particular interest. These simulations measure the spectrum of glue in the presence of a static quark and a static antiquark separated by some distance R. Not only are these potentials involved in heavy-hybrid-mass estimations in the Born–Oppenheimer approximation, but the large-R limit is important *per se*, since the formation of a confining string is expected at large distances, and direct measurements of string fluctuations become available. It is our purpose to investigate the large-distance behavior of adiabatic potentials in order to establish the kind of effective string degrees of freedom that are excited at large distances.

We perform these studies within the QCD string model. This model deals with quarks and pointlike gluons propagating in the confining QCD vacuum and is based on the method of vacuum background correlation functions [7]. The QCD string model was successfully applied to conventional mesons [8], hybrids [9, 10, 7], glueballs [11], and gluelump (gluon bound to the static adjoint source) [12].

The QCD string model for gluons is derived from perturbation theory against the nonperturbative background, developed in [13]. This formalism allows one to introduce constituent (valence) gluons as perturbations against the confining background. The latter is given by a set of gauge-invariant field-strength correlation functions that are responsible for the area law. The main feature of this approach is that, in contrast to the aforementioned models, one is able here to distinguish clearly between confining gluonic field configurations and confined valence gluons.

The starting point is the Green's function for the gluon propagating in a given background field B_μ [13],

$$G_{\mu\nu}(x,y) = (D^2(B)\delta_{\mu\nu} + 2igF_{\mu\nu}(B))^{-1}, \qquad (1)$$

where the covariant derivative $D^{ca}_\lambda(B)$ is

$$D^{ca}_\lambda(B) = \delta_{ca}\partial_\lambda + gf^{cba}B^b_\lambda. \qquad (2)$$

The term proportional to $F_{\mu\nu}(B)$ is responsible for the gluon spin interaction; in these first studies,

*This article was submitted by the authors in English.

**e-mail: yulia@heron.itep.ru

***e-mail: kuzmenko@heron.itep.ru

we neglect it, since it can be treated as a perturbation [11, 12]. The next step is to use the Feynman–Schwinger representation for the quark–antiquark–gluon Green's function [10], which is reduced, in the case of a static quark and a static antiquark, to the form

$$G(x_g, y_g) = \int_0^\infty ds \int Dz_g \exp(-K_g)\langle \mathcal{W}\rangle_B, \qquad (3)$$

where $K_g = \frac{1}{4}\int_0^s \dot{z}_g^2(\tau)\, d\tau$ and where the dependence on the vacuum gluonic field B_μ is entirely contained in the Wilson loop

$$\mathcal{W} = \mathrm{tr}(\lambda_a \Phi_q \lambda_b \Phi_{\bar{q}})\Phi^{ab}_{\Gamma_g}(y_g, x_g). \qquad (4)$$

Here, Φ_q and $\Phi_{\bar{q}}$ are the parallel transporters given by

$$\Phi_q = P\exp ig\int_{y_q}^{x_q} B_\mu(z_q) dz_{q\mu}, \qquad (5)$$

$$\Phi_{\bar{q}} = P\exp ig\int_{x_{\bar{q}}}^{y_{\bar{q}}} B_\mu(z_{\bar{q}}) dz_{\bar{q}\mu}.$$

In (5), the integration is performed along the classical trajectories $z_{q\mu} = (\tau, \mathbf{R}/2)$ and $z_{\bar{q}\mu} = (\tau, -\mathbf{R}/2)$ of a static quark and a static antiquark, P means path ordering,

$$\Phi^{ab}_{\Gamma_g}(y_g, x_g) = \Big(P\exp ig\int_{\Gamma_g} B_\mu(z_g)\, dz_{g\mu}\Big)^{ab}, \qquad (6)$$

a and b are adjoint color indices, λ_a are the Gell-Mann matrices, and the contour Γ_g runs along the gluon trajectory z_g.

The main assumption of the QCD string model is the minimal area law for the Wilson loop average, which yields, for the configuration in (4), the form [10]

$$\langle \mathcal{W}\rangle_B = \frac{N_c^2 - 1}{2}\exp\big(-\sigma(S_1 + S_2)\big), \qquad (7)$$

where S_1 and S_2 are the minimal areas inside the contours formed by the quark and gluon and by the antiquark and gluon trajectories, respectively, and σ is the string tension.

With the form (7) for $\langle \mathcal{W}\rangle_B$, the action of the system can be immediately read out of the representation (3),

$$A = \int_0^T d\tau \left\{ -\frac{\mu}{2} + \frac{\mu\dot{r}^2}{2} \right. \qquad (8)$$

$$\left. - \sigma\int_0^1 d\beta_1 \sqrt{(\dot{w}_1 w_1')^2 - \dot{w}_1^2 w_1'^2} \right.$$

$$\left. - \sigma\int_0^1 d\beta_2 \sqrt{(\dot{w}_2 w_2')^2 - \dot{w}_2^2 w_2'^2} \right\},$$

where the minimal surfaces S_1 and S_2 are parametrized by the coordinates $w_{i\mu}(\tau, \beta_i)$, i=1, 2, $\dot{w}_{i\mu} = \partial w_{i\mu}/\partial\tau$, $w'_{i\mu} = \partial w_{i\mu}/\partial\beta_i$.

In what follows, the straight-line ansatz is chosen for the minimal surface:

$$w_{i0} = \tau, \quad \mathbf{w}_{1,2} = \pm(1-\beta)\frac{\mathbf{R}}{2} + \beta\mathbf{r}. \qquad (9)$$

The quantity $\mu = \mu(\tau)$ in expression (8) for the action is the so-called einbein field [14]; here, one is forced to introduce it, since this is the only way to obtain meaningful dynamics for a massless particle. Moreover, we introduce another set of einbein fields, $\nu_i = \nu_i(\tau, \beta_i)$, to get rid of the Nambu–Goto square roots in (8) [8]. The resulting Lagrangian takes the form

$$L = -\frac{\mu}{2} + \frac{\mu\dot{r}^2}{2} - \int_0^1 d\beta_1 \frac{\sigma^2 r_1^2}{2\nu_1} \qquad (10)$$

$$- \int_0^1 d\beta_1 \frac{\nu_1}{2}\big(1 - \beta_1^2 l_1^2\big)$$

$$- \int_0^1 d\beta_2 \frac{\sigma^2 r_2^2}{2\nu_2} - \int_0^1 d\beta_2 \frac{\nu_2}{2}\big(1 - \beta_2^2 l_2^2\big),$$

$$l_{1,2}^2 = \dot{r}^2 - \frac{1}{r_{1,2}^2}\cdot(\mathbf{r}_{1,2}\cdot\dot{\mathbf{r}})^2, \quad \mathbf{r}_{1,2} = \mathbf{r} \pm \frac{\mathbf{R}}{2}.$$

It is clear from Eq. (10) that the einbein field μ can be treated as the kinetic energy of the constituent gluon and that the einbeins $\nu_i(\tau, \beta_i)$ describe the energy-density distribution along the string. These quantities are not introduced by hand, but they are calculated in the proposed formalism. Indeed, since no time derivatives of the einbeins appear in Lagrangian (10), it describes a constrained system, with the equations of motion

$$\frac{\partial L}{\partial\mu} = 0, \qquad \frac{\delta L}{\delta\nu_i(\beta_i)} = 0 \qquad (11)$$

playing the role of second-class constraints.

Now, one obtains the Hamiltonian $H = \mathbf{p}\cdot\dot{\mathbf{r}} - L$, with the result

$$H = H_0 + \frac{\mu}{2} + \int_0^1 d\beta_1 \frac{\sigma^2 r_1^2}{2\nu_1} \qquad (12)$$

$$+ \int_0^1 d\beta_2 \frac{\sigma^2 r_2^2}{2\nu_2} + \int_0^1 d\beta_1 \frac{\nu_1}{2} + \int_0^1 d\beta_2 \frac{\nu_2}{2},$$

$$H_0 = \frac{p^2}{2(\mu + J_1 + J_2)} \tag{13}$$
$$+\frac{1}{2\Delta(\mu + J_1 + J_2)} \left\{ \frac{(\mathbf{p}\cdot\mathbf{r}_1)^2}{r_1^2} J_1(\mu + J_1) \right.$$
$$+ \frac{(\mathbf{p}\cdot\mathbf{r}_2)^2}{r_2^2} J_2(\mu + J_2)$$
$$\left. + \frac{2J_1J_2}{r_1^2 r_2^2}(\mathbf{r}_1\cdot\mathbf{r}_2)(\mathbf{p}\cdot\mathbf{r}_1)(\mathbf{p}\cdot\mathbf{r}_2) \right\},$$

$$\Delta = (\mu + J_1)(\mu + J_2) - J_1J_2\frac{(\mathbf{r}_1\cdot\mathbf{r}_2)^2}{r_1^2 r_2^2},$$

$$J_i = \int_0^1 d\beta_i\, \beta_i^2 \nu_i(\beta_i), \quad i = 1, 2.$$

Since we deal with a constrained system, the extra variables μ and $\nu_{1,2}$ should be excluded by means of the conditions

$$\frac{\partial H}{\partial \mu} = 0, \qquad \frac{\delta H}{\delta \nu_i(\beta_i)} = 0 \tag{14}$$

before quantization; the extrema of the einbeins should be found from Eq. (14) and substituted into the Hamiltonian. Such a procedure is hardly possible analytically with the complicated structure specified by Eqs. (12) and (13) even at the classical level; after quantization, these extremal values of the einbeins would become nonlinear operator functions of coordinates and momenta, with inevitable ordering problems arising. In what follows, we use the approximation that treats μ and ν_i as c-number variational parameters. We find the eigenvalues of Hamiltonian (12) as functions of μ and ν_i and minimize them with respect to the einbeins to obtain the physical spectrum. This einbein method works surprisingly well in the calculations based on the QCD string model, with the accuracy of about 5–10% for the ground state [15].

Even with this simplifying assumption, the problem remains complicated because of the presence of the terms $J_{1,2}$ responsible for the string inertia. Suppose for a moment that one can neglect these terms in the kinetic energy (13). The Hamiltonian then takes the form [7, 10]

$$H = \frac{p^2}{2\mu} + \frac{\mu}{2} + \int_0^1 d\beta_1 \frac{\sigma^2 r_1^2}{2\nu_1} \tag{15}$$
$$+ \int_0^1 d\beta_2 \frac{\sigma^2 r_2^2}{2\nu_2} + \int_0^1 d\beta_1 \frac{\nu_1}{2} + \int_0^1 d\beta_2 \frac{\nu_2}{2},$$

which allows one to eliminate einbeins and to arrive at the potential-model Hamiltonian

$$H = \sqrt{p^2} + \sigma r_1 + \sigma r_2. \tag{16}$$

Let us now estimate whether the disregard of string inertia is justified. To this end, we find the spectrum of the Hamiltonian given by (15) and (16) using the einbein method described above. It is given by the set of equations

$$E_n(R) = \mu_n(R) + \frac{4(n + 3/2)^2\sigma^2}{\mu_n^3(R)}, \tag{17}$$
$$16\sigma^2\Big(n + \frac{3}{2}\Big)^4 = \mu_n^4(R)\Big(4\Big(n + \frac{3}{2}\Big)^2 + R^2\mu_n^2(R)\Big)$$

with ν_i independent of β_i,

$$\nu_{1n}(R) = \nu_{2n}(R) = \frac{2(n + 3/2)^2\sigma^2}{\mu_n^3(R)}, \tag{18}$$

where $n = n_z + n_\rho + \Lambda$, $\Lambda = |\mathbf{L}\cdot\mathbf{R}/R|$ being the projection of the orbital angular momentum onto the z axis ($\mathbf{z} \parallel \mathbf{R}$). Note that, while the angular momentum is not conserved in the exact Hamiltonian (16), it is a good quantum number in the approximate einbein method: we have compared the spectrum of the exact and the einbein-field Hamiltonian and found that the angular momentum is conserved in the potential problem (16) to within 5%. The same phenomenon is observed in the constituent gluon model [3] and is the consequence of linear potential confinement.

Let us first consider the small-R ($R \ll 1/\sqrt{\sigma}$) limit of the set of Eqs. (17):

$$E_n(R) = 2^{3/2}\sigma^{1/2}\Big(n + 3/2\Big)^{1/2} \tag{19}$$
$$+ \frac{\sigma^{3/2}R^2}{2^{3/2}(n + 3/2)^{1/2}},$$
$$\mu_n(R) = 2^{1/2}\sigma^{1/2}\Big(n + 3/2\Big)^{1/2} - \frac{\sigma^{3/2}R^2}{2^{5/2}(n + 3/2)^{1/2}},$$
$$\nu_{1,2n}(R) = \frac{(n + 3/2)^{1/2}\sigma^{1/2}}{2^{1/2}} + \frac{3\sigma^{3/2}R^2}{2^{7/2}(n + 3/2)^{1/2}}.$$

The last line in (19) yields $J_{1,2}/\mu \approx 1/6$. The situation here is similar to that in the light-quark, glueball, and gluelump QCD string calculations: the correction due to the string inertia is sizable but not large and can be taken into account as a perturbation [11, 12]. Note that it is the regime of small R that is relevant to heavy-hybrid-mass estimations [16]: the average distance between the heavy quark and antiquark is small, $\langle R^2\rangle \ll 1/\sigma$, so that the $q\bar{q}$ pair resides in the oscillator adiabatic potential, which, in the einbein method, is given by Eq. (19).

The situation changes drastically in the case of large R, $R \gg 1/\sqrt{\sigma}$. Now, a gluon enjoys small oscillation motion, and one has

$$E_n(R) = \sigma R + \frac{3}{2^{1/3}}\,\sigma^{1/3}\,\frac{(n+3/2)^{2/3}}{R^{1/3}}, \qquad (20)$$

$$\mu_n(R) = \frac{4\sigma^{1/3}(n+3/2)^{2/3}}{R^{1/3}}, \quad \nu_{1,2n}(R) = \frac{\sigma R}{2},$$

displaying the $(\sigma/R)^{1/3}$ subleading behavior typical of linear potential confinement at large distances [7]. In this case, we nevertheless have $J_{1,2} = \frac{1}{6}\sigma R \gg \mu_n$, so that the potential regime is inadequate at large R.

To obtain deeper insight into what happens at intermediate and large distances, we consider the semiclassical limit of large Λ, where only rotations about z axis are taken into account:

$$H = \frac{\Lambda^2}{2\rho^2(J_1+J_2)} + \frac{\sigma^2}{2}\Big(\rho^2 + \Big(z+\frac{R}{2}\Big)^2\Big) \qquad (21)$$
$$\times \int \frac{d\beta_1}{\nu_1} + \frac{\sigma^2}{2}\Big(\rho^2 + \Big(z-\frac{R}{2}\Big)^2\Big)\int \frac{d\beta_2}{\nu_2}$$
$$+ \int_0^1 d\beta_1 \frac{\nu_1}{2} + \int_0^1 d\beta_2 \frac{\nu_2}{2}.$$

Since no momenta p_z and $\dfrac{\mathbf{p}\cdot\boldsymbol{\rho}}{\rho}$ appear in the Hamiltonian, the system stabilizes itself at the points z_0 and ρ_0 given by the conditions

$$\frac{\partial H}{\partial z} = 0, \qquad \frac{\partial H}{\partial \rho} = 0. \qquad (22)$$

Combining Eq. (22) with the second condition in (14), one arrives at the expressions

$$z_0 = 0, \quad \rho_0 = \frac{\Lambda}{2\sigma\sqrt{Ja}}, \quad \nu_1(\beta) = \nu_2(\beta) = \nu(\beta), \qquad (23)$$

where

$$J = \int_0^1 d\beta \beta^2 \nu(\beta), \quad a = \int_0^1 \frac{d\beta}{\nu(\beta)} \qquad (24)$$

and the function $\nu(\beta)$ is given by

$$\nu(\beta) = \frac{\sqrt{A}}{\sqrt{1-B\beta^2}}, \qquad (25)$$

$$A = \frac{\sigma^2 R^2}{4} + \frac{\Lambda\sigma}{2\sqrt{aJ}}, \quad B = \frac{\Lambda\sigma}{2J}\sqrt{\frac{a}{J}}.$$

Substituting the form (25) into (24), one finds for the energy that

$$E = 2\sigma^{1/2}\Lambda^{1/2}\arcsin\sqrt{B} \qquad (26)$$
$$\times \frac{\{\arcsin\sqrt{B} + \sqrt{B(1-B)}\}^{1/4}}{\{\arcsin\sqrt{B} - \sqrt{B(1-B)}\}^{3/4}},$$

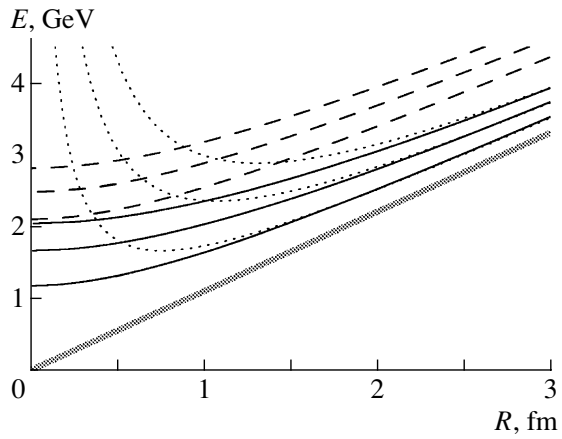

Fig. 1. Adiabatic hybrid potentials in various regimes. The semiclassical (solid), potential (dashed), and flux-tube (dotted) curves for $n_z = n_\rho = 0$ and $\Lambda = 1, 2, 3$ are presented here. The lowest curve is σR ($\sigma = 0.22$ GeV^2).

$$2\Lambda B^{3/2}\sqrt{1-B}$$
$$= \frac{\sigma R^2}{4}\{\arcsin\sqrt{B} + \sqrt{B(1-B)}\}^{1/2}$$
$$\times \{\arcsin\sqrt{B} - \sqrt{B(1-B)}\}^{3/2},$$

with the large-R limit of (26) given by

$$E(R) = \sigma R + 2\sqrt{3}\frac{\Lambda}{R}. \qquad (27)$$

Here, we have the $1/R$ subleading behavior typical of the naive Nambu–Goto string models. For example, the flux-tube model [4] predicts

$$E(R) = \sigma R + \frac{\pi\Lambda}{R} \qquad (28)$$

in the small-oscillation approximation. The energy curve (26) is shown in Fig. 1, along with the flux-tube (28) and potential-regime curve (17) for $n_z = n_\rho = 0$ and $\Lambda = 1, 2, 3$. The large-R limit of the semiclassical regime (26) is very close to the flux-tube one and deviates substantially from the potential regime, while, at small R, the unphysical divergent $1/R$ behavior is absent.

The case of large R can be treated directly by using the full Hamiltonian (12), which, in the small-oscillation limit, takes the form

$$H = \frac{\mu}{2} + \frac{p_z^2}{2\mu} + \frac{p_\perp^2}{2(\mu+J_1+J_2)} \qquad (29)$$
$$+ \sigma^2\Big(\rho^2 + \Big(z+\frac{R}{2}\Big)^2\Big)\int_0^1 \frac{d\beta_1}{2\nu_1}$$
$$+ \sigma^2\Big(\rho^2 + \Big(z-\frac{R}{2}\Big)^2\Big)\int_0^1 \frac{d\beta_2}{2\nu_2}$$

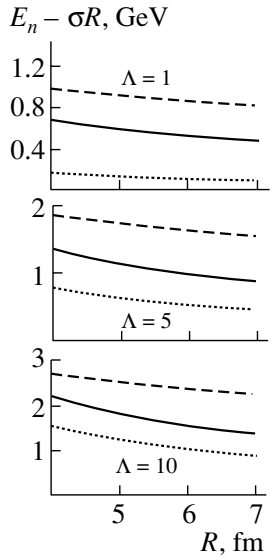

Fig. 2. Corrections to the linear behavior of the potentials. The QCD string (solid), potential (dashed), and flux-tube (dotted) curves for $n_z = n_\rho = 0$ and $\sigma = 0.22$ GeV^2 are presented here.

$$+ \int_0^1 d\beta_1 \frac{\nu_1}{2} + \int_0^1 d\beta_2 \frac{\nu_2}{2},$$

displaying two different kinds of string excitations, along the z axis and in the transverse direction. Indeed, for large R, one neglects the contribution of μ in the third term of (29) because the extremal values of $\nu_{1,2}$ are $\sigma R/2$. Oscillations in the longitudinal and transverse directions then decouple, and one has

$$E_n(R) = \sigma R + \frac{3}{2^{1/3}} \frac{\sigma^{1/3}(n_z + 1/2)^{2/3}}{R^{1/3}} + \frac{2 \times 3^{1/2}}{R}(n_\rho + \Lambda + 1). \quad (30)$$

The $(\sigma/R)^{1/3}$ regime is established at large R, but, at intermediate distances, there are sizable corrections from the Λ/R string regime, as is seen from Fig. 2.

Since we have not considered the gluon spin, we cannot yet compare our predictions with lattice results [6]. Nevertheless, some preliminary conclusions can be drawn. For separations less than 2 fm, the measured energies [6] lie much below the Nambu–Goto curves (28). There is no universal Nambu–Goto behavior even for R as large as 4 fm. The QCD string model is able to describe both these features: at small separations, the potential confinement regime dominates, while, at large distances, the situation is more complicated. Indeed, there is the contribution of the string-type gaps (27), which are due to transverse vibrations of the string, but the dominant subleading behavior is defined by potential-type longitudinal motion. In particular, even for semiclassically large values of Λ, there exists the contribution of oscillations in the longitudinal direction [second term in (30)].

Such peculiar behavior displays the most pronounced difference between the present approach and other models of constituent glue. In contrast to phonon-type models, QCD string vibrations are caused by a pointlike valence gluon, but, in contrast to potential models, the confining force follows from the minimal-area law, giving rise, at large distances, both to longitudinal vibrations with potential-type $(\sigma/r)^{1/3}$ dominant subleading behavior and to transverse vibrations with string-type Λ/R subleading behavior, which could be responsible for the observed Λ dependence. Full QCD string calculations with the gluon spin involved will provide, if confirmed by the lattice data, decisive evidence in favor of the QCD string model of valence glue.

ACKNOWLEDGMENTS

We are grateful to Yu.A. Simonov for stimulating discussions.

This work was supported by a joint grant (no. 97–0232) from INTAS and the Russian Foundation for Basic Research. The support of the Russian Foundation for Basic Research (project nos. 00–02–17836 and 00–15–96786) is also acknowledged.

REFERENCES

1. A. I. Vainshtein and L. B. Okun', Yad. Fiz. **23**, 1347 (1976) [Sov. J. Nucl. Phys. **23**, 716 (1976)].
2. D. Horn and J. Mandula, Phys. Rev. D **17**, 898 (1978).
3. E. S. Swanson and A. P. Szczepaniak, Phys. Rev. D **59**, 014035 (1999).
4. N. Isgur and J. Paton, Phys. Rev. D **31**, 2910 (1985).
5. A. Donnachie and P. R. Page, Phys. Rev. D **59**, 034016 (1999); A. Donnachie and Yu. S. Kalashnikova, Phys. Rev. D **60**, 114011 (1999).
6. K. J. Juge, J. Kuti, and C. Morningstar, in *Proceedings of the Third International Conference on Quark Confinement and the Hadron Spectrum, Jefferson Lab., 1998,* hep-lat/9809015; in *Proceedings of LATTICE98, Boulder, 1998;* Nucl. Phys. B (Proc. Suppl.) **73**, 590 (1999).
7. Yu. A. Simonov, in *Lectures at the XVII International School of Physics, Lisbon, 1999,* hep-ph/9911237.
8. A. Yu. Dubin, A. B. Kaidalov, and Yu. A. Simonov, Phys. Lett. B **323**, 41 (1994); Yad. Fiz. **56** (12), 213 (1993) [Phys. At. Nucl. **56**, 1745 (1993)].
9. Yu. A. Simonov, in *Proceedings of the Workshop on Physics and Detectors for DAΦNE, Frascati, 1991,* p. 399; in *Proceedings of HADRON'93 Conference, Como, 1993,* p. 2629.

10. Yu. S. Kalashnikova and Yu. B. Yufryakov, Phys. Lett. B **359**, 175 (1995); Yad. Fiz. **60**, 374 (1997) [Phys. At. Nucl. **60**, 307 (1997)].
11. A. B. Kaidalov and Yu. A. Simonov, Phys. Lett. B **477**, 163 (2000).
12. Yu. A. Simonov, Nucl. Phys. B **592**, 350 (2001).
13. Yu. A. Simonov, Yad. Fiz. **58**, 113 (1995) [Phys. At. Nucl. **58**, 107 (1995)].
14. Yu. S. Kalashnikova and A. V. Nefediev, Yad. Fiz. **60**, 1389 (1997) [Phys. At. Nucl. **60**, 1389 (1997)].
15. V. L. Morgunov, A. V. Nefediev, and Yu. A. Simonov, Phys. Lett. B **459**, 653 (1999).
16. Yu. B. Yufryakov, Yad. Fiz. **59**, 1692 (1996) [Phys. At. Nucl. **59**, 1636 (1996)]; Preprint ITEP-56-95 (Moscow, 1995).

Physics of Atomic Nuclei, Vol. 64, No. 9, 2001, pp. 1722–1728. Translated from Yadernaya Fizika, Vol. 64, No. 9, 2001, pp. 1802–1808.

ELEMENTARY PARTICLES AND FIELDS
Theory

Proton Structure Functions in the Quasielastic Limit

S. R. Kelner and D. A. Timashkov

Moscow State Engineering Physics Institute
(Technical University), Kashirskoe sh. 31, Moscow, 115409 Russia

Received June 13, 2000; in final form, September 7, 2000

Abstract—The evolution equation for the nonsinglet distribution of partons is solved in the leading order of perturbative QCD. It is shown that an exact analytic solution to the evolution equations can be found in the quasielastic limit. The Q^2 evolution of the structure function for $x \to 1$ is in good agreement with experimental data. © *2001 MAIK "Nauka/Interperiodica".*

1. INTRODUCTION

Investigation of quark distributions has a direct bearing on inelastic lepton–nucleon scattering. In relation to cross sections for other electromagnetic lepton–nucleon interactions, the inelastic-scattering cross section decreases more slowly with increasing momentum transfer ($\sim 1/q^4$). Therefore, inelastic scattering is a unique tool for studying the structure of nucleons at extremely small distances.

On the basis of the scaling property of the structure functions in inelastic scattering, Feynman [1] and Bjorken [2] proposed, in the late 1960s, the concept of partons as pointlike constituents of the nucleon that play the role of objects on which a virtual photon is scattered. This idea made it possible to interpret SLAC experimental data on inelastic electron–nucleon scattering [3].

The development of QCD enabled a construction of a consistent picture of the internal structure of nucleons that includes, along with valence quarks, a continuum of virtual sea quarks and gluons. It turned out that the distribution of partons (quarks and gluons) within the nucleon at an arbitrary value of the momentum transfer squared Q^2 can be expressed in terms of the distribution at a fixed value Q_0^2. This relation is provided by the evolution equations obtained by Dokshitzer, Gribov, and Lipatov and by Altarelli and Parisi [4–7] (DGLAP equations).

Despite a great number of ideas, models, and approaches proposed for describing inelastic interaction, there is no theory at the moment that could describe the behavior of inelastic form factors over the entire kinematically allowed region. Information about the behavior of the structure functions in various limiting cases near the boundaries of the kinematical region could be useful in seeking such a model.

The quasielastic limit is one of such cases. In this region, lepton–proton interaction at large values of the Bjorken variable, $x_B \sim 1$, is well described within the quark-parton model on the basis of the DGLAP equations. In this case, a virtual photon interacts with partons that carry a major fraction of the target-proton momentum. We denote by x_F the momentum fraction carried by the interacting parton and refer to it as the Feynman variable. Usually, the Feynman variable x_F is assumed to coincide with the Bjorken variable x_B. However, it is shown below that, for $x_B \to 1$ and at low momentum transfers, the difference of x_F and x_B is not negligible.

In this study, we obtain an expression for the variable x_F and show that, in the limit $x_F \to 1$, the evolution equation for the distribution of the valence quarks can be solved analytically. The expression obtained for F_2 describes the Q^2 evolution of the nucleon structure function in the quasielastic limit and agrees well with experimental data.

2. INELASTIC SCATTERING AND PARTONS

The cross section for the inelastic scattering of a charged lepton (an electron or a muon) by a proton in the laboratory frame (proton rest frame) is expressed in terms of two structure functions as [8]

$$\frac{d\sigma_{\text{in}}}{d\nu\, dQ^2} = \frac{2\pi\alpha^2}{Q^4E^2\nu}\Big\{\left(2EE' - Q^2/2\right)F_2 + \frac{\nu}{M}\left(Q^2 - 2\mu^2\right)F_1\Big\}. \quad (1)$$

The notation is illustrated in Fig. 1.

In the parton model, the structure functions are expressed in terms of the sum of quark distributions

$q_i(x_F)$ weighted with the squared charges. Specifically, we have

$$F_2 = x_F \sum_i e_i^2 q_i(x_F), \quad (2)$$

where x_F is the proton momentum fraction (in the Breit reference frame) carried by the parton that absorbs the virtual photon. Callan and Gross [9] showed that two structure functions in the simplest parton model are related by the equation

$$F_2 = 2x_F F_1. \quad (3)$$

In [10], it is proposed to use relation (3) for all Q^2 values because it provides a reliable description for $Q^2 \to 0$ as well.

The Bjorken variable is defined as

$$x_B = \frac{Q^2}{2M\nu}. \quad (4)$$

In order to find the expression for the Feynman variable x_F, we go over to the Breit reference frame defined as that which moves in the same direction as the virtual photon at a speed close to the speed of light with respect to the laboratory frame.

The momentum fraction carried by the parton is determined by the energy–momentum conservation law

$$\tilde{k} + \tilde{q} = \tilde{k}', \quad (5)$$

where $\tilde{k}$ and $\tilde{k}'$ are the parton 4-momenta before and after the scattering event, respectively. The tilde labels indicate that the variables in question are measured in the Breit reference frame. Squaring Eq. (5), we arrive at

$$2\tilde{k}\tilde{q} = Q^2$$

or

$$\tilde{k}_0\tilde{q}_0 - \tilde{k}_3\tilde{q}_3 = Q^2/2. \quad (6)$$

From the definition of the variable x_F, it follows that, in the Breit reference frame, the energy and the momentum of the parton are

$$\tilde{k}_3 = x_F\tilde{P}_3, \quad \tilde{k}_0 = \sqrt{m^2 + \tilde{k}_\perp^2 + \tilde{k}_3^2}. \quad (7)$$

For the energy and momentum of the virtual photon in the Breit frame, Lorentz transformations yield

$$\tilde{q}_0 = \frac{\nu - q_3\beta}{\sqrt{1-\beta^2}} = \frac{\nu\tilde{P}_0 + q_3\tilde{P}_3}{M}, \quad (8)$$

$$\tilde{q}_3 = \frac{q_3 - \nu\beta}{\sqrt{1-\beta^2}} = \frac{q_3\tilde{P}_0 + \nu\tilde{P}_3}{M}, \quad (9)$$

where m is the parton mass; $\tilde{k}_\perp$ is the transverse momentum of the parton; $q_3 = \sqrt{Q^2 + \nu^2}$ is the photon momentum in the laboratory frame; and $\tilde{P}_0$ and $\tilde{P}_3$ are, respectively, the energy and the momentum of the proton in the Breit frame. The exact equation for x_F is obtained by substituting (7)–(9) into Eq. (6) and by retaining terms that do not vanish in the limit $\tilde{P}_3 \to \infty$. The result is

$$x_F M(q_3 + \nu) - \frac{m^2 + \tilde{k}_\perp^2}{Mx_F}(q_3 - \nu) = Q^2. \quad (10)$$

The solution to this equation determines that proton momentum fraction which is used in relation (2):

$$x_F = \frac{Q^2}{2M\left(\nu + \sqrt{\nu^2 + Q^2}\right)} \times \left(1 + \sqrt{1 + 4\frac{m^2 + \tilde{k}_\perp^2}{Q^2}}\right). \quad (11)$$

We can neglect the quark mass m for the u, d, and s quarks. Assuming that $\tilde{k}_\perp^2 \ll Q^2$, we obtain

$$x_F = \frac{2x_B}{1 + \sqrt{1 + 4M^2x_B^2/Q^2}}. \quad (12)$$

Expression (12) determines the proton-momentum fraction in the Breit frame carried by the parton that interacts with the virtual photon. It is clear from (12) that, at $x_B \sim 1$, the relation $x_F \approx x_B$ is valid only for $Q^2 \gg M^2$. It is precisely the Feynman variable that must be substituted into expression (2)—this means that, at given ν and Q^2 values, the structure function is expressed in terms of the quark distributions at the point x_F determined by expression (12). Although the expression for the exact proton-momentum fraction carried by the parton in the quark-parton picture of inelastic scattering was obtained about 25 years ago [11–13], the above circumstance is often ignored in identifying x_F with x_B.

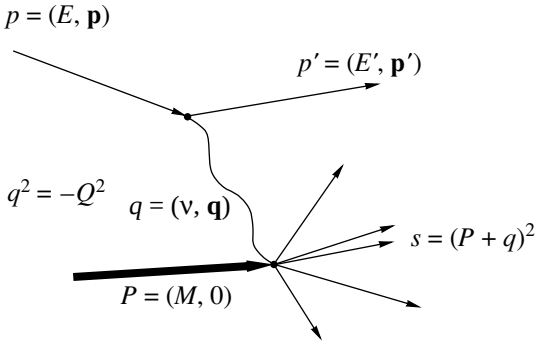

Fig. 1. Feynman diagram for the inelastic scattering of a charged lepton by a proton.

3. EVOLUTION EQUATION FOR THE DISTRIBUTIONS OF VALENCE QUARKS

Quark distributions appearing in (2) satisfy [together with the gluon distribution $g(x,Q^2)$] the set of integro-differential evolution equations that was obtained in the late 1970s [4–7] and which has the form (in order to avoid encumbering the ensuing expressions, we will henceforth suppress the subscript "F" on the Feynman variable using the notation x for it)

$$\frac{dq_i\left(x,Q^2\right)}{d\ln Q^2}=\frac{\alpha_s\left(Q^2\right)}{2\pi}\int\limits_x^1\frac{dy}{y}\left[q_i\left(y,Q^2\right)\times P_{qq}\left(\frac{x}{y}\right)+g\left(y,Q^2\right)P_{qg}\left(\frac{x}{y}\right)\right], \tag{13}$$

$$\frac{dg\left(x,Q^2\right)}{d\ln Q^2}=\frac{\alpha_s\left(Q^2\right)}{2\pi}\int\limits_x^1\frac{dy}{y}\left[\sum_i q_i\left(y,Q^2\right)\times P_{gq}\left(\frac{x}{y}\right)+g\left(y,Q^2\right)P_{gg}\left(\frac{x}{y}\right)\right],$$

where

$$\alpha_s\left(Q^2\right)=\frac{12\pi}{(33-2n_f)\ln(Q^2/\Lambda^2)}$$

is the QCD running coupling constant with $\Lambda=0.2$ GeV and n_f being the number of flavors.

The splitting functions P are given by

$$P_{qq}(z)=\frac{4}{3}\frac{1+z^2}{(1-z)_+}+2\delta(1-z), \tag{14}$$

$$P_{qg}(z)=\frac{z^2+(1-z)^2}{2}, \tag{15}$$

$$P_{gq}(z)=\frac{4}{3}\frac{1+(1-z)^2}{2}, \tag{16}$$

$$P_{gg}(z)=6\left(\frac{1-z}{z}+\frac{z}{(1-z)_+}+z(1-z)\right)+\left(\frac{11}{2}-\frac{n_f}{3}\right)\delta(1-z). \tag{17}$$

The symbol $\frac{1}{(1-z)_+}$ is spelled out as

$$\int\limits_0^1 dz\,\frac{f(z)}{(1-z)_+}=\int\limits_0^1 dz\,\frac{f(z)-f(1)}{(1-z)}. \tag{18}$$

Equations (13) make it possible to obtain the parton distributions for $Q^2>Q_0^2$ if the distributions at Q_0^2 are known. Usually, the value of Q_0^2 is on the order of a few GeV^2. The value used most often is $Q_0^2=4$ GeV^2. A detailed derivation of the evolution equations can be found in the review articles by Dokshitzer *et al.* [14], Reya [15], and Altarelli [16].

If we introduce the nonsinglet and singlet combinations of the quark distributions,

$$q^{\mathrm{NS}}\left(x,Q^2\right)=\sum_i\Big(q_i\left(x,Q^2\right)-\bar q_i\left(x,Q^2\right)\Big),$$

$$q^{\mathrm{S}}\left(x,Q^2\right)=\sum_i\Big(q_i\left(x,Q^2\right)+\bar q_i\left(x,Q^2\right)\Big),$$

the set of evolution equations splits into an equation for the nonsinglet function and the set that involves the singlet function and which is symmetric with respect to quarks and gluons:

$$\frac{dq_i^{\mathrm{NS}}\left(x,Q^2\right)}{d\ln Q^2}=\frac{\alpha_s\left(Q^2\right)}{2\pi}\times\int\limits_x^1\frac{dy}{y}\left[q_i^{\mathrm{NS}}\left(y,Q^2\right)P_{qq}\left(\frac{x}{y}\right)\right]; \tag{19}$$

$$\frac{dq_i^{\mathrm{S}}\left(x,Q^2\right)}{d\ln Q^2}=\frac{\alpha_s\left(Q^2\right)}{2\pi}\int\limits_x^1\frac{dy}{y}\left[q_i^{\mathrm{S}}\left(y,Q^2\right)\times P_{qq}\left(\frac{x}{y}\right)+2n_f g\left(y,Q^2\right)P_{qg}\left(\frac{x}{y}\right)\right], \tag{20}$$

$$\frac{dg\left(x,Q^2\right)}{d\ln Q^2}=\frac{\alpha_s\left(Q^2\right)}{2\pi}\int\limits_x^1\frac{dy}{y}\left[q_i^{\mathrm{S}}\left(y,Q^2\right)P_{gq}\left(\frac{x}{y}\right)+g\left(y,Q^2\right)P_{gg}\left(\frac{x}{y}\right)\right].$$

In the quasielastic limit, the main contribution to F_2 comes from the distributions of u_v and d_v valence quarks. They can be represented as

$$u_v=u-\bar u,\quad d_v=d-\bar d$$

and are described by the equation for the nonsinglet combination.

Instead of Q^2, we now introduce the variable

$$t=\frac{12}{33-2n_f}\ln\left(\frac{\ln(Q^2/\Lambda^2)}{\ln(Q_0^2/\Lambda^2)}\right). \tag{21}$$

It is more convenient to recast Eq. (19) for the nonsinglet combination into the form

$$\frac{dq_v\left(x,t\right)}{dt}=\frac{1}{2}\left\{\int\limits_x^1\frac{dy}{y}q_v\left(y,t\right)P_v\left(\frac{x}{y}\right)-q_v\left(x,t\right)\int\limits_0^1 dy\,P_v(y)\right\}, \tag{22}$$

where

$$P_v(z) = \frac{4}{3}\,\frac{1+z^2}{1-z}. \qquad (23)$$

The evolution equation written in this form is similar to the equations of cascade theory, the Feynman variable x and t corresponding to the particle energy and depth, respectively. The first term in Eq. (22) is equal to the income of valence quarks with the nucleon-momentum fraction x and the virtual-photon mass Q^2, while the second item is equal to the outcome of such quarks. In just the same way as in cascade theory, where the distribution of particles with energy E is determined exclusively by particles with energies $E' > E$, the distributions of partons with a given value of the variable x are determined exclusively by partons that carry nucleon-momentum fractions $x' > x$. It follows that, if we aim at determining the functions in the region $x_0 < x < 1$, the result will be independent of the choice of the initial values of the functions (at $Q^2 = Q_0^2$) in the interval $(0, x_0)$.

In order to solve Eq. (22) analytically, we first solve the equation

$$\frac{dq_v(x,t)}{dt} = \frac{1}{2}\left\{\int_x^\infty \frac{dy}{y} q_v(y,t)\, P_v\left(\frac{x}{y}\right) - q_v(x,t)\int_0^1 dy\, P_v(y)\right\}. \qquad (24)$$

In contrast to Eq. (22), this equation can be solved analytically. In order to do this, it is necessary to specify the initial function $q_v(x, t = 0)$ in the interval $0 < x < \infty$. It will be shown later that, if the initial function vanishes for $x > 1$, then $q_v(x > 1, t) = 0$ for $t > 0$. This can be qualitatively explained by invoking once again the similarity with cascade theory. If we assume that there are no particles with "energies" $x > 1$ at the boundary, it is obvious that no particles with such energies can appear in a further development of the cascade. Therefore, Eqs. (22) and (24) are equivalent in the class of functions $q_v(x > 1, t = 0) = 0$ under consideration.

4. SOLVING THE EQUATIONS FOR THE NONSINGLET COMBINATION

In order to solve Eq. (24), we apply the Mellin transformations

$$\int_0^1 dx\, x^{s-1}\varphi(x) = \tilde{\varphi}(s), \qquad (25)$$

$$\frac{1}{2\pi i}\int_{c-i\infty}^{c+i\infty} ds\, x^{-s}\tilde{\varphi}(s) = \varphi(x).$$

The contour of integration in the inverse transformation lies to the right of all singularities of the function $\tilde{\varphi}(s)$. The equation for the transform of the valence-quark distribution assumes the form

$$\frac{d\tilde{q}_v(s,t)}{dt} = \frac{1}{2}\tilde{q}_v(s,t)\left\{\int_0^1 dy\left(y^{s-1}-1\right) P_v(y)\right\}. \qquad (26)$$

If we applied the transformation in (25) to Eq. (22), it would not be possible to take the transform of the distribution outside the integral sign in expression (26). But now, the solution for the transform has the simple form

$$\tilde{q}_v(s,t) = \tilde{q}_v(s,0)\exp\left[-\beta(s)t\right], \qquad (27)$$

where

$$\beta(s) = \frac{1}{2}\int_0^1 dz\left(1 - z^{s-1}\right) P_v(z). \qquad (28)$$

Accordingly, the evolution of the valence-quark distribution in the proton is given by

$$q_v(x,t) = \frac{1}{2\pi i}\int_{c-i\infty}^{c+i\infty} ds\, x^{-s}\tilde{q}_v(s,0)\exp\left[-\beta(s)t\right]. \qquad (29)$$

By using the Mellin transformation (25), we substitute into (29) the initial condition

$$\tilde{q}_v(s,0) = \int_0^1 dy\, y^{s-1} q_v(y,0).$$

As a result, the solution of the evolution equation for the valence-quark distribution in the nucleon assumes the form

$$q_v(x,t) = \frac{1}{2\pi i}\int_{c-i\infty}^{c+i\infty} ds\, x^{-s}\exp\left[-\beta(s)t\right] \times \int_0^1 dy\, y^{s-1} q_v(y,0). \qquad (30)$$

By substituting the function $P_v(z)$ into expression (28), we find that $\beta(s)$ can be represented in the analytic form

$$\beta(s) = \frac{4}{3}\left(\frac{\psi(s) + \psi(s+2)}{2} + \gamma\right) - 1, \qquad (31)$$

where ψ is the logarithmic derivative of the gamma function and γ is the Euler constant.

Expressions (30) and (31) represent a solution to the evolution Eq. (22) for the nonsinglet combination

of the parton distributions. Indeed, we recast expression (30) into the alternative form

$$q_v(x,t) = \int_0^1 \frac{dz}{z}\, q_v(x/z,0) \times \frac{1}{2\pi i}\int_{c-i\infty}^{c+i\infty} ds\, x^{-s} \exp\left[-\beta(s)t\right].$$

If $q_v(x,0) = 0$ for $x > 1$, then $q_v(x > 1, t) = 0$ for $t > 0$ as well, because the integrand in the internal integral decreases exponentially for $\mathrm{Re}\, s \to +\infty$, so that the integral vanishes [the integrand has no singularities to the right of the integration contour in (30)]. Therefore, expression (30) satisfies Eqs. (24) and (22) simultaneously.

5. QUASIELASTIC LIMIT

In the quark-parton model, the structure function for inelastic scattering depends on all quark distributions. It has already been shown, however, that the quark distributions at a given value of x depend only on the parton distributions for $x' > x$. In the quasielastic limit, the structure function receives a contribution from the region where only the distributions of valence quarks are significant.

In order to determine the structure function in the quasielastic limit, we consider the solution in (30) to the evolution equation for valence quarks at $x_\mathrm{B} \sim 1$. For the initial condition, we take the standard expression

$$q_v(x,0) = q_0 x^k (1-x)^{n_0}, \tag{32}$$

which is used to fit experimental data. The transform of the initial condition can easily be found by substituting (32) into (25). The result is

$$\tilde{q}_v(s,0) = q_0 \mathrm{B}(s+k, n_0+1), \tag{33}$$

where B is the beta function.

For $t > 0$, the expression for the distribution of valence quarks assumes the form

$$q_v(x,t) = q_0 x^k e^{(1-4/3\gamma)t} \times \frac{1}{2\pi i}\int_{c-i\infty}^{c+i\infty} ds\, \mathrm{B}(s, n_0+1) \exp\left(-s\ln x - 2/3(\psi(s-k) + \psi(s-k+2))t\right). \tag{34}$$

All singularities of the beta function lie to the left of the integration contour. Therefore, we can take an arbitrarily large value of c in calculating the integral in (34). Using the asymptotic expressions for beta and psi functions,

$$\mathrm{B}(x,y) \xrightarrow[x\to\infty]{} x^{-y}\Gamma(y), \tag{35}$$

$$\psi(x) \xrightarrow[x\to\infty]{} \ln x, \tag{36}$$

we obtain expression (34) in the quasielastic limit:

$$q_v(x,t) = q_0 x^k e^{(1-4/3\gamma)t}\,\Gamma(n_0+1) \times \frac{1}{2\pi i}\int_{c-i\infty}^{c+i\infty} ds\, \exp\{-s\ln x\}\, s^{-(n_0+1+4/3t)}. \tag{37}$$

The integral in (37) is the standard inverse Laplace transform of s^{-p}:

$$\frac{1}{2\pi i}\int_{c-i\infty}^{c+i\infty} ds\, \frac{e^{ys}}{s^p} = \frac{y^{p-1}}{\Gamma(p)}. \tag{38}$$

After some simple algebra, we find that the evolution of the nucleon structure function in the quasielastic limit is described by the expression (hereafter, we recover the notation x_F for the Feynman variable)

$$F_2\left(x_\mathrm{B}, Q^2\right) = F_2\left(x_\mathrm{B}, Q_0^2\right)\left(1-x_\mathrm{F}\right)^{4/3t} \times \frac{\Gamma(n_0+1)}{\Gamma(n_0+1+4/3\cdot t)}\, e^{(1-4/3\gamma)t}. \tag{39}$$

A similar solution was obtained by Kuraev and Fadin [17], who considered radiative corrections to the cross section for one-photon annihilation.

6. CONCLUSION

Expression (39) describes the Q^2 evolution of the nucleon structure function in the quasielastic limit. The structure function decreases with increasing momentum transfer; as x_B approaches the kinematical boundary, F_2 decreases ever faster with increasing Q^2. Figure 2 displays the results of the calculations according to expression (39) for the values of $x_\mathrm{B} = 0.45$, 0.55, 0.65, 0.75, and 0.85. Also shown in Fig. 2 are the available experimental data at large x_B (in EMC and BCDMS experiments, the maximum value of x_B was 0.75; in the SLAC experiment, the structure function was measured up to $x_\mathrm{B} = 0.85$).

We have determined the boundary values of the structure function at $Q^2 = Q_0^2 = 4\ \mathrm{GeV}^2$ through fitting $F_2\left(x_\mathrm{B}, Q_0^2\right)$ in terms of the function $c\sqrt{x_\mathrm{F}}\left(1-x_\mathrm{F}\right)^{n_0}$, where $n_0 = 3$. We have set the normalization factor c to $c = 1.655$. This value was obtained from a comparison of the function F_2 calculated according to expression (39) at $x_\mathrm{B} = 0.85$ and $Q^2 = 10\ \mathrm{GeV}^2$ with the value of 0.00854 obtained in the SLAC experiment.

We have derived expression (39) in the limit $x_\mathrm{B} \to 1$, but it satisfactorily describes experimental data

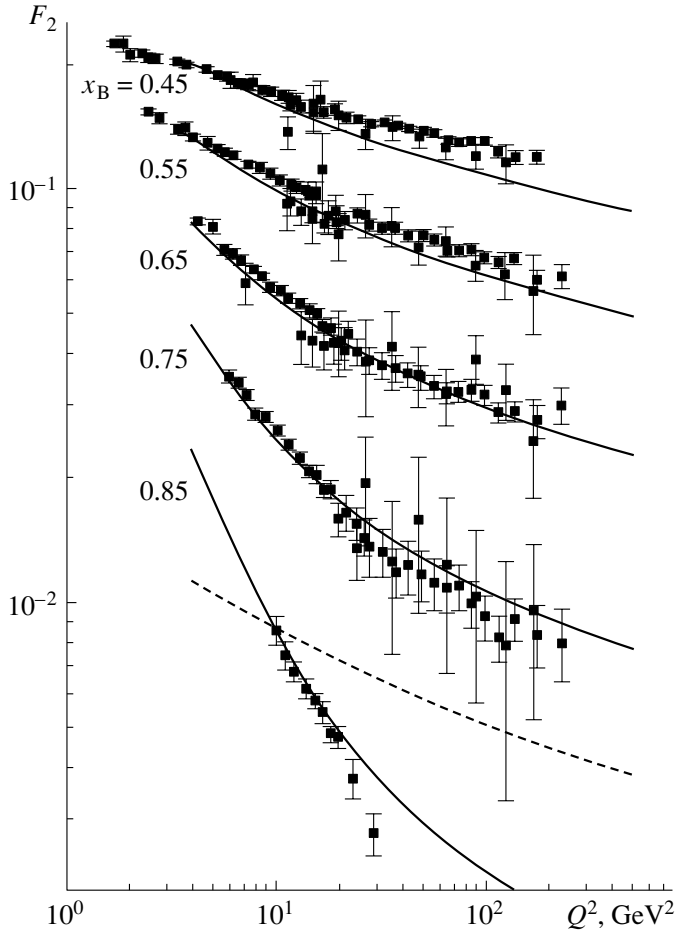

Fig. 2. Proton structure function versus Q^2 at large x_B: (solid curve) results of the calculation according to expression (39), (dashed curve) results of the calculation at $x_F = x_B = 0.85$, and (points) experimental data taken from [18].

down to $x_B = 0.65$. At lower values of x_B, the structure function calculated according to (39) falls short of experimental data. This is explained by an increase in the contribution from sea quarks and heavy flavors. In order to estimate the effect of the difference of x_F and x_B in the region of large x_B (about unity), the results of the calculations according to (39) at $x_F = x_B = 0.85$ are shown in Fig. 2. It is clear that the logarithmic violation of scaling as obtained in solving the evolution equations cannot explain quite an abrupt decrease in F_2 with increasing Q^2 at large values of x_B. In this region, the violation of scaling is due primarily to the distinction between the Feynman and the Bjorken variable.

The asymptotic dependence obtained for the proton structure function in the quasielastic limit can be used for a proper normalization of various approximate functions that describe the inelastic from factors and for a correct description of the quasielastic region $x_B \to 1$.

ACKNOWLEDGMENTS

We are grateful to Prof. A.A. Petrukhin, who stimulated this work, for numerous stimulating discussions and enlightening advice.

REFERENCES

1. R. P. Feynman, Phys. Rev. Lett. **23**, 1415 (1969).
2. J. D. Bjorken, Phys. Rev. **179**, 1547 (1969).
3. I. Friedman and H. W. Kendal, Annu. Rev. Nucl. Part. Sci. **22**, 203 (1972).
4. V. N. Gribov and L. N. Lipatov, Yad. Fiz. **15**, 781 (1972) [Sov. J. Nucl. Phys. **15**, 438 (1972)].
5. L. N. Lipatov, Yad. Fiz. **20**, 181 (1974) [Sov. J. Nucl. Phys. **20**, 94 (1975)].
6. G. Altarelli and G. Parisi, Nucl. Phys. B **126**, 298 (1977).
7. Yu. L. Dokshitser, Zh. Éksp. Teor. Fiz. **73**, 1216 (1977) [Sov. Phys. JETP **46**, 641 (1977)].
8. F. Halzen and A. Martin, *Quarks and Leptons: An Introduction Course in Modern Particle Physics* (Wiley, New York, 1984; Mir, Moscow, 1987).

9. G. Callan and D. J. Gross, Phys. Rev. Lett. **22**, 156 (1969).
10. D. A. Timashkov, in *Collection of Works of Scientific Session at the Moscow Engineering Physics Institute, 1998,* Part 8, p. 143.
11. H. Georgi and H. D. Politzer, Phys. Rev. D **14**, 1829 (1976).
12. H. Georgi and H. D. Politzer, Phys. Rev. Lett. **36**, 1281 (1976).
13. A. de Rujula *et al.,* Ann. Phys. (N.Y.) **103**, 315 (1977).
14. Yu. L. Dokshitzer *et al.,* Phys. Rep. **58**, 269 (1980).
15. E. Reya, Phys. Rep. **69**, 195 (1981).
16. G. Altarelli, Phys. Rep. **81**, 1 (1982).
17. É. V. Kuraev and V. S. Fadin, Yad. Fiz. **41**, 733 (1985) [Sov. J. Nucl. Phys. **41**, 466 (1985)].
18. Partical Data Group, Phys. Rev. D **54**, 1 (1996).

Translated by M. Kobrinsky